SANDIA REPORT
SAND2007-0217
Unlimited Release
Printed March 2007

Fundamental Science Investigations to Develop a 6-MV Laser Triggered Gas Switch for ZR: First Annual Report

John Maenchen, Jane Lehr, Larry K. Warne, Victor Anaya, Andy Benwell, David Bliss, John Corley, Randy Curry, Greg Feltz, Tony Fouracre, Martin Given, Doug Guthrie, Keith Hodge, David Johnson, Roy Jorgenson, Scott Kovaleski, John Krile, Hermann Krompholz, Keith LeChein, Scott MacGregor, G. Randy McKee, A. Richard Miller, Andreas Neuber, Michael Pasik, Ken Prestwich, David Rose, Stephen Rosenthal, Mark Savage, Ken Struve, Igor Timoshkin, Carsten Thoma, James Van den Avle, Russel Vela, Peter Wakeland, Zach Wallace, Dale Welch, Joseph Woodworth, and Chris Yeckel

Prepared by
Sandia National Laboratories
Albuquerque, New Mexico 87185 and Livermore, California 94550

Sandia is a multiprogram laboratory operated by Sandia Corporation,
a Lockheed Martin Company, for the United States Department of Energy's
National Nuclear Security Administration under Contract DE-AC04-94AL85000.

Issued by Sandia National Laboratories, operated for the United States Department of Energy by Sandia Corporation.

Available to DOE and DOE contractors from
U.S. Department of Energy
Office of Scientific and Technical Information
P.O. Box 62
Oak Ridge, TN 37831

Telephone: (865) 576-8401
Facsimile: (865) 576-5728
E-Mail: reports@adonis.osti.gov
Online ordering: http://www.osti.gov/bridge

Available to the public from
U.S. Department of Commerce
National Technical Information Service
5285 Port Royal Rd.
Springfield, VA 22161

Telephone: (800) 553-6847
Facsimile: (703) 605-6900
E-Mail: orders@ntis.fedworld.gov
Online order: http://www.ntis.gov/help/ordermethods.asp?loc=7-4-0#online

SAND2007-0217
Unlimited Release
Printed March 2007

Fundamental Science Investigations to Develop a 6-MV Laser Triggered Gas Switch for ZR: First Annual Report

J. Maenchen, J.M. Lehr, L.K. Warne, D. Bliss, R. Jorgenson, K. LeChein, G.R. McKee, M. Pasik, S. Rosenthal, M. Savage, K. Struve, J. Van den Avle, and J. Woodworth
Sandia National Laboratories
Advanced Pulsed Power Technologies
P.O. Box 5800
Albuquerque, New Mexico 87185-1193

J.P. Corley, V. Anaya, G. Feltz, D. Guthrie, K. Hodge, P. Wakeland, and Z. Wallace
Ktech Corporation
Albuquerque, New Mexico 87123

S. Kovaleski, A. Benwell, R. Curry, and C. Yeckel
University of Missouri-Columbia
Columbia, Missouri 65211

S. MacGregor, R.A. Fouracre, M. Given, and I. Timoshkin
University of Strathclyde
Glasgow, Scotland G1 1XW

D. Johnson and A.R. Miller
Titan Pulse Sciences Division

A. Neuber, J. Krile, H. Krompholz, and R. Vela
Texas Tech University
Lubbock, Texas 79409

K. Prestwich
Consultant

D. Rose, C. Thoma, and D. Welch
Voss Scientific
Albuquerque, New Mexico

ABSTRACT

In October 2005, an intensive three-year Laser Triggered Gas Switch (LTGS) development program was initiated to investigate and solve observed performance and reliability issues with the LTGS for ZR. The approach taken has been one of mission-focused research: to revisit and reassess the design, to establish a fundamental understanding of LTGS operation and failure modes, and to test evolving operational hypotheses. This effort is aimed toward deploying an initial switch for ZR in 2007, on supporting rolling upgrades to ZR as the technology can be developed, and to prepare with scientific understanding for the even higher voltage switches anticipated needed for future high-yield accelerators.

The ZR LTGS was identified as a potential area of concern quite early, but since initial assessments performed on a simplified Switch Test Bed (STB) at 5 MV showed 300-shot lifetimes on multiple switch builds, this component was judged acceptable. When the Z_{20} engineering module was brought online in October 2003 frequent flashovers of the plastic switch envelope were observed at the increased stresses required to compensate for the programmatically increased ZR load inductance. As of October 2006, there have been 1423 Z_{20} shots assessing a variety of LTGS designs. Numerous incremental and fundamental switch design modifications have been investigated.

As we continue to investigate the LTGS, the basic science of plastic surface tracking, laser triggering, cascade breakdown, and optics degradation remain high-priority mission-focused research topics. Significant progress has been made and, while the switch does not yet achieve design requirements, we are on the path to develop successively better switches for rolling upgrade improvements to ZR. This report summarizes the work performed in FY 2006 by the large team. A high-level summary is followed by detailed individual topical reports.

CONTENTS

FIGURES

ACRONYMS

EM	electromagnetic
FY	Fiscal Year
HPU	high-power ultrasound
HV	high voltage
ICCD	intensified charge-coupled device
ISC	Intermediate Storage Capacitor
LTGS	Laser Triggered Gas Switch
PFL	Pulse Forming Line
PIC	particle in cell
PMMA	Plexiglas
RC	Resistor-Capacitor
SEM	scanning electron microscopy
SSTB	Scaled Switch Test Bed
STB	Switch Test Bed
teff	t-effective
TWA	Transit-time Water Adder
UV	ultraviolet
VUV	vacuum ultraviolet

EXECUTIVE SUMMARY

In October 2005, an intensive three-year Laser Triggered Gas Switch (LTGS) development program was initiated to investigate and solve observed performance and reliability issues with the LTGS for ZR. The approach taken has been one of mission-focused research: to revisit and reassess the design, to establish a fundamental understanding of LTGS operation and failure modes, and to test evolving operational hypotheses. This effort is aimed toward deploying an initial switch for ZR in 2007, on supporting rolling upgrades to ZR as the technology can be developed, and to prepare with scientific understanding for the even higher voltage switches anticipated needed for future high-yield accelerators.

The ZR LTGS was identified as a potential area of concern quite early, but since initial assessments performed on a simplified Switch Test Bed (STB) at 5 MV showed 300-shot lifetimes on multiple switch builds, this component was judged acceptable. When the Z_{20} engineering module was brought online in October 2003 frequent flashovers of the plastic switch envelope were observed at the increased stresses required to compensate for the programmatically increased ZR load inductance. Its not that simple, however: there remains an unexplained discrepancy between STB and Z_{20} performance, and seemingly every hypothesis formulated to address Z_{20} issues can be countered with STB data, suggesting the problems observed are complex and likely a race between competing failure mechanisms.

As of October 2006 there have been 1423 Z_{20} shots assessing a variety of LTGS designs. In the first 1240 shots 74 plastic envelopes flashed. In some cases the switch was allowed to continue operation following a flash to assess subsequent shot performance impact and cumulative damage. The failure statistics are random, so the concept of "mean time to failure" has little value, but the anticipated impact of this failure frequency distribution on ZR operation is severe. Numerous incremental and fundamental switch design modifications have been investigated during FY 2006, resulting in only one plastic switch envelope flash in the last 300+ shots. We have not completed a scientific investigation of the flashing phenomena, but the pragmatic implications of just using this evolved switch design for the initial ZR deployment are quite encouraging.

As we continue to investigate the LTGS, the basic science of plastic surface tracking, laser triggering, overvoltage cascade breakdown, and electrode erosion leading to optics degradation remain high-priority mission-focused research topics. Significant progress has been made and, while the switch does not yet achieve design requirements, we are on the path to develop successively better switches for rolling upgrade improvements to ZR. This report summarizes the work performed in FY 2006 by the large team and identifies the focus of work to be performed in 2007. A high-level summary is followed by detailed information in the appendices.

HISTORICAL PERSPECTIVE

The Z accelerator at Sandia National Laboratories began as the Particle Beam Fusion Accelerator II in 1985, originally designed to create high-voltage ion beams for inertial confinement fusion research. In 1996 the power flow and output transmission line sections were modified from providing high voltage to high current for a six-month experimental study of z-pinch scaling. Those experiments were sufficiently successful that the machine was never converted back and was renamed Z in 1997.

Demand for Z shots has exceeded capacity by a factor of two, due in large part to the shot rate being limited by the 1985 vintage hardware.[1] Moreover, Z was not optimized for z-pinch operation nor designed for the rigors of daily use. The user community also desired higher currents, reproducibility, and precision. Thus, refurbishing the facility through redesign and upgrading most subsystems will provide significantly enhanced capability in several key areas of Sandia's high energy density physics mission. The ZR architecture is shown in Figure 1.

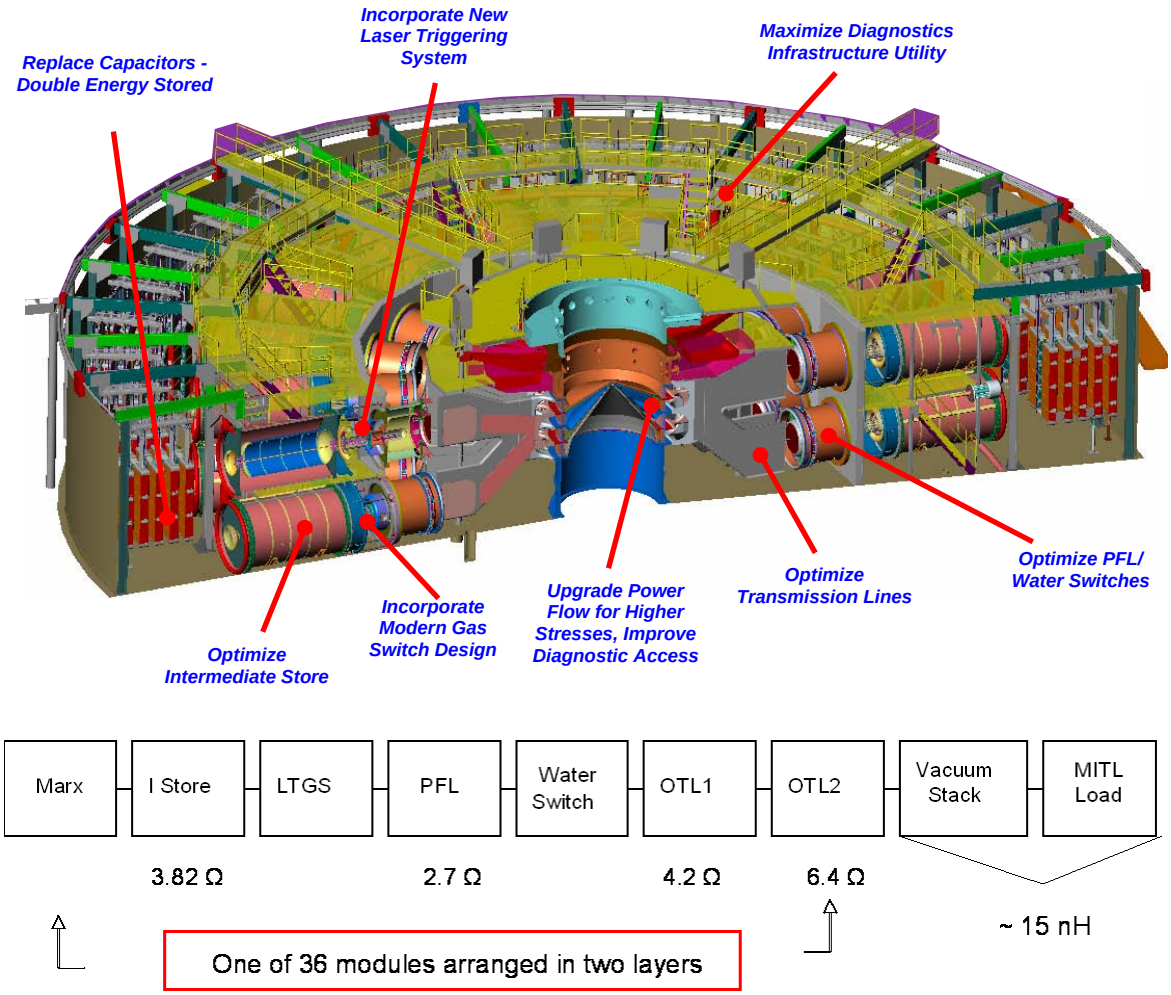

Figure 1. The ZR architecture.

A series of experiments were performed to assess the feasibility of the ZR architecture. The large single KrF laser used to trigger gas switches on Z was replaced by 36 modular Nd:YAG lasers designed for ZR.[2, 3] The lifetimes and reliability of the double-energy-density capacitors were tested[4] on the Simulation Test Facility. The Water Switch Test Stand (which later became the Z_{20} facility) was built to test and optimize the PFL/water switches.[5, 6] The ZR laser triggered gas switch (LTGS) was modeled with advanced electrodynamic techniques[7] and tested by converting the Transit-time Water Adder (TWA) accelerator into the Switch Test Bed (STB).[8,9] With each of these key components tested, the Z_{20} facility was populated with the first engineering version of a complete ZR module from Marx through output water transmission lines and the System Assessment Test Program[10] was initiated to validate the system modeling and the integrated ZR design.

The Z_{20} assessment identified various weaknesses in the design and components, and most were corrected. Open-shutter photographs showed that the LTGS inner surface of the plastic envelope had a tendency to flash. Tracking along the cascade section was found to typically lead to a prefire on subsequent shots. Flashover on the trigger housing, however, often had no lasting effects. Switching parameters such as delay time and jitter were vastly different on Z_{20} than had been exhaustively demonstrated on STB. Z_{20} also exhibited rapid and unacceptable degradation of the optical system components.

The LTGS flashover problems were exacerbated by the demands for ever-higher operating voltages. The ZR initial design assumed the vacuum inductance would remain at the Z value of 12 nH, so ZR could produce 26 MA with 5 MV on the intermediate store. The final ZR design increased the vacuum inductance by 25% to 15 nH, requiring a corresponding increase in voltage on all the upstream pulsed power components.

THE RIMFIRE CONCEPT AND THE ZR BASELINE SWITCH

The ZR LTGS design, shown in Figure 2, derives from an evolutionary sequence of similar switches used on previous accelerators[11-20] switching in the multi-megavolt regime with minimal inductance.

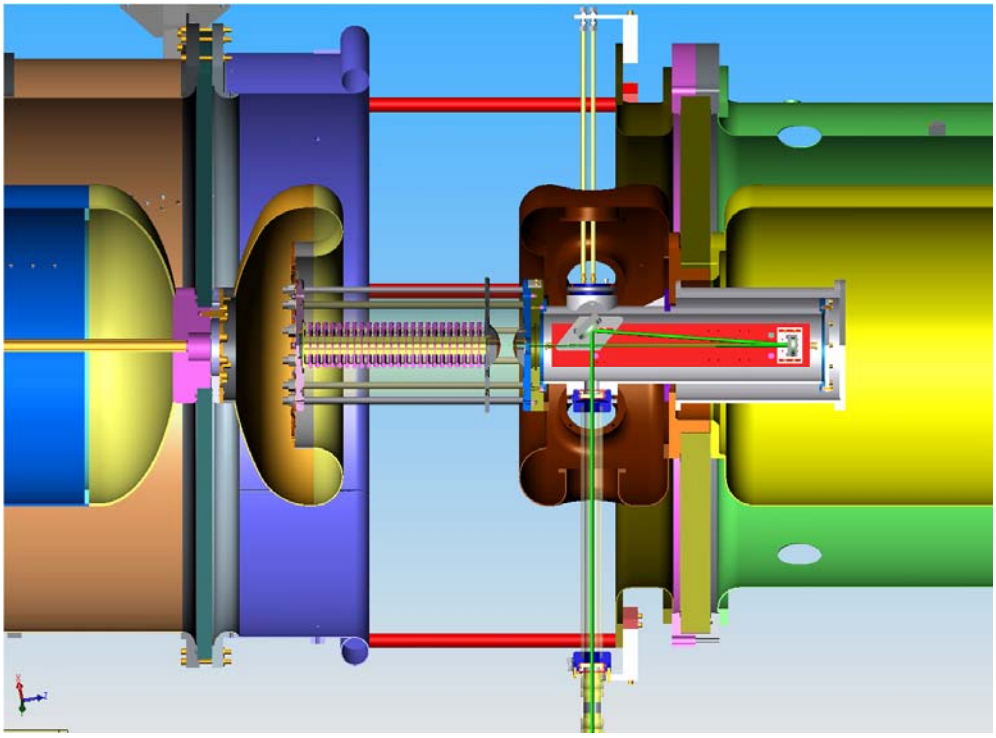

Figure 2. ZR laser triggered gas switch cross section. The electric fields are controlled by field shapers external to the LTGS housing.

The voltage is capacitively graded across the switch, reducing the electric fields in any electrode gap to below self-closure levels. A trigger gap is situated at one end and stressed to approximately 1 MV. The remainder of the voltage appears across the group of identical annular electrodes called the cascade (or rimfire or backbone) section. The switch is insulated with sulfur hexafluoride gas at a pressure that is empirically determined. A focused ultraviolet (UV) laser enters and initiates single-arc closure of the trigger gap and it is this voltage, applied as a transient to the cascade gaps on top of the previously applied fields, that initiates multi-site closure of the cascades and thereby closure of the entire switch. Appendix A documents a workshop discussing these switches. The ZR switch is immersed in oil, connecting a pulse-charged water-dielectric coaxial intermediate storage capacitor and a water coax pulse forming line. It serves as the final accelerator command control for pulse shape and timing. The Pulsed Power Sciences Center at Sandia has over 20 years experience with the design and operation of LTGS at progressively higher voltage operation, as shown in Figure 3. The quantity T_{eff} is

known as the “effective time” and is the time that the pulse is above 63% of its peak voltage. The Baseline switch for ZR was scaled from the HERMES III switch.

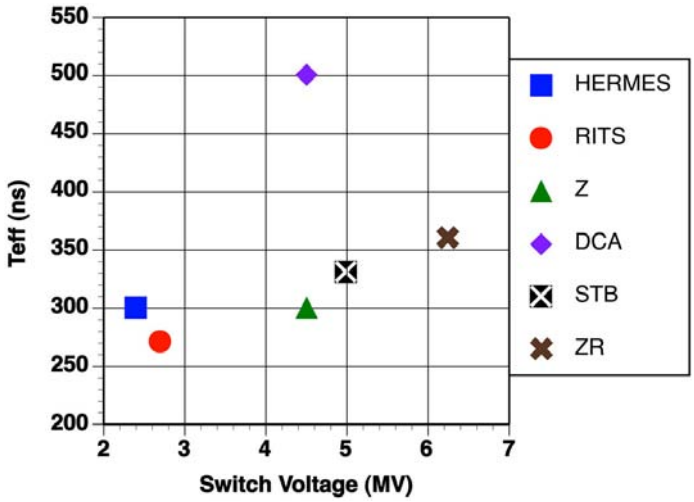

Figure 3. Laser triggered gas switch operating voltage and T_{eff} experience at Sandia.

The Baseline LTGS utilizes two separate plastic envelopes both fabricated from standard polished acrylic tubing separated by the trigger plate, which supports the cathode trigger electrode on one side and the first cascade electrode on the other. The anode trigger electrode has an axial hole the laser passes through. The cascade electrodes are separated by cylindrical acrylic spacers and the assembly is compressed with Belleville washers. The switch is held in compression with an array of rods.

The ZR LTGS original voltage specification was 5 MV (corresponding to 26 MA) and the switch was pragmatically designed for 5.5 MV (for margin and to occasionally deliver 30 MA). The increase in pulsed power requirements raised the normal operating voltage to 6.25 MV, corresponding to the following field stresses.

Peak Voltage	5 MV	5.5 MV	6.25 MV
Cascade Peak Field Stress	225 kV/cm	245 kV/cm	278 kV/cm
Trigger Gap Stress	268 kV/cm	294 kV/cm	337 kV/cm

Field uniformity across the cascade section is very important but quite difficult to achieve when using identical cascade-electrodes and spacers (a desired operational constraint). The baseline cascade electrode field uniformity is +0 and -18% (Figure 4). The field along the cascade housing is 81 kV/cm at 5.5 MV with a uniformity of -35% from its peak value, as shown in Figure 5. The trigger gap stress to the cascade gap stress is 1.2 and the housing to gap length ratio is 2.8.

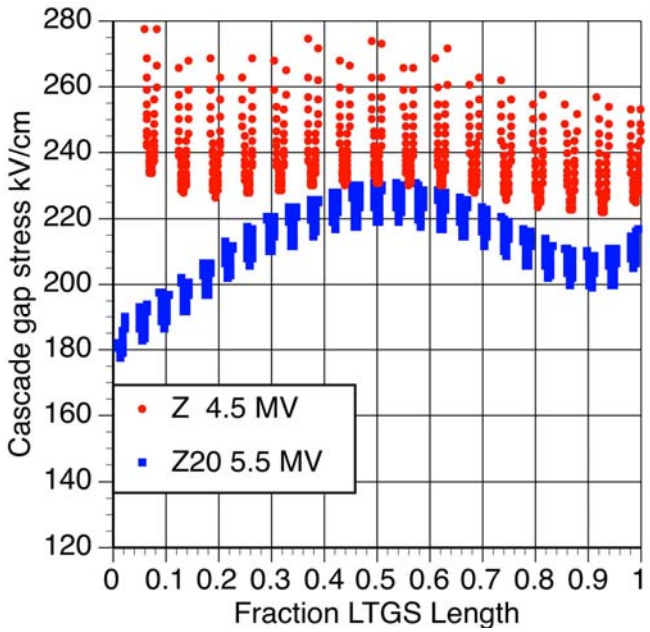

Figure 4. Electrostatic field stress profile through the LTGS cascade electrodes. The Z_{20} curve is the baseline switch discussed.

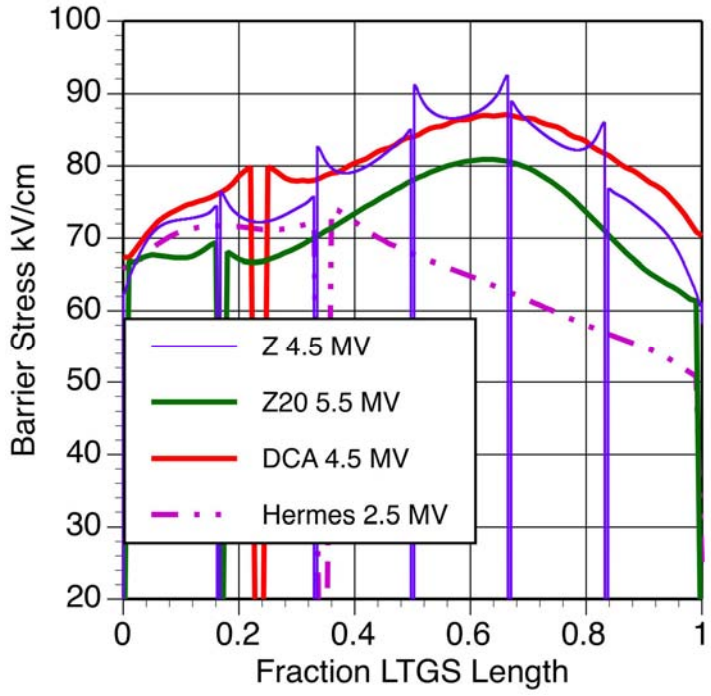

Figure 5. Electrostatic field stress profiles along LTGS cascade envelopes.

TESTING THE BASELINE LTGS

In July 2002, the TWA was modified to become the STB to support ZR switch development. LTGS testing began in early October 2002. In this initial configuration the STB was a 56-stage, 3.1-μF, 100-kV capacitor Marx generator that charged a 5.5-Ω, 20-nF water-insulated Intermediate Storage Capacitor (ISC) to a peak voltage of 6 MV in ~1.1 μs. The gas switch connected the output end of the ISC to a 5.5-Ω $CuSO_4$ resistive load. The gas switch was either electrically triggered with a TG-125 or laser triggered with a New Wave Tempest quadrupled Nd:YAG laser producing roughly 30 mJ of UV in 5 ns. The intermediate store voltage 21 ns upstream from the switch, the TG125 monitor 175 ns downstream, and a photo diode ~12 ns from the switch were used to characterize performance. Figure 6 shows the initial STB schematic.

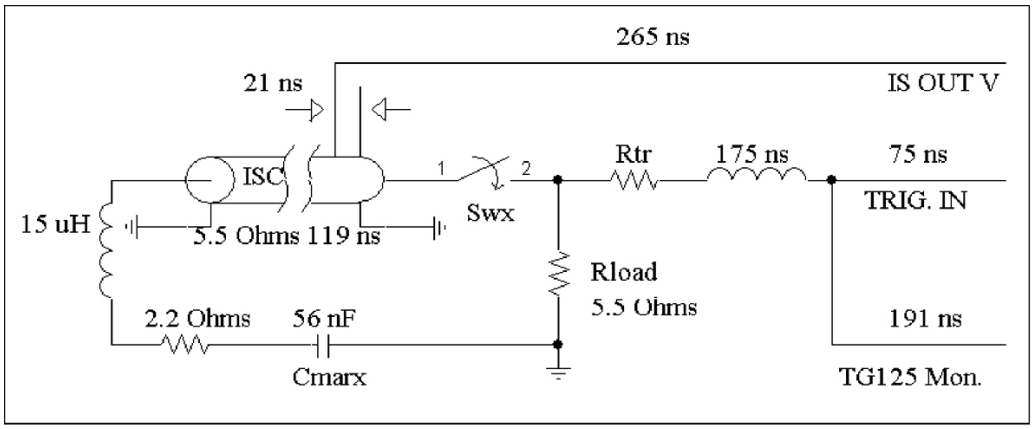

Figure 6. The initial Switch Test Bed schematic.

Several switches were tested including the "Cantilever," the "Hybrid," a Russian switch with SNL trigger, and three each of the "Baseline" switches. Before STB was shut down in June 2004, 1045 shots were taken. Of those, 977 were taken on the three "Baseline" switches with a mean time to failure of 325 shots. The Baseline switch was successfully triggered at voltages as high as 5.8 MV. Data shows that spread of this switch when laser triggered is ~4 ns (σ = 1.3 ns) with a runtime of approximately 24 ns from arrival of the laser pulse. Figure 7 shows the measurement of closure delay/switch spread for a series of 11 shots taken at ~4.6 MV switch voltage. It should be noted that the Baseline switch in STB was visually obscured. Thus, only electrical performance was an indicator of switch failures.

The STB was built to test the LTGS for ZR, and thus the relevant systems were made to look as much like the proposed (in 2002) hardware as possible. A comparison of the intermediate store output voltage waveforms for the STB and Z_{20} are shown in Figure 8. The intermediate store output voltage waveform shows both the LTGS charging waveform (the rising portion) as well as the LTGS discharge (the falling waveform). When the Baseline switch was installed on Z_{20} and exhibited a surprising failure rate, the resistive load was changed to put additional charge through the switch in an effort to isolate the source of LTGS failures. This same alteration of STB did not induce failure in the LTGS.

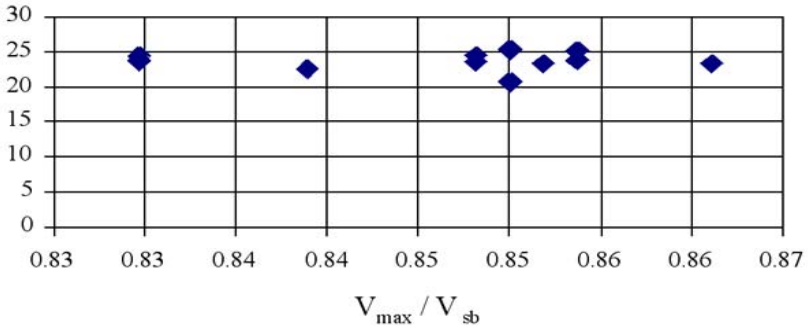

Figure 7. Delay time in nanoseconds for the Baseline switch design on STB. The jitter is on the order of 2 ns.

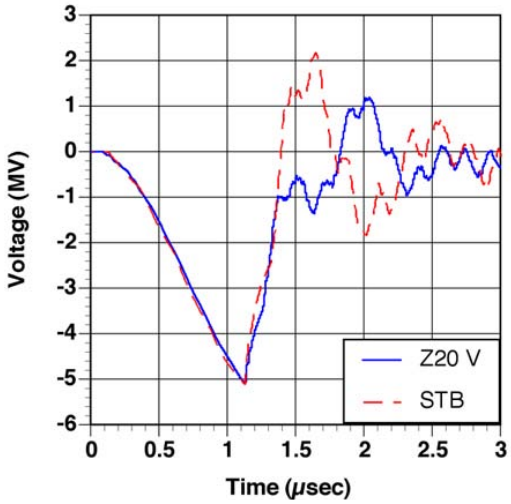

Figure 8. Typical ZR LTGS pulse charge and discharge waveforms. The same switch has been studied on Z_{20} (ZR-like waveforms) and on the switch test bed (STB) facility.

Since STB could not be operated reliably above 5 MV, the testing premise was changed to aid in the LTGS program: the switch was scaled to put much of the voltage on the trigger section. This modification (called SSTB for Scaled STB, described fully in Appendix E) was designed to enable a basic science approach to discriminate between various potential contributors to the LTGS surface flashover failures under realistic conditions. The switch, shown in Figure 9, was scaled so that the electric field in the trigger section at its lowest operating voltage of 2.5 MV was the same electric field as the Baseline Switch in Z_{20} at a peak charge voltage of 5.5 MV. A comparison of the field distribution along the trigger housing in the Z_{20} Baseline LTGS and SSTB is shown in Figure 10.

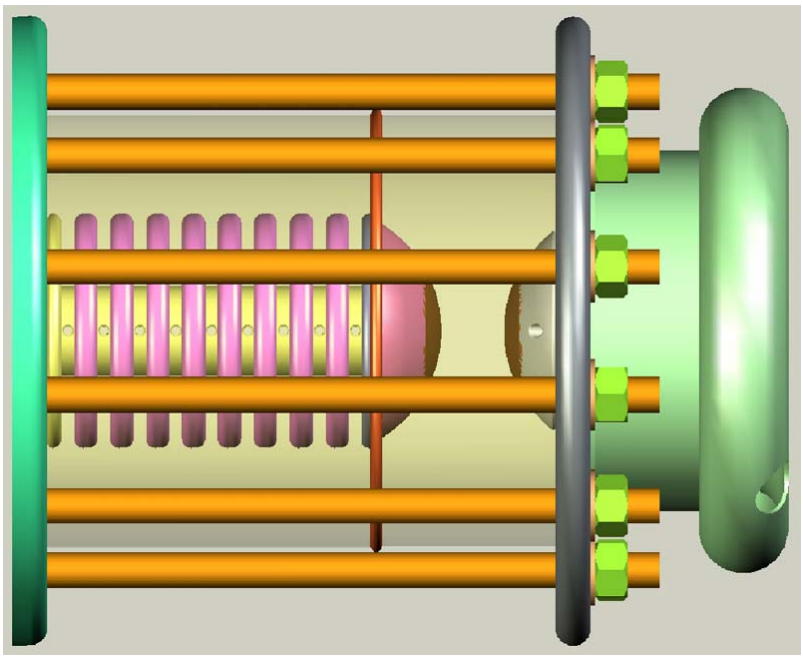

Figure 9. The SSTB LTGS has nine cascade gaps, forcing more of the total switch voltage into the trigger section.

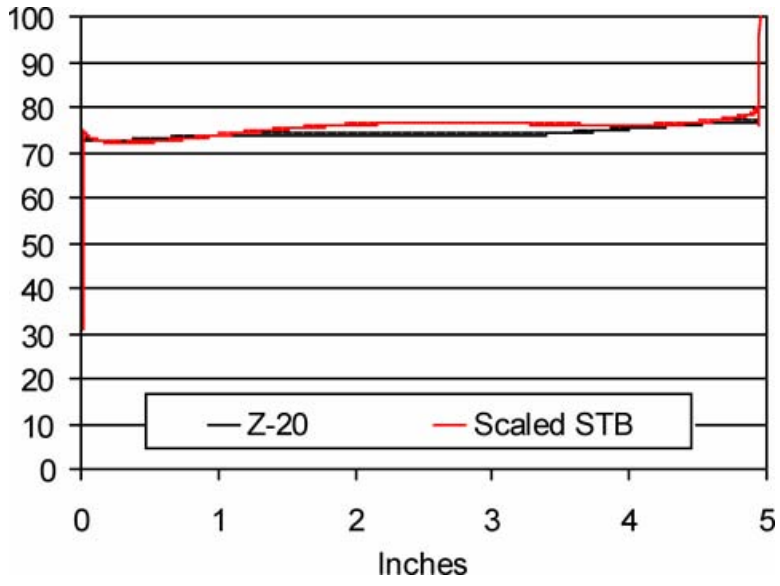

Figure 10. A comparison of the electric fields along the inner surface of the trigger housings of the LTGS on the SSTB and Z_{20} Baseline switches. In these plots, the charging voltage is 2.5 MV for SSTB and 5.5 MV for Z_{20}.

SSTB experiments were unable to replicate the flashovers observed on Z_{20}, even when the voltage was raised to nearly 4 MV. At this level the field in the trigger electrode is approximately 450 kV/cm and the field along the trigger housing is over 110 kV/cm, dramatically above the stresses induced for normal ZR operation. To test a hypothesis on the sensitivity of the triple points, a chamfer was introduced near the metal/gas/insulator interface to create even larger field enhancements. One surface flashover was observed on SSTB. Corroborative experiments at the University of Missouri yielded the same results. A theoretical analysis was developed that estimated that the fields at the triple point were too low to induce electron avalanching. These experiments and the supporting theoretical work lead us to conclude that field enhancement at the triple points in the LTGS are not a dominant mechanism leading to surface flashover.

The focus of SSTB was therefore shifted from trying to induce surface flashover on the inner trigger housing to providing support for the Z_{20} LTGS tests. A study to determine the effect of laser trigger energy on delay time and switch jitter was implemented on SSTB. The delay time is defined as the interval between the arrival of the laser beam, as measured at the zero crossing of a laser photodiode, to the arrival of current at the load. Switch delay times for SSTB are of the order of 15 ns. The delay time was not strongly affected with laser energies greater than 15 mJ and the switch could be triggered with laser energies as low as 5 mJ, as shown in Figure 11. This conclusion is supported by previous work where it was found that the laser trigger was not a strong variable in LTGS performance when the electric field stress was high in the trigger gap.

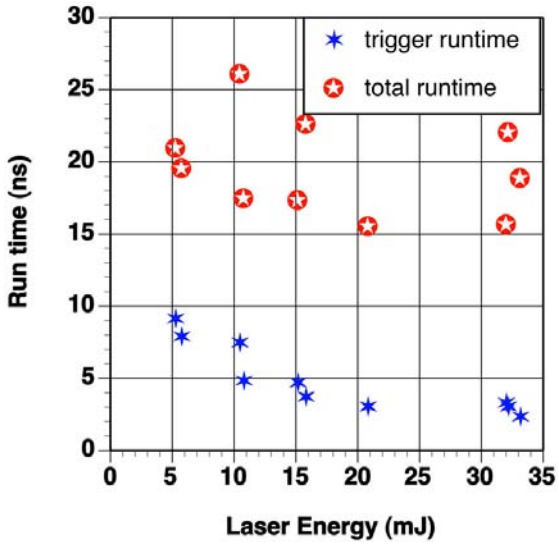

Figure 11. The effect of laser trigger energy on delay time for SSTB.

Z_{20}

Z_{20} (Figure 12) is a complete engineering version of a ZR module (Figure 1) from the Marx through the output transmission lines developed to assess the ZR design for verification of performance and reliability goals and the identification of areas for improvement. While component performance on other subsystem test facilities may be indicative, their performance on Z_{20} is definitive indication of ZR issues and capabilities. The 60-stage, 100-kV, 43-nF Marx generator charges a 26-nF, 100-ns ISC to a peak voltage in approximately 1.2 μs. An LTGS switches the ISC into a 2.6-Ω, 45-ns-long coaxial Pulse Forming Line (PFL) in approximately 200 ns. The negatively charged PFL is switched via self-closing water switches into a 4.2-Ω, 35-ns tri-plate transmission line (OTL1). Self-closing water pre-pulse/peaking switches are located between the output of OTL1 and a 6.4-Ω, 50-ns transmission line (OTL2). Z_{20} is terminated with fluid resistors that are undermatched to the line impedance to reduce the resistor voltage. Because Z_{20} has only one Marx, performance of the ZR output line combination, current adding of pairs of modules, the water convolute, and the vacuum regions cannot be evaluated. Z_{20} is extensively diagnosed with co-located current and voltage monitors at numerous positions throughout the system, along with optical time-integrated and time-resolved measurement systems.

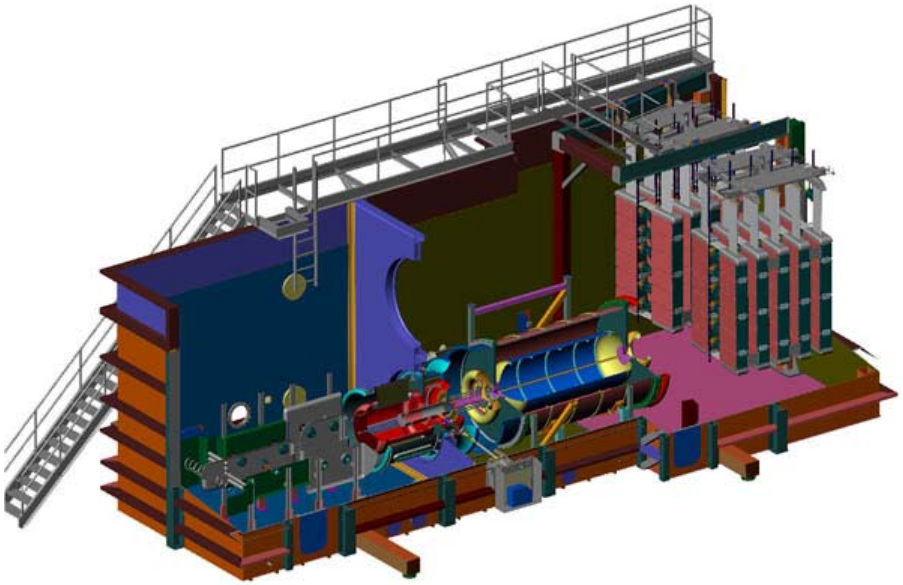

Figure 12. The assembled Z_{20} module.

LTGS open-shutter photographs, indicating the LTGS surface flashovers, are shown in Figure 13. Often these flashover events occur at the normal time of cascade switch closure and carry full current since the cascade gaps do not close. The flashover is not apparent in the experimental data and therefore does not affect the module shot performance, but rather serves as an indicator of the need for maintenance. Flashovers in the cascade section were found to be more detrimental to switch performance that those occurring in the trigger section. When a flashover occurs in the cascade section and the housing is not replaced, on subsequent shots the

switch will often prefire. It is inferred that a cascade flashover damages the surface to further reduce its ability to hold off voltage. Trigger housing flashovers frequently did not exhibit this trait and recover their insulating properties for subsequent shots. Open-shutter photographs or time resolved optical emission histories can identify envelope flashovers to provide useful information in prefire prevention.

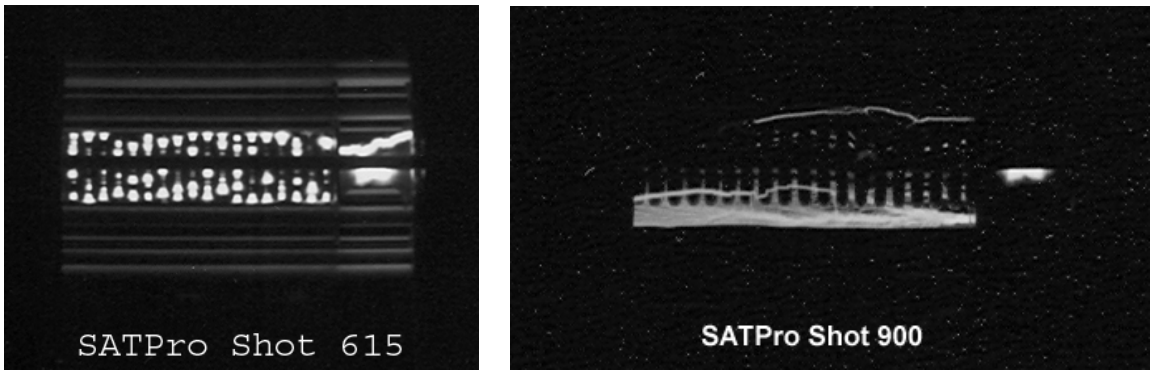

Figure 13. Time-integrated photographs of trigger and cascade housing flashovers.

The first Baseline LTGS tested on Z_{20} lasted over 200 shots at ~ 5 MV. This was consistent with the prior component testing performance on STB. After the first switch, and with an increasing voltage, reliability soon became an apparent issue. Extensive tests on STB investigated scaling with coulomb transfer and the action (made to be even greater than on Z_{20}) yielded the same results: the STB switches were longer lived.

To illustrate the extent of the problem on Z_{20} the switch failure log for Shots 199-1111 is shown in Figure 14. Because several of the LTGS housings were left in place for subsequent shots, the data is presented as number of shots to first failure and number of total pulses on a housing. The abscissa for this graph is the switch number, or switch chronology. Figure 15 shows the same data with the number of pulses to first flashover event in increasing order. The first flashover in one third of the Z_{20} Baseline switches occurs in less than 10 shots.

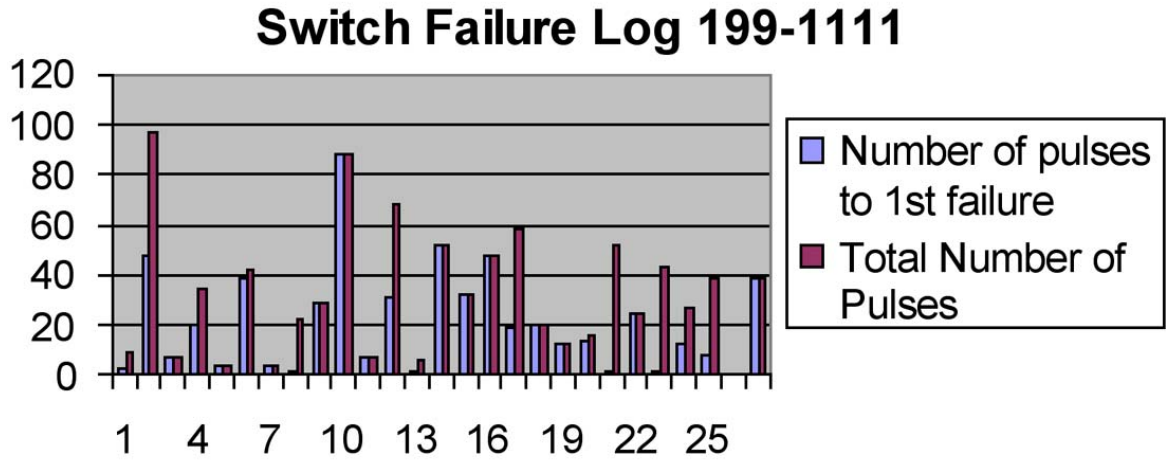

Figure 14. Analysis of flashover data in Z_{20} Switch Log for the Baseline LTGS.

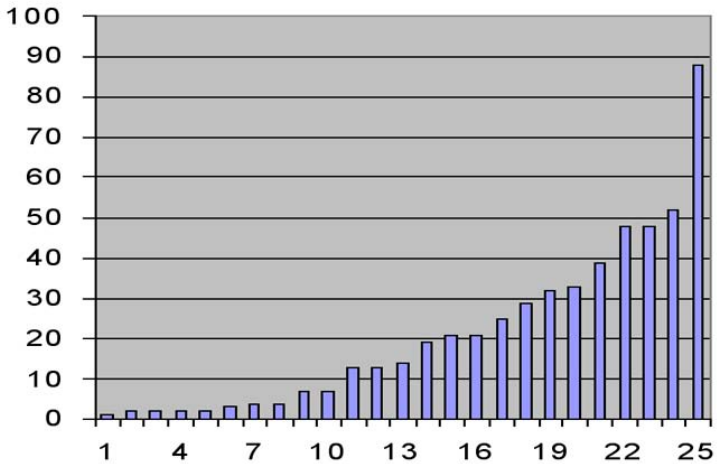

Figure 15. The first flashover data plotted in ascending order of number of shots to first flashover.

The data taken on STB is not consistent with the data on Z_{20}. The three switches tested on STB had a life in the 200- to 400-shot range before they had degraded electrically to the point that they were no longer functional. A similarly defined life for the last 28 switches tested in Z_{20} is somewhere between 1 and 97 shots. However, the life of the first switch in Z_{20} (not shown in this plot) was above 200 shots with many of those shots at low voltage, which may be the explanation. We believe the difference between STB and Z_{20} is real, and the effects of higher voltage (stress) is real also.

UPGRADED LTGS DESIGN TESTING ON Z_{20}

The ZR schedule drove the research efforts to deliver a reliable switch quickly. The time constraint can be easily seen in the near simultaneous changes in design and procedure, deferring careful confirmation activities. For example, between Shots 1071 and 1238, the trigger housing material, the laser trigger system, and the switch cleaning protocols were each changed and the baseline design was modified to increase the shielding on the triple points. Many on the project felt that we were just one Band-Aid away from a working ZR component, and constant effort was required to balance building the fundamental science basis and testing hypotheses, hoping for immediate deployment.

The trigger housing material and the cleaning procedures were changed following Shot 1070. Rexolite, a crosslinked polystyrene, is used extensively in vacuum stacks. Although the mechanisms of surface flashover in vacuum and in high-pressure gases are reported to be quite different, it is reasonable to assume the material surface properties contribute. At the same time the surface cleaning and handling protocols were modified. The initial cleaning procedure for the LTGS was the same as for Z, Saturn, and HERMES: Simple Green (a mild detergent) and tap water with a dry nitrogen purge through a anti-static blowing nozzle. This cleaning procedure was modified by adding a hexane swipe to the acrylic parts and ethyl alcohol for the Rexolite and metal components after the nitrogen drying. The immediate result of these two changes is noted in Figure 16 as a sudden reduction in surface flashover frequency.

It has long been known in LTGS design that the triple points where metal, plastic, and gas meet should operate at as low a field as possible. The baseline LTGS design was predicated on goals of operational simplicity and ease of fabrication, assembly, and maintainability. The long mean time to failure demonstrated on STB led to the assumption that the shielding of the triple points was "good enough." The true electric fields near the triple point cannot be computed to any degree of accuracy, but the maximum electric field along the insulator is ~80 kV/cm. As surface flashovers were identified as a serious concern limiting useful switch lifetime, the notion that propagating discharges might start at gaps between the insulator and metal plates motivated a design with reduced fields at the triple points. Recessing the joint into a region of reduced field, such as in a metal well, can effectively shield the triple point. This can also be accomplished with conductive inserts placed into the insulator housing (as in the ZR vacuum insulator design) and by shaping the plastic profile as it leaves the metal surface. The baseline design was modified to reduce the triple point fields by recessing the plastic into an electrode groove (Figure 17) beginning on Shot 1184. One important consequence of this shielded triple point approach is that the trigger plate became a larger diameter to allow a full radius on the trigger plate outer edge in the oil. This reduces the fields on the anode end of the cascade insulator after triggering, which may tend to inhibit flashover of both the cascade housing (desirable) as well as inhibiting self-closure of the cascade gaps (undesirable). This modification also noticeably reduced the frequency of envelope flashes. The "Z-like" physics-test switch was investigated at this point, whose flashovers have nothing to do with the baseline failure mechanism statistics. More information on this valuable experiment is available in the appendices.

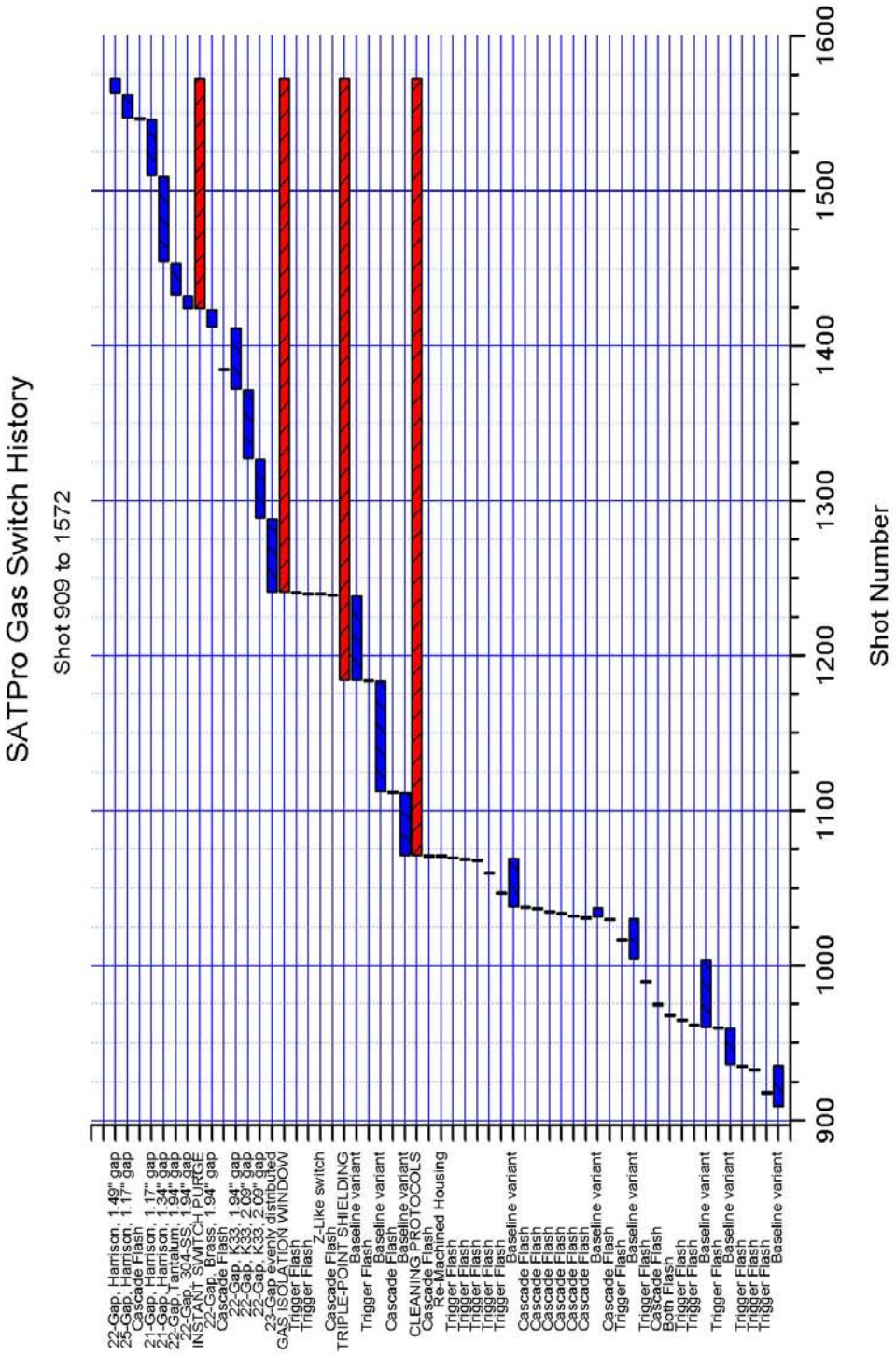

Figure 16. LTGS configuration failure history on Z_{20}.

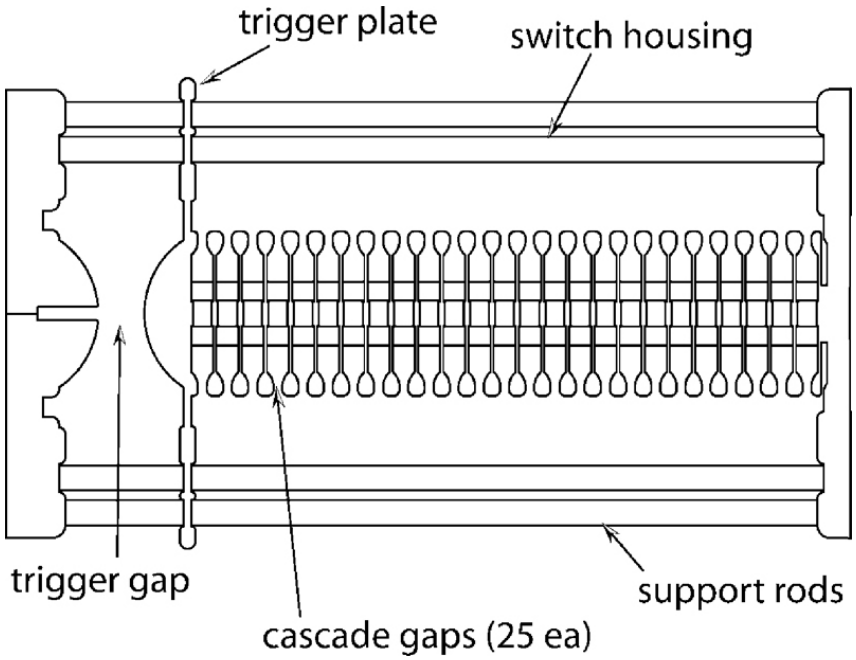

Figure 17. The shielded triple point design. The four locations where the insulator housing contacts the metal plates are recessed into low-field regions.

Around Shot 1240 the trigger optics were modified to investigate increasing their operational lifetime. It was discovered that the "smoke" from LTGS operation pervades the laser can where the trigger beam is relayed (see Figure 2), coating the optics therein and leading to rapid degradation (of order 10-shot lifetime). The result of the degradation of the optics is that the switch triggerability becomes progressively weaker with each shot. Material analysis reveals that very small (~30-nm diameter) Tungsten-oxide particles coat the optics and become baked in by subsequent laser irradiation, reducing the optical properties. Adding debris filters to baffle the vent holes between the LTGS and laser can was not effective, so these holes were closed and an additional window installed about 30 cm from the focal spot, sealing the LTGS. A one-way valve in this extension tube was added so the gas purge cycle could be accomplished by reducing LTGS pressure through the ISC, then refilling by overpressurizing the laser can, thereby blowing all switch debris away from the triggering optics. Combining this system with a prompt purge following every shot has significantly increased the optics lifetime, and combined with the other measures has consistently reduced the frequency of envelope flashover.

The reason why these modifications are successful at reducing the frequency of envelope flashover and increasing optics lifetime has not been established. However, with the relaxation of fundamental operational lifetime issues, the team discovered the switch-triggering reliability and jitter were unacceptable. It is believed this is due to a combination of large operating pressure and reduced laser-triggering effectiveness.

LTGS operating pressure has been a variable throughout the development program. To aid in the LTGS housing's resistance to surface flashover, the gas pressure was continually increased, which required the LTGS to work in a region of its self-break curve with a significant spread (Figure 18). The figure shows self-break is linear with pressure below 25 psig. Self-break data shows that for pressures above 40 psia the spread in voltage is over 1 MV, resulting in a saturation of the breakdown strength of pure SF_6. This is consistent with published literature stating that when SF_6 is used at high pressures there is a reduction of the withstand voltage caused by field enhancement associated with micro protrusions on the electrode surface.[21] While limited data was taken at high pressure, the effect can be seen with the inclusion of unintentional self-breaks on the self-break curve. These "unintentional self-breaks" will manifest as prefires in ZR. Further, at these elevated pressures the spread results in an increased prefire rate and increased jitter.

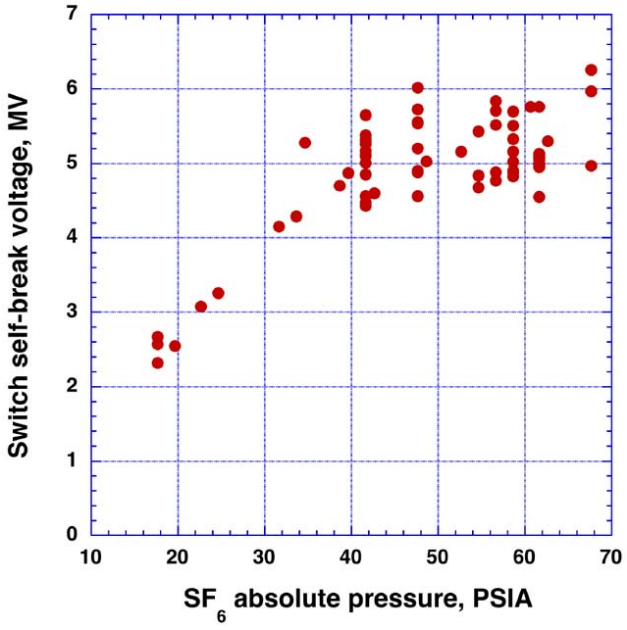

Figure 18. Z_{20} LTGS self-break curve including non-intentional self-break data at higher pressures. The breakdown strength appears to be linear at low pressure and saturated at higher pressures.

Investigations into the laser-triggering system are extensively described in the appendices, and this has become the near-term high priority for LTGS research. The combination of a low laser focal intensity and a high gas pressure make prompt triggering of the first gap problematic. A variety of triggering modifications are under investigation to develop solutions to this issue consistent with long envelope and optics lifetime and reliable operation at 6.25 MV.

At this point the data is suggestive that a few modifications to the original ZR LTGS design (which were abandoned over a year ago) could provide adequate capability for initial ZR operations, and that this research effort is on a sensible path toward identifying an improved generation of laser-triggered gas switches for rolling upgrades into that capability. The strength of this approach is based on combining the experimental demonstrations on Z_{20} with the efforts to develop an underlying science of gas switching, described in the next sections.

THEORY AND MODELING

The modeling activity has two main goals: (1) Understand intended processes in normal switch operation and (2) Understand unintended processes which may lead to switch failures. These two goals are not disjoint because changes to timing, levels, etc., in the intended mode of operation may enhance unintended processes, contributing to failure.

Specific processes of interest for intended operation are:

a. Gas ionization and attachment properties, which determine avalanche threshold field levels.
b. Electron avalanche through arc formation leading to switch closure timing.
c. Arc thermalization and expansion leading to switch closure impedance.
d. UV emission, some of which impinges on the insulator.
e. Particle emission, which may impinge on the insulator.
f. Electrode behavior and splatter leading to surface roughness (and insulator deposits).

Specific processes of interest for unintended operation are:

a. Insulator field levels and time behavior (oscillations), which drive breakdown events on the insulator.
b. Insulator surface properties and interactions (UV photons, electron and ion impact), which may modify avalanche thresholds by creating free electrons.
c. Insulator flashover thresholds.
d. Triple point effects, which can launch avalanches or leaders.
e. Macroscopic particle field enhancements (splattered macroscopic particles).
f. Insulator charging, which may modify surface drive fields.
g. Arc energy and insulator damage.

The theory and modeling capability required to understand these processes was not adequate at the outset of this project. The first task was to begin assembling a library of reference material on Quick Place. This library includes references for material properties as well as breakdown modeling and theory. Six additional areas have been worked on in FY 2006 to understand some of the above processes as well as to advance the state of the modeling capabilities, which will enable future applications to the other processes listed above.

EM Simulations

Axisymmetric electromagnetic (EM) simulations of switch closure have been performed in past years using TWOQUICK and a sigmoid closure function for arc conductivity. One main purpose of these simulations was to estimate field levels throughout the switch volume and particularly at the insulator as the switch closes. Figure 19 shows results for the insulator surface electric field during closure. Because many useful features are being added to the simulation tool QUICKSILVER, these EM simulations were converted over to this more general purpose code.

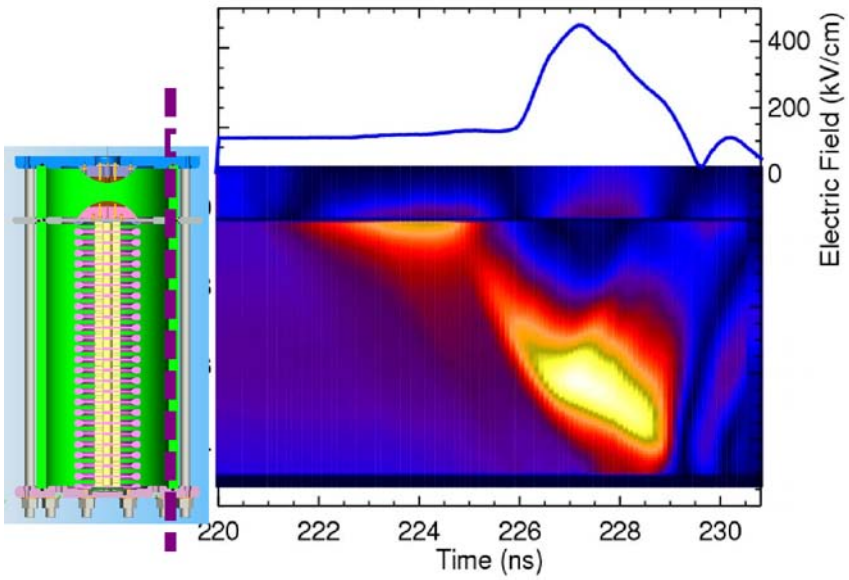

Figure 19. The insulator surface electric field during closure.

After this code conversion phase was completed, streak camera images indicated that cascade closure times were significantly longer than those obtained in the original EM simulations. This was attributed to the timing associated with the original sigmoid conductivity function. To bring these into better alignment, changes were made to the timing in this conductivity function to better match closure timing. Although this is not a first principles arc model, it was felt that this modification was the most expedient way to improve the EM simulations in the short term. Two times were introduced: the first corresponds to when the channel begins to affect the field (and might be thought of as the early time phase where the streamer first bridges the gap); the second corresponds to the intermediate and later time phases (where the channel thermalizes and expands to achieve high conductances). Figure 20 shows an example of modified cascade closure times in the simulation and a comparison with streak camera data.

Examination of the sigmoid function also revealed that, although the conductivity assumed reasonable values, mesh cell sizes forced the cascade arcs to take on a vastly overestimated cross-sectional area (several orders of magnitude larger). Because the total conductance may be important to the damping of the switching operation, and because in this axisymmetric model matching of the switch conductance is all that can be attained (since individual arc channels are not modeled directly), the conductivity in the sigmoid function is currently being increased to account for the ratio of channel areas.

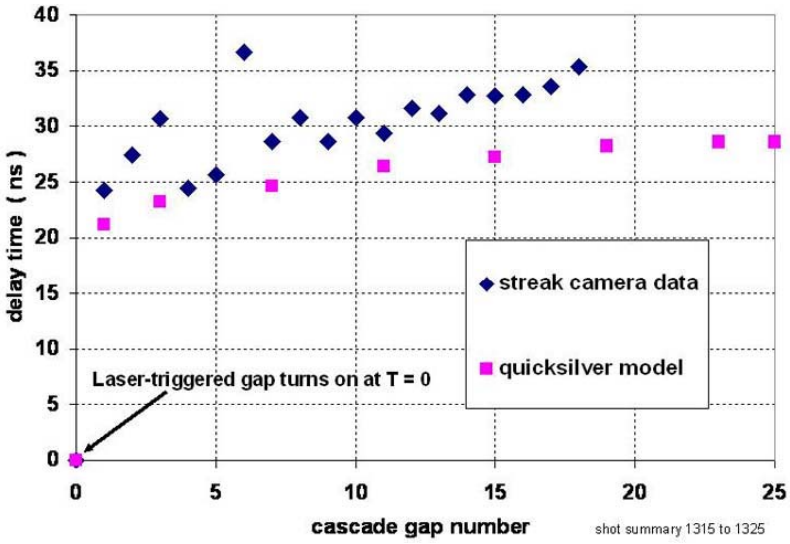

Figure 20. Comparison of measured and calculated cascade electrode closure times.

The initial runs with the timing modifications indicate that insulator envelope peak field levels during closure are sensitive to cascade closure timing. The figures below (Figure 21) show examples for variations in insulator field for two cascade run times. This is thought to be a consequence of changes to the time constant of the cascade gap closures, where long time constants correspond to electric field distributions that spread the voltage over the cascade train of gaps during closure, whereas short time constants correspond to a conductive protrusion of the cascade train into the cascade region during closure. This latter situation means that the voltage is concentrated at the end of the gap closure train as it progresses across the region; the radial and (to some extent) the axial electric fields are enhanced in this region as a result. Note that significant differences can exist between models which predict identical run times.

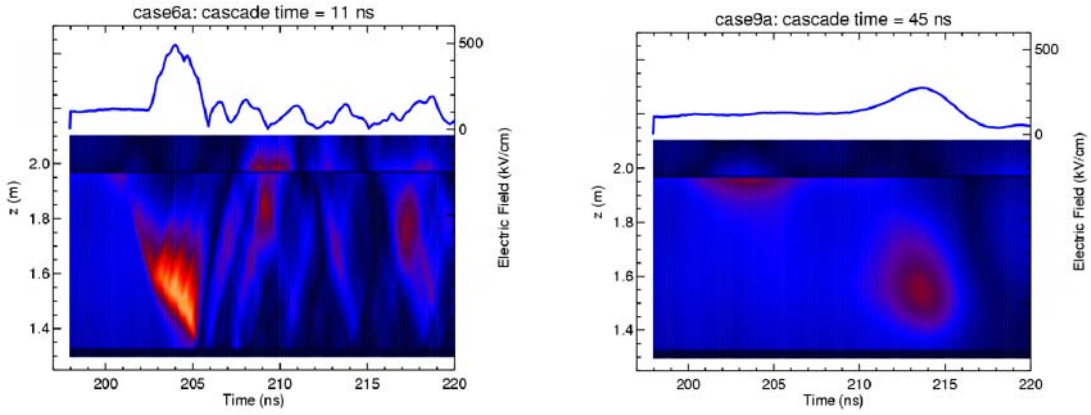

Figure 21. Quicksilver simulation predictions of the electric field evolution along the cascade envelope inner surface.

LSP and EEDF

Two particle in cell (PIC) codes are being used to simulate electron avalanche growth: LSP and QUICKSILVER. We are interested to see how far these simulations can be extended in time and electron density. For example we would like to have simulations carried out in the time regime from initial avalanche to streamer threshold (where the charge field is as large as the driving field) and further into channel thermalization (where the neutral temperature increases and the channel achieves significant conductivity). LSP simulation of electron avalanches in the simple gas hydrogen were originally carried out to get a feel for how it was performing with relatively simple gas interactions (no attachment processes) (see Figures 22 and 23).

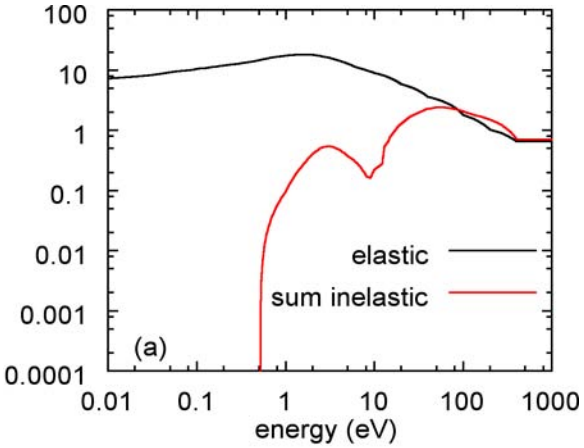

Figure 22. Total elastic and inelastic cross sections.

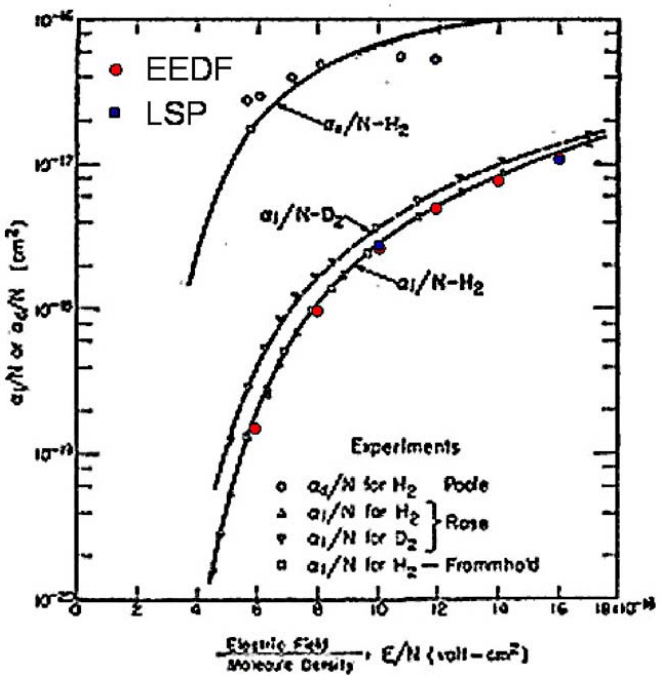

Figure 23. A comparison of the ionization coefficient with experimental data.

Simulations of electron avalanches in hydrogen were carried out. Improvements in the collision algorithm were made (including removal of ionization energy from the colliding electron). Charge density evolution is shown in the following sequence (Figure 24).

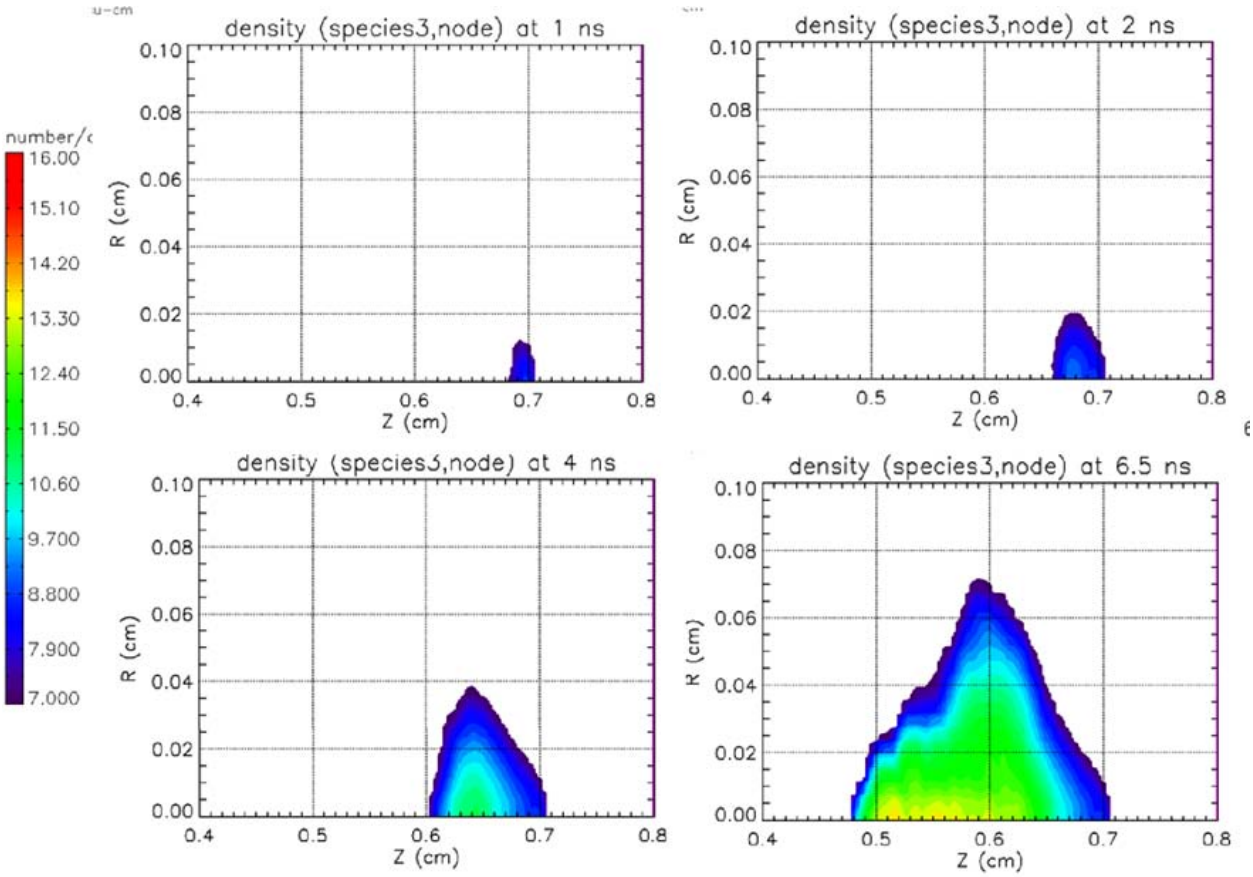

Figure 24. Plasma ion density evolution in a 30-kV/cm-atm LSP simulation.

Streamer threshold (where the charge field is comparable to the external drive field) has been reached, as can be seen in the following density plot (Figure 25). The bend-over in exponential growth rate indicates electrostatic screening in the body of the swarm.

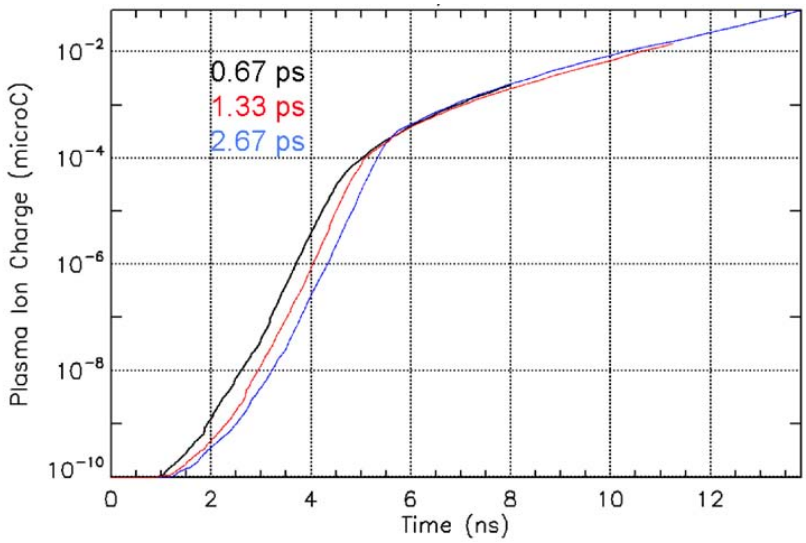

Figure 25. Total ion charge evolution in 3 stream simulations

Cross sections in SF_6 were examined. Figure 26 shows the total elastic and inelastic values, which illustrate the attachment process at low energies.

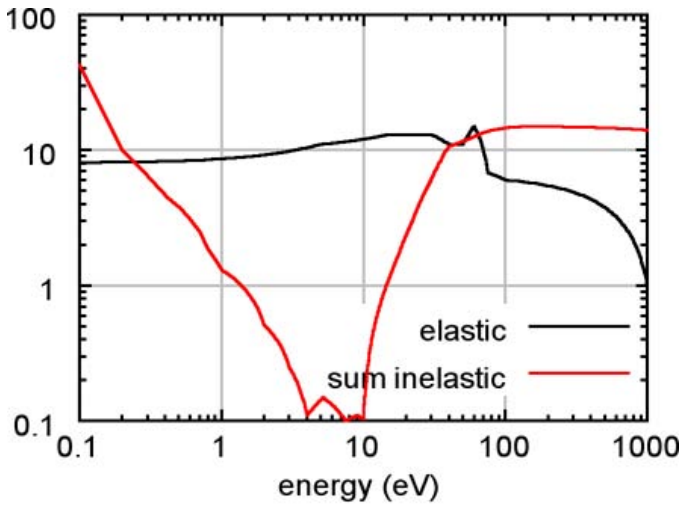

Figure 26. Kline cross section used to calculate transport coefficients.

Investigations were made on the value of the excitation cross sections, which are typically inferred by matching ionization rates to experimental data. Using the LSP-MCC kinetic calculations for the ionization rates, the excitation cross sections were similarly manipulated to match ionization thresholds. It was felt that with attachment processes dominant at low energies this approach represented an improvement over the Boltzmann approach (where the quasi-isotropic scattering assumption is questionable for these dominant inelastic processes). Figure 27 shows the effective ionization rates obtained in SF_6 versus experimental data. The plan now is to run streamer simulations in SF_6. Details are given in Appendix M.

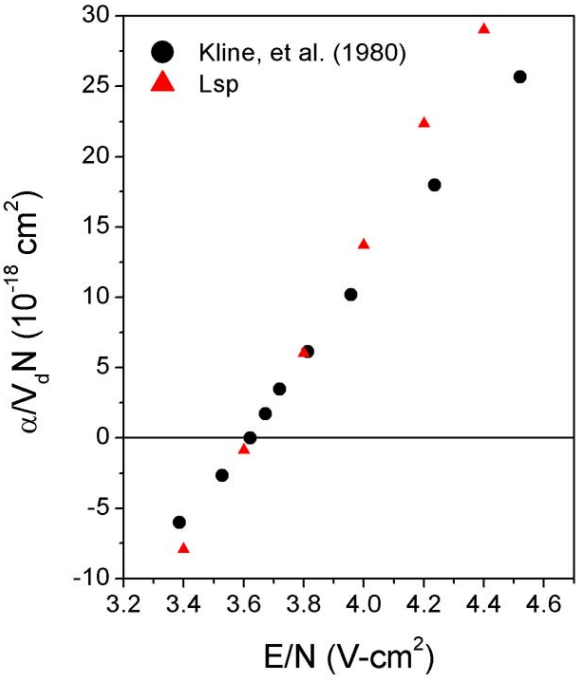

Figure 27. Effective ionization rate near the breakdown threshold in SF_6.

QUICKSILVER and MCSwarm

The PIC code QUICKSILVER is also being used to model streamer development by introducing an upward donor cell technique to allow charge convection from cell to cell. This algorithm has been prototyped in one dimension and the results for electron density and ion density are shown in Figures 28 and 29 for SF_6. This algorithm has advantages for three-dimensional simulations. It has been implemented in QUICKSILVER and is currently being examined in three dimensions.

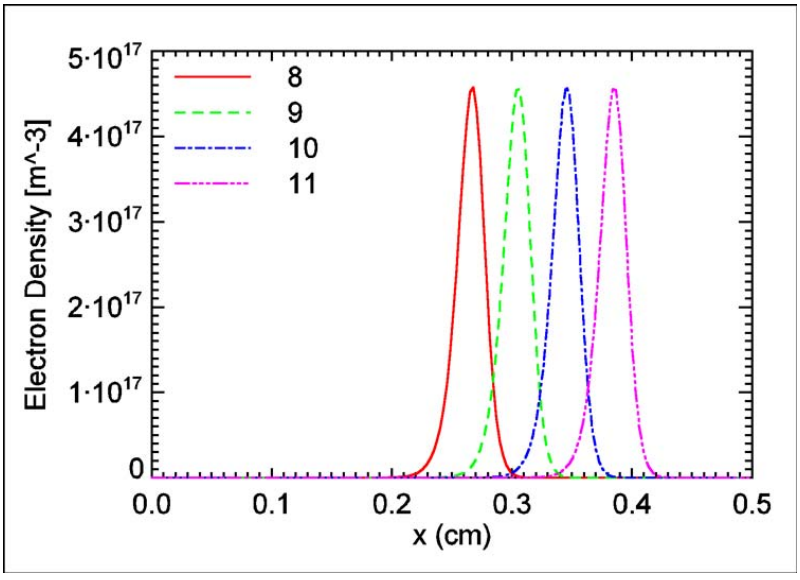

Figure 28. Electron density versus position at several times [ns].

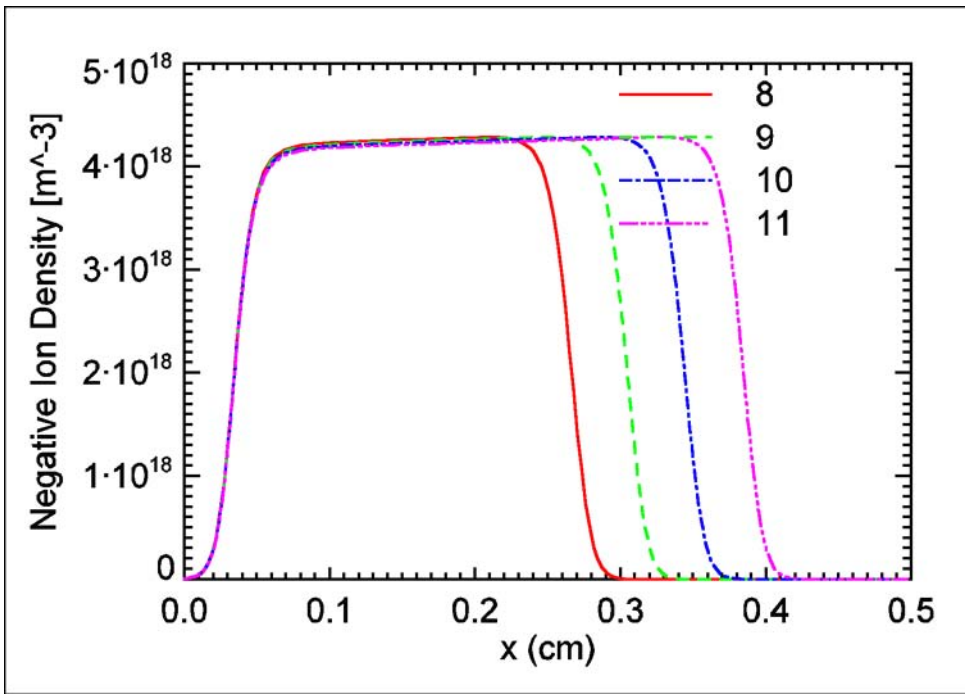

Figure 29. Negative ion density versus position at several times [ns].

SF_6 ionization properties were obtained from the NRL code MCSwarm. These are shown in Figure 30 and compared against existing data and against the LSP-MCC and EEDF simulations.

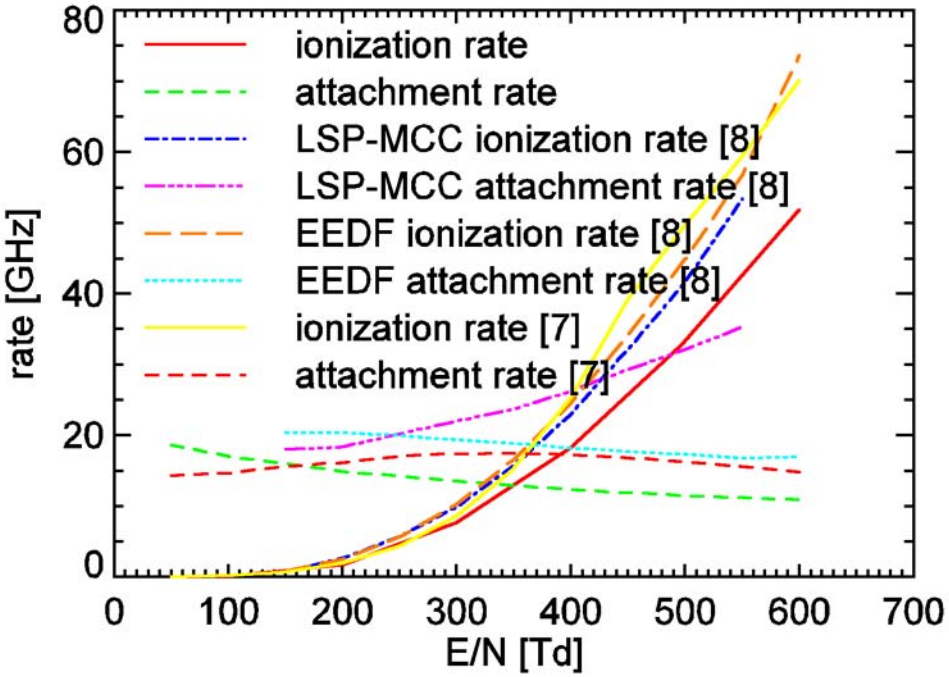

Figure 30. Comparison of SF_6 rate coefficients.

ALEGRA

The transition from a weakly conducting arc channel to a highly conductive channel typically occurs at later times due to expansion of the channel radius, shown in Figure 31. Braginskii developed a model for the hydrodynamic expansion associated with this phase in a variety of gases. We recently improved this model by incorporating conductivity variations in this later time phase for water arcs, using one-dimensional simulations with ALEGRA and 0D circuit models; we decided to apply a similar approach to high-pressure nitrogen and SF_6 for the current switch project. To expedite the process we went directly to the ALEGRA simulations.

We first did simulations in atmospheric pressure nitrogen. These are one-dimensional simulations driven by a fraction of the switch current waveform. Peculiarities in the results (including oscillatory behavior) motivated several improvements to the simulations such as the introduction of multi-group (multi-energy) radiated photons from the channel. These changes were sensible but did not have a significant effect on the results. We next went to higher pressures (nitrogen at five atmospheres absolute pressure) to see if better results could be obtained nearer to the operating regime of the switch. Figure 31 shows the resistance per unit length of a single channel as a function of time from the simulation. The drive current was a linear ramp with a rate of 3 kA/ns. We plan compare these simulations with 0D circuit models to investigate high-pressure SF_6.

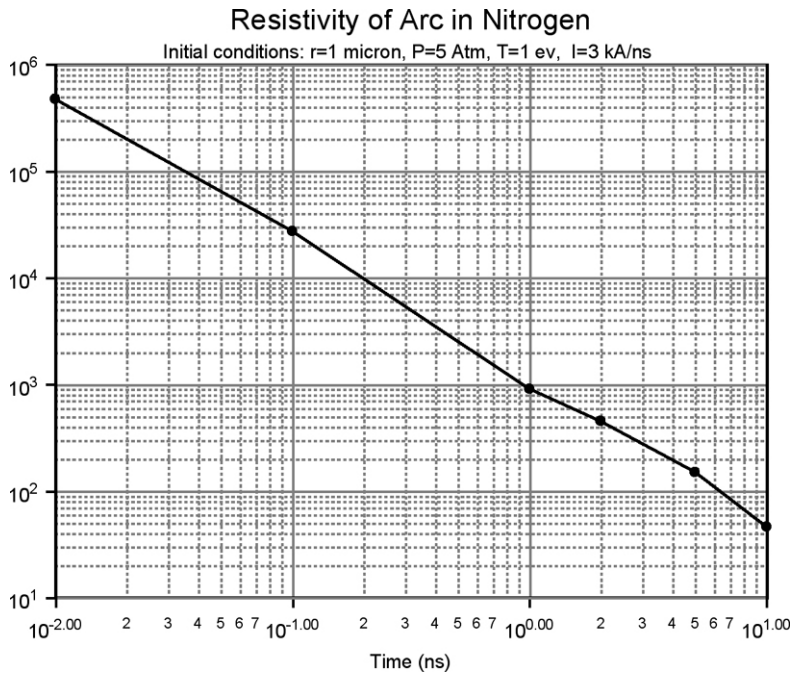

Figure 31. Resistance of a nitrogen arc from Allegra simulation.

UV emission from the arc can be extracted from the simulations. This is a quantity of interest, since parts of the spectrum make it out to the insulator, as demonstrated by the measured absorption of UV in SF_6 shown in Figure 32.[22]

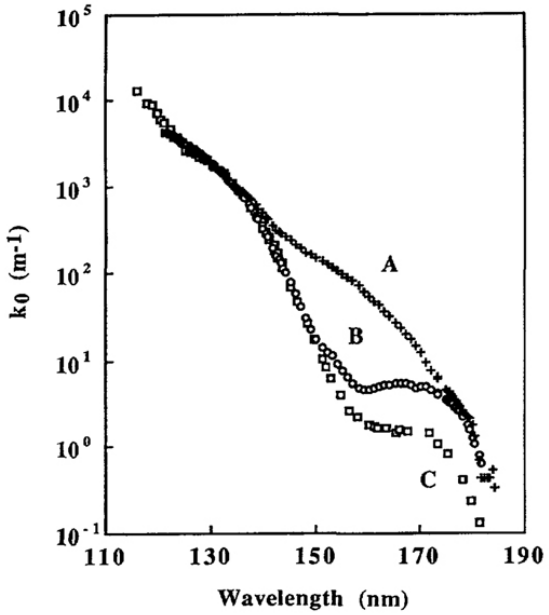

Figure 32. Measured absorption coefficient for three gaseous SF_6 samples at 298 °K and 100 kPa. A contains 600 ppm H_2O and 4500 ppm O_2. B contains 500 ppm H_2O and 60 ppm O_2. C contains 125 ppm H_2O and < 5 ppm O_2.

Breakdown_Alpha

Breakdown_Alpha is a code that solves for the static field distribution using the EIGER_S static boundary element code and then integrates the effective ionization coefficient (which typically depends on the field level in an exponential manner) along user-chosen electric field lines. The purpose is to see if breakdown or streamer thresholds have been reached (electron avalanche multiplication has reached critical levels). Because static field levels, or even switched field levels (not counting possible fast transient enhancements discussed above), along the insulator envelope are relatively small (and below avalanche threshold), there was a question about whether triple points could initiate streamers, which carry field enhancements at their head, and might be expected to propagate into somewhat lower field regions. To examine this issue further, we decided to look at avalanche multiplication in the field enhanced triple point gaps to see whether these critical electron levels could be reached. The first task was to build SF_6 ionization properties into Breakdown_Alpha. Next, several triple point geometries were set up. Sharp edges, rounded edges, and beveled edges were examined. A set of chosen field lines near a 1-mil sharp-edge triple point are shown in Figure 33.

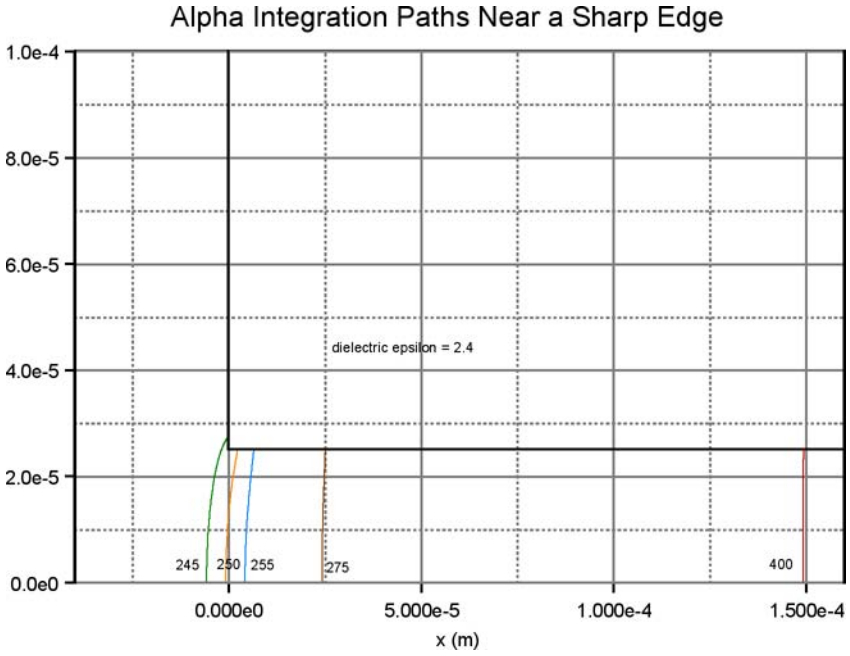

Figure 33. Breakdown calculation for SF_6

The exciting field outside the triple point region was taken to mimic static field levels of 70 kV/cm (charge field) and 140 kV/cm (switched field) as well as multiples of these levels. It was found that 44 psig pressure SF_6 never achieved streamer multiplication levels in these triple points. Approximately twice this switched external field level (or 280 kV/cm) was required to reach such thresholds.

Finally, the static solver EIGER_S currently has two-dimensional and three-dimensional capability only. The moments have been worked out to enable two-dimensional axisymmetric calculations to be performed as well. This will enable threshold calculations to be made on the entire switch envelope. These have been partly incorporated into Breakdown_Alpha and will be tested shortly.

Static Charge

A concern that has repeatedly arisen during the project is the possibility of surface charge existing on the insulator from shot to shot of the switch. To assess the seriousness of this effect, measurements were made using a commercial electrostatic field meter. This meter is basically an electronic field mill.

Measurements were made on an assembled switch located on a bench top before insertion into the Z_{20} system. These yielded field levels at or below about 0.8 kV/cm. The measurements were repeated after the switch was installed in the tank but before oil fill. These yielded less than or equal to 0.5 kV/cm. Following several shots, the oil was immediately drained, the pressure in the switch was brought down to a slight overpressure relative to atmospheric, and the measurements were repeated. These yielded levels below about 0.1 kV/cm.

Clearly all these measurements are small compared to the hypothesized significant residual static charge field levels where concerns would arise. However, there is certainly a question about the very small levels after the shots and oil immersion. Although the oil is an insulator, there is a very small leakage conductance. We do not know this value very well, but even very small levels may result in relaxation time constants on the order of milliseconds when the switch is immersed. It seems prudent to examine the relaxation time when a thin film is present (where this relaxation time would be lengthened considerably and would likely be observable). This would give us a better understanding of the role that conduction process might play in masking electric fields created by interior charges. Details of the measurement levels can be found in the appendices.

UNIVERSITY RESEARCH

Three universities with directly relevant experience in pulsed power and gas switching were included in the LTGS research project, both to leverage their unique and essential capabilities and to invest in developing a future pool of trained Pulsed Power Technologies scientists. In general their scope of efforts were divided with minimal overlap, but often benefited from significant cross-fertilization and joint investigation activities. Critical and time-urgent research needed to deploy an initial LTGS on ZR was retained at Sandia while elements of the fundamental underpinning science were studied at the universities. Regular team meetings, emails, and a shared QuickPlace web site were used to integrate these geographically diverse team efforts.

University of Strathclyde

Background work at the University of Strathclyde has been concerned with an understanding of the design and intended operation of the LTGS. This has included consideration and assessment of the cascade section of the switch along with recommendations as to how this could be proposed to operate for improved performance.

The experimental work conducted at Strathclyde has been concentrated on the study of (1) a single cascade gap switch subjected to high voltage and (2) the dielectric materials and their performance used in the LTGS housing.

The single cascade gap switch studies have included:

- Modeling of the electrical field distribution within the cascade gap with particular attention paid to triple points and field enhanced regions within the electrode/insulator system,
- The development of a single gap test system, a pulsed power supply, and high-voltage diagnostics,
- Development of a system for surface conductivity measurements, and
- Study of mechanical damage of the LTGS body (section of acrylic dielectric) caused by high-voltage spark channel formation and expansion.

During the course of the project a review of pulse breakdown data in SF_6, water, and insulating oil has been conducted. Specific attention has been paid to volt-time characteristics as they are of great importance for evaluation of the switch performance.

Electric Field Distributions in the Cascade Section

The distribution of electrical field in the cascade multi-electrode LTGS switch and the single gap test chamber has been analyzed using “Electro” software. Two versions of the test chamber model have been developed. One version is the model with a solid spacer between electrodes (Figure 34(a)) and the second version is the model with two separate dielectric spacers separated by a gap (Figure 34(b)). In the model with the single solid spacer, the spacer has no holes to

allow gas into the internal cavity. The presence of such holes with sharp edges could potentially generate high electrical fields. The second version models the presence of these holes by using a slot whose width is equal to the diameter of the holes drilled in the original spacer. This slot represents a limiting case, as there is no possibility to model real three-dimensional configurations using the two-dimensional "Electro" software.

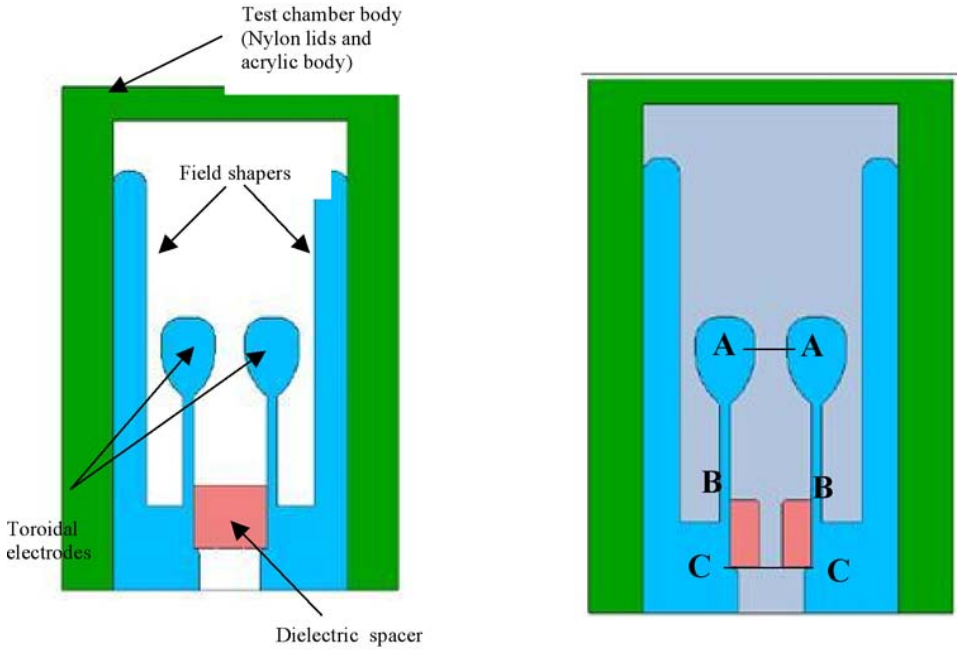

Figure 34. Single gap test chamber design used in "Electro" calculations. (a) Solid dielectric spacer; (b) Dielectric spacer with a gap. A-A, B-B, C-C indicate lines across which electric field has been obtained.

Figure 35(a) shows the field distribution along top surface of the solid dielectric spacer and Figure 35(b) shows the representation of the spacer with the slot. As can be seen, the electric field at the edges of the spacers could reach values that are similar (193 kV/cm) to the maximum electrical field in the gap between electrodes (250 kV/cm), and such high values of the electric field could potentially play a role in the initiation of breakdown. In this case the U field on the top surface of the dielectric spacer has much lower electric fields at ~90 kV/cm than the maximum field between electrodes. A similar analysis has been done for the lower spacer surface, and can be found in Appendix P.

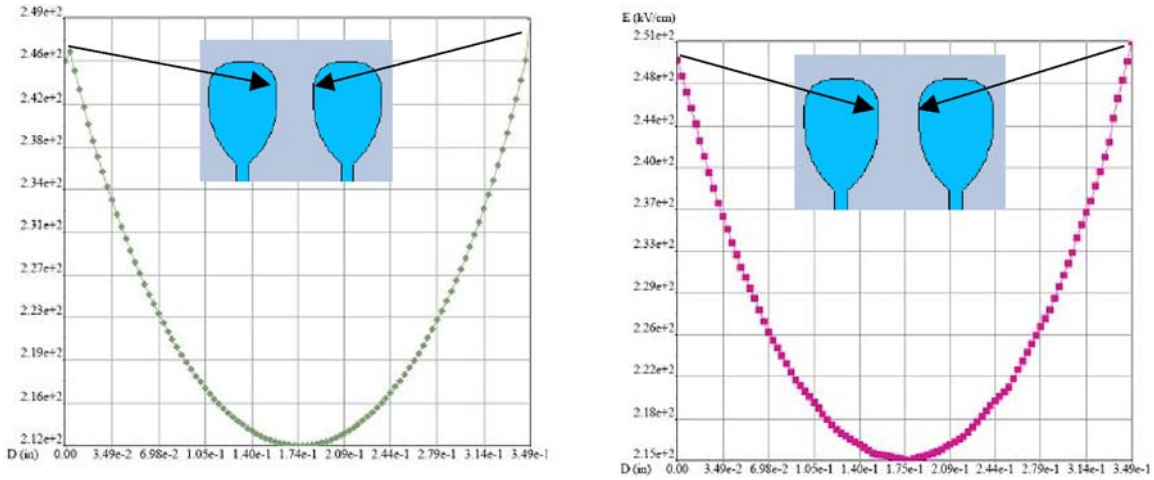

(a) (b)

Figure 35. Electric field along top surface of the dielectric spacer between electrodes.

Single Cascade Gap Switch Studies

The test chamber modeled above was fabricated to study pulsed breakdown properties of SF_6 in a single cascade gap, incorporating a pair of 4.5-inch-diameter symmetrical, toroidal electrodes along with dielectric spacer (puck), supplied by Sandia. The test chamber body uses an acrylic trigger housing provided by Sandia. Figure 36 shows the assembled test cell.

In order to study the pulse breakdown characteristics of the single gap, a Marx pulse generator has been developed. This 10-stage generator has a total erected capacitance of 8 nF and is configured to deliver high-voltage pulses with magnitudes up to 750 kV with a rise time of a few tens of ns. To satisfy the voltage rise and fall time conditions observed in Sandia experiments, the Marx generator has been modified. Using an additional Resistor-Capacitor (RC) circuit the voltage rise time has been increased to ~1 μs, which is close to the Sandia experimental parameters.

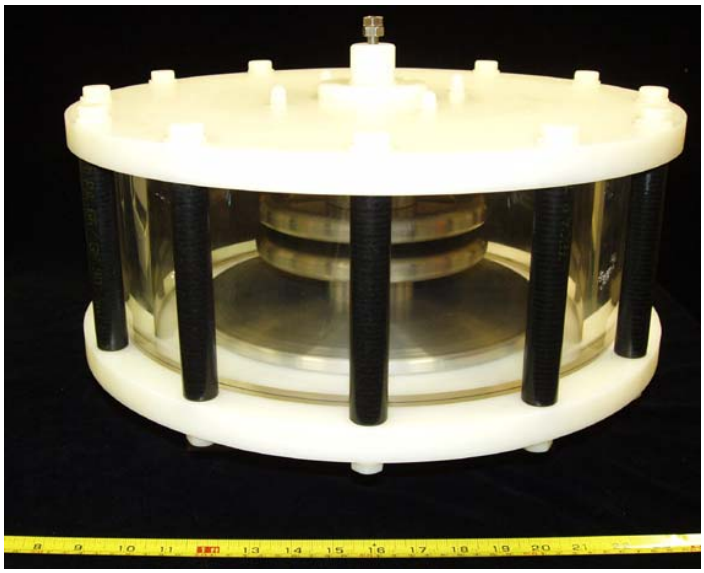

Figure 36. The photograph of the test cell.

Initiation of the Discharge in the Cascade Section

The laser-triggered gas switch consists of two sections. A gas discharge in the first section is initiated by a laser pulse; this causes the second cascade stage to become overvolted which results in subsequent breakdown of the cascade gaps, thereby effecting switch closure. It was indicated by Sandia that overvolting is one of the main mechanisms of discharge initiation in the cascade section. The switch is designed such that the nominal fields in the cascade gaps are ~250 kV/cm. When the trigger section closes, the fields on the first few cascade sections can increase significantly. Understanding the mechanisms by which discharges are initiated could lead to improvements in the LTGS design and operation.

It is clear that initiation of the discharge in the first stage of the switch occurs due to the dissipation of laser energy in the gas. In the case of the cascade section of the switch, there are several possible initiation mechanisms for the discharge. The discharge could be triggered in the gas by existing free electrons or ions that are subjected to the increased field occurring in the cascade sections. Free electrons can be created through the action of UV photons. These photons could be produced by the operation of the first section of the switch or by local partial flashovers in the cascade section. This may cause electron liberation through photoemission (cathode) or photo-ionization (in the gas). Finally, an electron avalanche could be initiated directly through field emission from the cascade electrode cathode surfaces.

Red arrows on Figure 37 shows potential sites for the emission of UV photons from the internal edges of the dielectric spacer. These photons could be generated by local discharges at the edge of the hole in the internal dielectric spacer. The electric field enhancement at the inner edge of the hole in the dielectric can be as high as ~160 kV/cm, which could be responsible for this. Such high values of the electric field may potentially lead to local breakdowns and play a noticeable role in initiation of the breakdown across the cascade gap at the points A and B through photoemission and photoionization.

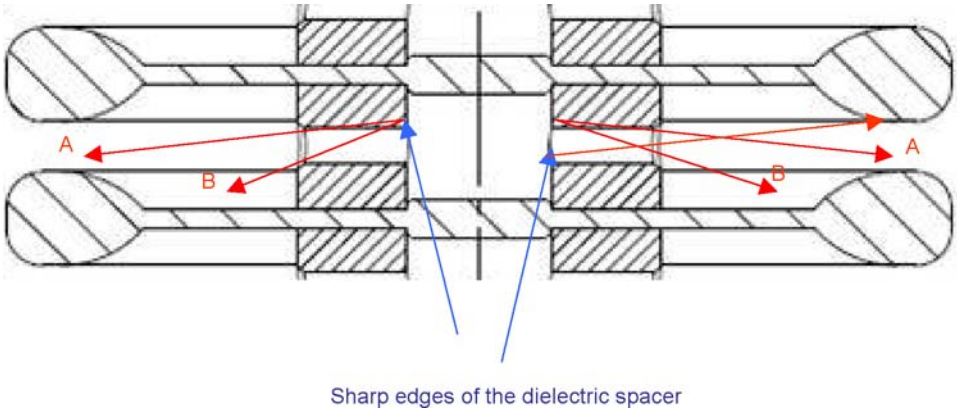

Figure 37. Potential emission of photons from the edges of dielectric spacer into inter-electrode gap.

If the laser-triggered section is “line of sight” blind from the cascade gaps, then photoemission and photoionization from the laser section can be ruled out as the source for initiatory electron production in the cascade section. This therefore means that free electrons from background radiation, field emission from the cascade electrodes, or photons from local flashovers are the only electron sources. The background ion-pair production rate (2 to 20 ion pairs per cc per sec) coupled with the short window of opportunity make it unlikely that a free electron will be produced in the switch gas volume due to background radiation at a time immediately following closure of the laser gap. The problems of local discharges within the gap due to the spacer configuration can be addressed by modifying its design to reduce the local field enhancements. This would leave field emission as the only source of initiatory electron production. Even though the gap breakdown mechanism is described as overvolting, there must be a production mechanism for the initiatory electrons. Field emission occurs for electric fields above 100 kV/cm. If the field on the electrodes is similar to the gas field, which is retained to a level below 250 kV/cm, then field emission must be considered. The big question is “not if, but when” does this start.

In addition, field emission may have already commenced before laser triggering and the rapid acceleration of existing ionization processes is subsequently influenced (accelerated) following the closure of the laser gap due to enhanced overvolting. Alternatively, the temporal statistics of field induced electron emission may be such that the cascade gaps are “silent” until laser gap closure, at which point the enhanced field causes spontaneous electron emission from the cascade electrodes (possibly from multiple sites, causing multi-channeling) leading to breakdown. It would therefore be useful to consider how the field emission process could be controlled to ensure better switch performance, or at least an increased understanding.

Unidirectional Electrodes

If the initiatory electron production does occur through field emission, then there is no advantage in using symmetrical cascade electrodes. Non-symmetrical floating “toroidal” electrodes as shown in Figure 38(b) will reduce the field enhancement at the negative electrodes and reduce field emission. This approach may allow the performance of the cascade section to be improved.

Non-symmetrical unidirectional electrodes will provide a field profile that influences electron production through field emission. It has been shown that the breakdown voltage for a system with a protrusion on a flat electrode surface behaves differently for negative and positive pulses. Figure 38 shows the electrode configuration considered in this paper with a hemispherical protrusion on the top electrode.

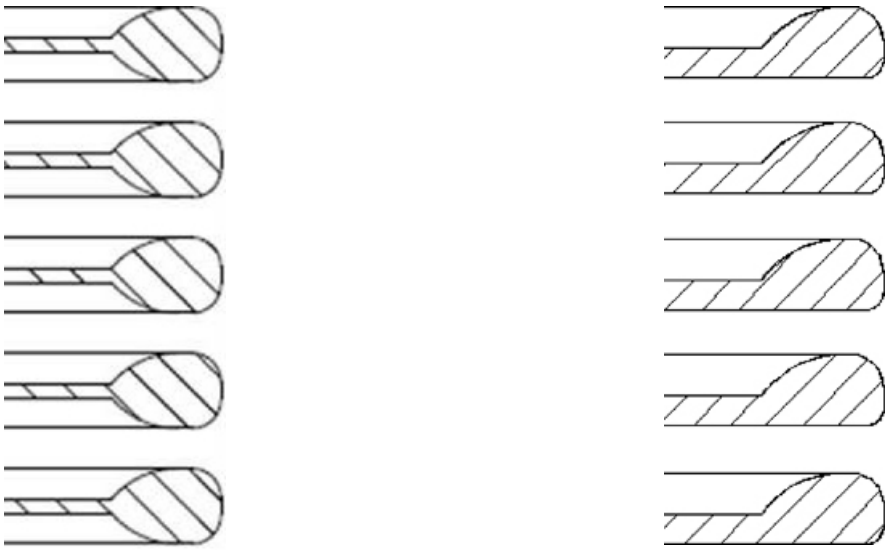

(a) (b)

Figure 38. (a) Cross-section view of the Sandia symmetrical toroidal cascade electrodes; (b) conceptual design of the unidirectional cascade electrodes.

When positive pulses are applied to the gap, electron emission occurs from the flat electrode without a protrusion. The field near the flat electrode is not significantly affected by the presence of the protrusion on the opposite electrode, and therefore for positive pulses the breakdown voltage will be very similar to the breakdown field for a pair of flat electrodes and will not be significantly affected by the size of the protrusion. Therefore there are advantages in designing an electrode system where the electrodes on the negative sides of the gap are flat, with protrusions on the electrodes on the positive side of the gap. This will allow the switch to be operated at higher pressures without the saturation effect on breakdown voltage occurring. This would make it possible to operate the cascade gaps at higher fields without breakdown before the operation of the laser-triggered section. A possible approach to reduce the probability of misfires in the cascade section is to reduce field emission from undesirable locations; this could be achieved by coating such regions of the cascade electrodes with an appropriate dielectric layer. This dielectric coating would minimize the electron emission from problematic areas such as triple points and reduces the effective area of the electrodes (Area Effect). Therefore, the probability of the discharge initiation from the uncovered electrode areas would be increased, allowing improved control of the cascade switch operation. The study of potential dielectric coatings for the electrodes is in progress.

Analysis of Shock Wave Action

In order to model the effects of shock waves on the insulator housing to the cascade section, it was proposed to manufacture a system for generating such shock waves in close proximity to samples of the housing material. The simplest method is to generate the shock waves in water using electrical discharges between two point-to-point electrodes or via a wire-guided discharge.

The discharge in water results in an efficient transfer of electrical energy to acoustic energy and the subsequent transfer of that energy to the insulator surface.

A test system has been developed to allow point-point electrodes or thin conductive wires to be located on the dielectric surface to explore shock wave effects. This test system was used to generate 80-mm wire-guided discharges. This arrangement causes the development of high-power ultrasound (HPU) pulses that impact on a section of the surface of the switch housing and allows the mechanical processes, which occur when the main switch housing flashes, to be simulated at relatively low voltages and energies.

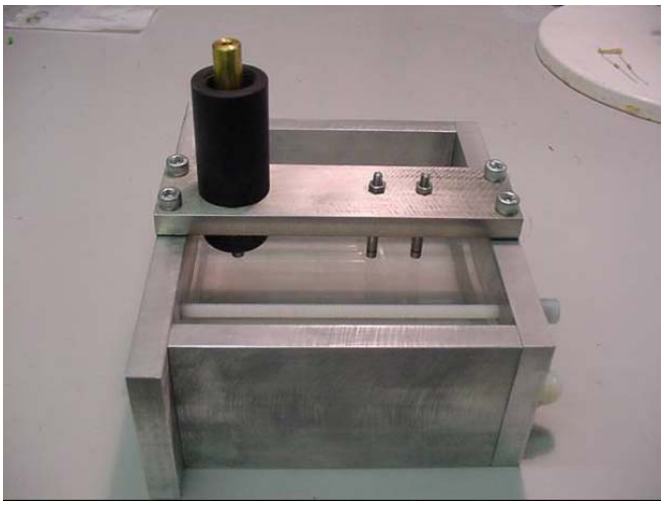

Figure 38. Photograph of the test frame with a section of the dielectric material.

A piece from the damaged insulation received from Sandia has been cut into sections and used to study the potential damage that shock pressure pulses could inflict on the dielectric body. In a preliminary series of the tests, the HPU pulses have been generated by relatively low-energy wire-guided spark discharges near the surface of the acrylic insulator. The distance between the wire and the acrylic surface was a few millimetres. In total 35 single shots were fired, with an exploding wire between the electrodes. Upon examination, the surface of the sample was not observed to have been damaged by the wire-guided spark discharges.

In the second series of HPU tests higher pulse energies (up to 900 J) have been used. The sections of the switch housing received from Sandia have been used in the tests. A 900-J pulse shattered the housing section. Tests with lower energies (340 to 717 J) provided clear evidence of fracturing in the acrylic sample similar to that observed in the original Sandia samples but to a much lesser extent. Two symmetrical lines on the insulator surface indicate small fractures have been produced by the acoustic wave. Energies of 300 to 900 J are currently being investigated and multiple HPU pulses will be applied to the housing parts.

Surface Conductivity Measurements on the Acrylic Switch Housing

The surface conductivity of the acrylic switch housing may have a significant impact on its flashover behavior. An experimental system to measure the surface conductivity of the housing of the laser-triggered gap is currently being developed and tested. Once the design parameters and the performance of this equipment has been established it will be used to establish the effects of the various processing and cleaning techniques used on the switch housing have on its surface conductivity.

For surface conductivity measurements to be meaningful it is necessary to design the measurement system so that the electric field applied to the sample is close to parallel to the surface of the sample. It is also necessary to design the measurement electrodes to ensure that the current-sensing electrode only detects the current that has passed along the surface of the sample and does not detect any current that has passed through the bulk of the sample. In addition, it is important that the field in the region of the electrodes is as uniform and parallel to the surface as possible to avoid high fields that can result in charge injection. In the case of the LTGS switch housing, this is made more complicated due to its cylindrical geometry.

The first requirement can be met by designing the current-sensing electrode such that this consists of a thin plate, surrounded by a larger electrode that acts as a guard ring. This concept is shown in Figure 40.

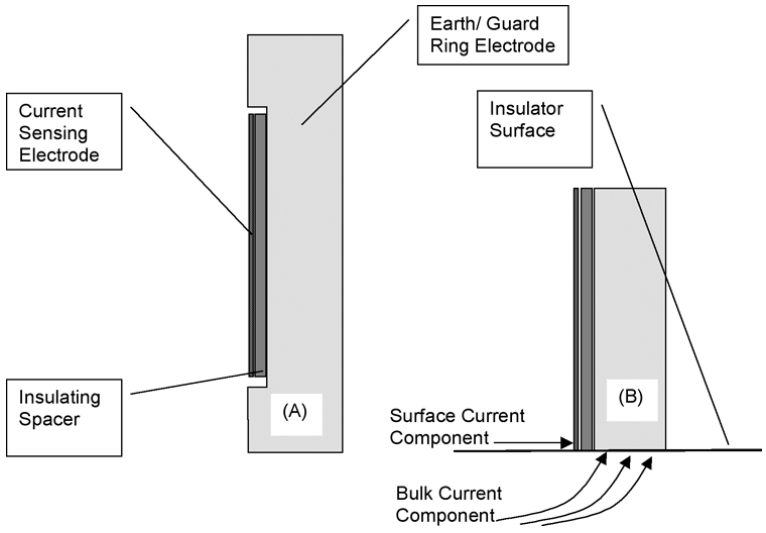

Figure 40. Surface current-sensing electrode.
(A) View from above the electrode system.
(B) Cross section showing current paths.

The thin current-sensing electrode presents a very small cross-sectional area to the surface of the dielectric so that this electrode collects a small proportion of the bulk current. The design of the earth/guard ring electrode ensures that the field in the region close to the sensing electrode will be close to uniform. The insulating layer prevents current flow between the guard and the

sensing electrodes. In operation the potential of the sensing electrode will be controlled to ensure that it is at the same potential as the guard electrode.

Field Across Surface of the Housing

In the Sandia switch, housing surface conductivity measurements are made more complex by the curvature of the surface and the thickness of the insulator housing. This complicates the design of the electrodes required to ensure that the electric field is parallel to the surface of the insulator. This has been addressed by using electrodes with surfaces normal to the insulator, and by having pairs of electrodes on the outer and inner surfaces of the sample.

To confirm that the proposed measurement system produces the field configuration required, field plots have been obtained for the electrode/insulator geometry using the QuickField two-dimensional finite element analysis package. Two pairs of radial electrodes (high-voltage (HV) and grounded) have been located on both sides of the curved section of the dielectric as shown in Figure 41. The end surface of the polymer has been set to the potential of the adjacent electrode. The equipotential between the electrodes is normal to the insulator surface with the field lines inside the dielectric following the curvature of the acrylic switch housing section. The normal component of the electric field across the air/dielectric interface will be a minimum and any charge flowing in the surface region will remain on the surface. In addition, volume conductivity is significantly smaller than surface conductivity so that the current measured is due to surface conduction processes. There is some distortion in the region of the electrode but this is small compared with other electrode configurations.

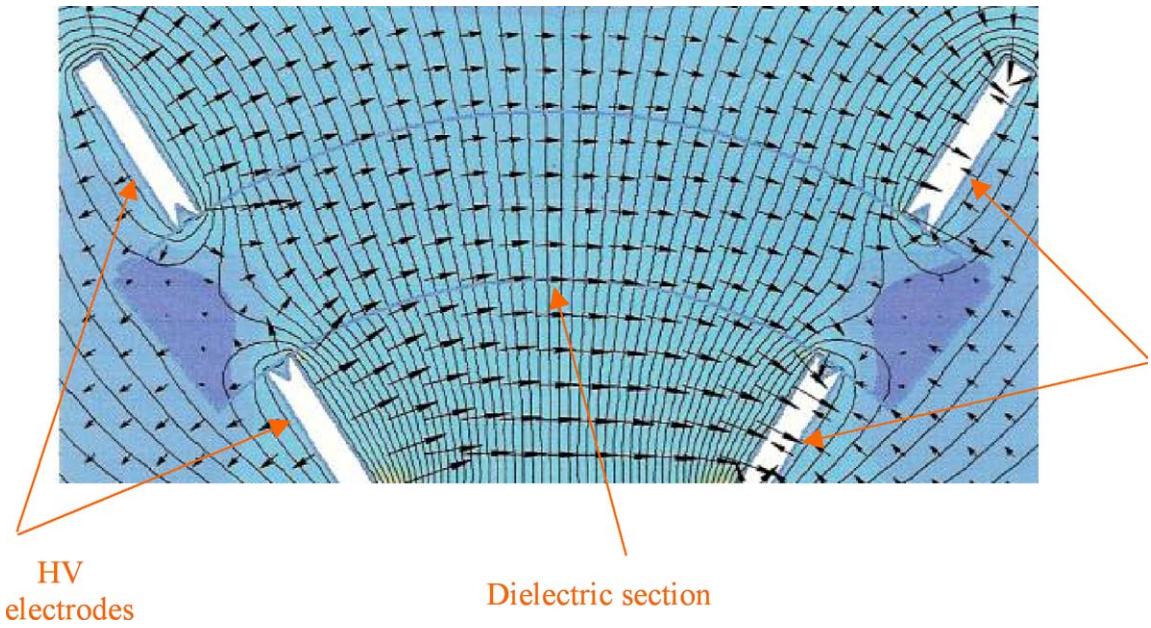

Figure 41. Field distribution in the section of the acrylic insulator. Sharp edge electrodes.

More information is available on the University of Strathclyde activities in the appendices.

Texas Tech University

Before the start of the LTGS program, Texas Tech was working with Sandia on surface breakdown in atmospheric nitrogen. Researchers found distinct differences in the flashover path for air and pure N_2 at 1 atm pressure, as shown in Figures 42 and 43.[23] Close to 100% of the discharges in air would follow the surface instead of the electric field lines, while roughly 80% of the discharges in N_2 would follow the electric field lines and lift off the surface. However, with the application of external UV light to the surface, the flashover path is easily forced to the surface in N_2 as well. Further, the breakdown delay time is reduced due to the UV solely applied to the surface either in air or N_2. This is a clear indication of the importance of photoelectric emission (UV photons release electrons from the surface) providing seed electrons for flashover/breakdown development.

It should be noted that the required light intensity affecting the flashover path is small, minimum ~ 0.3 μW/cm^2. Additionally, only the wavelength regime below ~ 320 nm has a clear impact on the flashover path. It should also be noted that under LTGS conditions SF_6 is transparent only for wavelengths above 160 nm, which reveals that the interesting wavelength regime extends from 160 nm to 320 nm in SF_6 surface flashover. This is observed in both pulsed and direct current excitations, provided conditions are dry.

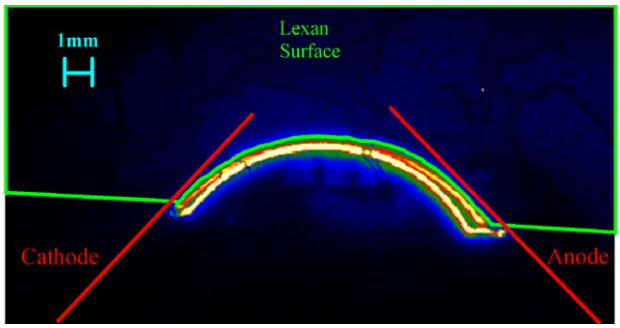

Figure 42. Side-on image of main breakdown in air with groove, 12-mm gap. Breakdown Voltage, Vb = 25 kV.

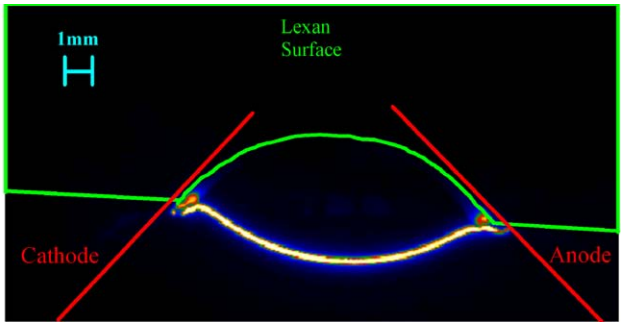

Figure 43. Side-on image of main breakdown in nitrogen with groove, 12-mm gap. Breakdown Voltage, Vb = 23.8 kV.

In the following sections, experimental results of pulsed surface flashover across different dielectric materials in SF_6 primarily at atmospheric pressure (60 μC transferred) as well as flashover and volume breakdown in SF_6 at pressures from 10 Torr to 40 psig (21.6 μC transferred) are presented. Besides fast voltage and current monitoring of the breakdown event, an increased emphasis was put on imaging the event as well as gathering optical emission spectra (~200 nm to 700 nm) from it. The role of UV emission due to a volume SF_6 arc as a potentially flashover hold-off reducing cause is discussed. As much as possible, the small-scale experiments were designed to reproduce at least partly the conditions as they are found in the large 5 MV Z switch.

Optical Emission Spectroscopy

In order to help determine some of the processes contributing to the flashover, a spectrograph is utilized to analyze the emissions from the discharge. This spectrograph has toroidal mirrors designed to allow multiple vertical points, or fiber optic inputs, to be diffracted at one time. This feature is used to collect spectra from multiple points along the discharge path, shown in Figure 44, using cylindrical quartz lenses to focus optical light emission from three rectangular areas between the electrodes into three fiber optic cables leading back to the spectrograph. In this way spatially resolved emission can be collected.

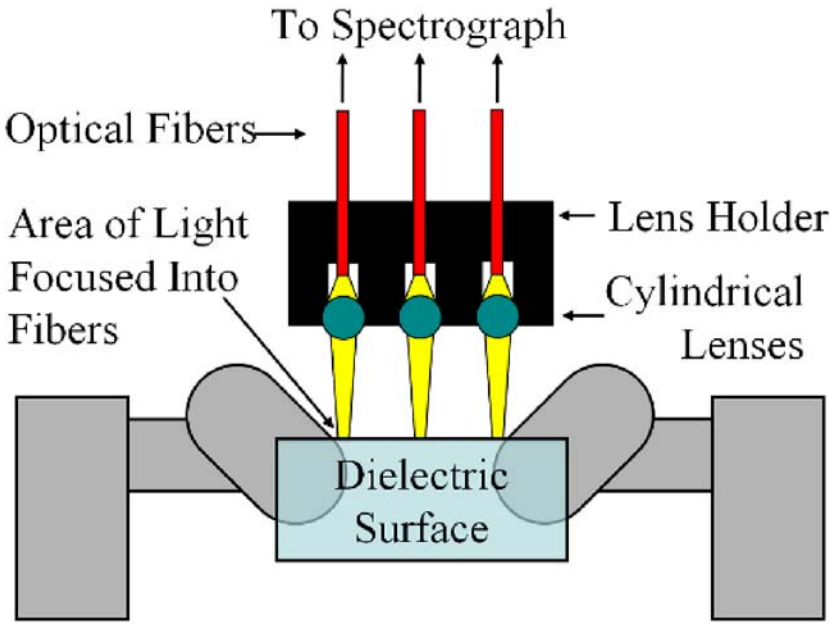

Figure 44. Cross section of the optical emission collection apparatus.

Utilizing absorption cross-section data available in the literature, the resulting transmission for the switch conditions, d = 2.75 inches, n corresponding to 40 psig of gas, reveals that light above 160 nm is easily transmitted in an SF_6 atmosphere, while this limit is roughly 180 nm for molecular oxygen. Hence, it should be assumed that virtually all light between 165 and 800 nm is transmitted easily through 2.75 inches of SF_6 at 40 psig. While the above clearly shows that

UV/vacuum ultraviolet (VUV) light can easily propagate in the conditions found in the Rimfire switch, experimental optical emission spectra of SF_6 discharges need to confirm that light in the relevant wavelength range ($\lambda < 320$ nm) is actually generated during switching.

Surface Flashover Testing

For each of the materials tested (Lexan, Rexolite, Teflon, Epox 826, High-Density Polyethylene, and Plexiglas (PMMA)), three different surface geometries were tested. The surface geometries were: Smooth, surface is one that was not altered or machined except for the electrode slots; Rough, surface was sanded with fine grit sandpaper to create micro protrusions on the surface; and Grooved, a dielectric sample having a groove machined along the surface of the sample. Although considerable effort went into creating uniformity in each sample and surface type, the machining of the groove depth varied slightly. This variation, although slight, showed an effect on the behavior of the flashover.

Material Flashover Analysis

The flashover analysis process consisted of many steps. One of the first steps that allowed us to obtain information on the flashover behavior was the data recorded from the intensified charge-coupled device (ICCD) camera. The images taken during the flashover event were angled on the surface of the dielectric such that the path of the event could be seen (see Figures 45 through 47). This proved important in the investigation of whether the flashover event followed the electric field lines or the surface of the dielectric. The results of the liftoff occurrences for each dielectric material are listed in the following section. In Figures 45 and 46, images of Teflon are shown because of its high percentage of liftoff occurrences. An interesting observation was that although it can be seen that Teflon flashover did follow the surface for some instances and distances, the flashover did not leave visible tracking on the surface. Even under scanning electron microscopy (SEM) imaging, surface distortions or abnormalities could not be detected.

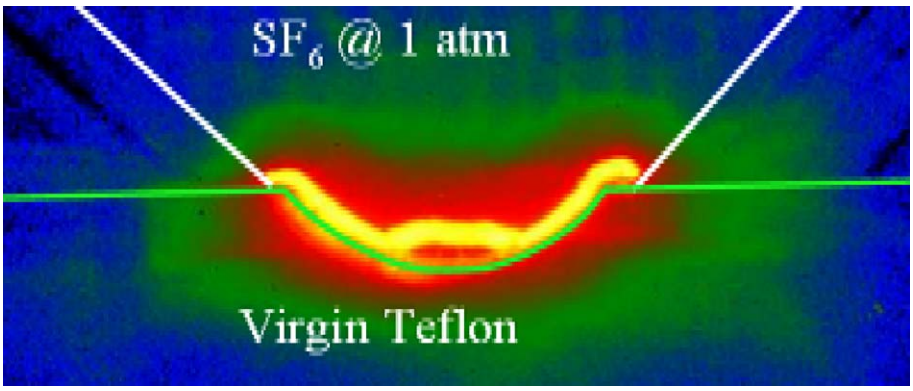

Figure 45. Grooved virgin Teflon sample at 1 atm of SF_6. Gap = 10.53 mm, T_{delay} = 92 ns, V_{pulse} = ~91 kV.

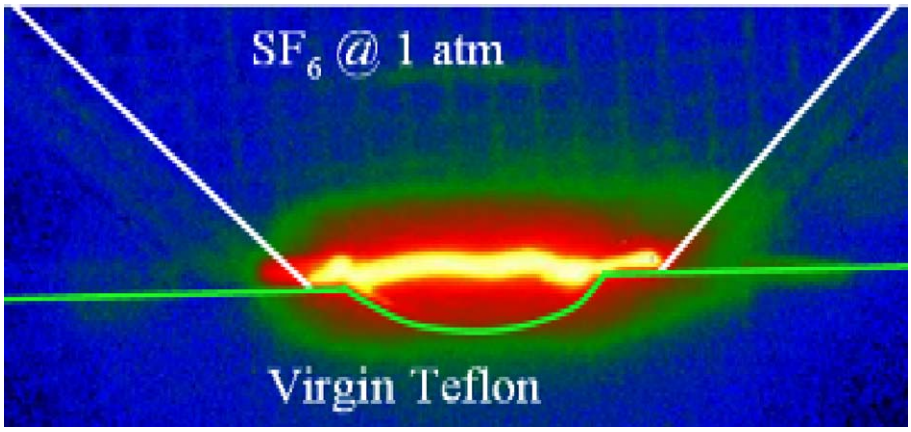

Figure 46. Grooved virgin Teflon sample at 1 atm of SF_6. Gap = 9.48 mm, T_{delay} = 307.3 ns, V_{pulse} = ~90 kV.

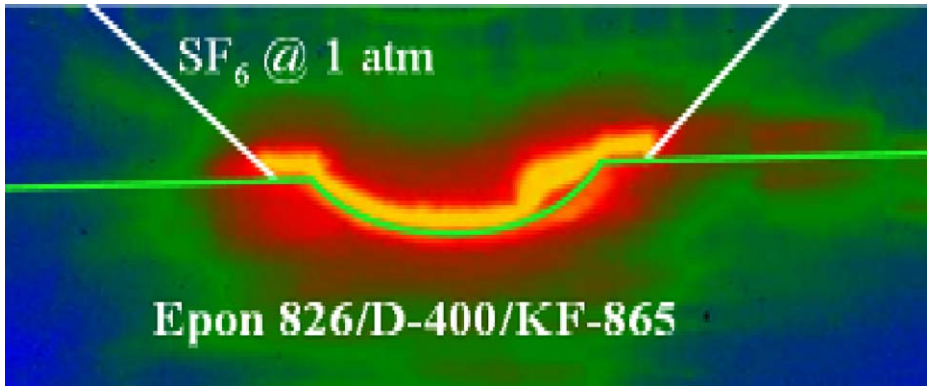

Figure 47. Grooved Epon 826/D-400/KF-865 sample at 1 atm of SF_6. Gap = 10.8 mm, T_{delay} = 50 ns, V_{pulse} = ~69 kV.

Material Comparisons

When a material flashes over a surface, the discharge usually, but not always, travels along the interface, as shown in Figure 47. The phenomena can be used to discriminate between materials by comparing the percentage of "liftoffs" for the total samples of that material. Table 1 gives the dielectric material comparisons of liftoff during a flashover event. Figure 48 shows a dielectric material comparison of average time delays.

Table 1. Dielectric material comparisons of liftoff during a flashover event. Each of the dielectric samples was flashed typically 10 times.

Material	Liftoff Percentage	Number of Samples	Permittivity	Comments
Teflon	50%	12	2-2.1	Partial liftoff (Grooved samples)
Lexan	0%	11	3	
HDP	0%	1	2.26@ 1Mhz	
Rexolite	0%	1	2.53 through 500 Ghz	
Plexiglas	50%	1	2.2-3.4	Very partial liftoff (Grooved sample)
Epon 826/T-403	13%	4	~5	Partial liftoff (Grooved samples)
826/D400/KF-865	18 %	3	~5	Partial liftoff (Grooved samples)

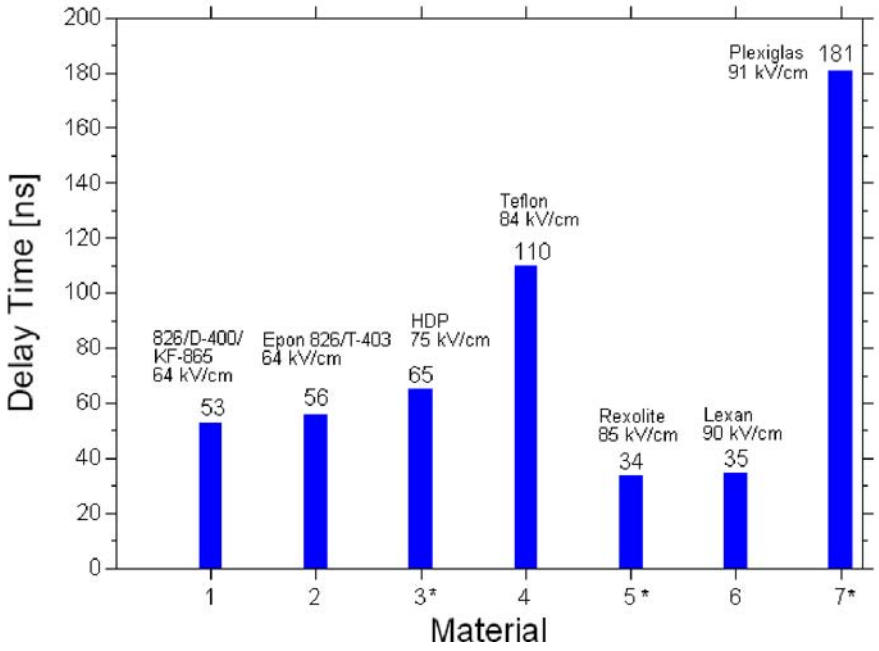

Figure 48. Dielectric material comparison of average time delays. Samples arranged by field strength (asterisk indicates one sample only tested).

Post-Flashover Analysis

In order to better understand the effects of flashover on the dielectric material, several dielectric samples underwent a postmortem imaging analysis at the Texas Tech University Imaging Center. First, each dielectric was imaged and photographed using a stereoscopic microscope. This process enables verifying if visible damage could be seen on the surface of the material. The second step was to utilize SEM to view the surface of the material and compare the images to the stereoscope. The third step was to use X-ray spectroscopy to identify elements on the surface of

the dielectric. This has the potential to give some insight into interactions between the arc, gas, and the dielectric.

The scanning electron microscope was utilized to obtain a closer view of the damage caused by the flashover. Although SEM can be used for obtaining topography, morphology, composition, and crystallographic information, the main utilization was on topography and composition. Through topography, images of the surface damage were obtained and compared to those of light microscopes. It should be noted that the employed scanning electron microscope imaging does not show what is on the surface, but rather what lies just below the surface. Typically when an area becomes charged, that is when the scanning electron microscope negatively charges an area, the image becomes brighter, but where the flashover path boundaries are black region is not expelling electrons. Speculation could be made that a positive charge is being left behind after surface flashover, or that there is a difference in the material.

A Lexan that underwent 40 flashovers was analyzed in detail. Flashover occurred five times at each of the following pressures: 10 Torr, 20 Torr, 50 Torr, 100 Torr, 250 Torr, 680 Torr, 20 psig, and 40 psig. This sample exhibited some cracking, which is only visible in the flashover region. Also, since changes in the structure of the material will show up in the scanning electron microscope images as well, it could be speculated that the internal cracking and discoloration of the material is due to a change in the composition of the material.

After obtaining images from the scanning electron microscope, X-ray spectroscopy analysis was performed on the sample surfaces (see Figure 49). Typically, the difficulty of the analysis spawns mainly from finding a suitable representative location or object to perform the analysis. Yet after obtaining scanning electron microscope images, a random pattern of white flakes could be seen on the surfaces. After performing the X-ray spectroscopy on some random white flakes, it was found that the flakes were comprised of sulfur (Figure 50). These arc by-products were found for all dielectric materials tested, although in some of the materials sulfur spheres were found rather than flakes.

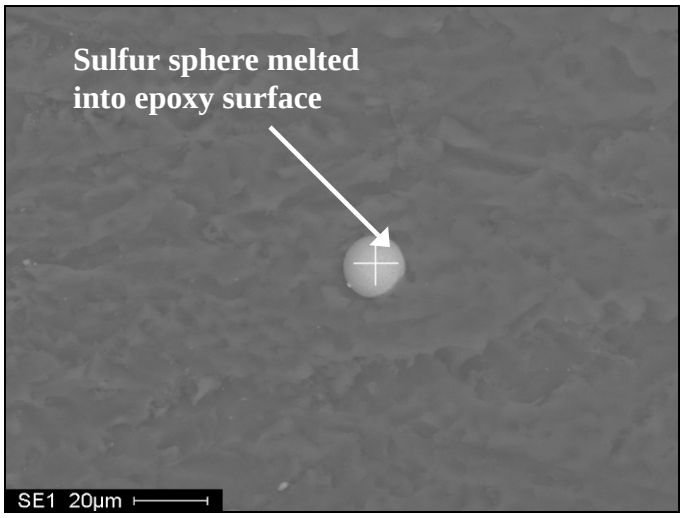

Figure 49. Scanning electron microscope image from dielectric material 826/D400/KF-865 used for X-ray spectroscopy analysis (1 atm SF_6, 30 µC).

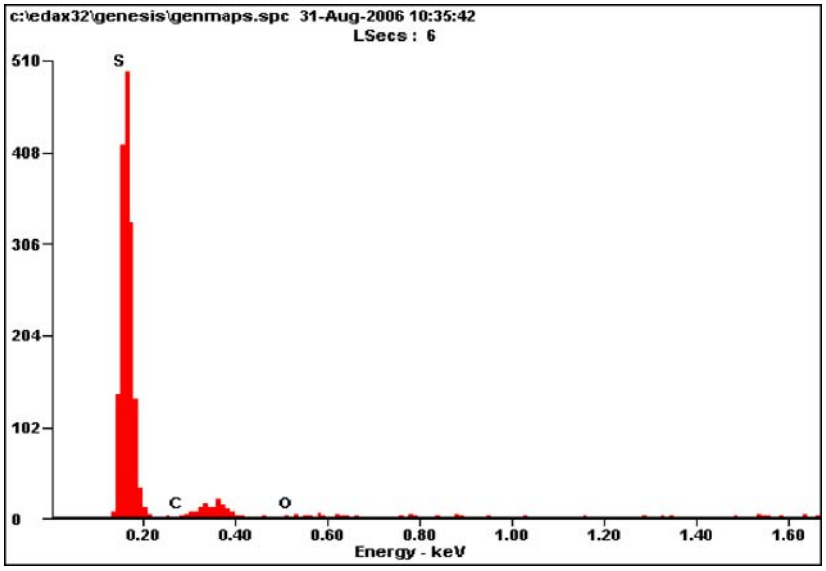

Figure 50. X-ray spectroscopy results for crosshair location in Figure 49. X-ray spectroscopy indicates sulfur deposit.

Optical Emission Spectra, Surface Flashover

Optical spectra were collected from three points along the arc channel as described above. The first lens collects optical emissions from just in front of the of the excitation electrode, the second observes the middle of the gap, and the third observes just in front of the grounded electrode. Figure 51 shows several of the peaks that have been identified so far, including sulfur, fluorine, hydrogen, and carbon. The carbon and hydrogen are of particular significance because they indicate the discharge is removing material from the surface and exciting it.

Spectra collected from three points along the discharge path are in general very consistent over the length of the gap. One notable difference is the increased UV content just in front of the charging electrode. Typically, metal lines would be present in the regions near the electrodes; however, in this case the Marx generator is unable to provide sufficient current to erode the stainless steel electrodes. This is further supported by the lack of significant damage to the electrodes after repeated firing. In addition to the distinct peaks, there is a broadband contribution to the spectra as well. This broad signature becomes more and more pronounced at higher pressures, where the discharge is more intense and as a minimum pressure broadened. At higher pressures the carbon line is dominant, which could be due to a more constricted arc channel, or the increased gas/ion temperature of the discharge. The more intense discharge is able to effectively remove the carbon from the surface and excite it.

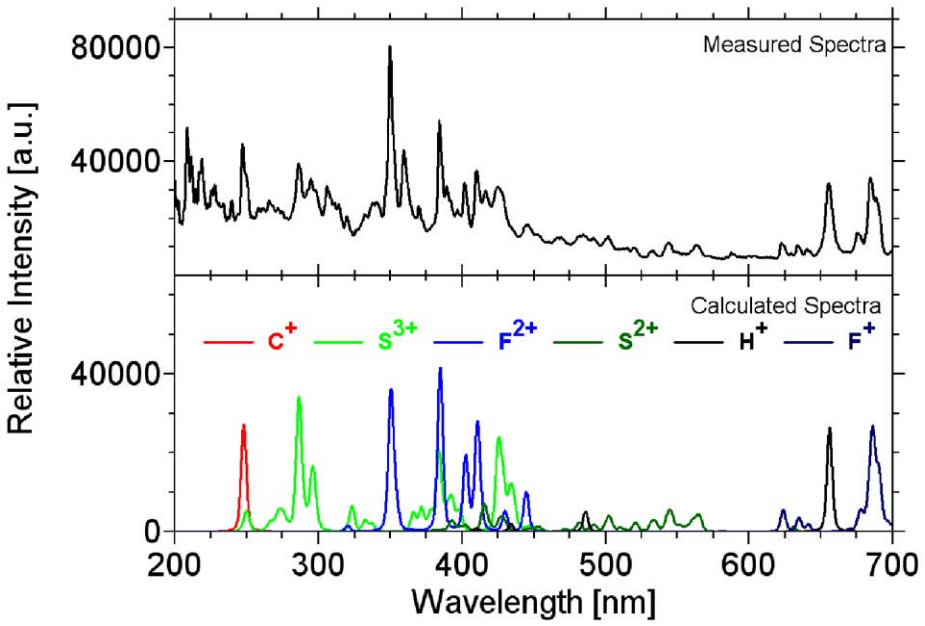

Figure 51. Spectra peak identification using calculated atomic spectra. Measured spectra collected in SF_6 environment, across a polycarbonate sample, at 50 torr. The calculated spectra is given for an temperature of 30,000 K.

SF_6 Volume Breakdown, 10 torr to 40 psig

Spectra line identification as shown in Figures 52 through 54 indicates three important differences in optical emissions of surface flashover across polycarbonate and that of volume breakdown. The first is the lack of carbon and hydrogen lines, which tends to support the initial conclusion that they were the result of damage to the surface. The second is the absence of some of the sulfur and fluorine lines, which were initially assumed to be a result of the dissociation of the SF_6 gas in the environment. Their absence in volume breakdown could indicate that they were a result of damage to the polycarbonate surface, which contains both elements. Finally, there is the presence of nitrogen lines, which is likely due to small leak in the system at the time, allowing small amounts of air into the chamber. It should be noted that previous research under controlled mixing conditions has revealed that small amounts of nitrogen (few percent) in SF_6 already show up prominently in the emission spectrum of a spark. Looking at the intensity of the lines with respect to background reveals that the N_2 lines fade as the pressure increases, disappearing altogether at 500 torr. Obviously, a small leak has lesser consequences at the higher pressures.

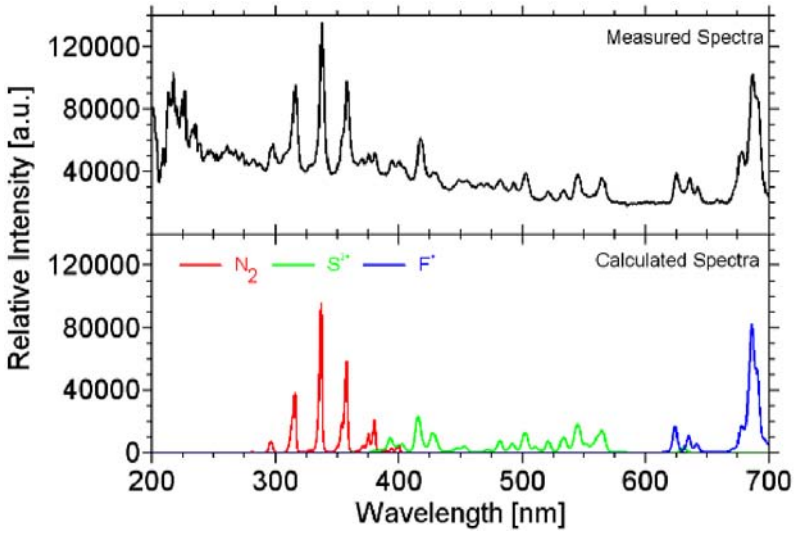

Figure 52. Spectra peak identification using calculated atomic and diatomic spectra. Measured spectra collected in SF_6 environment at 100 torr.

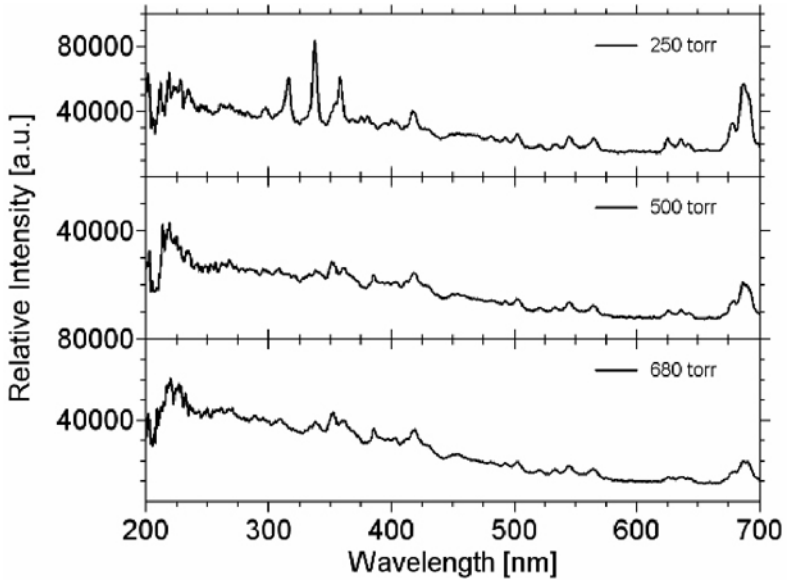

Figure 53. Spectra collected from a volume discharge in SF_6 at various pressures.

Photoemission of electrons by UV photons impacting the envelope is one of the suspected reasons that can initiate the unwanted tracking along the inside envelope surface in the ZR switch. We have quantitatively shown that a significant amount of UV light is produced by both a volume arc and surface flashover in high-pressure SF_6. The more intense light output is in the wavelength regime below 320 nm, a regime that has been identified in previous research as having a distinct effect on the arc path of flashover in atmospheric nitrogen. The majority of species contributing to the observed optical emission spectra between 200 and 700 nm has been identified. While it was possible to estimate the volume arc's electronic temperature (~35,000 K) for the lower pressures (50 torr), the spectra at 40 psig are problematic due to their more broadband features that mask distinct atomic or molecular lines. The differences between volume and surface flashover become apparent in Figure 55.

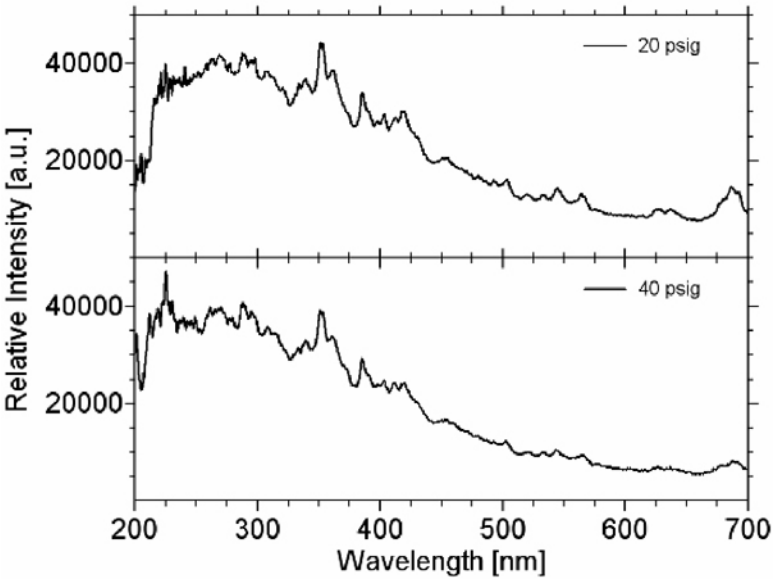

Figure 54. Spectra collected from a volume discharge in SF_6 at various pressures.

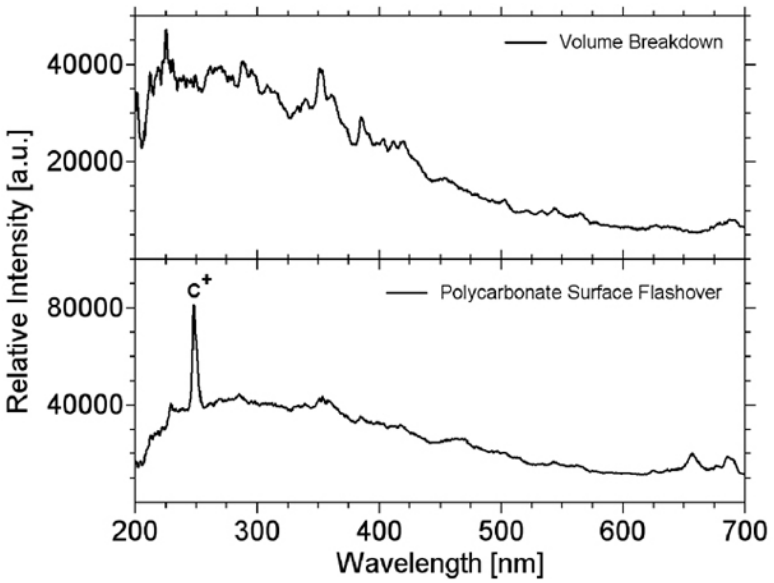

Figure 55. Volume breakdown (top) and surface flashover (bottom) at 40 psig SF_6.

Most prominently, the peak at 250 nm in the surface flashover spectrum is due to singly ionized carbon produced by erosion followed by electron impact ionization and excitation of dielectric material (all tested materials were hydrocarbon-based). The absence of metal lines in any of the observed spectra is a result of the rather low coulomb transfer and low current amplitude (~ 2 kA) in the test setup. It should be assumed that the spectral shape will change with the current amplitude increased into the 100-kA regime in future research. Overall, our results support the hypothesis of UV radiation contributing to the initiation of switch failure.

The breakdown delay time of several dielectric materials was recorded and compared for several dielectric materials with the initial setup limited to 1 atmosphere of SF_6. Most of the materials (Lexan, Teflon, High-Density Polyethylene, Rexolite, Plexiglass) have dielectric constants between ~ 2 to 3, while the Epoxy-based materials fall out of this range with a permittivity of ~ 5. Of all tested materials, Teflon and Plexiglass performed the best, i.e., they exhibited the longest flashover delay time at a given pulsed voltage amplitude. Clear differences in erosion became apparent. For instance, Epoxy and Rexolite exhibited very distinct surface damage. Teflon exhibited the least surface damage, and postmortem surface analysis (40 psig flashover) did not reveal any sulfur deposits. With the recent completion of the high-pressure SF_6 breakdown chamber, it will now be possible to test the diverse materials more rigorously with improved statistics.

Postmortem analysis of surface flashover samples revealed sulfur deposits on the dielectric surface, essentially a layer of sulfur with some sulfur drops. Depending on the material, the deposits were more or less distinct; virtually no sulfur was found on Teflon. The occurrence of sulfur on the dielectric surface is consistent with the more prevalent appearance of sulfur ionic lines in the flashover spectrum (SII and SIII) as compared to the volume breakdown spectra (SII only).

University of Missouri Columbia

The University of Missouri's test stand, MUTTS, was once part of Sandia's Proto machine and contains an LTGS. As part of the LTGS program, it conducted a study of flashover in several atmospheres of SF_6, voltages to 1.5 MV, peak currents of 150 kA, and intermediate store charge times of about 550 ns. MUTTS has the same basic experimental layout as STB, with STB having peak voltage of 4 MV and charge time of 800 ns. However, both machines have similar rates of charge. The MUTTS experiments focus on the importance of parameters like triple point field enhancement, time at high voltage, or t-effective (teff) and UV effects on the insulator. The switch was configured to operate in both self-break and laser-triggered mode and uses the same quadrupled Nd-YAG laser at 266 nm as the LTGSs at Sandia.

At the MUTTS facility, a 4-MV Rimfire LTGS has been modified to test only the trigger gap section of the original switch. The cascade section of the switch has been electrically shorted for the purpose of testing only the trigger gap. Most of the cascade electrodes have been removed so that the cascade section fits in a single switch envelope insulator, as shown in Figure 56. The switch has four field shaping rings surrounding it. Figure 57 shows the electric field along the insulator of the MUTTS switch with 938 kV across the trigger gap and the electric field of a Z_{20} trigger gap. The electric field on the insulator varies less than 4% between the two switches.

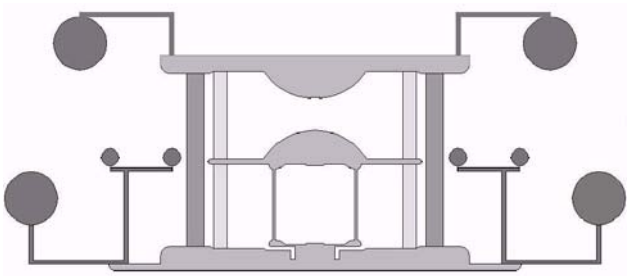

Figure 56. MUTTS trigger gap switch with electric field shaping conductors.

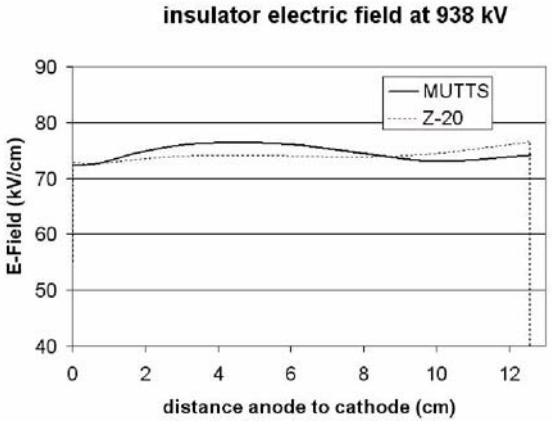

Figure 57. Electric field for MUTTS and Z_{20} along the trigger gap of the switch insulator with 938 kV applied. The electric field varies less than 4% between the two insulators.

Asymmetric Torque

The effect of cantilevering shift on the insulator due to the mounting of the switch was tested. In order to mimic a cantilevered shift on the insulator with a vertically mounted switch, an asymmetric torque was put on the nylon rods holding the switch together. This created a measurable difference in the endplate-to-endplate dimension of the switch. A total of 26 shots were taken on the asymmetrically torqued switch at voltages on the order of 1.25 MV without flashover.

Grooved Insulator

The possibility of flashover caused by small gaps between endplate and insulator was also tested. Field enhancement caused by these gaps is considered to be a possible cause of insulator flashover. Gaps were machined into the insulator in two separate tests. A test consisting of 17 shots and a mean breakdown voltage of 1.31 MV did not result in flashover along the insulator.

An extreme test was conducted in an attempt to induce flashover. An insulator was rigged so that it had a series of gaps, increasing in depth, around the circumference of the switch. This test showed the effect of both very small and very large gaps near the insulator-cathode junction. Figure 58 is a drawing of a section of the multi-grooved insulator, showing the largest and smallest grooves, separated by a section with no groove. The multi-grooved concept was installed on the cathode side of the trigger gap and then on the anode side. Neither set of tests resulted in flashover.

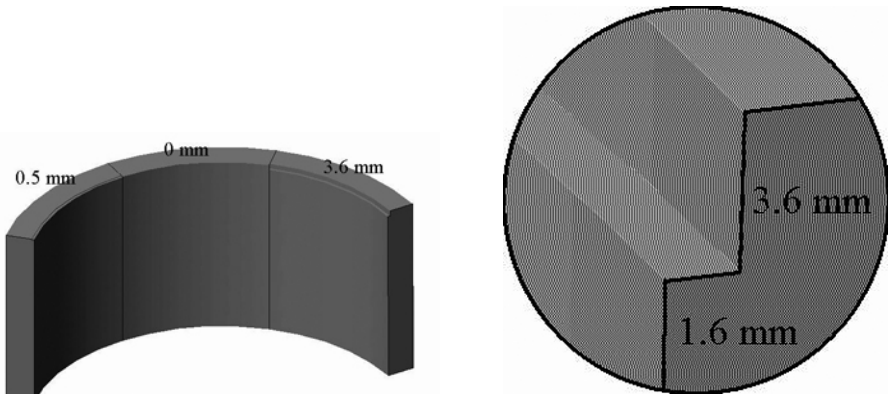

Figure 58. Section of multi-grooved insulator.

Removed Trigger Hemispheres

In an effort to force the insulator to flash, the trigger hemispheres were removed from the endplate and trigger plate of the switch in order to decrease the trigger gap to insulator length ratio. The bronze laser tube was left in place extending 2.54 cm from the anode into the trigger gap. The first shot with this configuration caused an arc to jump from the bronze tube to the cathode plate. A second, less intense arc formed near the insulator, flashing the insulator for the first time. Figure 59(a) shows the switch during operation without the trigger hemispheres with the more intense arc and the less intense flashover and Figure 59(b) shows the switch under normal operating conditions.

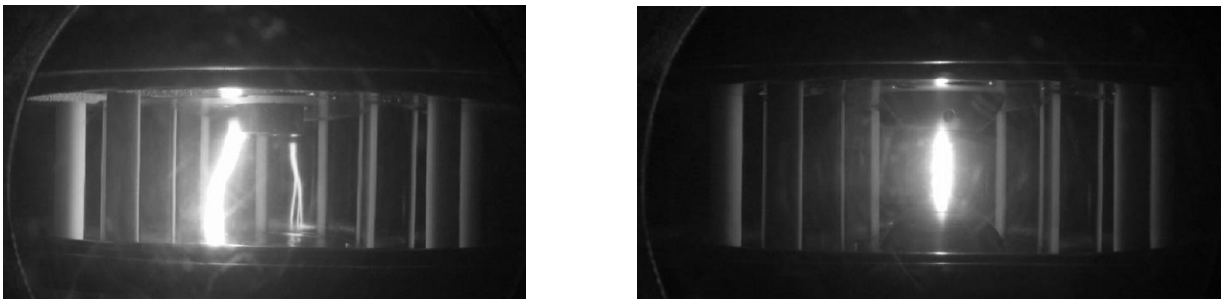

(a) (b)

Figure 59. Shot 212 with trigger hemispheres removed.
The flashover event is less intense than the arc near the switch center.

Increased Teff

Inductance was added between the Marx bank and the I-store to increase the teff on the insulator. The dV/dt on the switch was decreased from 2.9×10^{12} V/s to 2.71×10^{12} V/s. Thirty-five shots were taken with a decreased rate of voltage rise and shots with similar rise times were compared. Figure 60 shows two shots with similar rise times and a different dV/dt.

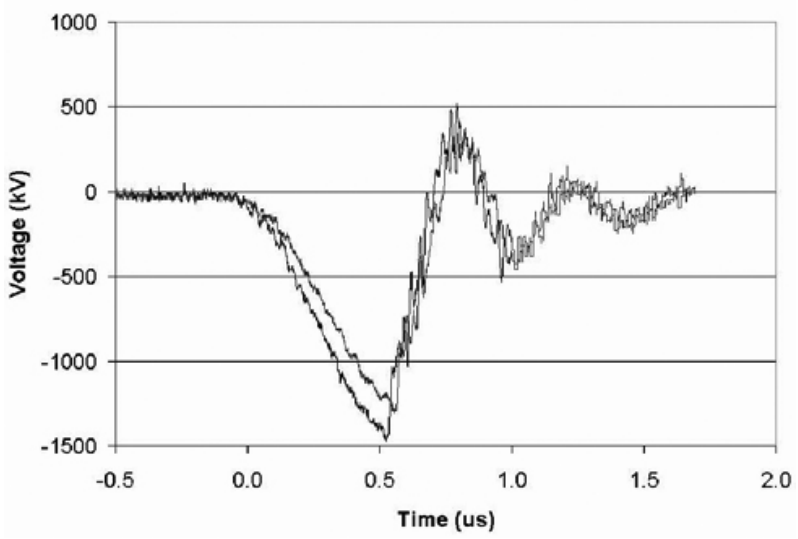

Figure 60. Switch voltages before and after changing teff.

The increased charge time resulted in lower breakdown voltages at a given pressure, as shown in Figure 61, and did not result in flashover. The multi-grooved insulator was shot an additional 20 times with the inductance added to decrease dV/dt; no flashover was observed.

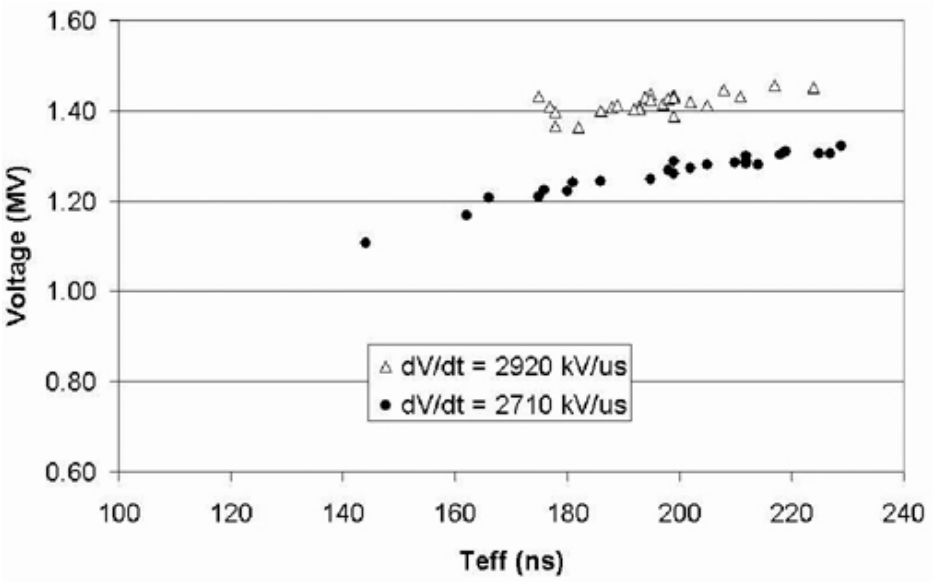

Figure 61. Decreased dV/dt effect on breakdown voltage at 4.40 atm.

Isolated Trigger Hemispheres

To investigate the effect of UV illumination of triple points, a gap was introduced between the cathode trigger hemisphere and the trigger plate with several layers of Kapton tape, resulting in an arc shining directly on the triple point, as shown in Figure 62. The separation allowed an arc to form between the hemisphere and trigger plate. The arc acted as a UV source shining more directly on the triple point. No flashover was observed.

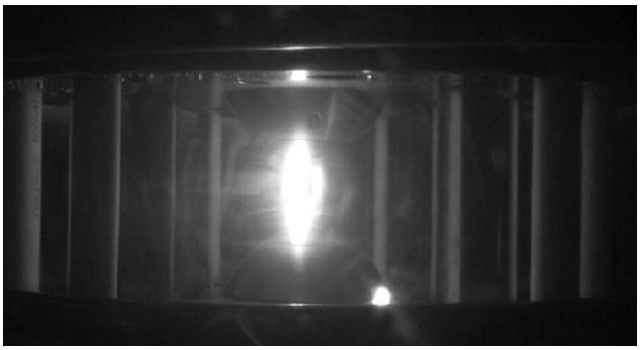

Figure 62. With the trigger plate hemisphere slightly removed from the cathode, a spark forms between the hemisphere and cathode, shining directly on the triple point.

Transmissivity of PMMA

The percentage of UV light transmitted, reflected, and absorbed was measured for samples prepared with various cleaning procedures on a UV-visible spectrophotometer. Three cleaning procedures on PMMA were tested: (1) simply wiped with a lint-free cloth, (2) wiped with hexane using a lint-free cloth, and (3) wiped with Windex using a lint-free cloth. A spectrum ranging from 190 to 1000 nm was taken on the first sample set (three pieces) with all three cleaning procedures. The last two sample sets (six pieces) were scanned at very low speed from 370 to 410 nm to focus on the transmissivity cutoff. Percent transmitted (%T), percent reflected (%R), and absorption were all measured.

PMMA exhibits a distinct cutoff region between 380 and 400 nm. Over this range the %T and %R of light drop nearly 80% while absorption increases dramatically. The PMMA cleaned with hexane exhibits slightly lower %T nearing cutoff. Figure 63 shows the transmissivity near cutoff.

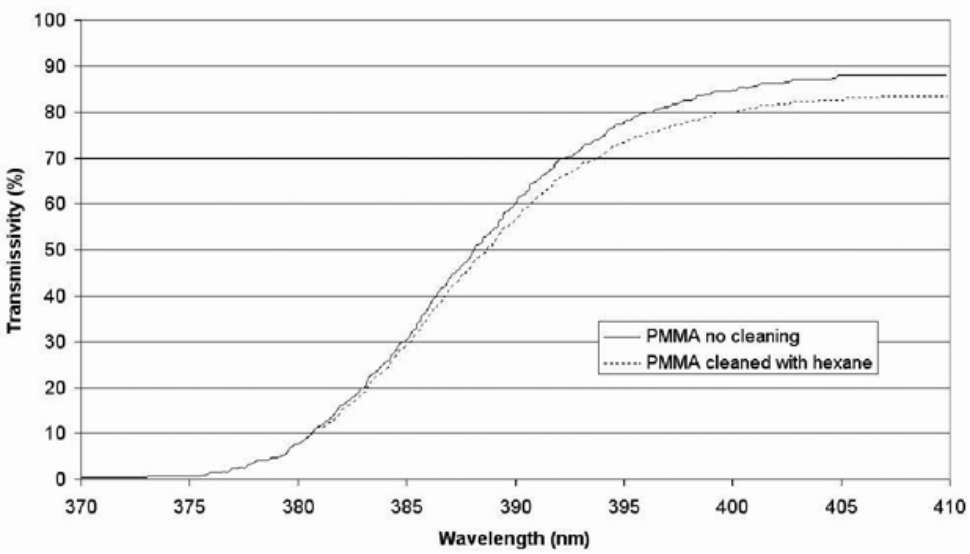

Figure 63. Percent transmitted vs. wavelength through the sample of PMMA.

No sizable difference between %T, %R, and absorption was found for the three cleaning procedures, although hexane appears to absorb slightly more near the cutoff region.

Over 350 shots have now been taken on the trigger gap switch and flashover has occurred on the trigger gap insulator only once, when the switch hemispheres were removed. One of the more interesting observations of this study was that significant triple-point field enhancement did not lead to any flashover events in this configuration. A cantilever effect due to a horizontal switch mount was also not shown to lead to flashover. The experiments also provide some perspective on the relative importance of parameters like triple-point field enhancement and teff. We believe that these experiments will provide some guidance in designing future experiments that directly test the causes and mitigating factors of switch flashover.

REFERENCES

1. E.A. Weinbrect, D.H. McDaniel, and D.D. Bloomquist, The Z Refurbishment Project at Sandia National Laboratories, *Proc. of the IEEE Int. Pulsed Power Conference*, p. 157, Edited by M. Giesselmann and A. Neuber, 2003.

2. D.E. Bliss, R.T. Collins, D.G. Dalton, E.J. Dawson, Jr., R.L. Doty, T.L. Downey, H.C. Harjes, E.A. Illescas, M.D. Knudson, B.A. Lewis, J.A. Mills, S.D. Ploor, J.W. Podsednik, S.T. Rogowski, M.S. Shams, and K.W. Struve, A New Laser Trigger System for Current Pulse Shaping and Jitter Reduction on Z, *Proc. of the IEEE Int. Pulsed Power Conference*, p. 179, Edited by M. Giesselmann and A. Neuber, 2003.

3. T.D. Pointon, H.C. Harjes, M.E. Savage, D.E. Bliss, and R.W. Lemke, Pulse Shaping of the Load Current on the Z Accelerator, *Proc. of the IEEE Int. Pulsed Power Conferenc*e, p. 175, Edited by M. Giesselmann and A. Neuber, 2003.

4. D.L. Smith, M.E. Savage, J.E. Maenchen, D.H. McDaniel, M.J. Slattery, E.A. Weinbrect, D.L. Kitterman and R.L. Starbird, ZR Marx Capacitor Vendor Evaluation Results and Procurement Strategy, *Proc. of the IEEE Int. Pulsed Power Conference*, p. 1205, Edited by M. Giesselmann and A. Neuber, 2003.

5. J.M. Lehr, J.E. Maenchen, J.R. Woodworth, W.A. Johnson, R.S. Coates, L.K. Warne, L.P. Mix, D.L. Johnson, I.D. Smith, J.P. Corley, S.A. Drennan, K.C. Hodge, D.W. Guthrie, J.M. Navarro, and G.S. Sarkisov, Multi-Megavolt Water Breakdown Experiments, *Proc. of the IEEE Int. Pulsed Power Conference*, p. 609, Edited by M. Giesselmann and A. Neuber, 2003.

6. J. Woodworth, J.M. Lehr, P.A. Miller, B. Aragon, J. Elizondo, W. Fowler, J.W. Maenchen, G.S. Sarkisov, J.P. Corley, K. Hodge, S. Drennan, D. Guthrie, G. Mowrer, M. Navarro and D.L. Johnson, Optical Diagnostics of 4-MV Water Switches in the Z_{20} Test Facility, *Proc. of the IEEE Int. Pulsed Power Conference*, p. 167, Edited by M. Giesselmann and A. Neuber, 2003.

7. S.E. Rosenthal, J.M. Elizondo, J.E. Maenchen, K.W. Struve, D.H. McDaniel, J.P. Corley, D.L. Johnson, and B.V. Oliver, Modeling 6-MV Gas Switches for the ZR Accelerator, *Proc. of the IEEE Int. Pulsed Power Conferenc*e, p. 163, Edited by M. Giesselmann and A. Neuber, 2003.

8. J.P. Corley, K.C. Hodge, S.A. Drennan, D.W. Guthrie, J.M. Navarro, D.L. Johnson, J.M. Lehr, S.E. Rosenthal, and J.M. Elizondo, Development/Tests of 6-MV Triggered Gas Switches at SNL, *Proc. of the IEEE Int. Pulsed Power Conference*, p. 875, Edited by M. Giesselmann and A. Neuber, 2003.

9. J.P. Corley, M.A. Dixon, A.A. Kim, B.M. Kovalchuk, V.A. Sinebryukhov, S.N. Volkov, K.C. Hodge, S.A. Drennan, J.M. Navarro, D.L. Johnson, G. Avrillaud, and F. Lassalle, Tests of 6-MV Triggered Switches on APPRM at SNL, *Proc. of the Int. Pulsed Power Conference*, Edited by R. Reinovsky and M. Newton, 2001.

10. J.M. Lehr, D.D. Bloomquist, J.E. Maenchen, J.P. Corley, S.A. Drennan, H.C. Harjes, K.C. Hodge, D. Guthrie, D.L. Johnson, D.H. McDaniel, and K.W. Struve, SATPRo: The System Assessment Test Program for ZR, *Proc. of the IEEE Int. Power Modulator Conference*, 2004.

11. J.B.N. Turman, W.B.S. Moore, J.F. Seamen, F. Morgan, J. Penn, and D.R. Humphreys, Development Tests of a 6 MV, Multistage Gas Switch For PBFA II, *Proceedings of the 4th International Pulsed Power Conference*, pp. 617-619, Albuquerque, NM, 1983.

12. D.R. Humphreys, K.J. Penn, J.S. Cap, R.G. Adams, J.F. Seamen, and B.N. Turman, RIMFIRE: A Six Megavolt Laser-Triggered Gas-Filled Switch For PBFA II, *Proceedings of the 5th International Pulsed Power Conference*, pp. 262-265, 1985.

13. D.D. Bloomquist, G.R. Montry, S.E. Downie, and G.R. Peterson, Cascade Switch Implementation on PBFA I, *Proceedings of the 5th International Pulsed Power Conference*, pp. 266-269, 1985.

14. J.M. Wilson and G.L. Donovan, Laser-Triggered Gas Switch Improvements On PBFA-II, *Proceedings of the 6th International Pulsed Power Conference*, pp. 361-364, 1987.

15. G.J. Denison, J.P. Corley, D.L. Johnson, G.J. Weber, R.A. Hamil, G.W. Crowder, J.A. Alexander, D.A. Petmecky, L.P. Schanwald, and J.J. Ramirez, A High-Voltage Multistage Laser-Triggered Gas Switch, *Proceedings of the 6th International Pulsed Power Conference*, pp. 490-493, 1987.

16. B.N. Turman and D.R. Humphreys, Interstage Closure Times For The Rimfire Multistage Gas Switch, *Proceedings of the 7th International Pulsed Power Conference*, Monterey, CA, pp. 555-558, 1989.

17. G.J. Denison, J.A. Alexander. J.P. Corley, D.L. Johnson, K.C. Hodge. M.M. Manzanares, G. Weber, R.A. Hamil. L.P. Schanwald, and J.J. Ramirez, Performance Of The HERMES-111 Laser-Triggered Gas Switches, *Proceedings of the 7th International Pulsed Power Conference*, pp. 579-582, Monterey, CA, 1989.

18. B.N. Turman and D.H. Humphreys, Scaling Relationships for the Rimfire Multi-Stage Gas Switches, *Proceedings of the 6th International Pulsed Power Conference*, pp. 347-353, 1987.

19. R.G. Adams, W.B. Moore, J.R. Woodworth, M.M. Dillon, F. Morgan, and K.J. Penn, *Proceedings of the 4th IEEE Pulsed Power Conference*, pp. 613-616, 1983.

20. J.P. Corley, K.C. Hodge, S.A. Drennan, D.W. Guthrie, J.M. Navarro, D.L. Johnson , J.M. Lehr, S.E. Rosenthal, and J.M. Elizondo, Development/Tests of 6-Mv Triggered Gas Switches at SNL, *Proceedings of the 14th IEEE International Pulsed Power Conference*, Dallas, Texas, 2003, pp. 875-878.

21. A. Pederson, The Effect of Surface Roughness on Breakdown in SF_6, *IEEE PES Winter Power Meeting*, New York, 1975.

22. C. Pradayrol, A.-M. Casanovas, and J. Casanovas, Absorption of SF_6, SF_4, SOF_2 and SO_2F_2 in the 115-220 nm Region, *1996 International Symposium on Electrical Insulation*, Montreal, Quebec, Canada, June 16-19, 1996.

23. K. Morales, J. Krile, A. Neuber, and H. Krompholz, Pulsed Dielectric Surface Flashover in Nitrogen at Atmospheric Conditions, *IEEE Trans. Dielect. Elect. Insulation*, vol. 13, pp. 803-809, August 2006.

APPENDIX A. Gas Switch Workshop Notes
May 8, 2001

The goal of this workshop was to gather and share the community's experience and intuition in triggered high-voltage gas switch design, performance, triggering, operational issues, problems, and potential flaws to guide future gas switch research activities. The baseline switch specifications are:

5 to 6 MV operating voltage (85 kV to 100 kV Marx charge)
Switchout time ~ 1 μs
Triggering jitter 3 to 4 ns (standard deviation)
Prefire probability < one shot in 20 on the full array of 36 switches for the 6-MV mode
Lifetime > 200 shots before servicing of switch or trigger components
Surrounding dielectric: undetermined (either oil or water)

Discussion suggested that these specifications should be refined to include
Lifetime > 400 shots before servicing of switch or trigger components
Design for switch replacement without draining fluids
Design for simplified (faster, easier) laser alignment

John Corley reviewed the gas switch development history in 963. Beginning with a Z switch (Figure A-1), he discovered they operate to the same level in oil as in water: about 4.8 MV. The failure mode was predominantly tracking of the plastic inner cylinder that supports the cascade section around the trigger electrode. Debris was observed along the bottom – probably switch electrode material, which limited the lifetime to less than 100 shots in the APPRM application. Doug observed the same behavior on a similar switch in Saturn and solved it by successively cutting out the tracked region (eventually the whole bottom third azimuth) of the inner envelope. This solution was not tested extensively, but is suggestive.

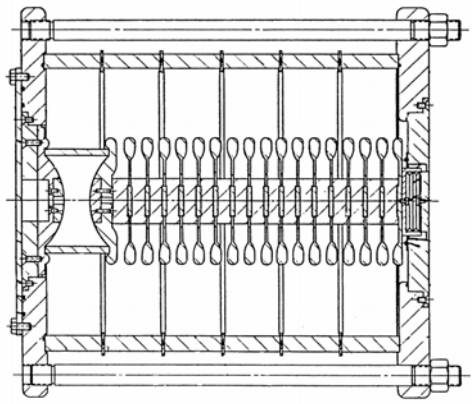

Figure A-1. Z switch.

The next switch tested was an extended Hermes switch (from 2.5 to 4.5 MV). Several iterations to reduce cost and size of the PBFA switch led to the version shown in Figure A-2, which has an increased cascade puck diameter from HERMES III. In about 1800+ switch shots at 3.8 MV, at 80 to 85% of self-break, this switch failed approximately six times in which the failure was not associated with external influence (i.e., something left on top of switch). With 6-10 mJ of laser energy it demonstrated a 3.2-ns spread, 2.4-ns σ, and a 20-ns run time from the laser pulse to closure.

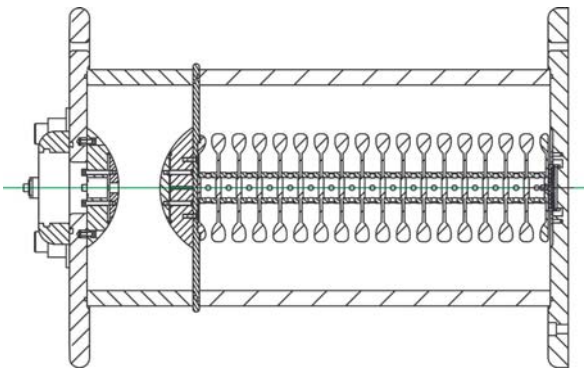

Figure A-2. Extended Hermes switch.

A concern raised is that the trigger electrode extending through the housing into the outer dielectric could shield the first cascade stage (interfering with breakdown). This switch has been tested in self-break to 4.5 MV.

A smaller (16-inch-long) full-cascade self-break gas switch was developed that operated at ~3 MV, ~30 psig with a 12-cm gap length (Figure A-3). For charge times below 180 ns four of these switches closed reliably with a 1.5-ns spread, while for larger charge times, approaching 200 ns, the spread grew catastrophically. This behavior is unexplained. Typically the first puck shows a few channels, while later stages show many more.

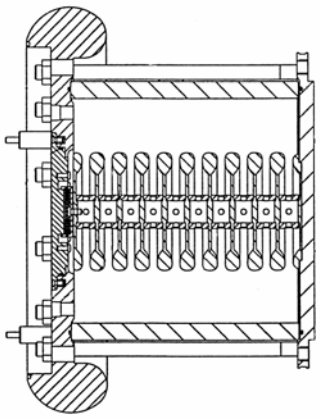

Figure A-3. Self break switch.

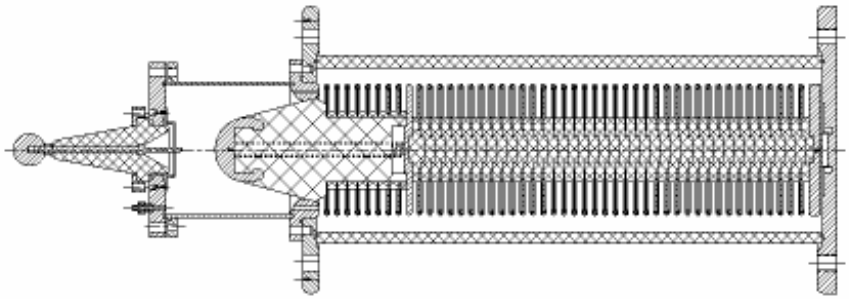

Figure A-4. Russian switch.

Boris Kovolchuk and Sasha Kim developed a high-voltage gas switch that uses unique materials and a novel approach (Figure A-4). The trigger section is extruded beyond the main switch but is inductively connected to the seventh electrode in a continuous 32-cascade stack. This leads to poor electrical grading but dramatically (10x) reduces the current in the trigatron gap, and hence reduces both debris and overall inductance. The large capacitance of the triggered cascade section and the inductance of the connection lead to a slow (100 ns) ringing of that section. The triggering increases the voltage on the cascade section, leading to switching. Perhaps due to the poor grading, this switch was unable to operate at voltages approaching 6 MV.

A Hybrid Sandia National Laboratories (SNL)-Russian switch was constructed, coupling the Russian swinging section to the extended Hermes cascade section (Figure A-5). This composite switch consisting of 26 SNL cascade electrodes (25 gaps) and 6 HCEI electrodes in the trigger section has been tested. The self-break voltage of the switch is controlled by peak electrical field on the first gap of the cascade section of the switch. Fields in this gap are ~410 kV/cm with 6 MV across the switch, resulting in a 25% reduction in self-break voltage compared to the extended HIII switch. The switch has been tested in triggered mode to ~4.5 MV.

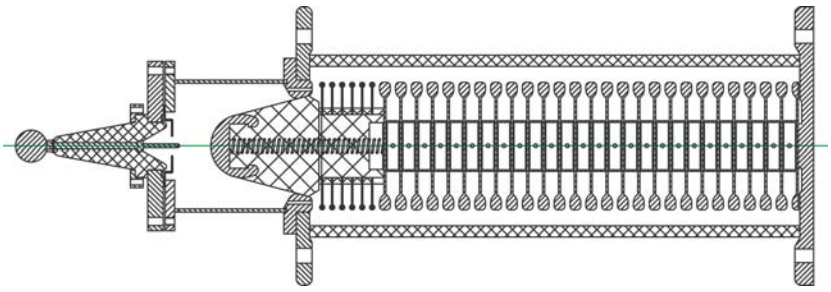

Figure A-5. Hybrid switch.

General switch design criteria developed in this research are:

Switch > 15% of the charge voltage to control run time spread
Keep axial stresses on the gas gaps below 250 kV/cm to avoid prefires
Keep axial stresses in the trigger region above those in the cascade to control self-break
Keep plastic length above three times the gas gap length

Switch	Overall Length (inch) Phys/ Elect.	Insu-lator Length (inch)	Gap length Cascade/ Trig. (inch)	Ratio	Oper-ating Voltage (MV)	Pres-sure (psig)	% SB	Self-Break Peak V
Z	27 / 23.5	23	6.63 / 1.75	2.7	4.5	50		~5.0 MV 48 psig
Saturn								
Extended Hermes	24.3 / 22.5	22.2	5.8 / 1.85	2.9	4.5	40	80	4.5 MV 30 psig
6-MV	32.2/ 30.5	30.2	8.5 / 1.85	2.9	6.0	TBD	TBD	5.5 MV 41psig
Russian	49.2 / 30.9	30.1	14.8	2	ND	ND	ND	*4.8 MV 20psig
Hybrid	49.2 / 30.6	30.7	8.5 / 2.17	2.9	4.5	48	80	5.5 MV 48 psig
Self-break - Short	11.7 / 9.8	10.1	3.4	3	2.5	36	N/A	3.30 MV 36 psig
Self-break - Long	13.7 / 11.8	12.1	4.1	3	3	ND	N/A	ND

* highest self-break voltage achieved, with 70 mm trigger pin; 4.3 MV @ 35 psig with 100mm trigger pin. Were unable to positively trigger in any configuration.

Different gas switch envelopes were discussed and compared. A significant concern was expressed regarding the ratio of plastic insulation length to gas switch gap length. Judd suggested a factor of 7 was desired, although a factor of 2.5 was probably acceptable. This is really a balance of surface breakdown to gas breakdown, and depends on gas pressure as well as on configuration. Design for low prefires is contrary to low jitter, but certainly the preferred breakdown path is through the gas. The Z switch tracks the plastic at 5.1 MV as measured in the ISC several ns from the switch. Ian noted that the switch envelope needs to be designed for fault mode (longer) $t_{effective}$. There was concern that the scale up from low to higher voltage perhaps has missed the optimum of low prefire probability with minimum jitter, and that variation testing is needed.

Monolithic single-tube cylinders were historically believed to be overly expensive, especially when compared to the cost of repairing and replacing shorter sections when damaged in operation. Typically metal grading rings are used with the combined purpose of coupling several shorter sections, grading the triple points (2x), and arresting surface arcs before they can become destructive. However, streamers are observed to grow from these metal grading rings into the surrounding dielectric. In some cases a non-damaging internal track was observed adjacent to a switch-destroying water detonation outside the next enclosure ring. Whether this is from a fundamental surface track issue or from a combination event where the pucks arc radially through the gas to the enclosure grading ring, thereby driving a more serious outside arc, is

unclear. It is felt that this failure mode might be fixed by either returning to monolithic enclosures or removing the metal grading rings (step indexing and incorporating o-rings into the plastic cylinders), leading to a less-expensive more robust design.

There is a suspicion that significant radial electric fields may oscillate through the envelope. Saturn envelopes (Figure A-6) are regularly punched in the trigger region, and fixed by drilling out the damage and threading in a sealed nylon screw. A thicker plastic envelope might be indicated, and electromagnetic simulations are needed to assess this phenomenon.

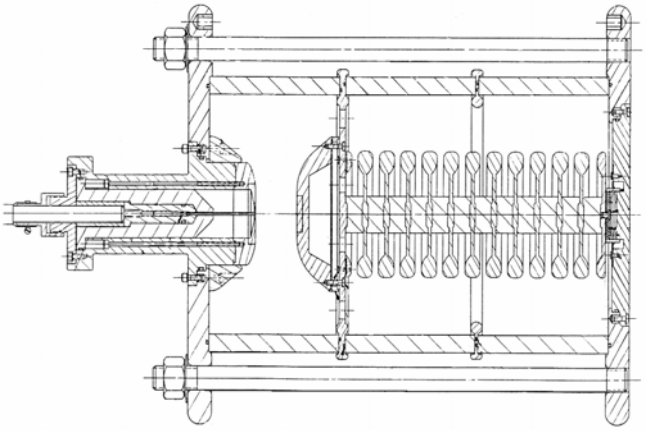

Figure A-6. Saturn switch.

One major concern increasing the voltage for ZR is coupling the trigger laser through the highly stressed PFL inter-electrode gap. Dave Bliss presented experimental measurements of quadrupled YAG light propagation through water (see table). The results suggest that while clean water works well (as seen on Nike and Electra), the open Z tank is far too polluted to apply this approach. The principal maintenance element in Z is cleaning the laser optic nearest the gas switch: the damage suggests trigger electrode metal adheres to the optic surface and is subsequently burned into the glass by successive laser pulses. Several suggestions should be studied: perhaps purging the switch by blowing gas across the surface of this optic could clean it before damage is incurred, or a longer focal length might reduce the debris, or perhaps focusing the laser on the inside of an annular trigger electrode (instead on normal to the electrode surface) could reduce the debris on this surface.

	Res MΩ/cm	E0(mJ)	Short Ef (mJ)	T	E0 (mJ)	Long Ef (mJ)	T	Twind	α (cm^{-1})	T(12") AR
Z Tank	1.4	32.9	3.9	0.119	32.4	1.8	0.056	0.227	0.021	0.522
Z DI Spigot	12	32.4	15.8	0.49	32.7	9.9	0.30	0.73	0.013	0.664
Z DI Spigot	17.5	32.6	16.2	0.5	32.8	11.6	0.35	0.66	0.009	0.75
Z DI Spigot	17.5	32	15.7	0.49	32.2	10.2	0.32	0.71	0.012	0.69
Z DI Overnight	--	32.8	4.1	0.12	32.6	1.5	0.05	0.29	0.03	0.42

Fred Zutavern presented results using a PCSS laser triggered GaAs switch to trigger a 300-kV spark gap with very small (100 ps) jitter. It was suggested that this approach might enable a self-contained electrical trigger system attached to each gas switch, where the applied electric field on the IS charges a pulser that is discharged when a laser pulse is provided to the PCSS switch. The only external connection would then be the laser (perhaps through fiber optics?), as is done now.

The water switch development program schedule is:

1. Immediate start of DCA oil-environment laser triggering tests, ending either with 25 repeated shots at 5.5 MV or June 30.
2. Repeat in water on Z_{20} (probably October).
3. Switch variations in water through November (longer envelope, modified grading rings, radial spacings, various trigger systems, etc.).
4. Test to failure (tbd).
5. Transient modeling (tbd).
6. Acquisition of operational statistical data (tbd).

This community will reassemble to discuss the DCA laser-triggered gas switch data and to revisit the issues discussed here, hopefully bringing more historical information relevant to the ZR switch regime. For example, Bob Turman has offered to resurrect his database of gas switch performance characterization and help integrate it with more recent information in the fall, about when Z_{20} becomes available to investigate new and iterated gas switch designs in oil and water.

APPENDIX B. Z_{20} Gas Switch Development Report

The Z_{20} test bed is a full-scale test facility for upgraded Z components. The primary energy store system consists of a 60-stage Marx generator built from 2.6-μF capacitors operated at up to 95 kV charge voltage. The Marx energy is switched into an intermediate storage capacitor, and subsequently switched into the water-insulated pulse-forming line by the laser triggered gas switch (LTGS). The pulse energy transfers through two sets of water-insulated self-closing switches and two water-insulated transmission lines to the load. The load on Z_{20} is a set of resistors, undermatched to the line impedance to reduce the resistor voltage. Because Z_{20} has only one Marx, the line combination and current adding of pairs of modules that will happen on ZR is not present on Z_{20}. Apart from the line combination and the load, Z_{20} closely matches one module of the ZR system.

The primary interest at present is the LTGS. The performance and reliability of the gas switch are both substantially inferior to the project goals. The primary requirements are 20-ns switching spread relative to the laser pulse, at least 50-shot lifetime, and operation at 6.25 MV peak. The switch conducts 720 kA peak at 6.1 MV peak switch voltage. The charge through the switch is about 0.7 coulombs. The switch current action ($\int_{-\infty}^{\infty} I_{switch}^2 dt$) is about 200 kJ/Ω at 6.1 MV peak switch voltage.

The switch suffers from several major problems. The switch housing (either the trigger insulator or the main insulator) flashes (often coincidentally with triggering), generally within 50 shots. The switch jitter was about 12 ns on a recent 12-shot run, with 45 ns spread, exceeding the project goals by a factor of about two. The switch has a prefire rate that is in excess of the project requirements. The jitter increases dramatically when considering larger groups of shots. The trigger laser optics becomes contaminated with debris from the 720-kA metal arc, and the switch triggering becomes progressively weaker with more shots. This means that a long series of shots must be done at pressures relatively close to self-break to allow for the degradation. This makes prefires relatively common.

The issue of housing flashes has been relegated to lower priority. This is because both the housing flash rate seems to have dropped precipitously, and because the switch jitter and prefire rate is more alarming. Table B-1 shows some basic parameters for recent operations with switch configurations on Z_{20}. It is not clear why the housing flashover rate has dropped substantially; Table B-1 data does not indicate a specific corrective action because of overlapping changes. However, assuming that the trigger insulator material does not reduce the likelihood of main insulator flashing, the hexane and alcohol cleaning protocol might be a factor in the flash rate reduction. Switch housing cleaning had been done with Simple Green and tap water before Shot 1071. After Shot 1070, the acrylic and polycarbonate parts were cleaned with hexane after Simple Green and water; the Rexolite parts were cleaned with filtered ethanol. The metal parts are cleaned with filtered ethanol.

Figure B-1 shows the Z_{20} system. The pulser can be operated ten or more times per day. A typical number of full-energy tests is eight on a day with no problems. The time between shots

is about an hour minimum, due to load resistor heat dissipation concerns. The switch gas is purged after each test; the SF_6 is reprocessed in a standard reclaimer. The laser is aligned before each test. A fiber monitor near the trigger section records visible light from the laser spark. The signal from this monitor is used to gauge the laser alignment and roughly estimate the condition of the final optical surface. The primary diagnostic for laser alignment and energy is the runtime of the trigger section of the switch. This is monitored by the displacement current due to the change in total (end-to-end) switch capacitance caused by the closure of the trigger section. The switch voltage is monitored by voltage diagnostics in the intermediate store capacitor. The transit time from the voltage monitor to the switch endplate is ~30 ns. The current through the switch is recorded with Bdots mounted in the feed gap downstream of the switch (the same monitors as are used to resolve the trigger switch closure).

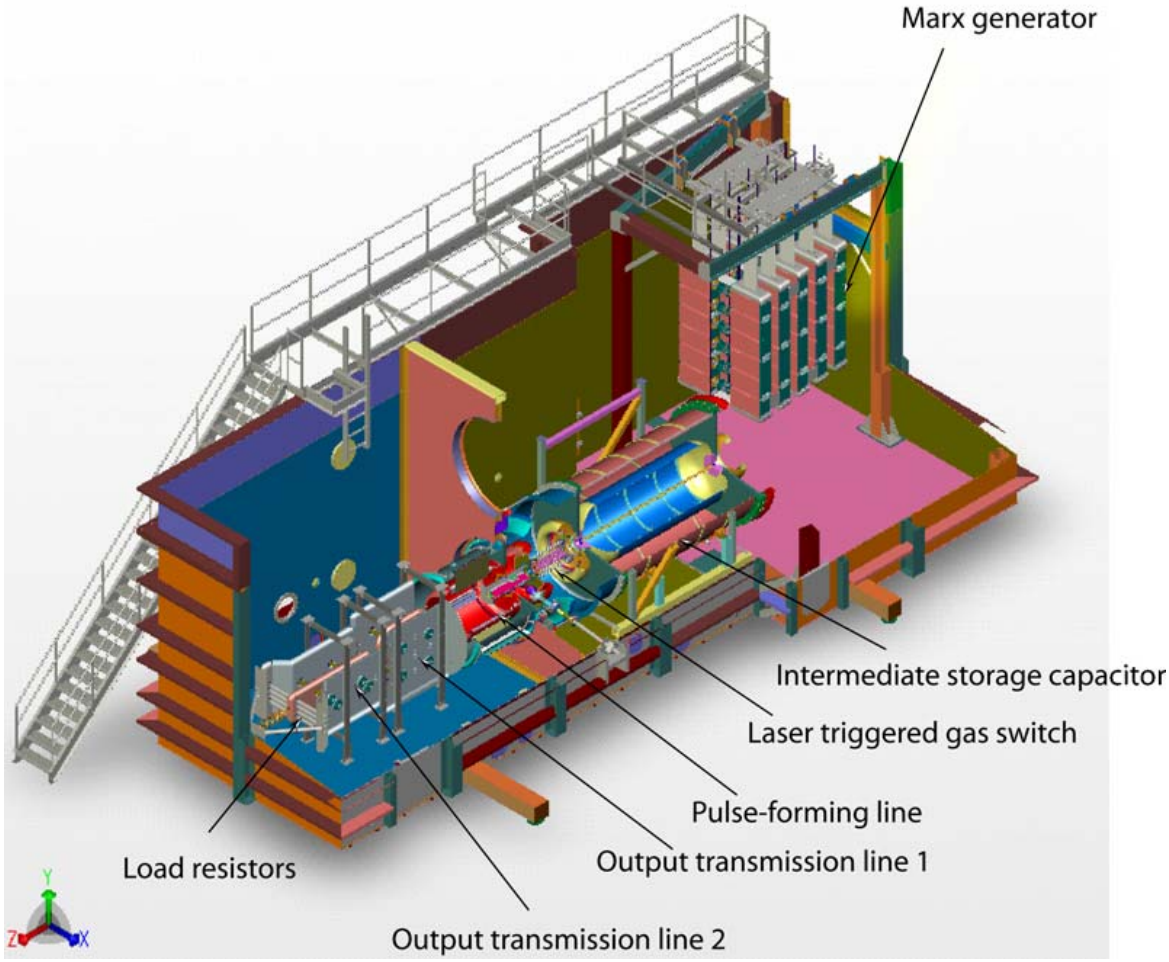

Figure B-1. The Z_{20} pulser. The right-hand Marx generator and the upper pulse-forming system are not shown and not installed.

Table B-1. Housing flash and switch runtime parameters for recent tests on Z_{20}. The runtime numbers are extracted by performing a least-squares waveform comparison between individual shots and a reference shot, using only shots above 5.9 MV switch voltage, on which the runtime was less than 200 ns and shots on which the switch closed after the laser arrived. This is a brutal (realistic) assessment of jitter, not accounting for trigger optics condition or operating pressure.

Switch	Shot Numbers	Shots Above 5.9 MV	Number of Trigger Flashes	Number of Cascade Flashes	Mean Runtime, ns	Runtime Jitter, ns
Recent old configuration	800-1070	60	18	14	42.1	21.2
Rexolite trigger insulator	1071-1326	87	1	2	55.9	30.2
Cleaned with hexane and alcohol	1071-1429	165	1	2	63.6	25.9
Triple-point shielded	1183-1429	146	0[†]	2[†]	63.4	21.3
Z-like	1239-1240	2	2[*]	2[*]	33.0	0.3
Triple-point shielded 23 gaps	1241-1288	0	0	0	N/A	N/A
Triple-point shielded 22 gaps	1289-1429	100	0	1	68.1	17.8
Return of acrylic trigger housing	1326-1429	78	0	1	72.2	16.5
Laser window	1238-1429	103	0	1	67.0	18.7

[†] Does not include Z-like switch flashovers (Z-like does not use trigger plate).

[*] Both tests of Z-like switch arced radially from the trigger cathode to housing late in time (more than 500 ns after switch closure).

Gas Switch Design

Baseline Switch

The so-called baseline switch is the switch used until Z_{20} Shot 1070. This switch uses standard polished acrylic tubing for the housing. The laser-triggered section and the rest of the switch (the self-breaking "cascade" section) use insulators separated by the trigger plate. The trigger plate divides the two parts of the switch and supports the trigger cathode electrode. The laser light enters through a hole in the trigger anode electrode. Cylindrical acrylic spacers support the cascade section electrodes. The switch cathode plate and the trigger plate support the cascade electrode stack. The cascade stack is sprung on Belleville washers to allow for parts tolerances. Figure B-2 shows a view of the baseline switch.

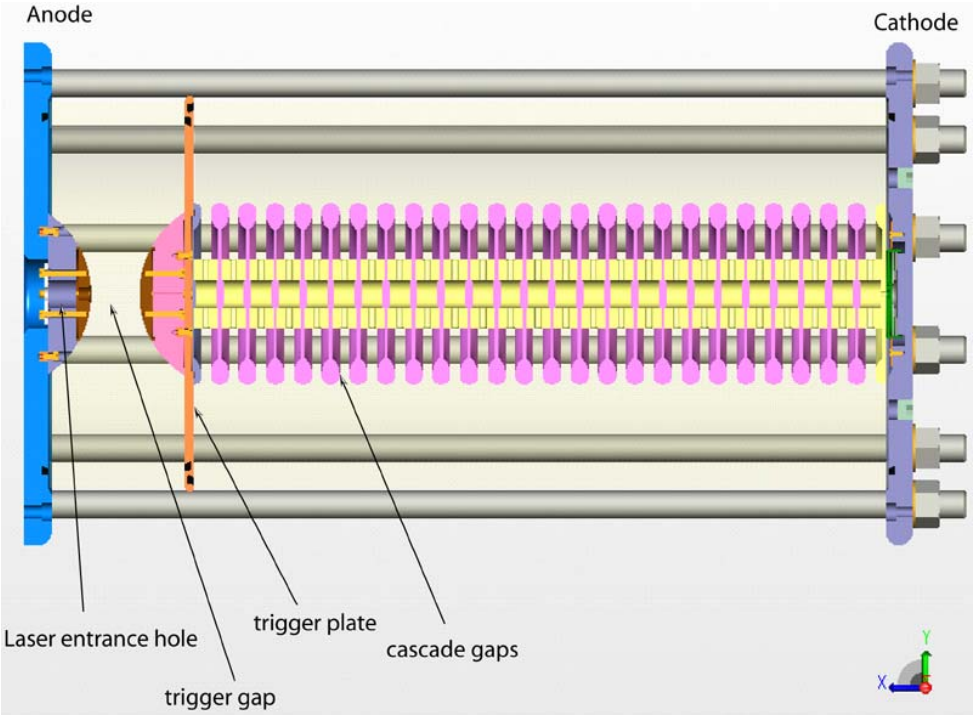

Figure B-2. The baseline Z_{20} laser triggered gas switch.

Rexolite Trigger Housing

Starting at Shot 1071, the acrylic trigger insulator was replaced with cross-linked polystyrene (Rexolite™ 1422). Rexolite is used on large vacuum insulators. Rexolite has a lower dielectric constant than acrylic, which reduces peak fields near gaps. Rexolite is much more chemically stable than acrylic, allowing cleaning with ethanol without inducing crazing.

Shielded Triple Point

The notion that propagating discharges might start at gaps between the insulator and metal plates motivated a design with reduced fields at the triple points. Recessing the joint into a region of reduced field (a metal well) does this. This can also be done with conductive inserts placed into the insulator housing. The shielded triple points could also provide tolerance to debris that might be near a triple point. One important difference with the shielded triple point design is that the trigger plate is larger diameter to allow a full radius on the trigger plate outer edge (see Figure B-3). This was not possible inside the switch support rods, so the trigger plate extends outside the support rods. This reduces the fields on the anode end of the cascade insulator after triggering. The reduced fields might tend to inhibit cascade insulator flashing (such flashing often happens upon triggering), but reduce the triggering wave amplitude on the first few gaps of the cascade section. Table B-1 shows that the mean runtime for the triple point shielded switch is longer than the previous switches. This design has been used on several switches, with 146 shots above 5.9 MV to date.

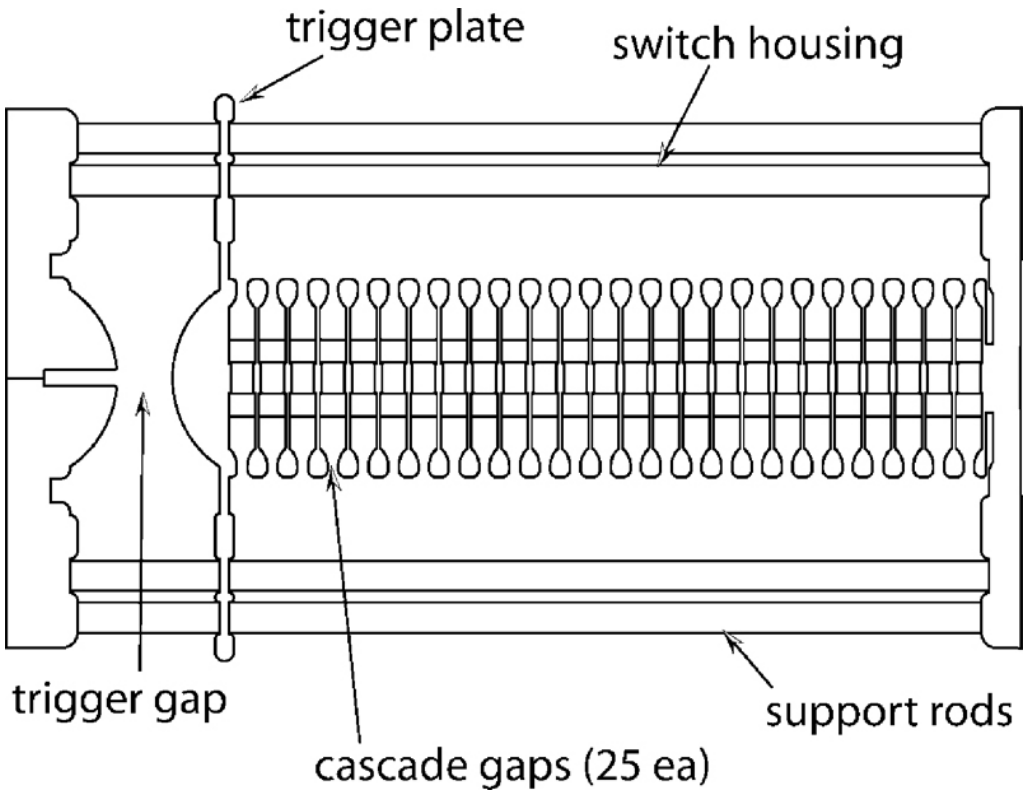

Figure B-3. The shielded triple point design. The four locations where the insulator housing contacts the metal plates are recessed into low-field regions.

Z-like

The Z-like switch (Figure B-4) was intended to be a comparison to the switch used on Z. This switch uses a smaller-diameter insulator to support the trigger gap. On Z, this is a cylinder. The Z-like switch tested on Z_{20} used six posts for the trigger gap support. This design moves the high fields present after triggering into the gas (the baseline switch has those high fields outside the switch envelope, in oil). This helps in the triggering process (the Z-like switch had relatively short runtimes on Z_{20}) but the switch arced in the gas from the trigger gap cathode to the housing. The radial fields present on the outer edge of the trigger cathode electrode are about 500 kV/cm after triggering. Notably, the breakdowns on both tests were late in time (hundreds of nanoseconds after switch closure). Switch performance on both tests was adequate; however, the arcing to the housing is not a sustainable course of events. The proximity of the support posts to the trigger arc stirred concerns of UV-induced flashing of the posts. In the short two-shot run, however, there was no evidence of support post flashing. The Z switch has a larger main housing diameter. It is possible that a larger housing with a Z-like switch would avoid the radial arcing. Such a test will be done later.

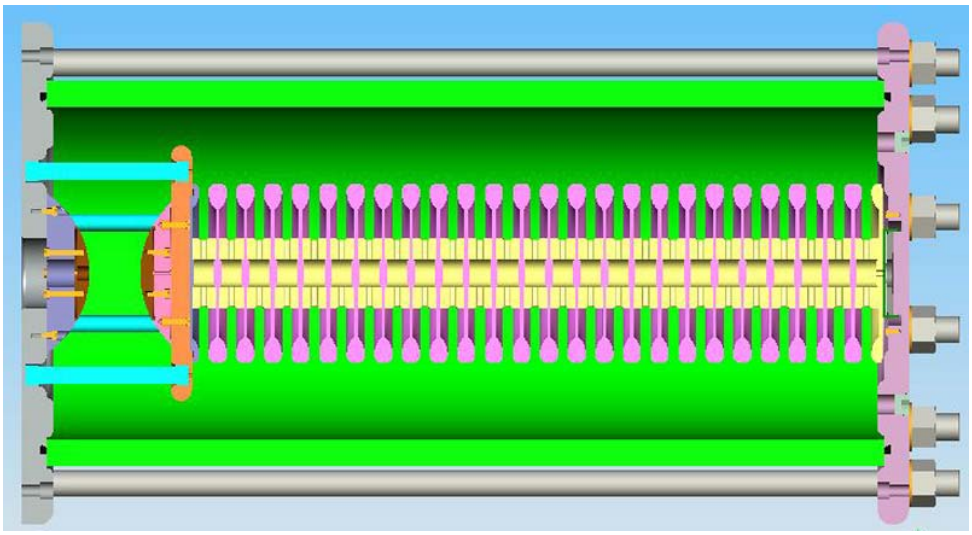

Figure B-4. The Z-like switch. The six insulating rods, instead of the trigger housing, maintain the trigger gap.

Untested: The Cantilever Switch

The cantilever switch is similar to the Z-like switch but supports the trigger gap with an insulating rod in the middle of the cascade stack. This rod is tensioned with a nut outside the switch housing. This design is similar to the Z-like switch, but does not require the six support posts to maintain the trigger gap (see Figure B-5). The support rod is under substantial mechanical stress. The support rod is made from an advanced high-strength material such as Torlon.

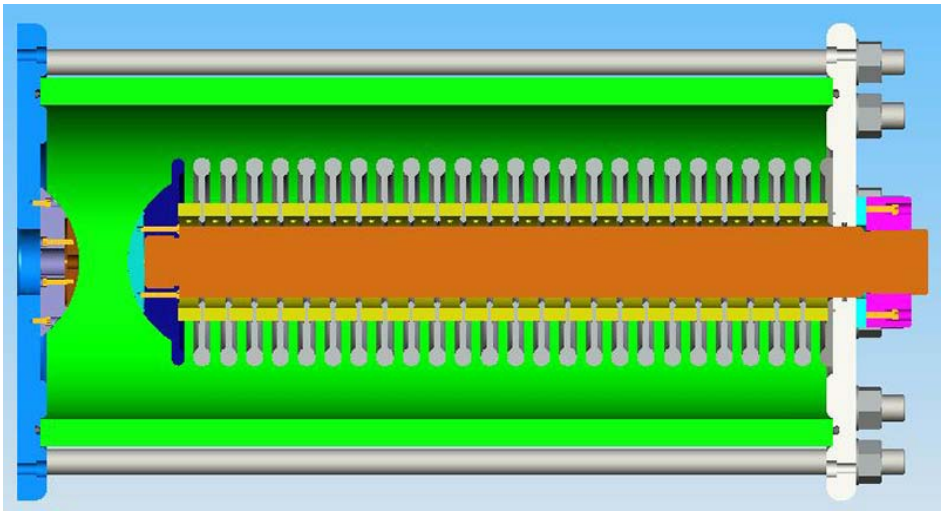

Figure B-5. The cantilever switch design. The support rod (under tension) applies compression force from the trigger cathode to the cathode end plate.

Untested: The Segmented Switch

The segmented switch design relies on the well-known statistical nature of flashover to improve the reliability under some conditions. One very simple estimate for the minimum number of insulators (stages) is

$$N > \frac{k\sigma_{selfbreak}}{1-\eta_{selfbreak}-k\sigma_{selfbreak}}$$

where N is the number of stages, k is the number of standard deviations away from self-break required for reliability, $\sigma_{selfbreak}$ is the fractional spread in the self-break (flash) distribution (presumed to be substantially less than one), and $\eta_{selfbreak}$ is the operating fraction of self-break (flash) voltage. Of course, the standard deviation of the self-flash voltage may be unknown to a large degree. The equation ignores "packing fraction" effects of lost insulator length from the metal grading rings. The segmented switch naturally allows electrical and optical shielding of the insulator triple points. One estimate of improvement with a segmented gas switch is a factor of two increase in holdoff strength for a 3-MV high-pressure trigatron switch.[1] The switches on Z were comprised of about five separate insulators. It is known that those switches can function for hundreds of shots even with one insulator clearly tracked. A monolithic insulator has no such tolerance: arc damage will spread and lengthen.

The segmented switch suffers from mechanical complexity. There are more sealing surfaces in such a switch. However, the o-ring compression is additive; a switch of many segments has more axial travel before leakage than a single o-ring of the same minor diameter.

The segmented switch design uses shaped insulators to reduce the fields at the triple points (see Figure B-6). This design also uses teardrop features on the grading rings inside the gas to shield the insulators from light and direct debris, as well as provide an alternate fault breakdown path to the insulator surface.

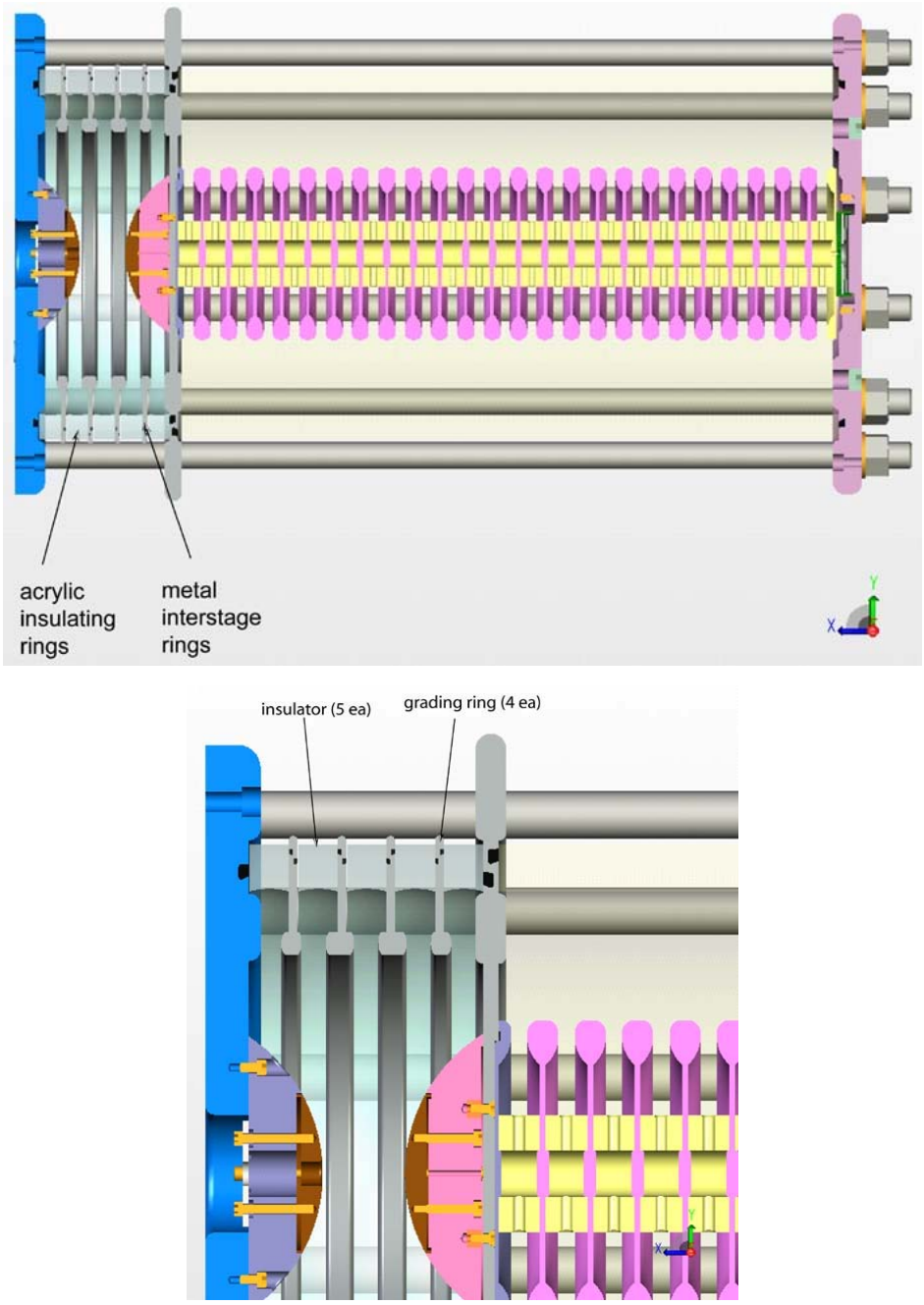

Figure B-6. The segmented switch. The trigger section is built from small insulators cut from tube or sheet, and metal grading rings with o-rings. The trigger section would be the first test of the segmented concept.

Untested: The Lined Switch

The lined switch concept is based on the observation that certain materials may have desirable electrical properties, but might not be mechanically able to support the pressure inside the switch. Since the Z_{20} switch very rarely arcs in the oil outside the envelope, it seems possible to

build a switch that uses oil to mechanically support an inner liner. It is well known that Teflon has superior flashover resistance, lower surface charging, and reduced accumulated damage from discharges.[2] Since Teflon would flow and be unable to hold the required SF_6 pressure for reasonable wall thickness, we considered a design with an internal liner that would not need to tolerate a pressure difference. In principle, a simple sleeve inside an acrylic housing would accomplish this. However, if the contact between the sleeve and the acrylic housing were not void-free, it is likely that arcing would be *enhanced* and not eliminated. The oil buffer shown in Figure B-7 allows observation of the interface quality (lack of bubbles) and simple assembly.

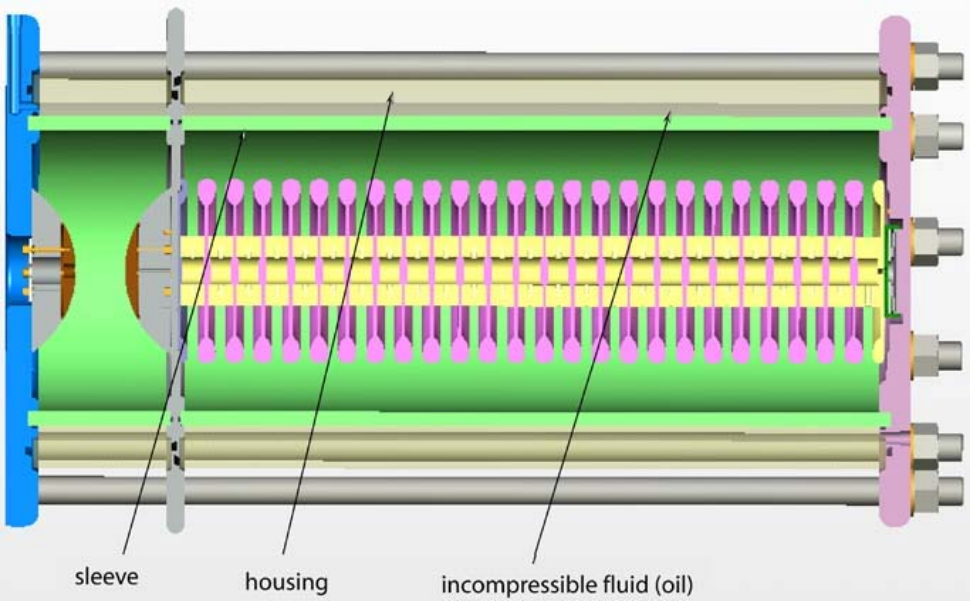

Figure B-7. The lined switch. An inner liner, which may lack adequate mechanical strength to support the internal switch gas pressure, is supported radially with an incompressible fluid that transfers force to the outer housing.

Untested: The Scalloped Housing

The scalloped housing is another concept to reduce complete housing flashes. The Z gas switch housings are grooved in a round screw-thread configuration. Historically, grooving is believed to increase flashover tolerance.[3] However, grooving greatly enhances the electric field in places, while increasing the tracking distance. The original Saturn switches were grooved, but in a cost-reduction effort, new Saturn gas switch insulators are not grooved. There is no clear difference in housing flashover rates between the grooved housings and the straight housings. In an attempt to understand the effect of housing surface, we designed a switch insulator surface for the Z_{20} trigger section that has a small increase in peak field compared to the average field, but has regions of greatly reduced field. The housing design is shown in Figure B-8. Figure B-9 shows the relative tangential and normal electric fields on the interior of the housing. To lower the field in one place requires raising it elsewhere. In the design shown below, an 8% increase in peak tangential field is accompanied by a 50% reduction in the field at the tips of the scallops. The concept was to see if local periodic regions of low field would tend to stop an avalanching surface discharge.

Other work on more dramatic surface contouring for the power industry[2] indicates that large grooves maintain or even reduce the flashover strength of clean insulators, but typically improve the flashover strength of contaminated insulators.

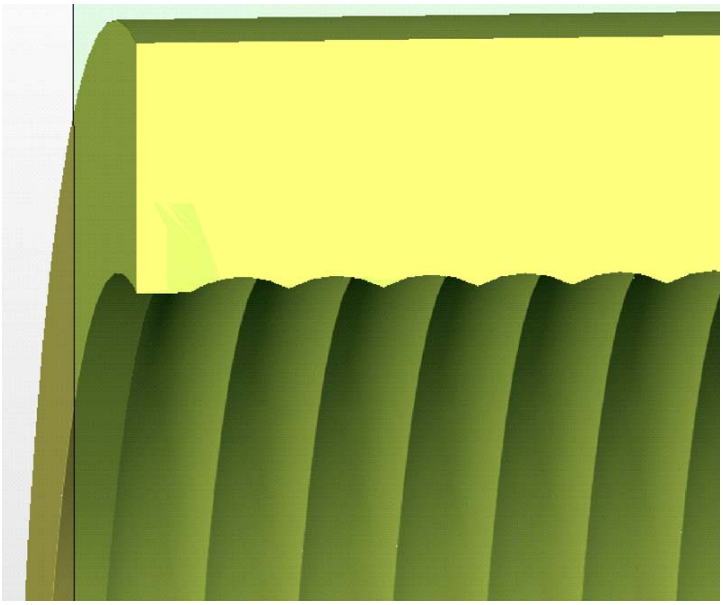

Figure B-8. The scalloped switch insulator. Before switch closure when equipotentials are normal to the housing axis, the field is lowest at the peaks (smallest radius).

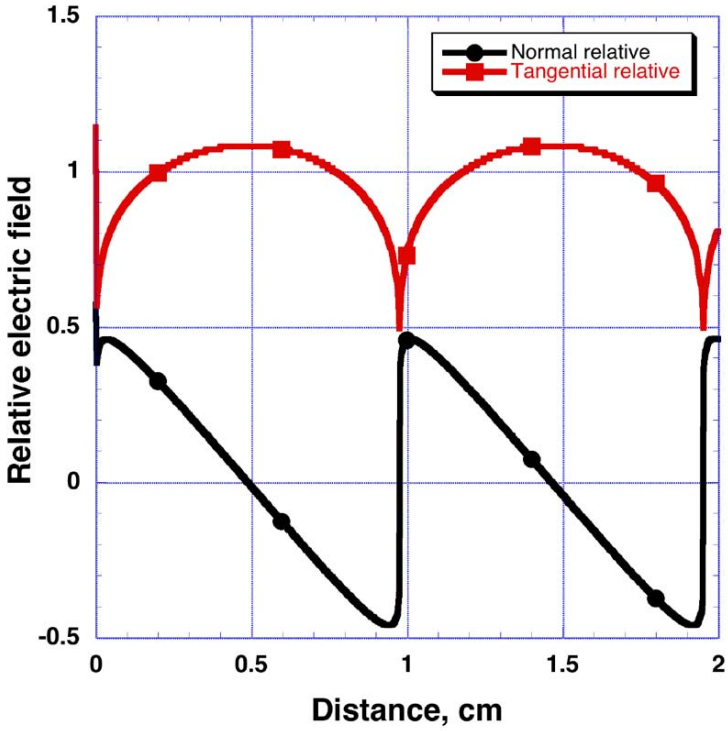

Figure B-9. Relative electric fields on the interior of the scalloped housing. Both tangential and normal fields are shown, relative to total voltage divided by insulator height.

Gas Switch Self-Break Characteristics

The Z_{20} gas switch has typical SF_6-insulated breakdown behavior. As the pressure is raised, the electron path lengths get shorter and the surface acts as less smooth.[4] The relative breakdown resistance along an insulator compared to bulk gas breakdown (insulator efficiency) falls at higher pressures.[5] It is clear that minimizing fields for a given voltage is a desirable practice. Figure B-10 shows self-breakdown characteristics for the Z_{20} baseline switch (shots up to 1175). The self-break voltage does not increase at higher pressures (above ~45 psia) and the spread in self-breakdown voltage increases at higher pressure. The spread in breakdown voltage is the most detrimental. A large spread in breakdown voltage forces operation at a lower fraction of self-break voltage. This requires a larger trigger mechanism, and likely increases the jitter in the self-breaking cascade section.

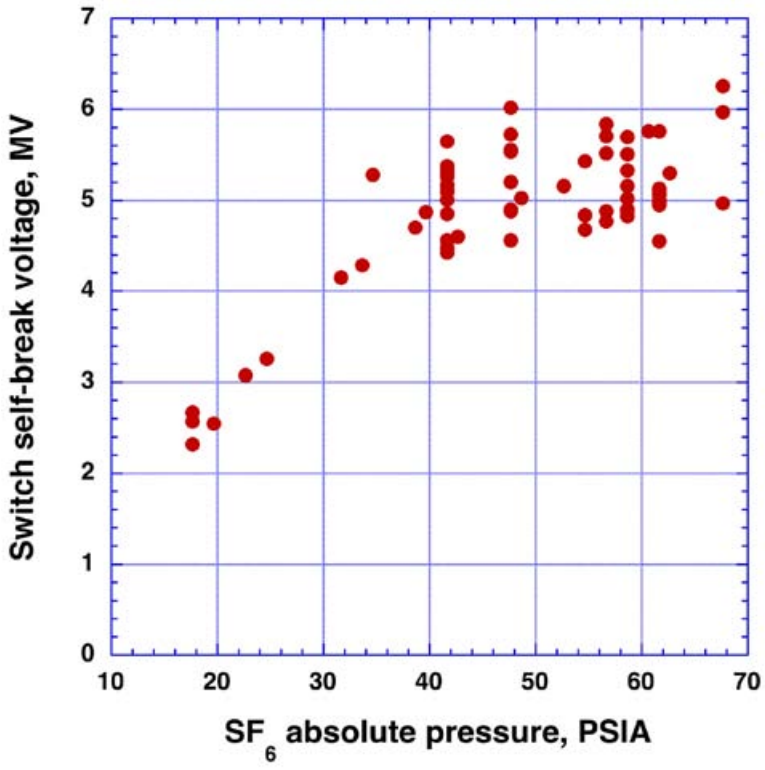

Figure B-10. Self-breakdown characteristics of the Z_{20} baseline switch. It is intended that the trigger gap self-break before the cascade section self-breaks, but this does not always happen.

Gas Switch Trigger Characteristics

The switch on Z_{20} has substantial jitter. This is due largely to a small laser spark in the trigger gap, which is basically a weak trigger. This forces operation close to self-break voltage. Operation close to self-break causes poor reliability and larger jitter. Wilson[6] discusses two design philosophies for triggered gas switches. One proposes using a low field in the trigger section, so that the laser must close a large fraction of the gap. This was used in the design of the

original PBFA-II gas switches. The second philosophy suggests higher fields in the trigger section than in the untriggered section. The prefire rate of the switch would then be controlled by the triggered section, but the switch runtime characteristics would be less sensitive to the laser spark. This was applied in a modification to the PBFA-II gas switches. It is likely that a reoptimization of the electric potential distribution in the switch will be necessary for a more reliable switch.

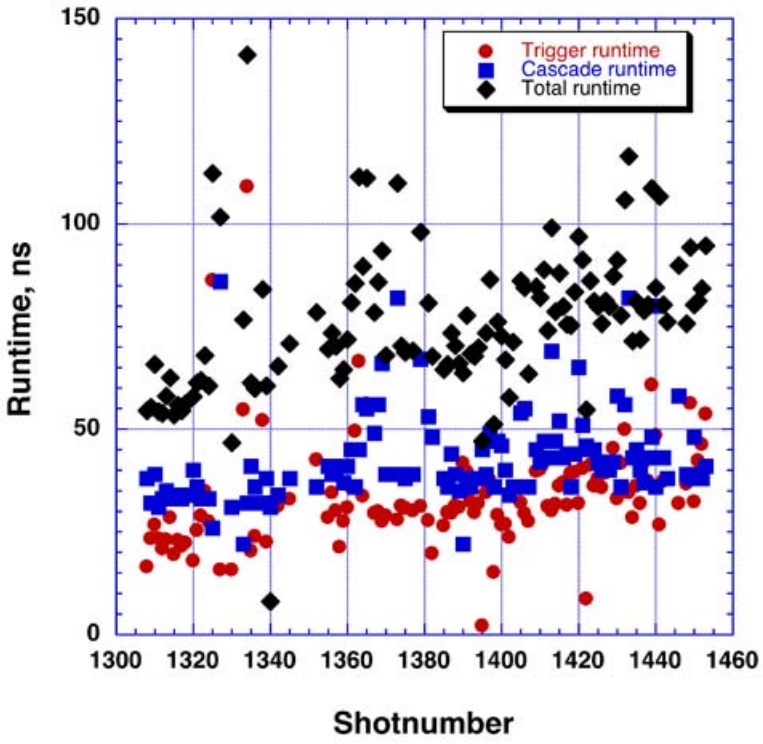

Figure B-11. Trigger, cascade, and total runtime for a recent number of Z_{20} tests. Long runtimes and prefires have been discarded.

References

1. S. Mercer, I. Smith, and T. Martin, *A Compact, Multiple Channel 3 MV Gas Switch*, Italy.

2. H.F.A. Verhaart and A.J.L. Verhage, Insulator Flashover in SF_6 Gas, N.V. Kema, Arnhem, The Netherlands, *Kema Scientific and Technical Reports*, 6(9), 1988.

3. B.N. Turman, W. B.S. Moore, J.F. Seamen, F. Morgan, J. Penn, and D.R. Humphreys, Development tests of a 6 MV, multistage gas switch for PBFA II, presented at *4th IEEE International Pulsed Power Conference*, Albuquerque, NM, 1983.

4. T.H. Martin, Pulse Charged Gas Breakdown, presented at *5th IEEE International Pulsed Power Conference*, Arlington, VA.

5. J.R. Laghari, Spacer Flashover in Compressed Gases, *IEEE Trans. on Electrical Ins.*, vol. EI-20, pp. 83-92, 1985.

6. J.M. Wilson and G.L. Donovan, Laser-Triggered Gas Switch Improvements on PBFA-II, presented at *6th IEEE International Pulsed Power Conference*, Arlington, VA, 1987.

APPENDIX C. LTGS Optical Diagnostics

Gas Switch Flashover Problems

During the first half of 2005, the Z_{20} gas switch had an unexplained fault mode in which the trigger or cascade section plastic insulators would flash over on the inside during a shot. While the switch delivered a normal power pulse on the shot with the first flashover, the switch often prefired on subsequent shots, leading to unacceptable power pulses. Figure C-1 shows framing camera images of the switch during a normal shot. The laser-triggered portion of the switch lights up (i.e., breaks down) in the 20-ns frame. The cascade section has begun breaking down by the 40-ns frame and the entire switch has broken down by the end of the 50-ns frame. Figure C-2 shows a shot in which the cascade insulator flashed, with the flashover beginning in the first frame (0 ns) at least 30 ns before the laser-triggered segment of the switch broke down. The insulator flashover in Figure C-2 is behind the cascade insulators and hence backlights the cascade electrodes. None of the cascade electrode gaps themselves broke down.

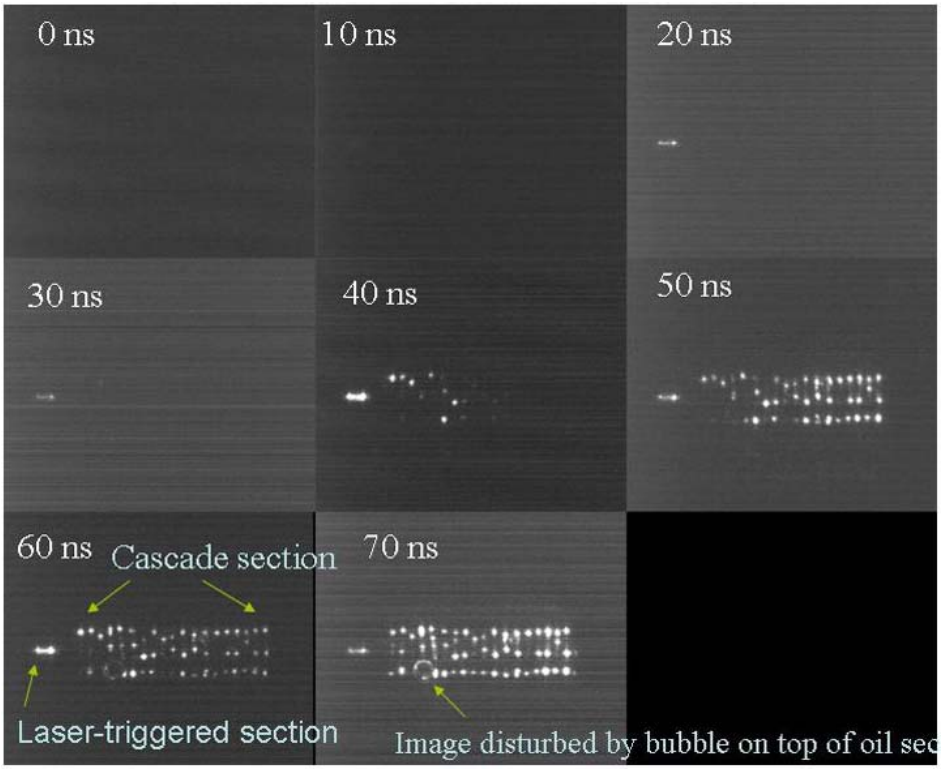

Figure C-1. Framing photographs of a normal operation LTGS progression for Z_{20} Shot 858. There are eight 5-ns-wide frames, starting from the top left, spaced 10 ns apart.

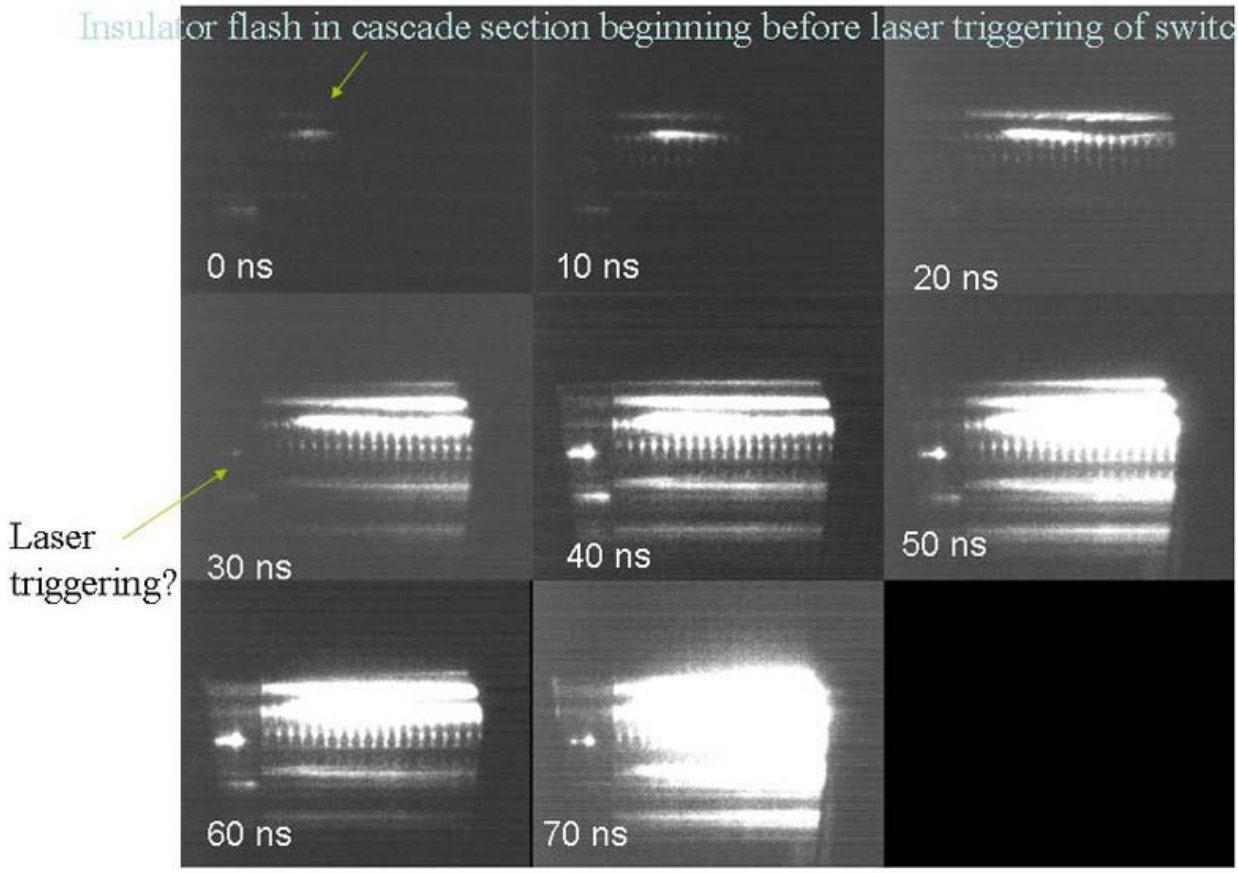

Figure C-2. Framing camera pictures of the Z_{20} gas switch breaking down on an abnormal shot. In this shot, the insulator around the cascade section flashed over on the inside surface before the switch was laser triggered.

Several modifications were made to the switch including increasing the insulator diameter and trying different insulator materials. These modifications did not solve the insulator flashover problem. This insulator flashover problem was much reduced after instituting different cleaning and handling protocols, and the longer lifetimes continued when using triple-point shielding, and when adding a gas-tight final window to separate the gas switch and "laser can" (which contains the final turning and focusing optics). The laser can volume is comparable to that of the gas switch. Inserting a window between these two volumes appears to keep the insulators much cleaner and, apparently, less susceptible to flashovers.

Cascade Switch Breakdown Timing with Streak Camera

A streak camera was used to look at the breakdown of the gas switch on Z_{20} on a number of shots. The streak camera record shows when the laser-triggered gap and 18 of the cascade gaps break down as a function of time (the remaining 5 cascade gaps were behind a metal field shaper and could not be imaged by the streak camera). Figure C-3 shows a typical trace from the streak camera. In addition to the timing marks at the top of the picture, the streak image shows a one-dimensional image of light emitted from various parts of the switch versus time. The laser-

triggered gap, which is just below the timing marks in the picture, lights up roughly 25 ns before the cascade gaps begin to light up. The individual cascade gaps can be seen breaking down over the next ~30 ns. Note that the ~8 cascade gaps just below the laser-triggered gap do not break down in perfect sequential order.

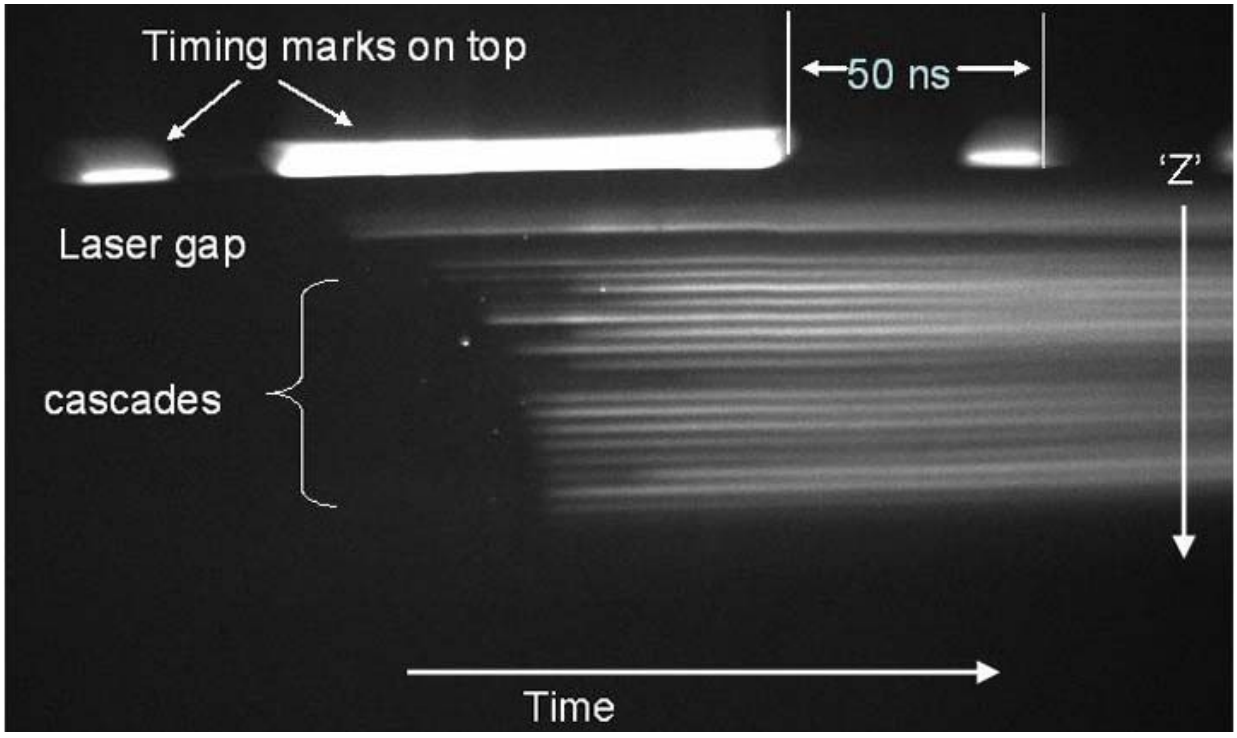

Figure C-3. Streak camera picture of the Z_{20} gas switch on Shot 1315. Timing marks are on the top of the picture, with light from the laser gap and then the cascade gaps below the timing marks. Note that the first ~8 cascade gaps do not break down in order.

Figure C-4 shows data taken by the streak camera on 9 different shots. This figure shows the time of breakdown of each of the 18 individual cascade gaps we could see, relative to the breakdown of the laser gap. In these shots the gas switch was pressurized to 44 PSIG of SF_6 and held off 6.15 MV before being triggered. In Figure C-4, there is a 20-to-40-ns delay between breakdown of the laser trigger gap and breakdown of the first cascade gap. As seen in Figure C-3, the cascade gaps do not break down in numerical order. Further, for the first 6 gaps, the delay between the breakdown of one gap and its nearest neighbor can be $\pm$ 20 ns. After gap 8, the cascade gaps begin breaking down very rapidly and the difference in breakdown time between a gap and its neighbor is usually less than 5 ns.

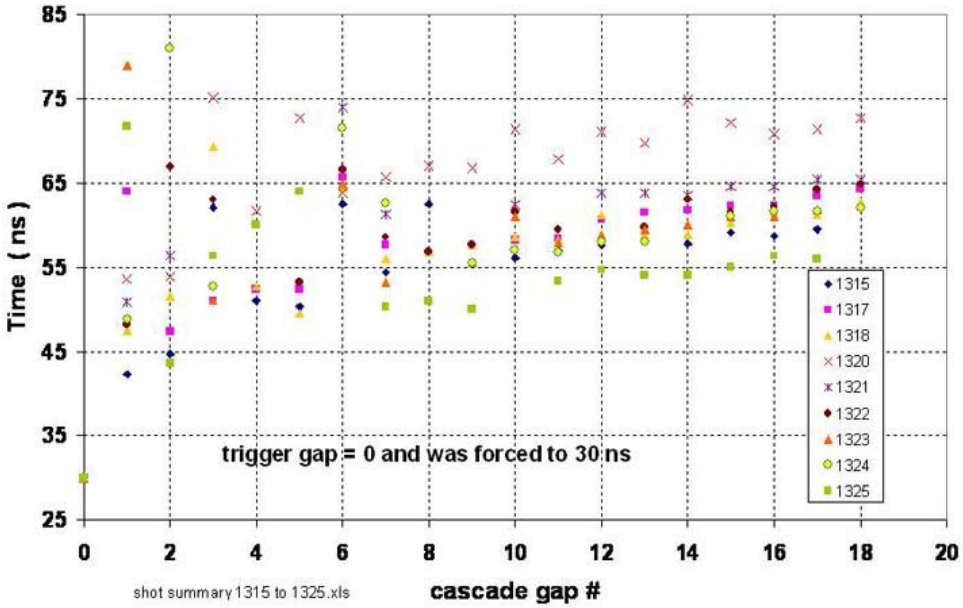

Figure C-4. Breakdown times for the cascade gaps in the Z_{20} gas switch on 10 shots.

Figure C-5 shows a statistical analysis of the cascade gap breakdown times. The top data points (diamonds) show the average breakdown times, with the laser-trigger gap breakdown time arbitrarily defined at 30 ns. On the average, there is 25-ns delay between the laser-triggered section breakdown and the first cascade gap breakdown. The rest of the cascade section breaks down in ~10 ns. Anything that could decrease the delay between the laser-trigger gap and the start of the cascade section breakdowns would have a large effect on the switch's run time.

The bottom two sets of data points show the standard deviation of breakdown times, and more importantly, the standard deviation of the differences in breakdown times between nearest neighbor gaps. The plot of standard deviation of differences indicates that almost all of the jitter in the cascade run time is contained in the first 8 cascade gaps and that the remaining 15 gaps contribute very little to the jitter.

Figure C-6 shows a comparison of the average cascade gap breakdowns shown in Figure C-5 and results of an electromagnetic (EM) calculation of the breakdown of the cascade gaps using the "Quicksilver" EM code. There is reasonable agreement between the streak camera data and the Quicksilver simulations, with both predicting a relatively long delay between the laser-triggered gap and the first cascade gap and a fast breakdown of the rest of the gaps. Note that the Quicksilver calculations were done on a version of the switch with 25 cascade gaps whereas the switch the streak camera looked at had only 23 gaps.

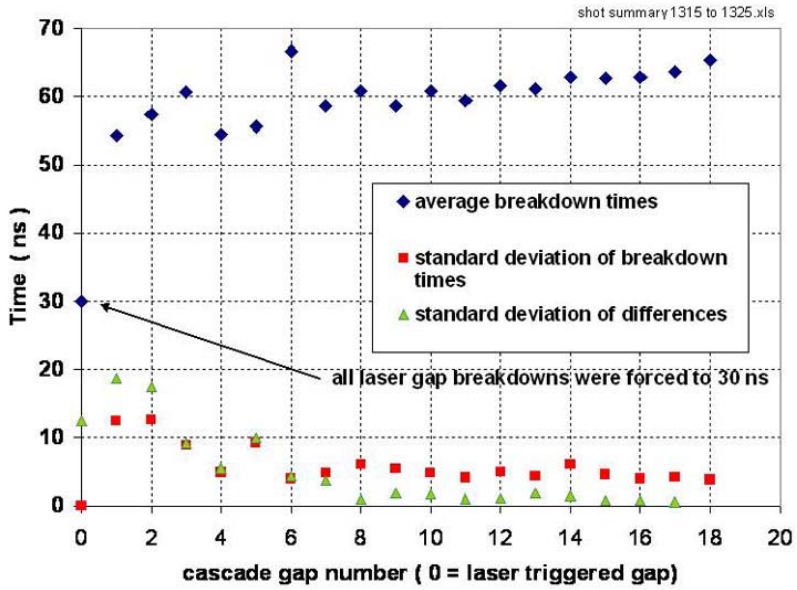

Figure C-5. Statistical analysis of breakdown times of cascade segments in Z_{20} gas switch. Most of the delay is caused by the turn-on time of the first cascade segment and most of the jitter occurs in the first eight cascade segments.

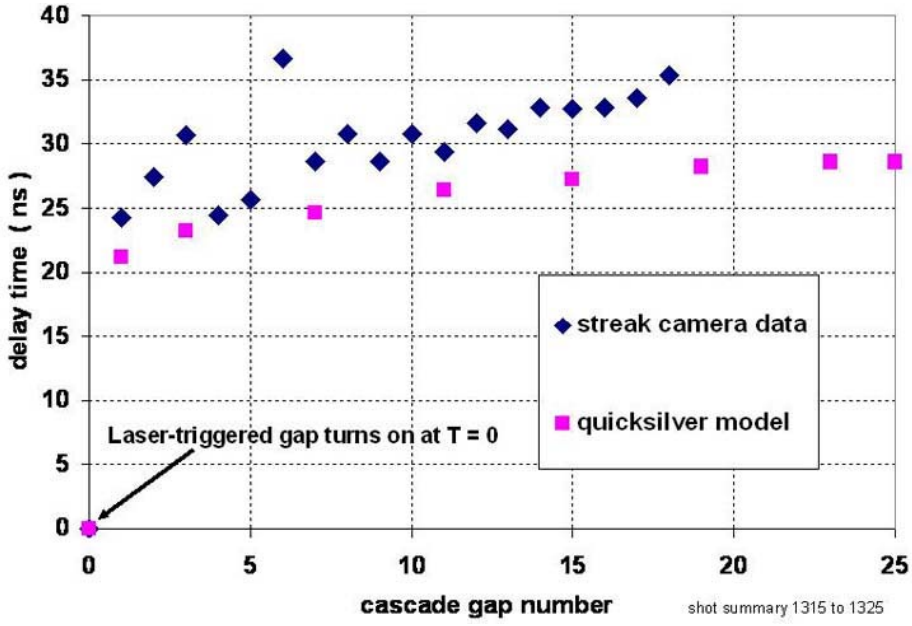

Figure C-6. Comparison of average cascade segment breakdown times with Quicksilver electromagnetic simulations of the switch.

We have had problems accurately determining when the laser pulse reaches the laser gap relative to the time the other gaps break down as seen by the streak camera. We have, therefore, recently taken some of the waste green energy from the laser to generate a timing marker directly on the streak pictures. The green laser energy is led through an optical fiber to the streak camera slit and produces a short, bright mark on the streak image as seen in Figure C-7. After correcting for time-of-flight distances of the laser light both in the fiber and on the way to the switch, this laser mark tells us when the laser energy reached the switch, relative to the time the various segments of the switch broke down, with an accuracy of a few nanoseconds.

Of particular interest, an initial check with the laser monitor indicates that the laser-triggered section of the switch is breaking down about 32 ns after the laser pulse arrives, in agreement with electrical data. This is a very long breakdown time for a laser-triggered switch and suggests that our laser triggering is currently marginal. We will investigate how to improve the triggering in the next fiscal year.

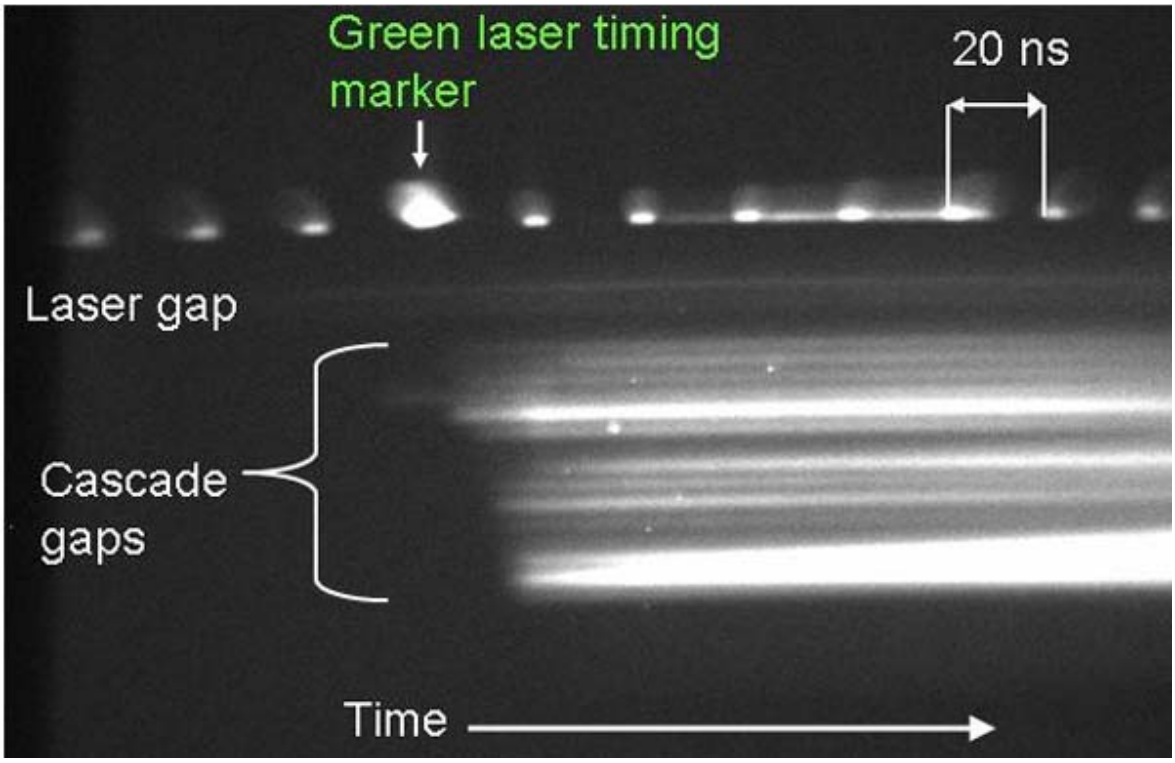

Figure C-7. Streak camera picture of Z_{20} gas switch on Shot 1416. The green laser timing mark gives an absolute timing reference of when the laser arrived at the switch.

APPENDIX D. Laser Trigger System

Introduction

At Sandia National Laboratories (SNL), a long and successful history exists for operating Rimfire cascade gas switches on pulsed power machines. These switches have been operated in a self-break mode (DCA) and a triggered mode with both electrical (Saturn) and laser-driven (Z, Hermes, RITS) trigger arcs. Now, most large multi-module machines use a laser-based trigger because of the more accurate timing a laser provides.

Going into the Z Refurbishment (ZR) project there was little worry about the Laser Trigger System (LTS) since laser triggering of recent Rimfire switches had been stable. LTS was primarily an afterthought, an exercise in system integration: Get the laser focused into the switch and it will work. To route the beam from the existing fixed position of the laser tower to the new location of the gas switch, add two extra mirrors. To prevent flashover of the laser crossover tube, add one extra window so the SF_6 pressure can be independently increased in the tube. To prevent oil from ever leaking down the laser tower, add another extra window for insurance. LTS for ZR should be set.

Unfortunately, the number and quality of the optics appears to make a difference in the spark length and brightness, which in turn can dominate the runtime and associated timing jitter of the switch. It is also unfortunate that every machine parameter considered, including the time of day, appears to influence switch performance, in particular the runtime of the switch trigger gap. This sensitivity to so many parameters causes confusion by making it difficult to perform well-controlled experiments. Perhaps if the trigger gap were not operating so close to the edge then isolating the most important controlling parameters would be easier. For now, on the higher-voltage ZR switch, the runtime jitter is more sensitive to the spark length for the than it was on the Z switch. With the Inertial Confinement Fusion program making demands for higher-current, shorter-pulse-length machines, peak operating voltages and E-field stress on switch components will only increase. Therefore a comprehensive understanding of how switch performance depends on gas switch parameters is critical to the success of all next-generation high-current machines. This report summarizes work in progress but is not yet a definitive treatise on the topic of laser-triggering MV class gas switches.

The main objective of LTS for a pulsed power gas switch could be stated simply as,

LTS must trigger the switch consistently shot after shot.

The success in meeting this objective is typically quantified by overall switch performance requirements such as timing jitter, soft failure rates (prefires, no-fires, or surface flashover of insulators) and lifetimes of components. LTS contributes to meeting these requirements but is not the only factor. Both LTS and the switch design are responsible for the overall switch performance. However, one could isolate a more specific objective for LTS. For example,

LTS must reliably generate a spark of some specified length in the trigger gap at a specified SF_6 pressure shot after shot.

At this point it is not possible to specify a minimum length for the laser spark to properly trigger the Z_{20} switch with a specified jitter. A primary goal for laser triggered gas switch (LTGS) research is to understand the relationship between the laser spark length and the runtime of the trigger gap. Perhaps it is beneficial that no spark length specification exists. The system can only produce a certain length spark. Then we must determine if that is sufficient to meet jitter requirements on the switch. Presently, we do not understand how the trigger gap runtime (and hence the jitter) depends on the length of the spark for the current Z_{20} switch.

Physical Layout of the Various LTS

Z Layout

As a reference, the optical layout of the Tempest LTS on Z is shown in a CAD drawing in Figure D-1. This is the original Tempest LTS that was operated successfully on Z since January 2003.[1,2,3] This LTS was the first hardware installed as part of the ZR upgrade but has now been removed in preparation for installing ZR pulsed power components. Figure D-2 shows a cartoon schematic of the LTS for a single module on Z. It shows the order and general layout of the optical components. The drawing is not to scale. The laser is a quadrupled Nd:YAG laser with 30 mJ of λ = 266nm light in a ~3 ns pulse. The beam path of the Z LTS was relatively simple, utilizing four mirrors and one window to deliver the beam to the final focusing lens and into the switch. The operator aligns the system at a computer workstation by monitoring images of targets behind the mirrors and adjusting motorized mirror mounts.[2]

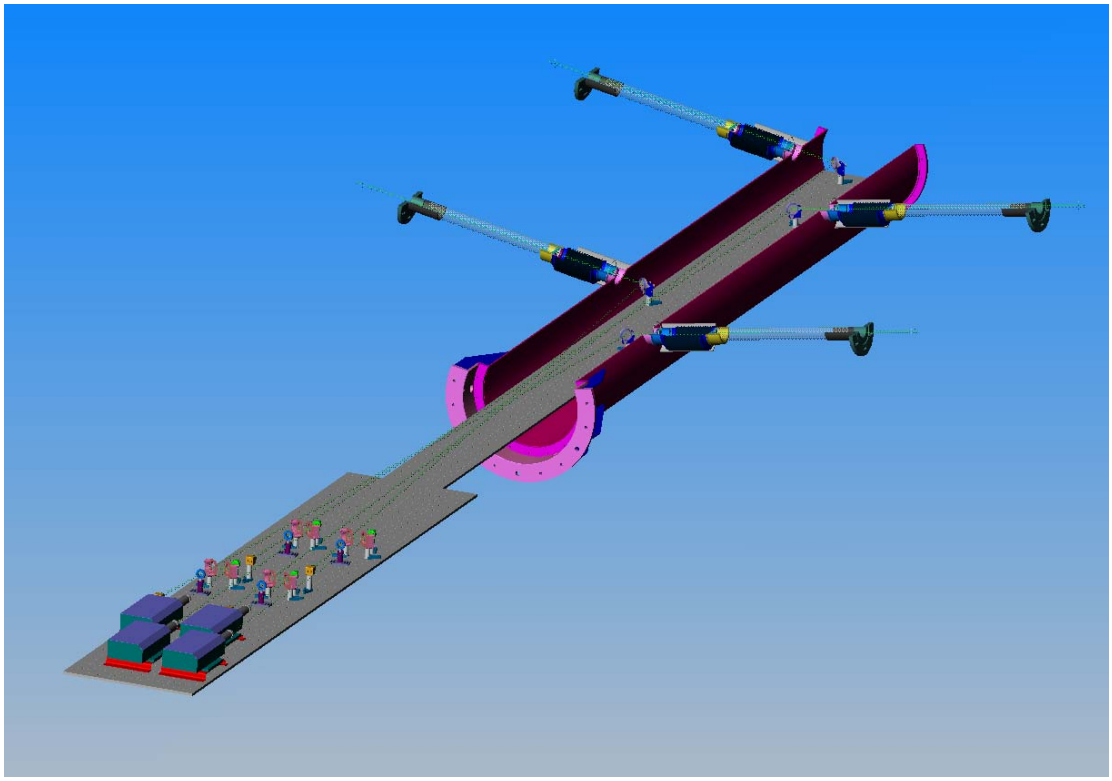

Figure D-1. Z: CAD drawing showing the physical layout of the original Tempest LTS components in the laser tower and through the crossover tube.

ZR Layout

The primary difference between LTSs on ZR and Z is that the ZR system was initially designed with an off-axis focusing mirror, f = 1 m, instead of the f = 0.5 m lens used on Z. The intent was to move the focusing optic further away from the switch to reduce contamination by debris generated during switching. LTSs with longer focal lengths, f = 1 m, have been used successfully to trigger megavolt gas switches on other pulsed power machines at SNL: Switch Test Bed (STB), Hermes, and RITS. Also on ZR, the beam path inside the laser can needed to be folded to accommodate geometry constraints between the laser tower, laser can, gas switch, and the oil/water tank wall. Use of a focusing mirror instead of a lens reduced the number of optics required in the laser can.

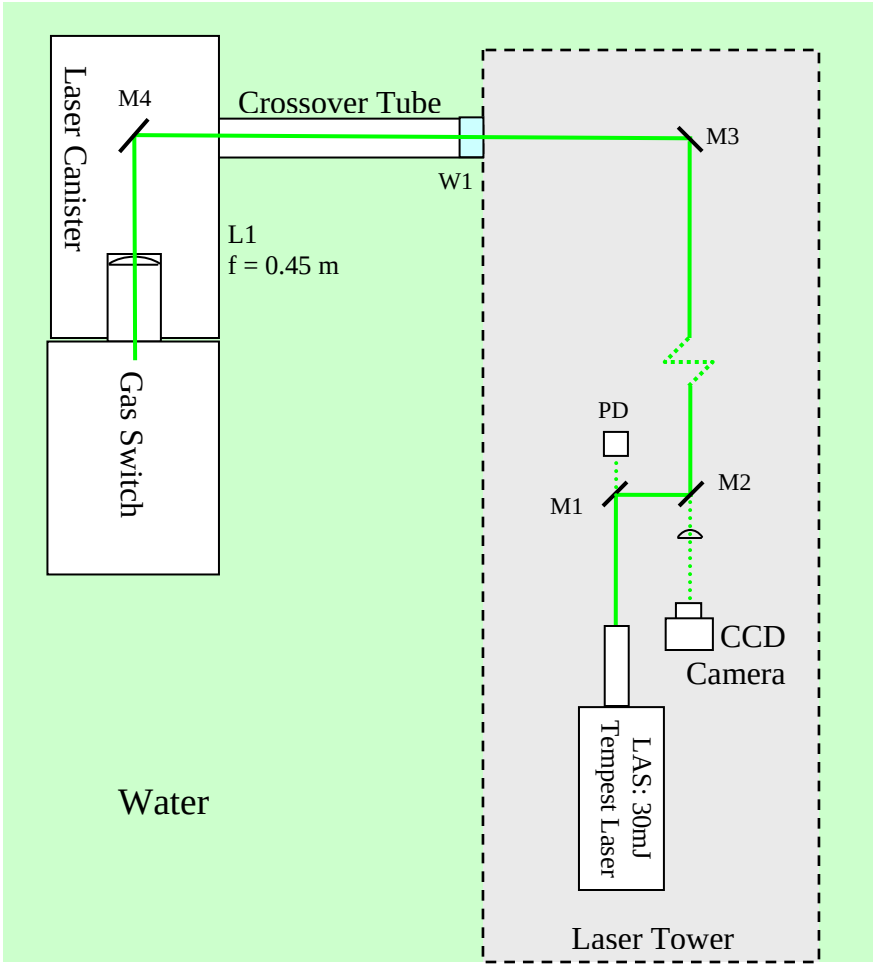

Figure D-2. Z: Schematic layout of the primary Tempest LTS optical components for a single module.

Unfortunately, ZR still uses two more mirrors and two more windows than Z to get from the laser tower to the gas switch. The extra optics were added to accommodate the gas switch being immersed in oil and the fact that the LTS towers were constrained to not move for structural reasons. Two extra windows were placed in the beam path to prevent oil from leaking down the tower or into the laser can if (when!) a crossover tube fails. Two extra mirrors were added to deliver the beam to the new switch position. Figure D-3 shows a CAD drawing of the laser tower and sidecar used to deliver the beam to the switch. The pulsed power modules have been removed to expose the folded path of the laser beam. Figure D-4 is a schematic cartoon of the LTS for a single module on ZR. It shows the order and general layout of the optical components. Again, this drawing is not to scale.

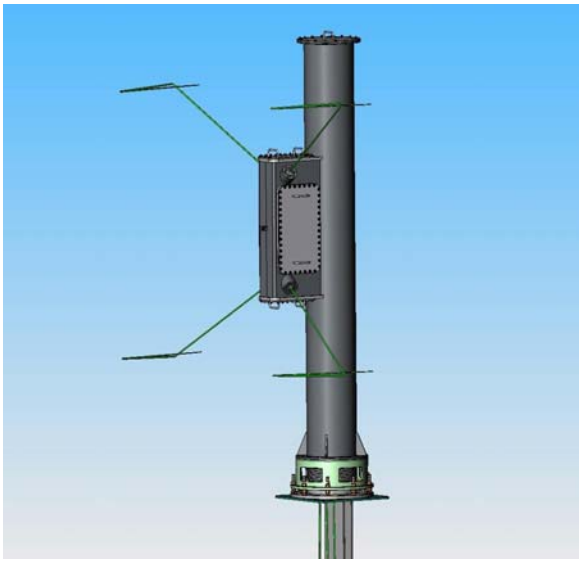

Figure D-3. ZR: CAD drawing of the laser tower indicating the laser beam path after the laser exits the sidecar attached to the laser tower. Modules and crossover tubes have been removed to reveal the folded path of the laser to each of the four modules. The center of the machine is to the left.

The problem with off-axis collecting mirrors, as most amateur astronomers know, is that they can create strong astigmatism and coma aberrations as the angle of incidence increases. Aberrations limit resolution and reduce the focusable intensity of a laser beam. Aberrations created by the off-axis spherical mirror were a concern and analyzed early in the project. Ray tracing and Gaussian laser beam propagation tools were used to analyze the optical system. Figure D-5 plots the peak focusable intensity along the optical axis for each of the systems assuming that the peak power in the laser beam is 10 MW. Again one can observe the sharp drop in peak focusable intensity as the off-axis angle is increased from 3º to 5º. This plot also shows how the astigmatism shortens the focal length of the reflective mirror. Figure D-6 shows the spatial distribution of laser intensity in the xy plane moving through the focus of the laser in the z direction. The three columns represent different angles of incidence, 0º, 3º, and 5º, between the laser and the normal to the mirror surface. The total included angle between the incident and reflected laser beam is twice this amount. The baseline ZR design has a 3º angle of incidence, which is the blue trace in Figure D-5 and the center column in Figure D-6. Shown to the left of each row in Figure D-6 is the distance from the focal waist of the on-axis (0º) case to the position of the intensity map shown. The calculation only includes aberration terms up to astigmatism so it does not include coma or higher-order terms. Also, the calculation does not include nonlinear optical effects in the SF_6 gas such as ionization, self-phase modulation and self-focusing, which are certainly occurring. After all, the intent of LTS is to laser-ionize the gas. Self-phase modulation and self-focusing effects always occur just under the intensity threshold for ionization. The only question is the amplitude of these non-linear effects in SF_6. Therefore, the intent of the calculation is to indicate the general quality of the optical system and not to duplicate the exact intensity profile of the laser focus. The intensity distribution is not significantly different between the 0º and 3º setups, although, some slight amount of astigmatism is observed at 3º that becomes much worse at 5º.

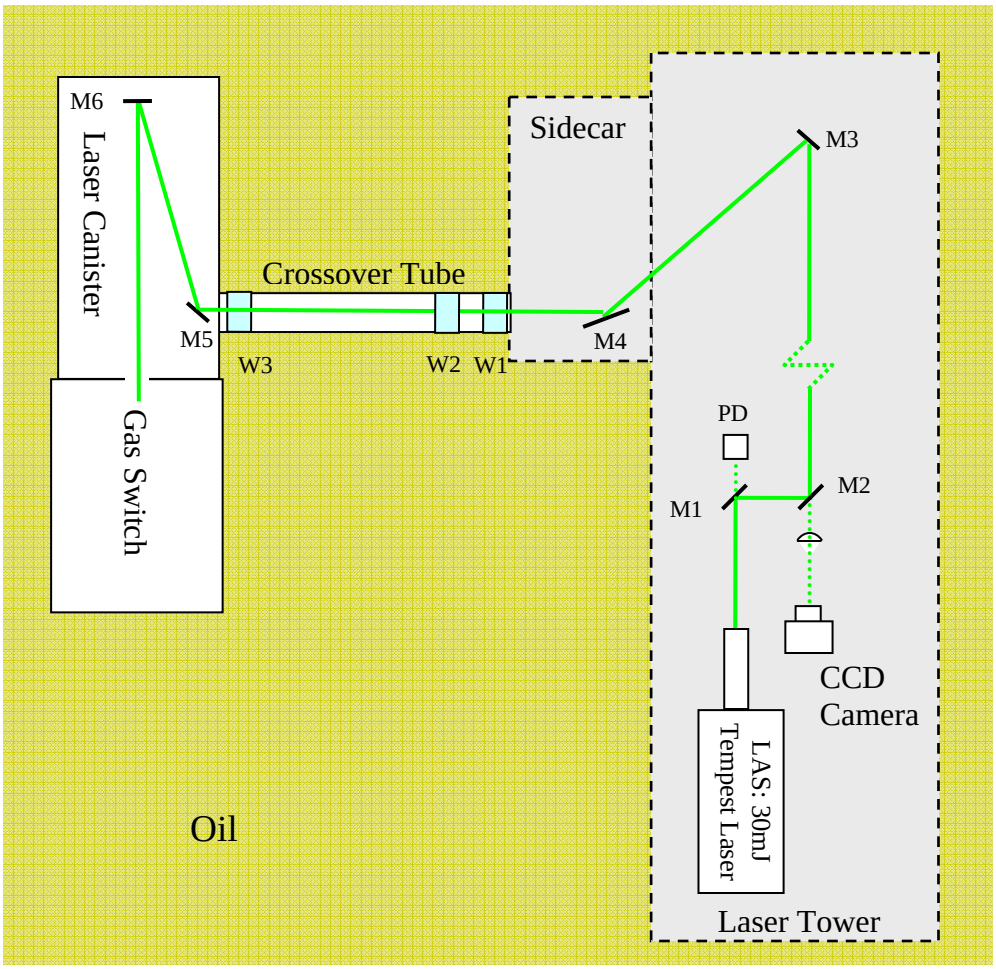

Figure D-4. Schematic layout of the primary Tempest LTS optical components for a single module on ZR. M6 is a concave focusing mirror with f = 1 m. Note: there is no isolation between the laser can and the switch. Optical components M6, M5, and W3 are all contaminated by metal and SF_6 byproducts during switching.

Unlike astronomical telescopes that utilize large apertures (a 400-mm-diameter Newtonian would be a large amateur telescope), LTS systems have smaller apertures, defined by the diameter of the laser beam instead of the diameter of the optic. The Tempest LTS uses a 12-mm-diameter beam after the 3x beam expander. Fortunately for LTS, optically slow systems, with small F/ numbers, have significantly smaller aberration terms.

The baseline design for ZR still includes an off-axis mirror, f = 1 m, and does not have a window to isolate the laser can from the switch volume. The consequence of not isolating the laser can is rapid contamination of all the optics within the laser can. Maintenance would be required on all modules every 10 to 20 shots to clean and replace contaminated optics. Also, some Z_{20} data suggests the probability for flashing the switch envelope is reduced with this same isolation window used to increase optics lifetime. A trigger plate with shielded triple points and new procedures for cleaning the insulator housing were implemented on Z_{20} at approximately the same time as installing the window.

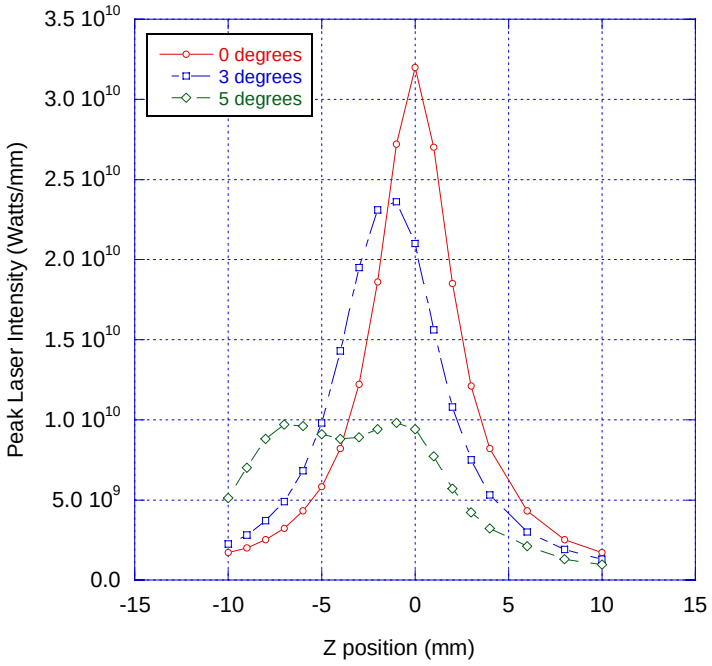

Figure D-5. Intensity of a Gaussian laser beam along the optical axis at the time of peak power as calculated with ZEMAX physical optics propagator. The focusing optic was a spherical mirror with a 2-m radius of curvature. Curves are shown for 0°, 3° and 5° angle of incidence relative to the optic normal. The baseline design for ZR is the 3° case shown in blue. Total included angles are twice this value. The beam conditions were set for a 12-mm diameter waist located 10 m before the focusing optic. The total power in the beam at the peak of the pulse is set to 10 MW (30 mJ in 3 ns).

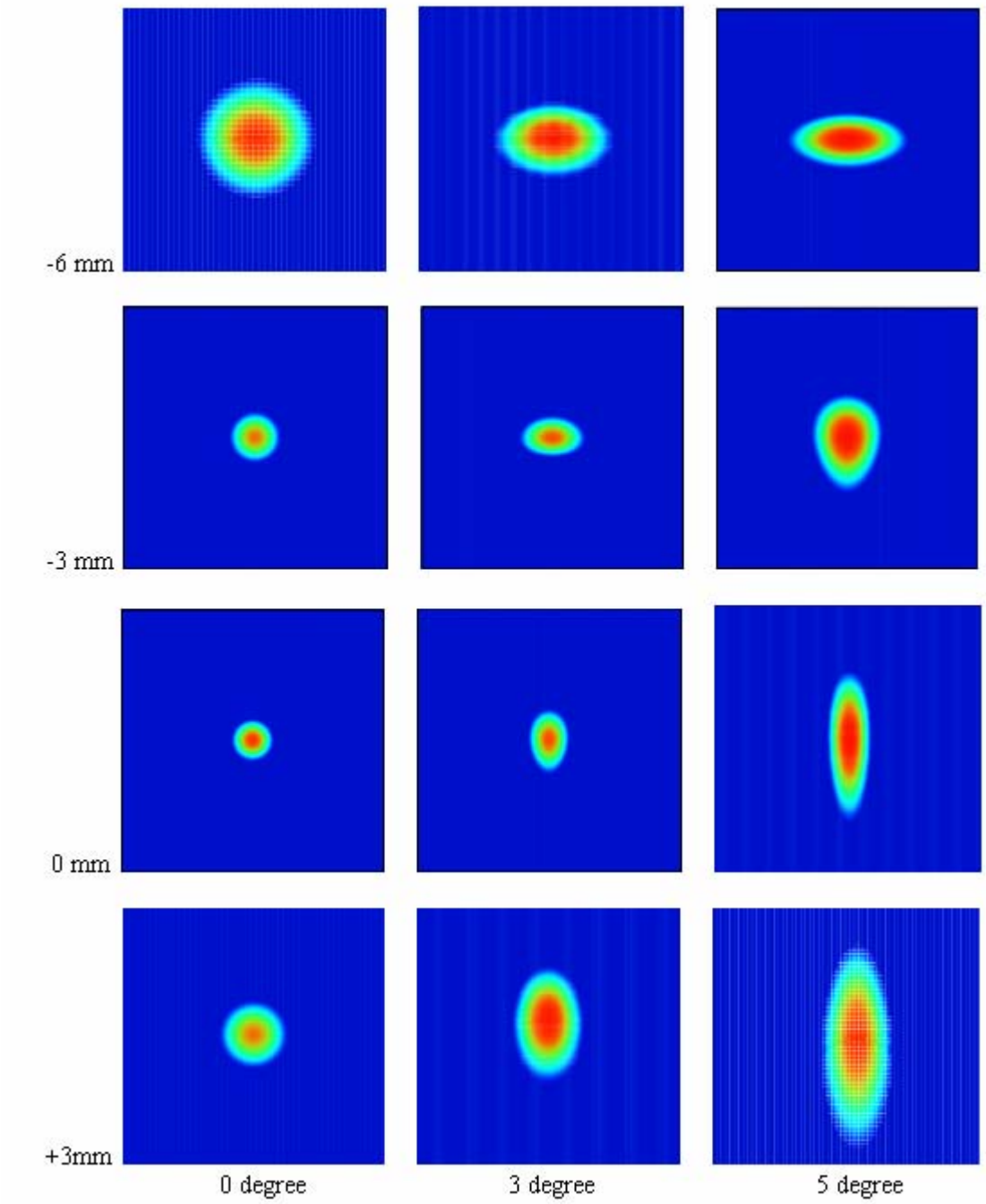

Figure D-6. Relative intensity profiles for a Gaussian laser beam through the focal waist of a f = 1 m spherical mirror at 0°, 3° and 5° angles of incidence. The baseline design for ZR is the 3° case shown in the center column. The total included angle between the incident and reflected beam is twice the angle of incidence. The distance specified for each row of images is the distance away from the waist of the 0° case, along the axis of propagation. The spatial extent of each image is 0.4 mm. Refer to Figure D-5 for the peak intensity on the axis.

Z_{20} Layout

The LTS layout on Z_{20} has evolved over the last two years. The initial LTS design mimicked ZR as shown previously in Figure D-4, using the same number of mirrors and windows. The overall architecture is the same for Z_{20} and ZR but the distance between optics is different.

Problems were immediately encountered on Z_{20} with the contamination of optics in the can. Since the switch and laser can volumes were not isolated, SF_6 and tungsten by-products created during switching could coat the optics and reduce the transmitted laser intensity. A window was added to isolate the laser can from the switch volume but still used a focusing mirror. The current configuration is shown in Figure D-7. The isolation window added to the laser can is represented by component W4. A focusing lens, f = 0.5 m, was used to create a shorter but brighter spark. A focusing mirror could not be used because it would place a window too close to the switch, exposing it to too much debris. Another problem with a short focal length mirror is that the angle of incidence would increase, creating more astigmatic aberrations. See Figure D-5.

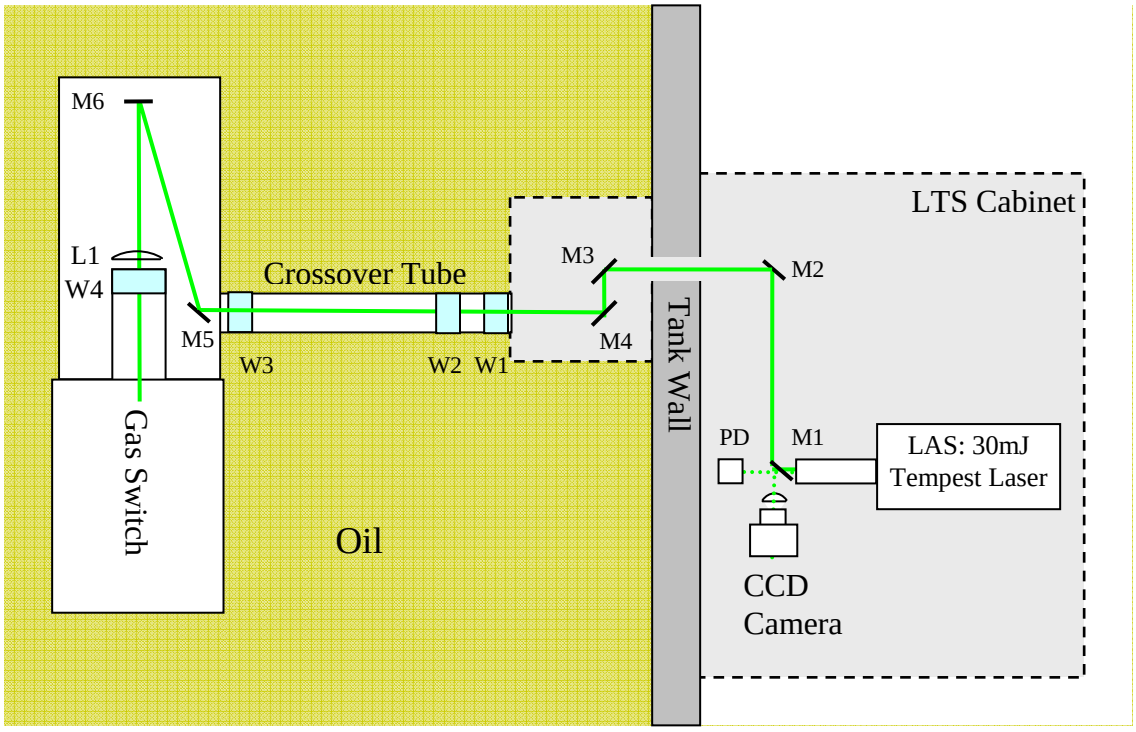

Figure D-7. Schematic layout of the LTS optical components on Z_{20}.

STB Layout

STB has the simplest LTS layout of any of the machines. A beam splitter, two mirrors, and one lens are the only components in the beam path. Figure D-8 shows the schematic layout of the optical components in the STB LTS.

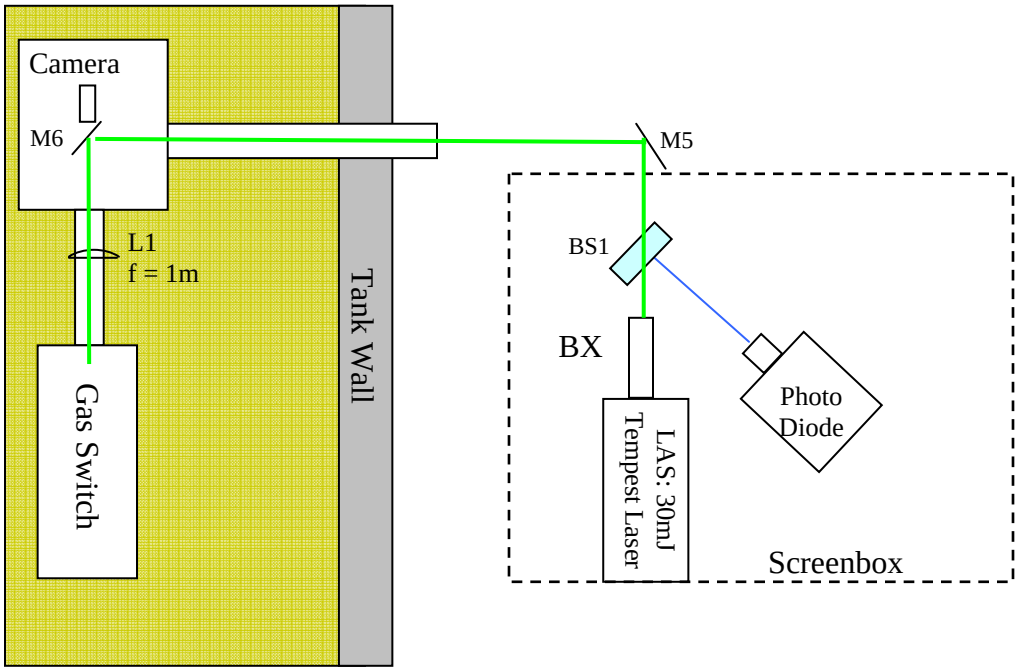

Figure D-8. Schematic Layout of the original LTS for STB.

Comparison of the LTS Layouts

The LTSs on the different machines can be compared based on the following criteria: the F/# of the focus, whether the focusing optic is a mirror or lens, the off-axis angle, the number of mirror and window surfaces, the amount of glass, the total path length, etc. The length of glass and the total number of surfaces used in the various LTS setups is summarized in Table D-1 and shown graphically in Figure D-9. Optical components inside the laser and the 3x beam expander are left out of the comparison since they are common to all the LTSs. Note that STB and Z have the least amount of glass and the fewest optical surfaces. These are the two systems that function the best with Tempest-based LTSs.

Table D-1. Comparison of the total number of optical surfaces and the length of glass for the LTS on several pulsed power machines considered in the LTGS program. Note the total number of surfaces includes lenses, windows, and mirrors.

	ZR, off-axis mirror	**ZR Lens focus**	**Z**	**Original STB**	**Z_{20}**	**Current Z_{20}**	**Modified STB**
Number of surfaces	12	14	8	6	16	14	18
Length of glass (mm)	38.1	43.1	20	10	52.6	43.1	58

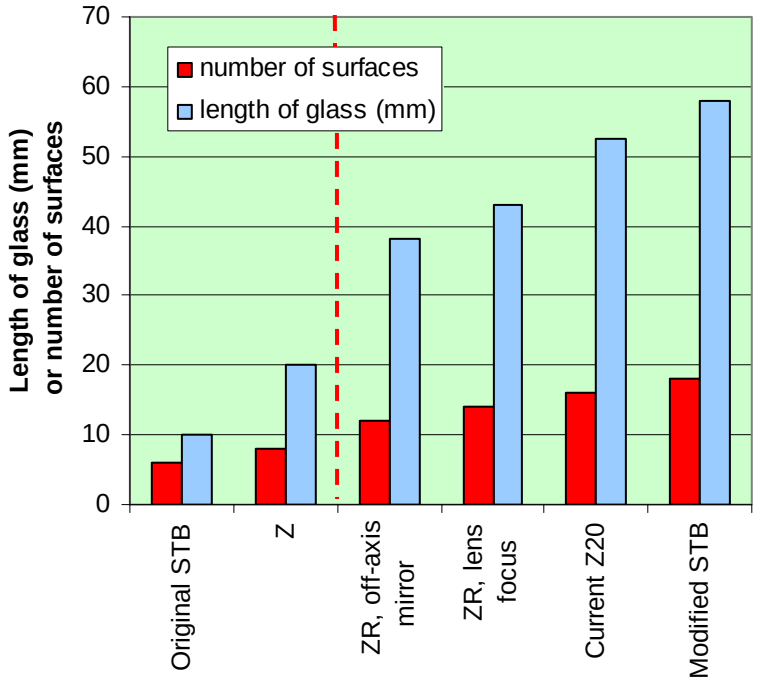

Figure D-9. Bar chart comparison of the number of active optical surfaces and the length of glass for the various LTSs on different machines (from Table D-1). Note that Z, the current Z_{20} and ZR all have f = 0.5 m focusing elements while the other systems are f=1 m. The dashed red line separates systems that run with short runtimes and low jitter (<5 ns) to the left from high jitter systems to the right.

Laser Alignment

A new scheme to align the LTS has been developed on Z_{20} for use on ZR. Previously on Z, the LTS was aligned by viewing reflective targets located behind the mirrors.[2] The targets were illuminated by residual green light leaking through specially designed ultraviolet (UV) mirrors that had R = 50% reflectivity in the green but R = 100% in the UV. Alignment on Z_{20} and ZR is still based on residual green second harmonic light propagating colinearly with the fourth harmonic UV. However, now, unlike before, the operator can observe the spark directly in the switch. Figures D-10 and D-11 illustrate the alignment scheme for a focusing mirror and focusing lens based LTS, respectively. In the past, since the spark could not be observed by the alignment camera, the orientation of the final mirror was assumed not to change after installation. Previously, in an attempt to verify that the final mirror had not moved and that the laser was indeed in the switch, "light-ups" were performed. During a light-up, the lights in the hi-bay would be extinguished and observers positioned around the mezzanine attempted to observe the laser spark through the frosted switch insulator housing sitting under several feet of water. Even when properly aligned, the laser flash was barely visible so that light-ups were a highly unreliable procedure.

Now the laser spark can be observed directly in the switch, making alignment more reliable. Direct observation of the spark could also improve optic lifetime because it allows the possibility

of shrinking the aperture in the anode electrode from a diameter of ½ inch anywhere down to ¼ inch. A smaller aperture should reduce the flow of contamination from the switch onto the optics. The primary drawback of the current alignment scheme is the increased number of mirrors (six versus four) in the LTS. Imaging each of the six mirrors to verify that the beam is not clipping is difficult if not impossible with a fixed focal length camera. Remote control of the alignment camera focus would help, but with 36 cameras cost and reliability are an issue. Ultimately, the simplest camera system that achieves proper alignment will be the most robust system. For now, to ensure that the beam is not clipping on a mirror mount, LTS operators will perform a visual observation of the top sets of mirrors in the tower. They will also use the camera to look for unfocused glare if a beam is clipping on a mount. As operations gains experience with the multi-module ZR system, improvements to the alignment scheme will be implemented.

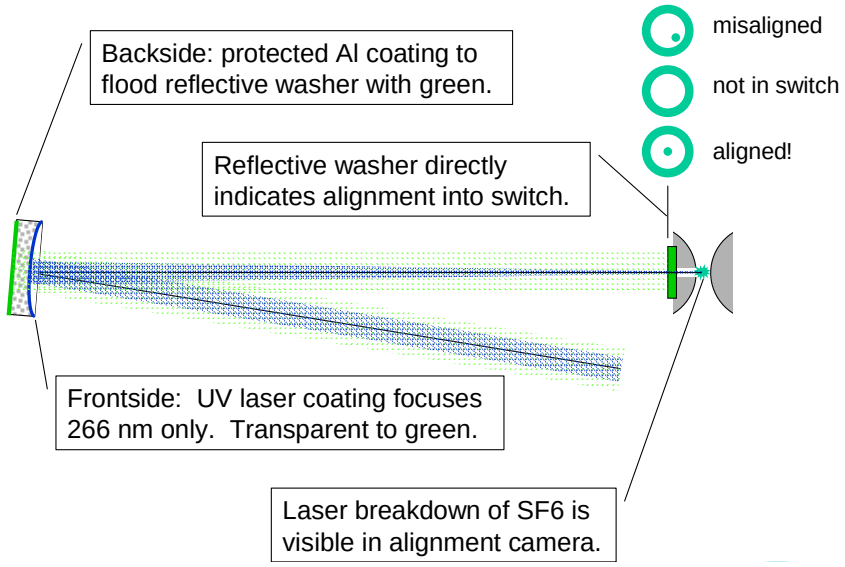

Figure D-10. Focusing mirror alignment scheme. Schematic layout of the LTS optical components inside the laser canister illustrating how the laser would be aligned with a focusing mirror. The UV beam and the green 2nd harmonic are shown in blue and green. The back, flat surface of the focusing mirror is used to reflect the green and illuminate the reflective alignment washer while the colinear UV beam is focused in the gap.

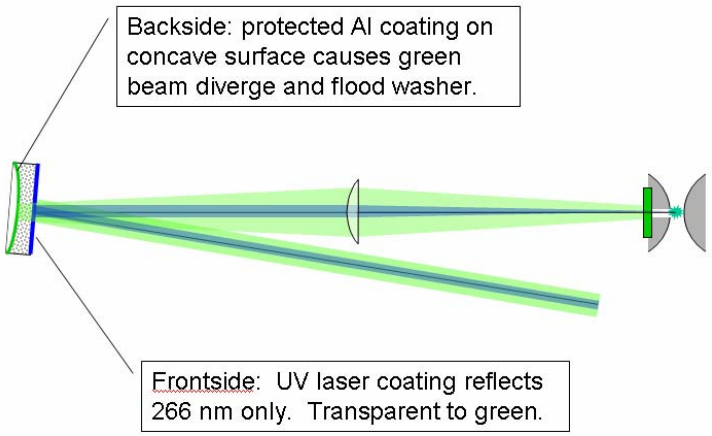

Figure D-11. Focusing lens alignment scheme. Schematic layout of the LTS optical components inside the laser canister illustrating how the laser would be aligned with a focusing lens. Note that the final mirror has been flipped and the coatings reversed. The back Al-coated surface now causes the green beam to diverge so that the lens cannot focus it completely before reaching the reflective washer to illuminate it.

Experiments

Characterizing Z_{20} Trigger Performance: The "Squiggle"

The best indicator of LTS performance is the runtime of the trigger gap, which is the time it takes for the trigger gap to close after the arrival of the laser pulse. Short trigger runtimes indicate a switch that will operate with low jitter. On Z_{20}, no specific monitors are in place to detect closure of the trigger gap. Instead, a "squiggle" on the PFL monitor was observed by Keith Hodge and John Corley to coincide with closure of the trigger gap. On shots where the cascade section pre-fired, no squiggle was observed. The PFL voltage is shown in green in Figure D-12. The start of the squiggle occurs when a high-frequency ringing associated with shorting the trigger electrode capacitance breaks from the background noise, which has a lower amplitude and frequency. The time between the photodiode (PD) signal and the start of the squiggle is the trigger section runtime. The PD signal is normalized to the same peak value as the PFL and a threshold of -10^5 V is used to determine the laser time. Cascade closure is indicated by the break in the PFL voltage. Again a threshold of -10^5 V is used. In this fashion the total runtime (and jitter) of the switch can be broken down into trigger and cascade components.

John Corley made a slight modification to the Screamer model for Z_{20} to verify that the origin of the squiggle could be the shorting of the trigger electrode capacitance. The Z_{20} Screamer model with modifications is listed in Appendix D1. The modifications are highlighted in blue in the "Trigger Plate" section of the circuit code. An ELECTRO model of the switch determined the trigger capacitance to be ~15 pF. Figure D-13 shows a comparison of the Screamer output and the measured PFL voltage for Shot 1235. The sign of the squiggle is correct and period is approximately the same. Little effort was made to match all the features precisely but it seems sufficient to justify associating the "squiggle" with closure of the trigger gap.

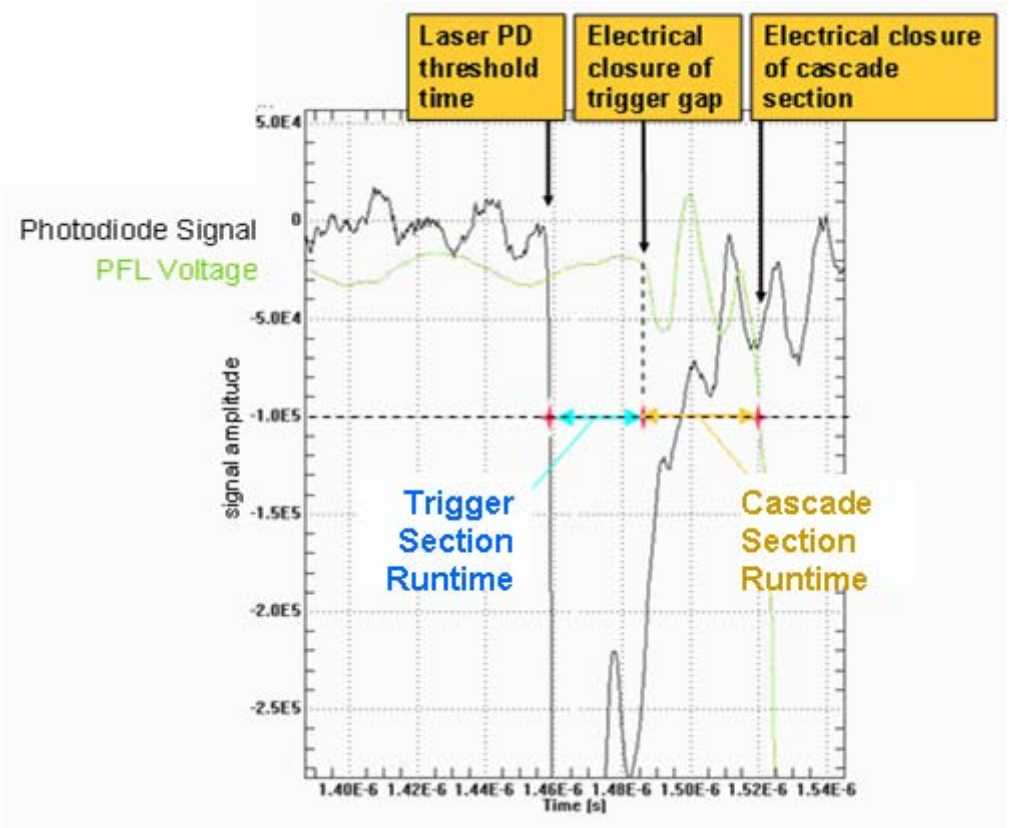

Figure D-12. Photodiode and PFL voltage waveforms on Z_{20} illustrating the trigger and cascade section runtimes.

An Ideal Laser Focus

The bottom line for any LTS is to create the most effective "needle" possible to break down the trigger gap of a switch. Effective implies that the spark has the proper combination of length and conductivity to create sufficient E field stress in the trigger gap to cause breakdown of the gas in a timely, low-jitter fashion. A possible indicator of a large change in conductivity is the "brightness" of the spark. Brightness should indicate that a large concentration of SF_6 molecules have been ionized, creating a large change in conductivity. A simple image of the spark should indicate how well it might trigger a switch.

Basic laser textbooks treat the focusing properties of a laser beam with a Gaussian intensity profile.[4,5] The focal spot size is typically characterized by the radius, *w*, where the intensity drops by *1/e*. Eight-six percent of the total power in the beam is contained in the diameter 2*w*. The minimum spot radius or waist, w_0, is related to the focal length, *f*, by

$$w_0 = \frac{f\lambda}{\pi w_s}, \qquad \text{(D-1)}$$

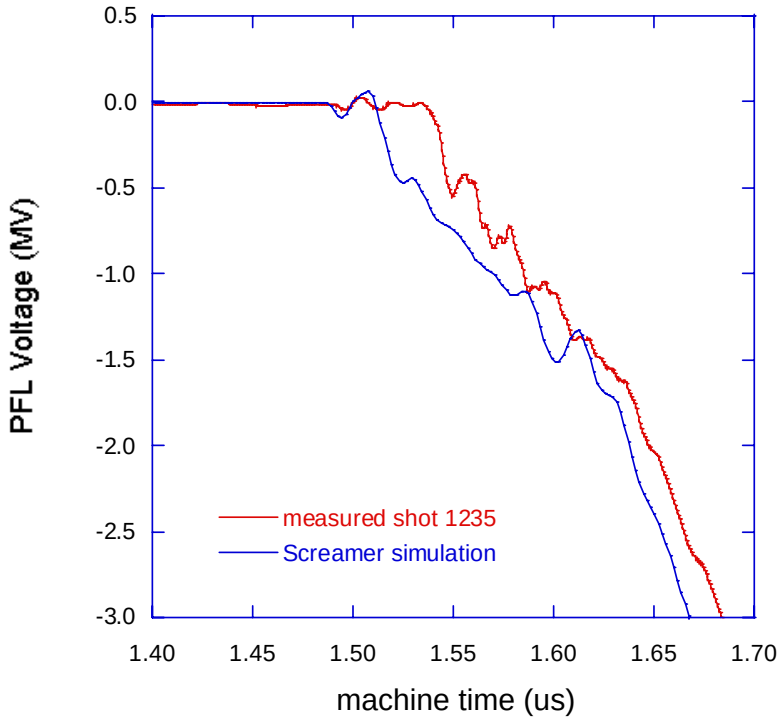

Figure D-13. Plot of the measured and calculated PFL voltages for Shot 1235 that compares the "squiggle." The Screamer circuit code has been modified to include the switching of the trigger gap capacitance and is shown is Appendix D1.

where λ is the wavelength and w_s is the beam radius on the focusing optic. The waist length, $2Z_R$, is defined as the point along the optical axis to either side of the waist where the spot size has increased by $\sqrt{2}$ compared to w_0 or the intensity on-axis has dropped by a factor of 2. The Rayleigh length, Z_R, is related to the waist by

$$Z_R = \frac{\pi w_0^2}{\lambda}. \qquad \text{(D-2)}$$

The waist extends approximately one Rayleigh range to either side of the minimum. Figure D-14 illustrates the parameters used in Equations D-1 and D-2 and Table D-2 summarizes them. The length of the spark can be increased by reducing the F/# of the focal system, which can be achieved by either increasing the focal length or reducing the beam diameter. Inversely, the focusable intensity can be increase by increasing the F/#. Because of the inverse relationship between the Z_R and w_0, the length and brightness of the laser spark must be traded in an engineering compromise by adjusting only the F/# of the focal system. For a fixed-diameter laser beam, increasing the focal length reduces the peak intensity, I_P, while increasing the Rayleigh range, Z_R, where

$$I_P \propto \frac{1}{f^2} \quad \text{and} \quad Z_R \propto f^2. \qquad \text{(D-3, D-4)}$$

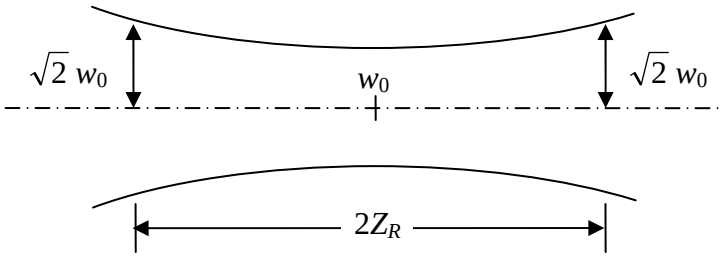

Figure D-14. The waist region and Rayleigh range near the focus of an ideal Gaussian laser beam.

Table D-2. The calculated waist diameter and full Rayleigh range for an ideal Gaussian beam. The expanded beam diameter is 12 mm and the wavelength is l = 266 nm.

Focal Length (m)	Waist Diameter $2w_0$ (μm)	Rayleigh Range $2Z_R$ (mm)
0.5	14.1	1.2
1.0	28.2	4.7

Aberrations

Aberrations only reduce the focusable intensity from the diffraction limit[1] and therefore must be kept to a minimum. Passive optical components such as windows, mirrors and lenses as well as index fluctuations in the optical path can only add aberrations. Aberrations can be removed by actively controlled adaptive optics (AO) such as those used on the latest generation of astronomical telescopes to remove atmospheric fluctuations or to clean up the beam of high-powered lasers. However, these systems are complicated and somewhat finicky to operate. The expense and practicality of operating 36 AO systems in a pulsed power environment might be questionable if not impossible. Therefore, high-quality optics should be used and the number of optics kept to a minimum. High quality does not necessarily imply that an expensive, hard-to-acquire optic must be used everywhere in the optics train. This is because root-mean-squared (RMS) wavefront distortions add in quadrature. High quality means that the optic that dominates the aberration with the worst surface figure must be as perfect as possible.

Mirrors, windows, and a lens comprise the set of optical components in the beam path of the LTS. Mirrors are typically characterized by a surface figure that specifies the maximum excursion of the surface, over 85% of the active area. Optical surfaces are typically measured by an interferometer at the HeNe wavelength $\lambda = 632.8$ nm. A $\lambda/10$ surface would have excursions that are less than 63 nm. The wavefront aberration for a mirror will be twice the surface error since the reflected light double passes any surface deviation. Lenses and windows are characterized by a similar specification that includes the effects of surface irregularities and volume fluctuations in the index of refraction.

[1] OK, the diffraction limit can be tricked, but it takes a very specific aberration, e.g., see David R. Smith, Beating the diffraction limit, *Physics World*, 2004, vol. 17, no. 5, pp. 23-24, or google the world wide web.

Figures D-15 through D-20 show maps of the wavefront distortions of several of the optics used in the LTS. Table D-3 summarizes typical measured values of the peak-to-valley (PV) and RMS wavefront distortions. The units are given in fractions of a wave at 632.8 nm. *Important note*: At the LTS operational wavelength of 266 nm, the phase aberration is 2.38 times larger than at the HeNe measurement wavelength, 632.8 nm.

Table D-3. Typical values for the wavefront distortions of individual LTS optical components. Units are given in fractions of a wave. Measurements are made over a 0.5-in. aperture, equivalent to the laser beam diameter. Peak-to-valley (PV) and root-mean-squared (RMS) values are measured at l = 632.8 nm and scaled (2.38x) to the operational wavelength, 266 nm.

	Wavefront Aberration of LTS Optics (wave)			
Component	**PV 633 nm**	**PV 266 nm**	**RMS 633 nm**	**RMS 266 nm**
Mirror, R=1 @ 2x/4x	0.03	0.071	0.004	0.010
Mirror, R= 0.5 @ 2x	0.03	0.071	0.005	0.012
Mirror, Excimer & HeNe	0.01	0.024	0.001	0.002
Window, A0	0.01	0.024	0.001	0.002
Window, D1	0.02	0.048	0.002	0.005
Error bar	±0.01	±0.024	±0.001	±0.003

All the optics have comparable low levels of aberration and none stand out as particularly bad optics. In general, the windows have less aberration than the mirrors. Of the windows, the A0 grade are slightly better than the D1 grade, $\omega_{rms} = 0.001 \pm 0.001$ versus 0.002 ± 0.001, but any measured difference is at the detection limit of the interferometer. The various grades of Corning's fused silica are summarized in Table D-4. The D1 grade has a maximum index fluctuation of $\leq$3 ppm measured over the clear aperture of a 1-in.-thick blank. For a 0.5-in.-thick window, this corresponds to a maximum path difference of 27 nm. RMS fluctuations are typically 1/6 of the PV amount, which yields an estimated RMS wavefront distortion of 0.017 over the entire aperture. The measured aberration over a 0.5-in. aperture appears to be an order of magnitude better. One cautionary note is that the measurements are made at 632.8 nm and not 266 nm. The assumption that the index fluctuations are the same at both wavelengths might be questionable since the value of the refractive index is larger at 266 nm. The fluctuations could be larger too. Ideally the wavefront distortion should be measured at 266 nm also.

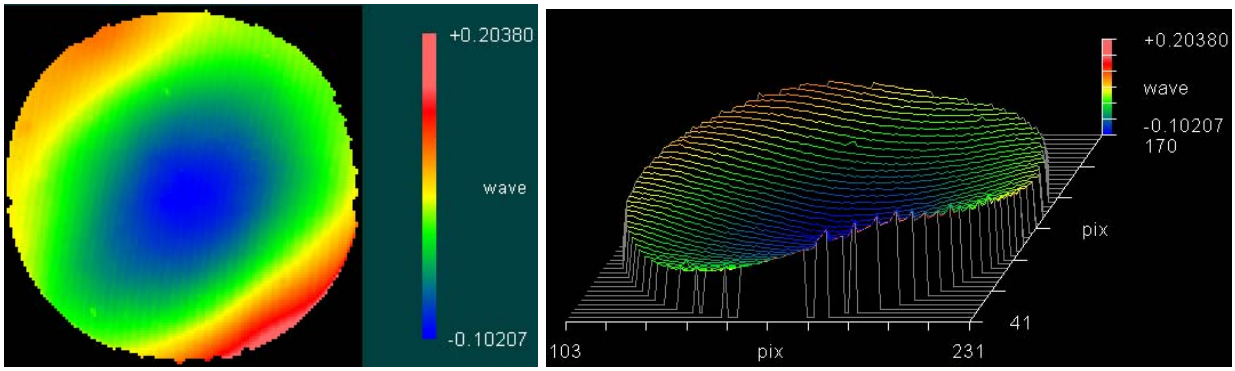

Figure D-15. Map of wavefront aberrations of a D1 grade fused silica window used on Z_{20} dual wavelength mirror (reflects both 2nd and 4th harmonic light) used in the LTS as measured by the Zygo interferometer. The map coves the active aperture, 1.8 in. of a 2 in. mirror. Only tilt has been removed. Note the slightly astigmatic "potato chip" deformation created by stress in the optical coating.

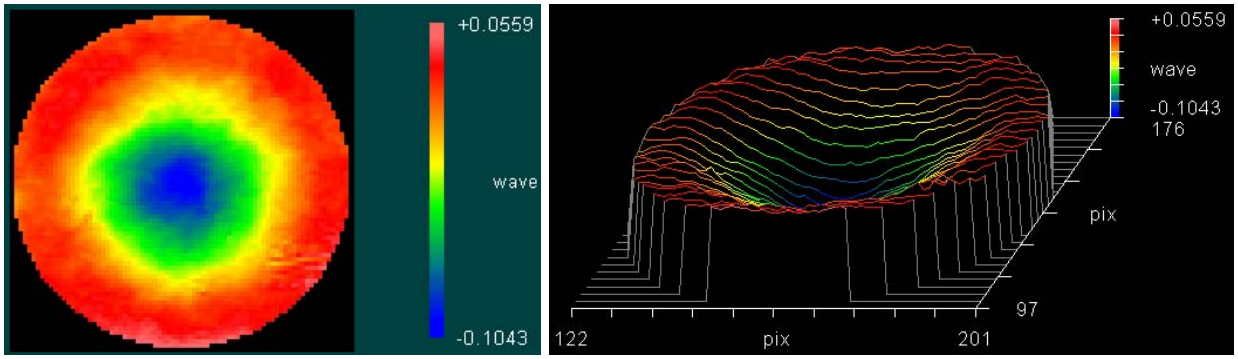

Figure D-16. Wavefront map of a different dual wavelength mirror shows symmetric strain. Power and tilt are removed.

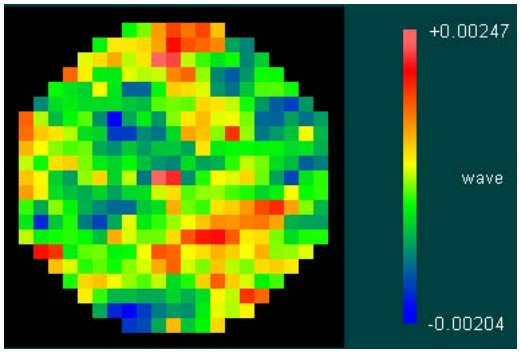

Figure D-17. Zygo wavefront map of the used AO grade window in Figure D-15 taken over a 0.5-in.-diameter aperture. Piston, tilt, and power terms have been removed. The wpv, the PV wavefront fluctuation, is less than 0.01 waves while the RMS fluctuation is 0.001 waves.

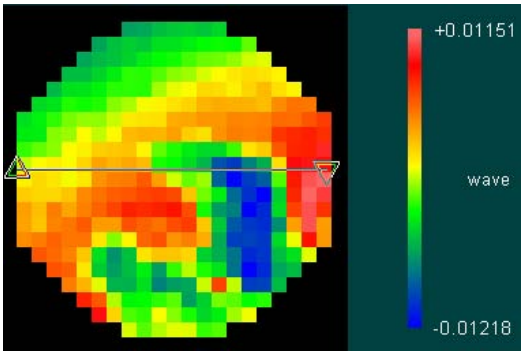

Figure D-18. Zygo wavefront map of the laser-damaged spot on the used AO grade window in Figure D-16 taken over a 0.5-in.-diameter aperture. Piston, tilt, and power terms have been removed. The PV fluctuation is less than 0.02 waves while the RMS fluctuation is 0.005 waves.

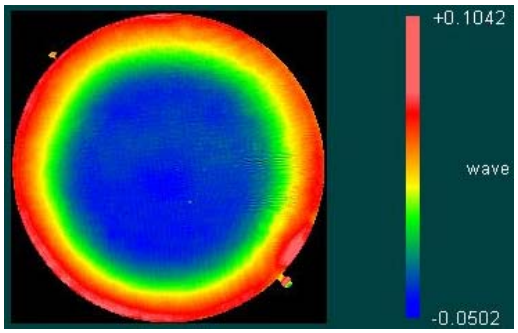

Figure D-19. Wavefront aberrations over the full aperture of a 45° UV mirror. This mirror has R = 50% in the green and is used on Z in front of targets and the camera. Power has been removed. Note the larger deformation-free region in the center.

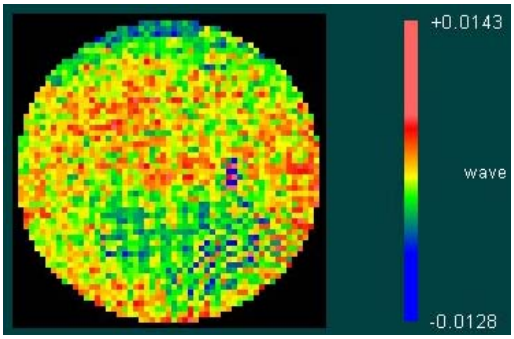

Figure D-20. Wavefront aberrations over a 0.5-in. aperture of a 45° UV mirror. This mirror has R = 50% in the green and is used on Z in front of targets and the camera. Power has been removed.

Table D-4. Summary of Corning's standard fused-silica grades.

Inclusion Class			Homogeneity[3,4] ppm							
			Grade							
Class	Total Inclusion[1] Cross Section [mm²]	Maximum[2] Size [mm]	AA ≤ 0.5	A ≤ 1	B ≤ 1.5	C ≤ 2	D ≤ 3	E ≤ 4	F ≤ 5	G[5] NS
0	≤ 0.03	0.10	■	■	■	■	■	■	■	■
1	≤ 0.10	0.28		■	■	■	■	■	■	■
2	≤ 0.25	0.50			■	■	■	■	■	■
3	≤ 0.50	0.76				■	■	■	■	■
4	≤ 1.00	1.00					■	■	■	■
5	≤ 2.00	1.27					■	■	■	■

NOTES:

1. Defines the sum of the cross section in mm² of inclusions per 100 cm³ of glass. Inclusions with a diameter ≤ 0.10 mm are disregarded.
2. Refers to the diameter of the largest single inclusion.
3. Index homogeneity: the maximum index variation (relative), measured over the clear aperture of the blank.
4. Index homogeneity is certified using an interferometer at 632.8 nm. The numerical homogeneity is reported as the average through the piece thickness. Blanks with a diameter up to 450 mm can be analyzed over the full aperture. Larger parts can be analyzed using multiple overlapping apertures. The minimum thickness for index homogeneity verification is 20 mm. For thinner parts, the parent piece is certified.
5. NS (not specified)

None of the inherent aberrations measured in the optics should drastically reduce the focusable intensity. The dashed line in Figure D-21 shows typical worst-case aberration measured for any of the optics. The cumulative effect on the Strehl ratio of one, two, and up to six optics is shown. Peak intensity should only be reduced a few percent at most.

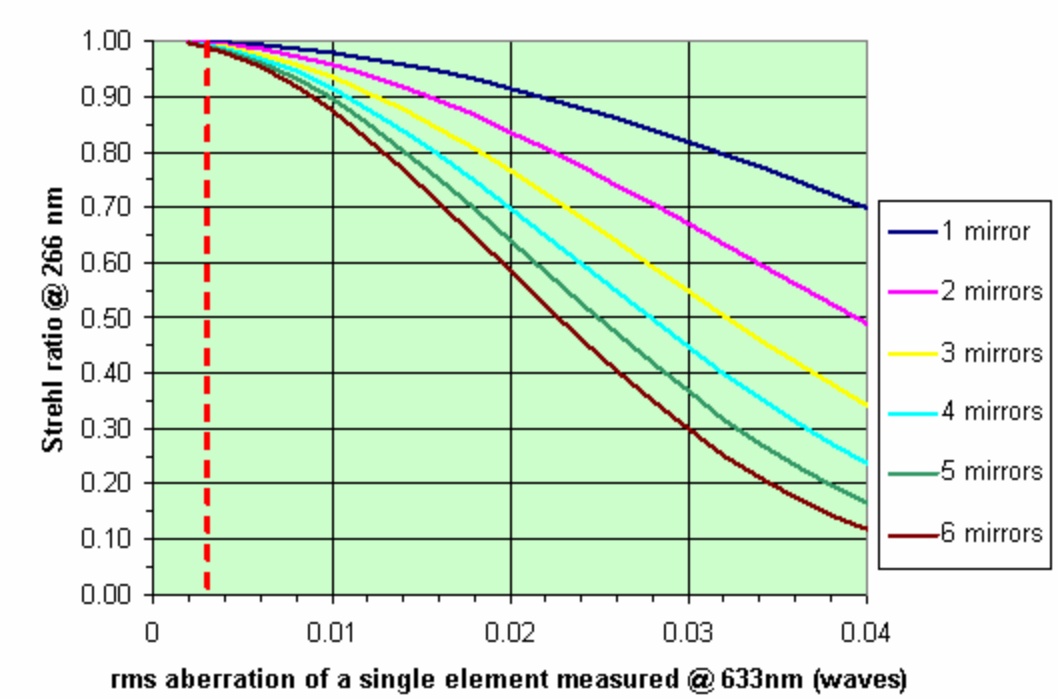

Figure D-21: The Strehl ratio, S, at l = 266 nm, plotted as a function of the RMS wavefront aberration, W_{rms}, measured over a 0.5-in. aperture, which is the diameter of the laser beam. The unit of the aberration is given in waves measured at l = 633 nm, which is the standard output for the Zygo interferometer used to measure the optics. The function plotted is S = exp[-(2pwrms)2]. Curves for multiple mirrors are shown. The total RMS wavefront error, W_{rms}, for n equivalent mirrors is the sum in quadrature of the individual aberrations or $W_{rms} = \sqrt{n}\omega_{rms}$. *The dashed red line shows a typical value of W_{rms} measured for the 45º turning mirrors.*

STB Experiment

Purpose of STB Experiment

This section summarizes the preliminary results of modifications to the STB LTS to make it mimic the Z_{20} system. Before the modification, the runtime of the trigger gap on Z_{20} was an order of magnitude longer than for STB, 40 ±10 ns versus 4 ±1 ns respectively. Attempts to improve the runtime of the trigger gap on Z_{20} were not successful. They included:

1. Verifying the laser alignment,
2. Checking that the position of laser can had not shifted after filling with fluids such that the laser beam might clip or miss an optic,
3. Replacing used optics with new optics,
4. The replacement of the off-axis, f = 1 m focusing mirror with a shorter focal length lens, f = 0.5 m, mounted on axis, and
5. Swapping the Z_{20} and STB lasers.

Since none of the above steps improved the Z_{20} LTS, an alternate approach was taken: modify the STB LTS to make it more like Z_{20}. Ironically, the goal of this experiment is to make the STB switch run ***worse*** in order to understand which LTS parameters have the greatest influence on switch operation. The objective is to observe any degradation in the spark length and/or the trigger runtime as optics are added to the system. Figure D-22 shows a schematic drawing of the optical layout within the STB LTS screen box. In brief, compared to the much simpler STB LTS, the Z_{20}-like LTS cut down on the length and brightness of the laser spark. In addition, the runtime of the trigger gap was successfully increased. Further experiments will verify and expand on these preliminary results. We hope to identify which optical components influence runtime the greatest and then develop a feasible corrective action for ZR.

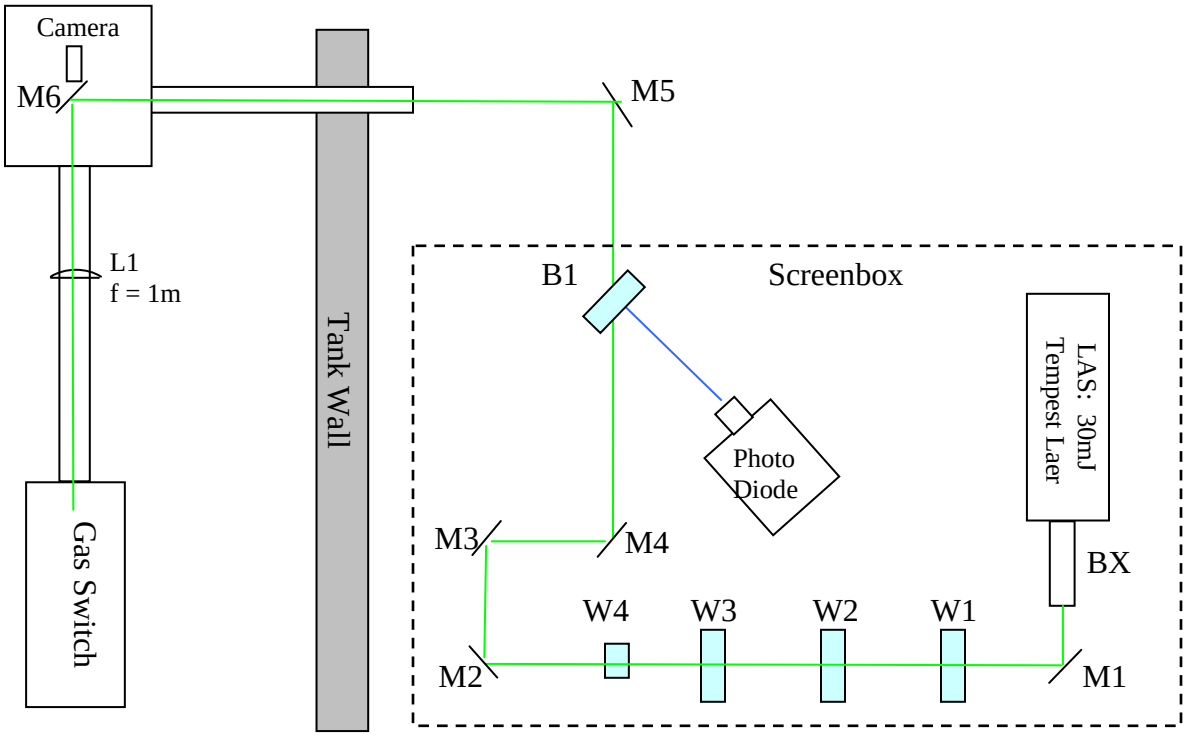

Figure D-22. Schematic layout of the LTS for STB modified to simulate the number of optics in the Z_{20} system.

Results and Discussion

On STB, electrical closure of the trigger gap is monitored directly by a Rogowski coil wound around the trigger electrode. Analysis of the trigger runtime need not rely on the "squiggle." The measured runtime for Z_{20} is an order of magnitude higher than STB, ~40 ±10 ns versus ~4 ±1 ns respectively. All cable length delays were checked and rechecked.

Only a few shots have been fired after making the Z_{20}-like modifications to the STB LTS so statistical precision is limited. Clearly, though, the modification increased the trigger-gap runtime to ~40 ns, the Z_{20} value. To understand the effect of the mirrors on the runtime, pairs of mirrors were removed from the LTS. LTS configurations with six, four and two mirrors were

utilized with runtimes and decreasing jitter of 35.4 ±14.8 ns, 39.8 ±10.8 ns and 15.4 ±3.2 ns respectively. Oddly, however, the runtime and jitter did not return to the original value of ~4 ± 1 ns with two mirrors. The probable cause for the hysteresis in the trigger runtime is contamination of the focusing lens. The lens on Z_{20} typically lasts ~300 shots, unlike on Z_{20} where the final window lasts only ~20 shots. The lens is being replaced and we will see if the runtimes return to initial values. STB is also operating with a different laser than before. In the past the runtime has not depended on the specific laser used. I do not expect the laser to be the cause of the difference but it is being considered. Also, the power supply for the new laser was positioned where the cooling fan caused more turbulence in the laser beam paths. Values for the average runtime and standard deviation are summarized in Table D-5 for the various LTS configurations tested. Another series of shots will have to be performed to precisely quantify the runtime dependence on the number of optics.

Achieving low runtime jitter requires a bright laser spark, easily visible to the eye. A dim spark has not been sufficient on Z_{20} or STB. Also, the spark must span a significant fraction of the trigger gap. On the original STB, the spark extended across 85% of the 2-in. gap as seen in Figure D-23a and D-23b. Also, the spark needs to be observed at the SF_6 pressure used during the shot, typically 45 to 60 psig. At lower pressures, the spark is much brighter. We were able to observe laser sparks on Z_{20} at 5 to 10 psig. However, at 60 psig the spark disappeared (Figure D-24). Figure D-25 shows the laser spark at 55 psig at full laser energy. Table D-6 summarizes the results of the laser spark observations on Z_{20} and STB.

Table D-5. List of optical components for the original STB and modified Z_{20}-like LTS.

a) Optical components common to both LTS Systems.

Optic	Description	Manufacturer & Part No.
LAS	30 mJ Tempest laser	New Wave Tempest 10
BX	3x UV Beam Expander	CVI: BXUV-10.0-3X-266

b) Modified Z_{20}-like optics train: (These are the extra optics in the STB screen box.)

Optic	Description	Manufacturer & Part No.
M1	45° mirror, R>99% @ λ=532 & 266 nm, 2-in. dia	CVI:BS RS266/RP532-PW-2037-UV-45
W1	UV window (AR coated 1 side), 3-in. dia.	[1,2]CVI: W1-PW1-3050-UV-266-0
W2	UV window (AR coated 1 side), 3-in. dia.	CVI: W1-PW1-3050-UV-266-0
W3	UV window (AR coated 1 side), 3-in. dia.	CVI: W1-PW1-3050-UV-266-0
W4	UV window (AR coated 1 side), 1.5-in. dia.	CVI: W1-PW1-1537-UV-266-0
M2	45° mirror, R>99% @ λ=532 & 266 nm, 2-in. dia	CVI:BS RS266/RP532-PW-2037-UV-45
M3	45° mirror, R>99% @ λ=532 & 266 nm, 2-in. dia	CVI:BS RS266/RP532-PW-2037-UV-45
M4	45° mirror, R>99% @ λ=532 & 266 nm, 2-in. dia	CVI:BS RS266/RP532-PW-2037-UV-45
BS1	10% Beam Splitter	

[1]An alternate optic was tested. [2]An alternate optic was tested.

c) Optics in the STB Laser can.

Optic	Description	Manufacturer & Part No.
M5	45° Excimer UV mirror, 2-in. dia	CVI:
M6	45° Excimer UV mirror, 2-in. dia	CVI:
L1	Fused Silica Lens, f = 1 m	CVI:

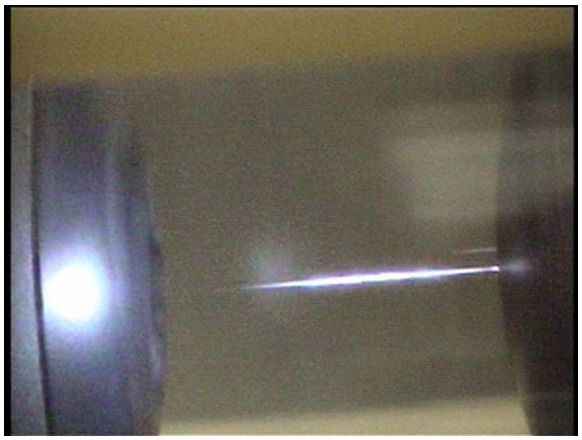

(a) $P(SF_6)$ = 5 psig

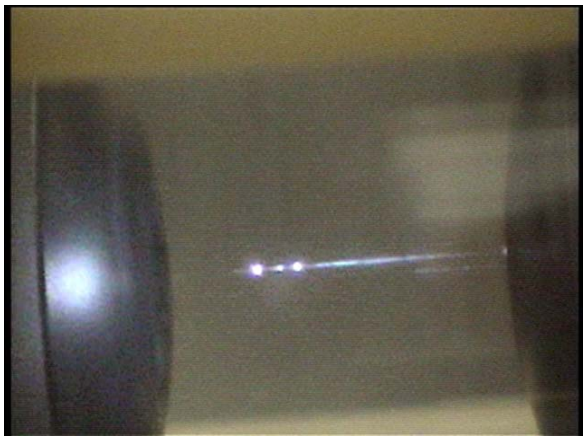

(b) $P(SF_6)$ = 60 psig

Figure D-23. Laser spark on STB with the original LTS. E = 32 mJ at laser. Estimate E = 28 mJ in the switch. The electrode separation is 50 mm for reference.

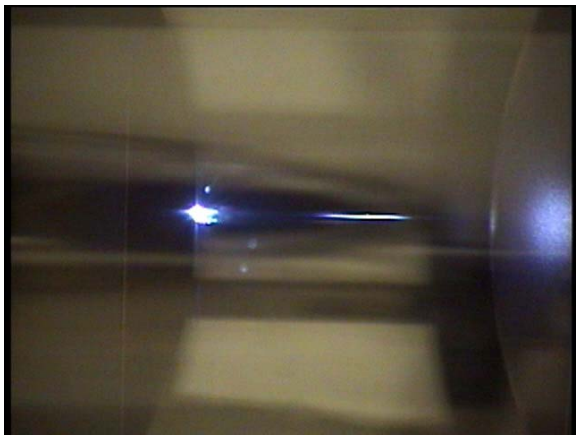

(a) $P(SF_6)$ = 5 psig

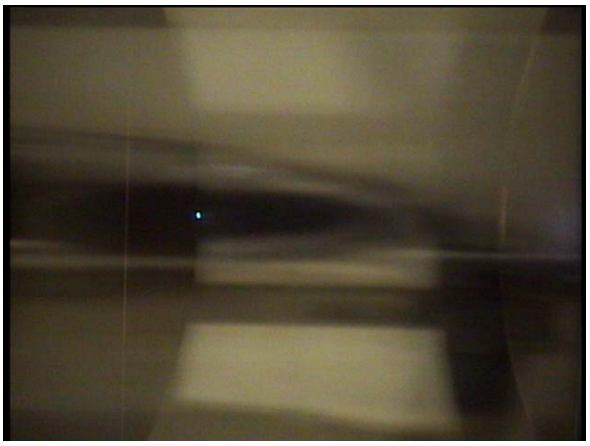

(b) $P(SF_6)$ = 60 psig

Figure D-24. Laser spark on Z_{20} with the f = 1 m off axis focusing mirror at full laser energy. (a) Shows that the spark spans 1/3 of the gap at low pressure. No spark occurs at high pressure (b). Only a small plume on the far electrode is visible.

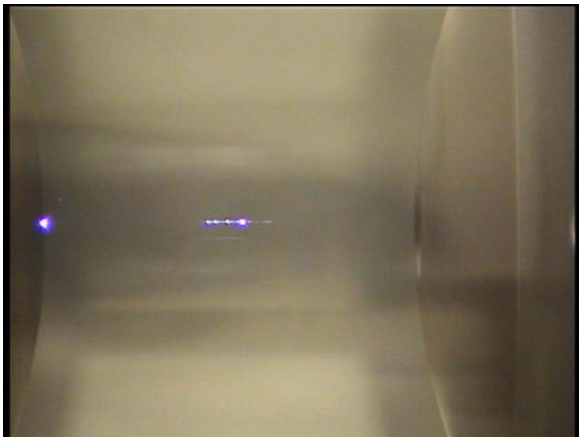

Figure D-25. Z_{20} laser spark with f = 515 mm lens and $P(SF_6)$= 55 psig at full laser energy.

Table D-6. Summary of laser spark observations made on STB. Tests conducted by the experienced eyes of Dave Bliss and Zach Wallace. Comments in table are from Zach Wallace.*

Test #	Optic Changes	Switch Pressure (psig)	Laser Energy @ Laser Head (mJ)	Laser Energy @ into Tank (mJ)	Comment
1	Added four 45° HR turning optics, three new, one used.	5	30.05	20.13	No spark across the trigger gap.
2	Replaced the used 45° HR turning optic with a new one.	5	31.2	21.8	Bright spark across the entire trigger gap with bulges along the length (think bright ball bearings)
3	None	5	Adjusting laser power.		Dropped laser power until the spark disappeared. Spark disappears @8.8 mJ into the tank; 13.3 mJ from the laser head.
4	None	10	31.2	21.8	No change in the spark length or brightness.
5	Added three 3-inch windows and one 1.5-inch window.	5	29.47	17.89	Spark starts at the trigger plate electrode and goes approximately 0.25-0.5 inch into the gap. Spark is very dim, barely visible with the naked eye.
6	none	5	Adjusting laser power.		Dropped laser power until the spark disappeared. Spark disappears @13 mJ into the tank; 19.5 mJ from the laser head.

*Note: Observations were made by eye since the remote camera and the video card were damaged by EMP produced during a Z_{20} MTG trigger test. Experience is all relative.

During observations on STB, both new and "used" optics were introduced. "Used" refers to optics that have been exposed to switch by-products on Z_{20}. We found that inserting just one mirror that had previously been exposed to 30 shots severely degraded the spark (Table D-6, test #1) even though the reflected laser energy only measured slightly less. The addition of windows used previously in the crossover tube also degraded the spark. Waylon Clark will work to characterize the laser spark in SF_6 (length, brightness, change in capacitance) in a laboratory setup.

Summary of STB Experiment

Interpretation of the results on the STB experiments has been very confusing. Ultimately we have discovered that the quality of the laser spark degrades through the course of the day because of problems with the SF_6 reclaimer.

Optic Lifetime

On Z, one of the most common reasons for draining the water section was to replace the final focusing optic. The combination of diffusive particulates and ballistic debris from the metal electrodes, SF_6 gas breakdown by-products, and intense UV illumination causes a complicated mix of processes that attack the surface of the final optic. Deposition, etching, and photo-chemistry all combine to degrade the flat surface of the lens. The bar chart in Figure D-26 shows, by module, the mean time between replacement (MTBR) for the final optic on Z. MTBR is measured in number of shots. The plot is for Z shots between 844 and 1720. The MTBR for each module varies significantly from 31 to 116 shots depending on the module. We suspect the cause of the variation is due to differences in the purge rates of the individual modules. The MTBR averaged over all the modules on Z is 57 ±54 shots. This number is certainly less than the true lifetime of an optic because often an optic is replaced as preventative maintenance when the switch is replaced or while the water has been drained for some other reason. A histogram of the frequency for replacing an optic is shown in Figure D-27. It is interesting that the frequency steadily decays towards longer lifetime and does not show any dominant mode. This probably has more to do with the infant mortality of gas switches than true optic lifetime. Towards the end of Z's operational life preventative maintenance was less important. If a switch were functioning properly, both the optic and switch were left in the machine. Two switches with 400+ shot lifetimes were pulled only after Z was decommissioned. The longest-lived optic lasted 369 shots! This is certainly a goal to strive for on ZR.

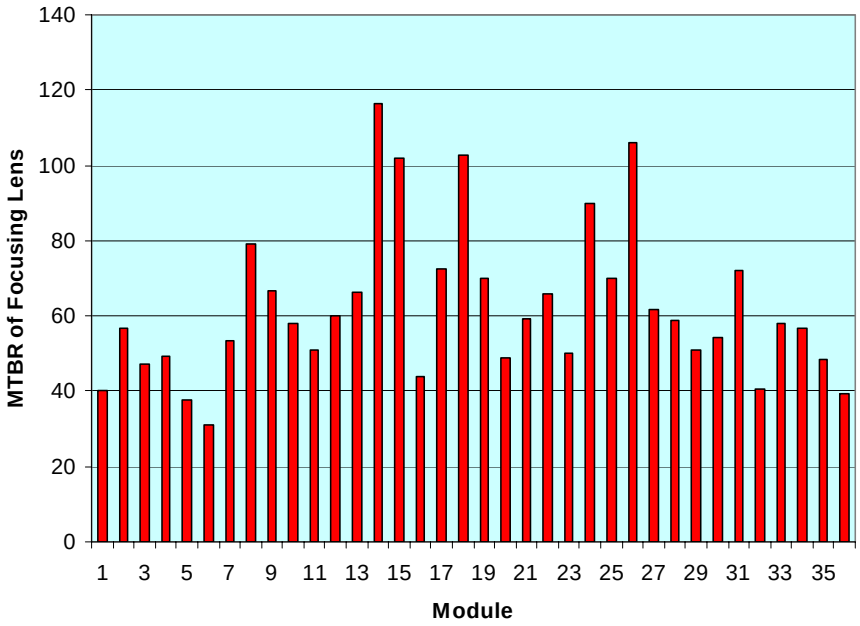

Figure D-26. Graph of the MTBR of the final focusing lens on Z by module. Variation between modules is suspected to be caused by different purge rates. The overall MTBR for the entire machine is 57 ±54 shots.

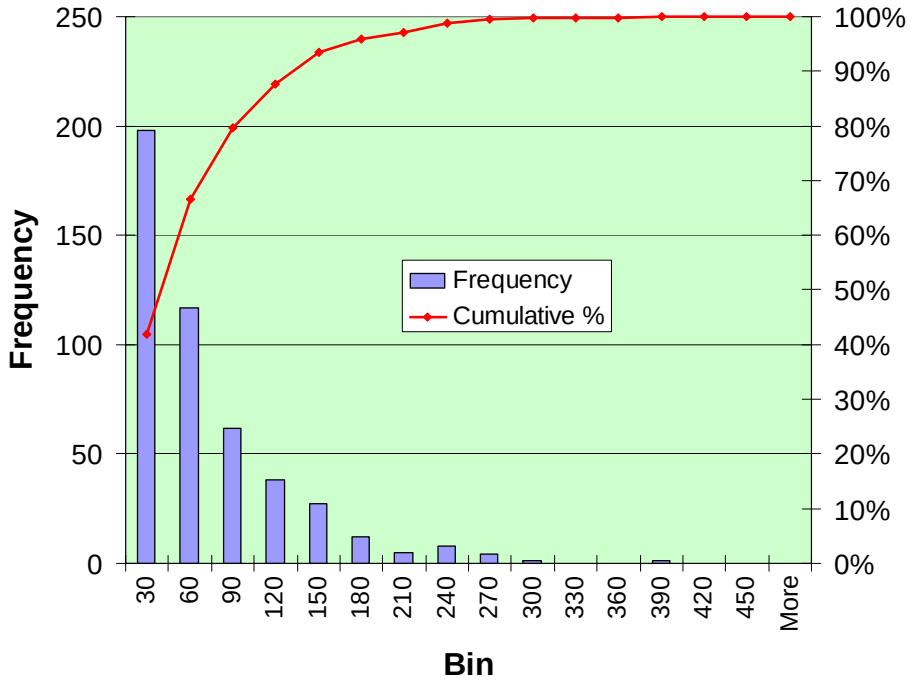

Figure D-27. Histogram of the replacement frequency of the final lens on Z. Notice that one lens lasted 369 shots. The cumulative percentage of optics replaced is shown in red. The median indicates that half the optics on Z were replaced after only 39 shots.

On Z_{20} we have observed many modes of degrading the optics. When a MgF anti-reflective (AR) coating was accidentally inserted facing the switch, it was attacked by SF_6 by-products. Figure D-28 shows the resulting damage to the coating. In another case, the surface of a bare fused silica lens was etched by breakdown products from a laser spark running at 5 Hertz. The switch was only fired four times but the surface looked as though it were exposed to HF. In an open configuration, the mirrors lost reflectivity at an initial rate of 0.5 mJ per shot. All of these failure modes can be greatly reduced by use of an isolation window or lens and an immediate purge after firing the shot.

Conclusions

In brief, LTS needs

1. to be sealed from the switch, to have the fewest optical components possible,
2. the shortest pathlength in SF_6 to reduce sensitivity to any UV absorbing gas impurities,
3. the fewest number of optical components,
4. the longest focal length optic that generates a stable spark over the lifetime of the optics, and
5. to be purged immediately after the shot.

With improvements to the gas handling system to reduce contamination of the SF_6, the LTS should function properly on ZR.

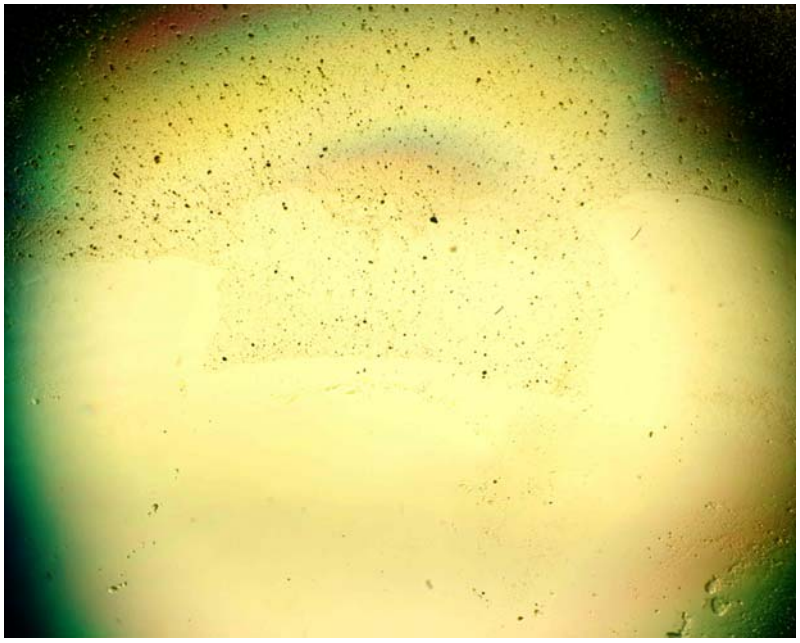

Figure D-28. Image of isolation window with MgF anti-reflective coating facing the switch. Most of the black spots are bubbles in the coating and not debris defocusing the light. The coating is attacked by SF_6 by-products.

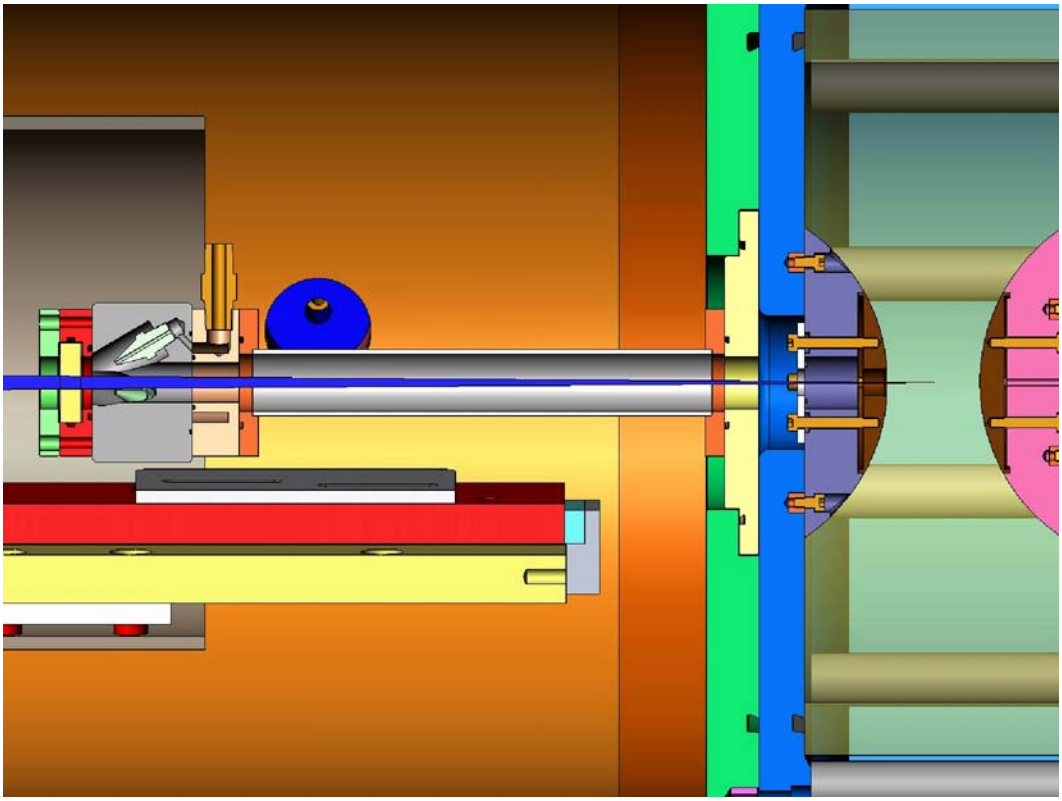

Figure D-29. Schematic drawing of gas jet assembly to use SF_6 gas to blow off particulates from the surface of the final isolation optic. Unfortunately the assembly does not significantly reduce particulates and risks contaminating the window with impurities in the SF_6 system. See Figure D-30 for an example of vacuum grease contamination.

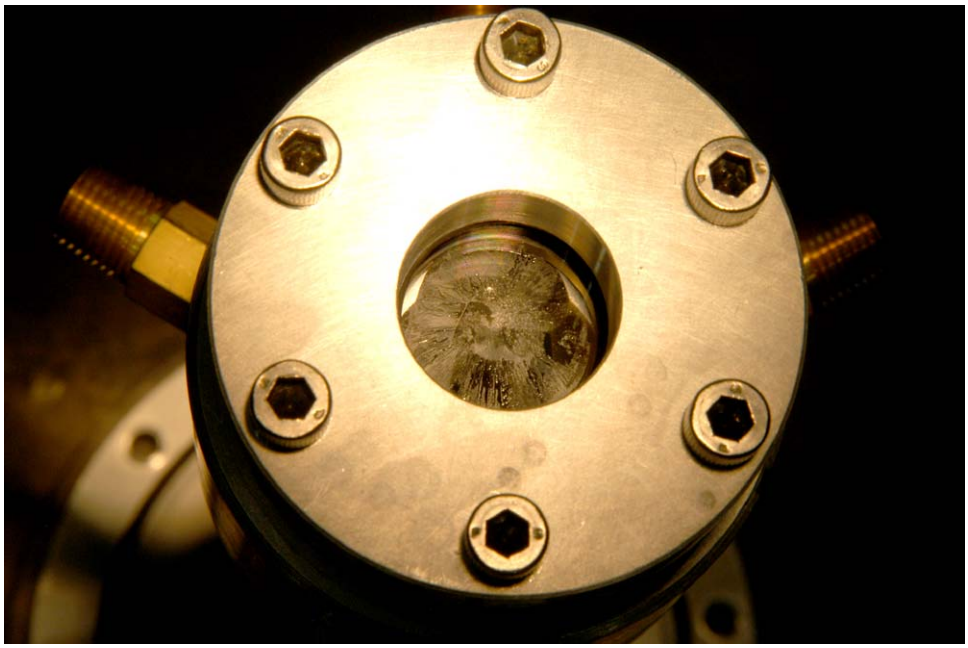

Figure D-30. Contamination of laser can isolation window with vacuum grease blown onto window by SF_6 gas jets.

Figure D-31. The STB final optic pulled on 09-27-2006 after 93 shots. Optic shows features of HF etching, metal deposition and laser-generated UV photo-chemistry.

Purging?

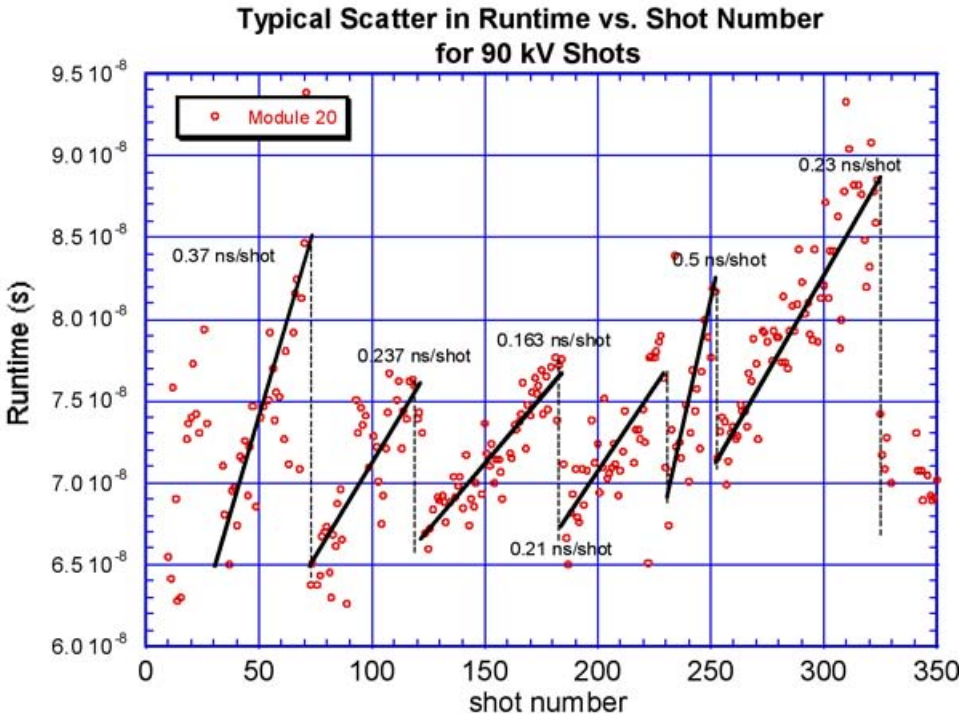

Figure D-32. Sawtooth runtime variations on the initial shots on Z illustrating the importance of a strong purge immediately following a shot. The stainless steel SF_6 return lines had been crushed by zingers in the water tank. After replacement of the gas lines the sawtooth variations went away.

APPENDIX D1.

Screamer code for Z_{20} modified to include independent closure of the trigger gap.

```
Z20/SatPro SUBMODULE CIRCUIT --- Corley's
version
TIME-STEP             .5E-9
RESOLUTION-TIME       .5E-9
END-TIME              5.5E-6
NUMBER-PRINTS         1
EXECUTE-CYCLES        ALL
MAX-POINTS            3000
BRANCH
!
!*****SHOT 80KV charge PEAKING GAP 4
electrode shorted gap WITH 2.5 OHM LOAD 3
Main gap switch sites 12.7cm**************
rcg  1e6  43e-9
INITIAL   VC1     -5.4e6
CSV VC1
$CapRev
CSV Qc1
$Q
CSV Eout
$Marx E
!
!Next is MARX series R&L!
rls  1.4  11e-6
!Next is Marx CVR
rls .00489
csv ir2
$MarxCVR
CSV pr2
$Marx p
!Next is Marx Parallel
rcg  .342e3
CSV IR1
$Marx Shunt
endbranch
!Next is Marx Rmon
rcg   10e3  0
csv vr1
$MarxRM
rls   0   .9e-6
trl lin    9e-9   95
Trl lin   6e-9   95
!
!  INTERMEDIATE STORAGE CAP
!!!!!NEXT IS ADDITIONAL C FROM ELECTRO for
cone sec!!!!!!
RCG    1e6    .09E-9
!!!!!!!!NEXT IS INPUT CONE!!!!!!!!!!!!!!!
trl lin  1.18e-9     36    64
!!!!!!NEXT IS INPUT BARRIER!!!!!!!!!!!
trl lin  .25e-9  36 36  .2e-9
!!!!!!NEXT IS NECK SECTION!!!!!!!!!
trl lin  2.275e-9   6   6
!!!!!NEXT IS TANK HEAD INNER
CONDUCTOR!!!!!!!!
trl lin    7.76e-9   6     3.817
TRL LIN 18.27e-9   3.817
CSV Vout
$IS_IN_V
CSV Iout
$I_IN
TRL LIN 38e-9   3.817
CSV Vout
$IS_OUT
CSV Iout
$ISC Iout
CSV Eout
$ISC Eout
Trl lin 18.27e-9   3.817
!!!!!!!!!NEXT IS OUTPUT TANK HEAD INNER
CONDUCTOR!!!!!!!!
trl lin  7.76E-9  3.817   6
trl lin  2.275e-9  6   6
!!!!!NEXT IS OUTPUT BARRIER!!!!!!!!!
trl lin  .25e-9  36     36  .2e-9
!!!!!!!!NEXT IS OUTPUT CONE!!!!!!!
trl lin 1.9e-9  64   23.6  .1e-9
!!!!!!NEXT IS ADDITIONAL C FR0M
ELECTRO!!!!!!
Rcg   1e6   .09E-9
csv vout
$swx Voltage
!!!!END OF ISC
!
!ISC SWITCH
!!!!!TRL FOR ISC SWITCH SPACE!!!!!!!!!!
 trl lin .5e-9   90   90   .05e-9
rls   1e6   400e-9
Var R2 exp
  1e6  .1   1.206e-6   30e-9   6
CSV Qr2
$Switch Q
CSV Vr2
$ISSWX
CSV Vl2
$Daves Swx out
!csv er2
!$Energy r2
csv ir2
$IS_SW_I
csv qr2
$QSwx
Topbranch
Trl lin .5e-9  90  90  .05
!!!!!TRL FOR ISC SWITCH SPACE!!!!!!!!!!
 trl lin .3e-9   90   90   .03e-9
RCG 1e6 0
Csv Vr1
$Trigger Plate
RLS 1e6  110e-9
Var r2 exp
  1e6 .1   1.186e-6  10e-9   6
Topbranch
Trl lin .3e-9  90  90  .03
!NEXT IS THE PFL OIL SIDE!
TRL LIN   .46e-9   80   12   .04e-9
TRL LIN    .46e-9    12    15.4   .04e-9
Trl lin   1e-9   15.4  15.4   .1e-9
CSV Vout
$PFL  V_in_oil
CSV Iout
$PFL I-IN
TRL LIN    .59e-9  15.4   15.4  .1e-9
TRL LIN   .23e-9   15.4    31   .02e-9
TRL LIN   .25e-9   31   31   .01e-9
!Rcg   1e6   .1e-9
```

```
!!!!!!!!NEXT IS PFL BARRIER!!!!!!
TRL LIN   .23E-9   40   40  .02e-9
!!!!!!!!NEXT IS PFL WATER SIDE!!!!!!
TRL LIN  .9e-9   5.25   5.25   .1e-9
!Rcg   1e6   .5e-9
TRL LIN  2.575e-9  5.25   2.7
TRL LIN 4.55e-9   2.7
CSV Vout
$PFL in_H20
CSV Iout
$Bar_I
TRL LIN   16.3e-9   2.7
CSV Vout
$PFL OUTPUT_V
CSV Iout
$PFL OUTPUT I
CSV Eout
$PFL E
Trl lin   9.5e-9   2.7
TRL LIN  2.64e-9   2.7
CSV Vin
$PFL-0ld
!!!!!!!NEXT IS PFL OUTPUT RADIUS!!!!!!!
Trl lin   6.44e-9   2.7  7
Rcg 1e6   5e-9
!CSV Vin
!$PFL OUTPUT_V
csv Iin
$PFL I Swx_in
CSV pout
$ PFL p
!!!!!!NEXT IS 1st Part WATER Gap
Spacing!!!!!!!!!!!!
!!!!!
rls   1e6  40e-9
!!!!!!NEXT IS WATER GAP!!!!!
Var R2 exp
  1e6  .32   1.430e-6   15e-9   7
!!!!!!!NEXT IS 2nd Part WATER Gap
Spacing!!!!!!!!
CSV Er2
$Energy R2
Csv ir2
$Swx I OUT
topbranch
TRL LIN   8.8e-9   11.2
TRL LIN   4e-9  9
CSV IOUT
$SWX I TRIPLATE_in
!!!!!!
TRL LIN   1.9e-9   9   4.2
!!!!!!!NEXT IS LINE 1!!!!!!!
Trl lin  4.9e-9   4.2
CSV Vout
$OTL1N_V
CSV Iout
$OTL1N_I
trl lin 10.8e-9   4.2
CSV VOUT
$OTL1 mid V
CSV IOUT
$OTL1 mid I
!endbranch
CSV Eout
$OTL1 E
trl lin 12.52e-9   4.2
TRL LIN   1.9e-9   4.2 7
!!!!!!NEXT US 1st 1/2 PrePulse Swx
Spacing!!!!!
Trl lin 2.27e-9  11
!!!!!!
!!!!!!NEXT IS PrePulse SWX
RLS  .25e6  10e-9
Var R2 exp
.25e6   .2   1.510e-6  10e-9   11
!!!!!!NEXT IS 2nd 1/2 PrePulse Swx
Spacing!!!!!
CSV Ir2
$PrePulse Swx I
topbranch
Trl lin 2.27e-9  11
!!!!!!
TRL LIN   1.9e-9   7  6.4
!!!!!!!NEXT IS LINE 2!!!!!!
Trl lin  6.7e-9   6.4
CSV VOUT
$OTL2n_V
CSV IOUT
$OTL2n_I
TRL LIN  18.4E-9   6.4
CSV VOUT
$OTL2 Mid_V
CSV IOUT
$OTL2 Mid_I
TRL LIN 18e-9   6.4
!!!!NEXT IS FLARE FOR LOAD
TRL LIN   9.4e-9   6.4   10.7
RCG  3  3e-10
CSV Er1
$Load Energy
CSV Vr1
$Load V
CSV IR1
$Load I
!!!CROWBAR
Branch
rls   1e6  650e-9
Var R2 exp
  1e6  .4   1.580e-6   20e-9   10
Rls   7.1  650e-9
Csv ir2
$Crowbar I
Rcg   0
!!!GAS SWX COUPLING CAP!!
Branch
Rcg   1e6   .3e-10
CSV Vr1
$Daves2
Branch
Rcg   1e6   .5e-10
!!!NEXT IS Water SWX COUPLING CAP!!!!!!
Branch
RLS 0 20e-9
RCG   .5e6    .75e-9
!Var R1 exp
!   .5e6   40   1.381e-6   20e-9   8
csv ir1
$Swx Shunt
!branch
!rls   0   48e-9
!TRL LIN   190E-9   20
!Rls 0   48e-9
!CSV IOUT
!$Inductor
!RCG   0
!!!!NEXT IS PEAKING SWX COUPLING C!!!!!
Branch
!Rls   0   3.5e-9
Rcg   1e6   5e-10
```

References

1. D.E. Bliss et al., A New Laser Trigger System for Current Pulse Shaping and Jitter Reduction on Z, PPC-2003, *14th IEEE International Pulsed Power Conference*, June 15-18, 2003, Dallas, TX, USA, pp. 179-182, Vol. 1.

2. J.W. Podsednik and D.E. Bliss, Operation of a Multiple Laser Trigger System on the Z Facility, PPC-2003, *14th IEEE International Pulsed Power Conference*, June 15-18, 2003, Dallas, TX, USA, pp. 1375-1378, Vol. 1.

3. S.T. Rogowski, D.E. Bliss, R.G. Adams, and K.W. Struve, A Study of Timing Jitter Improvments on Z with a New Laser Triggering System, PPC-2003, *14th IEEE International Pulsed Power Conference*, June 15-18, 2003, Dallas, TX, USA, pp. 1371-1374, Vol. 1.

4. Wolfgang Demtroder, *Laser Spectroscopy*, Springer Series in Chemical Physics 5, Springer-Verlag, Berlin, 1982, pp. 267-271.

5. Anthony E. Siegman, *Lasers*, University Science Books, Sausalito, CA, 1986.

APPENDIX E. Scaled STB

Introduction

The Switch Test Bed (STB) was modified in first quarter of FY 2006 to accommodate a 2.5-MV Rimfire laser triggered gas switch (LTGS). The LTGS has nine cascade gaps and a trigger gap identical to the Z_{20} 25-gap baseline (not triple point shielded). A depiction of the LTGS on STB is shown in Figure E-1. The insulators were PMMA at an inner diameter of 10 inches. This gas switch was scaled in voltage, but was designed to have similar trigger insulator field stress as a Z_{20} 25-gap baseline switch at 5.5 MV (field comparisons depicted in Figure E-2). With Z_{20} operating at 6 MV and MUTTS operating at 1.5 MV, modifying STB for 2.5 to 3.5 MV allowed a diverse range of test beds available to the LTGS program. This modification, called Scaled STB (SSTB) in this document, consisted of upgrading the original STB Marx to 56, 2.6 μF capacitors. The intermediate store water capacitor was relocated to accommodate the addition of a view port in the tank wall. The return sheath that surrounded the switch in the original STB was removed in lieu of adding five discrete return conductors. Photographic and electrical diagnostics were added, allowing closer observation of switch operation.

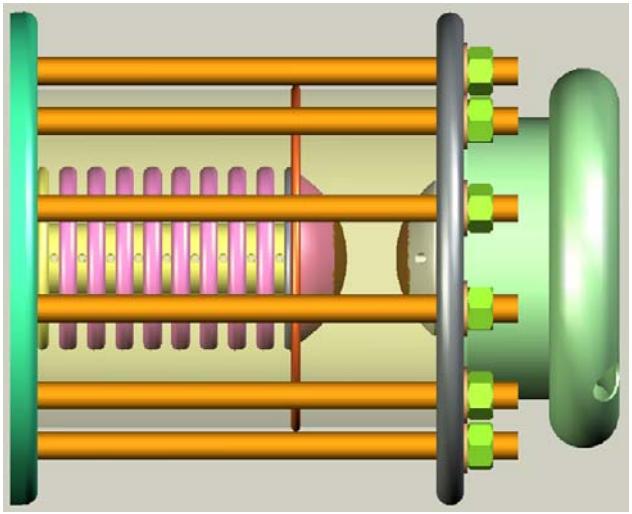

Figure E-1. Nine-gap SSTB Rimfire switch.

The long-term goal of SSTB is to serve as a scaled test bed for hypotheses that would improve LTGS operation on Z_{20} and therefore ZR. It will also serve as an initial test bed to Z_{20} for any improvements or new topographies. For the first year of the LTGS program the main focus of SSTB was the pursuit of fundamental understanding of gas switches and the physics that governs them as opposed to quick-fix gas switch design and improvement.

Before the modification of STB it was assumed that conditions on Z_{20} leading to insulator flashover (the most perceived problem facing the LTGS on Z_{20} for the majority of FY 2006) could be replicated on SSTB and scaled up to Z_{20} once remedied. If this assumption were true

two things could be conducted on SSTB at once. They were to identify and fix the issue causing flashovers on Z_{20} and to do basic science research regarding switch housing materials. Unfortunately, this assumption proved to be false.

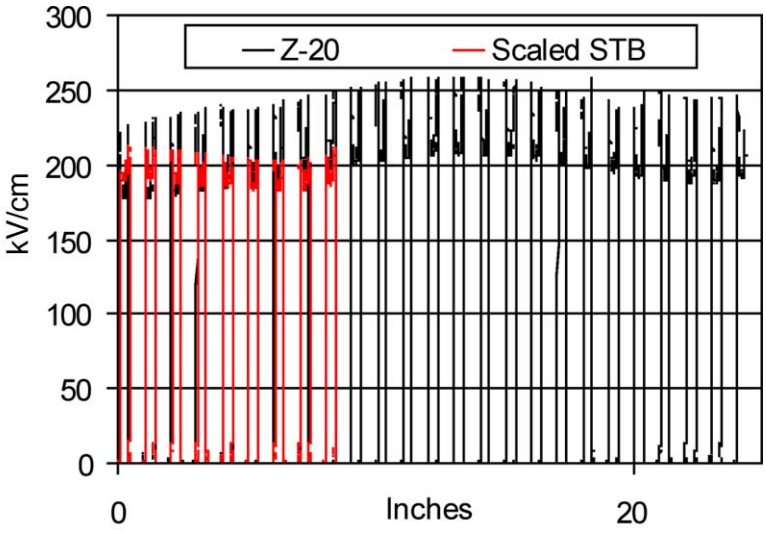

Figure E-2a. Cascade electrode field (electric field at the location arcs are observed to occur on the cascade electrodes) comparison between Z_{20} at 5.5 MV and SSTB ("Scaled STB") at 2.5 MV. Trigger gap at x = 0.

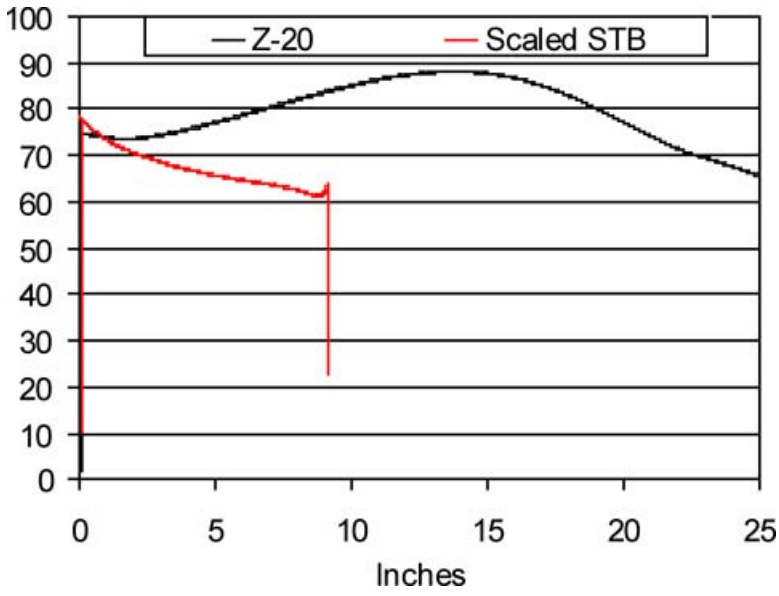

Figure E-2b. Inner cascade insulator field (electric field on the inner surface of the cascade insulator) comparison between Z_{20} at 5.5 MV and SSTB ("Scaled STB") at 2.5 MV. Trigger section at x = 0.

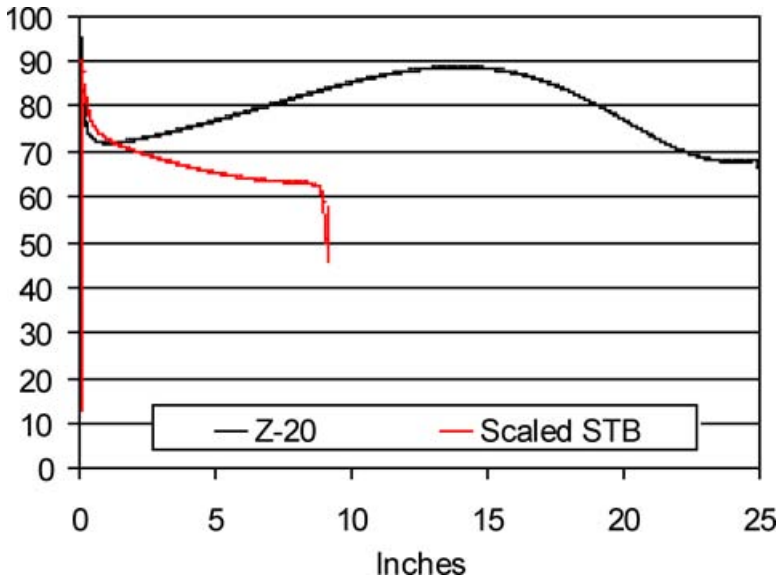

Figure E-2c. Outer cascade insulator field (electric field on the outer surface of the cascade insulator) comparison between Z_{20} at 5.5 MV and SSTB ("Scaled STB") at 2.5 MV. Trigger section at x = 0.

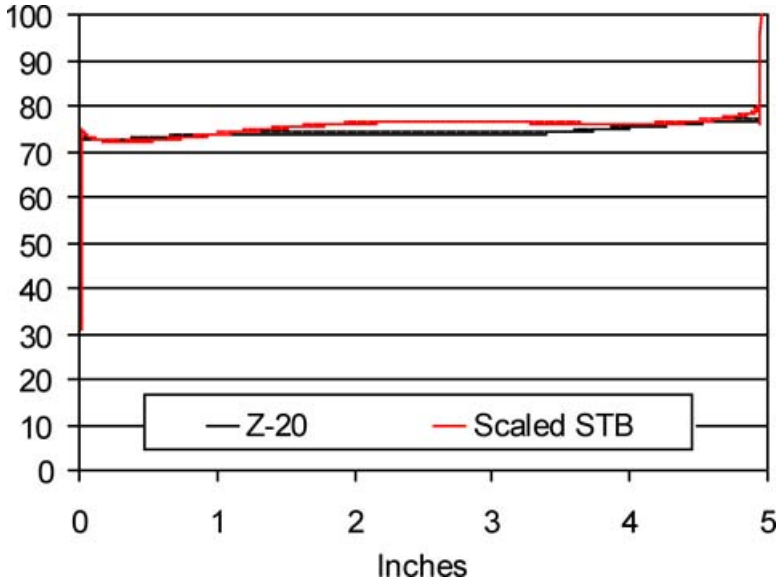

Figure E-2d. Inner trigger insulator field (electric field on the inner surface of the trigger insulator) comparison between Z_{20} at 5.5 MV and SSTB ("Scaled STB") at 2.5 MV. Switch output at x = 0.

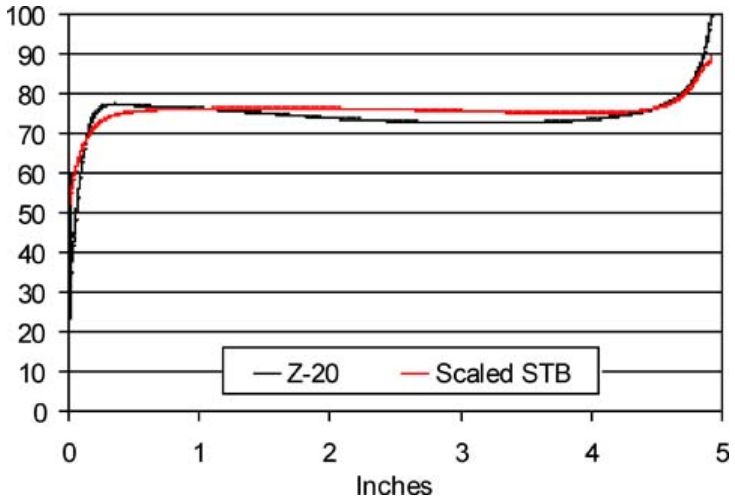

Figure E-2e. Outer trigger insulator field (electric field on the outer surface of the trigger insulator) comparison between Z_{20} at 5.5 MV and SSTB ("Scaled STB") at 2.5 MV. Switch output at x = 0.

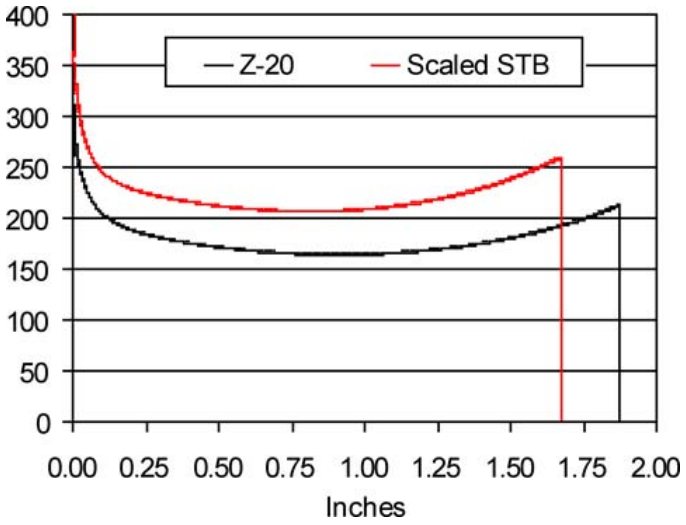

Figure E-2f. Axial trigger field (electric field between trigger electrodes) comparison between Z_{20} at 5.5 MV and SSTB ("Scaled STB") at 2.5 MV. Switch output at x = 0.

Fault modes hypothesized by the LTGS community to cause flashover were implemented on SSTB in order to achieve similar flashover rates as Z_{20}. They were (1) tangential electric field overstress of the insulator exceeding many other Rimfires used at Sandia National Laboratories; (2) reasonable triple point marring of the trigger insulator simulating a gap that might be caused by physical stress due to cantilevering the LTGS from the PFL in Z_{20}; and (3) accumulating debris on the housing in conjunction with (1) and (2). Despite these efforts made to worsen SSTB we were unable to achieve the same flashover rates for PMMA insulators as Z_{20}. This null result, however, is the most gleaming success for SSTB.

The direction of research on SSTB was augmented in the last quarter of FY 2006 once it was proven that insulator failures were not occurring on SSTB as on Z_{20}. This also coincided with a decreased flashover rate observed on Z_{20} with a change in the cleaning protocol. At this time the most perceived problem shifted from insulator flashover to switch jitter and laser issues. Short test runs (40 shots or less) that would undeniably prove or disprove a hypothesis were implemented and aimed at obtaining fast results toward solution of the new most-perceived problem. Two such hypotheses were observing runtime as laser energy was decreased and utilizing an SF_6/air gas mixture to tighten the self-break curve at elevated pressures.[1]

Shots on SSTB began on March 16, 2006, with Shot 1306. As of the date of this publication the last shot in the log was 1728 taken August 25, 2006. There were three major shot runs tailored to address the proposed hypotheses mentioned above. Shots 1306 to 1525 were focused on achieving flashover with no modifications to evaluate the hypothesis that overstress or number of shots (insulator aging or memory) could replicate the Z_{20} flashover rate on SSTB. Shots 1526 to 1705 were attempts at flashover with a chamfered triple point as to evaluate the hypothesis that the triple point is the cause of flashovers in the presence of overstress/aging. This shot run also contained varying laser energy runtime tests and the addition of a diagnostic endplate. Shots 1706 to 1728 were self-break shots utilizing the SF_6/air gas mixture.

Experimental Results

No Switch Modifications (Scaled Z_{20} Baseline)

In March 2006, the Z_{20} PMMA insulators were flashing an average of 1 in 30 shots. There were 194 shots taken on a scaled non-triple point shielded baseline switch in SSTB in which one flash occurred. A self-break curve for this switch is depicted in Figure E-3. Most shots in the shot run occurred at 85% of self-break. Approximately 20 were at 90% with approximately 10 at 80% of SB. In this shot series there were:

Breakdown Voltage (MV)	Number of Shots
<2.5	66
2.51 – 3	40
3.01 – 3.25	12
3.26 – 3.5	41
3.51 – 4	18

The trigger housing was replaced and an additional 26 shots were conducted, 22 of which exceeded 3.25 MV (an overstress of 30% compared to Z_{20} design levels). No flashes occurred in this run.

[1] This hypothesis was suggested by Scott MacGregor upon a trip by John Maenchen and Jane Lehr to Strathclyde.

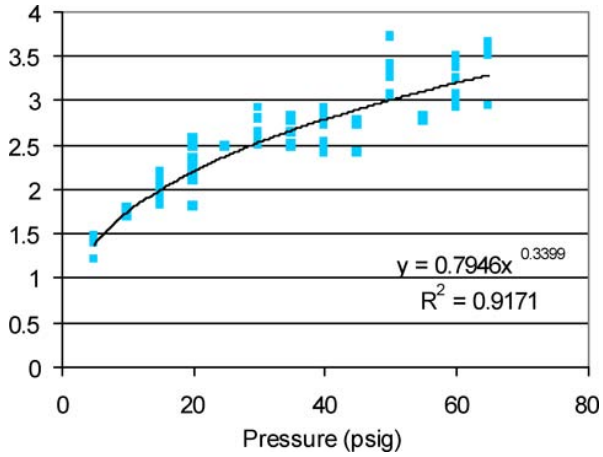

Figure E-3. Self-break curve for nine-gap Rimfire with 38% of total voltage in the trigger gap. The field enhancement on the trigger electrode that does not have a laser hole is 20%.

Chamfered Trigger Housing

Since it was clear Z_{20} flashover rate was not duplicated on SSTB, modifications were proposed to the insulator as a possible means to increase flashover rate. At the time, only reasonable changes were considered that could lead to worsening insulator performance. One such suggestion was to chamfer the inner triple point, at both the anode and cathode, in order to simulate a gap that may occur as a result of self-load stress when the switch was installed in Z_{20}. The chamfer shape in Figure E-4 was chosen since it provide large field enhancement (also depicted in Figure E-4) and was of reasonable size. The fields in the gap exceeded 300 kV/cm at 2.5 MV charge. This is an overstress of Z_{20} design levels of roughly 400%.

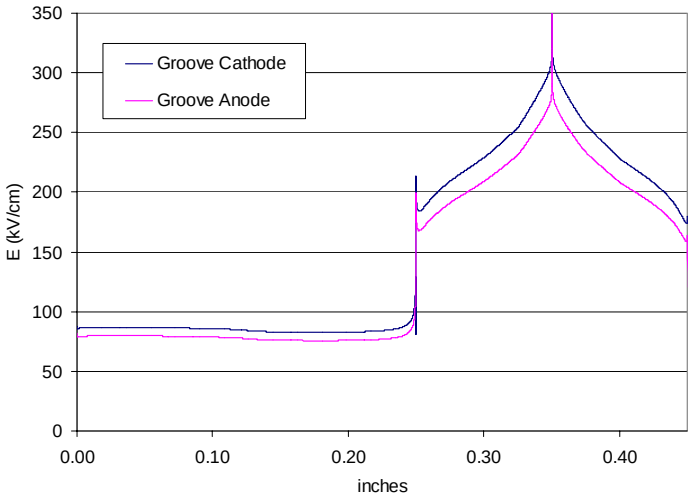

Figure E-4. Field profiles for chamfered triple point modification.

The groove was linearly tapered from 0.010 inch to zero into the insulator face with the maximum gap occurring at the inner circumference and tapering to zero at a radial depth of 0.100 inch into the insulator face. This chamfer was added on both the anode and cathode triple points for the full circumference of the trigger housing.

There were 179 shots with this insulator with no flashes. Most shots were taken at 85% of self-break. A synopsis of the breakdown voltages is below.

Breakdown Voltage (MV)	Number of Shots
<2.5	10
2.51 – 3	56
3.01 – 3.25	16
3.26 – 3.5	73
3.51 – 4	3

Photographs of debris from this run are depicted in Figure E-5. The rather large (~1 mm) particles present on the bottom of the switch housing, in conjunction with over 30% of the designed field levels on the insulator surface, indicate this macroscopic debris, even in the triple point, is likely not a major culprit contributing to switch insulator failures.

Varying Laser Energy

The robustness of the switch in SSTB led to the conclusion that obtaining a flashover rate similar to that of Z_{20} was not possible without major modifications. It was also at this time that flashover as a switch failure mode seemed less pressing than runtime and jitter issues. The focus of SSTB shifted from a flashover/insulator materials test bed to a rapid results test bed for Z_{20}.

Jitter issues were determined to be a result of poor laser energy or poor laser beam quality or both. They were also assumed to be a function of pressure and gap length. Therefore, an experiment was conducted on SSTB that would address laser beam energy as the major culprit to large trigger runtime jitter.

Table E-1 is a table of data collected in which the laser energy was reduced from 35 mJ to 5 mJ. Trigger runtime is defined as the time between the laser photo diode zero crossing to the breakdown point of the voltage monitors in the switch end plate (diagnostic setup described in the section titled “Diagnostics”), corrected by 5 ns. Total runtime is defined as the time between the zero crossing of the laser photo diode signal to the squiggle on the integrated Rogowski coil in the switch end plate. Figure E-6 depicts the results of that test, which show that trigger runtime begins to increase with less than 15 mJ of laser energy. Absolute values for these runtimes (debatable within 2 ns) are nowhere near runtimes experienced on Z_{20}, which vary from 10 to 60 ns.

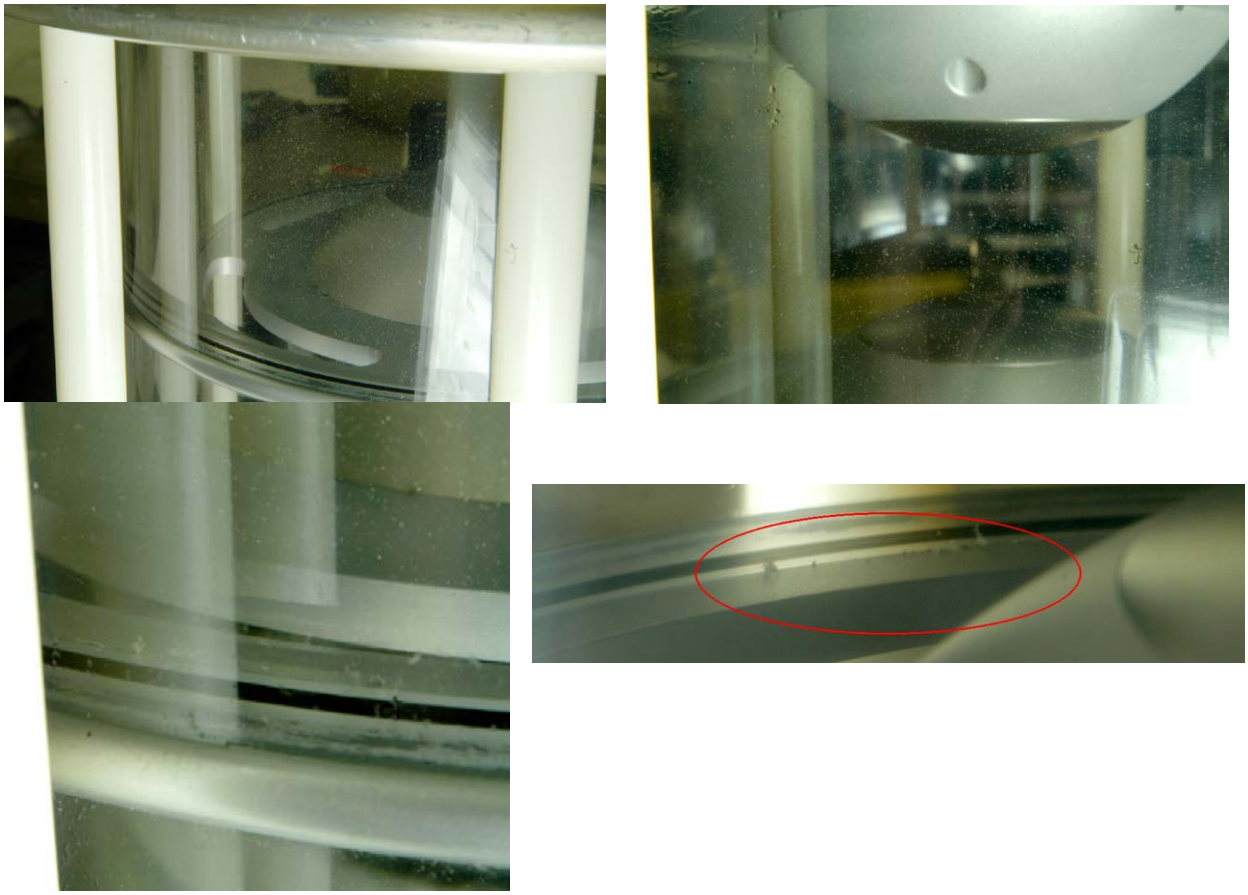

Figure E-5. Photographs of debris after a 26-shot run at 3.4 MV with the chamfered triple point. Debris was located on bottom 180° of the trigger section. Nearly uniform coverage with roughly 0.125-inch spacing between individual pieces was noted over entire trigger housing length. Large mm size pieces were located at BDC at the triple point. No flashes occurred.

Table E-1. Laser runtime data from the 2.5 MV Rimfire in STB.

Shot #	Energy (mJ) measured pre-shot after the beam expander	Trigger runtime	Total Run
1631	32	3.22	11.37
1632	33.2	2.29	11.08
1633	32.2	3.13	11.27
1636	15.2	4.68	13.65
1637	15.9	0.78	12.45
1638	10.8	1.48	13.33
1639	10.5	6.6	15.94
1640	5.8	7.35	16.66
1641	5.4	5.02	18.47

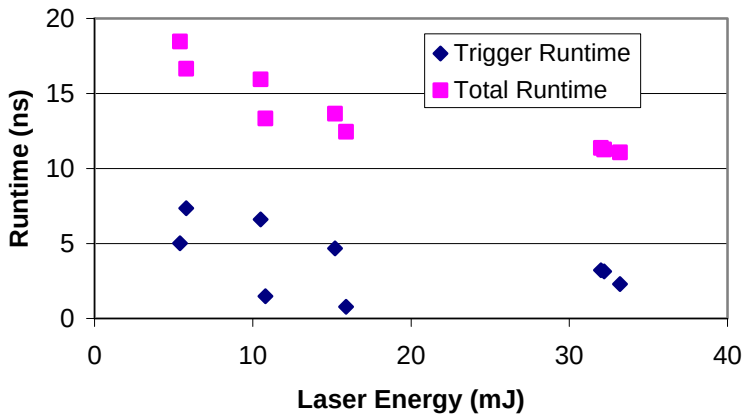

Figure E-6. Summary of runtime versus laser energy.

It is reasonable to conclude from these data that although trigger runtime increases with energies below 15 mJ, it does not exceed 10 ns with as low as 5 mJ. Therefore laser energy alone cannot explain the incredible discrepancy in runtimes between SSTB and Z_{20}. That is, laser energy by itself should not be a figure of merit when determining sufficient beam presence for acceptable triggering. This leaves laser focusable intensity, which is related to optics and beam quality, as the remaining culprit for long trigger runtimes on Z_{20}.

At 40 psig the average runtime on SSTB was 12.56 ns with a standard deviation of 2.75 ns over 41 shots. At 50 psig the average runtime was 11 ns with a standard deviation of 3.72 ns for 77 shots. At 60 psig, the average runtime was 11.85 ns with a standard deviation of 4.62 ns over 39 shots.

SF_6/Air Mixture

Another rapid results experiment included utilizing a 75%/25% SF_6/air mixture. This mixture was hypothesized to have a tight self-break curve at elevated pressures (beyond 30 psig) unlike pure SF_6. Tests were conducted at 40 and 60 psig. The results are depicted in Figure E-7. Though the spread may have improved very slightly at 40 psig, a few outliers make the spread worse at 60 psig. This experiment was abandoned to field more pressing laser optics issues with Z_{20} and should be revisited on a smaller system to truly evaluate the benefits of a mixture gas.

Diagnostics

We recently installed a number of electrical diagnostics directly on the endplate of the laser trigger section of the STB gas switch. Since this endplate rises to ~1 MV during each pulse, we installed a transit-time-isolating inductor from the endplate to ground with all the signal leads from the diagnostics running inside the inductor. The diagnostics included two V-dot probes to sense the voltage directly across the laser-triggered gap, a Rogowski probe to measure current through the same gap, and pressure probes at two different locations.

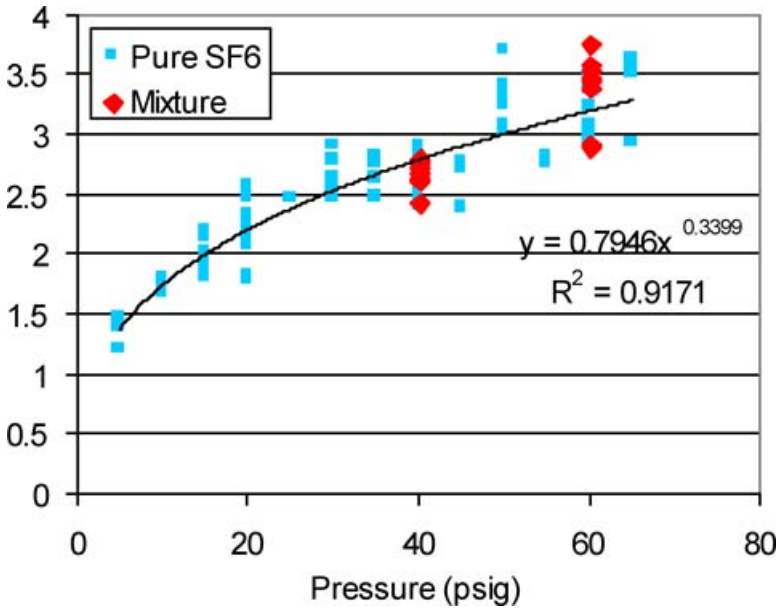

Figure E-7. Self-break comparison of pure SF_6 and a 25% air, balance SF_6 mixture.

We are still troubleshooting the information from these diagnostics but can draw a few conclusions from them.

1) The cascade section in the STB switch appears to be closing in a time on the order of 10 ns. This is much faster than the ~35-ns closure times of the cascade section in the Z_{20} gas switch. There are at least two factors contributing to this increased closure speed. First, for shots exceeding 2.5 MV, field stresses are higher in the SSTB switch than for Z_{20}. Second, the SSTB the cascade section had only ~1/3 as many gaps as the Z_{20} switch.

2) The pressure probes indicate that there is a narrow shock wave in the switch during each shot, peaking at a few tens of psi, with much shot-to-shot variation. The apparent widths of the shocks are equal to the 1-ms response time of the detectors. The pressure returns to about ~1 psi above the original pressure immediately after the shock and then returns to the original pressure within a few milliseconds. These narrow shocks were probably responsible for transporting arc by-products from the Z_{20} gas switch into the optics can before a window was added between the Z_{20} switch and the optics can.

APPENDIX F. LTGS Engineering and Materials Report

Over the last year the Z_{20} facility has fired 475 shots using five different switch configurations, with approximately 15 flashed trigger housings and 13 flashed cascade housings. Due to cost and availability the selection of types of housing materials to study was limited to Acrylic and Rexolite. Table F-1 shows the shot matrix comparing switch configuration, housing materials, and failures.

Table F-1. Insulator housing material shot matrix for LTGS program.

	Dates	Shot #'s	Trigger Flashes	Cascade Flashes	PMMA UVA	PMMA Re-machined/ polished	Rexolite	PMMA UVT	PMMA UVA-Annealed	NOTES:
Baseline	8/23 - 11/3	959 - 1037	6	9	Trigger/ Cascade					Shots 1031 - 1037 flashed 5 times in cascade without noticeable effect on switch performance, until 1037 pre-fire flash.
Baseline	11/08 - 11/17	1038 - 1069	4 (5?)	0	Re-used Trigger/ new Cascade					
Baseline	7-Dec	1070	0	1 (1st shot)		Cascade	Trigger			Both trigger and cascade had machined I.D.'s and polished using Novus plastic polish. Changed to cleaning procedure 2.
Baseline	12/12 - 1/4/06	1071 - 1111	0	1	Re-used Cascade		Trigger (previous)			
Baseline	1/9 - 2/9	1112 -1183	1	0	Cascade		Trigger (previous)			Trigger flashed Late time.
Triple point shielded	2/16 - 3/23	1184 - 1238	0	1			Trigger	Cascade		
Z-like	4/3 - 4/4	1239 - 1240	2					Housing		Flashed Housing 2 out of 2 shots.
Triple point shielded reduced field	4/10 - 4/19	1241 - 1288	0	0	Cascade		Trigger (previous)			All Intentional self breaks
Triple point shielded tailored field.	5/23 - 6/13	1289 - 1326	0	0	Cascade (previous)					Tracked 4th cascade gap puck (from trigger); K-33 electrodes.
Triple point shielded tailored field.	6/21 - 7/18	1327 - 1371	0	0					Trigger/ Cascade	Trigger plate bowed; opened trigger gap to 2.082"
Triple point shielded tailored field.	7/21 - 8/3	1372 - 1384	0	1			Trigger (previous		Trigger/ Cascade (previous)	Decreased trigger gap 1.942

Cleaning procedure 1: Washed with Simple Green, rinsed, dried with paper towel, wiped with lint-free cloth, dusted with air.

Cleaning procedure 2: Washed with Simple Green, rinsed, dried with paper towel, wiped with lint-free cloth, dusted with air, wiped with ethanol.

Shot History Notes From The Previous Table

Shots 959 – 1003: On Shot 959 the trigger envelope flashed at some point during the previous 24-shot series and did not adversely affect switch performance. Replaced switch, flashed trigger envelope two shots later. Switch flashed the trigger section three more times and the cascade section twice. On Shot 967 flashed trigger then cascade. Switch was eventually removed due to powder and large particles in housing (see powder residue analysis, Jim Van Den Avyle).

Shots 1004 – 1030: Trigger envelope flashed late in time. The cascade envelope flashed twice (4.98 MV and 3.37 MV) before laser, no apparent gap closures, flash carried full energy.

Shots 1031 – 1037: Cascade envelope flashes coincident with the trigger, no cascade closures. The cascade envelope flashes three times after the trigger; again no apparent cascade closures. Cascade envelope flash appears to be self-break carrying all the current.

Shots 1038 – 1069: Replaced the envelope on the previous switch with minimal refurbishment, all of the flashes occurred late time in the trigger section.

Shot 1070: Cascade envelope was remachined from a previously shot housing, which then flashed on the very first shot.

Shots 1071 – 1111: Cleaned the envelopes (procedure 2) after 36 shots for a 30-shot survivability test (i.e., what would be the lifetime if we routinely maintained the envelopes). A white film cleaned off easily and there was a very light flash on the cascade. Cleaned the envelopes on Shot 1108, which then flashed on Shot 1111, whereupon we stopped the 30-shot cleaning procedure.

Shots 1112 – 1183: Cascade envelope had visible crazing and inclusions before assembly. Late time trigger (Rexolite) flash (6.38 MV). The Rexolite retained a large carbon track after the flash and could not be reused. The Rexolite envelope demonstrated a 113-shot life.

Shots 1184 – 1238: The cascade envelope flash occurring on the final shot appears to originate at the trigger plate.

Shots 1239 – 1240: The flashes appear to jump from the cascade side of the trigger plate to the envelope (angling back toward the cascade section) then reversing direction and following the housing to the output endplate. There are multiple dendrites all around the inner wall of the housing directly across from the trigger output endplate.

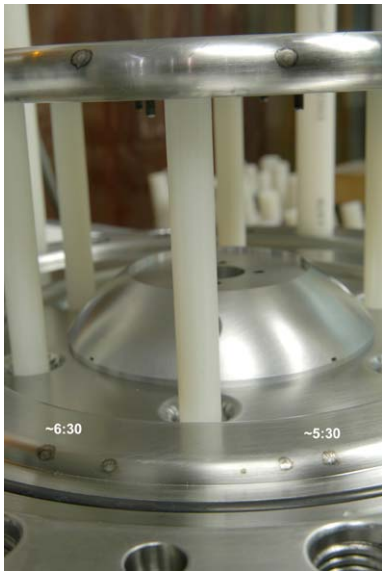

Shots 1241 – 1288: No switch failure, but unusual loop patterns predominantly in trigger section, output plate side.

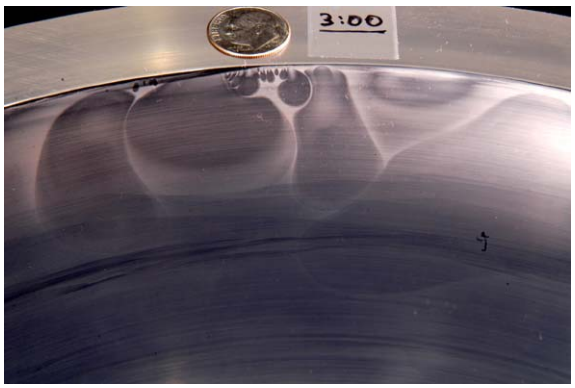

Figure on right (Z-like) shows cross pattern created by gas escaping from behind the electrode holder; these parts were subsequently redesigned to prevent this.

Shots 1289 – 1326: No housing failure. Flashed the cascade insulator puck (4th gap from IS end). K-33 trigger electrodes (for more information, see report by Jim Van den Avyle) show minimal wear.

Shots 1327 – 1371: No housing flashed. Trigger plate bowed.

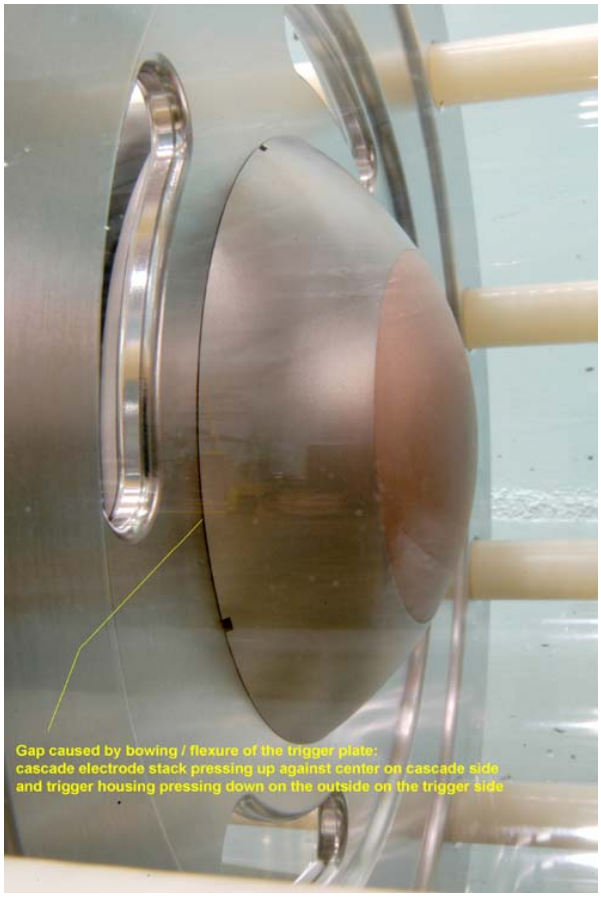

Shots 1372 – 1384: Flashed cascade after the trigger gap closed; no cascades closed so the envelope track coupled all the current. It was noted in the images that the flash may have resulted from ultraviolet (UV) illumination.

Because of the rate and unpredictability in envelope flashes, considerable emphasis was given to insulator materials, their fabrication and stress-removal protocols, surface treatment, handling and surface finish. It was anticipated that we would study an extensive matrix of different material compositions, surface finishes and stress-relief methods. Table F-2 lists materials and housings fabricated for the LTGS effort. Due to other events most of these remain to be tested.

Table F-2. Insulator housing materials used for LTGS testing.

CASCADE	REXOLITE; 1200 grit silicon carbide/32microinch; POLISHED
Z-LIKE	REXOLITE; 1200 grit silicon carbide/32microinch; POLISHED
CASCADE	REXOLITE; 2000 grit silicon carbide/32microinch; POLISHED
Z-LIKE	REXOLITE; 2000 grit silicon carbide/32microinch; POLISHED
TRIGGER	REXOLITE; 2000 grit silicon carbide/32microinch; POLISHED
Z-LIKE	PMMA UVT BD
Z-LIKE	PMMA UVT BD
Z-LIKE	PMMA UVT BD
CASCADE	PMMA UVA STAND; ANNEALED; STOCK
CASCADE	PMMA UVA STAND; ANNEALED; STOCK
TRIGGER	PMMA UVA STAND; ANNEALED; STOCK
TRIGGER	PMMA UVA STAND; ANNEALED; STOCK
TRIGGER	PMMA UVA STAND; ANNEALED; STOCK
TRIGGER	PMMA UVA STAND; ANNEALED; STOCK
CASCADE	PMMA UVA STAND; ANNEALED; POLISHED
TRIGGER	PMMA UVA STAND; ANNEALED; MACHINED; SANDED
CASCADE	PMMA UVA STAND; ANNEALED; MACHINED; SANDED
TRIGGER	PMMA UVA STAND; ANNEALED; POLISHED
TRIGGER	PMMA UVA STAND; ANNEALED; MACHINED; SANDED
CASCADE	PMMA UVA STAND; ANNEALED; MACHINED
CASCADE	PMMA NBD UVT; ANNEALED; POLISHED
TRIGGER	PMMA NBD UVT; ANNEALED; MACHINED
CASCADE	PMMA NBD UVT; ANNEALED; POLISHED
TRIGGER	PMMA NBD UVT; ANNEALED; POLISHED
TRIGGER	PMMA NBD UVT; ANNEALED; POLISHED
CASCADE	PMMA NBD UVA; ANNEALED;POLISHED
CASCADE	PMMA NBD UVA; ANNEALED; MACHINED; SANDED
TRIGGER	PMMA NBD UVA; ANNEALED; POLISHED
TRIGGER	PMMA NBD UVA; ANNEALED;POLISHED
CASCADE	PMMA NBD UVA; ANNEALED;MACHINED; SANDED
TRIGGER	PMMA NBD UVA; ANNEALED; POLISHED

PMMA with UVA has a UV stabilizer. UVT has no stabilizer, and NBD is no blue dye (an ingredient common in standard acrylic tubes).

Based on the initial success of the Rexolite, a cross-linked polystyrene, other cross-linked materials were obtained. UVT acrylic tubes with no blue dye were purchased containing a 0.5% and 2% cross-linking chemical agent. These were the upper and lower limits suggested by the vendor and remain to be machined and tested. Highly cross-linked epoxy resin has also been cast. Optical polarization analysis of the machined Rexolite showed stress bands.

Polishing Procedures

Basic methodology:

1. Sanding begins with a wet-sand using 600-grit silicone carbide paper.
2. Wet-sand using a 1200-grit silicone carbide paper.
3. Next use 9-micron diamond polishing cloth.
4. Finish sanding with a 3-micron diamond polishing cloth.
5. Buff with Novus plastic polish #2.
6. Wipe with Glass-plus (a non-ammonia based cleaner).

For an even finer finish, add a 2000-grit silicone carbide wet sand after step 2 to obtain optical clarity.

Manufacturing Guidelines

1. Sufficient process control shall be used to prevent material from contacting chemicals other than water or a water and liquid soap mixture.
2. Overall caution: leave the masking on during all fabrication operations to prevent damaging the surface. Other chemicals may cause short- or long-term surface crazing and swelling. Remove any chemicals immediately.
3. Tooling should be tungsten carbide, with top rake no greater than 3 degrees. Clearance and side rake between 8-17 degrees. Inserts are also acceptable. Tools must be sharp! Good results for achieving optical clarity were found using a very shallow final cut at slow feed rate using a Kennametal (GP 443K; Grade KC5410) cutting insert.
4. No oils or petroleum-based cutting fluids should be used.
5. Coolant should be a mixture of water and dish soap.
6. Parts shall be cleaned within two hours after completion of machined operations; post-machining cleaning shall be done with plain water and mild detergent.
7. All fabrication (sawing or machining) induces stress in acrylic sheet. Annealing to relieve this stress is recommended to minimize crazing or cracking that can occur.
8. Anneal acrylic parts in a forced air-circulating oven. Ramp the acrylic to 180 °F (just below its deflection temperature). Heat for one hour per every 0.040 inch of cross-sectional thickness for a minimum of two hours. Cooling time should be a minimum of two hours. For sheet thicknesses above 8 mm, cooling time in hours should equal thickness in millimeters divided by four. Ramp down to 80 °F.

Instituting these machining, handling, and cleaning protocols seemed to reduce the occurrence of envelope flashover, although triple-point shielding was installed at this same general time and could be contributory to solving this problem as well.

The continuing problem with short optics lifetimes led to an effort to reduce the dust and debris pollution of the equipment in the optics can. On April 4, 2006, the gas transfer holes in the LTGS baseplate were sealed and a gas isolation window was installed during the Z-like switch test. Because of this, material selection and focus has shifted towards understanding electrode materials (Table F-3) that produce the debris limiting optics lifetime.

Table F-3. Shot matrix for August 2006 shot series.

	Date	Shot #'s	Trigger Flashes	Cascade Flashes	PMMA UVA	PMMA Re-machined/ polished	Rexolite	PMMA UVT	PMMA UVA Annealed	PMMA UVA Sanded Annealed	Notes
TPS Tailored field	8/9 – 8/16	1385 – 1411	0	0				Trigger (previous)		Cascade	Welded plugs in trigger plate slots
TPS Tailored field	8/21 – 8/22	1412 – 1423	0	0					Trigger	Cascade (previous)	Brass Electrodes
TPS Tailored field	8/24 – 8/28	1424 – 1432	0	0					Trigger (previous)	Cascade (previous)	Stainless 304 Electrodes
TPS Tailored field	8/30 - Present	1433…	0	0					Trigger (previous)	Cascade (previous)	Tantalum Electrodes

Shot History Notes From The Previous Table

Shots 1385 – 1411: Plugs were welded into trigger plate slots to eliminate UV illumination on cascade section. It was a conjecture that this illumination might assist cascade envelope breakdown. No confirmation has been obtained, but it still seems a reasonable modification with no downside.

Shots 1412 – 1423: Replaced trigger housing to inspect old one due to interesting crazing marks. Brass electrodes showed bad erosion and large (mm-scale) particles in the bottom of the trigger envelope.

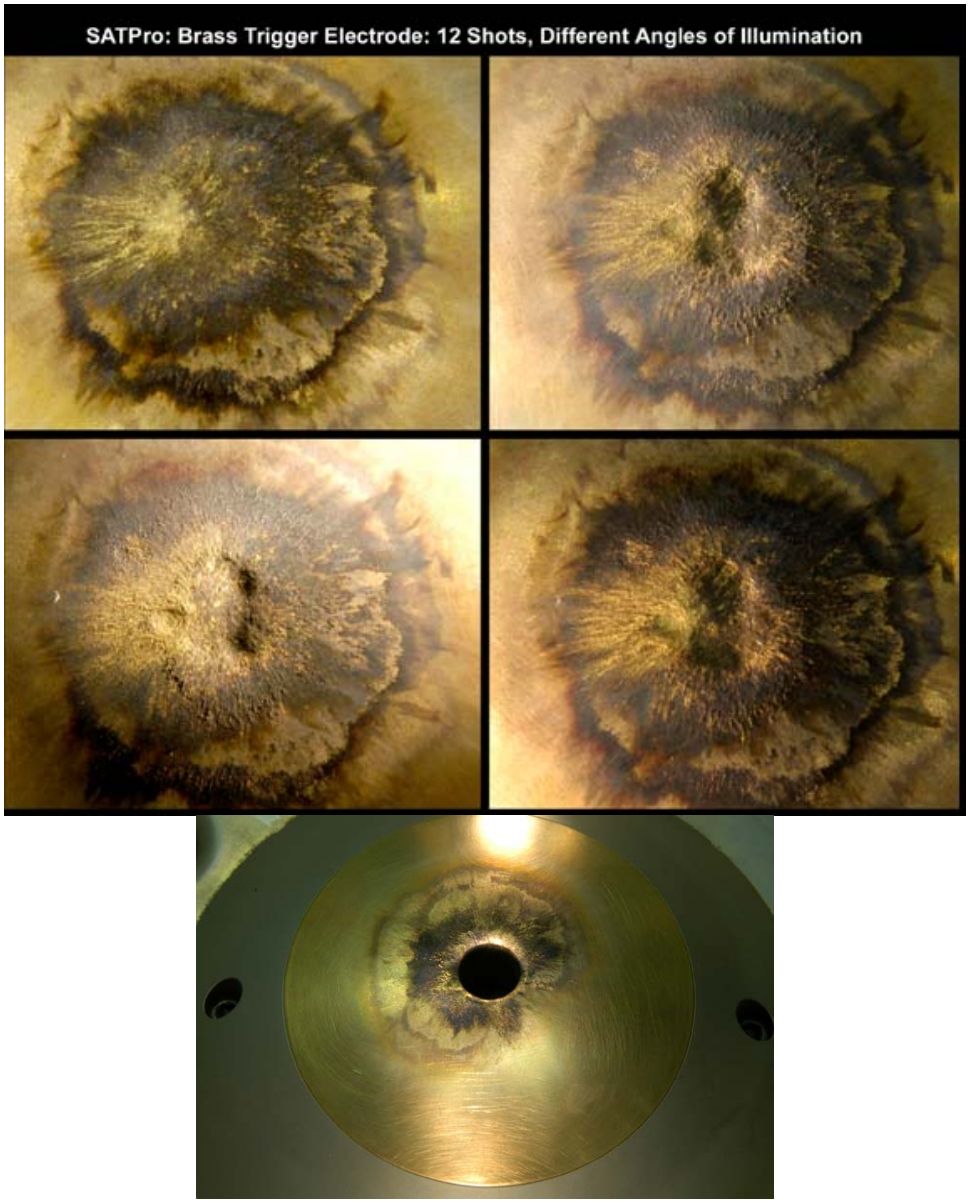

Shots 1424 – 1432: Fair amount of erosion occurs on stainless electrodes; one can count craters for each shot. Started to purge the switch immediately following each shot to remove vapor-debris from the optical window.

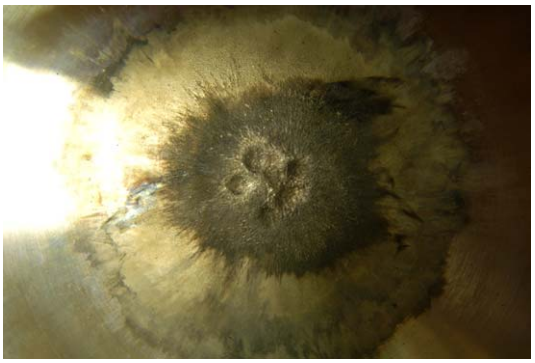

Tungsten Electrode Materials

Historically tungsten alloy inserts have been used in the single-channel triggered gap of gas switches. There is a great deal of confusion regarding which tungsten alloy has been used in the past, for which switches, and with what results. Some electrodes are visibly redder in color, some show slight wear, and some dramatic pitting. No electrode-specific historical records are available, so we are vaguely believing some are better than others. On Z_{20} recent results (below) demonstrate minimal wear after 100 shots, but we do not know the source of the alloy used.

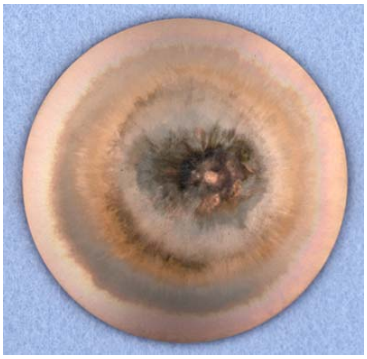

Various tungsten/copper alloys available for testing include Mallory 1000, HD-17, and Fansteel 77. In general tungsten alloys are made of sintered tungsten particles with Ni-Cu binder, typically 90w/o W, 6w/o Ni, 3w/o Cu. During sintering, some of the tungsten is dissolved into the Ni-Cu binder phase, and the resulting alloy microstructure has 75-81% W particles by volume. Alloy structure and compositions taken from eight used electrodes show a consistent volume fraction tungsten and average tungsten particle diameter from 25 to 30 µm. Recently purchased tungsten alloy material shows a significant difference of twice the W particle diameter (50 to 60 µm), albeit with similar volume fraction tungsten particles and similar binder alloy compositions. All samples contain a modest amount of porosity that causes material pull-out during machining, leading to rough surfaces (photo on left).

The table below lists the advertised constituent fractions of several tungsten alloys.

CMW Metals: Elconite	W	Cu
5W3	70%	30%
10W3	75%	25%
10W53	75%	25%
30W3	80%	20%
40W3	87%	13%
Mallory (UK) Elkanite	**W**	**Cu**
10W3	72%	28%
30W3	78%	22%
Eagle Alloys Corp	**W**	**Cu**
CW70 class10	70%	30%
CW75 class 11	75%	25%
CW78 class 11 and 12	78%	22%
CW80 class 12	80%	20%

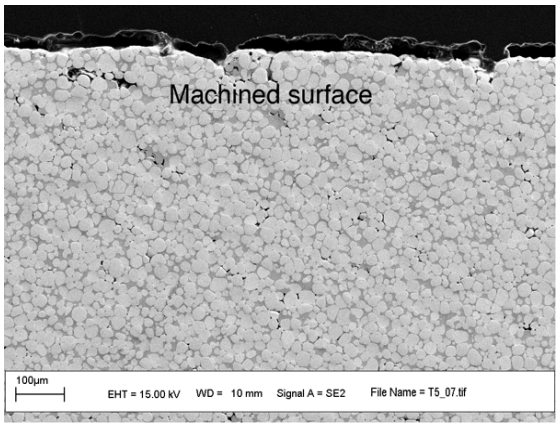

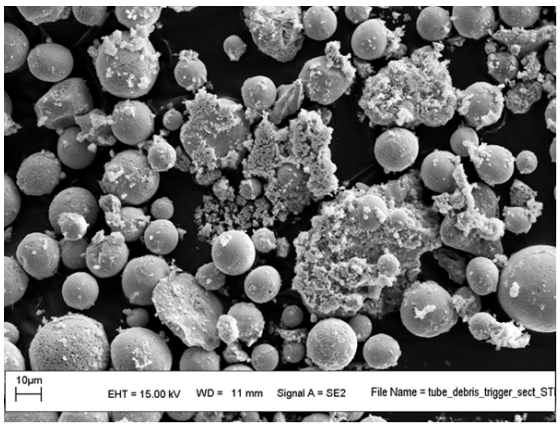

Debris recovered from the trigger section of the LTGS (photo on right) shows arc-melted tungsten spheres sized 5 to 50 µm diameter and fine powder debris containing tungsten compounds as well as Fe-Ni-Cr oxides from the cascade section electrodes. There is evidence of tungsten vaporization (flat particles found on surfaces), tungsten melting, tungsten particle loss, preferential vaporization of Ni-Cu-W binder at the surface, and a low porosity zone extending approximately 0.05 inch below arc-melted surface (likely due to melting and pore consolidation of the Ni-Cu binder alloy well below the surface). No apparent differences in local damage mechanism were found between used electrodes exhibiting shallow craters and those with deep craters, suggesting the major effect is arc energy density, not alloy structure.

Fansteel utilizes an infiltration process reproduced for us by Wah-Chang that has the highest tungsten to copper ratio of all the tungsten electrodes analyzed. Its average matrix composition is 52w/o Ni, 28w/o Cu, 20w/o W. More tungsten particles are sintered or bonded together than seen in any other tungsten alloy samples. The measured area fraction of tungsten particles is 0.79. The measured density is 17.05 g/cc (as compared to 16.93 g/cc of historical electrode samples). Since the ideal density would be 17.3 g/cc, Fansteel 77 is about 98.6% dense, more

than the historical samples of 97.9% dense. This suggests an alloy that provide significantly improved erosion rates; however, it has not yet been tested.

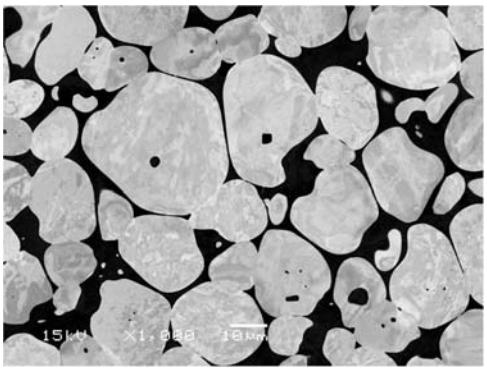

Fansteel micrograph

APPENDIX G.
Z Gas Switch Lifetimes

Number of shots per switch before removal/rebuild

Individual Gas Switch Lifetimes

- Data from Oct 1997 to present
- 47 different sets of switch endplates
  - After failure (or PM removal), each switch is completely rebuilt
- Shot Lifetime does not seem to depend on date of rebuild

Switch Lifetimes (number of Shots)	
Mean	99
Standard Error	3.31
Median	90
Mode	1
Standard Deviation	72
Sample Variance	5224
Kurtosis	-0.90
Skewness	0.39
Range	288
Minimum	0
Maximum	288
Sum	47419
Count	478
Confidence Level(95.0%)	6

Shot Number Lifetimes for Four Typical sets of Switch Hardware

- The “Rebuild Date” below is the time when the switch was removed after the corresponding number of shots

Switch #20		Switch #21		Switch #33		Switch #45	
Number of Shots	Rebuild Date	Number of Shots	Rebuild Date	Number of Shots	Rebuild Date	Number of Shots	Rebuild Date
5	May05	0	Jun05	131	Feb06	110	Jan06
157	Jan05	1	Oct04	229	Jun05	49	Aug04
58	Feb04	64	Jul04	89	Feb04	49	May04
44	Sep03	42	Apr04	60	Sep03	101	Nov03
1	Jun03	131	Sep03	12	May03	93	Jan03
161	May03	13	Jun03	73	Oct02	96	Jun02
86	Apr02	10	Oct02	216	Aug02	16	Mar01
2	Apr01	122	Sep02	78	Apr01	15	Sep00
18	Dec00	146	Mar02	7	Feb01	9	Apr00
162	Sep00	22	May01	127	May00	89	Feb00
100	Apr99	64	Mar00	68	Apr99	127	May99
121	Sep98	178	Mar99	138	Jul98	37	Jun98
159	Nov97	159	Oct97	4	Apr98	100	Mar98

Histogram of Switch Shot Lifetimes

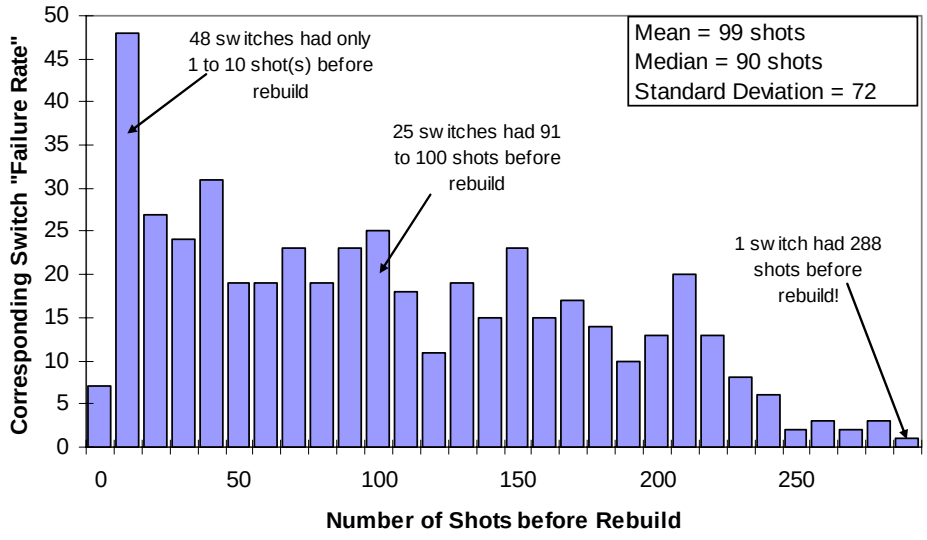

Z Gas Switch Lifetimes

Removal rate for failure vs.
preventative maintenance

Gas Switch Failure/Lifetime Data

- Time period from Feb 02 to Present
  - 50 months
- Total number of gas switches replaced
  - 255
- Gas switches replaced due to failure
  - 226
- Gas switches replaced for preventative maintenance
  - 21
- Average total monthly gas switch replacement (failure and PM) rate
  - 5 per month (mean and median)

Preventative Maintenance

- In the past switches were removed after approximately 200 shots
  - If not removed sooner for failure (more likely)
- Approximately 1 year ago this policy was changed
  - Why replace a fully functioning switch with a new, uncharacterized switch?

Gas Switch Failure/Lifetime Data (continued)

- Total number of shots on Z during this period
  - 817
- Monthly gas switch replacement does not seem to depend on number of shots per month
  - Correlation = 0.23
- Rough "average" number of shots per switch
  - 115

Number of months	50
Total Number of switches replaced	255
Total Number of switches replaced due to PM	21
Total Number of switches replaced due to Failure	226
Total Number replaced for No Reason Listed	8
Average Monthly Replacement Rate	5
Total Number of Z Shots	817
Shots * (36 Switches) / Replaced Switches	115

Histogram of number of months with the specified number of gas switches replaced (median = 5)

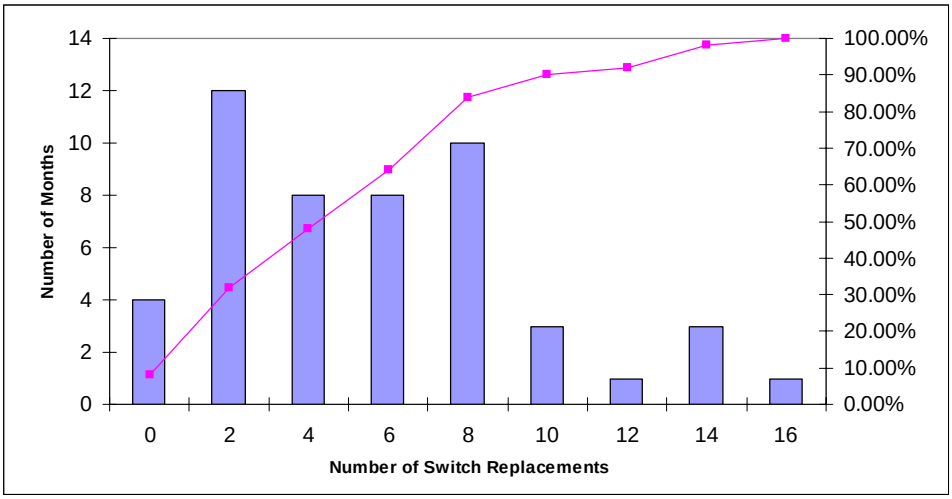

Comparison of the number of shots per month with the number of switches replaced per month

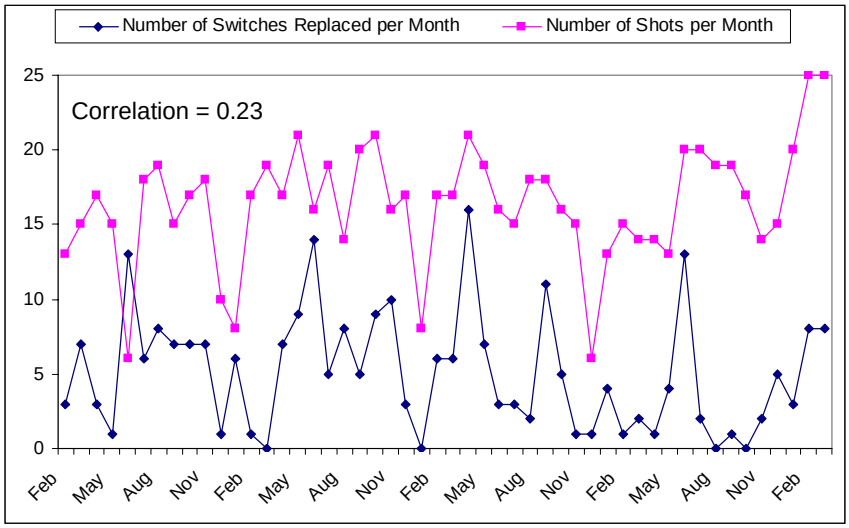

APPENDIX H. Analysis of Operation and Development Data for Z_{20} Shots 199-1111 and STB Shots 63-1305 That Includes Data from the Testing 32 Laser Trigger Gas Switches

H.1 Summary

Z_{20} is the development and engineering module created to evaluate and improve the design of the ZR module[1-3] and to obtain data for projecting the reliability of ZR and for establishing planned preventive maintenance procedures. Z_{20} has been in operation since October 16, 2003. In this report Z_{20} data taken over the period from March 2, 2004 (Shot 199), to April 6, 2006 (Shot 1199), is analyzed to quantify the module design and testing success and failures and to do a detailed evaluation of the laser triggered gas switch (LTGS) data. Three different module configurations were tested in this shot sequence and 29 LTGSs were tested. The first five ZR LTGSs were tested on the Switch Test Bed (STB).[4,5] These switches functioned as required for a successful ZR with four of the five having lifetimes between 200-400 shots (mean time to failure 220 shots) and with the shot-to-shot jitter significantly under the 4 ns required to meet the ZR goals (see Section H.4.5.3.3). This mean time to failure is comparable to the best switches on Z (see Section H.4.4). Self-breakdown data from these five switches is used to compare with formulas for predicting the most probable self-breakdown voltages as a function of pressure and for predicting the probability of prefires as a function of pressure. Excellent agreement in measured and predicted self-breakdown voltage is found with procedures provided in a paper on effects on electrode roughness and insulator flashover by Nitta et al.[6] (see Section H.4.5.3.3). The next 27 LTGSs were tested on Z_{20} and in all cases they have not performed to the standard of the first five and must be improved to meet the ZR goals. The performance of these switches is discussed at the end of this summary and in Section H.4.5. A summary of Z LTGS performance over a ten-year period is reproduced in Section H.4.4.[7] Weibull analysis of this data shows two distinct populations. One population containing 62% of the data has an early failure rate that accounts for the need to replace one switch on every fourth shot. Of the 36 switches operating on each shot on Z, 62% would represent 24 switches. A second population containing 38% of the data has a failure rate that increases with number of shots and only becomes significant after the 200th shot, accounting for the long lives of some Z switches. This population would represent the remaining 12 switches on Z.

In all of the 1184 shots taken from March 2, 2003, until August 30, 2006, on $Z_{20,}$ only one water breakdown has occurred in the Intermediate Storage Capacitor (ISC). The effective Z_{20} ISC 5 MV shots are 1.77 times the projected number to the first breakdown and the effective ISC 6 MV shots are 1.68 times the projected number to the first breakdown. Bulk breakdowns have not occurred in the Pulse Forming Line (PFL), Line 1 and Line 2. Of those shots 764 were on the Value Engineering Module with a new PFL design. ISC 5 MV and 6 MV shots had 4.6 MV and 5.6 MV respectively on the PFL. The effective Z_{20} 4.6 MV shots are 1.5 times the projected number to the first breakdown and the effective 5.6 MV shots are 0.92 times the projected number to the first breakdown. (See summary in Table H-2.) The power law scaling relationship that was used in the design process was applied to the ISC and PFL voltages to determine an effective number of shots. This power law scaling formula with an exponent of 17.2 was used to select electric field values in the design that would provide a low probability of bulk breakdown

in the insulating liquids.[8-13] The ISC Z_{20} data suggests that this relationship provides a conservative design since we have significantly exceeded the scaled expected number of shots to breakdown. The facts, that only one bulk breakdown has occurred in these components for 1384 shots with the voltage level as high as 6.5 MV on some shots and that the one bulk breakdown that did occur produced minimal mechanical damage, are positive findings with respect to projected ZR reliability and maintenance.

Even with this positive finding, there are significant concerns about meeting the ZR goals for peak current, timing, and less than 2% lost shots due to pulsed power system failures. Some of the reasons for these concerns follow:

1. Z_{20} PFL inner cylinder support rods have tracked periodically. This observation led to a design change that allows the PFL inner cylinder to be cantilevered, eliminating the PFL rods. Since barrier flashovers have not been observed in Z_{20}, this approach should be more conservative than the rod design approach, but the thicker PFL barriers are being installed on ZR without testing on Z_{20}. The consequences of tracked barriers are usually more severe than tracked rods.

2. The scaling formulas are based on limited data and may not be accurate for predicting low-probability breakdowns. In the pulsed power community, data on systems that work well is not analyzed. Small changes in the exponent can significantly affect projections of number of shots to breakdown. It could also affect our conclusion that the effective shots exceed the breakdown projection. For example, the value of an effective 5 MV shot is calculated by $(V_{shot}/5)^{17.2}$. With this scaling one 5.5 MV Z_{20} shot counts as five 5 MV effective shots and 0.2 6 MV effective shots.

3. The ZR operation point moved from 5 MV to over 6 MV peak voltage on the Intermediate Storage Capacitor and across the LTGS during the period of Z_{20} operation that was analyzed in this report. This increase in operating voltage was primarily to accommodate a 25% increase in the total inductance of the water convolute, vacuum stack, and magnetically insulated transmission lines (MITLs). This change resulted in almost continuous change in the operating voltage for Z_{20} during the data set that was analyzed in this report and only at the end of the period was testing done at 6 MV. It also reduced the projected number of ZR shots before failure of these components to a small number. The ISC projection is ten shots, which corresponds to 360 Z_{20} shots.

4. The LTGS, laser and optics, Marx generator, Marx trigger system, and divertor are not functioning with the reliability required for ZR. To assess the reliability, these components need to be functioning sufficiently well that 900 shots can be taken with the same Marx charge voltage, laser timing, and gas switch pressure with less than three failures in the complete system. With the continuously changing parameters to attempt to resolve the problems with these components and to find a 6 MV stable operating point, 27% of the shots have had faults. Many of these faults would either cause a delay in the shot or a slight decrease in the load current. About 6.2% have a high probability of destroying the ZR shot. (See Section H.3.) Thus with a LTGS system that is not functioning well and a shot pattern that likely causes more LTGS prefires, we are within a factor of three of the 2% goal. This statement assumes that all modules will operate the same, although they

may not. The water convolute and stack will not be tested until ZR is functioning. A new Marx trigger system with improved reliability has been developed by a team led by Mark Savage, but has not been implemented on Z_{20}.[14] Although this change would only have a small impact on the 6.2%, it could substantially reduce the number of delayed shots on ZR and would improve the shot rate on Z_{20}.

As mentioned above the first five LTGSs that were tested on STB exceeded the initial ZR requirements in failure rate, mean time to failure, and jitter.[4,5] These results were established while the design voltage level was 5 MV. The next 27 switches were tested on Z_{20} with insulator flashovers and prefires occurring at too high a rate. The rate of these failures does not appear to be a strong function of the operating voltage. In addition, the run times of those switches have been highly variable, leading to the conclusion that the ZR jitter requirement could not be met without improving the LTGSs. Run time is defined as the time from arrival of the laser trigger pulse to the closure of the LTGS. The number of shots to the first switch housing flashover was between 1 and 88. (See Figure H-14.) In many cases testing continued after first flashover with negligible impact on the operation of the LTGS, especially if the first flashover was just the trigger section housing. End of life for these 27 switches varied from 1-96 shots. (See Figure H-19.) Failure rates were analyzed for shots to first failure and found to decrease with increased number of shots similar to the left side of a typical bathtub failure rate curve. That type of failure curve is usually attributed to design or assembly errors rather than material wear out.[15] The mean time to failure (MTTF) of a single switch for this mode was 12 shots. For the end-of-life data the failure rate increases with the number of shot to the 0.17 power and the mean time to failure of a single switch is 27 shots. In either case, if things have not improved, multiple (1-3) switches would have to be replaced after each ZR shot.

We defined a goal for the first-generation switch to be a mean time to failure of 100 shots with 95% failing by the 200^{th} shot. The Weibull parameters to meet that goal are $\beta = 2.1$ and $\eta = 115$ shots. β is the Weibull shape factor and η is the number of shots for 63% of switches to fail.[16,17] If we can achieve these parameters, the replacement rate would be very low in the beginning (1/280) and increase to the nominal Z value of 1:4 by the 50^{th} shot. This type of loss rate would be amenable to scheduled maintenance of replacing switches before failure. Calculations were done to see what types of test protocol would be needed to have confidence that an improved switch met these parameters. It would take between 400 shots (4 switches for 100 shots without any failures) and 900 shots (5 switches for 180 shots with 3 failures) to provide 95% confidence that we had met the goal. If things are working well the shot rate for Z_{20} is 50 shots/week.

In 1987 Turman and Humphreys published a paper entitled “Scaling Relations for the Rimfire Multi-Stage Gas Switch” in which they tabulated the scaling relationships developed from the PBFA-II, Hermes III, and Saturn switches.[18] They analyzed data from development and operation of switches for these three accelerators and established E/P relationships required to achieve low probability of insulator flashover and of prefires and to avoid long run times. They associated long run times with high jitter. We compared our data to these E/P requirements and found that even though we met the criteria, we had flashovers, prefires, and long run times. As mentioned in the first paragraph of this section, we found that the procedures outlined in a paper by Nitta et al.,[6] which was published nine years after the Nitta et al. paper[19] that Turman and Humphreys followed to evaluate their data, predicted with good accuracy the STB voltage self-

breakdown curve. To use this procedure to establish LTGS criteria, we need an improved method for defining an effective area for this multigap switch and to define a roughness parameter for electrode damage done by our high-current flow. I did a Weibull analysis of the STB data to define an $(E-E_0)/P$ value for one prefire in 3600 shots. From this value of $(E-E_0)/P$, I determined that it would be necessary to operate at 80 percent of self-breakdown voltage to achieve the low prefire rate.

In exploring the trends of the data, we observed that for fixed E/P the run times appeared to be bimodal. We describe a possible explanation for this observation starting with the assumption that a weak laser trigger is the cause. Time to breakdown for SF_6 is polarity sensitive. In point plane data, it takes almost an order of magnitude longer for a streamer that initiates at a negative point to close a few centimeter gap than it does a streamer that initiates at a positive point. Video camera pictures of the light emitted when the Z_{20} laser was repetitively focused in the center of the gap did not show light in the center on all of the laser pulses. Light appeared at the negative electrode on all laser pulses.[20] With light in the middle, the point plane data suggests that the two gaps on each side of the ionized location close in sequence in about 2 ns. With light only on the negative electrode, it takes about 51 ns to close (see Subsection H.4.5.3.2). The 2 ns is a shorter closure time than shown by almost all of the data but the trend suggests that this may be an explanation of the bimodal run times.

A substantial portion of the LTGS data analyzed in this report occurred before the implementation of the enhanced R&D program that was set up to resolve the continuing issues with these switches and to provide a better basic understanding of the operation of these switches. During the past few months improvements have been made that have decreased the frequency of the housing insulator flashovers. This improvement resulted from following three changes: (1) changing the insulator cleaning procedure, (2) shielding the triple junctions on the trigger electrode support plate, and (3) adding a window that stopped the heated gas from sloshing back and forth between the triggers section and final optics area and between the trigger section and the cascade section. As stated in the previous paragraph, recent data indicates that the laser focus intensity is such that it is only providing a week trigger. STB has a different optical setup that provides strong triggering and indications are that fixing this focusing problem could have a major impact on the way the LTGSs operate.

H.2 Introduction

ZR is a project to refurbish and upgrade the Z accelerator to improve the reliability, shot-to-shot reproducibility, and the timing precision and to increase the z-pinch current from 18 MA to 26 MA.[1-3] A ZR project requirement is that the pulsed power system be sufficiently reliable that failures in its subsystems and components cause less than 2% loss of ZR shots. Z_{20} is the development and engineering module created to evaluate and improve the design of the ZR module and to obtain data for projecting the reliability of ZR and for establishing planned preventive maintenance procedures. Z_{20} has been in operation since October 16, 2003. The operation logs provide detailed information for three distinct phases of operation:

1. Marx and PFL Dummy Load Tests, which includes Shots 1 to 162 performed from October 16, 2003, to December 17, 2003, with the primary purpose of initial system checkout through the PFL,

2. OTL-Shots-Original PFL, which includes Shots 163 to 619 performed from February 3, 2004, to November 2, 2004, for the purpose of evaluating and improving the first unit design, developing an oil spark gap diverter, and analyzing and improving the LTGS, and

3. Value Engineered PFL, which includes Shots 620 (December 9, 2004) to >1400 at the present date and continuing for the purpose of evaluating and improving the final module design, establishing an operation point that will provide 26 MA to the ZR load, and continuing development of the LTGS and diverter.

In this report we discuss the data from the operation of Z_{20}, the implications of this data on the operation of ZR, and suggestions for improving the percentage of shots without module problems. There are two classes of potential ZR module problems:

1. Dielectric breakdown problems of subsystem components.

   These components were designed with detailed electric field analysis and scaling formulas. Z_{20} data may be used to confirm or refute the analysis approach. Electric fields were chosen for low probability of breakdown in the 36 modules of ZR, which means dielectric breakdown should be a rare event in Z_{20}. In most cases the frequency of occurrence of this class of failures on Z_{20} is consistent with the procedures used to project ZR reliability.

2. Malfunctions that cause a module to deliver energy to load either prematurely (prefires of Marx generator or LTGS) or late (deceasing the peak load current), or which create maintenance work. The use of Z_{20} to identify and resolve these issues leads to tests of radically different system configurations, and therefore much of this data cannot be used to extrapolate to ZR operational reliability.

At this stage of the development, problems with the Z_{20} LTGS and Marx generator make it unlikely that the 2% goal will be met without significant improvements to these subsystems. Extensive work is under way to improve the LTGS. All of the component malfunctions encountered in Z_{20} were observed on Z and ways were developed to work around these problems.[21, 22] It is not clear at this point whether the same workaround procedures can be used with the higher currents and voltages of ZR. It is clear that we must develop a better understanding of the cause of these malfunctions and attempt to mitigate each of them.

In Section H.3 of this appendix, we discuss the system operation data for Z_{20} and the potential implication of the observed Z_{20} successes and failures on ZR operations. In Section H.4, we provide the analysis of data on the LTGS including data from STB and Z. Section H.5 contains the References and Appendix H1 contains supporting material for the main body of the report.

H.3 Z_{20} Operation Analysis

The ZR operation point has moved from 5 MV to over 6 MV peak voltage on the Intermediate Storage Capacitor, ISC, and the LTGS during the period of Z_{20} operation. This increase in operating voltage was primarily to accommodate increases in inductance in the water convolute, vacuum stack, and MITLs. Much of the recent effort has therefore been devoted to establishing operation at 6.0 MV on the ISC and LTGS.

The design analysis for those two components used 5.0 MV for the nominal operation level and 5.5 MV for occasional (<10%) of the ZR shots. Since the probability of breakdown of the oil, water, and gas insulated components usually varies as E^{-a} where a is between 7 and 17 (see Table H-1), we have moved into an area where the expected reliability will be much lower than was projected for the initial design.

Table H-1. Exponents for probability of breakdown scaling.

Dielectric	Polarity	Exponents	References
Oil	Positive	13.7	8
Oil	Negative	13.7	8
Water	Positive	17.2	8
Water	Negative	14.5	8
SF^6	Both	7-10	6,19,23,24

For example, the projected number of shots until a water arc occurs in the ISC on ZR is 220 shots at 5.0 MV, 34 shots at 5.5 MV,[11] and 10 shots at 6.0 MV. For Z_{20} these numbers are 7920 shots at 5.0 MV, 1224 at 5.5 MV, and 360 at 6.0 MV. Using the same scaling as in Reference 11, an equivalent number of shots for the ISC for phases 2 and 3 of Z_{20} testing for 5 MV operation is determined by the sum of $(Visc/5)^{17.2}$ for all shots. This gives 14,000 equivalent 5 MV shots if we include all data up until August 30, 2006. Similarly, for 6 MV operation level we get 398 equivalent shots. During this time, only one water breakdown occurred in the ISC. That breakdown occurred immediately after replacing the barrier with new material for evaluation purposes. This breakdown could be an assembly error or it could be a low-probability statistical breakdown of the water dielectric. The arc did not damage the electrodes or the barrier and the ISC has remained in Z_{20} without further problems. The lack of arc damage may be due a robust ISC mechanical design. Based on the equivalent shot number for the 5 MV level of operation, we have exceeded the expected number of shots until breakdown by a factor of 1.77 (14000/7920 = 1.77). At the 6 MV level we have exceeded the expected number of shots to breakdown by a factor of 1.69 (607/360 = 1.69). This observation provides a moderate level of confidence that the design techniques and margins are conservative, but more data is needed at 6 MV and above to project the probability of failure of ZR with confidence. Uncertainty in the scaling relationships and the limited number of shots that can be done of Z_{20} will always limit the confidence in our projections.

Table H-2 is a summary of these numbers and similar calculations of the Value Engineering PFL. We did not include OTL shots for the PFL because there were significant changes in de-

sign for the Value Engineering version. ISC did not change from OTL to Value Engineering modules. In the PFL we have not observed bulk water breakdown and we have exceeded the equivalent number of shots by 1.5 and at 4.6 MV, the original design level, and are at 0.9 times the projected number of shots to the first breakdown at 5.6 MV, the present design operating level. The total number of shots in this analysis was 1184 and 204 of these were above 5.6 MV. Additional data is needed at the 5.6 MV level to help predict the component failure rate on ZR.

Table H-2. Comparison of projected number of shots to bulk breakdown versus actual number of breakdowns.

Test Sequence	**Shots Analyzed**	**Initial Design Level Number of Equivalent Shots**		**Final Design Level Number of Equivalent Shots**		**Actual shots with voltage above final design level**
		ISC	PFL	ISC	PFL	
OTL	420	2,080		90		
Value Engineering Module	764	11,920	11,272	517	382	206
Total	1184	14,000	11,272	607	382	206
Projected shots to first breakdown		7,920	7,512	360	416	
Total Shots/ Projected Shots		1.77	1.50	1.69	0.92	
No. Breakdowns		1	0	0	0	
Equivalent number of ZR shots-Total/36	33	389	313	17	12	6

Although bulk breakdown has not been a problem during testing on Z_{20}, nine PFL inner cylinder support rods have tracked during the 832 shots of testing of the Value Engineering Module. The tracks were predominately in one azimuthal location even though the profile and amplitude of the electric field is the same in the vicinity of the other five rods.[12] Two approaches to correct this problem were considered: In the first, we keep the design as is and spend more effort on understanding why the low probability of tracking occurred; in the second (chosen), we change the barrier design to allow the PFL to be cantilevered and remove the PFL rods. We will return to understanding rod tracking at a later date; the problem has not gone away, but because of the design modification it can be deferred. Since we have not observed any barrier flashes in Z_{20}, it is believed our barrier design approach is more conservative than the rod design approach, but it must be recognized as also being unverified since the thicker PFL barrier has not been tested.

Although the probabilities of breakdowns in the ISC and the water section are proving to be less than the predicted probabilities in the design calculations, malfunctioning component faults have been observed on 27% of the Z_{20} developmental shots. Recall that some of these components are not in the final ZR configuration (which is still evolving) so these failures cannot be simply extrapolated to ZR performance. They are at best indicative of areas of concern, but in that regard are quite valuable. If these faults occur in ZR, many of them could result in a loss of a ZR shot

or a delay in a ZR shot. Table H-3 and Figure H-1 summarize the frequency that these faults were observed and the predicted impact on ZR. The data for these tables and for Figure H-1 is provided in Tables H.1-1 and H.1-3 in Appendix H1.

In Table H-3, all faults were counted even if multiple faults occurred on a single shot. The number of shots in which faults did not occur was tabulated independent of the fault count. Row 10 of Table H-3 indicates that multiple faults occurred on about 8.8% of the shots. To counteract the counting of multiple faults on single shots appearing as a higher failure rate, to help understand the progress being made over the duration of Z_{20} operations, and to help understand the differences in failure rates with the higher-voltage operation in the Z_{20} value engineering test mode than in the previous two test modes, the data in Table H.1-3 in Appendix H1 was compiled from the Z_{20} shot logs. Table H.1-3 shows the successful shots and various failure modes for each Z_{20} 30-shot increment to Shot 1111. In the data in Table H.1-3, the sum of the "No. of shots with faults" shown in the far right column and the "number of shot without problems that effect shot or output" given in the third column always equals the total number of shots in the test increment. The test increment is 30 unless the increment being considered is at the end or beginning of one of the three test phases. The sum of the numbers given for the various faults does not always equal the "No. of shots with faults" if there were multiple faults on a single shot. Column 4 is "Percentage of shots without problems." The numbers from this column are shown versus the initial shot number in each test increment in the bar chart in Figure H-1. The x-axis of Figure H-1 is column 2 of Table H.1-3.

Table H-3. Percentage of occurrence of various faults on Z_{20} for Shots 199 to 1184.

		Total Number of Shots	**Number of Faults Observed**	**Percentage**
1	Fraction of shots with problems	1184	705	59.5
2	Fraction of shots with problems excluding diverter late or no closure data	1184	562	47.5
3	Energy storage system failures w/o diverter failures	1184	69	5.8
4	Diverter electrical or mechanical failures	1088	19	1.8
5	Diverter closure problems	1021	415	40.7
6	LTGS problems	1072	103	9.6
7	Laser Problems including long closure times	1072	92	8.6
8	All other problems	1072	8	0.8
9	Good Shots ignoring diverter late closure or no closure	1184	726	61.3
10	Sum of percentage in Row 2 and Row 9. It appears that multiple problems are observed and listed on 8.8% of the shots.			108.8

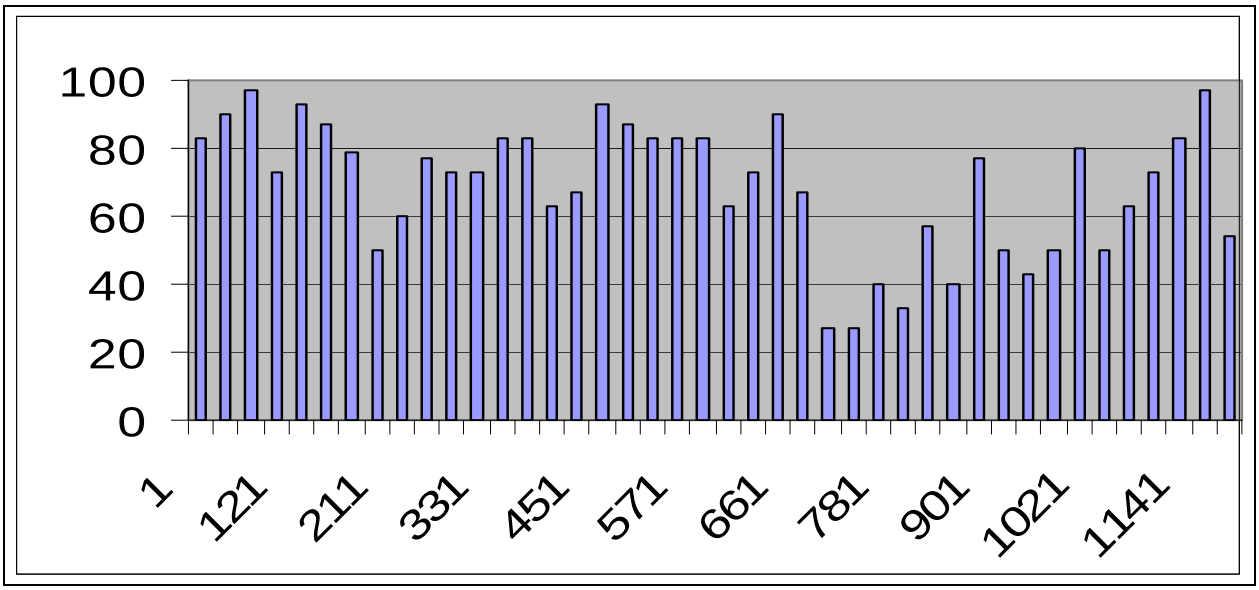

Figure H-1. Bar chart showing percentage of Z_{20} shots without failure in 30-shot increments versus first shot number in increment. X-axis scale is non-linear. The numbers are the first shot in each sequence. Each fourth bar has a number. All bars represent results from 30 shots except for the following four bars: Counting from the origin, the seventh bar is results from 12 shots, the eighth bar is results from 19 shots, the 23rd bar is results from 19 shots and the 24th bar is results from 10 shots. These four bars occur at the end and beginning of Z_{20} test phases.

Table H-4. The primary cause for each drop in percentage of shots without failures

Shot Numbers	Causes of Failures
91-120	Diverter development
181-240	Laser not properly triggering LTGS
391-450	LTGS-multiple flashovers and prefires on each switch before removal
601-619	LTGS
620	Value Engineering module installed
691-750	Diverter development
901-960	Energy storage and LTGS
1021-1080	Diverter and LTGS
1081-1140	Energy Storage

Important goals of the Z_{20} test program are the following:

1. Provide the data to project the successful shot rate on ZR.
2. Provide information needed to project the required maintenance activities.
3. Provide information needed to project the manpower to achieve the desired 200-400 shots annually.

The first step in the process to reach these goals is to understand the impact of the above failures on ZR shots. Table H-5 is the results of an initial analysis of the Z_{20} data for that purpose.

Table H-5. Projected impact of Z_{20} faults on the operation of ZR. Data from Z_{20} test data fault analysis-impact trends in Table H.1-2 in Appendix H1.

1.	2.	3.	4.	5.	6.	7.	8.
	Shots	Number of shot with faults	Number of shots with failures that would not impact ZR shot (within 20 ns of shot time)	Number of shots with questionable impact-failures that provide energy within +/- 20-40 ns of shot time	Number of shots with failures that would delay ZR shot	Number of shots with failures that would cause a loss of that module energy for a ZR shot	Number of shots with failures in which the module energy is supplied >40 ns before shot
Total	1-1184	297	77	19	70	64	67
Percent		27	7.1	1.8	6.5	5.9	6.2

The third row of Table H-5 gives the number of shots on which faults occurred and the fourth row gives the percentage of shots that each event occurred. The third column shows that faults occurred on 27% of the shots. The 297 shots with faults are then distributed according to expected impact on a ZR shot. On 7.1% of the shots there would not be an impact. Since the implosion occurs in 100 ns and the Z-pinch load does not require a precise current waveform, circuit simulations by Chuck Harje show that if the forward-going wave occurs within a 20 ns window from planned shot time that the impact on the load will be negligible.[25] Switch closure time as compared with other shots in the immediate sequence was used to determine whether each shot with faults occurred in that 20 ns window. Of interest was the fact that in a fairly high percentage of shots in which the LTGS housing flashed the closure occurred within this window. This implies that either these faults are being triggered by the laser or that this fault mode has a strong voltage dependence. Similarly, almost all of the water and rod failures fell into this window with the LTGS closing at the planned time.

Circuit analysis has been requested to determine the impact of shots where the LTGS closes in a window 20 to 40 ns from the intended shot time. On 6.2% of the shots, the forward-going pulse occurs 40 ns before the intended shot time. In this case it is likely that the experiments on these shots will fail since there will be a change in the last portion of the 200 ns prepulse. The impact of this type of change in prepulse on the Z-pinch implosion needs to be addressed. If the module LTGS closes 40 ns after the intended time, it will provide either a small amount of energy or not supply any energy to the Z-pinch. Column 5 shows that on Z_{20} 1.8% of the shots occurred in this window.

Column 6 indicates that on 6.5% of the shots, a failure occurred that would require a delay in the ZR shot. These failures are Marx generator or Marx generator trigger system prefires that occur

before disconnect from the clamp resistor. In Z_{20} and ZR during charging of the Marx capacitor, the Marx output terminal is connected to an 8-ohm resistor with the diverter hydraulic system. When the Marx is fully charged the hydraulic system separates two electrodes that are between the capacitor and the 8-ohm resistor. If the LTGS does not fire then this oil gap should close to prevent ringing of the ISC. A major difference between Z and ZR is that the ZR connection to the ISC remains in place at all times whereas in Z a swing arm is disconnected from the resistor and connected to the ISC. The potential for arcing from the swing arm to the oil water interface has been removed. The voltage across the 8-ohm resistor in parallel with the ISC is usually sufficiently small in amplitude that the gas switch cascade section will not break down even if the laser trigger arrives on time. In all of the shots when the Marx generator prefired, the clamp circuit functioned as designed and prevented any energy from going down line. When this fault occurs in ZR, there will be delay of the shot while an assessment of the cause of the prefire is made and corrective measures to prevent a reoccurrence are taken. Although it is not always clear whether the trigger generator or the Marx generator prefired, it appears that a high percentage of these failures are due to the trigger generator. This has been a problem on Z[21,22] and it is time to replace the trigger generators with an improved design.

Column 7 indicates that 5.9% of the shots were such that the gas switch closed more than 40 ns after the arrival of the laser and the down-line energy from that module would arrive too late to contribute to the Z-pinch load. In this case the pinch current would be down 3 to 5%. For many experiments, this change in current would still allow valuable information to be obtained. In all of the cases discussed to this point, there is a high probability of a successful Z-pinch shot if success is defined as 23-26 MA at the load. These cases represent 77% of the shots out of the total of 29% that had faults (230 of the 297 that had faults).

The information in column 8 indicates that in about 6% of the shots on Z_{20} the fault mode sends energy down line $\geq$ 40 ns before the LTGS trigger arrives. Simulations show that in this case the prepulse will be an order of magnitude larger than the projected ZR prepulse. Having that much energy around up to few hundred nanoseconds before the shot will set up initial conditions much different than a normal Z-pinch shot and the probabilities are high that the shot will be a failure. If all modules had faults of this sort on 6% of the shots, ZR with 36 modules would never have a successful Z-pinch shot. The situation is not that bleak. In the development of the Z switch on Demon and during the first one or two years of PBFA-II operation, an operating voltage-pressure range (E/P) was defined that would give less than 0.1% of the shots with prefires or long runtimes. In the case of Z_{20}, the operating voltage required to produce the forward-going pulse needed to produce 26 MA has increased by 20% during the operation of Z_{20}. This change and the problems with the LTGS housing flashover has led to very frequent changes in operating parameters. A significant fraction of the data was taken E/P values outside of the values used in Z or suggested in the scaling formulae. Since it was unknown whether the diverter would close to prevent the ISC from ringing over, much of the data was also taken a higher percent of self-break voltage than may be necessary during ZR operation. These conditions lead to a higher percent of the shots being prefires. In addition, when an LTGS housing flashover occurs, in many cases the damage is minimal and the switch can continued to be used. In some cases the switch tracks on subsequent shots at voltages as low as 60% of the planned operating voltage. These shots are also included in column 8. There have been and will continue to be conflicts over time spent on Z_{20} to understanding the causes of faults and methods to correct the faults that are occurring too

frequently and time spent on collecting statistics to show that ZR will function as promised. When the module is operating reliably, it takes two days to get enough shots for the equivalent of one shot on ZR. To know whether the 2% lost shot on ZR goal can be achieved, one would needed the equivalent of 100-200 ZR shots. This is 3600-7200 Z_{20} shots or 180 to 360 reliable days of operation. Clearly the final statistics will need to be developed on ZR.

H.4 Laser Triggered Gas Switch Data and Observations

H.4.1 LTGS Introduction

The 6 MV LTGSs are the last actively controlled subsystems that determine the timing of the forward-going pulses. Upon closing these switches, transfer of energy from the ISC to the PFL is initiated and the voltage waveform from this transfer of energy determines the timing of the self-closing water switches. Precise timing of the LTGS closure is required to achieve the nearly simultaneous arrival of all 36 pulses at the vacuum insulator stack such that the sum of these pulses produces the required 26 MA at the load. Another ZR goal is to provide a jitter of one nanosecond where jitter is defined as the root mean square of the deviations from the average closure time. With 36 modules operating in parallel, the jitter of each module must be ~6 ns.[26] The module jitter is defined as the standard deviation from the average timing of the forward going waves. The module jitter includes both the LTGS and the two sets of water switches. From the Z_{20} data on these three sets of switches, the LTGS jitter must be ~4 ns. There have been data sets on STB and Z_{20} in which the overall module jitter including the LTGS jitter have been achieved with the LTGS voltage up to 5.5 MV. Work is continuing to establish a switch and laser configuration and pressure regime in which this requirement can be achieved at 6.2 MV.

The ZR Project goals for the LTGS are stated as follows:

> *Normal operational performance (launching the correct forward-going voltage pulse) must be coupled with the reliability requirement of no more than 2% loss-of-shots from the entire pulsed power chain due to on-shot performance or delays. The shot-delay impact was estimated, based on guesses of manpower access and switch maintenance requirements, to be: The laser triggered gas switch shall be routinely replaceable within 4 hours, including oil fill/drain, without impacting normal next-shot preparation procedures.*

Table H-6 compares original and enhanced design parameters to present Z_{20} operational parameters. Table H-6 indicates that all of the parameters except reliability have been met for a limited numbers of shots. At the failure rates in the sequence of shots analyzed in this report, it is unlikely that consistent performance of ZR can be achieved. The LTGS issues that need to be resolved to achieve MTTF and jitter acceptable for initial operation of ZR are housing flashover, prefire rates, and variations in run times. Following development of the initial LTGS for ZR, the research and development effort will continue with a goal to increase our understanding of the physics of these switches to develop a switch that will maintain a low jitter throughout a lifetime that is greater than 400 shots. The R&D Program will also provide the physics understanding and engineering scaling information required for reliable designs of these types of switches over wide parameter ranges.

Table H-6. ZR LTGS design and test parameters.

	Original Goal	12/2004 ZR Requirement	Z_{20} Performance 4/2006
Peak voltage at switch out	5 MV	6 MV	MTTF 40 shots in range of 5 MV to 6 MV
Peak Design Current	550 kA	660 kA	660 kA
Jitter (1 STD)	<4 ns	< 4 ns	1.7 ns at 5 MV
Cascade Section Design Fields	<250 kV/cm	<250 kV/cm	250 kV/cm @ 5.5 MV 270 kV/cm @ 6.0 MV
Trigger/Cascade Field Stress Ratio	1.1	1.1	1.2
Cascade Section Field Uniformity	< 15%	<15%	12%
Reliability	MTF≥100 shots, Pre-fires 1:3600 greater* than 40 ns before nominal switch out time.	MTF≥100 shots, Pre-fires 1:3600 greater than 40 ns before nominal switch out time.	MTF 40 shots Prefires ~1/17
* Assumes that LTGS prefires will contribute less than 1 lost ZR shot per 100 ZR shots. This allows the complete rest of the pulse power system one failure in 100 shots to meet the less than 2% loss of shots due to pulsed power system problems.			

H.4.2 Description of Laser Trigger Switch

The ZR LTGS design (Figure H-2) derives from an evolutionary sequence of similar switches used on previous accelerators that provides an extensive data base of experience at progressively higher-voltage operation.[4,5,7,18,27-34] The trigger section has about 1 MV across it with 6 MV across the switch. The trigger electrode inserts are tungsten allow (usually Mallory 1000). The remainder of the voltage appears across about 25 gaps formed by a group of identical annular electrodes. This section is usually called the cascade section but is sometimes referred to as the rimfire section or as the backbone section. The stainless steel cascade electrodes are 15 cm in diameter. In ZR the switch is immersed in oil, connecting a pulse-charged, water-dielectric, coaxial intermediate storage capacitor and a water-dielectric, coaxial PFL.[1,2,11-13] PMMA housings that are either 25 cm or 30 cm in diameter have been extensively tested. A laser pulse focused in the center of the 4.8-cm gap in the trigger section initiates a single arc. The formation of that arc shorts the trigger section, creating a wave that sequentially closes the gaps in the cascade section. Approximately six arcs form in each of the cascades gaps. When the switch is functioning as designed the trigger section closes in about 5 ns after arrival of the laser pulse and it takes about 30 ns for all of the cascade gaps to close.

As stated in Section H.1, the ZR pulsed power system was designed assuming the load and vacuum interface inductance would remain 12 nH, the same as Z. With this inductance, circuit calculations representing the full ZR system indicated that 26 MA could be achieved with 5 MV across the LTGS. When ZR design was completed this inductance had risen to 15 nH. This 25% increase in inductance required at least a 20% increase in the voltage across LTGS to develop 26 MA in 100 ns. Z_{20} testing proceeded while these requirements were changed.

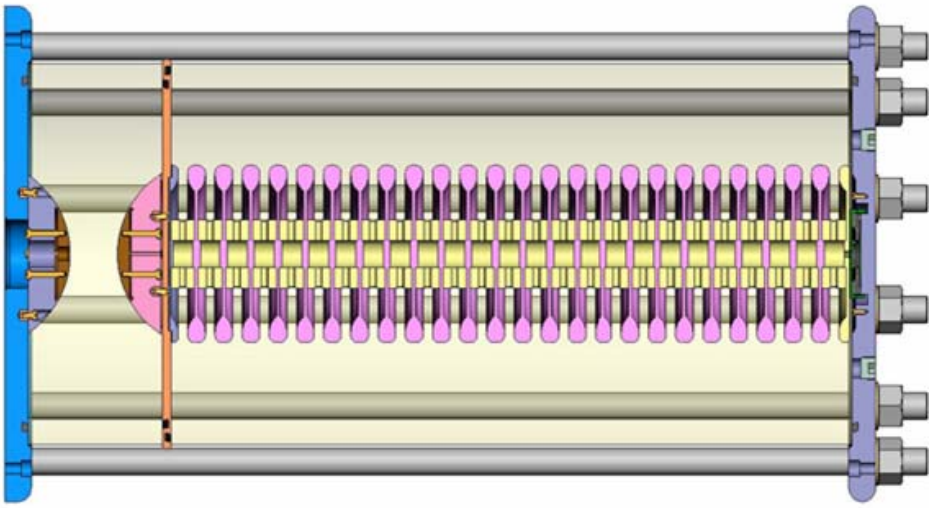

Figure H-2. ZR LTGS.

H.4.3 STB Results at 5 MV Level

Initial testing of the ZR baseline switch was done on the STB.[4,5] The system for these tests consisted of a 6 MV Marx generator (28 nF erected capacitance), an ISC (24 nF), LTGS, 8-ohm resistor, and the laser system. These parameters limit the voltage across the switch to about 5 MV if the switch closes at less than 90% of the peak voltage on the ISC. In contrast to the problems in Z_{20}, excellent results were obtained in these early tests. Table H-7 gives the results of these tests, including switch lifetime, frequency of insulator flashover, and voltage levels of the tests.

It should be noted that optical diagnostics to observe flashovers could not be installed on the STB. Degradation in the electrical signals was used to determine insulator flashover. In many cases in Z_{20}, flashover occurs without degradation in the electrical signals on that shot or subsequent shots.

One of the problems in developing components and subsystems in conjunction with establishing reliability for that module is that time needs to be spent understanding causes for failures and changes in operational characteristics. These efforts to understand the physics, engineering, and scaling laws can limit the consecutive shots at the same operation parameters. In the case of the LTGS, data is needed with the same Marx generator charge voltage, time of laser arrival, and switch pressure to establish switch voltage repeatability and jitter. Table H-7 contains consecutive shot runs that were greater than 20 shots in STB in which these three parameters were unchanged. In all cases, the parameters were set for the switch to close with 5 MV across it. The standard deviations of the voltage in Table H-7 are given in megavolts. The percentage of the standard deviation of the average voltage varies from 0.046% to 1.56%, which is within the specifications required to give 1% reproducibility of ZR output. The jitter varies from 1.1 ns to 4.8 ns with all but the first series less than the 4 ns requirement.

One should note that even with this extensive test sequence on a single shot facility, it only represents 30 ZR shots. This is insufficient data to evaluate whether less than 1% of the shots on ZR will be lost due to LTGS failures.

Table H-7. Summary of LTGS data on STB including failure summary, lifetime data and test voltages.

Shot		Failures Observed	Total Shots on Switch	Number of shots the switch voltage in megavolts was in the bins.					
				No Data	<3.75	3.76-4.25	4.26-4.75	4.76-5.25	5.25-5.75
63-185	Original Switch	2/149 prefired, 8/149 had long run times, 13/149 all in the sequence from 263 to 282 the laser did not trigger	123	6	10	3	6	98	0
258-283	Baseline #1	On Shot 283 the main housing flashed. Oil contamination observed.	26 (149)	0	5	6	6	4	5
351-563	Baseline #2	4 of the 213 were prefires, 33 of the 213 had long run times -30 of long run times were in sequence form 427 to 460. The cascade housing flashed on Shot 563.	213	0	25	38	33	117	0
564-1045	Baseline #3	6 of 482 were prefires, 60 of the 482 had long run times-52 of long run time were in sequence 574-698. On Shot 1045, the cascade and trigger housings flashed.	482	9	42	23	9	398	1
1046-1305	Baseline #4	Shots 1249 to 1305 had higher current, higher coulomb transfer and higher action. More than half of these shots had either prefires or long run times. On Shot 1305 the cascade and trigger housings flashed.	260	10	115	21	33	78	3
	Total		1104	25	197	91	87	695	9

Table H-8. Summary of average voltage and time from laser arrival to the rise of the PFL current pulse on consecutive shots with the same parameters and without failures on the STB.

First Shot No.	Last Shot No.	Number of Shots	LTGS Pressure psig	Laser Delay	Average Switch Voltage MV	Standard Deviation MV	Average Run Time ns	Standard Deviation ns
108	150	43	25	1320	4.91	0.026	41.5	4.8
162	181	20	25	1320	4.85	0.048	32.2	2.5
478	561	83	34	1225	5.04	0.060	45.7	2.2
580	599	20	34	1225	4.99	0.048	45.3	1.1
602	634	33	34	1225	5.05	0.079	49.3	2.4
729	835	107	31.5	1260	5.07	0.043	44.5	2.5
847	906	60	31.5	1260	5.07	0.026	42.2	2.5
908	941	24	31.5	1260	5.03	0.023	44.2	2.8
		390						

H.4.4 Statistical Analysis of Z LTGS

The Z-LTGS was developed in the early 1980s and implemented on PBFA-II (later converted to the Z accelerator) in 1983.[35,36] Papers describing the development of this switch and similar ones for Hermes and Saturn were presented at the 1983 and 1985 pulsed power conferences.[18,27-34] Improvements to LTGS were made during the first two years of operation of PBFA to achieve the desired reliability and jitter requirements.[18,30] The switch has limited lifetime and some improvements have been made by the PBFA-II and Z operations teams over the 20 years of operation. Even with these improvements many of the problems that are now being addressed on Z_{20} have limited the lifetime and reliability of the Z LTGS.[7,21,22] These switches have been one of the high-maintenance items during the successful operation of Z. The LTGSs are one of the items that needed to be improved to achieve the ZR goals to improve the reliability, shot-shot reproducibility, and precision. In this subsection, we reproduce the Z operation team data on the Z switch and provide information on Weibull analysis of that data.

The Z switch is same basic design as the ZR switch but somewhat different in dimensions and operational parameters. The nominal operation peak voltage and current are 4.5 MV and 300 kA.[27] The size and number of cascade gaps are significantly different. The Z-switch has 15 cascade gaps compared to 25 for the ZR switches discussed in this report. Figure H-3 is a sketch of the Z-LTGS. The outer diameter of the insulator is 50 cm and the length of the switch is 68 cm.

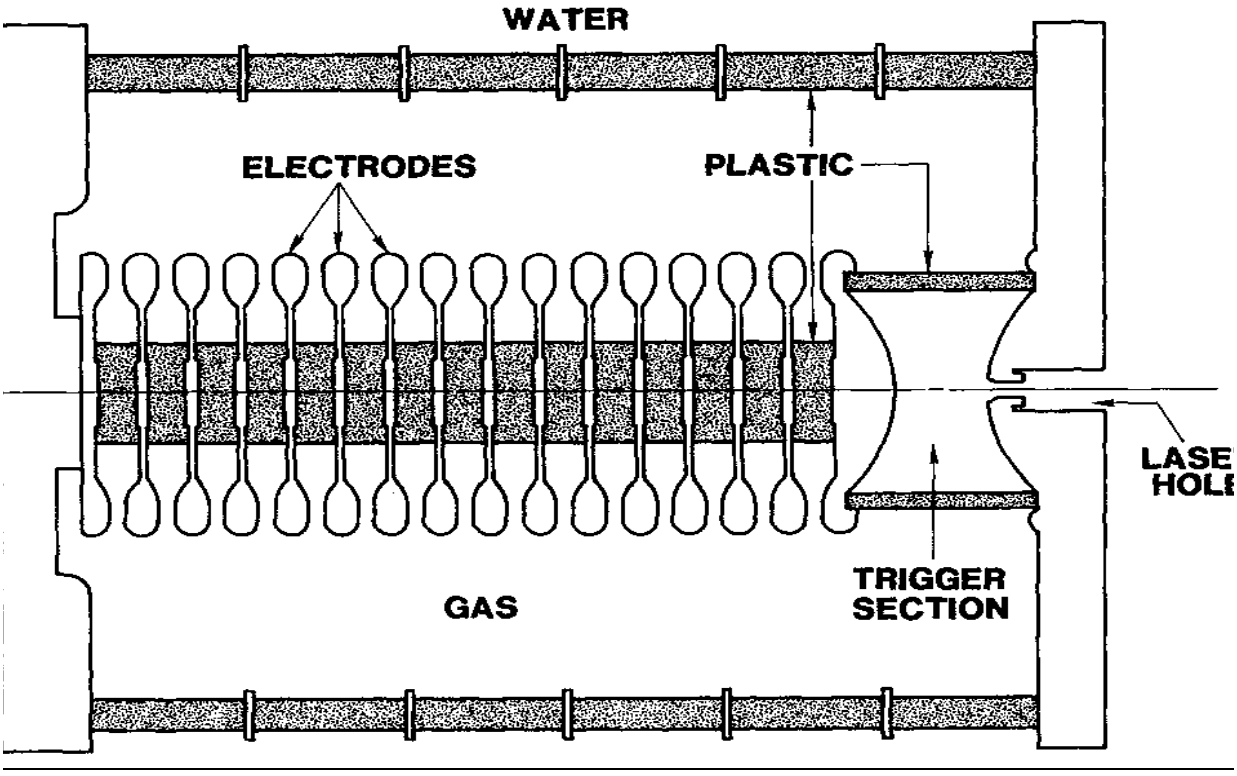

Figure H-3. Sketch of Z-LTGS.

William White of the Z operations team analyzed Z LTGS lifetime data for the period from 1997 to 2006.[7] Figure H-4 is a summary of the data and Figure H-5 is a bar chart of that data. In Figure H-5, the number of shots before replacement is given on the X axis in 10-shot bins with the label for the bin the minimum number of shots in that bin (i.e., 0-10 shots is labeled 0). There are 47 switches that were rebuilt about ten times each for a total switch count of 476 switches and a total switch shot count of 47,419. (The total number of Z shots in that period was 1317 (47,419/36).) The mean lifetime of the 476 switches was 99 shots and the standard deviation of the lifetime is 72 shots.

The Relia code[37] was used by Ken Prestwich to determine a Weibull distribution for the Z switch data. The best fit of the data to the unreliability curve is a two population Weibull distribution with one population containing 62% of the data having Beta equal 1.3 and Eta equal 75 and a second population containing 38% of the data having Beta equal 3.8 and Eta equal 191. The unreliability curve is shown in Figure H-6 and the probability density function is shown in Figure H-7. β is the Weibull plot slope, which determines the shape of the probability curve; η is the value at 63% probability of failure.[16,17]

Individual Gas Switch Lifetimes

- Data from Oct 1997 to present
- 47 different switches
- Lifetime does not seem to depend on date of install

Switch Lifetimes (number of Shots)	
Mean	99
Standard Error	3.31
Median	90
Mode	1
Standard Deviation	72
Sample Variance	5224
Kurtosis	-0.90
Skewness	0.39
Range	288
Minimum	0
Maximum	288
Sum	47419
Count	478
Confidence Level(95.0%)	6

Figure H-4. Summary of Z switch lifetime data.

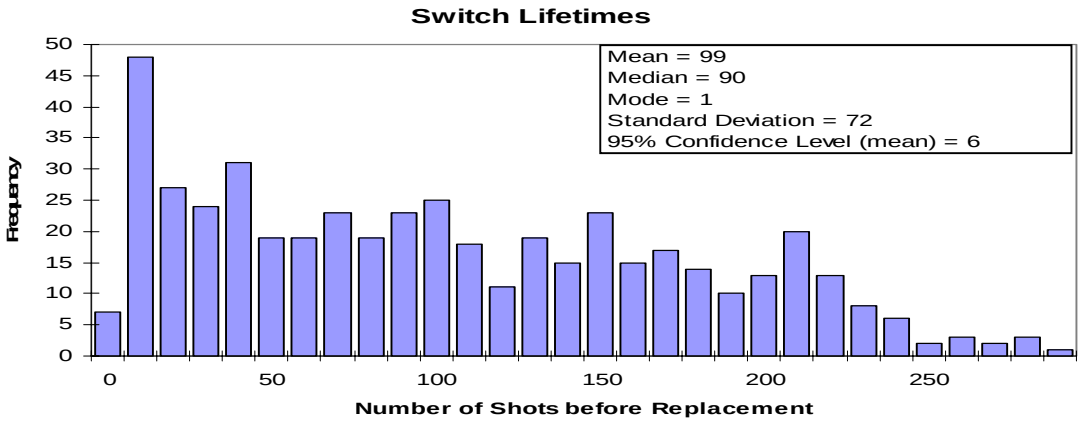

Figure H-5. Z-LTGS lifetime data for switches in service from 1997 to 2006.

Figure H-8 is a histogram of the Z data plotted with the probability density function. The low number of failures in 112-139 bin resulted in the need for two populations to fit the data. Whether the low failure in this shot bin is just a coincidence or there are two distinct failure modes is yet to be determined. Figure H-9 is a plot of the failure rate for this two population Weibull distribution. This curve is similar to the right portion of a bathtub curve. Between Shots 12 and 96, the failure rate in Figure H-9 is constant at 0.0078. The probability of a switch failure on a single shot in this band is 36x.0078, which equals 0.28, which is consistent with the loss of one switch in four shots shown in the data. Figure H-9 does not explain how the two distributions affect the failure rate.

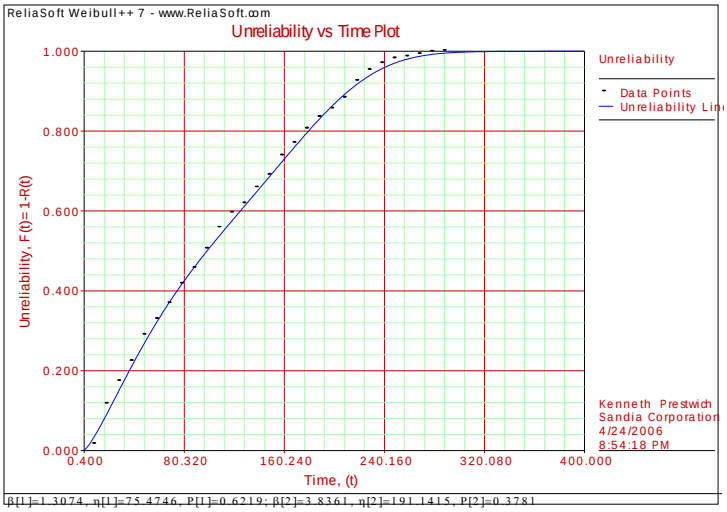

Figure H-6. Unreliability curve for Z LTGS data two population Weibull distribution.

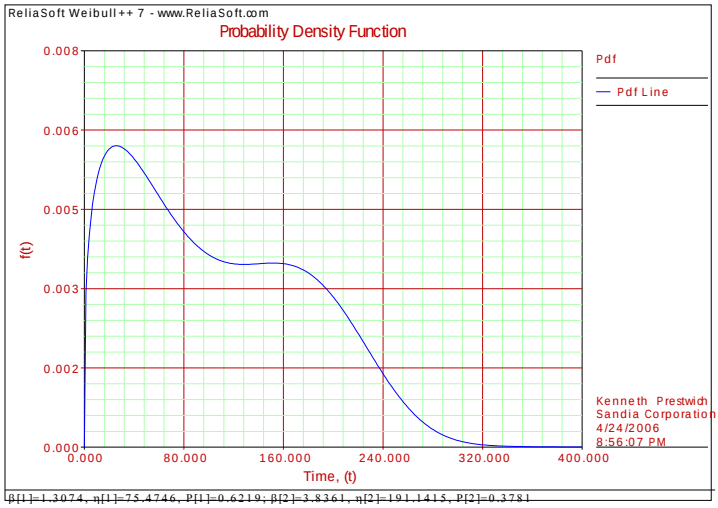

Figure H-7. Z switch data two population probability density function.

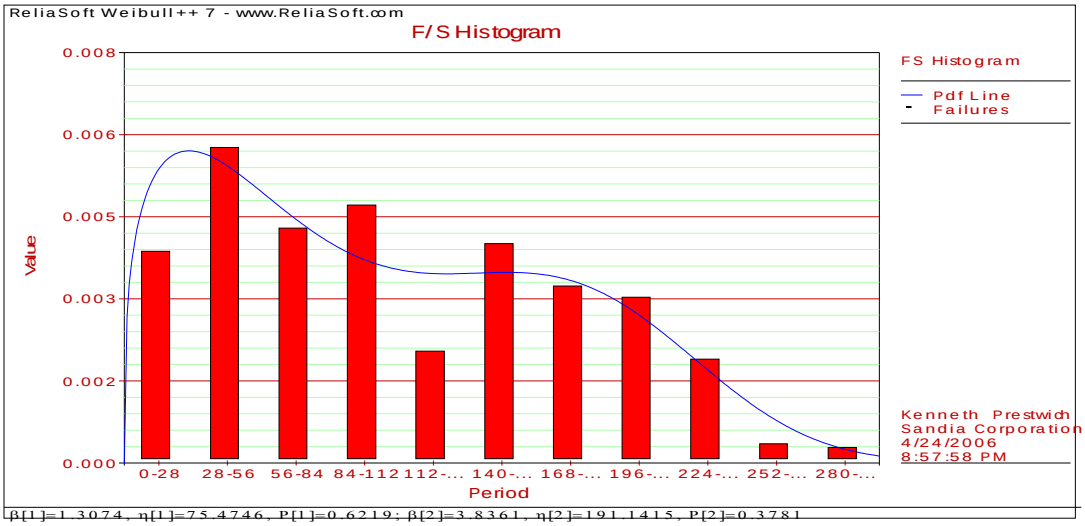

Figure H-8. Histogram of Z data with two population probability density function.

In the Weibull distribution, the failure rate can be found at any shot number from Equation H-1.[17]

$$\lambda(n) = \beta n^{\beta-1} / \eta^{\beta} \qquad \text{(H-1)}$$

where λ is s the failure rate, β is the Weibull plot slope, which determines the shape of the probability curve, η is the value at 63% probability of failure, and n is the number of shots at which the failure rate is being analyzed. The two population distribution has 24 switches with $\beta = 1.3$ and $\eta = 75$, which gives $\lambda = 4\text{-}7 \times 10^{-3} n^{0.3}$ and 12 switches with $\beta = 3.8$ and $\eta = 191$, which gives $\lambda = 8.2 \times 10^{-9} n^{2.8}$. For the 24 switches, the formula gives a failure rate of 0.01 at 12 shots and 0.018 at 96 shots. Both of these numbers are greater than the .0078 from Figure H-9. The reason for this discrepancy has not been explained at this time. Twenty-four times 0.01 is 0.24 and 20 times 0.018 is 0.43, which is not constant, as shown in Figure H-9. At the 12th shot, the probability of losing one switch is consistent with the one in four shots observed on Z. The rate has increased one in 2.3 shots by the 96th shot. These numbers may still be consistent with the observed one switch failure in four observed in the Z-data since we are continually replacing switches and the sample is not 24 after 96 shots. The probability of a failure in the other 12 switches at the 96th shot is 0.035 or one in 29 shots. The probability of one loss in four shots for this distribution does not occur until the 200th shot. This picture is qualitatively consistent with the Z data in that the switch replacement rate is about one in four shots and that the life of some switches is in the range of 200 to 400 shots. At this point in time, the reasons for two populations with vastly different failure rates and lifetimes have not been explained. Any data that would show distinct differences in materials, voltages, currents, laser energy, assembly procedure, or switch location could be valuable in helping explain the lifetime physics of cascade switches.

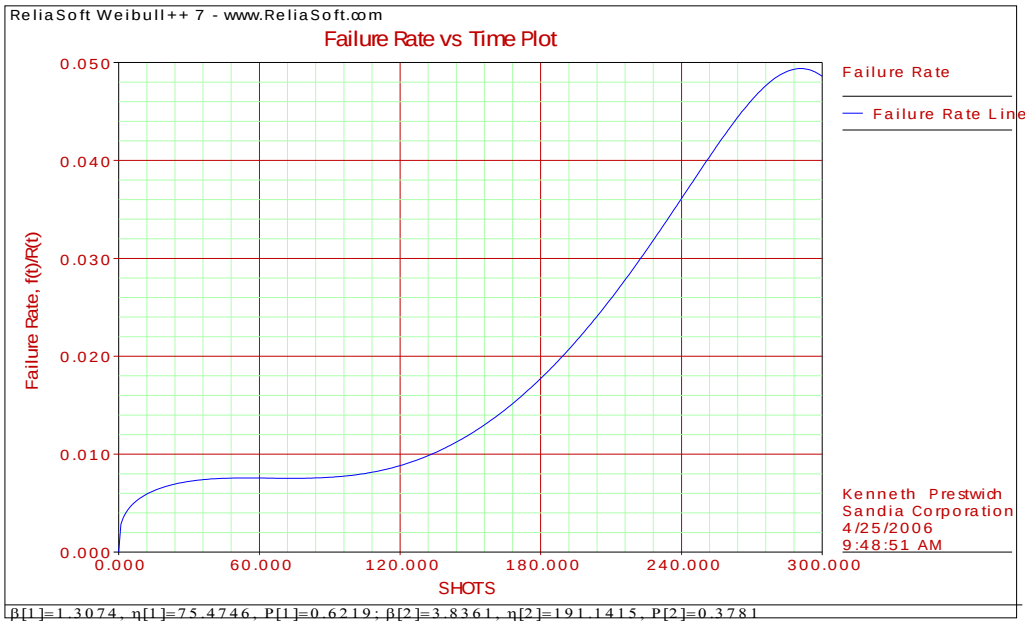

Figure H-9. Failure rate for two population Z switch Weibull distribution.

Figure H-10 is the Relia Code analysis of the data using normal distribution. The difference in the mean from the Z team analysis is the difference in how we labeled each bin in the data set. In the Z team analysis, they listed life versus frequency in bins with the bin labeled as the lower end of the ten-shot bin (i.e., 0-10 is listed as 0). I labeled the same bin 10, which accounts for the ten-shot difference in the distribution mean. The standard deviation for the two listings is almost the same. The probability density function for the normal distribution does not seem to properly account for the early failures. An explanation for the two populations is needed.

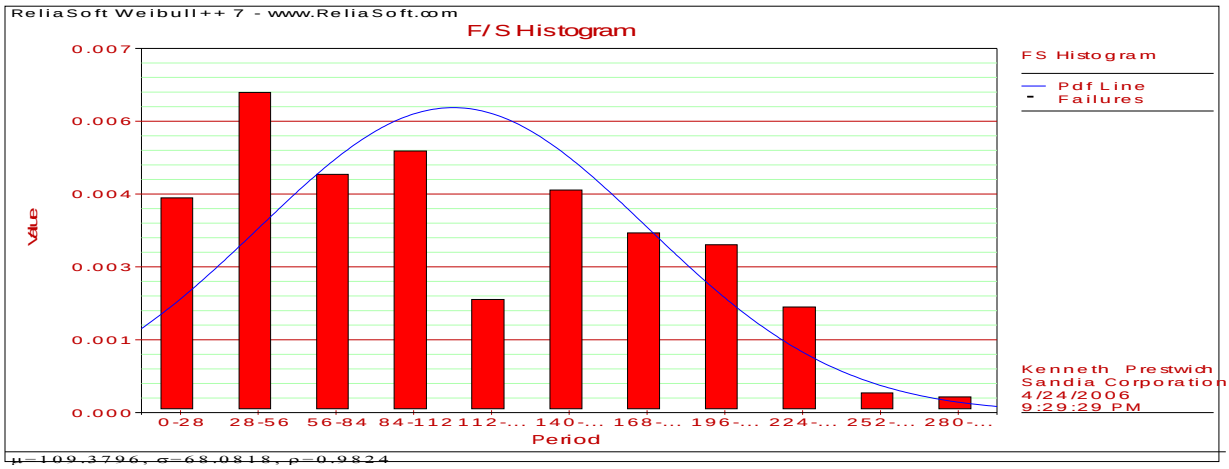

Figure H-10. Relia code histogram and normal distribution for Z LTGS lifetime data.

For the normal distribution shown in Figure H-10 the mean lifetime is 109 shots and standard deviation is 68 shots. The difference in the mean from the analysis by William White is in the Relia analysis the highest shot number in each ten-shot bin was used to identify that bin.

William White also analyzed the lifetimes of four switches for each rebuilt during the period from 1997 to 2006. Figure H-11 is a summary of that analysis. That data indicates the lifetime is a random process of the rebuild process or the location of the switches in the accelerator. William White also analyzed the monthly switch replacements rate for 50 months from February 2002 through March 2006. The results of that analysis are shown in Figures H-12 and H-13. The total number of gas switches replaced during this period was 255. The number replaced due to failure was 226. The number replaced for preventative maintenance was 21. The average total monthly LTGS replacement on Z including failures and planned maintenance was five per month (mean and median). Figure H-13 shows there is not a particular correlation between number of switches replaced each month and the number of Z shots that month. This lack of correlation implies the switch failure rate has little to do with the Z shot rate and that the switch replacements were not the determining factor in the number of Z shots per month.

Switch	20	21	33	45	
Number of Shots	5	0	131	110	Present
	157	1	229	49	
	58	64	89	49	
	44	42	60	101	
	1	131	12	93	
	161	13	73	96	
	86	10	216	16	
	2	122	78	15	
	18	146	7	9	
	162	22	127	89	
	100	64	68	127	
	121	178	138	37	
	159	159	4	100	Oct-97

Figure H-11. Shot lifetimes for four typical Z switches.

The data shows the lifetime of each of the 12 times that the four switches were rebuilt, indicating the lifetime is a random function of the rebuild process.

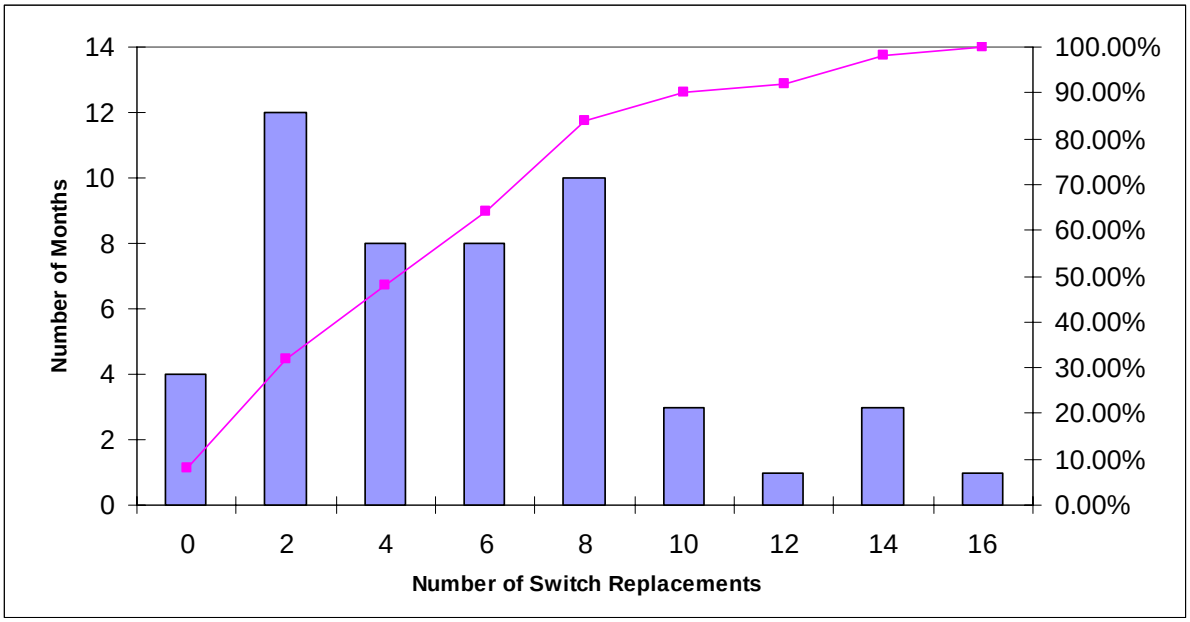

Figure H-12. Histogram of number of months with the specified number of gas switches replaced on the Z accelerator (median = 5) for the period from February 2002 to March 2006. Mean replacement rate is five per month.

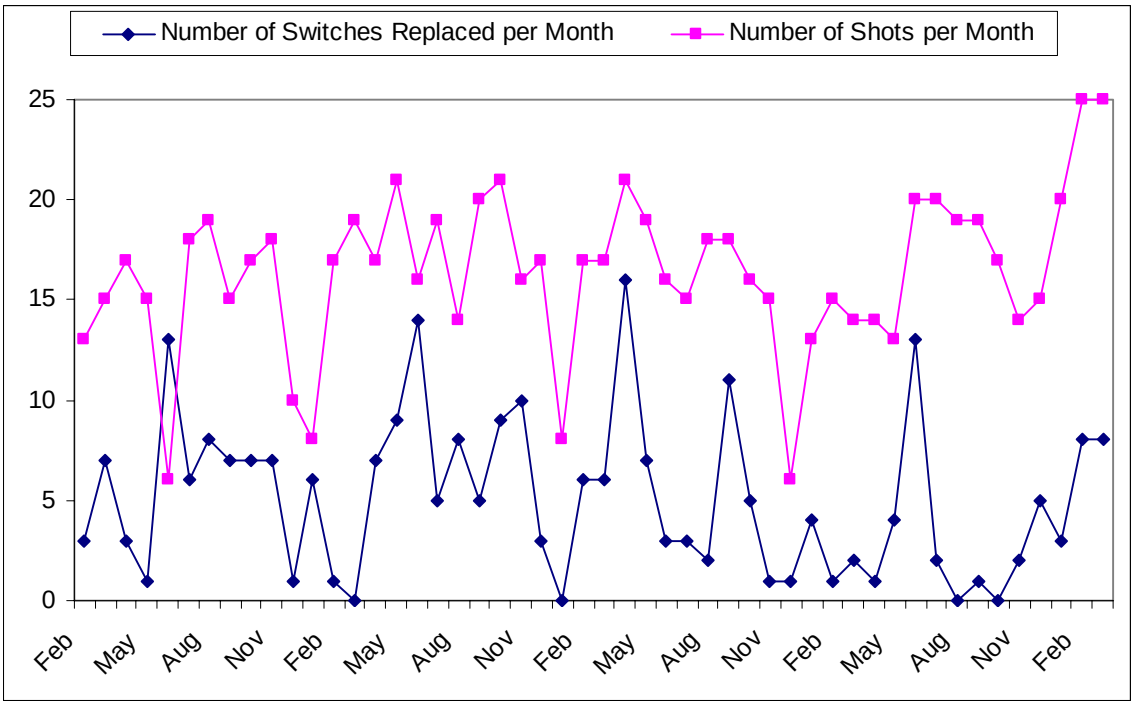

Figure H-13. Comparison of the number of shots per month with the number of switches replaced per month.

H.4.5 Z_{20} Switch Data Analysis

H.4.5.1 Failure Rate Analysis

In the first 1111 shots on Z_{20}, 27 LTGS were tested. Figure H-14 is a bar chart showing the history of these 27 switches. Twenty-six of these were removed because of a failure of the LTGS or of the associated gas or laser optics system.

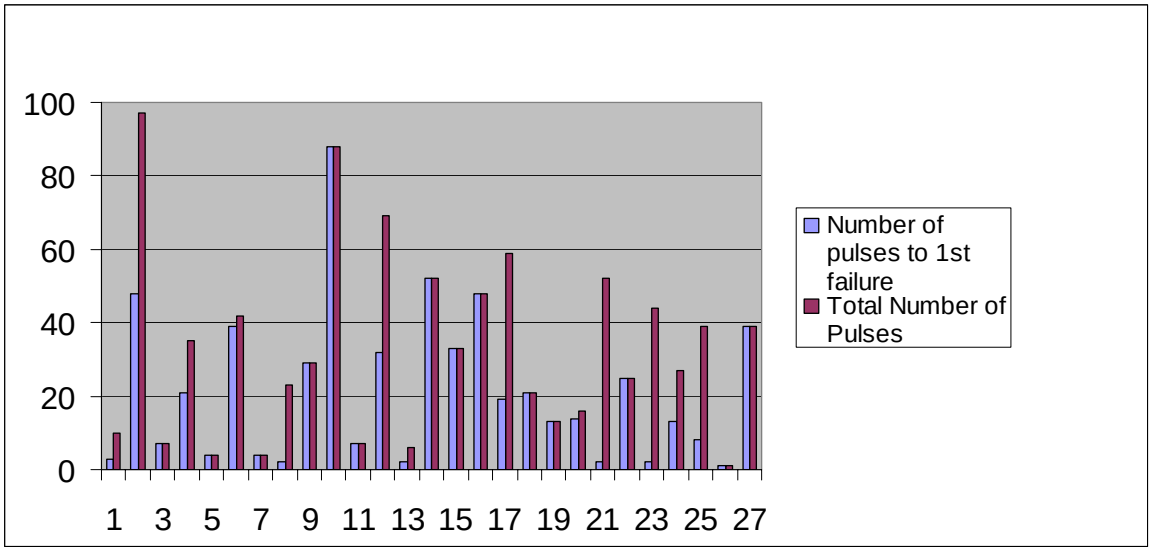

Figure H-14. Number of shots to first failure and number of shots until the switch was removed for the 27 switches in the sequence that they were tested on Z_{20}.

Table H.1-4 in Appendix H1 gives the test data for this chart including number of flashovers before removal, average E/P for normal run times, and average voltage for the test sequence. The switch listed as number 11 in Figure H-14 had not failed. It was removed to allow testing of a new design. For all other switch data shown in Figure H-14, the blue line represents the number of shots until the first flashover of one of the two housings and the red line represents the number of shots until the switch was removed. Table H-9 is the data for Figures H-14 and H-15 listed in ascending order of switch lifetime. Figure H-15 is a plot of the first flashover for the switches tested in Z_{20} in the same order as listed in Table H-9. Figure H-16 is a plot of the failure rate calculation shown in the last column of Table H-9.

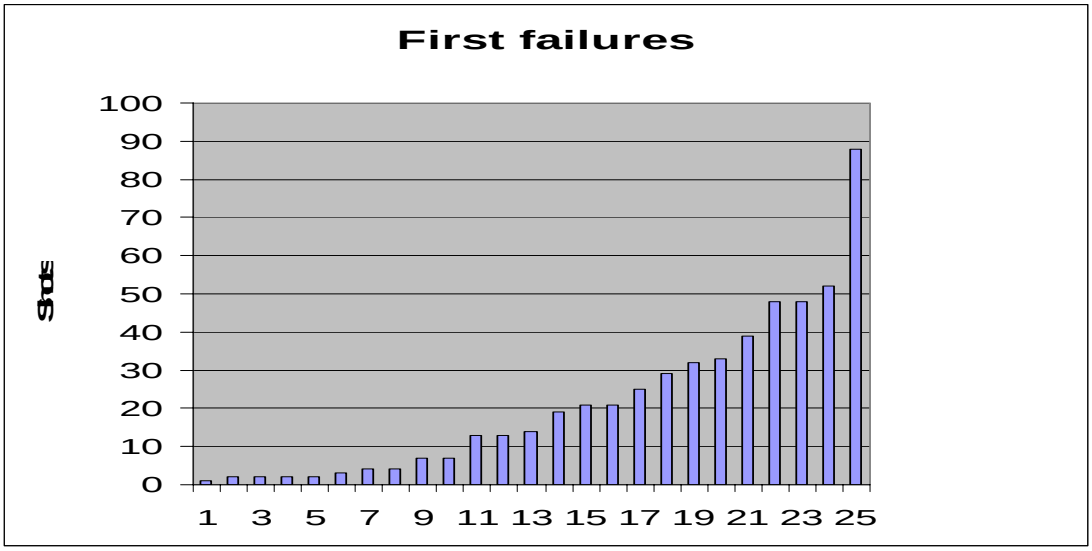

Figure H-15. Plot of data in Table H-7 showing switch failures in ascending order.

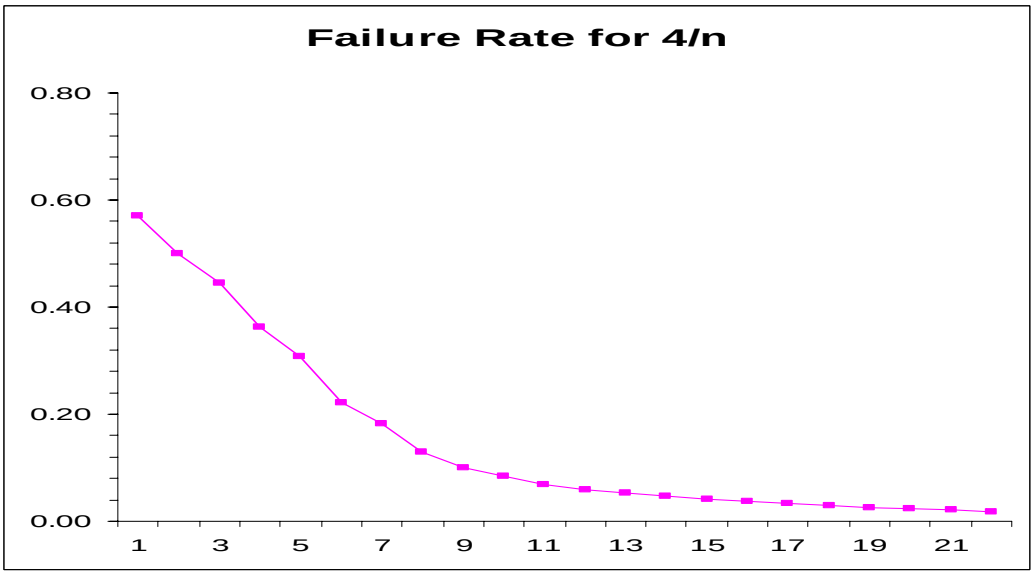

Figure H-16. Failure rate as given in final column of tabulated data in Table H-9.

This type of plot could be construed as left side of a typical bathtub failure rate curve. Usually this type of curve implies the device under test has faulty material, assembly, or design. Weibull distributions with beta >2 have failure rate curves that increase with number of shots as the Z LTGS distribution curves usually indicate problems or lifetimes due to wearout or a change in parameters due accumulated damage with use. This is not completely consistent with Figure H-11 that shows the random nature of the lifetimes for each of the 12 times that four Z switches were rebuilt.

To assess whether this failure rate curve is consistent with the Weibull distribution for this data, the first three columns of Table H-9 were analyzed using the Relia code, giving the results shown in Figures H-17 and H-18.

Table H-9. Data for Figure H-14 listed with shots to first flashover in ascending order. The last column is the failure rate calculated by 4/n where n is the total number of shots to first flashover for that switch and the three preceding switches.

Switch	1st Shot	1st Failure	Last Failure	Number of Pulses to 1st Failure	Failure Rate Calculate for Four Shot Intervals
25	1031	1031	1069	1	
8	398	399	420	2	
13	614	615	619	2	
21	883	884	934	2	0.57
23	960	961	1003	2	0.50
1	199	201	208	3	0.44
5	348	351	351	4	0.36
7	394	397	397	4	0.31
3	306	312	312	7	0.22
11	538	544	544	7	0.18
19	854	866	866	13	0.13
24	1004	1016	1030	13	0.10
20	867	880	882	14	0.09
17	753	771	811	19	0.07
4	313	333	347	21	0.06
18	812	832	832	21	0.05
22	935	959	959	25	0.05
9	421	449	449	29	0.04
12	545	576	613	32	0.04
15	672	704	704	33	0.03
6	352	390	393	39	0.03
2	209	256	305	48	0.03
16	705	752	752	48	0.02
14	620	671	671	52	0.02
10	450	537	537	88	0.02

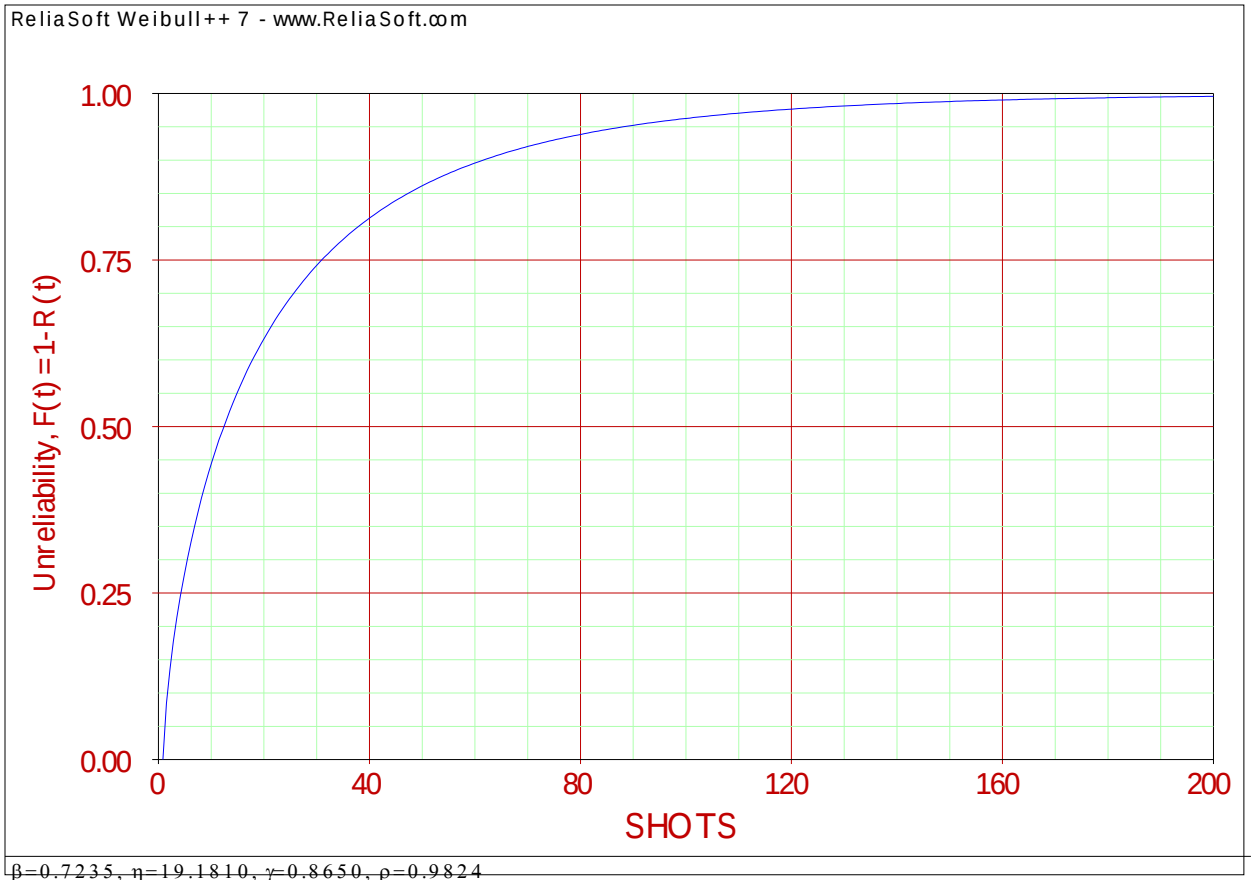

Figure H-17. Unreliability plot for first failure of the 27 switches tested between Z_{20} Shots 199-1111.

Figure H-18. Failure rate from first flashover data Weibull distribution calculated by ReliaSoft from data in Table H-9. Beta is equal to 0.72 and eta is 19.

In the Weilbull distribution, the failure rate can be found at any shot number from Equation H-1 (repeated here for convenience).

$$\lambda(n) = \beta n^{\beta-1} / \eta^{\beta} \qquad \text{(H-1)}$$

where λ is s the failure rate, β is the Weilbull plot slope, which determines the shape of the probability curve, η is the value at 63% probability of failure and n is the number of shots at which the failure rate is being analyzed. For beta less than 1 the failure rate is decreasing function with number of shots, left side of the bath tub curve-early failure portion. For β equal 1, the failure rate is constant, the bottom of the bathtub curve-normal operating life portion. For $\beta>1$, the failure rate increases with number of shots, right side of bathtub curve-wear out portion. For the first flashover data, β is 0.72 and η is 19, which makes the λ = proportional to $0.086/n^{0.28}$. In this case the failure rate tends to infinity as the number of shots approaches zero and the Relia program is not consistent on the failure rate for the first few shots. In the program, the failure rate is the number failing as the original sample is depleted by failures. The failure rate trend is the same as our crude calculation in Figure H-16.

As shown in Figure H-14, testing of many switches continued after the first failure. Table H.1-5 in Appendix H1 gives the data for each of these switches. Figure H-19 is an unreliability plot for the number of shots until removal for the switch test data shown in Figure H-14.

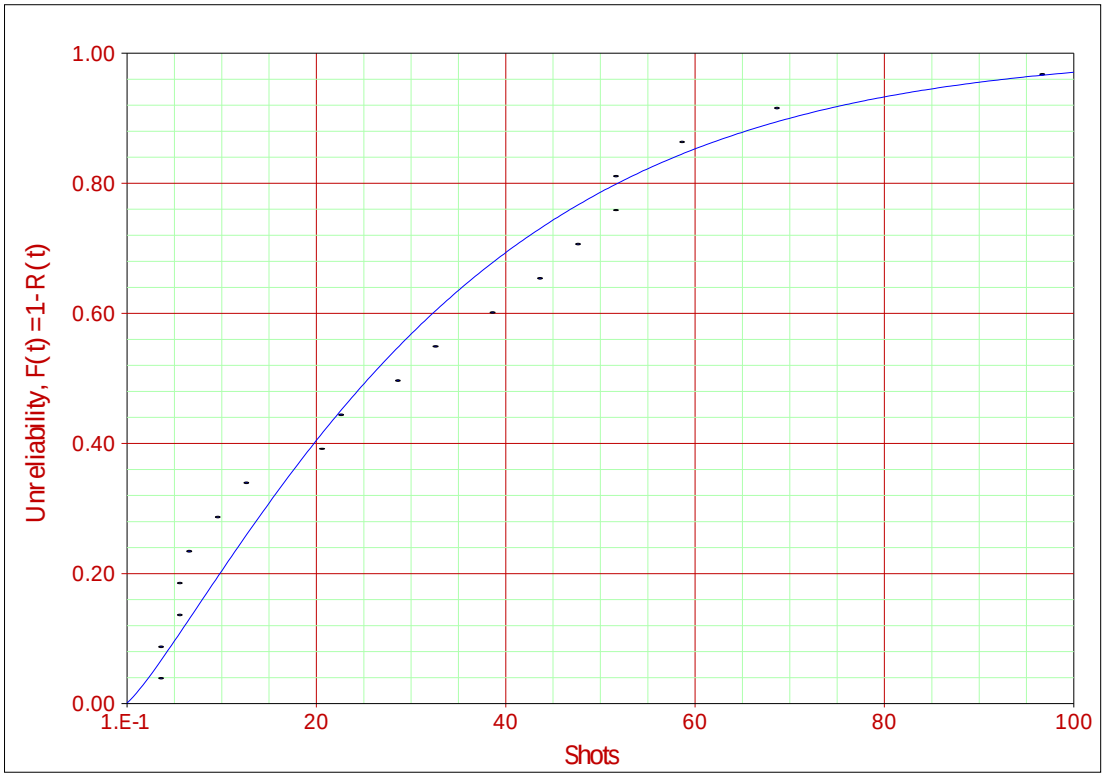

Figure H-19. Unreliability plot for number of shots until removal of switches for the 27 switches tested on Z_{20} between Shots 199 to 1111. For this analysis β =1.19 and η =35.

This change from $\beta<1$ for shots to first time failures to $\beta>1$ for shots to removal is an important observation. In Z_{20}, a still camera and a framing camera are used to clearly identify every flashover. On a significant percentage of the shots in which flashovers occur, the downstream electrical signals are the same as if the switch closed and did not flash the insulator. In some cases, the switch closes normally and the housing tracks either almost simultaneously or at a later time. Usually in these cases there is negligible change in the voltage and power of the forward-going wave. In Z and STB, deviations from the normal electrical signals are the determining factor on whether a switch failure has occurred. In this comparison, βs for Z_{20} and the Z population containing 62% of the switches are similar, but η is considerably smaller for the Z_{20} data for Shots 199-1111 than in Z giving a failure rate of one switch per ZR shot rather than the one switch per four shots in Z.

Using the methods described with Equation H-1, the failure rate as a function of n, the number of shots on a switch, is given in Equation H-2.

$$\lambda(n) = 0.017n^{0.19} \qquad \text{(H-2)}$$

The failure rate curve is plotted in Figure H-20.

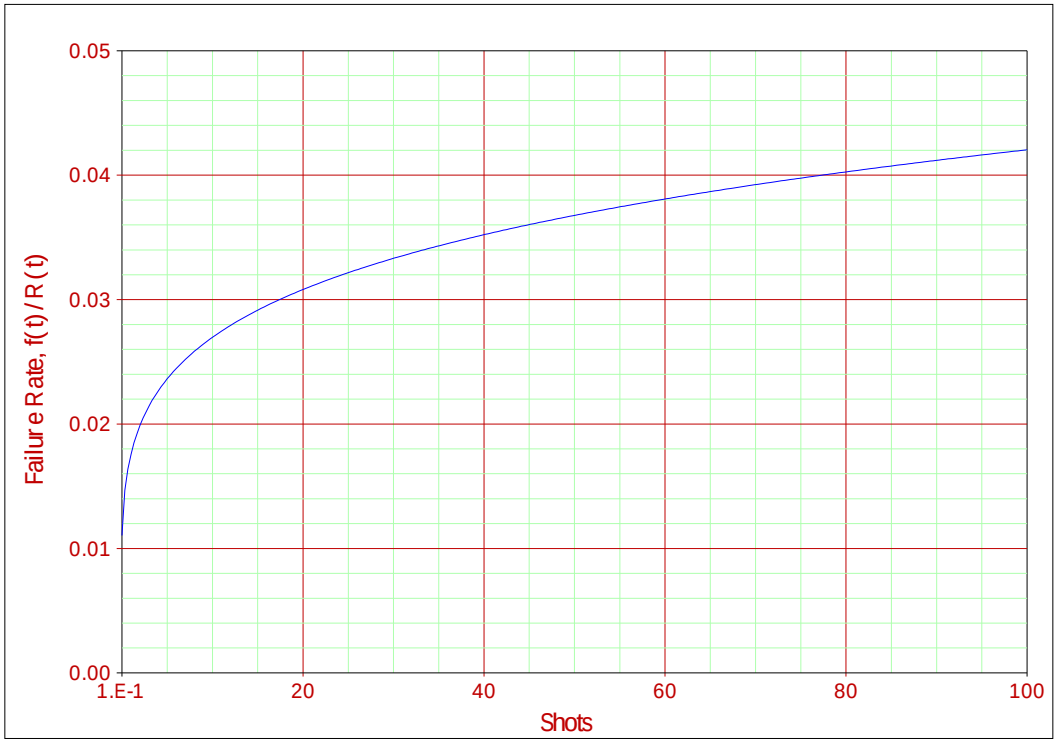

Figure H-20. Failure rate curve for Weibull analysis of Z_{20} data on number of shots to removal of each switch in the shot sequence from 199 to 1111.

The above analysis defined the number of failures and failure rates. Many unsuccessful attempts have been made to correlate the flashovers and prefires with particular switch parameters; some of those are reported in this section. The plot of voltage versus shot number done by Porter showed that about 10% of the shots were at voltages 10 to 20% higher than the average voltage for any particular switch.[38] Concerns were expressed in the switch R&D planning meeting that these high-voltage shots were causing the flashover problems. Comparing the voltage on a flashover shot or to the shot immediately before flashover with the maximum voltage applied to that switch and to the number of shots between the occurrence of the maximum voltage and the flashover has not shown a trend to establish that maximum voltage on a switch is the cause of flashover. The data to make this comparison is Table H.1-5 in Appendix H1.

H.4.5.2 Discussion of Differences on Z_{20} and STB

The LTGS team has spent considerable amount of time evaluating the differences between Z_{20} and STB and between Z_{20} and all other Sandia facilities that use Rimfire switches. The expected number of shots to failure in virtually all other facilities except Z_{20} is in the 100-400 shot range and the expected number of shots to failure in Z_{20} is in the 20-40 shot range. In the case of the STB and Z_{20}, the switches that have been tested are identical and the assembly procedures are the same. Tests in the 5.5 MV range have been done where STB has the same or greater coulomb transfer and current action than Z_{20}. Four out five switches tested on STB had a life in the 100-400 shot range before they had degraded electrically to the point that they were no longer functional. The fifth switch flashed after 28 shots. It had oil contamination and was the first switch installed after an arc in the PFL. A similarly defined life for the last 28 switches tested in Z_{20} is between 1 and 97 shots. Twenty-nine switches have been tested on Z_{20} by Shot 1199. The number of pulses to first failure and the total number of pulses until the switch was removed are given in Figure H-14. The first switch in Z_{20} is not shown in this plot. The life for that switch as defined above was about 200 shots. The voltage across the switch in almost all of the shots was less than 5 MV. The system configuration for these first 200 shots changed frequently and for a large fraction of these shots the downstream side of the switch was connected directly to resistors. The STB tests were done with this direct connection to resistors.

The odds that the first switch on Z_{20} and the four switches tested on STB would be the five best switches of the 33 that had the same manufacturing and assembly processes is 1/237,336. This number was calculated as follows: $(5\times4\times3\times2\times1)/(33\times32\times31\times30\times29)$. If we include the five switches that had a life equal to or better than 60 shots (four shown in Figure H-14 and the switch tested immediately after the data set being considered in this report, which had about 80 shots before flashover) in the sample of good switches, the odds are still 1:5650 against selecting the best four switches for STB.

The Weibull distribution for the Z_{20} switch removal data shown in Figure H-19 has $\beta = 1.19$ and $\eta = 35$, which gives a failure rate versus number $0.017n^{0.019}$. If this failure rate is not improved, one would expect to have to replace one switch in the first two shots, by the tenth shot the replacement rate would be one each shot, and by the 100^{th} shot it would be three replacements in two shots. This rate of replacement will have a negative impact on the ZR goal to improve reliability. If one replaces the switches after the first flashover the situation is even worse. For the STB data $\beta\sim1$ and $\eta = 256$. This gives a failure rate of one switch replacement in seven shots,

which would be acceptable for the first switches on ZR. This data indicates that one or more significant differences in these two test facilities have caused a large change in the lifetime of the switches. Identifying that crucial difference has been a slow and difficult process. The highest-priority goal of the LTGS Research Program is to understand this difference and to improve the LTGS failure rate.

The following are some of differences in the STB and Z_{20} that have been evaluated and when appropriate action was taken to mitigate:

1. Z_{20} has water switches with the associated shock waves.

   Rimfire switches operate in close proximity to water switches on many other facilities; we have assumed at this point that this not the significant difference.

2. The techniques for supporting the switches are different.

   Rimfire switches in all facilities are supported by cantilevering the switches from one endplate attached to the center electrode of either the ISC or the PFL. In all of the facilities except Z_{20}, the switches are attached rigidly to the center electrode of the ISC and have a flexible attachment to the PFL. In Z_{20} the switch is rigidly attached to the center electrode of the PFL with a flexible attachment to the ISC.

The Z_{20} switch is designed such that gaps should not occur at the triple junctions. It is possible that deflections due to change in cantilevering could open gaps in Z_{20} that do not exist on STB. Flashover of insulators is not well understood because of the many material variables. For design purposes, it is generally agreed that the differences in dielectric constants between the insulator and the gas cause enhanced electric fields at the triple junction that can initiate flashovers. These enhancements are created when a gap exists between the insulator and the electrode in the direction of the electric field. In the gap, the electric field in the gas is about εE if the field in the plastic in the immediate area is E and ε is the relative dielectric constant of the plastic. For Lucite (PMMA), ε is 2.7 at 1 MHZ. At 6 MV on the Z_{20} gas switch, the electric field at the triple junctions during charging of the PFL without this enhancement is in the range of 76-82 kV/cm and in the main electrodes the electric field is in the range of 220-250 kV/cm. In a gap at the insulator, the field will increase to 205-220 kV/cm. These levels indicate that if a gap exists, we are as likely to begin ionization of the gas at the insulator as in the main electrodes. At the insulator the electrodes are aluminum. The cascade electrodes are stainless steel. The onset of electron emission is usually lower for aluminum (~100 kV/cm) than for stainless steel (~200 kV/cm). Since we depend on the impulse electric strength of the gas, the initial ionization may occur before triggering the gap. When the trigger gap closes, the electric field increases in the first cascade gaps and at the triple junction on the support plate by at least a factor of 1.4. (Rosenthal's simulations give larger increases.[39]) It is then a matter of whether the insulator flashover or the cascade gap breakdown develops faster. Since the peak field in the flashover case only occurs over the gap that must be less than about 60 mils wide for the switch to remain sealed, the flashover is developing into a low field (70 kV/cm) and may take longer to develop. These competing processes may be consistent with a phenomenon that occurs randomly from 1 to 97 shots.

The two end electrodes have recesses to help align the switch. Those recesses provide some shielding of the triple junction. The plate that supports one trigger electrode and one end of the cascade assembly is smooth. When the switch is cantilevered from the PFL, the moments to cause a gap at this smooth plate appear to be greater because the lever arms are much longer. There are seven ways to alleviate this problem: (1) change the design of the smooth plate to lower the triple junction fields on the smooth plate, (2) change to a Z like design, (3) increase the clamping forces, (4) cantilever from the other end, (5) provide a pliable material between the insulator and the metal plates that will fill any gaps that may be created, (6) glue the insulator to the end plates with a void-free-high-dielectric strength insulator or a conducting material, and (7) form the insulators with portions of the endplates as part of the insulator assembly. The design and testing of Option 1 was completed in 2006 and it appears to be contributing factor to the decrease in the probability of flashovers that occurred in the summer of 2006. This option lowers the electric fields at the triple junctions to about 40 kV/cm, significantly lowering the probability that flashover will initiate from those triple points even if gaps exist. In addition, the electrodes have been changed from aluminum to stainless steel. Studies are also under way to understand the function of the width of the gap on the arc initiation process. Option 2 was also tested in the summer of 2006 and an arc occurred from the edge of the trigger support blade to the housing, causing a flashover. Option 3 has been evaluated in the past with respect to the mechanical stability of the switch during installation and operation. It is difficult to determine if gaps, perhaps as small as a few mils, are formed in the cantilevering process. The implementation of Option 1 that shielded the triple junction decreased the concern of gaps forming near triple junctions due to differences in cantilevering. Options 5-7 are items to be considered if the ultimate flashover frequency is not sufficiently small to meet the LTGS reliability goals.

3. The return current geometries are different.

   Since both return current geometries have been used in other facilities this does not appear to be the major difference that we are seeking.

4. The volume behind the trigger section that houses the optics is different in the two setups and allow hot gases to slosh back and forth between the switch volume and the optics housing volume in Z_{20} to a much greater extent than in STB.

   This sloshing appears to have distributed a larger fraction of the by-products from the arcing on the cascade section insulator. Installing a window between these two volumes appears to have been a major factor in reducing the frequency of flashovers during the summer of 2006. The size of the holes in the trigger support plate was also reduced at this time to limit the sloshing between the two parts of the switch. This reduction in hole size also limits the flow of UV light from the trigger section to the cascade housing. At this point the data to quantify this decrease in frequency is limited, and testing to see if it meets our goals for the first-generation ZR switch is under way.

5. The laser intensity that creates an arc in the SF_6 is much weaker in Z_{20} than in STB.

   After installation of the window described above in item 4, the ability to get a small spread in shot-to-shot switch closure times would last for less than 20 shots after cleaning

and realigning all of the optics. This process required pulling the switch and hampered the rate of acquiring data on Z_{20}. In addition, it was taking 20-30 ns after arrival of the laser for the trigger section to close in Z_{20} as compared to 2-5 ns in STB. The laser energy was similar in the two facilities and tests in STB indicated that trigger closure time was not a strong function of laser energy. This observation is supported by data in the development of the PBFA-II switch. A number of considerations in the design of ZR and in the configurations and data collection on Z_{20} led to an optical train with more elements and interfaces than previous designs. There was a ZR design decision to continue to use the optical towers without moving them. Tests showed that the crossover tube, which provides the path for getting the laser to the center of the PFL and into the switch, needs to operate at higher pressure than the LTGS to prevent flashovers of that tube. This added two additional windows. The net result appears to be that the Z_{20} laser beam can not be focused to as high a level of intensity as STB and therefore is a weaker trigger. Recent experiments duplicating the STB optics and interfaces on STB seem to confirm the loss of ability to achieve the desired ionization intensity.[40] These experiments and bench tests on the optical train continued in October 2006.

The weak triggering discussed in item 5 has also limited the percentage of the average self-breakdown voltage that experiments on Z_{20} could be done without large spreads in the shot to shot closure times. Operating at a higher percentage of average self-breakdown voltage significantly increases the probability of prefires and insulator flashover.

H.4.5.3 E/P Analysis

In 1987 Turman and Humphreys published a paper entitled *Scaling Relationships for the Rimfire Multi-Stage Gas Switch* in which they tabulated the scaling relationships developed from the PBFA-II, Hermes III, and Saturn switches.[18] They analyzed data from development and operation of switches for these three accelerators and established the following E/P relationships for insulator flashover, prefire rates, and to avoid the variations in run times that result in unacceptable jitter. In this section, the relationship between E/P and flashovers and E/P and run times are explored for the Z_{20} data that is the subject of this report.

1. The maximum E-field that can be tolerated without prefire is derived from self-breakdown Weibull statistics. This Maximum field, for a 0.003 probability of prefire per switch, is

$$\mathbf{E / P < 82 - 3.5P} \quad \text{for } P<4 \text{ bars} \tag{H-3}$$

2. The maximum allowable insulator field

$$\mathbf{E / P_{ins} < 25} \quad \text{kV/cm-bar.} \tag{H-4}$$

3. The standard deviation for the trigger delay time increases rapidly for fields lower than 46 kV/cm-bar with a laser energy of 10 mJ or greater. This criteria is associated with the minimum electric field in the trigger section.

4. The voltage across the trigger section should be at least 20% of the total voltage.

H.4.5.3.1 E/P Analysis of Flashover Data

The principal failure that has been addressed up until this point in this section is insulator flashover covered by relationship number 2. The criteria come from the analysis of flashover data taken on the Demon test facility during the development of the PBFA-II (Z) module. Flashovers were recorded with a still camera. The best straight line fit to a Weibull plot of the data yields the following equation for probability of flashover occurring.

$$F(E)=1-\exp(-4.3 \times 10^{-11} (E/P)^{5.6}) . \quad \text{(H-5)}$$

This equation yields the <25 kV/cm-bar criteria for the probability of flashover of 0.003, the PBFA-II goal. A paper published at the same time by Wilson and Donavan discussed modifications required to the LTGS assembly needed to meet the module-to-module jitter requirement.[30] In that paper the authors state that prefires and flashovers in the first 40 shots on PBFA-II contributed to the module-to-module timing spread. The paper states that the prefires and flashovers happen occasionally. The criterion of probability of flashover of 0.003 implies that one flashover would occur in 333 switch firings. With 36 LTGSs firing on each shot, the possibility exists that one housing would flash every nine shots; similarly, one prefire could occur every nine shots. The paper does not state whether that was the case. The Z_{20} data clearly indicates that multiple flashover can occur before significant impact on the electrical signals. Using Equation H-5 we can scale $(E/P/25)^{5.6}$ and predict an expected number of shots until flashover.

An E/P analysis of the peak electric field on the Z_{20} LTGS cascade section insulator has been done for each switch tested between Shots 199 and 1111. The results are summarized in Table H-10. E/P at last flashover is the value for either the actual flashover or the value for the shot immediately preceding the flashover. If the flashover shot had a significantly lower electric field than the shots immediately preceding the flashover, the E/P for the preceding shot was used. The column labeled Maximum E/P is the maximum value for all shots on that switch. The maximum value has exceeded 25 kV/cm-bar on seven of the 26 switches. The column labeled E/P average is the average value for the peak insulator E/P for all of the shots on the switch in which data was available. We note that the average E/P only exceeds 25 kV/cm-bar for one switch. In the column labeled projected life, we use the relationship at the end of the preceding paragraph to predict expected number of shots to flashover. The last column compares the actual life of the switch, which in many cases includes several flashovers (column labeled Number to Last Flashover) to the projected life. Clearly the equation from the Demon data does not describe the Z_{20} flashover data.

Turman and Humphreys discuss a flashover problem that existed on Demon and was solved before obtaining the data that gave Equation H-5. They believed that changing housing material from slurry-cast PMMA to monomer-cast PMMA significantly reduced the flashover frequency. During the intervening 20 years that operations teams on both Z and Hermes III have reverted to slurry-cast PMMA due to availability of materials. This change in materials did not appear to change the frequency of flashovers on these machines. The switch housings on STB and Z_{20} during the test sequence analyzed in this paper were slurry-cast. Investigations of the impact of these PMMA materials as well as other materials are under way.

Table H-11 is a listing of the data give in Table H-10 sorted by switch lifetime (Number to Last Flashover). Figures H-21 through H-23 are plots of the data in the three E/P columns in Table H-11. Figure H-21 seems to show a slight trend for the highest peak E/P to occur on the switches with the longest lifetimes. Figures H-22 and H-23 show that in the Z_{20} case switch lifetime due to flashovers is independent of E/P.

Table H-10. E/P of Z_{20} switch cascade insulator analysis for all switches tested between Shots 199-1111.

Switch	Number to Last Flashover	Number to Last Flashover	E/P at Last Flashover	E/P Maximum	E/P Average	Projected Life	Actual Life/ Projected Life
1	3	10	22	28.8	25.3	75	0.133
2	48	97	22.1	29.4	23.6	452	0.215
3	7	7	21	21.6	20.4	1023	0.007
4	21	35	20.9	24.6	23	527	0.066
5	4	4	18.6	20.7	18.2	1980	0.002
6	39	42	18.7	24.2	20.7	958	0.044
7	4	4	19.3	20.8	19.3	1601	0.002
8	2	23	19.3	19.3	19	1500	0.015
9	29	29	19.1	23.7	20.2	1097	0.026
10	88	88	19.8	24.9	19.1	1481	0.059
11	7	7	19.4	20.2	20.2	1088	0.006
12	32	69	17.9	29.4	18.4	1848	0.037
13	2	6	17.9	18	17.9	2162	0.003
14	52	52	20.6	30.2	24.5	372	0.140
15	33	33	25	26.6	25	333	0.099
16	48	48	21.2	22.4	20.8	945	0.051
17	19	59	19.2	22.1	19.7	1237	0.048
18	21	21	21	21.3	19.7	1271	0.017
19	13	13	19.8	19.8	18.8	1622	0.008
20	14	16	18.4	18.6	18.3	1915	0.008
21	2	52	17.5	21.4	18.6	1769	0.029
22	25	25	20.4	20.4	18.6	1758	0.014
23	2	44	25.5	29.8	23.1	520	0.085
24	13	27	19.3	27.7	19.2	1457	0.019
25	8	39	18	18.5	18.1	2026	0.019
26	1	1	17.9	17.9	17.9	2148	0.000
27	41	41	17.3	19.4	17.2	2690	0.015

Table H-11. Peak E/P on cascade housing data in ascending order of number of shots to last flashover.

Switch	Number to Last Flashover	Number to Last Flashover	E/P at Last Flashover	E/P Peak	E/P Average
26	1	1	17.9	17.9	17.9
5	4	4	18.6	20.7	18.2
7	4	4	19.3	20.8	19.3
3	7	7	21	21.6	20.4
11	7	7	19.4	20.2	20.2
1	3	10	22	28.8	25.3
19	13	13	19.8	19.8	18.8
20	14	16	18.4	18.6	18.3
18	21	21	21	21.3	19.7
8	2	23	19.3	19.3	19
22	25	25	20.4	20.4	18.6
24	13	27	19.3	27.7	19.2
15	33	33	25	26.6	25
4	21	35	20.9	24.6	23
6	39	42	18.7	24.2	20.7
9	29	29	19.1	23.7	20.2
25	8	39	18	18.5	18.1
27	41	41	17.3	19.4	17.2
23	2	44	25.5	29.8	23.1
16	48	48	21.2	22.4	20.8
14	52	52	20.6	30.2	24.5
21	2	52	17.5	21.4	18.6
17	19	59	19.2	22.1	19.7
12	32	69	17.9	29.4	18.4
10	88	88	19.8	24.9	19.1
2	48	97	22.1	29.4	23.6

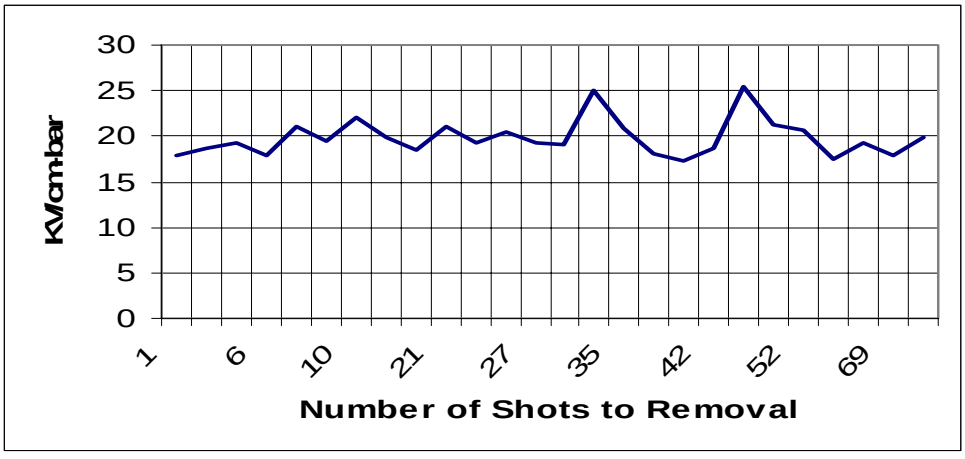

Figure H-21. Maximum E/P on the cascade housing at final flashover versus lifetime of all Z_{20} switches tested between Shots 199-1111.

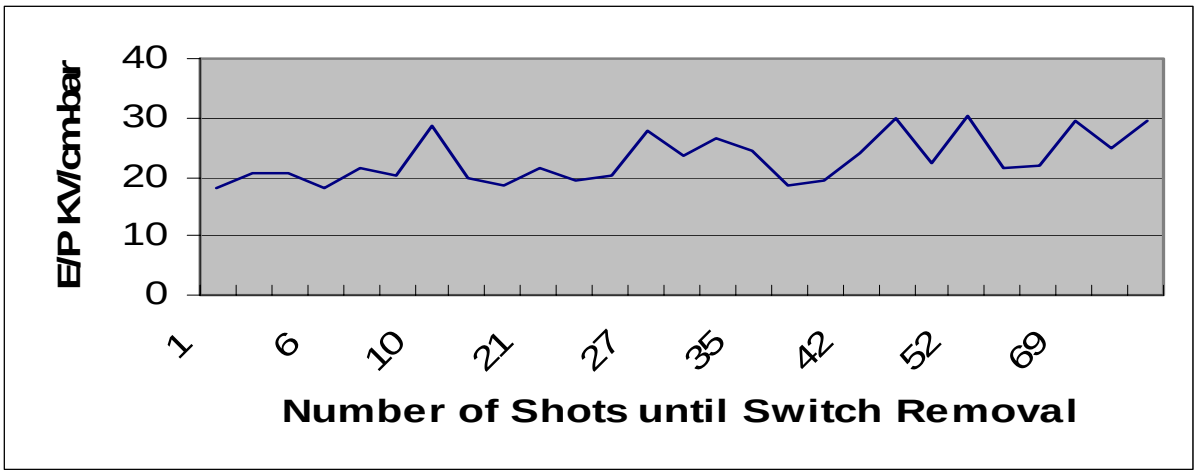

Figure H-22. The maximum E/P on cascade housing observed during the lifetime of each switch versus switch lifetime for all switches tested between Shots 199-1111.

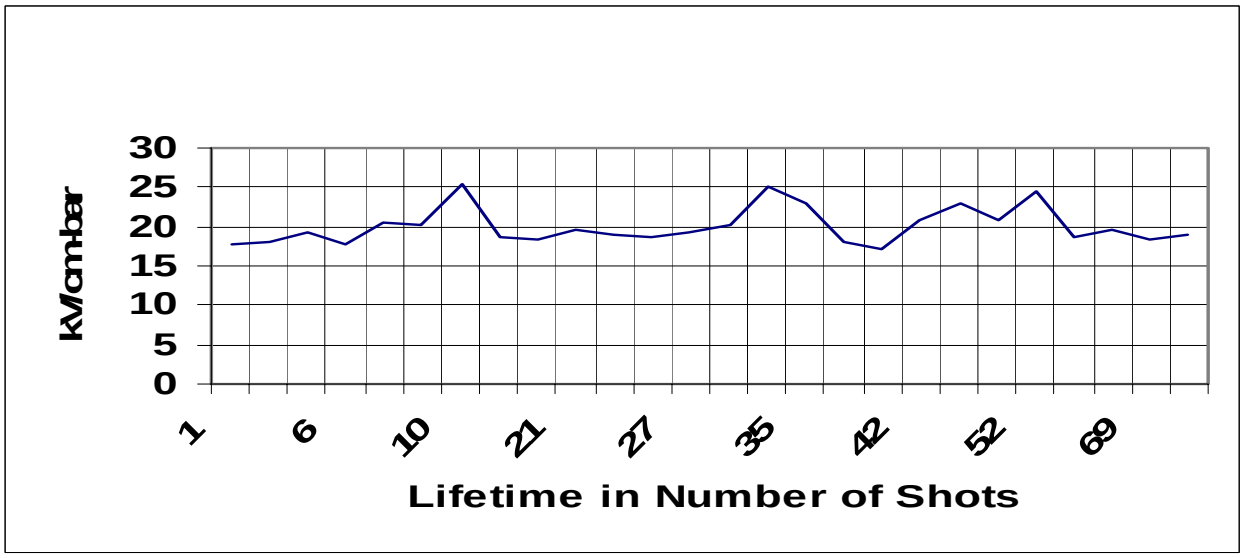

Figure H-23. The average value of the peak E/P values on the cascade housing versus number of shots until removal for the 27 switches tested between Shots 199-1111.

H.4.5.3.2 E/P Analysis of Switch Runtime Data for Shots 800-1184

In order to meet the timing requirement for ZR, the jitter (standard deviation of the timing spread) must be less than 4 ns. In ZR the timing spread of concern is both module-to-module and average time to closure from laser trigger on a shot-to-shot basis. In the single module test on Z_{20}, jitter is the standard deviation of the shot-to-shot variations in the time to closure from the arrival of the laser trigger system. Mark Savage analyzed the time to closure of Shots 800-1184 and found a large spread in the data.[41] His plot of the data is shown in Figure H-24. This data indicates there is serious problems with timing shot-to-shot spread on all eight switches in this data set. Since eight switches were tested and many different voltage and pressures were

used in this sequence, further analysis of the timing was warranted. In this section we discuss the relationship of timing with E/P and percent of self-breakdown voltage. In Figure H-25 we plot percentage of shots with run times greater than 60 ns along with the percentage with run time less than 60 ns. E/P must be low to prevent prefires, but if E/P is too low the run time spread (jitter) is expected to be too large. This analysis is the first step in determining if the Turman-Humphreys relationships apply to the ZR switch and, if not, to generate similar relationships for this switch. We also will attempt to relate these relationships to basic physics phenomena.

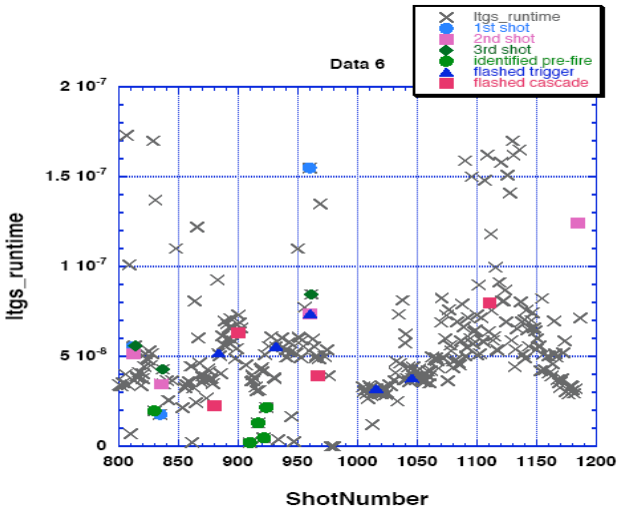

Figure H-24. Run time versus shot number for Z_{20} shots between 800 and 1084. Eight switches were tested in this data set and voltage, pressure, and laser timing were changed frequently.[41]

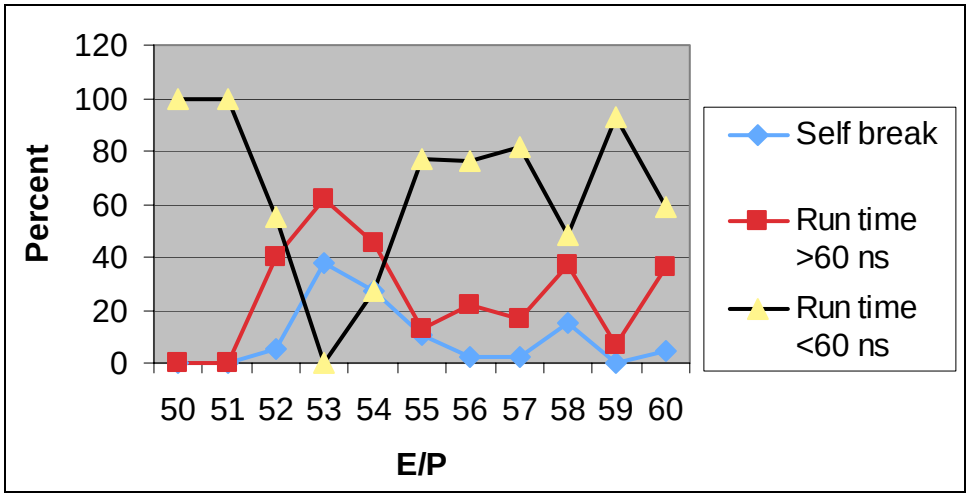

Figure H-25. Percent of Z_{20} shots in the sequence 800-1184 that had run times >60 ns, run times < 60 ns and that were self-break as a function of peak E/P in cascade section. E=246 kV/cm with 5.5 MV across the switch.

In Figure H-25 comparisons are made in percentage of shots that have long run times (>60 ns), more normal run time (<60 ns), and prefires. The E/P in this chart is the peak E/P in the cascade section electrodes. The E/P trends that we expected are not apparent in this chart. About 80% of the data have run times less than 60 ns. We need to understand why 20% of the data has long run times. Poor laser performance was the suspected reason at the time that the data was taken in the spring of 2006. It appears in September 2006 that poor focus of the laser is highly likely to be the cause. Video pictures of trigger section with laser operating at about one pulse per five seconds shows that light from laser breakdown of the SF_6 appears in the center of the gap on a large fraction of the shots but not on all shots. There is light on the negative electrode on all shots. These two modes of breakdown could account for the long run times on at least 20% of the shots. The closure time of the trigger section in Z_{20} is usually 20 ns or greater whereas in STB the trigger section closure time is less than 5 ns.

In Figures H-26 through H-32, the run time data for each value of minimum E/P in the trigger gap is plotted for Z_{20} shots 800-1084. This field is 176 kV/cm with 5.5 MV across the switch. Each data point is numbered to create the X axis. These plots show definite trends for two modes of operation, one mode with normal short run times and one mode with long and somewhat erratic run time. In Figure H-33, the average run time, the crudely estimated average value of short run time and long run time are given for each value of E/P. The short run time, which is somewhat representative of normal operation of the LTGSs does show a trend for shorter run times as E/P is increased.

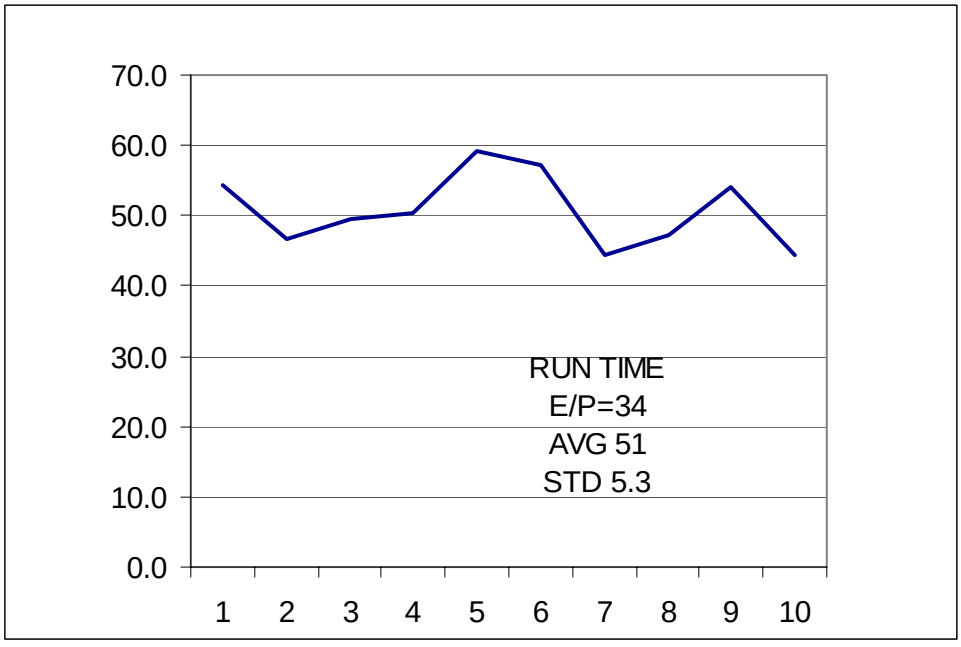

Figure H-26. Switch run time in nanoseconds plotted for each data point with E/P=34 kV/cm-bar in the Z_{20} shot sequence 800-1084. Prefires were removed from the data for this analysis.

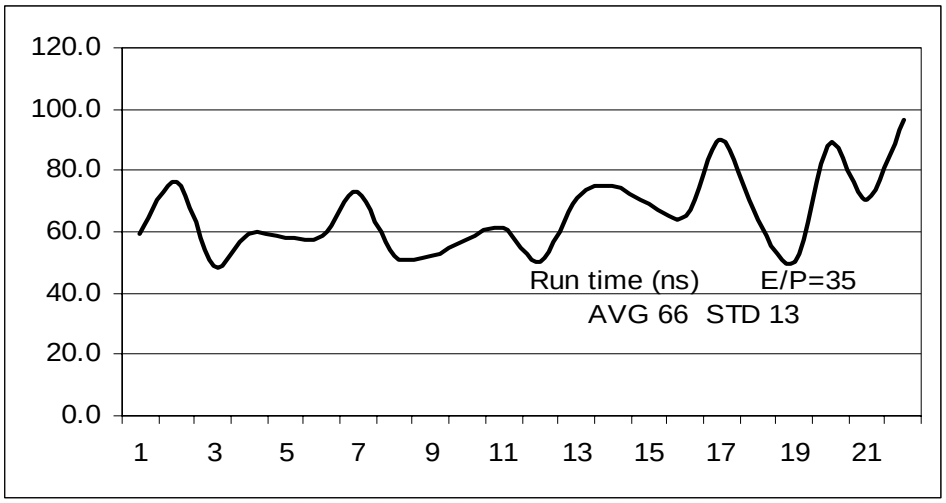

Figure H-27. Switch run time in nanoseconds plotted for each data point with E/P=35 kV/cm-bar in the Z_{20} shot sequence 800-1084. Prefires were removed from the data for this analysis.

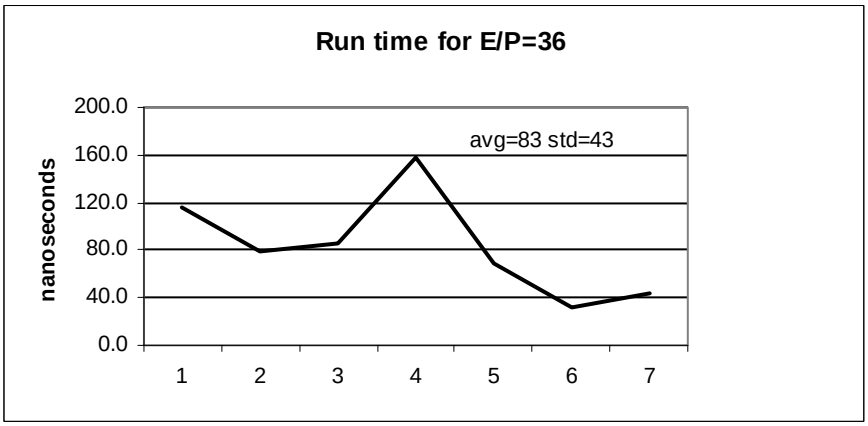

Figure H-28. Switch run time in nanoseconds plotted for each data point with E/P=36 kV/cm-bar in the Z_{20} shot sequence 800-1084. Prefires were removed from the data for this analysis.

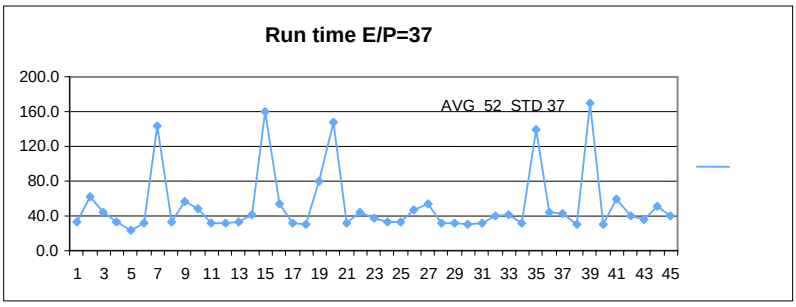

Figure H-29. Switch run time in nanoseconds plotted for each data point with E/P=37kV/cm-bar in the Z_{20} shot sequence 800-1084. Prefires were removed from the data for this analysis.

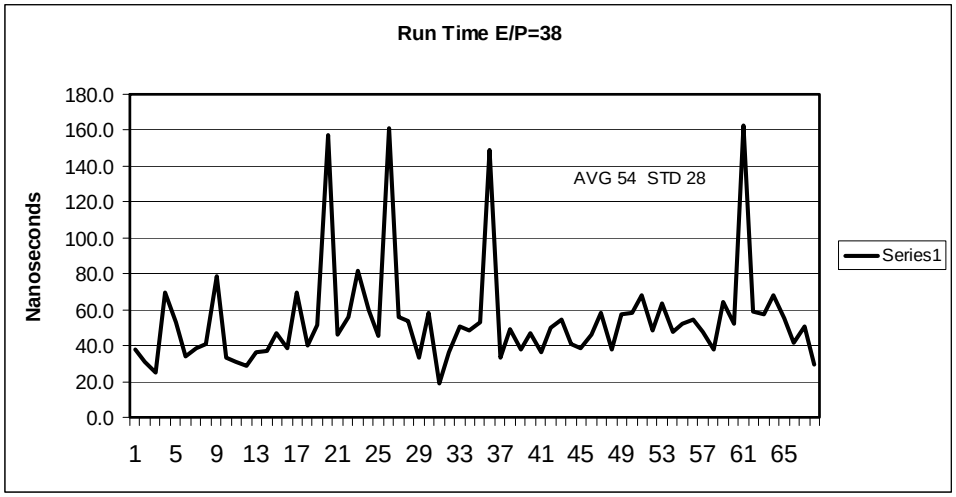

Figure H-30. Switch run time in nanoseconds plotted for each data point with E/P=38 kV/cm-bar in the Z_{20} shot sequence 800-1084. Prefires were removed from the data for this analysis.

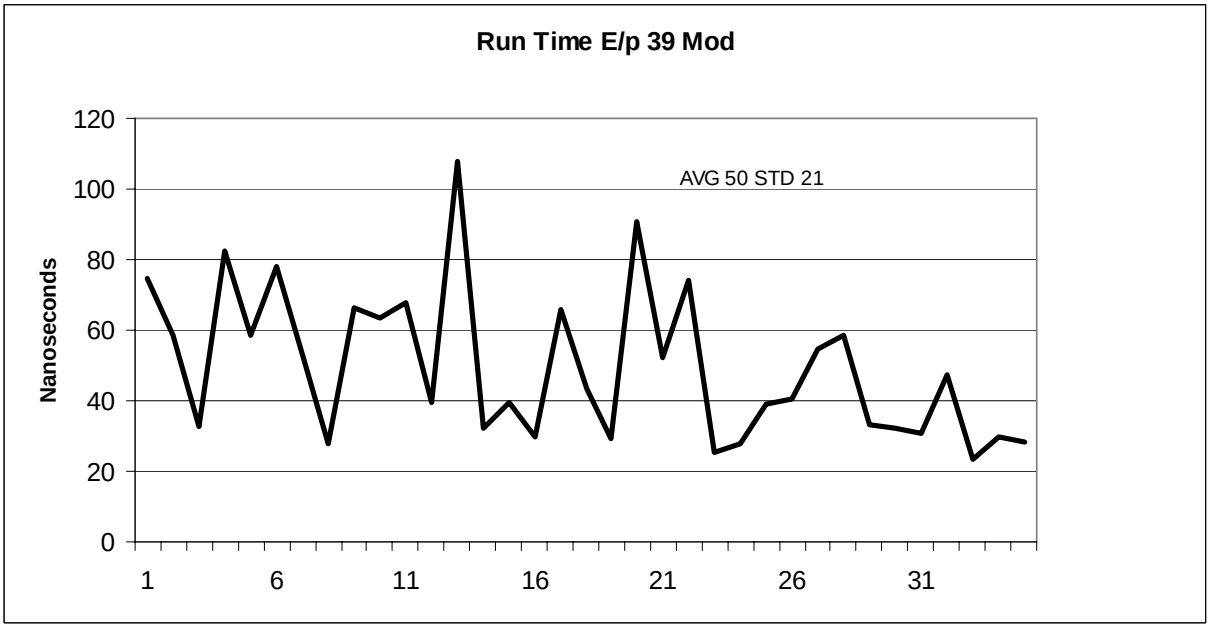

Figure H-31. Switch run time in nanoseconds plotted for each data point with E/P=39 kV/cm-bar in the Z_{20} shot sequence 800-1084. Prefires were removed from the data for this analysis.

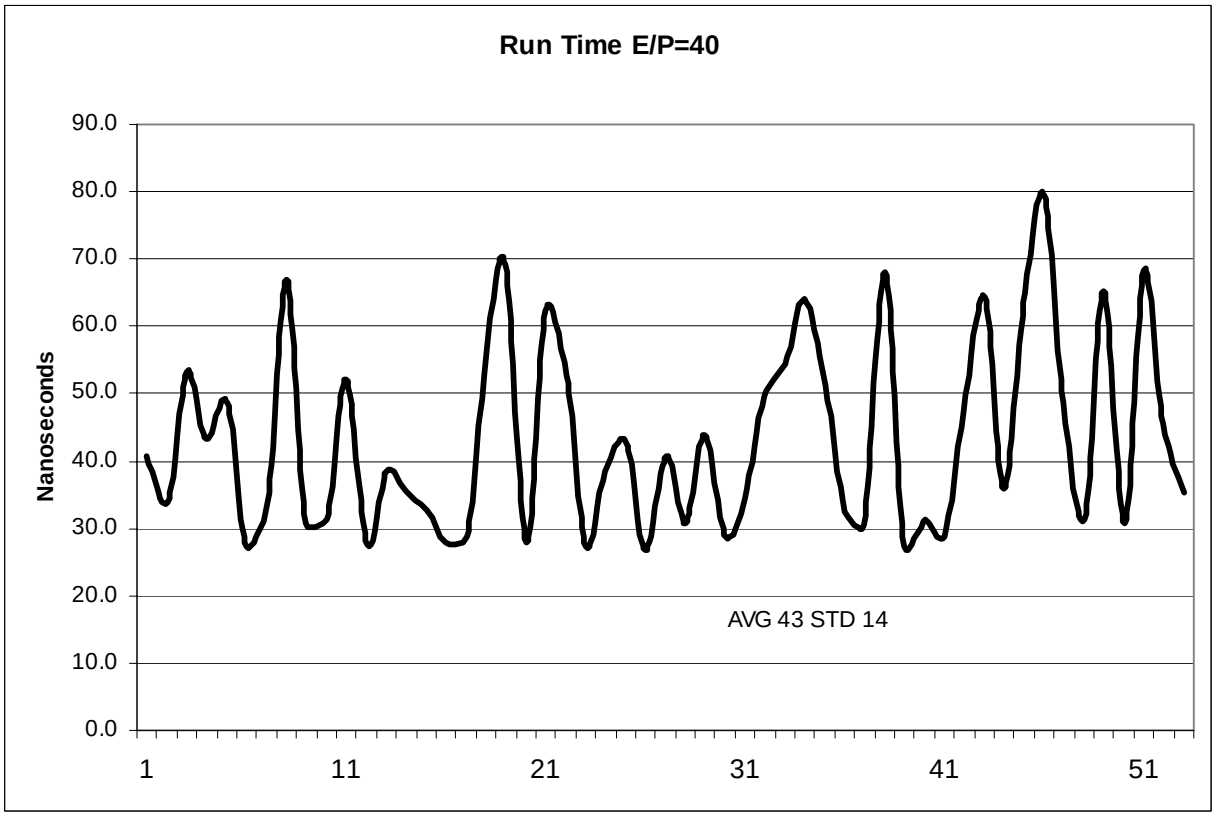

Figure H-32. Switch run time in nanoseconds plotted for each data point with E/P=40 in the Z_{20} shot sequence 800-1084. Prefires were removed from the data for this analysis.

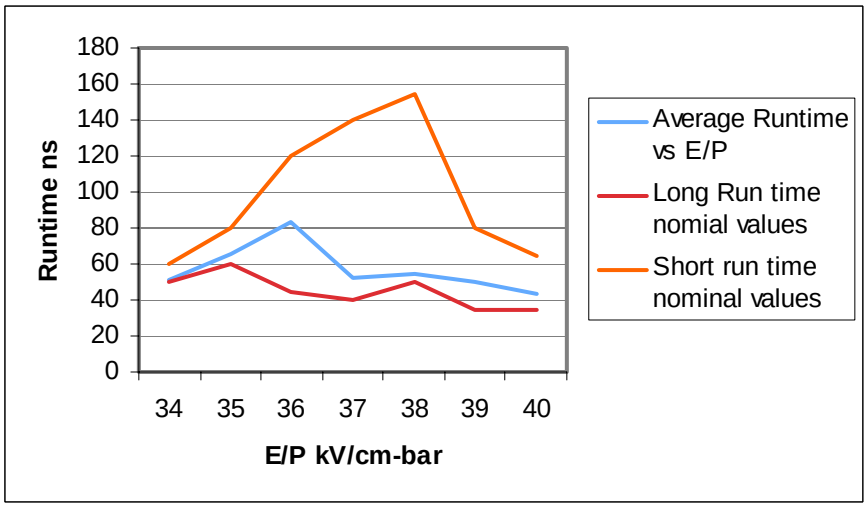

Figure H-33. Average Switch Run Time Versus E/P for Z_{20} Shot Sequence 800-1084. Estimated average values of the long run times and short run times for each E/P data set are also included. Prefires were removed from the data for this analysis.

As stated above and shown by these graphs, there seem to be two distinct modes of operation. If the two modes are due to laser creating conditions for the arc to start in the center of the gap for some of the shots and for the arc to start at the negative electrode for the rest of the shots, we can get an idea of the difference in run times for these two modes by comparing point plane scaling relationships for the two conditions. J.C. Martin, Dave Forester, and Phil Champney took SF_6 point plane breakdown data for various pressures and produced the scaling relationship and constants given in tables that are reproduced here from pages 137 and 138 of Reference 24.

Table 6a-II

Values of $k = Ft^{1/6}d^{1/10}$ for positive point or small sphere

	p absolute P.S.I	15	25	35
AIR	Point	24	33	37
	Small Sphere	20	28	33
FREON	Point	40	43	46
	Small Sphere	45	51	55
SF_6	Point	48	55	59
	Small Sphere	60	66	69

Table 6a-III

Values for k- for negative point and small sphere

	p absolute p.s.i	15	25	35
AIR	Point	25	38	49
	Small Sphere	17	-	28
FREON	Point	67	84	100
	Small Sphere	47	-	77
SF_6	Point	79	-	116
	Small Sphere	49	-	93

Figure H-34. Breakdown constants versus pressure for point plane and 2.5-cm-diameter sphere for equation in top graph.

In the experiments described in this note, d was varied from 2 to 15 cm and the effective time, t, was always in the range of 100-200 ns. In the equation at the top of the figure t is in microseconds, d in centimeters and F, the average electric field at breakdown, is in kV/cm. The $d^{0.1}$ was derived from the data. The $t^{1/6}$ was assumed from values found in previous experiments. In the data in the above E/P plots the pressure was between 46 psig (61 psia) and 60 psig (72 psia). Since k increases with pressure for the point plane SF_6 data, I assumed it increases as P^a and calculated a to be 0.2 for positive polarity and 0.8 for negative polarity. Using this procedure, I get k_+=67 and k_- to be 145. If I solve the equation in Figure H-34 for t, I get Equation H-3.

$$\mathbf{t = k^6 /(Fd^{0.1})^6} \qquad \text{(H-6)}$$

If I assume that the laser produces a 2-mm ionized point in the center of the trigger gap for mode A and a 2-mm gap at the far electrode for Mode B, I can use Equation H-6 to estimate differences in closure times of the trigger gap for the two modes. For mode A, F is 205 kV/cm and $d^{0.1}$ is 1.08, giving 222 for the term in the brackets. For positive polarity half of the gap, the closure time is $(66/222)^6$, which gives 0.7 ns. The negative half of the gap closure time is $(145/222)^6$, which gives 78 ns. This implies that for this mode the gap closes sequentially and all of the voltage appears across the negative gap after positive closes. In that case the negative closure time is $(145/444)^6$, which gives 1.2 ns. The total closure time for this mode is 2.0 ns. For closure times in Figure H-33, we have to add 20-30 ns for the all of the cascade gaps to close. This gives a total closure time for Mode A in the range of 25 ns to 35 ns. In Mode B we only have a streamer from an ionization region near the negative electrode. The field is still 205 kV/cm, $d^{0.1}$ is 1.16 for the 4.4 cm gap. The numerator in this case is 238. The closure time is $(145/238)^6$ which gives 51 ns. Adding the 20 ns to 30 ns cascade gap closure gives an estimated closure time of 71 to 81 ns.

The value of this exercise is to point out the impact of the SF_6 breakdown polarity effect as one possible explanation for the long run times if the laser does not start the arc in the same fashion each time. The calculated short run times are about a factor of two below those in Figure H-33. The 71 to 81 ns is reasonable agreement with the long run times shown in Figures H-26 to H-33. Slight changes in the negative constant can make significant differences in the estimated closure time. The laser ionization is not a needle, but the breakdown process could be similar if the desired focus is achieved. Data taken in the LTGS R&D Program should provide a more accurate way of estimating closure time versus various switching parameters.

Since the run times seemed to be independent of E/P, we evaluated how run time varied as a percent of average self-breakdown voltage. There is considerable spread in the higher-pressure self-breakdown voltage data, which means there is greater uncertainty in the actual self-breakdown voltage value at these pressures. Intentional self-breakdowns to generate data for a self-breakdown curve are only taken at pressure up to 40 psig. Figure H-35 is an Excel plot for all the data from all 285 shots. Since there is not an equal number of data points at each percent of self-breakdown voltage, there is a nonlinear scale and 83 and 85 appear twice on the scale. Figure H-36 gives the average value of run time versus percent of self-breakdown voltage and Figure H-37 gives the standard deviation at each percent of self-breakdown voltage. We know that for this data set there were at least three sequences of shots when the laser was providing a weak trigger. The statistics given in the next section infer that we will need to operate at 80% of the self-breakdown voltage to achieve the very low prefire rate required to meet the one prefire in 100 ZR shots. The standard deviation of the runtime for the data between 80 to 90% self-breakdown voltage is 2.5-2 times the allowable standard deviation to meet the ZR jitter specification of 4 ns. Above 90% of the self-breakdown voltage the jitter is below the specification but it is highly likely the prefire rate will be too high. This data needs to be repeated when the laser is providing a more effective trigger.

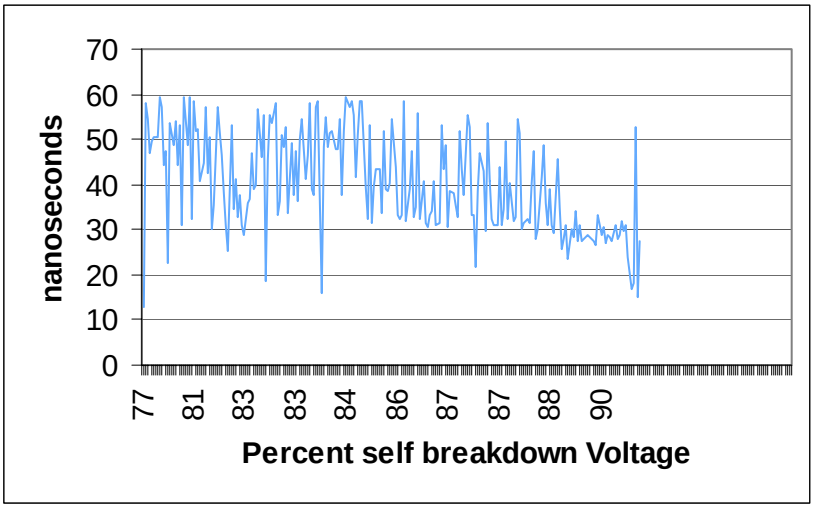

Figure H-35. Run time versus percent of the average self-breakdown voltage for Z_{20} shot sequence 800-1084 showing all data points at each percentage to indicate the spread in data. Prefires were removed from data. The x-axis is not linear because there is not equal number of data points at each value of percent of self-breakdown voltage.

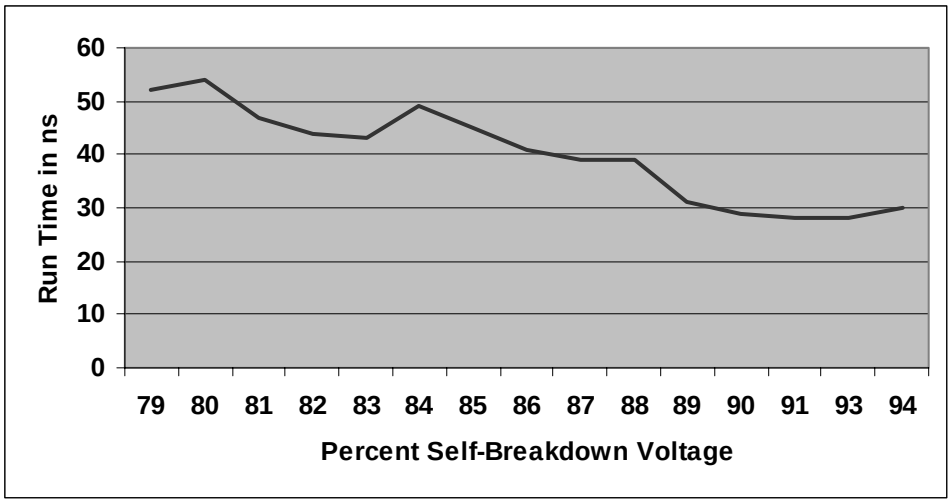

Figure H-36. Average run time versus percent of the average self-breakdown voltage for Z_{20} shot sequence 800-1084 showing all data points at each percentage point. Data shows expected trend of shorter run times for increased percentage of self-breakdown voltage.

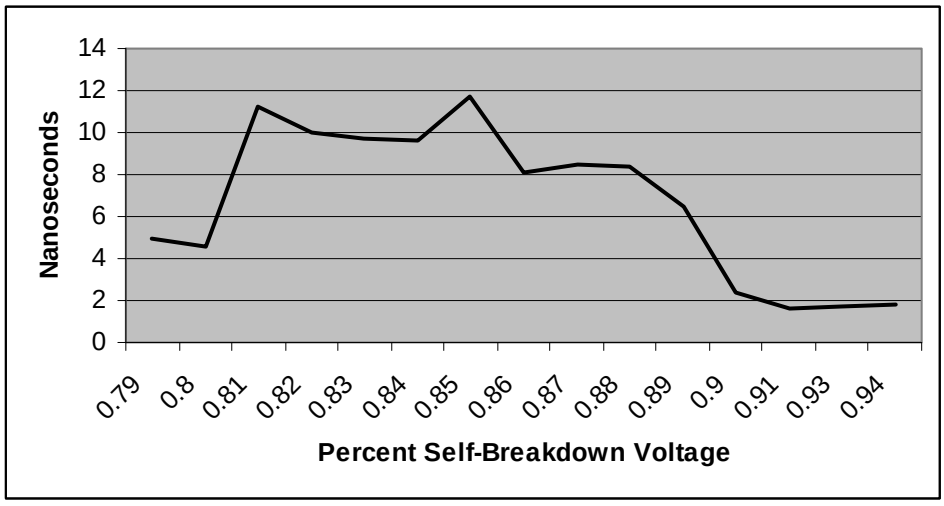

Figure H-37. Standard deviation of runtime as a function of percent of self-breakdown voltage.

H.4.5.3.3 Comparison of Turman-Humphreys and Nitta et al. Probability of Breakdown Formulas to STB Self-Breakdown Data

As stated above, the combination of prefires and switch housing flashovers should not occur more frequently than 1/3600 shots to meet the goal that pulsed power problems will cause less than 2% of the ZR shots. A further check was needed to see if the Turman-Humphreys' E/P scaling relationships[18] could be used to project the operation parameters needed to achieve this goal when the Z_{20} switch is reliable and reproducibility has been improved. To make this check, the original STB data is used due to the success of the first five switches tested on this facility. The STB log shows that there was a large number of intentional self-breakdown shots in that series. All of the self-breakdown shots (intentional and otherwise) were analyzed to see if the scaling

relationships predicted these breakdowns. There are 99 self-breakdown shots at 19 different pressures (bins) in the range of 3.5-36 psig with the data in each bin varying from one shot to 20 shots. Only one shot out of 11 in the five highest pressure bins was an intentional self-breakdown shot and the other possibly should have been recorded as lower-probability events than was used in this analysis.

If a bin has one self-breakdown shot, it has a greater than or equal to 50% probability of breakdown. If a bin has 20 shots and all broke down, the probability of breakdown is greater than or equal to 95%. I plotted these probabilities of breakdowns on Turman and Humphreys Figure 5, that is reproduced here as Figure H-38. The pink line is the STB data. This line is below the 50% probability of breakdown for all of the high-pressure data. From the data given in Figure 5 in Reference 1, Turman and Humphreys derived Equation H-1 in Reference 18 to predict the probability of breakdown on rimfire switches. This equation and Equation H-2 for E_o from Reference 18 are reproduced here as Equations H-7 and H-8. F is the probability of breakdown, A is the effective area, E and E_o are in kV/cm and P is in atmospheres. E_o is the projected breakdown strength for infinitely large area electrodes.

$$\mathbf{F = 1 - exp\left[- 2x10^{-18} A\left(\frac{E - E_0}{P} \right)^{10} \right]} \qquad \text{(H-7)}$$

$$\mathbf{E_0 = 62P - 3.5P^2} \qquad \text{(H-8)}$$

I set F = 0.5 in Equation H-1 and calculated a value for the term in brackets and did a similar calculation for F = 0.95. From these numbers, I determined that E/P- E_o/P should not vary more than 10% over the full pressure range of the STB self-breakdown voltage data range. I used the average breakdown voltage in each pressure bin to calculate an electric field, E, for that pressure. Using that data, I found that E/P- E_o/P continuously decreased as pressure is increased with the value 48 at 15.5 psia (3.5 psig) and 17 at 48 psia (36 psig) for a ratio from lowest pressure to highest pressure of 2.7. As stated above there is some question whether I should be using the five highest pressure bins. If I eliminate these bins, the ratio becomes 1.7. If these ratios hold after further analysis, we will not be able to use the above equations to predict probability of breakdown for ZR switches.

To compare the STB data to other spark gap data, I compared the average self-breakdown values of the STB data with the self-breakdown curve that Bill Tucker used when he developed a 3 MV trigatron for Hydra.[42] This is shown in Figure H-39. To match the 3.5 psig point, I needed to divide the STB value by four. The red dots are the STB self-breakdown voltage data divided by 4 and plotted at the appropriate pressures. Up to 25 psig, the STB data follow Tucker's curve. The five high-pressure data points that should be reevaluated fall below his curve. Tucker's curve is the average of three independent tests at pressures from 10 to 100 psig. The switch SF_6 was purged after each shot. The maximum spread in the data at any one pressure was 5%. The maximum current through the switch in these tests was 139 kA. The switch was submersed in oil.

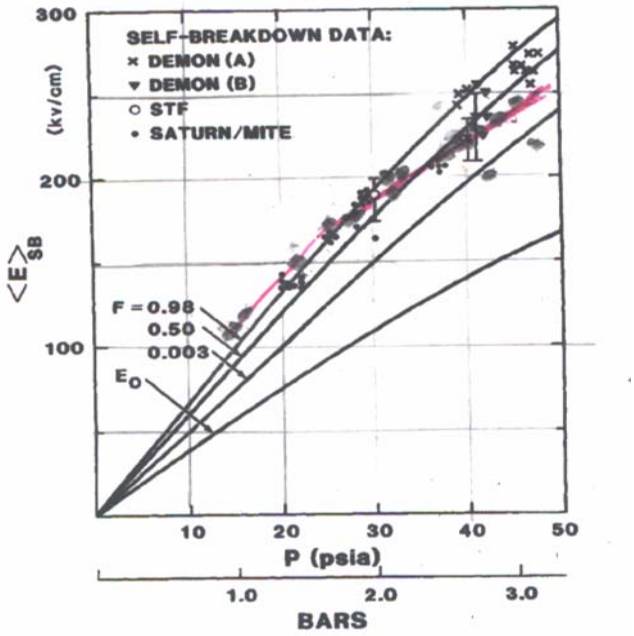

Fig. 5 Self-breakdown electric field as a function of pressure. Solid curves are predicted from Eq. (6). Data points were collected from Demon, STF, and MITE accelerators between 2.4 - 6 MV.

Figure H-38. Figure copied from Reference 18 with STB self-breakdown data superimposed as a pink line.

Since STB self-breakdown data has a similar slope to the Tucker data for pressures up to 27 psig, I looked for reasons that Turman-Humphreys' equations did not describe the STB data. They followed procedures outlined by Nitta et al. in References 19 and 22 published in 1971 and 1974 and Tom Martin's adoption of that technique to pulsed data in Reference 43. The form of Equation H-1 above comes from fundamental data on ionization and recombination taken by Bhalla and Craggs in Reference 44. In Reference 6 published 12 years later than Reference 19, Nitta et al. start by stating that the area effect infers a density of weak points as defined in Equation H-9.

$$N(E) = \lambda\left(\frac{E - E_o}{E_d}\right)^m \qquad \text{(H-9)}$$

where E_d is the breakdown strength if electrode effects are negligible and increases linearly with pressure (E_d = 89P with P in atmospheres). λ is a function of the surface roughness. In each of the three references by Nitta et al., they call λ a constant and then point out that it is a function of pressure. Turman and Humphreys recognized this, but by using the effective area treatment and a constant derived from Weibull plots of their data found a way to treat λ as a constant.

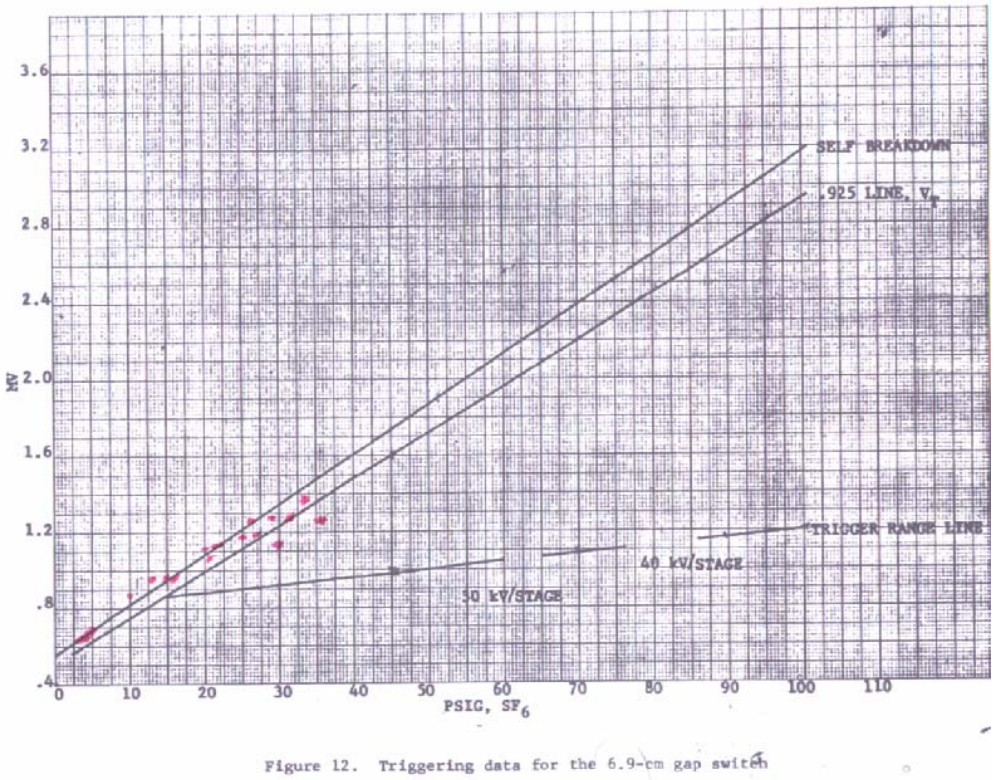

Figure H-39. SF_6 self-breakdown curve reproduced from W.K. Tucker, "3 MV Sulfur Hexafloride Trigatron," Sandia National Laboratories Report, SC-DR 72-056. Pink points are STB self-breakdown voltage data.

In Reference 7, Nitta et al. describe λ with Equation H-10.

$$\lambda = \lambda_o \circ e^{1.15P} \tag{H-10}$$

Values for λ_o for stainless steel are 0.4 for a highly polished surface and 12 for a carefully machined surface as used in gas insulated apparatus. If I set λ_o equal to 1, the value from Equation H-4 varies from 3.4 at 1.1 atm (3.5 psig in Albuquerque) to 42.7 at 3.27 atm (36 psig in Albuquerque). Adapting this change λ with the value a function of pressure to the 1.15 power as given in Equation H-10 eliminates the problem of the large change in difference of E/P-E_o/P described above.

Nitta et al. also have a different equation for E_o than the one derived by Tom Martin from Nitta et al. data. This equation is given in Equation H-11.

$$E_o = E_d / (1 + 0.355P^{0.7}) \tag{H-11}$$

Over our pressure range the values of E_o from Equation H-11 agree with those from Equation H-8 within 10%.

Nitta et al. develop a probability of breakdown expression given in Equation H-12 beginning with Equation H-9. Equation H-12 is similar to Equation H-7.

$$F(S,E) = 1 - \exp(-\lambda A(\frac{E - E_o}{E_d})^m) \quad \text{(H-12)}$$

Since E_d is 89P, this equation converts to the form of Equation H-7 if the constant is $\lambda A/(89^m)$. Nitta et al. found m = 7.4 rather than the 10 that Turman and Humphreys found from the Weibull plot of their cascade switch data. From Equation H-12, Nitta et al. calculated the most probable value of the self-breakdown electric field as a function of pressure to be Equation H-13.

$$E_m = E_o + E_d\left(\frac{m-1}{\lambda \cdot A \cdot m}\right)^{1/m} \quad \text{(H-13)}$$

If I set $\lambda_o A$ =120 and m = 7.4 and convert the electric field calculations to voltage with $5.5E_m/246$, I get good agreement with the STB data over the full pressure range as shown in Figure H-40 and in the values in Table H-12. This scaling is for the cascade section, which is inconsistent with the rest of this paragraph. If I use the peak field of the trigger section, $\lambda_o A$ will decrease. The pressure dependence should not change with either voltage scaling. If we assume the trigger section broke down first for this complete data section, A should be the trigger electrode area for which the electric field is greater than 90% of the peak value of the field. I estimate this area to be about 3 cm^2. This would imply that λ_o is 40. After a few breakdowns the ZR switch electrode surfaces are rougher than a carefully machined surface and sintered tungsten alloy is likely to have a rougher surface than stainless steel. Therefore 40 is a reasonable number for λ_o. (The value of λ_o for carefully machined aluminum is 100.)

The Weibull parameters for the data in Reference 6 indicate that the breakdown data can be described by normal distributions. Nitta et al. derived formulas for upper and lower bounds of the data by setting the probability of breakdown in Equation H-6 to 0.135% for the lower bound and 99.865% for the upper bound corresponding to the three sigma values of normal distributions. These equations are given in Equations H-14 and H-15 and are used to compare the upper and lower limits of the STB data at each pressure bin where there were three or more data points. The comparisons are given in Table H-12.

$$E_u = E_o + E_d \cdot \left(\frac{6.61}{\lambda \cdot A}\right)^{1/m} \quad \text{(H-14)}$$

$$E_L = E_o + E_d \cdot \left(\frac{0.00135}{\lambda \cdot A}\right)^{1/m} \quad \text{(H-15)}$$

In all three cases the agreement between measured and calculated values is excellent for the complete pressure range. For the calculated and average measured self-breakdown values, the

differences are less than 8% for all cases except two of the final four pressures. We would need much larger sets of data at each pressure to establish the three sigma points. Therefore the measured maximum voltage for each data set should be less than the three-sigma upper-value limit and our minimum value should be greater than the three-sigma lower-voltage limit. These conditions are true for all cases except the minimum value for 30 psig data. The 30 psig data points may be associated with an insulator flashover.

Using Equations H-10 through H-13 resolves the issues raised by attempts to fit our data to Equation H-7. It is rare to find a scaling relationship that describes spark gap breakdown as well as these equations. Determining the appropriate E for voltage scaling, λ_0 and the effective area for the LTGS electrodes will be needed to further evaluate this technique. Comparing Equation H-6 predictions to long runs without breakdowns will also be a next step in this evaluation.

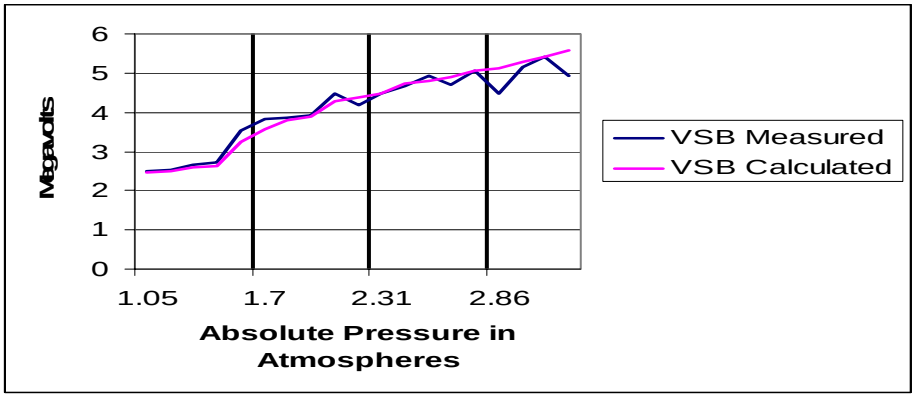

Figure H-40. Plots of STB self-breakdown voltage versus pressure. The calculations are the most probable value of breakdown voltage using Equation H-1.

Because of the uncertainty in the self-breakdown data due to not treating the high-pressure data as low probability of breakdown data, I created a Weibull plot for all of the STB data considered in this report. The data is plotted as probability of breakdown versus $(E-E_o)/P$ in Figure H-41. β is 7.8, which is similar to the Nitta et al. value of 7.4. The 90% confidence limits are shown as red lines. The ZR desired prefire rate is 1/3600, which equals 0.00028. The Y-axis in Figure H-41 is given in percent probability of breakdown. I located the point where the upper confidence limit intercepted 0.028% as $(E-E_o)/P=11.7$.

Setting $(E_{op}-E_0)/P$ equal to 11.7, we can solve for the operating electric fields and voltages for each value of pressure. These values are given in Table H-13 for the switch design tested in STB and in Table H-14 for the new switch criteria[43] where the goal is to have the peak electric field in the cascade section 220 kV/cm at 6.25 MV. The challenge for the LTGS Research Team in FY 2007 is to determine whether the low prefire rate and low probability of insulator tracking can actually be achieved at 80% of self-breakdown voltage and whether the 4 ns standard deviation of the run time can be achieved at this same $(E_{op}-E_0)/P$ level.

Table H-12. Comparison of original STB data average self-breakdown voltage, minimum and maximum breakdown voltages at each pressure with the calculated most probable breakdown voltage, and the three-sigma minimum and maximum values from Equations H-11 though H-15.

PSIG	P-ATM	Data Points	VSB Average Measured	VSB Calculated	Vmin Measured	Vmin Calculated	Vmax Measured	Vmax Calculated
3.5	1.05	3	2.51	2.45	2.26	1.92	2.65	2.74
4.0	1.09	3	2.53	2.51	2.49	1.97	2.58	2.81
4.5	1.12	2	2.65	2.58	2.64	2.01	2.66	2.88
5.0	1.16	9	2.73	2.64	2.67	2.06	2.81	2.95
10.0	1.50	2	3.53	3.24	3.52	2.53	3.53	3.62
13.0	1.70	3	3.84	3.57	3.81	2.79	3.9	3.99
15.0	1.84	3	3.87	3.78	3.82	2.96	3.91	4.22
16.0	1.90	18	3.93	3.88	3.74	3.04	4.11	4.34
20	2.18	3	4.49	4.27	4.39	3.35	4.66	4.77
21	2.24	5	4.2	4.37	3.7	3.42	4.53	4.88
22	2.31	5	4.49	4.46	4.09	3.50	4.63	4.98
25	2.52	12	4.66	4.72	3.68	3.71	5.06	5.28
26	2.59	1	4.92	4.81		3.78		5.37
27	2.65	20	4.7	4.9	3.90	3.85	5.27	5.46
29	2.79	2	5.05	5.06	4.80	3.98	5.29	5.64
30	2.86	2	4.49	5.14	4.38	4.05	4.6	5.73
32	2.99	1	5.15	5.30		4.18		5.90
33.5	3.10	1	5.43	5.41		4.27		6.03
36	3.27	4	4.93	5.59	4.35	4.42	5.46	6.23

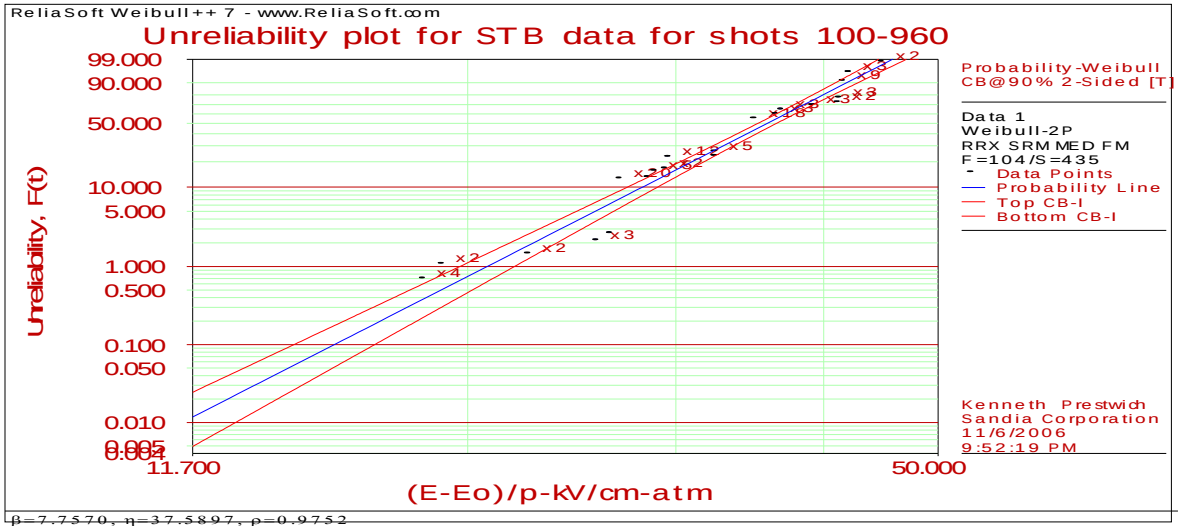

Figure H-41. Weibull probability of prefire plot as a function of $(E_{op}-E_0)/P$ for the original STB data. The data for this plots includes intentional self-breakdown data and data for successful LTGS tests.

Table H-13. Operating electric field and voltage from $(E_{op}-E_0)/P=11.7$, the value from Figure H-41 for 1:3600 prefires.

PSIG	E_{OP}	V_{OP}	E_{SB}	V_{SB}	V_{OP}/V_{SB}
40	210	4.7	263	5.9	0.80
45	225	5.0	277	6.2	0.81
50	239	5.4	290	6.5	0.82
55	253	5.7	303	6.8	0.83
60	267	6.0	314	7.0	0.85

Table H-14. Operating voltages for $(E_{op}-E_0)/P=11.7$ for new switch criteria with peak cascade electric field 220 kV/cm at 6.25 MV.

PSIG	E_{OP}	V_{OP}	E_{SB}	V_{SB}	V_{OP}/V_{SB}
40	210	6.0	263	7.5	0.80
45	225	6.4	277	7.9	0.81
50	239	6.8	290	8.2	0.82

H.5 References

1. K.W. Struve, J.P. Corley, D.L. Johnson, H.C. Harjes, D.H. McDaniel, R.W. Shoup, D.L. Smith, W.A. Stygar, and E.A. Weinbrecht, Design Options for a Pulsed-Power Upgrade of the Z Accelerator, *Proceedings of the 13th IEEE International Pulsed Power Conference*, Las Vegas, NV, 2001, p. 440.

2. E.A. Weinbrecht, D.H. McDaniel, and D.D. Bloomquist, The Z Refurbishment Project (ZR) at Sandia National Laboratories, Digest of Technical Papers, *14th IEEE International Pulsed Power Conference*, Dallas, Texas, June 15-18, 2003, p. 157.

3. J. Maenchen, D. Bliss, J. Corley, J. Elizando, K. Hodges, D.L. Johnson, S. Kovaleski, K. LeChien, J. Lehr, S. MacGregor, D. McDaniel, R. McKee, A.R. Miller, A. Neuber, T. Poiton, K. Prestwich, M. Savage, K. Struve, J. Van den Avyle, P. Wakeland, L. Warne, and J. Woodworth, Pulsed Power Technology Development for ZR, *2006 International Conference on High Power Beams*.

4. J.P. Corley, K.C. Hodge, S.A. Drennan, D.W. Guthrie, J.M. Navarro, D.L. Johnson, J.M. Lehr, S.E. Rosenthal, and J.M. Elizondo, Development/Tests of 6-Mv Triggered Gas Switches at SNL, *Proceedings of the 14th IEEE International Pulsed Power Conference*, Dallas, Texas, 2003, pp. 875-878.

5. J.P. Corley, M.A. Dixon, A.A. Kim, B.M. Kovalchuk, V.A. Sinebryukhov, S.N. Volkov, K.C. Hodge, S.A. Drennan, J.M. Navarro, D.L. Johnson, G. Avrillaud, and F. Lassalle, Tests of 6-MV Triggered Switches on APPRM at SNL, *Proceedings of the 13th IEEE International Pulsed Power Conference*, Las Vegas, Nevada, June 2001, pp. 1778-1781.

6. T. Nitta, Y. Fujiwara, F. Endo, and J. Ozawa, Effects of Electrode and Solid Insulator on the Flashover in Compressed SF_6, *CIGRE*, Paris, France, 1986, Paper 15.04.

7. William White and John Porter, Private Communications, Sandia National Laboratories, April 13, 2006.

8. R.A. Eilbert and W.H. Lupton, *Extrapolation of AWRE Breakdown Data*, Naval Research Laboratory, Washington, D.C., Unpublished Report.

9. I.D. Smith, *Impulse Breakdown of Deionized Water*, SSWA/JCM/6511/B, ULAEA, Atomic Weapons Research Establishment, Aldermaston, England, November 1965.

10. K.E. Neilsen, H.A. Davis, E.O. Ballard, J.M. Elizondo, R.F. Gribble, B. T. McCuistian, and W.M. Parsons, Atlas Transmission Line Breakdown Analysis, *Proceedings of the 12th IEEE International Pulsed Power Conference*, Monterey, California, June 27-30, 1999, pp. 381-384.

11. J.M. Elizondo, D.L. Johnson, D. McDaniel, K. Struve, J. Maenchen, J. Corley, L. Bennett, and H. Ives, ZR Technical Note #17, *ZR Intermediate Store Probability of Failure Calculations*, Unpublished data, Sandia National Laboratories, May 2002.

12. J.M. Elizondo, H. Ives, L. Bennett, J. Corley, K. Struve, and D.L. Johnson, ZR Technical Note #26, *ZR PFL Electric Field Distribution and their Probability of Failure*, Unpublished Data, Sandia National Laboratories, February 2003.

13. J.M. Elizondo and L. Bennett, ZR Tech Note #36, *Simplified PFL Design with Improved Reliability*, Unpublished data, Sandia National Laboratories, October 2003.

14. Mark Savage, Private Communications, Sandia National Laboratories, July 2006.

15. J.E. Gilbert and J.B. Ennis, *Reliability and Lifetime for High-Energy-Density Capacitors*, Maxwell Laboratories Report MLR-3732, March 1991.

16. W. Hauschild and W. Mosch, *Statistical Techniques for High-Voltage Engineering*, Peter Peregrinus Ltd., London, United Kingdom, 1992.

17. Life Data Analysis Reference, ReliaSoft Corporation, Tucson, Arizona, 1997.

18. B.N. Turman and D.H. Humphreys, Scaling Relationships for the Rimfire Multi-Stage Gas Switches, *Proceedings of the 6th International Pulsed Power Conference*, 1987, pp. 347-353.

19. T. Nitta, N. Yamada, and Y. Fujiwara, Area Effect of Electrical Breakdown in Compressed SF_6, *IEEE Transaction of Power Apparatus and Systems*, PAS-93, pp. 623, 1974.

20. Dave Bliss, Joe Woodworth, and Keith Hodges, Private Communications, Sandia National Laboratories, August 2006.

21. D.J. Anderson and D. Briand, ZR Reliability and Operation Analysis, *Digest of Technical Papers, 14th IEEE International Pulsed Power Conference*, Dallas, Texas, June 15-18, 2003, p. 157.

22. D. Briand and D.J. Anderson, *Z/ZR Reliability and Operations Timeline Analysis*, Sandia National Laboratories Report, October 31, 2003.

23. T. Nitta and Y. Shibuya, Electrical Breakdown of Long Gaps in Sulfur Hexafluoride, *IEEE Trans. of Power Apparatus and Systems*, PAS-90, No. 3, p. 1065, 1971.

24. *J.C. Martin on Pulsed Power*, Plenum Press, New York, 1996, Edited by T.H. Martin, A.H. Guenther, and M. Kristiansen.

25. Chuck Harjes, Private Communications, Sandia National Laboratories, May 2006.

26. D.L. Johnson Private Communications, Sandia National Laboratories, 1985.

27. B.N. Turman, W.B.S. Moore, J.F. Seamen, F. Morgan, J. Penn, and D.R. Humphreys, Development Tests of a 6 MV, Multistage Gas Switch For PBFA II, *Proceedings of the 4th International Pulsed Power Conference*, Albuquerque, NM, 1983, pp. 617 - 619.

28. D.R. Humphreys, K.J. Penn, J.S. Cap, R.G. Adams, J.F. Seamen, and B.N. Turman, RIMFIRE: A Six Megavolt Laser-Triggered Gas-Filled Switch for PBFA II, *Proceedings of the 5th International Pulsed Power Conference*, 1985, pp. 262-265.

29. D.D. Bloomquist, G.R. Montry, S.E. Downie, and G.R. Peterson, Cascade Switch Implementation on PBFA I, *Proceedings of the 5th International Pulsed Power Conference*, 1985, pp. 266-269.

30. J.M. Wilson and G.L. Donovan, Laser-Triggered Gas Switch Improvements on PBFA-II, *Proceedings of the 6th International Pulsed Power Conference*, 1987, pp. 361-364.

31. G.J. Denison, J.P. Corley, D. L. Johnson, G.J. Weber, R.A. Hamil, G.W. Crowder, J.A. Alexander, D.A. etmecky, L.P. Schanwald, and J.J. Ramirez, A High-Voltage Multistage Laser-Triggered Gas Switch, *Proceedings of the 6th International Pulsed Power Conference*, 1987, pp. 490-493.

32. B.N. Turman and D.R. Humphreys, Interstage Closure Times for the Rimfire Multistage Gas Switch, *Proceedings of the 7th International Pulsed Power Conference*, Monterey, CA, 1989, pp. 555 - 558.

33. G.J. Denison, J.A. Alexander, J.P. Corley, D.L. Johnson, K.C. Hodge, M.M. Manzanares, G. Weber, R.A. Hamil, L.P. Schanwald, and J.J. Ramirez, Performance Of The HERMES-111 Laser-Triggered Gas Switches, *Proceedings of the 7th International Pulsed Power Conference*, Monterey, CA, 1989, pp. 579-582.

34. R.G. Adams, W.B. Moore, J.R. Woodworth, M.M. Dillon, F. Morgan, and K.J. Penn, *Proceedings of the 4th IEEE Pulsed Power Conference*, 1983, pp. 613-616.

35. T.H. Martin, B.N. Turman, S.A. Goldstein, J.M. Wilson, D.L. Cook, D.H. McDaniel, E.L. Burgess, G.E. Rochau, E.L. Neau, and D.R. Humphreys, PBFA II, The Pulsed Power Characterization Phase, *Proceedings of the 6th International Pulsed Power Conference*, 1987, pp. 294-299.

36. R.B. Spielman et al., PBFAZ: A 60 TW/5MJ Z-pinch Driver, *Proceedings of the 4th International Conference on Dense Z-pinches*, AIP Conf. Proc. #409, 1997, p. 101.

37. Relia Software Company, Tucson, Arizona

38. John Porter Private Communications, Sandia National Laboratories, March 2006.

39. Rosenthal, Private Communications, Sandia National Laboratories, March 2006.

40. Keith LeChien, Dave Bliss, Joe Woodworth, and Keith Hodges Private Communications, Sandia National Laboratories, October 2006.

41. Mark Savage, Private Communications, Sandia National Laboratories, June 2006.

42. W.K. Tucker, *A 3-Megavolt Sulphur Hexafluoride Trigatron*, Sandia National Laboratories Development Report SC-DR-72-0506, September 1972.

43. T.H. Martin, Pulsed Charged Gas Breakdown, *Proceedings of the 5th International Pulsed Power Conference*, 1985, pp. 74-83.

44. M.S. Bhalla and J.D. Craggs, Measurement of Ionization and Attachments Coefficients in Sulphur Hexafluoride in Uniform Fields, *Proc. Phys. Soc.*, Vol. 80, 1961, p.151.

Appendix H1

Table H.1-1. Potential ZR module faults modes and record of observance in the first 1084 shots on Z_{20}. All faults were listed even if more than one occurred on a single shot. Some intentional prefires of LTGS may have been included in this summary.

	Possible Module Fault Modes	**Shots**	**Number of Times That the Fault Occurred in the 1184 Shots**	**Frequency of Observance on Z_{20} Percent**	**Consequence**	**ZR Current-MA**	**Maintenance**
	Energy Storage System						
1	Marx Generator Prefire	1184	10	0.84	Diverter takes energy-one module with nothing down line.	25.3	Nothing first time-replace Marx generator second time.
2	Charge Resistor Track	1184	3	0.25	Usually operation ok-worst case ISC voltage drops and LTGS has long delay	26-25.3	Replace Marx
3	Interstage Resistor Tracks	1184	1	0.08	Usually operation ok-worst case ISC voltage drops and LTGS has long delay	26-25.4	Replace Marx
4	Trigger Resistor Tracks or acrs to capacitor causing failures in trigger generator	1184	1	0.08	Usually operation ok-worst case ISC voltage drops and LTGS has long delay	26-25.5	Replace Marx and rebuild trigger generator
5	Arc through Marx Generator Gas Lines	1184	2	0.17	Usually operation ok-worst case ISC voltage drops and LTGS has long delay	26-25.6	Replace Marx
6	Marx Charge Cables shorted with arc	1184	?	Y	Shot probably ok-Delay of next shot	26	Replace cable
7	Marx Generator automatic shorting support track	1184	1	0.08	Usually operation ok-worst case ISC voltage drops and LTGS has long delay	26.0-25.6	Replace support or Marx generator
8	Marx Generator trigger rod support track	1184	?	Y	Usually operation ok-worst case ISC voltage drops and LTGS has long delay		Replace support or Marx generator

	Possible Module Fault Modes	Shots	Number of Times That the Fault Occurred in the 1184 Shots	Frequency of Observance on Z_{20} Percent	Consequence	ZR Current-MA	Maintenance
9	Marx Capacitor Failure	1184	1	0.08	loss of shot		Replace Marx generator
10	Marx spark gap failure	1184	2	0.17	Prefire-loss of shot		Replace Marx generator
11	Marx Capacitor Charge Voltage uncertainty 2 kV of 94 kV	1184	all	Y	Could impact run time of switch increasing jitter	26	Improve instrumentation
12	Trigger Generator Prefire	1174	26	2.21	Same as 1	25.3	Rebuild trigger generator
13	Trigger Generator No Fire	1184	18	1.52	Loss of Module	25.3	Repair trigger and control circuitry
14	MTG charge cable arc	1184	3	0.25			
15	MTG Capacitors and support failure	1184	1	0.08			
16	Diverter support track	1027	5	0.49	Loss of Module	25.3	Rebuild diverter
17	diverter closes early	1027	87	8.47	Loss of Module if >30 ns before laser arrival. Otherwise ok	25.3-26	Adjust setting on Diverter electrodes
18	diverter closes late	1027	56	5.45	Loss of Marx protection	26	Adjust setting on Diverter electrodes
19	diverter does not close	1027	272	26.48	Loss of Marx protection	26	Adjust setting on Diverter electrodes
20	diverter clamp switch does not open	1094	4	0.37	Delay shot		Rebuild diverter
21	diverter green light not on	1094	6	0.55	Delay shot		Improve diverter control circuitry
22	ISC water arcs	1073	1	0.09	Worst Case LTGS does not close-Loss of module Best case late in time and all energy down line	25.3-26	Rebuild or Replace ISC?

	Possible Module Fault Modes	Shots	Number of Times That the Fault Occurred in the 1184 Shots	Frequency of Observance on Z_{20} Percent	Consequence	ZR Current-MA	Maintenance
23	ISC Barrier Track	1073	0	0.00	Worst Case LTGS does not close-Loss of module Best case late in time and all energy down line	25.3-26	Rebuilt or Replace ISC?
24	LTGS Prefire	1073	33	3.08	<20 ns before laser negligible impact on output >100 ns before laser loss of module	25.3-26	Replace Switch after second prefire
25	LTGS trigger housing flash	1073	38	3.54	shot usually ok	26	Replace Switch if detected optically or if track marks seen by diver
26	LTGS Cascade housing flash	1073	24	2.24	<20 ns before laser negligible impact on output >100 ns before laser loss of module	25.3-26	Replace Switch if detected electrically or optically or if track marks seen by diver
27	LTGS Cascade pucks tracked	1073	3	0.28			
28	LTGS oil leak	1073	2	0.19			
29	LTGS gas line failure	1073	3	0.28			
30	LTGS long run time	1073	33	3.08	<closure 20 ns after nominal closure time negligible impact on output >100 ns after nominal closure time loss of module	25.3-26	Check laser alignment and optics
31	LTGS no fire	1073	attributed all to laser system	Y	loss of module	25.3	Check laser alignment and optics
32	Laser failure	1073	42	3.91	loss of module	25.3	Replace Laser
33	Laser Early	1073	3	0.28			
34	Oil leak in laser feedthru tube	1073	2	0.19	Loss of Module if missed by divers and if reduced laser energy causes closure time >30 ns longer than nominal closure time. Otherwise ok.	25.3-26	Replace feed thru tube and optics

	Possible Module Fault Modes	Shots	Number of Times That the Fault Occurred in the 1184 Shots	Frequency of Observance on Z_{20} Percent	Consequence	ZR Current-MA	Maintenance
35	Flashover of laser feedthru tube orig. Design	529	12	2.27			
36	Flashover of laser feed thru tube-New Design	544	3	0.55	Loss of Module if missed by divers and if reduced laser energy causes closure time >30 ns longer than nominal closure time. Otherwise ok.	25.3-26	Replace feed thru tube and optics
37	PFL barrier or rod track original design	529	0	0.00			
38	PFL barrier or rod track-Value Engineering design	544	5	0.92	Loss of Module if track occurs >30 ns before water switch closure. Otherwise ok	25.3-26	Replace barrier or PFL
39	PFL Water arcs original design	529	?	?			
40	PFL water arcs-value engr design	544	?	?	Loss of Module if arc occurs >30 ns before water switch closure. Otherwise ok	25.3-26	Inspect and remove if necessary
41	Water switch early fire	1073	1	0.09	Increase jitter small reduction in output current	~26	Check and possibly replace switch electrodes
42	One or two water switch no fire	1073	?	?	Slight reduction in module current	~26	Check and possibly replace switch electrodes
43	Line 1 support rod track	954	?	?	Reduction in module current	~26	Replace support rod
44	Prepulse switch close early	954	1	0.10	Increase prepulse amplitude	26	Tighten or replace switch electrodes
45	Line 2 support rod track	954	?	?	Reduction in module current	~26	Replace support rod
46	Water convolute arc			Not tested on ZR	Reduction in total current-needs circuit code analysis	?	Repair arc damage

	Possible Module Fault Modes	Shots	Number of Times That the Fault Occurred in the 1184 Shots	Frequency of Observance on Z_{20} Percent	Consequence	ZR Current-MA	Maintenance
47	Vacuum Insulator flashover during pulse			Model tests and Saturn tests	Reduction in total current-needs circuit code analysis	?	Repair arc damage

Table H.1-2. Analysis of impact of Z_{20} failure modes on ZR operations.

Start	End	Num-ber of Prob-lems	Number of shots with failures that should not impact ZR- within 20 ns of shot	Number of shots with question-able impact-module within ±20-40 ns of shot	Number of shots in which the module energy is supplied >40 ns be-fore shot	Number of shots with failures that would delay ZR shot	Number of shots with failures that would cause a loss of that module en-ergy for a ZR shot	
1	30	5			2	3		
31	60	3	1		2			
61	90	1				1		
91	120	7		2	1	4		
121	150	2		1		1		
151	162	2			1	1		
162	180	4	1		2	1		
181	210	12	4	2	1	2	3	
211	240	10				5	5	
241	270	7	3	2			2	
271	300	10	2	2		2	4	
301	330	8	3		3	1	1	
331	360	5	1		2	1	1	
361	390	8	1	1	1	3	1	
391	420	11	3	1	5		2	
421	450	6	2		2		2	
451	480	2	1			1		
481	510	4	1	1		1	1	
511	540	6	2		1	1	2	
541	570	5	1	1	2	1	1	
571	600	5	2		2		1	
601	619	7	5				2	
620	630	2	2					
631	660	3	1		1		1	
661	690	7	5		1		1	
691	720	15		1	5	8	1	
721	750	6	2		2		2	
751	780	12	3		6		3	
781	810	12			3	3	6	
811	840	9	1		4	1	3	
841	870	12	1		5	2	4	
871	900	8	4	1	2		1	
901	930	12	1	1	2	4	4	
931	960	15	1	1	1	8	4	
961	990	15	4	1	2	6	2	
991	1020	3	3					
1021	1050	10	6		3	1		
1051	1080	10	6	1	1	1	1	
1081	1110	6	1			5		
1111	1140	5	1			2	2	
1141	1170	1					1	

Start	End	Number of Problems	Number of shots with failures that should not impact ZR- within 20 ns of shot	Number of shots with questionable impact-module within ±20-40 ns of shot	Number of shots in which the module energy is supplied >40 ns before shot	Number of shots with failures that would delay ZR shot	Number of shots with failures that would cause a loss of that module energy for a ZR shot	
1171	1183	4	2		2			
Total	1184	297	77	19	67	70	64	297
Percent		25	26	6	23	24	22	100

Table H.1-3. Record of Z_{20} successful shots and problems summarized in 30-shot increments.

Start	End	Number of shot without prob-lems that ef-fect shot or out-put	Percent-age of shots without problems	Number of shots with problems in the Energy Storage subsys-tem	Num-ber of shots on which the di-verter closed early	Number of shots on with diverter electrical or me-chanical problems	Number of shots on which there were prob-lems with the LTGS	Number of shots on which there were prob-lems with the laser	Number of shots on which other prob-lems oc-curred	No. of shots with faults
1	30	25	83	3	0			2		5
31	60	27	90				1	2		3
61	90	29	97	1						1
91	120	23	73	2		2	3			7
121	150	28	93	1			1			2
151	162	10	87	2						2
162	180	15	79	1			1	2		4
181	210	15	50	2				13		15
211	240	18	60	4				8		12
241	270	23	77				5	2		7
271	300	22	73	3	1		2	2		8
301	330	22	73				8			8
331	360	25	83	1			4			5
361	390	25	83	3			1	1		5
391	420	19	63				11			11
421	450	22	67	1			4	3		8
451	480	28	93	1				1		2
481	510	26	87	1			1	2		4
511	540	25	83				3	2		5
541	570	25	83	1	1		3			5
571	600	25	83				4	1		5
601	619	12	63				7			7
620	630	10	73					1		1
631	660	27	90	1			1	1		3
661	690	20	67		2		3	4	1	10
691	720	8	27		18		1	3	1	22
721	750	18	27		7	1	4			12
751	780	12	40		8		6	2	2	18
781	810	10	33	1	15	1	3		2	20
811	840	17	57	2	2		5	4	1	13
841	870	12	40	1	10	1	4	2		18
871	900	23	77		1		4	2		7
901	930	15	50	5		3	6	1		15
931	960	13	43	9			6	4		17
961	990	15	50	8		1	5	4		15
991	1020	24	80	1	3		1	1		6
1021	1050	15	50	1	8		7			15
1051	1080	19	63	1	5	1	3		1	11

Start	End	Number of shot without prob-lems that ef-fect shot or out-put	Percent-age of shots without problems	Number of shots with problems in the Energy Storage subsys-tem	Num-ber of shots on which the di-verter closed early	Number of shots on with diverter electrical or me-chanical problems	Number of shots on which there were prob-lems with the LTGS	Number of shots on which there were prob-lems with the laser	Number of shots on which other prob-lems oc-curred	No. of shots with faults
1081	1110	22	73	5		3				8
1111	1140	25	83	3			1	1		5
1141	1170	29	97					1		1
1171	1183	7	54	1	2		2		1	6
Total	1184	830	70	66	83	13	121	72	9	354
Percent				5.57	7.01	1.10	10.22	6.08	0.76	30

Table H.1-4. Tabulation of Z_{20} LTGS failures for Shots 199 to 1111. Each line is data on a particular switch assembly. After removal, switches were rebuilt and tested again. Each rebuilt switch has a separate line in this chart.

Switch	1st shot	1st failure	last failure	Number of pulses to 1st failure	Total Number of Pulses	Switch Failures	Number trigger housing flashes	Number of cascade housing flashes	Number of times switch SB without housing flash	Number of switch run times >60 ns	Other Issues
1	199	201	208	3	10	3		3			199-204 self-break shots, 0il in switch just prior to this sequence
2	209	256	305	48	97	9	7	2			209-220 sys-tem problems
3	306	312	312	7	7	1		1			May have been 7 cascade housing flash-overs. These were self-break shots.
4	313	333	347	21	35	2	1	1			
5	348	351	351	4	4	1		1			
6	352	390	393	39	42	4	4				
7	394	397	397	4	4	1		1			one hockey puck flashed-S
8	398	399	420	2	23	3	2	1			
9	421	449	449	29	29	0					one hockey puck flashed, curved back-bone-S
10	450	537	537	88	88	1		1			
11	538	544	544	7	7	0					Switch had not failed replace with modified switch-S
12	545	576	613	32	69	4	3	1			
13	614	615	619	2	6	5	5				
14	620	671	671	52	52	5		1	2	2	
15	672	704	704	33	33	2	1		0	1	
16	705	752	752	48	48	7			6	1	ISC arc shot before first failure
17	753	771	811	19	59	9	3		6	0	Switch had not failed replace with modified switch
18	812	832	832	21	21	3		1	1	1	didn't trigger right
19	854	866	866	13	13	4			1	3	oil in switch
20	867	880	882	14	16	3		2		1	
21	883	884	934	2	52	19	4	1	5	9	
22	935	959	959	25	25	6	1		2	3	

Switch	1st shot	1st failure	last failure	Number of pulses to 1st failure	Total Number of Pulses	Switch Failures	Number trigger housing flashes	Number of cascade housing flashes	Number of times switch SB without housing flash	Number of switch run times >60 ns	Other Issues
23	960	961	1003	2	44	23	4	2	10	7	oil on optics
24	1004	1016	1030	13	27	7	1	5	0	1	
25	1031	1038	1069	8	39	5	4		0	1	
26	1070	1070	1070	1	1	1		1			Rexolite triggering housing-remachined cascade housing
27	1071	1111	1111	39	39	1		1	17		Same Rexolite housing-1082 and 1108 were not fired
Total				533	840	127	40	26	33	30	
				21	37	5.1	1.6	1.0	1.3	1.2	

Table H.1-5. Comparison of flashover voltage to the maximum voltage applied to the switch for each switch tested in the Z_{20} shots sequence 199-1111. The number of shots between the occurrence of the maximum voltage shot and the flashover shots is given.

	Sequence	Number of shots	Flashover Voltage MV	Peak Voltage in Sequence	Number of shots between peak voltage and flashover	Comments
1	199-208	10	4.8,4.5,4.3	5.1	2,8,10	Intentional SB shots first 7@26pisg, 208@30psig
2	209-305	95	5.4	6.8	16	
3	306-312	7	5.4	5.6	2	all>4.7
4	313-347	35	5.5	5.5		oil side track, four 5.5 MV in row
5	348-351	4	4.8	5.4	4	
6	352-393	42	4.7	6.0	15	Many in 5.3 MV RANGE
7	394-397	6	5.4	5.4		
8	398-420	20	5.0	5.0		
9	421-449	37	5.0	5.7	33	Most shots lower than 5.0 MV
10a	450-526	66	5.0	5.8	3	Most shots about 5.0 MV
10b	527-537	11	4.4	5.1	8	
11	538-544	39	5.0	5.1	6	all shots less than or equal to 5.0 MV
12	545-613	33	4.4	5.0	4	Most <5.0 MV
13	614-619	6				
14	620-671	52	4.8	4.9		all shots less than or equal to 4.9 MV
15	672-704	33	4.8	5.0	25	
16	705-752	47	5.7	6.0	2	All but 5 shots >5.3 MV
17a	753-771	14	5.4	5.4		All but 2 >5.2 MV
17b	772-790	19	5.9	5.9		All > 5.1 MV
17c	791-811	21				
18	812-844	33	5.8	5.8		All > 5.2 MV
19a	845-851	7	4.9	6.0	4	Most shots self break
19b	854-866	13	5.6	5.6		Range 4.6 MV-5.6 MV
20	867-880	14	5.2	5.3	8	Range 5.1 MV-5.3 MV
21a	885-900	16	5.3	6.0	4	Range 5.2 MV-6.0 MV
21b	901-917	17	5.1	6.0	10	Range 4.4 MV to 6.0 MV
21c	918-932	15	5.3	5.3		Range 4.9 MV to 5.3 MV

APPENDIX I. The Z-like Switch

Overview

Suggestions made at the August 16, 2005, meeting on laser triggered gas switches (LTGSs) led a small group to consider simple, rapid-to-implement modifications of the Z_{20} LTGS that might provide near-term insights into the envelope failure problems experienced at about and above 5 MV. The desired near-term insight was the role the triple point has played in the Z_{20} LTGS low-frequency flashover. The premise is to have a switch as much like the Z_{20} LTGS as possible, but eliminate (or relocate) the triple point to see what effect it has on lifetime. Figure I-1 shows the proposed switch, which is called "Z-like," as the trigger electrode (which in the Z_{20} design extends radially to penetrate the outer envelope) is replaced with a smaller-diameter plate supported by axial compression of six plastic rods. The posts replace a pair of outer housing triple point rings with six smaller-diameter triple point rings at smaller radius (closer to the trigger arc) and should yield valuable information regarding the role the triple point played in the Z_{20} LTGS failure. The mechanical construction approach is similar to the Z LTGS, although the details are quite different.

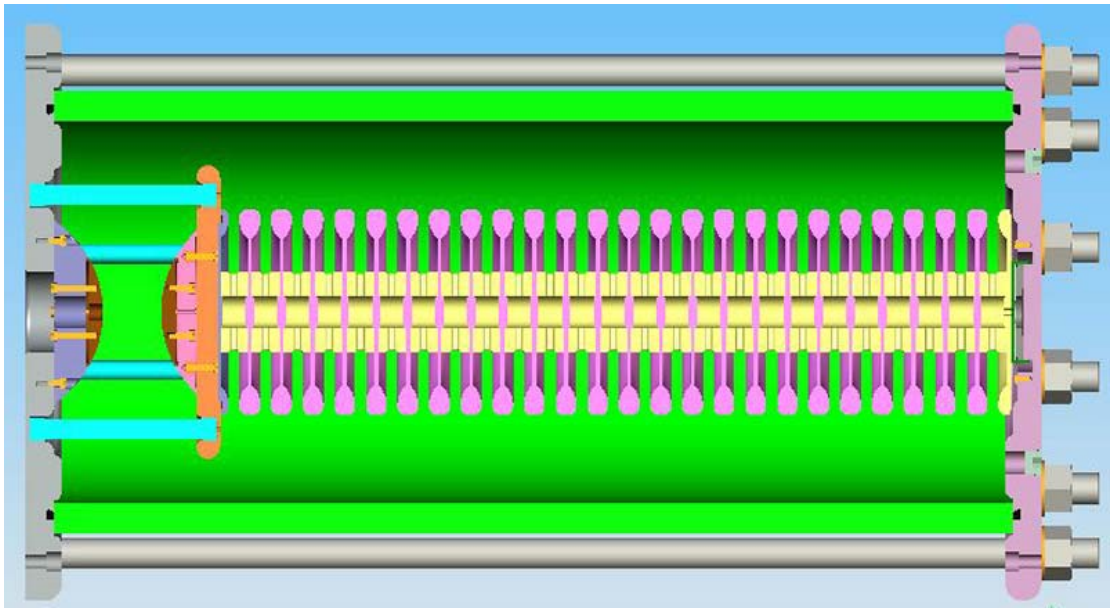

Figure I-1. Z-Like Switch.

While investigating this configuration was not planned until later in the two-year project, it was the easiest to quickly implement on Z_{20} to provide a "quick look" at eliminating the outer housing trigger electrode triple points. A video conference on October 5, 2005, provided part of the community an opportunity to discuss the design basis, the critical issues, and likely outcomes of testing this LTGS on Z_{20}.

The switch was experimentally investigated on Shots 1239 and 1240 with curious results: the highly stressed axial posts were unaffected while the envelope flashed, initiating across from the downstream trigger electrode. This appendix details the design intent, the design analysis, and insights developed in this investigation, which is not yet complete, to explain the experimental performance.

Video Conference Issues

- Jim Dickens will find and provide references on impulse breakdown of SF_6 at relevant stress times (100 ns – 1 μs).

- Concern was expressed that the trigger plate diameter should be further reduced to lower the probability that a streamer might connect the trigger plate to the outer envelope. The proposed design is the smallest that can accommodate support rod grading outside the existing central electrodes. The stress on the trigger electrode outer radius was subsequently analyzed, and is found to be identical to that in the present Z_{20} switch (located in oil) and higher in the cantilever design. The cascade gap stress is similar for both all-open and trigger-closed conditions, as this is largely set by external grading.

- Concern was raised that this design (as compared to Z_{20}) just moves the problem from the envelope to the posts, which are even closer to the arc channel and therefore subject to even greater ultraviolet (UV) and debris.

- Extensive discussion focused on what might be an optimal triple point (3-pt) design. This, along with grading and flashover reduction, is a purpose of the entire two-year effort and cannot be determined in a single teleconference. However, some analysis can be performed to address immediate concerns, which are presented next.

The following are subsequent considerations given to topics discussed.

1. Recommendations were made on construction details, tolerances, fits and finishes.
The switch drawings reviewed were early versions, not ready for release to manufacture, but suggestions are relevant to whatever may eventually be built. The new interfaces need revision to reduce the triple point fields as discussed later. Additionally the effect of mechanical gaps at the triple points was considered. The recommendations were:

- Locate part numbers on the non-electrically-stressed region of the plastic

- Radius support rod releifs and replace vent grooves with flats.

- Post and post-hole dimensions should be consistent for a plug (to close) but not as an interference fit.

- Housing specifications should include clarity (or optical quality). Checking or crazing, bubbles, or particulates should be avoided. Material should be delivered stress-free (annealed).

- Half of the full radius on the baseplate can be omitted as it is shielded when mounted.
- All holes (counterbores and vents) exposed to electric fields should be radiused.
- Outer housing options should include Rexolite and monomer cast acrylic (PMMA).
- Wet-sand the housing with 400-grit silicon carbide paper to a matte finish, approximately 32 micro inch, to provide a reliable and repeatable surface for experimental assessment.

2. Post and cylinder grading needs to be better studied.
In the Z_{20} LTGS at 5.5 MV, the trigger plate voltage before triggering is 900 kV and the stress at the trigger electrode plate triple points (3-pt) with the outer housing envelope is 70-75 kV/cm. This agrees with a simple "back of the envelope" calculation of 0.9 MV/12.7 cm = 71 kV/cm and (5.5 – 0.9) MV/2.5 MV x 2.54 cm 72 kV/cm, a level which should not flash over. What field enhancement is needed to induce flashover? Impulse breakdown of SF_6 occurs around

E = (100 to 120)P, with P in atmospheres and E in kV/cm.

For a gas switch pressure of ~ 3.5 atm the mean field would have to be enhanced to ~ 350 kV/cm, giving a required field enhancement factor of ~ 350/75 ~ 4.7 x.

An estimate of the enhancement produced at the 3-pt by a gas gap due to misfit or damage of the housing (below) is about 3.5x, or about 250 kV/cm. This enhancement, combined with other factors, may result in the low frequency of observed flashover. A low-pressure test should be performed with a deliberately enhanced triple point to develop pressure scaling and statistics.

Field Enhancement in low dielectric constant media

Consider a plane parallel set of biased electrodes separated by a gap D, with the gap divided between two dielectrics. The local fields are shown in Figure I-2. For D = 12.7 cm, $\kappa_1 = 3.5$, $\kappa_2 = 1$, V = 0.9 MV, Figure I-3 shows the enhancement levels.

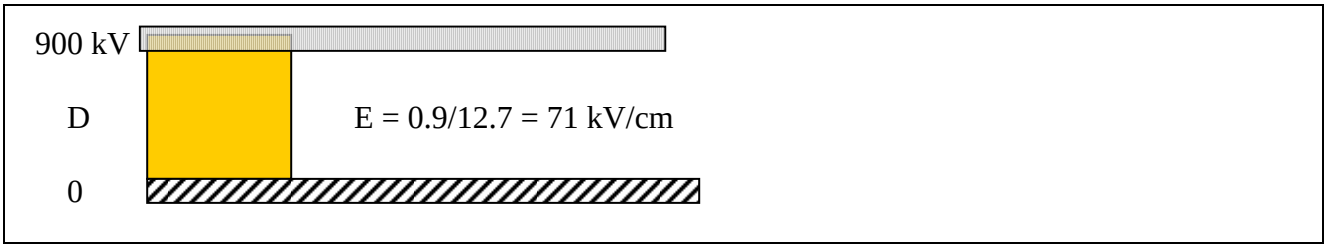

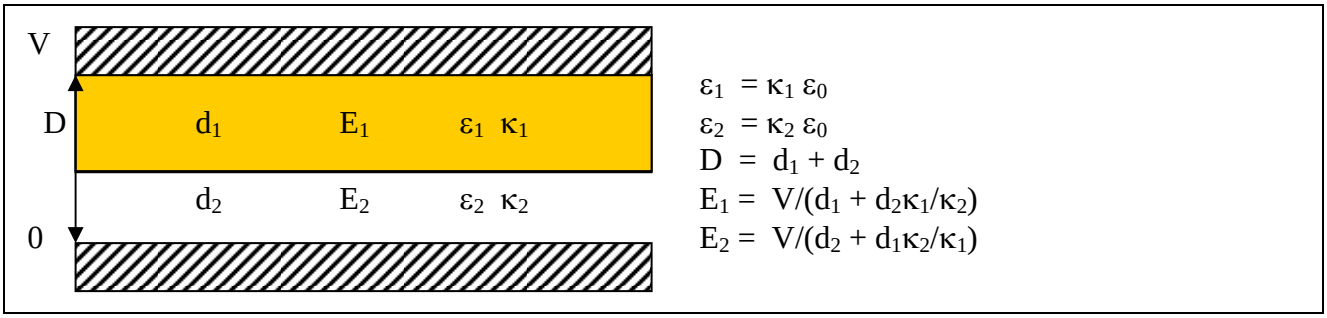

Figure I-2. Local fields.

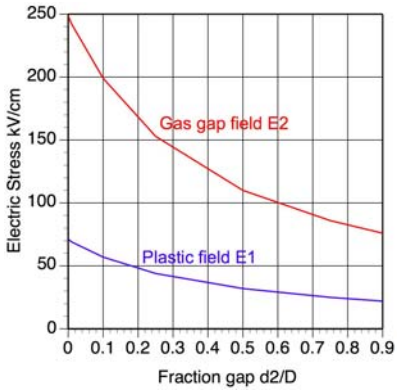

Figure I-3. Fields in a gas gap and plastic as a percentage of total spacing.

Note that $E_2/E_1 = \kappa_1/\kappa_2$ independent of d_1, d_2, or V. For this case $E_2/E_1 = 3.5$. For a simple triple point configuration (sketched below) the fields are as shown and the addition of a small gap ($d << D$) results in a gap field of $E\kappa_1/\kappa_2 = 248$ kV/cm.

Electro calculations were performed to look at this specifically. Figure I-4 shows the fields and profile of a 1-mm triple point mechanical gap. Figure I-5 shows the same for a 0.015 inch more typical mechanical gap. Both increase the local fields by about 3.3 to 4.4 (since $k_1 \sim 4.5$).

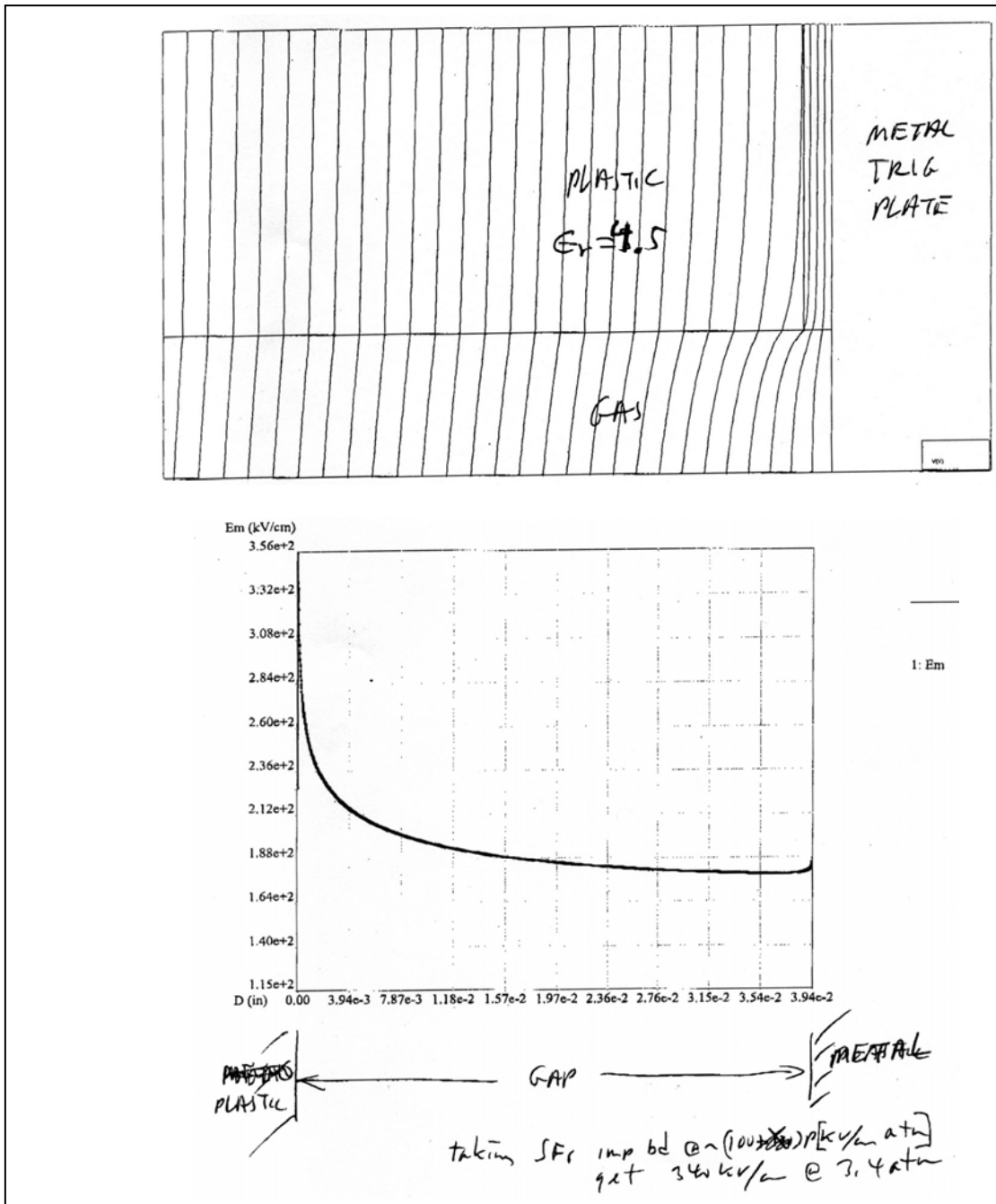

Figure I-4. 1-mm triple point gap fields.

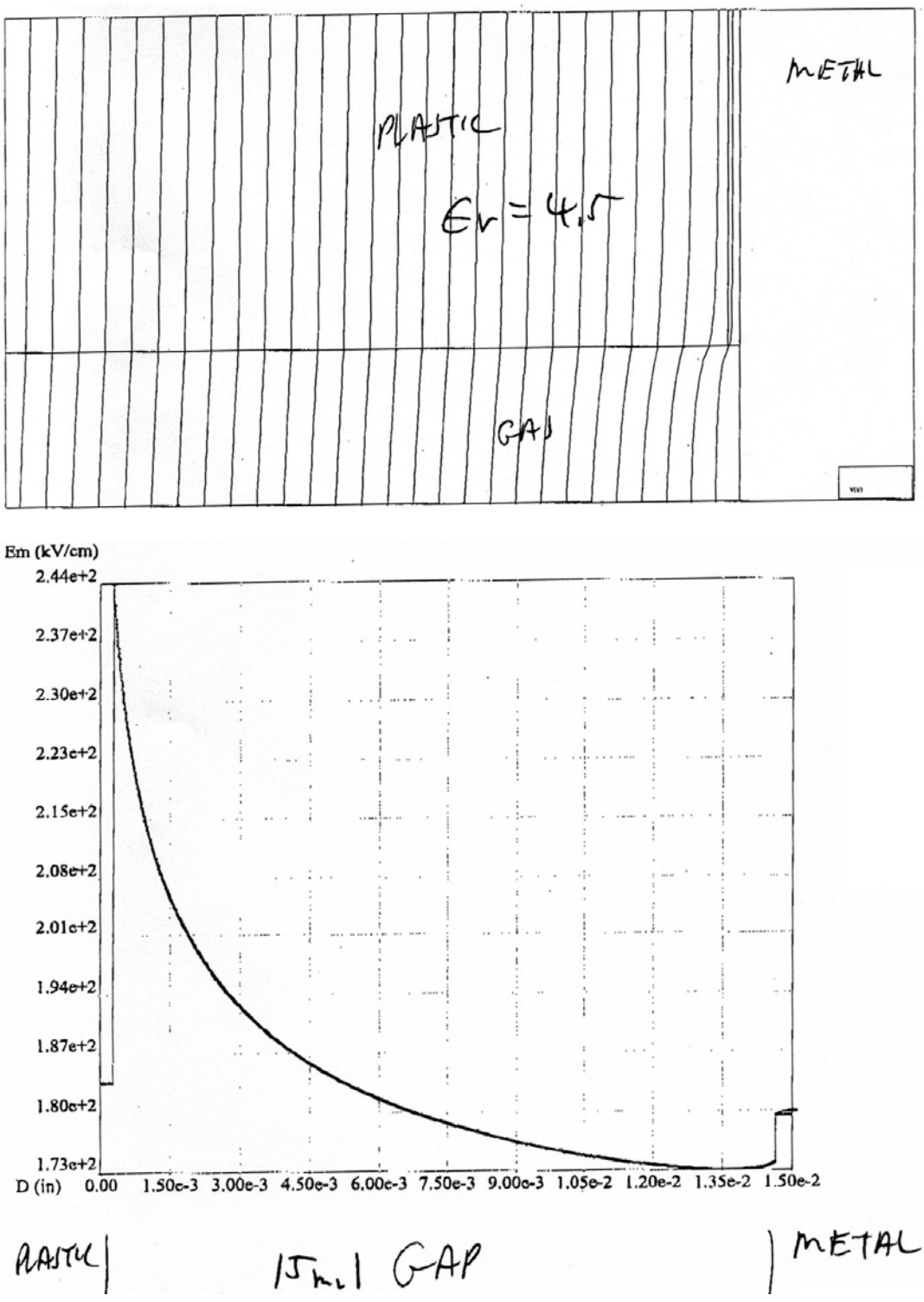

Figure I-5. 15-mil triple point gap enhancements.

Subsequent to the video conference, field plots for Z-like LTGS trigger section (Figures 1 through 6) were preformed. These are:

Figure 1: This is the initial field profile near to one of the six nylon posts as proposed. In Electro this is a two-dimensional cylinder approximation. In all cases, this is the pre-trigger stress configuration where 900 kV is dropped from the trigger electrode to the endplate. The trigger electrode is more negative than the endplate in all cases. The 0.75-inch rod is recessed into the plates to provide mechanical stability supporting the cascade electrode structure. This induces significant enhanced fields immediately adjacent to the post as it enters the recess. There is a concern that streamers initiating from these highly enhanced locations could accelerate down the electric field gradient to intercept the dielectric, inducing a flashover.

Figure 2: Is a demonstration that the field enhancements seen in Figure 1 are due to the change in dielectric constant – in this case the post is set equal to the gas and no enhancements are observed.

Figure 3: investigates the effect of small (0.010-inch) mechanical gaps, due to misalignment or tolerance buildup. The stresses concentrate at the post, and are severe. These field enhancements due to misaligned "air gaps" may be an explanation for flashovers at low overall fields.

Figure 4: Shows the effect of reducing the recess distance into the plate. Here the nylon only steps in as far as the depth of the electrode radius, producing a significant reduction in stress buildup near the post (as compared to Figure 1). Reduced recess (not re-entrant) designs may be effective where assembly compression is adequate to maintain position.

Figure 5: There are two ways to reduce the stress buildup: either protrude the electrode material inside the post (an anode bump as suggested by several, see Neuber's sketch, Figure 5a) or by removing the plastic to allow the field lines to smoothly flare out into the gap. This figure shows the latter, a "waisted" post profile. "Waisting" reduced the mechanical shear and moment bearing capability in exchange for reducing 3-pt electric fields.

Figure 5a: Neuber's pre-conference suggestions for field grading the triple point areas.

Figure 6: For comparison, this is the proposed field profile where the outer envelope (PMMA) meets the endplate. Inside is SF_6, outside is oil. Again, there is concern that a streamer originating on the enhanced electrode will impinge on the dielectric, inducing a flashover. This is similar to Andreas' re-entrant sketch, especially for penetrations approaching a post-diameter. In that configuration the 3-pt fields may be quite low but breakdown risk still exists from the adjacent field shapers.

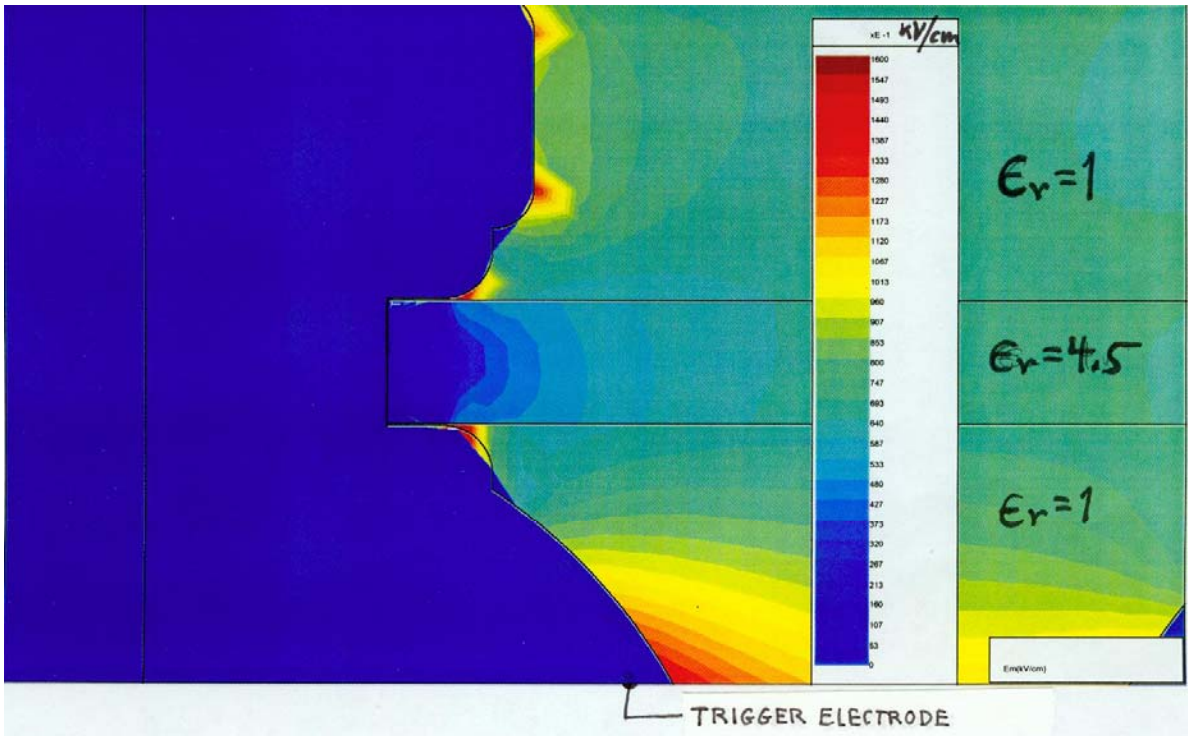

FIG 1 Z-LIKE TRIGGER SECTION INSULATOR @ 0.9 MV. POSTS MODELED AS CYLINDER. RECESSED INTO PLATE.

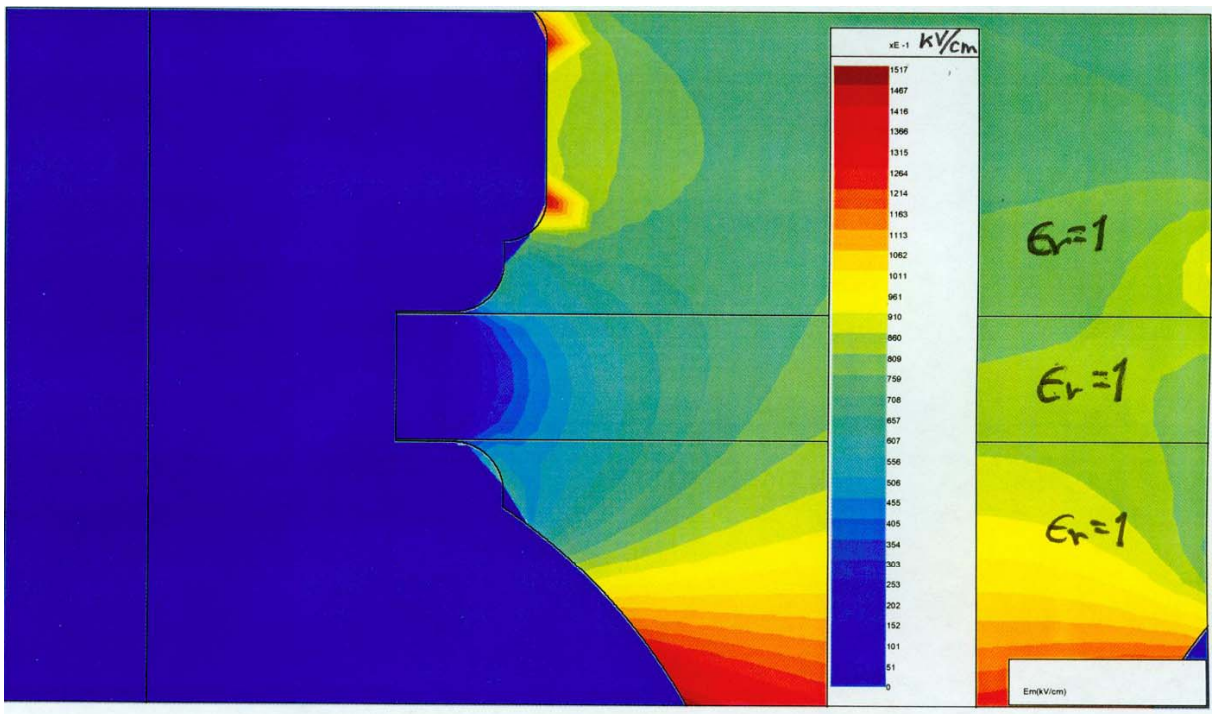

FIG 2 Z-LIKE TRIGGER SECTION INSULATOR @ 0.9MV, DIELECTRIC CONSTANT SET TO 1 TO VERIFY ENHANCEMENT DUE TO HIGH ϵ_r IN FIG. 1

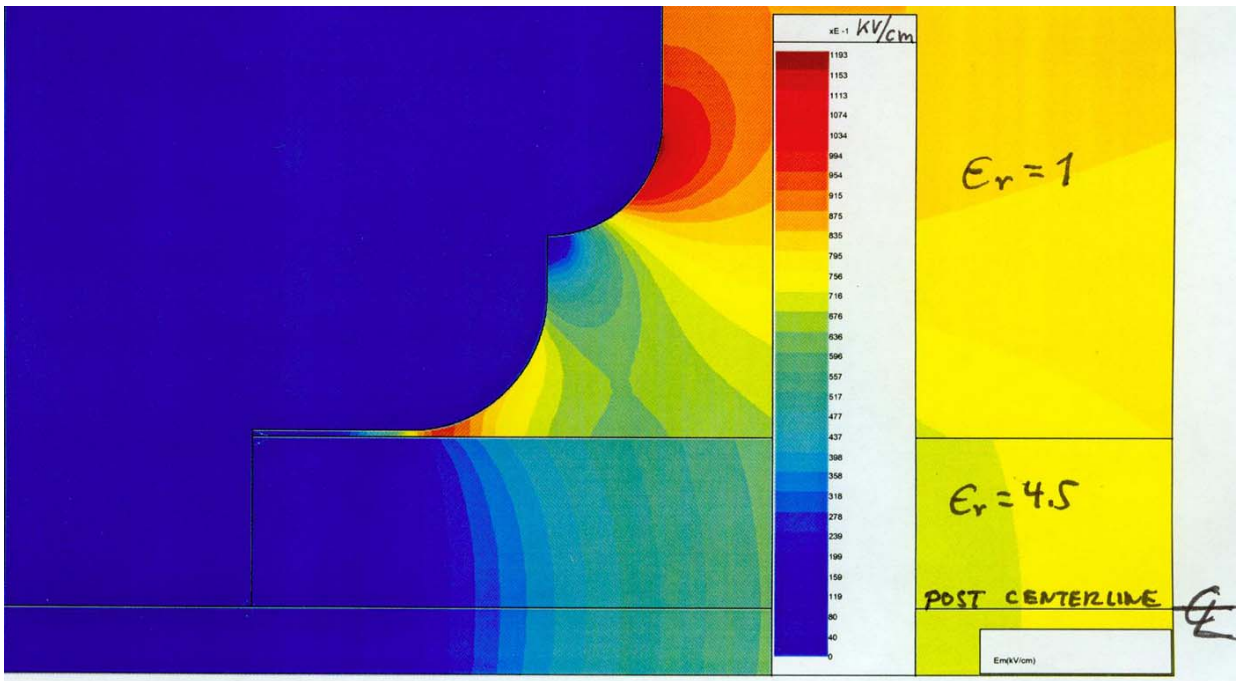

FIG 3 RIGHT CIRCULAR CYLINDRICAL POST WITH Z-LIKE CYLINDER MODEL. FOR COMPARISON OF STRESSES, (AT 0.9 MV) NOTE SIMILARITY PLATE NOTE RECESS INTO

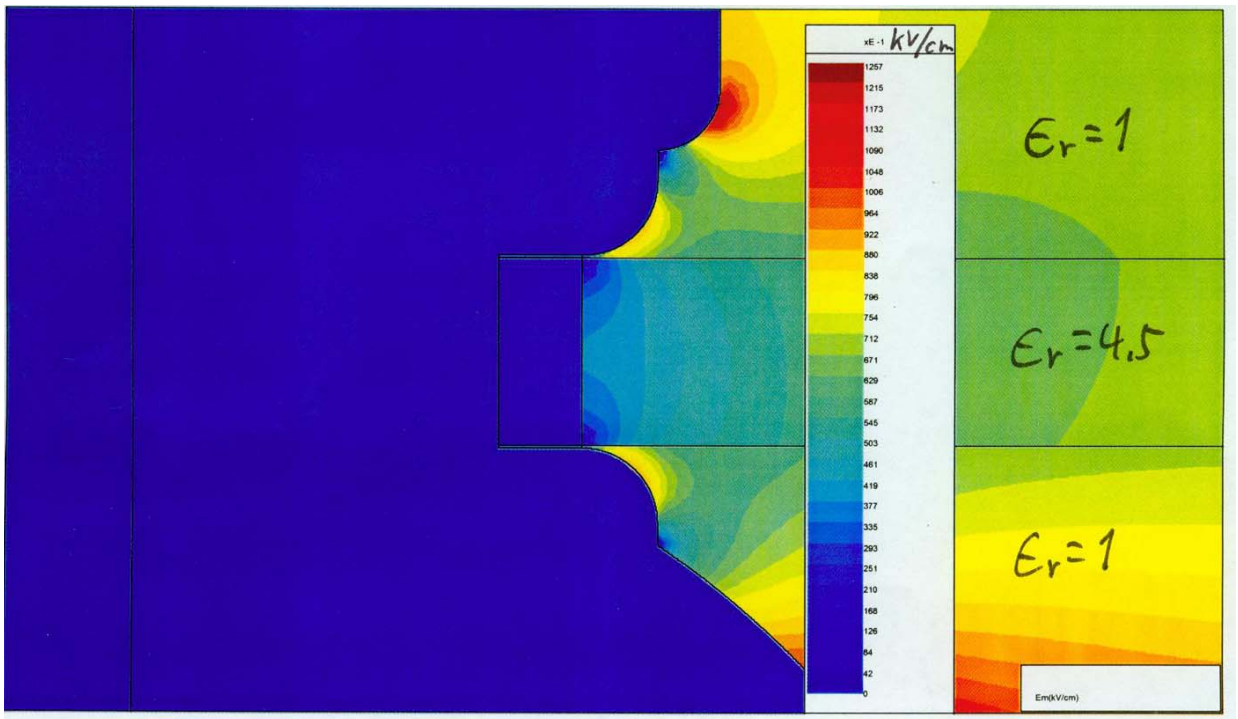

FIG 4 Z-LIKE CYLINDRICAL TRIGGER SECTION INSULATOR. SHORTER CYLINDER WITH FILLED RECESS. NOTE REDUCED 3-PT FIELDS (AT 0.9 MV)

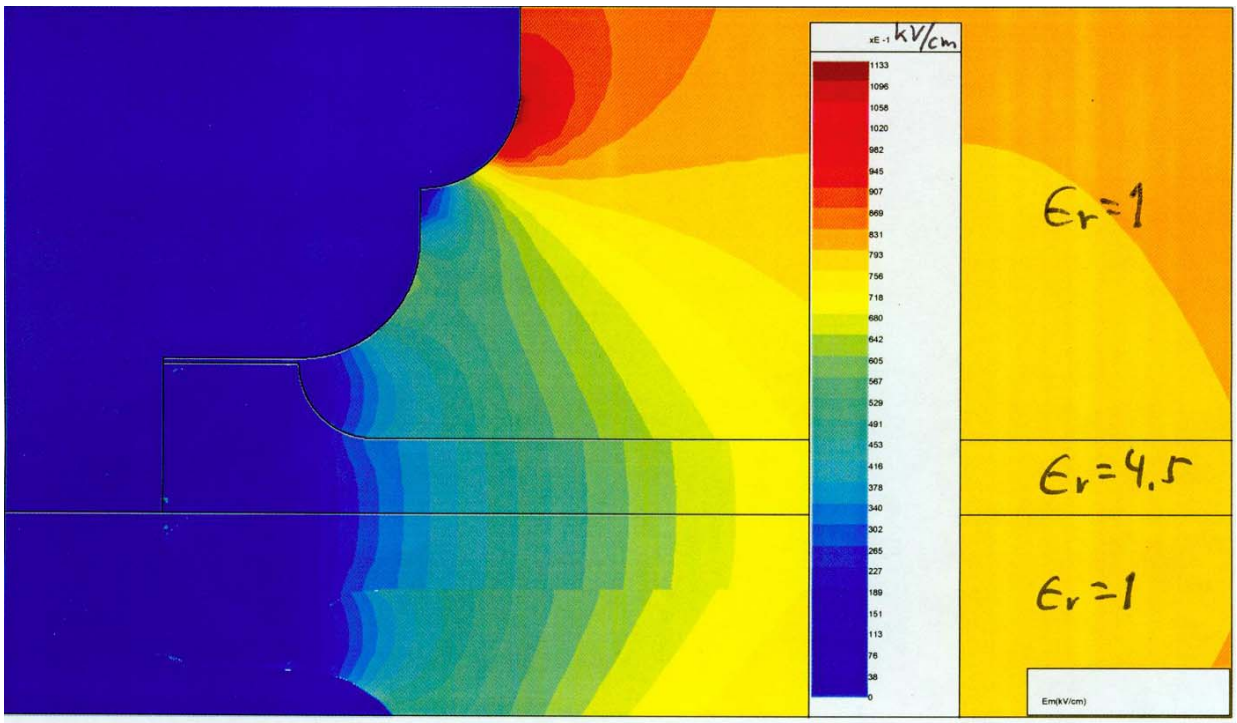

FIG 5 WAISTED POST (OR CYLINDER) FOR Z-LIKE TRIGGER SECTION INSULATOR SUPPORTED IN RECESS IN PLATE. NOTE MARKED REDUCTION IN FIELDS AT 3-PT. (AT 0.9MV)

10-4-05
A. Neuber

Suggested design change where PMMA tube meets input/output end

Current: (O-ring not shown)

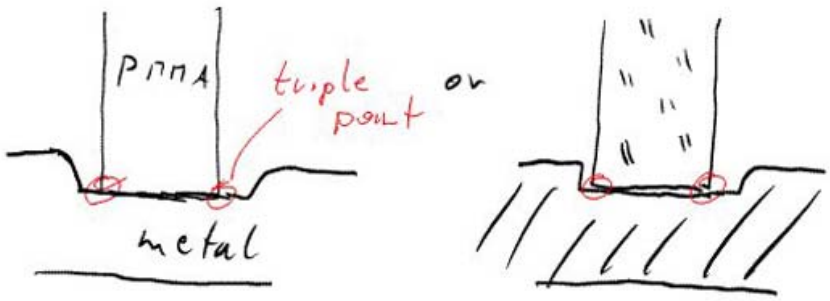

To minimize field at triple point:

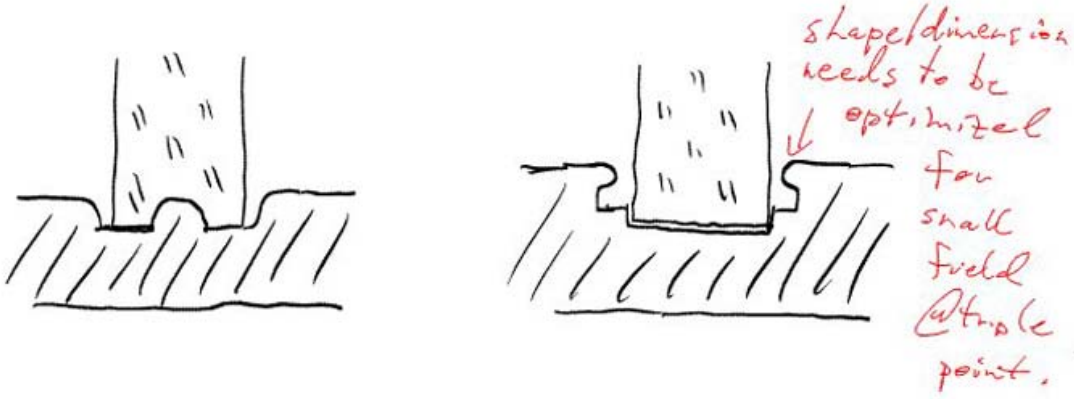

Figure 5a. Neuber's initial suggestions on shielding the triple points for the posts and envelope.

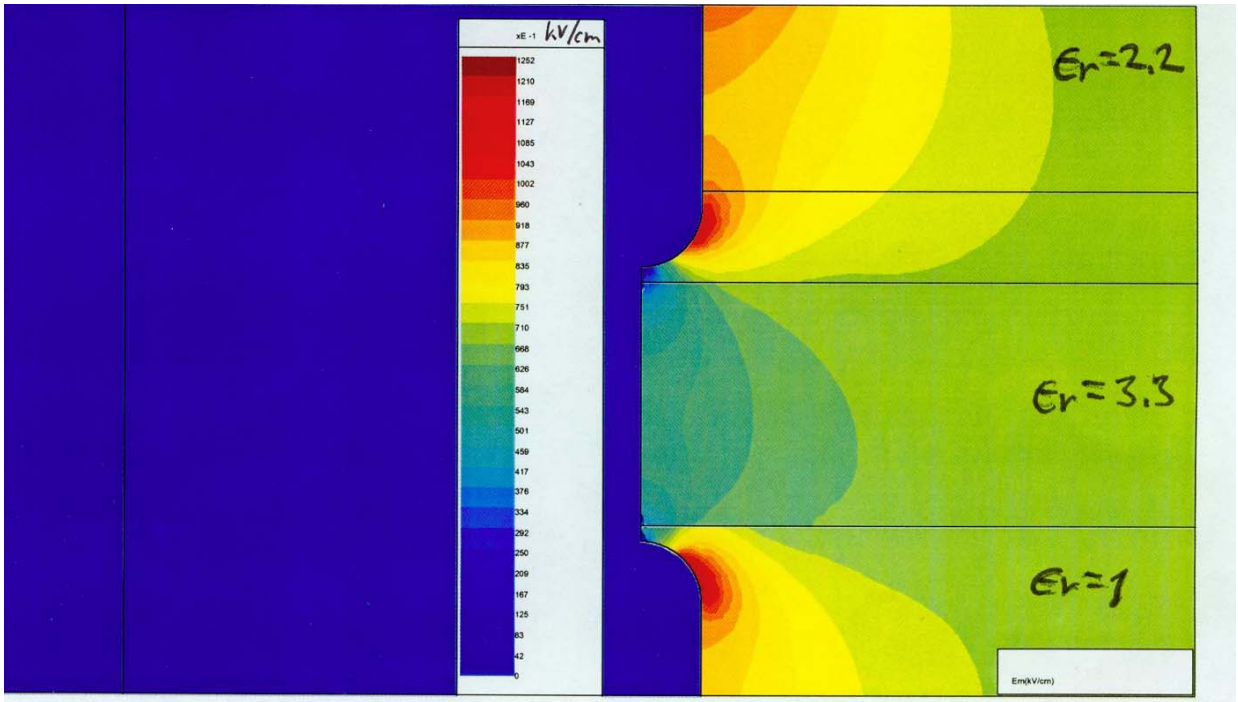

FIG 6 TRIGGER SECTION END OF OUTER HOUSING. NOTE ENHANCEMENT ON FIELD SHAPER ADJACENT TO 3-PT. (AT 0.9 MV)

℄

3. More thorough field analysis was performed to study the trigger plates.

The concern was emission from the trigger electrode crossing the gas to impact the outer envelope for each of the proposed designs (Z_{20}, Z-like, and Cantilever) before an axial arc to the cascade stages removes the voltage. In the following figures we see that the trigger plate edge stresses increase a little from baseline to Z-like, and substantially to cantilever, as the separation similarly increases: 430 to 450 to 585 kV/cm. The stresses on the first cascade gap increase from ~250 to 495 to 533. Ideally the latter should equal or exceed the former so an arc will occur along the cascade rather than to the envelope. The cascade base stage stresses are set by the external grading and are unaffected by these trigger variations.

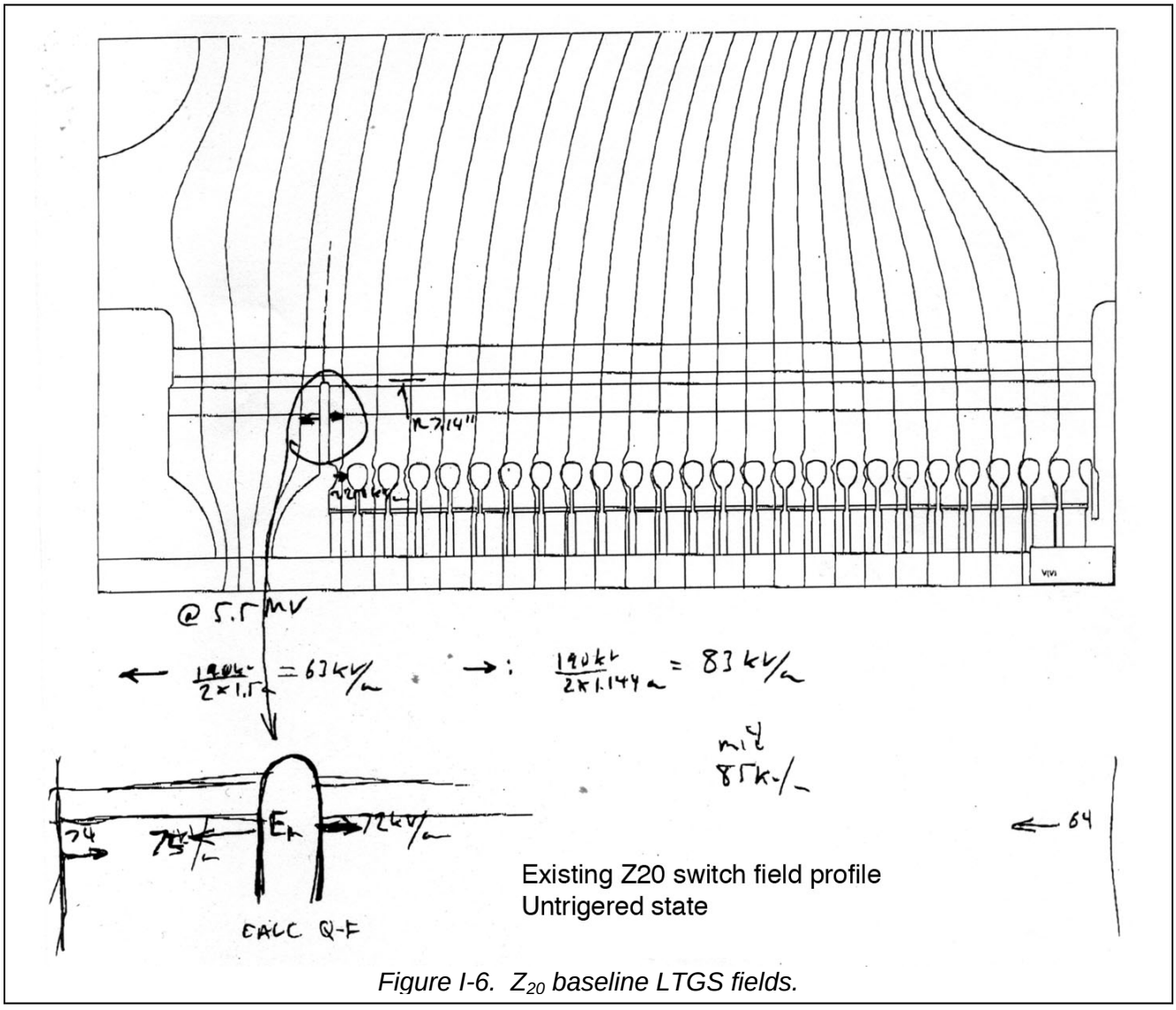

Figure I-6. Z_{20} baseline LTGS fields.

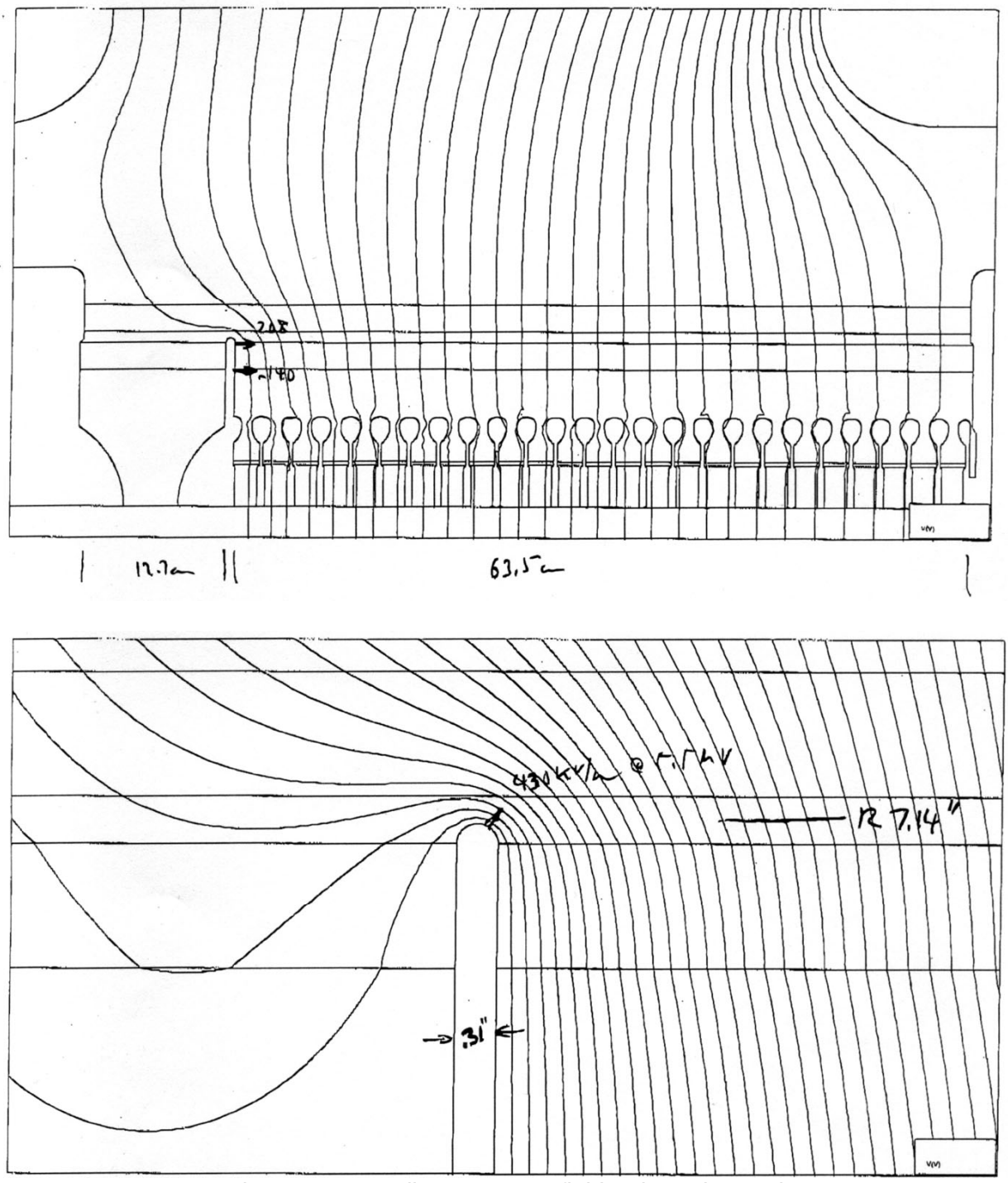

Figure I-7. Baseline Z_{20} LTGS fields when triggered.

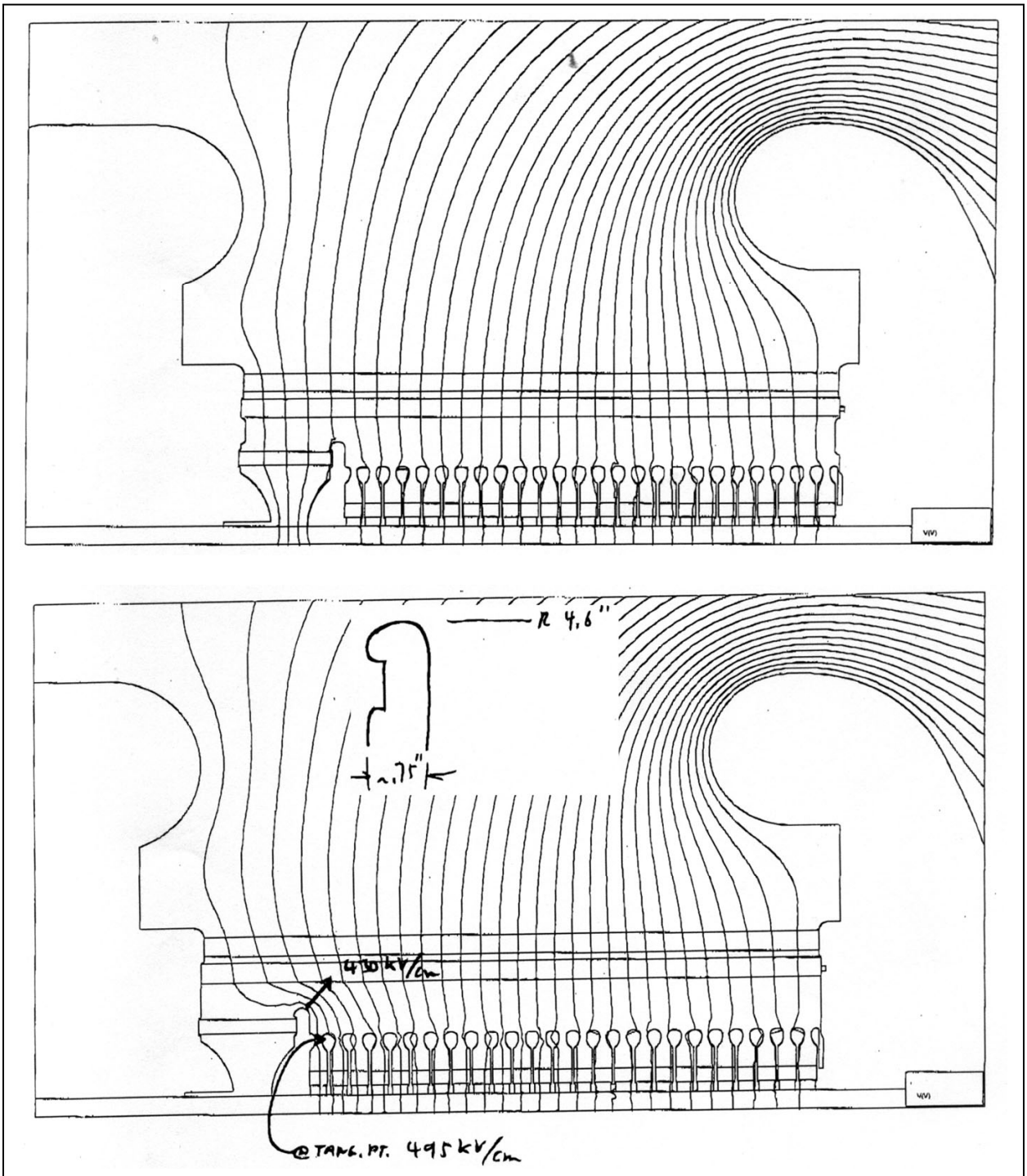

Figure I-8. Z-like LTGS fields when triggered.

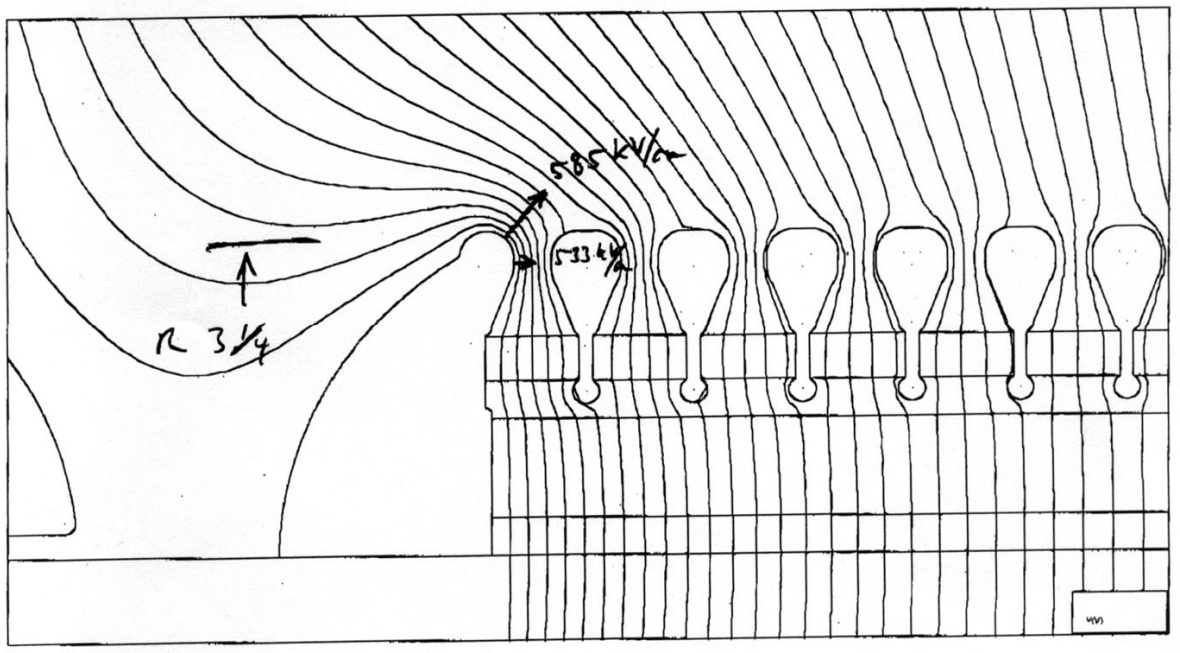

Figure I-9. Cantilever LTGS fields when triggered.

4. Consideration of the self break curve.

The self-break curve from the Z_{20} (and Switch Test Bed, STB) LTGS have few points above ~ 5 MV and at pressures > 25 psig. A number of routine test shots appear to have self-fired before laser pulse arrival in the trigger section, which could be considered self-break data points with laser backup. However, inclusion of such shots produces a self-break curve that is flat (V independent of pressure) above 5 MV. This is an issue separate from the housing flashover problem. The breakdown voltages for these non-laser-assisted shots, are, for the most part, surprisingly the same independent of pressure, with the exception of two fired with no laser. This suggests a possible misalignment of diagnostics timing that needs to be reviewed. More no-laser shots are needed in the range of 25 to 55 psig. The effect of electrode erosion should be determined, and continuous monitoring of SF_6 quality needs to be implemented. Inclusion of data from shots with negative run times (i.e., closure before the laser phase) results in a curve that is almost flat vs. pressure above 5 MV. Diagnostic verification and more data are needed for the range of 20 to 50 psig.

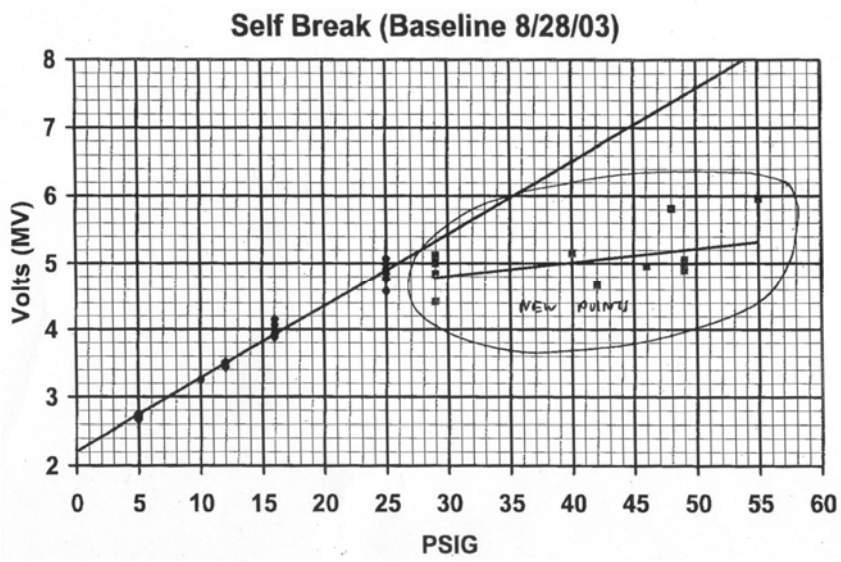

Figure I-10. Baseline Z_{20} LTGS self-break data.

Conclusions and Recommendations

While this Z-like design for test was developed before implementing our plan, and hence the roles and responsibilities for the people involved were a bit out of line from our intended structure, the work is timely and an excellent opportunity for us to start working together. The initial design presented on October 5, 2005, applied existing mechanical and electrical design approaches to the issue of how to remove the triple point between the trigger electrode and the outer envelope. The simplest engineering modification envisioned was to change only the trigger electrode, replacing the external positioning system with six axially compressed dielectric rods. These could have been a cylinder (as in the Z switch), but it was recognized that the danger was being moved from the outer to the inner cylinder and, since a pressure boundary was not needed, the area (and subsequent the probability of tracking) could be reduced by using an array of rods. Electrical and mechanical analysis suggested the approach was sensible, which led to the proposal. The video conference provided very useful diverse viewpoints and concerns that have all been considered and the analysis presented above. Some fundamental conclusions to date are:

1. There is little value in reducing the trigger electrode diameter further – the principal danger seems to be post flashover, which becomes worse as the space for grading the post ends is reduced. The risk of launching a streamer to the outer envelope appears low.

2. Triple point enhancements from dimensional clearances and mechanical positioning errors have been estimated, suggesting an explanation for the apparent “low stress” breakdowns observed. More study is needed to verify this analysis is correct and pertinent.

3. Several new approaches to grading the post ends (and hence to joining all dielectrics to electrodes) have been proposed – an electrode protrusion within the dielectric and a “waisted” dielectric profile. Tests of both, as well as of designs intended to fail, are needed.

This report is an experiment to develop a method of communicating advances in insight and (eventually) in understanding across the entire team. Suggestions for improvement for this Z-like switch and in communications are solicited from all!

LTGS: Further Considerations

J. Corley and A.R. Miller 11/23/2005

A variety of efforts relevant to the LTGS were reported on after the October 5, 2005, video conference. This note covers further efforts subsequent to that report. Those are:

Further analysis of interface triple-point designs including those recommended by A. Neuber, modeling of a gap at the 3-point and of a crazed plastic surface.

Calculation of trigger gap fields for a post-supported Z-like switch.

Comparison of cascade gap voltages for Z_{20}, Z-like, and cantilevered switches with the laser triggered gap closed.

Collection of papers and references on SF_6 and SF_6 breakdown.

Switch shot logs and commentary.

Correction

Before reviewing the interface studies a correction is relevant. In the previous report the field enhancement required to initiate an interface flashover was considered. It was shown that small gas gaps under the plastic at the triple point (3-pt) result in a field enhancement that scales like the dielectric constant of the plastic relative to the gas or about 3.5 X the field with no gap for nylon. In the Z_{20} LTGS at 5.5 MV a 0.015-inch gap would enhance 3-pt fields to about 250 kv/cm.

It was assumed that the SF_6 impulse breakdown strength was ~ (100 to 120) P kv/cm - atm, providing a withstand capability approaching 400 kv/cm at 4.0 atm, and other factors would be needed to initiate flashover. A review of literature on SF_6 breakdown does not support this assumed breakdown strength. Interface (or boundary) data for interface lengths of a few cm at 1 to 4 atm, are in the range of (70 to 50) P kv/cm - atm and breakdown at the gap stress of ~ 250 kv/cm is therefore likely.

Insulator Triple Point Designs: “Waisted” Interface

It was shown previously that “waisting” the plastic support at the triple-point (3-pt) provides the maximum reduction in 3-pt fields. The design shown in Figure 5 of that report shows a waist considerably smaller than the major diameter. This reduces mechanical moment bearing and buckling resistance of the interface. Further modeling with less severe diameter reduction shows similar electric field reduction even with a 12-mil radial gap at the post base (Figure 1). Thus ¾-in.-diameter rods with 1/16 inch radii (5/8 inch waist diameter) will be used in the Z-like switch.

The entire length of the Z-like trigger section support and part of the external envelope is shown in Figure 1a. Stresses at 3-pts are seen to be low (~50 kv/cm) for both posts and envelope.

Adjacent fields are higher (~124 kv/cm) but not above SF_6 breakdown and the likely streamer trajectories are not directed at the plastic. The envelope could also be waisted if re-entrant. If envelopes are to be machined to net shape this may be considered. Other surface contours are being considered. Figure 1a is to be compared with Figure 1b where the rod length is only partially waisted. This would further stiffen the rod, but stresses adjacent to 3-pts are increased and likely streamer trajectories intercept the plastic.

Chip-Out Defect

The field enhancement due to a 3-pt defect such as a small chip-out of the plastic edge is shown in Figure 2. A 15-mil gap extends back 45 mils. A maximum enhancement of ~2.5 times to ~175 kv/cm at the gap apex is noted in the model as would be expected for a dielectric constant of 2.4 and average stress of 70 kv/cm when the switch is charged to 5.5 MV. After laser gap closure this defect, if on the cascade side of the trigger plate, would be stressed to ~ 350 kv/cm, which is above predicted breakdown stress for SF_6 at 4 atm and would probably initiate a breakdown.

Other 3-pt Shielding Designs: Metal Insert

The previous report showed notional design changes suggested by A. Neuber for reducing 3-pt fields (Figure 5a of that report). These have been modeled with the following results. The first utilizes a metal protrusion into the plastic (e.q. anode bump) to lift fields off the 3 pts. This was first evaluated as re-entrant to provide mechanical bending strength. The metal post contacts the plastic and there is a small radial gap. The result is shown in Figure 3. This has not been optimized. A larger insert would probably help. There may be some other combination of radii giving better results. 3-pt fields adjacent to the plastic are higher than before and fields in plastic at metal sharper are high, but not near strength of plastic. While not an immediate concern for the plastic, experience with similar configurations is that of eventual treeing of the plastic, especially if there is a gas gap above the shaper where there will be partial discharges.

For the case with an embedded field shaper that is not required to support mechanical moments (as in A. Neuber's originally suggested configuration), the 3-pt fields are relieved while the internal shaper to plastic fields are still high. This is shown in Figure 4. If the effect of manufacturing tolerances are considered, two conditions result; a gap at end of plastic or a gap above the field shaper. A gap at the end of the plastic (i.e., supported on the protrusion only) is modeled in Figure 5, and shows gap fields of ~150 kv/cm with average fields of ~70 kv/cm. This condition should be avoided.

Other 3-Pt Shielding Designs: Re-entrant External Shield

Two versions of the re-entrant shielded design suggested by A. Neuber were modeled, one where the plastic is placed into the baseplate for mechanical rigidity, the other as sketched by Neuber. In both cases the 3-pt is hidden and stresses are low, but the adjacent shroud enhances fields and likely streamer trajectories could intercept the plastic. These are shown in Figures 6 and 7. The models shown have not been optimized for minimum stress, but with the dielectric constant difference and shroud aperture significant further reduction is unlikely.

Laser Triggered Gap Fields

The Z-like switch had been modeled as if the discreet posts supporting the trigger section were a plastic cylinder. There was concern about the effect this would have on grading and the trigger gap voltage. Trigger gap shunt capacitance was calculated for the cases:

No plastic support

A ¾-inch-thick plastic cylinder

A 0.114-inch-thick plastic cylinder equivalent to 6 rods

Gap voltage with 5.5 MV across the switch was also calculated. The results are in Table 1.

Table 1. Trigger gap capacitance and voltage.

	C Shunt	**V Gap**
No plastic support	10.45 pF	890 kV
¾-inch-thick cylinder	13 pF	792 kV
6 post equivalent (0.114-inch-thick wall cyl)	10.75 pF	874 kV

The difference between cases 2 and 3 (~10%) does not significantly alter the results of any previous analyses of trigger plate and cascade section stresses.

Cascade Gap Voltage

The peak fields and voltages produced across the first four cascade gaps by closure of the laser triggered gap were calculated for three switch designs and are given in Table 2.

Table 2. Cascade gaps; Fields (E) and Voltages (V), (kV/cm and kV).

	E	V	E	V	E	V	E	V
Gap	**1**		**2**		**3**		**4**	
Z_{20}	362	282	352	284	345	277	335	272
Z-like	355	347	408	327	372	296	342	267
Cantilever	489	395	405	327	362	286	332	260

The first gap of the cantilever design is the least shielded as the trigger electrode plate is the smallest diameter. Note that Z_{20} switch cascade section run time after trigger gap closure is usually 20 to 30 ns with a δ of a few ns. Triggerability of Z_{20} is not at issue. Z-like and cantilevered switches are yet to be tested.

SF_6 Gas

Reference information on SF_6 is being collected. Specifications, physical properties, and papers citing dielectric strength are included. A partial list follows. A compilation of breakdown data relevant to the LTGS from various sources is shown in Figure 8. There seems not to be a standard breakdown strength for SF_6 under impulse conditions, and while there are general similarities much data is unique to specific test conditions. Design criteria avoiding breakdown are given for specific applications, sometimes with confidence levels. Non-paschen Law scaling of breakdown strength with pressure is sometimes noted as is gap and area dependence of E/P vs. P. A rational approach to SF_6 use in the LTGS application would be to specify and control SF_6 purity and develop breakdown scaling parameters relevant to the specific requirements of the application (e.g., at relevant gaps, pressures, and voltages for the various features specific to the switch design). Comparison with data from other applications is useful when results are far from expected.

SF_6 Literature

Specifications:
ASTM D2472-00; standard specification for sulfur hexafluoride.

ASTM D2477-02; standard test method for dielectric breakdown voltage and dielectric strength of insulating gases at commercial power frequencies.

IEEE STD4-1995; IEEE Standard Techniques for High Voltage Testing.

CEI-IEC 60376 International Standard, 2nd Ed., Specification of Technical Grade Sulfur Hexaflouride (SF_6) For Use in Electrical Equipment.

Example of Purchase Order Specification for SF_6 (Titan PSD).

Physical Properties:
Sulfur Hexafluoride for Gaseous Insulation, Allied Chemical, Specialty Chemicals Division. TB-85603, 22 pgs.

Sulphur Hexaflouride Data Sheets, Solvay Fluor Corp., 6 pp.

SF_6 Properties, and Use in MV and HV Switch Gear, Cahier Technique No. 188, Groupe Schneider, 25 pp.

Sulfur Hexaflouride (SF_6), PFPC Science
Website: http://64.177.90.157/science/html/sf6.html

Papers and Articles:
A Review of Insulation Breakdown and Switching in Gas Insulation, M. J. Mulcahy et al., Ion Physics Corp., *Insulation/Circuits*, August 1970, pp. 55-61.

Dielectric Materials and Their Applications - A·Dielectric Materials, by John G. Trump, pp. 147-156.

Criteria for Spark Breakdown in Sulfur Hexafluoride, A. Pedersen, *IEEE Winter Power Meeting*, New York, NY, January 25-30, 1970.

Gas Insulated Cables, Alan H. Cookson, *IEEE Transactions of Electrical Insulation*, Vol. EI-20, Vol. 5, October 1985.

SF_6 Decomposition in Gas-Insulated Equipment, F.U. Chu, *IEEE Transactions on Electrical Insulation*, Vol. EI-21, No. 5, October 1986.

On the Toxicity of SF6 Insulating Gas, S. Wock, *IEEE Transactions on Electrical Insulation*, Vol. EI-14, No. 2, April 1984.

A Potent Greenhouse Gas Identified in the Atmosphere: SF_5CF_3, W. T. Sturges et al., *Science*, Vol. 289, July 28, 2000, pp. 611-613.

Statistical Techniques for High Voltage Engineering, W. Hauschild and W. Mosch, Peter Peregrinus Ltd, ISBN 0 86341 205 x, Chapter 5.3 on Compressed Gas Insulation.

High-Voltage Insulation Technology, Dieter Kind and Hermann Karner, Friedr. Vieweg & Sohn, ISBN 3-528-08599-1.

An Introduction to High-Voltage Experimental Technique, Dieter Kind, Friedr, Vieweg & Sohn, ISBN 3-528-08383-2.

Scaling Relations for the Rimfire Multi-stage Gas Switch, B.N. Turman and D.R. Humphreys, *6th IEEE Pulsed Power Conf.*, Arlington, VA, 1987.

Electrical Breakdown in SF_6 Under Negative Impulse Voltage, Koukos, MacGregor, Farish and Spyrou, *6th Int Symp on High Voltage Engineering*, New Orleans, LA, USA, 28 August-1 September 1989.

Dielectric Behavior of SF_6 Point-plane Gap Subjected to Fast Rising Impulse Voltage, Gilbert, Dupuy, Riquel, *6th ISHVE*, September 1, 1984.

The Effect of Surface Imperfections on the Breakdown Strength of SF_6 Under Very Fast Transients, va der Zel, Reynders, *6th ISHVE*, September 1, 1984.

LTGS Shot Logs

Performance of individual switches is being extracted from the shot record for comparisons and detection of trends and similarities. Peak voltage at switch at time of closure and switch closure run time are tracked and occurrence of envelope flashovers noted. Correlations with pre- and post-shot observations are attempted. For example, switch #031 had a cascade section flashover on its first shot out from buildup. The flash occurred subsequent to laser triggering at 6.04 MV. Origin appears to be mid span with branching in both directions toward base electrodes. On five subsequent shots, two were normal (no flashover) and three flashed. Switch run times for all six shots were similar, indicating triggering of the flashover or of the cascade gaps. The mid span flash origin and diffuse structure could be explained by an extensively crazed inner surface as new, with minimal time from cleaning with Simple Green and no vacuum processing.

SWX 031 Shot Log					
			Flashover ?		
Shot #	V (MV)	Trun (ns)	T-sect	C-sec	Other
1031	6.04	30.4		Yes	All shots @ Vmg=+/-90kV,Pswx = 60 psig bottled SF6
1032	6.05	37.6			
1033	6.02	30.4		Yes	
1034	6.06	21.6		Yes	
1035	6.16	69.6			
1036	6.09	31.3		Yes	
1037	5.44	-110		Yes	Withstand V deteriorating remove and replace housing

Notes:

Without photos there is little to discriminate flashover from normal switch shots.
Cascade F.O. and Cascade gap closure appear ~ equally probable with similar run times.
C-sect operating point may be near “crossover” at 60 psig
Housing was crazed from new –probably the worst yet – had not been under vacuum-cleaned in Simple Green before assembly.

SWZ 004 Shot Log					
Shot #	V (MV)	trun (ns)	Flash Over? T-Sect	C-Sect	Other
1004	6.01	—			35 psig all other shots @ 55 psig
1005	5.93	29.2			All on bottled SF6
1006	5.95	28.0			
1007	6.04	28.8			
1008	6.02	27.8			
1009	5.97	23.6			
1010	5.55	29.6			
1011	5.90	30.0			
1012	5.94	25.6			
1013	5.92	10.0			
1014	5.89	28.0			
1015	6.04	28.0			
1016	6.04	28.04	Yes		
1017	6.01	27.3			
1018	5.99	28.4			
1019	6.04	27.4			
1020	6.05	26.8			
1021	6.02	28.0			
1022	6.08	30.4			
1023	6.06	28.8			
1024	6.08	27.2			
1025	6.09	28.8			
1026	—	—			PF: rolled over V = 6.34 MV teff = 825 ns no SWX closure
1027	6.01	31.2			
1028	5.97	30.8			
1029	4.79	-207.2		Yes	
1030	3.31	-414		Yes	Rapid degradation of housing withstand V, replace SWX
27 Shots Total					

Did rollover #1026 damage envelope and predispose it to flash 3rd shot later at 4.8 MV?

SWX #960 Shot Log					
			Flash Over?		
Shot #	V (MV)	Trun (ns)	T-sect	C-sect	Other
960	5.64	149.2			VMG = ±86 kv Psig = 49 psig
961	5.33	72.0	Yes		
962	5.22	81.6			
963	5.26	58.4			
964	5.28	54.8	Yes		
965	5.28	46.4			
966	5.29	48.0			
9.67	5.20	37.6	Yes	Yes	
968	5.24	48.4			
969	5.05	132.0			
970	—	—			No data – MG malfunction
971	—	—			
972	—	—			
973	5.09	48.8			
974	4.55	-114		Yes	
975	5.24	52.8			
976	5.26	37.6			
977	4.42	-124			VMG = ±80kV P_{swx} = 29 psig
978	5.12	16.8			
979	4.84	-77			
980	—	—			
981	5.00	-68			
982	—	—			
983	—	—			MG prefires – rebuild
984	—	—			MG DL shot
985	5.10	-12			
986	5.31	15.2			
987	5.64	No laser			
988	5.09	No laser			Laser blocked for all remaining shots to 1003
989	4.47	-153.9			
990	5.37	27.6			

SWX #960 Shot Log					
Shot #	V (MV)	Trun(ns)	Flash Over? T-sect	C-sect	Other
991	5.25	-8.4			Laser blocked on shots 988 thru 1003
992	5.29	No laser			5.12 ±0.379 MV n = 9
993	5.16	-23.6			
994	5.26	93.2			
995	4.55	-135.6			
996	4.87	-79.9			VMG = ± 86 kv raise Pswx to 35 psig
997	5.19	-11.2			
998	6.01	218.4			
999	5.55	52.8			VMG = ± 90 kv
1000	5.72	92.8			
1001	4.89	-83.9			
1002	5.53	18.1			5.29 ± 0.496 MV n = 8
1003	4.55	-139.2			
44 shots (incl MG Problems)					Switch removed as contaminated by powdery substance and chunks of crud

- Majority of contamination in cascade sect – to be analyzed.
- Self-break (no laser) Shots 987 through 1003 in two groups; 29 psig and 35 psig. Difference seems not significant +20% increase in P vs + 3% increase in Vbd.
- After three T-sect FOs and two C-set FOs SWX continued 25 shots w/o FO at voltages from ~ 5 to 6 MV despite contamination and significant envelope damage (esp. C-sect).
- Housing was crazed from new. Additional craze-cracks produced by FO streamers along arc path. Plane of these is perpendicular to hoop stress and constitutes tension sensitive notch, which could lead to disruptive failure.

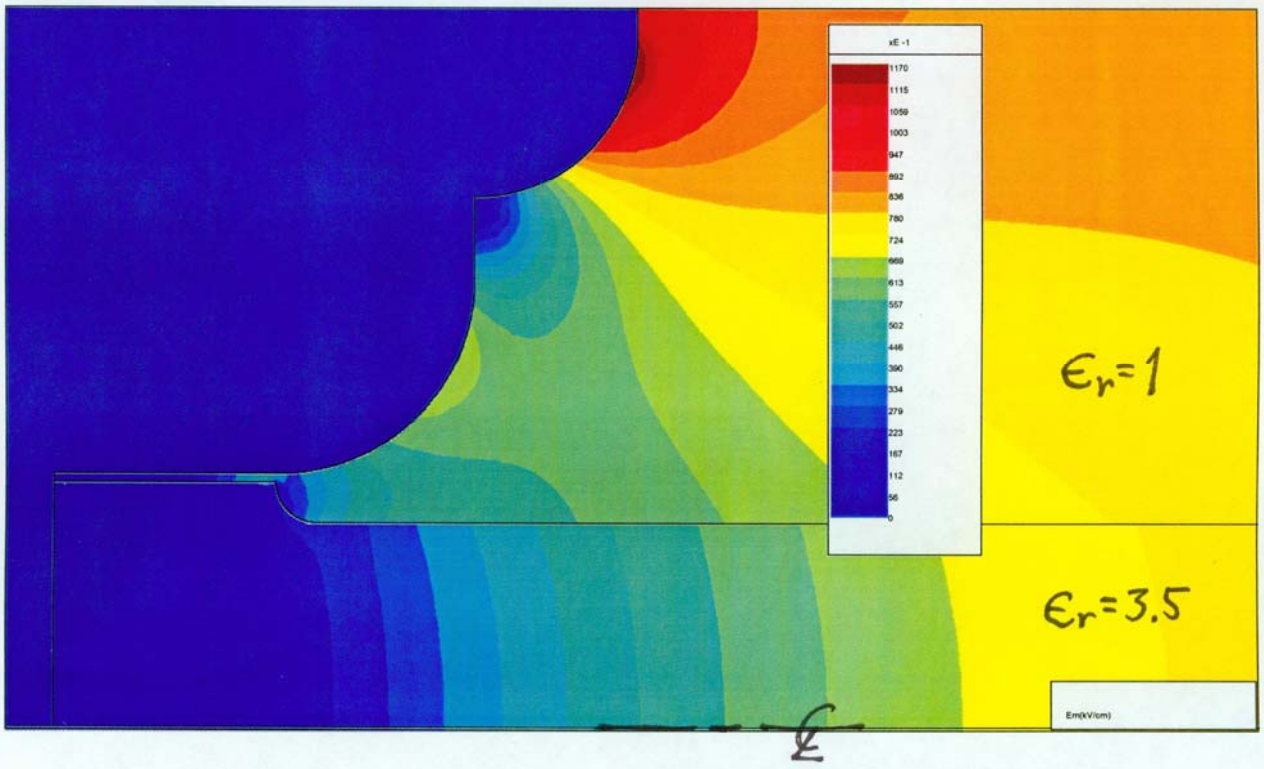

FIG 1. ϕ 0.75 in. ROD WITH 1/16 in. RADIUS WAIST AND 12 mil RADIAL GAP. (NYLON)

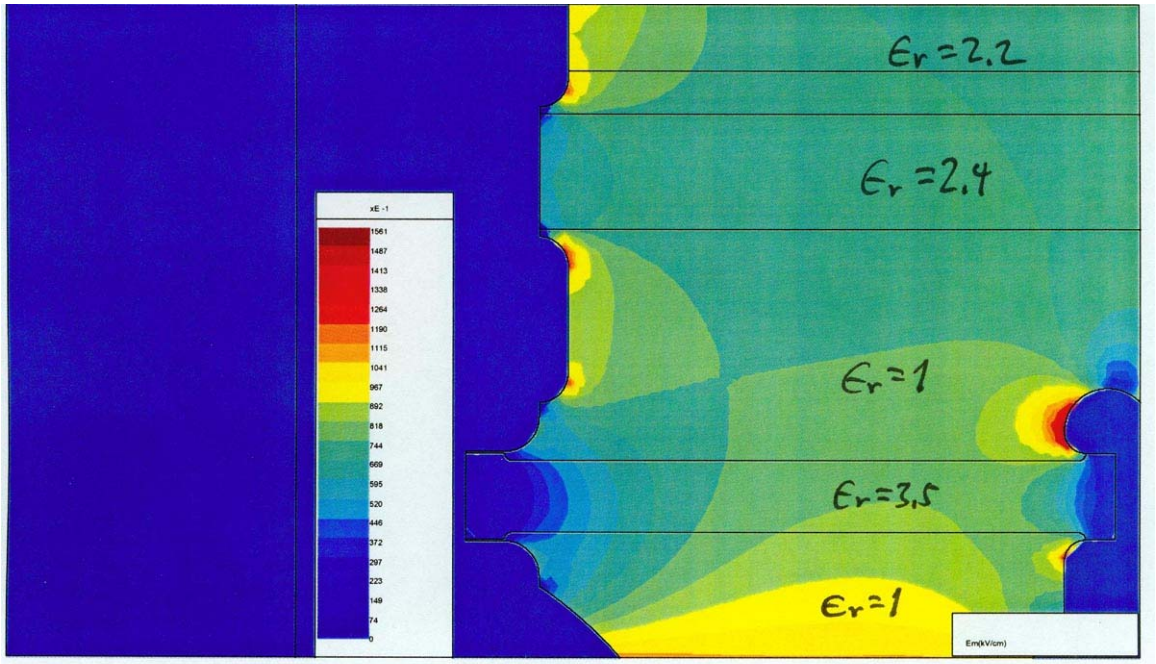

FIG 1a. TRIGGER SECTION WITH WAISTED ROD SUPPORTS AND OUTER ENVELOPE. SWITCH @ 5.5 MV —— - ℄

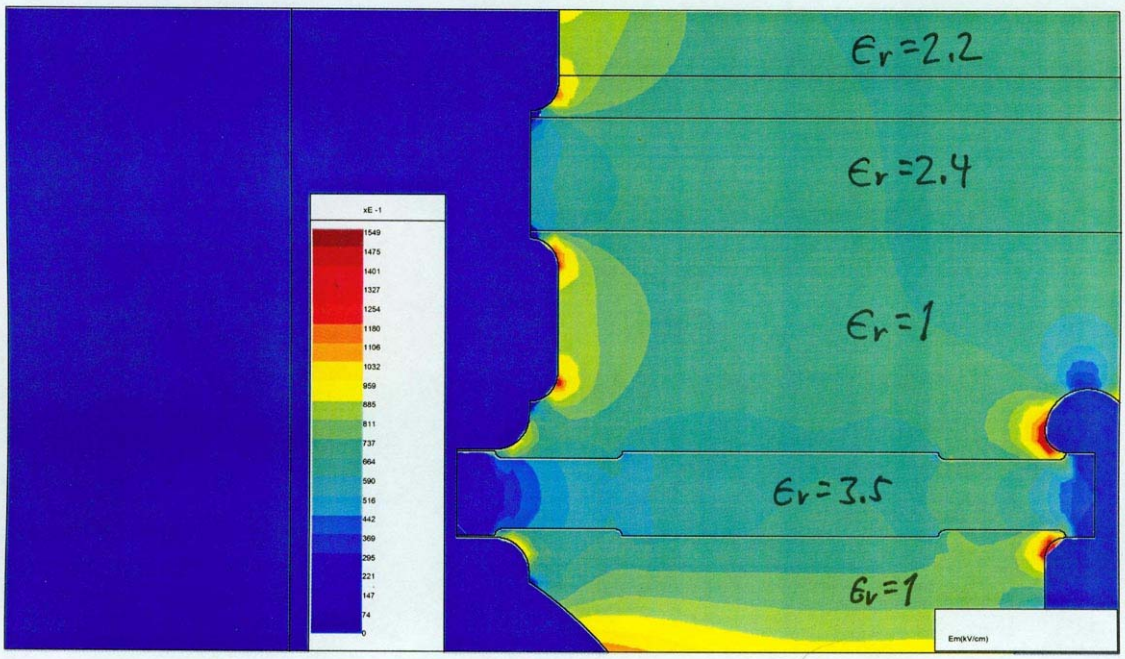

FIG 1b. TRIGGER SECTION WITH PARTIALLY WAISTED SUPPORT RODS

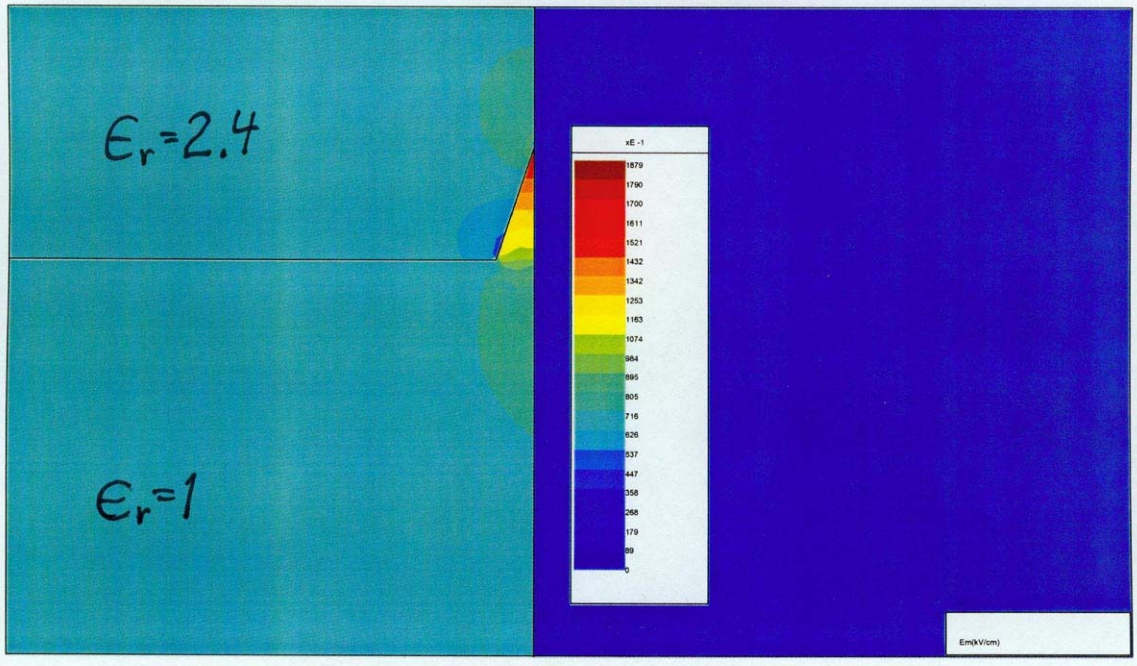

FIG 2. STRESS MODEL OF 15 mil WIDE X 45 mil DEEP CHIP-OUT IN PMMA ENVELOPE AT 3-PT.

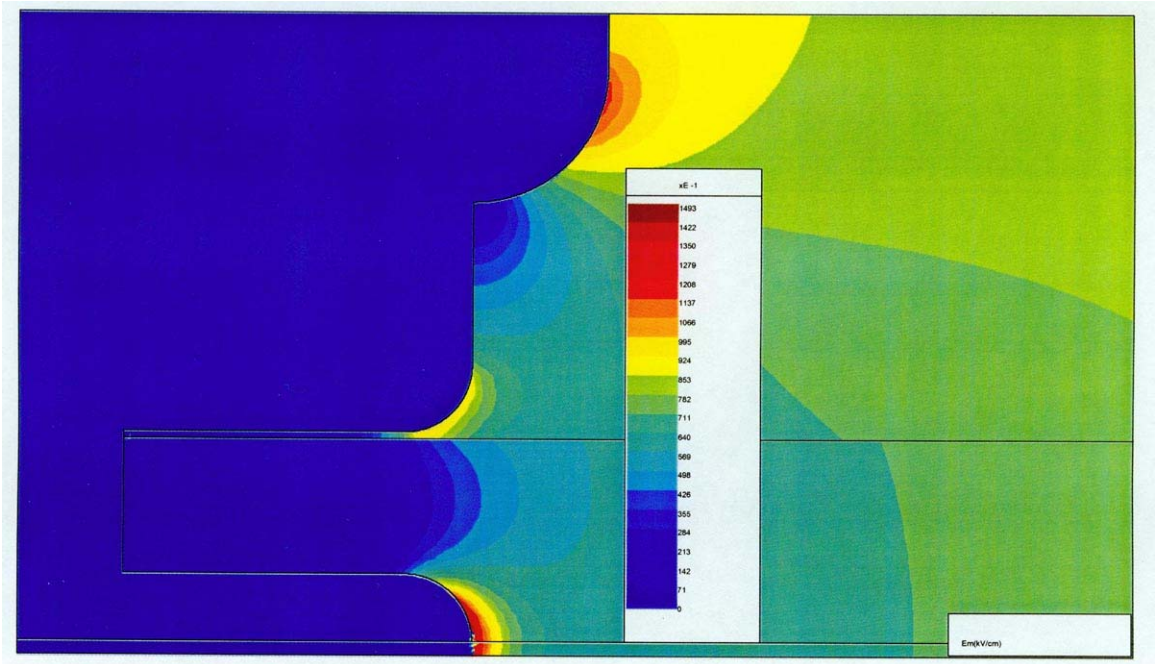

FIG 3. FIELD SHAPER IN PLASTIC, RE-ENTRANT VERSION OF A. NEUBER SUGGESTION.

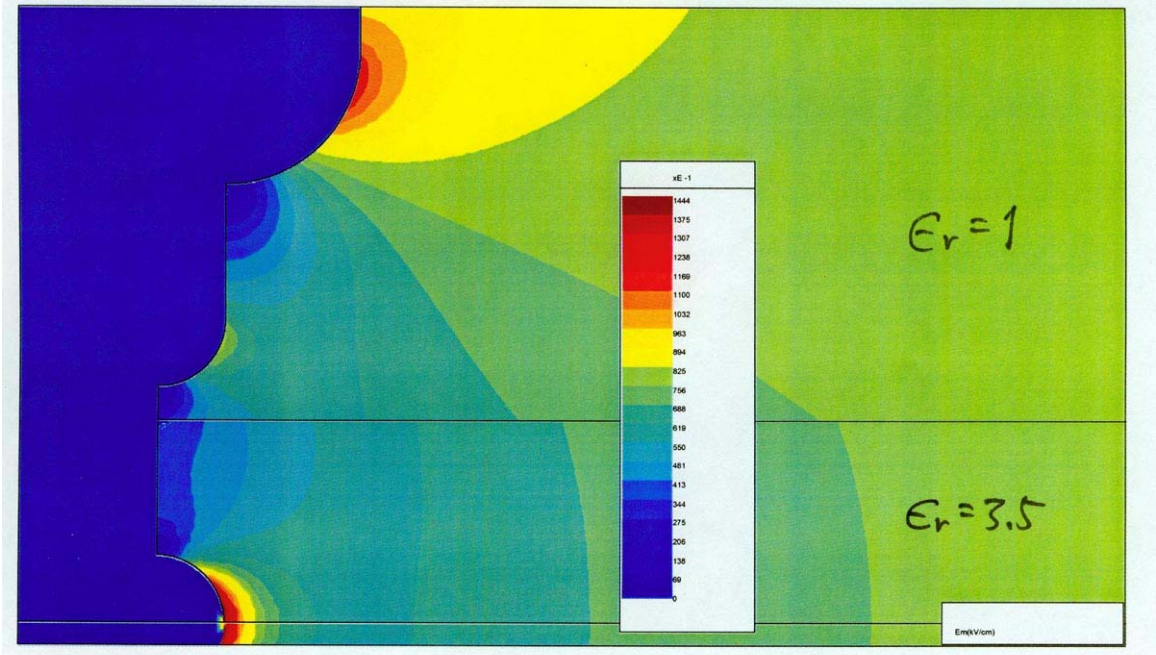

FIG 4. GRADING AND STRESS REDUCTION AT 3-PT BY FIELD SHAPER EMBEDED IN PLASTIC AS IN SUGGESTION BY A. NEUBER.

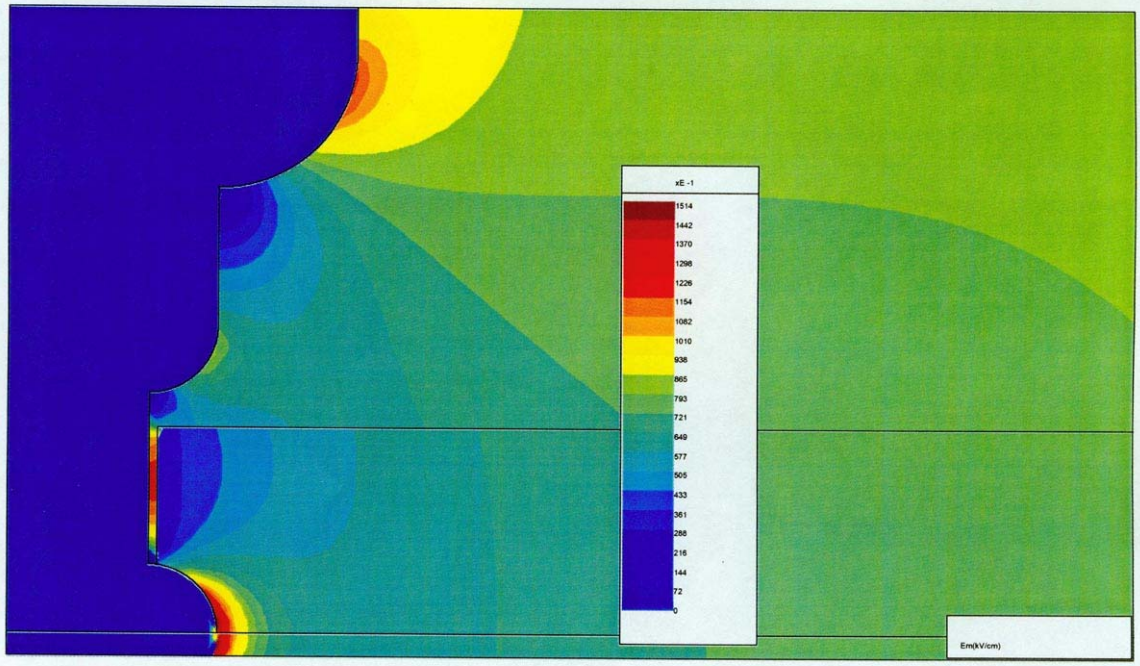

FIG 5. FIELD ENHANCEMENT IN GAP AT END OF PLASTIC FOR INTERNAL FIELD SHAPER DESIGN SUGGESTED BY A. NEUBER.

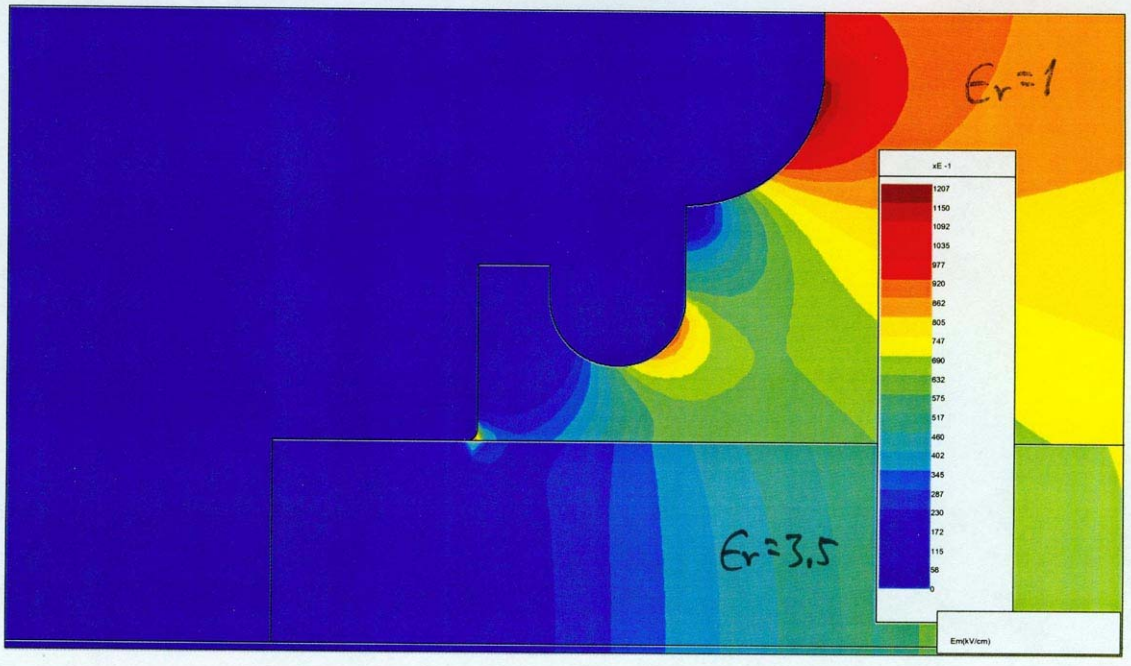

FIG 6 REENTRANT DESIGN SHIELDED BY RETRACTED FALSEWORK (MOMENT BEARING) SUGGESTED BY A. NEUBER.

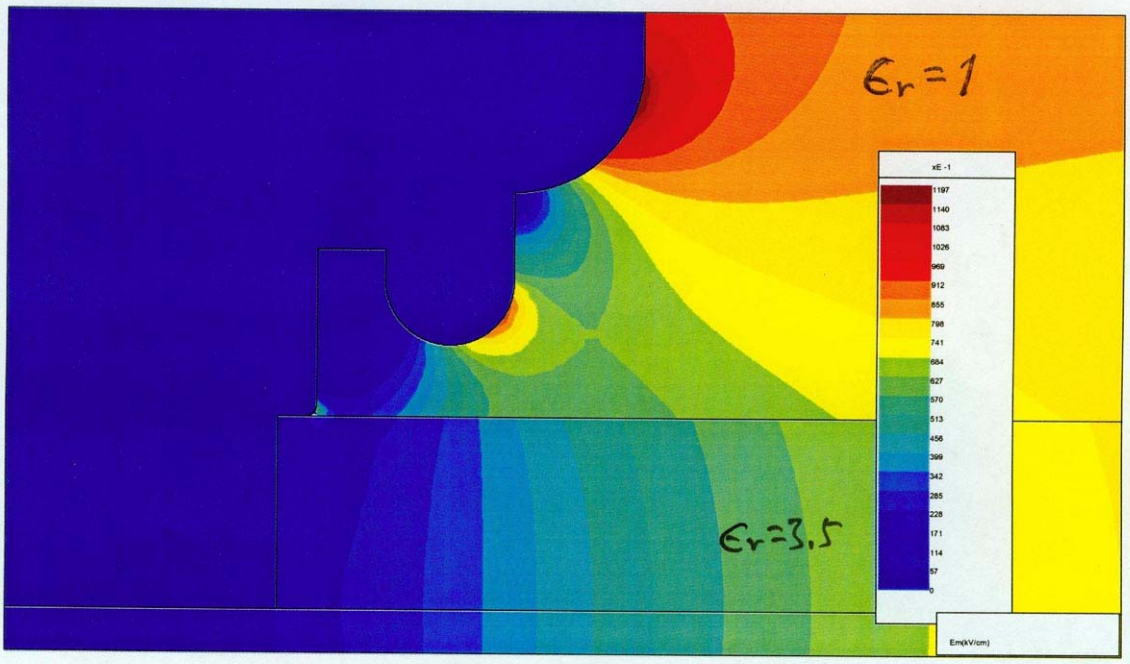

FIG 7. REENTRANT DESIGN SHIELDED BY RETRACTED FALSE WORK (NON-MOMENT BEARING) SUGGESTED BY A. NEUBER

APPENDIX J. Axisymmetric Moments

INTRODUCTION

The potential moments for the axisymmetric modification are formulated.

AXISYMMETRIC SOLUTION

In general we have Poisson's equation

$$\nabla^2\phi = -\rho_v\left(\underline{r}\right)/\varepsilon_0$$

with volume charge density ρ_v and solution

$$\phi\left(\underline{r}\right) = \frac{1}{4\pi\varepsilon_0}\int_V \frac{\rho_v\left(\underline{r}'\right)}{|\underline{r}-\underline{r}'|}dV'$$

The potential for a delta function charge Q satisfies

$$\nabla^2\phi = -Q\delta\left(\underline{r}-\underline{r}'\right) = -Q\frac{1}{\rho}\delta\left(\rho-\rho'\right)\delta\left(\varphi-\varphi'\right)\delta\left(z-z'\right)$$

with solution

$$\phi\left(\underline{r}\right) = \frac{1}{4\pi\varepsilon_0}\frac{Q}{|\underline{r}-\underline{r}'|}$$

The potential for a loop charge of constant line density $q = Q/\left(2\pi\rho'\right)$ satisfies

$$\nabla^2\phi = -q\frac{1}{\rho}\delta\left(\rho-\rho'\right)\int_0^{2\pi}\rho'\delta\left(\varphi-\varphi'\right)d\varphi'\delta\left(z-z'\right) = -\left(q/\varepsilon_0\right)\left(\rho'/\rho\right)\delta\left(z-z'\right)\delta\left(\rho-\rho'\right)$$

$$= -\left(q/\varepsilon_0\right)\delta\left(z-z'\right)\delta\left(\rho-\rho'\right)$$

The solution is then

$$\phi\left(\underline{r}\right) = \frac{1}{4\pi\varepsilon_0}\int_0^{2\pi}\frac{q}{|\underline{r}-\underline{r}'|}\rho'd\varphi'$$

$$= \frac{1}{4\pi\varepsilon_0}\int_0^{2\pi}\rho'd\varphi'\frac{q}{\sqrt{\left(\rho\cos\varphi-\rho'\cos\varphi'\right)^2+\left(\rho\sin\varphi-\rho'\sin\varphi'\right)^2+\left(z-z'\right)^2}}$$

$$= \frac{q\rho'}{4\pi\varepsilon_0}\int_{\varphi}^{2\pi+\varphi}\frac{d\varphi'}{\sqrt{\rho^2+\rho'^2-2\rho\rho'\cos\left(\varphi-\varphi'\right)+\left(z-z'\right)^2}}$$

$$= \frac{q\rho'}{4\pi\varepsilon_0} \int_{-\pi}^{\pi} \frac{d\varphi'}{\sqrt{\rho^2 + \rho'^2 - 2\rho\rho' \cos(\varphi' + \pi) + (z - z')^2}}$$

$$= \frac{q\rho'}{2\pi\varepsilon_0} \int_{0}^{\pi} \frac{d\varphi'}{\sqrt{\rho^2 + \rho'^2 + 2\rho\rho' \cos\varphi' + (z - z')^2}}$$

Using $\cos\varphi' = 1 - 2\sin^2(\varphi'/2)$ gives

$$\phi(\rho, z) = \frac{q\rho'}{\pi\varepsilon_0} \int_{0}^{\pi/2} \frac{du}{\sqrt{(\rho + \rho')^2 + (z - z')^2 - 4\rho\rho' \sin^2 u}}$$

$$= \frac{q}{\pi\varepsilon_0} \frac{\rho'}{\sqrt{(\rho + \rho')^2 + (z - z')^2}} \int_{0}^{\pi/2} \frac{du}{\sqrt{1 - k^2 \sin^2 u}}$$

$$= \frac{q}{\pi\varepsilon_0} \frac{\rho'}{\sqrt{(\rho + \rho')^2 + (z - z')^2}} K(k)$$

where

$$k = \frac{2\sqrt{\rho\rho'}}{\sqrt{(\rho + \rho')^2 + (z - z')^2}}$$

$$k' = \sqrt{1 - k^2} = \sqrt{\frac{(\rho - \rho')^2 + (z - z')^2}{(\rho + \rho')^2 + (z - z')^2}}$$

and

$$K(k) = \int_{0}^{\pi/2} \frac{d\theta}{\sqrt{1 - k^2 \sin^2\theta}}$$

is the complete elliptic integral of the first kind.

GREEN'S FUNCTION

The three-dimensional Green's function satisfies

$$\nabla^2 g = -\delta(\underline{r} - \underline{r}') = -\frac{1}{\rho}\delta(\rho - \rho')\,\delta(z - z')\,\delta(\varphi - \varphi')$$

The axisymmetric Green's function for this problem satisfies

$$\nabla^2 G = -\delta(\rho - \rho')\,\delta(z - z')$$

and is thus given by

$$G = \int_0^{2\pi} \rho' g d\varphi' = \frac{\rho'}{\pi R} K(k)$$

where

$$k = \frac{2\sqrt{\rho\rho'}}{R}$$

and

$$R = \sqrt{(\rho + \rho')^2 + (z - z')^2}$$

GREEN'S THEOREM

The three-dimensional Green's function satisfies

$$\nabla^2 g = -\delta(\underline{r} - \underline{r}')$$

Taking the difference with the Poisson equation

$$\nabla^2 \phi = -\rho_v / \varepsilon_0$$

and integrating over the volume gives

$$\int_V \left(g\nabla^2\phi - \phi\nabla^2 g\right) dV = \int_V \nabla \cdot (g\nabla\phi - \phi\nabla g)\, dV$$

$$= \oint \left(g\frac{\partial\phi}{\partial n} - \phi\frac{\partial g}{\partial n}\right) dS = \phi(\underline{r}') - \frac{1}{\varepsilon_0}\int_V g\rho_v dV$$

where we used the divergence theorem

$$\int_V \nabla \cdot \underline{A} dV = \oint_S \underline{A} \cdot \underline{n} dS$$

Now specializing the final equality to axisymmetric potential and surface charge density

$$\oint_C \left[\left(\int_0^{2\pi} g d\varphi\right)\frac{\partial\phi}{\partial n} - \phi\left(\int_0^{2\pi}\frac{\partial g}{\partial n} d\varphi\right)\right]\rho d\ell = \phi(\rho', z') - \frac{1}{\varepsilon_0}\int\int \rho_s \left(\int_0^{2\pi} g d\varphi\right)\rho d\rho dz$$

where we have taken the two-dimensional axisymmetric potential to satisfy

$$\nabla^2\phi = \frac{1}{\rho}\left(\rho\frac{\partial\phi}{\partial\rho}\right) + \frac{\partial^2\phi}{\partial z^2} = -\rho_s(\rho, z)/\varepsilon_0$$

and using the axisymmetric Green's function equation

$$\nabla^2 G = \frac{1}{\rho}\left(\rho\frac{\partial G}{\partial \rho}\right) + \frac{\partial^2 G}{\partial z^2} = -\delta\left(\rho-\rho'\right)\delta\left(z-z'\right)$$

we see that

$$G = \int_0^{2\pi} \rho' g d\varphi' = \int_0^{2\pi} \rho' g d\varphi$$

Thus we write the above Green's theorem as

$$\oint_C \left[\left(\int_0^{2\pi} \rho g d\varphi\right)\frac{\partial \phi}{\partial n} - \phi\left(\int_0^{2\pi} \rho \frac{\partial g}{\partial n} d\varphi\right)\right] d\ell = \phi\left(\rho', z'\right) - \frac{1}{\varepsilon_0}\int\int \rho_s \left(\int_0^{2\pi} \rho g d\varphi\right) d\rho dz$$

Let us examine

$$\int_0^{2\pi} \rho g d\varphi = \left(\rho/\rho'\right) G$$

Noting that

$$\int_0^{2\pi} \rho \frac{\partial g}{\partial z} d\varphi = \left(\rho/\rho'\right)\frac{\partial G}{\partial z} = \frac{\partial}{\partial z}\left[\left(\rho/\rho'\right) G\right]$$

$$\int_0^{2\pi} \rho \frac{\partial g}{\partial \rho} d\varphi = \left(\rho/\rho'\right)\frac{\partial G}{\partial \rho} = \frac{\partial}{\partial \rho}\left[\left(\rho/\rho'\right) G\right] - G/\rho'$$

gives

$$\int_0^{2\pi} \rho \frac{\partial g}{\partial n} d\varphi = \left(\rho/\rho'\right)\frac{\partial G}{\partial n}$$

Thus Green's theorem becomes

$$\oint_C \left[\left(\rho/\rho'\right) G\frac{\partial \phi}{\partial n} - \phi\left(\rho/\rho'\right)\frac{\partial G}{\partial n}\right] d\ell = \phi\left(\rho', z'\right) - \frac{1}{\varepsilon_0}\int\int \rho_s \left(\rho/\rho'\right) G d\rho dz$$

or alternatively if we define

$$\widetilde{G} = \left(\rho/\rho'\right) G = \frac{\rho}{\pi R} K\left(k\right)$$

$$\oint_C \left[\widetilde{G}\frac{\partial \phi}{\partial n} - \phi\left(\frac{\partial \widetilde{G}}{\partial n} - \underline{n}\cdot\underline{e}_\rho \widetilde{G}/\rho\right)\right] d\ell = \phi\left(\rho', z'\right) - \frac{1}{\varepsilon_0}\int\int \rho_s \widetilde{G} d\rho dz$$

It seems that there is a slight change to the ϕ boundary term from a strictly two-dimensional problem.

Change of Coordinates

Interchanging coordinates

$$G = \frac{\rho'}{\pi R} K(k)$$

$$\oint_C \left[G \frac{\partial \phi}{\partial n'} - \phi \left(\frac{\partial G}{\partial n'} - \underline{n}' \cdot \underline{e}'_\rho G / \rho' \right) \right] d\ell' = \phi(\rho, z) - \frac{1}{\varepsilon_0} \int \int_S \rho_s G d\rho' dz'$$

GREEN'S FUNCTION DERIVATIVES

The radial and axial derivatives are now found. The axial derivative is

$$\frac{\partial G}{\partial z} = -\frac{\rho'}{\pi R^3} (z - z') [K(k) + kK'(k)]$$

$$\frac{\partial \widetilde{G}}{\partial z} = -\frac{\rho}{\pi R^3} (z - z') [K(k) + kK'(k)]$$

The radial derivative is

$$\frac{\partial G}{\partial \rho} = -\frac{\rho'/\rho}{2\pi R} K(k) + \frac{\rho'/\rho}{2\pi R} \left[1 - \frac{2\rho}{R^2} (\rho + \rho') \right] [K(k) + kK'(k)]$$

$$\frac{\partial \widetilde{G}}{\partial \rho} = \frac{1}{2\pi R} K(k) + \frac{1}{2\pi R} \left[1 - \frac{2\rho}{R^2} (\rho + \rho') \right] [K(k) + kK'(k)]$$

The derivatives of the complete elliptic integral are replaced by means of the identity

$$K(k) + kK'(k) = \frac{1}{k'^2} E(k)$$

where

$$k' = \sqrt{1 - k^2}$$

and

$$E(k) = \int_0^{\pi/2} \sqrt{1 - k^2 \sin^2 \theta} d\theta$$

is the complete elliptic integral of the second kind.

INTEGRATION WITH BASIS FUNCTIONS

We now wish to integrate the Green's function gradient with linear basis functions and the Green's function with pulse basis functions. If we take a path C in the ρ, z plane, specified by identifying points (ρ_j, z_j) with each point s_j, and a pulse basis function along the path

$$p_j(s) = 1 \ , \ s_j < s < s_{j+1}$$

$$= 0 \ , \ \text{otherwise}$$

then we can write

$$\rho' = \rho_j + \left(\rho_{j+1} - \rho_j\right) \frac{s - s_j}{s_{j+1} - s_j}$$

$$z' = z_j + \left(z_{j+1} - z_j\right) \frac{s - s_j}{s_{j+1} - s_j}$$

$$|s_{j+1} - s_j| = \sqrt{\left(\rho_{j+1} - \rho_j\right)^2 + \left(z_{j+1} - z_j\right)^2}$$

Let us take $s_j = 0$ and $s_{j+1} = \ell$

$$\ell = \sqrt{\left(\rho_{j+1} - \rho_j\right)^2 + \left(z_{j+1} - z_j\right)^2}$$

$$s = \sqrt{\left(\rho - \rho_j\right)^2 + \left(z - z_j\right)^2}$$

$$s' = \sqrt{\left(\rho' - \rho_j\right)^2 + \left(z' - z_j\right)^2}$$

when (ρ, z) is on the segment then we can take $s = s_0$ such that

$$\rho = \rho_j + \left(\rho_{j+1} - \rho_j\right) \frac{s_0}{\ell}$$

$$z = z_j + \left(z_{j+1} - z_j\right) \frac{s_0}{\ell}$$

Note that

$$\left(\rho - \rho'\right)^2 + \left(z - z'\right)^2 = \left(s_0 - s'\right)^2$$

Let us in general define the projections

$$\underline{e}_s = \underline{e}_\rho \left(\rho_{j+1} - \rho_j\right) / \ell + \underline{e}_z \left(z_{j+1} - z_j\right) / \ell$$

$$\underline{e}_n = \underline{e}_\varphi \times \underline{e}_s = -\underline{e}_z \left(\rho_{j+1} - \rho_j\right) / \ell + \underline{e}_\rho \left(z_{j+1} - z_j\right) / \ell$$

$$\underline{e}_s \cdot \left(\underline{\rho} - \underline{\rho}_j\right) = \left(\rho_{j+1} - \rho_j\right) \left(\rho - \rho_j\right) / \ell + \left(z_{j+1} - z_j\right) \left(z - z_j\right) / \ell = s_0$$

$$\underline{e}_n \cdot \left(\underline{\rho} - \underline{\rho}_j\right) = \left(z_{j+1} - z_j\right) \left(\rho - \rho_j\right) / \ell - \left(\rho_{j+1} - \rho_j\right) \left(z - z_j\right) / \ell = n_0$$

$$s^2 = s_0^2 + n_0^2$$

$$\underline{e}_s \cdot \left(\underline{\rho}' - \underline{\rho}_j\right) = \left(\rho_{j+1} - \rho_j\right)\left(\rho' - \rho_j\right)/\ell + \left(z_{j+1} - z_j\right)\left(z' - z_j\right)/\ell = s'$$

$$\underline{e}_n \cdot \left(\underline{\rho}' - \underline{\rho}_j\right) = 0$$

$$s_0 - s' = \left(\rho_{j+1} - \rho_j\right)\left(\rho - \rho'\right)/\ell + \left(z_{j+1} - z_j\right)\left(z - z'\right)/\ell$$

$$n_0 - n' = \left(z_{j+1} - z_j\right)\left(\rho - \rho'\right)/\ell - \left(\rho_{j+1} - \rho_j\right)\left(z - z'\right)/\ell = n_0$$

$$\left[\underline{e}_s \cdot \left(\underline{\rho} - \underline{\rho}'\right)\right]^2 + \left[\underline{e}_n \cdot \left(\underline{\rho} - \underline{\rho}_j\right)\right]^2 = \left(\rho - \rho'\right)^2 + \left(z - z'\right)^2 = \left(s_0 - s'\right)^2 + n_0^2$$

Note that

$$\lim_{n_0 \to \pm 0} \frac{n_0}{\left(s_0 - s'\right)^2 + n_0^2} = \pm\pi\delta\left(s_0 - s'\right)$$

First Term

$$\int_C p_j\left(s'\right) G ds' = \int_0^\ell G ds'$$

$$G = \frac{\rho'}{\pi R} K\left(k\right)$$

$$k = \frac{2\sqrt{\rho\rho'}}{\sqrt{\left(\rho + \rho'\right)^2 + \left(z - z'\right)^2}}$$

$$\rho' = \rho_1 + \left(\rho_2 - \rho_1\right) s/\ell$$

$$z' = z_1 + \left(z_2 - z_1\right) s/\ell$$

Second Term

$$\frac{\partial}{\partial n} \int_C p_j\left(s'\right) G ds' = \frac{\partial}{\partial n} \int_0^\ell G ds'$$

$$\frac{\partial G}{\partial z} = -\frac{\rho'}{\pi R^3}(z-z')\left[K(k) + kK'(k)\right]$$

$$\frac{\partial G}{\partial \rho} = -\frac{\rho'/\rho}{2\pi R}K(k) + \frac{\rho'/\rho}{2\pi R}\left[1 - \frac{2\rho}{R^2}(\rho+\rho')\right]\left[K(k) + kK'(k)\right]$$

$$\frac{\partial G}{\partial n} = \underline{e}_n \cdot \underline{e}_\rho \frac{\partial G}{\partial \rho} + \underline{e}_n \cdot \underline{e}_z \frac{\partial G}{\partial z}$$

$$= \frac{\partial G}{\partial \rho}(z_{j+1} - z_j)/\ell - \frac{\partial G}{\partial z}(\rho_{j+1} - \rho_j)/\ell$$

$$k' = \sqrt{1-k^2} = \sqrt{\frac{(\rho-\rho')^2 + (z-z')^2}{(\rho+\rho')^2 + (z-z')^2}}$$

On the segment

$$\frac{\partial G}{\partial \rho} = -\frac{\rho'/\rho}{2\pi R}K(k) + \frac{\rho'/\rho}{2\pi R^3}\left[(\rho-\rho')^2 + (z-z')^2 - 2\rho(\rho-\rho')\right]\frac{(\rho+\rho')^2 + (z-z')^2}{(\rho-\rho')^2 + (z-z')^2}E(k)$$

$$= -\frac{\rho'/\rho}{2\pi R}K(k) + \frac{\rho'/\rho}{2\pi R^3}\left[(\rho+\rho')^2 + (z-z')^2 - 2\rho(\rho-\rho') - \frac{8\rho^2\rho'(\rho-\rho')}{(\rho-\rho')^2 + (z-z')^2}\right]E(k)$$

$$\frac{\partial G}{\partial z} = -\frac{\rho'}{\pi R^3}(z-z')\frac{4\rho\rho' + (\rho-\rho')^2 + (z-z')^2}{(\rho-\rho')^2 + (z-z')^2}E(k)$$

$$= -\frac{\rho'}{\pi R^3}(z-z')\left[\frac{4\rho\rho'}{(\rho-\rho')^2 + (z-z')^2} + 1\right]E(k)$$

$$\frac{\partial G}{\partial n} = \frac{\partial G}{\partial \rho}(z_{j+1} - z_j)/\ell - \frac{\partial G}{\partial z}(\rho_{j+1} - \rho_j)/\ell$$

$$= -\frac{\rho'/\rho}{2\pi R}K(k)(z_{j+1} - z_j)/\ell$$

$$+\frac{\rho'/\rho}{2\pi R^3}\left[R^2(z_{j+1} - z_j)/\ell + 2\rho\left\{(\rho_{j+1} - \rho_j)(z-z')/\ell - (\rho-\rho')(z_{j+1} - z_j)/\ell\right\}\right]E(k)$$

$$+\frac{4\rho\rho'^2}{\pi R^3}\frac{\left\{(\rho_{j+1} - \rho_j)(z-z')/\ell - (\rho-\rho')(z_{j+1} - z_j)/\ell\right\}}{(\rho-\rho')^2 + (z-z')^2}E(k)$$

or

$$\frac{\partial G}{\partial n} = \frac{\rho'/\rho}{2\pi R}\left[-K\left(k\right)+E\left(k\right)\right]\left(z_{j+1}-z_j\right)/\ell - \frac{\rho'/\rho}{\pi R^3}\rho n_0 E\left(k\right)$$

$$-\frac{4\rho\rho'^2}{\pi R^3}\frac{n_0}{\left(s_0-s'\right)^2+n_0^2}E\left(k\right)$$

Thus in the limit where the observation point is in the segment $n_0 \to \pm 0$

$$\frac{\partial G}{\partial n} = \frac{\rho'/\rho}{2\pi R}\left[-K\left(k\right)+E\left(k\right)\right]\left(z_{j+1}-z_j\right)/\ell - \frac{1}{2}\delta\left(s_0-s'\right)$$

$$\frac{\partial}{\partial n}\int_C p_j\left(s'\right)G ds' = \int_0^\ell \frac{\rho'/\rho}{2\pi R}\left[-K\left(k\right)+E\left(k\right)\right]\left[\left(z_{j+1}-z_j\right)/\ell\right]ds' - \frac{1}{2}$$

Third Term

If we take

$$\Lambda_j\left(s\right) = \frac{s-s_{j-1}}{s_j-s_{j-1}}\ ,\ s_{j-1}<s<s_j$$

$$= \frac{s_{j+1}-s}{s_{j+1}-s_j}\ ,\ s_j<s<s_{j+1}$$

$$= 0\ ,\ \text{otherwise}$$

$$\int_C \Lambda_j\left(s'\right)\frac{\partial G}{\partial n'}ds' = \int_0^{\ell_j}\frac{s'}{\ell_j}\frac{\partial G}{\partial n'}ds' + \int_0^{\ell_{j+1}}\frac{\ell_{j+1}-s'}{\ell_{j+1}}\frac{\partial G}{\partial n'}ds'$$

$$\ell_j = \sqrt{\left(\rho_j-\rho_{j-1}\right)^2+\left(z_j-z_{j-1}\right)^2}$$

$$\rho' = \rho_{j-1}+\left(\rho_j-\rho_{j-1}\right)s'/\ell_j$$

$$z' = z_{j-1}+\left(z_j-z_{j-1}\right)s'/\ell_j$$

$$\ell_{j+1} = \sqrt{\left(\rho_{j+1}-\rho_j\right)^2+\left(z_{j+1}-z_j\right)^2}$$

$$\rho' = \rho_j+\left(\rho_{j+1}-\rho_j\right)s'/\ell_{j+1}$$

$$z' = z_j + (z_{j+1} - z_j)\, s'/\ell_{j+1}$$

$$s'' = \ell_{j+1} - s'$$

$$\int_0^{\ell_{j+1}} \frac{\ell_{j+1} - s'}{\ell_{j+1}} \frac{\partial G}{\partial n'} ds' = \int_0^{\ell_{j+1}} \frac{s''}{\ell_{j+1}} \frac{\partial G}{\partial n'} ds''$$

$$\rho' = \rho_{j+1} + \left(\rho_j - \rho_{j+1}\right) s''/\ell_{j+1}$$

$$z' = z_{j+1} + (z_j - z_{j+1})\, s''/\ell_{j+1}$$

$$\frac{\partial G}{\partial \rho'} = \frac{1}{2\pi R} K(k) + \frac{1}{2\pi R}\left[1 - \frac{2\rho'}{R^2}(\rho + \rho')\right] \frac{1}{k'^2} E(k)$$

$$= \frac{1}{2\pi R}\left[K(k) + E(k)\right] + \frac{1}{\pi R} \frac{\rho'(\rho - \rho')}{(\rho - \rho')^2 + (z - z')^2} E(k)$$

$$\frac{\partial G}{\partial z'} = \frac{\rho'}{\pi R^3}(z - z') \frac{1}{k'^2} E(k)$$

$$= \frac{1}{\pi R} \frac{\rho'(z - z')}{(\rho - \rho')^2 + (z - z')^2} E(k)$$

$$\frac{\partial G}{\partial n'} = \underline{e}_{n'} \cdot \underline{e}_\rho \frac{\partial G}{\partial \rho} + \underline{e}_{n'} \cdot \underline{e}_z \frac{\partial G}{\partial z}$$

$$= \frac{\partial G}{\partial \rho'}(z_{j+1} - z_j)/\ell - \frac{\partial G}{\partial z'}\left(\rho_{j+1} - \rho_j\right)/\ell$$

$$= \frac{1}{2\pi R}\left[K(k) + E(k)\right](z_{j+1} - z_j)/\ell + \frac{\rho'}{\pi R} \frac{(\rho - \rho')(z_{j+1} - z_j)/\ell - (z - z')\left(\rho_{j+1} - \rho_j\right)/\ell}{(\rho - \rho')^2 + (z - z')^2} E(k)$$

$$= \frac{1}{2\pi R}\left[K(k) + E(k)\right](z_{j+1} - z_j)/\ell + \frac{\rho'}{\pi R} \frac{n_0}{(s_0 - s')^2 + n_0^2} E(k)$$

In the limit $n_0 \to 0$

$$\frac{\partial G}{\partial n'} = \frac{1}{2\pi R}\left[K(k) + E(k)\right](z_{j+1} - z_j)/\ell + \frac{1}{2}\delta(s_0 - s')$$

$$\int_0^{\ell_j} \frac{s'}{\ell_j} \frac{\partial G}{\partial n'} ds' = \int_0^{\ell_j} \frac{s'}{\ell_j} \frac{1}{2\pi R} \left[K(k) + E(k) \right] \left[(z_j - z_{j-1}) / \ell_j \right] ds' + \frac{1}{2} \frac{s_0}{\ell_j} \ , \ 0 < s_0 < \ell_j$$

Fourth Term

$$\frac{\partial}{\partial n} \int_C \Lambda_j(s') \frac{\partial G}{\partial n'} ds' = \frac{\partial}{\partial n} \int_0^{\ell_j} \frac{s'}{\ell_j} \frac{\partial G}{\partial n'} ds' + \frac{\partial}{\partial n} \int_0^{\ell_{j+1}} \frac{\ell_{j+1} - s'}{\ell_{j+1}} \frac{\partial G}{\partial n'} ds'$$

$$\frac{\partial}{\partial n} \int_0^{\ell_{j+1}} \frac{\ell_{j+1} - s'}{\ell_{j+1}} \frac{\partial G}{\partial n'} ds' = \frac{\partial}{\partial n} \int_0^{\ell_{j+1}} \frac{s''}{\ell_{j+1}} \frac{\partial G}{\partial n'} ds''$$

$$\frac{\partial G}{\partial \rho'} = \frac{1}{2\pi R} K(k) + \frac{1}{2\pi R} \left[1 - \frac{2\rho'}{R^2} (\rho + \rho') \right] \frac{1}{k'^2} E(k)$$

$$= \frac{1}{2\pi R} \left[K(k) + E(k) \right] + \frac{1}{\pi R} \frac{\rho' (\rho - \rho')}{(\rho - \rho')^2 + (z - z')^2} E(k)$$

$$\frac{\partial G}{\partial z'} = \frac{\rho'}{\pi R^3} (z - z') \frac{1}{k'^2} E(k)$$

$$= \frac{1}{\pi R} \frac{\rho' (z - z')}{(\rho - \rho')^2 + (z - z')^2} E(k)$$

The quantities $\frac{\partial^2 G}{\partial \rho \partial \rho'}$, $\frac{\partial^2 G}{\partial z \partial \rho'}$, $\frac{\partial^2 G}{\partial \rho \partial z'}$, $\frac{\partial^2 G}{\partial z \partial z'}$ are also needed in the code.

Fifth Term

$$\int_C \Lambda_j(s') \frac{G}{\rho'} \underline{n}' \cdot \underline{e}_{\rho'} ds'$$

$$= \int_0^{\ell_j} \frac{s'}{\ell_j} \left[\frac{1}{\pi R} K(k) (z_j - z_{j-1}) / \ell_j \right] ds' + \int_0^{\ell_{j+1}} \frac{s'}{\ell_{j+1}} \left[\frac{1}{\pi R} K(k) (z_{j+1} - z_j) / \ell_{j+1} \right] ds'$$

The subtraction of this term simply changes the third self term to

$$\int_0^{\ell_j} \frac{s'}{\ell_j} \frac{\partial G}{\partial n'} ds' = \int_0^{\ell_j} \frac{s'}{\ell_j} \frac{1}{2\pi R} \left[E(k) - K(k) \right] \left[(z_j - z_{j-1}) / \ell_j \right] ds' + \frac{1}{2} \frac{s_0}{\ell_j} \ , \ 0 < s_0 < \ell_j$$

APPENDIX K. Electron Avalanche Across Small Gaps

Introduction

In this section we will examine the integral of the primary ionization coefficient (α) in SF_6 across small gaps between the cathode and the dielectric wall of the gas switch. We will impose a field E (nominally $1\times$ $2\times$ and 4×70 kV/cm) outside the gap. The 70 kV/cm field is the expected static field present near the envelope of the switch. Doubling and quadrupling this field accounts for dynamic effects seen in some of the electromagnetic simulations of the switch. The gaps in the gas switch are small compared to the length of the dielectric wall. We expect that the electric field in the gap will be enhanced by a factor of ε_r – the relative dielectric constant of the wall. In these simulations we will be solving a smaller problem where the size of the dielectric may be on the same order as the gap. Therefore, it is important to understand these enhancements so we can scale the field in the smaller problem appropriately.

Let us examine the infinite, parallel-plate geometry shown in Figure K-1.

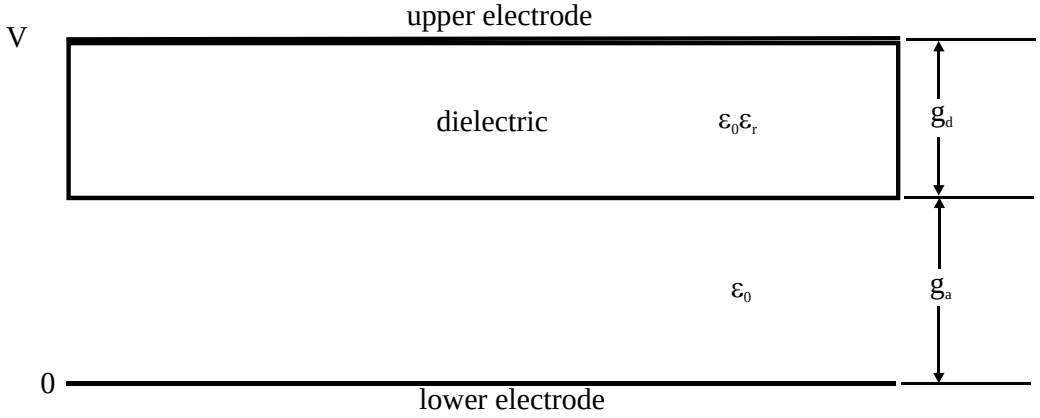

Figure K-1. Parallel plate gap.

If D is the electric flux density, the normal component of which is continuous across the dielectric interface, E_{ag} is the electric field in the air gap

$$E_{ag} = \frac{D}{\varepsilon_0}$$

and E_d is the electric field in the dielectric

$$E_d = \frac{D}{\varepsilon_r \varepsilon_0}$$

The voltage between cathode and anode is

$$\begin{aligned} V &= E_{ag} g_a + E_d g_d \\ &= \frac{D}{\varepsilon_0} g_a + \frac{D}{\varepsilon_r \varepsilon_0} g_d \\ &= \frac{D}{\varepsilon_0} \left[g_a + \frac{g_d}{\varepsilon_r} \right] \end{aligned}$$

rearranging

$$E_{ag} = \frac{V}{\left[g_a + \frac{g_d}{\varepsilon_r} \right]}$$

If there were no dielectric present

$$E_a = \frac{V}{g_a + g_d}$$

so the enhancement of E_{ag} over E_a is

$$\frac{E_{ag}}{E_a} = \frac{g_a + g_d}{\left[g_a + \frac{g_d}{\varepsilon_r} \right]} \qquad \text{(K-1)}$$

if $g_d >> g_a$, like in the actual gas switch, $E_{ag}/E_a \approx \varepsilon_r$ as expected.

Sharp Edge

Our first simulation is for a sharp, dielectric edge, as shown in Figure K-2. The purpose of all these simulations is to determine if the field enhancement in the vicinity of an edge can cause streamering, even though the field in the volume is too small for this to occur. Using $g_a = g_d = 5\mu m$ in Equation K-1, we would expect a field enhancement in the region between the dielectric and cathode and halfway between the two dielectric edges of $E_{ag}/E_a = 1.41$ According to the numerical solution, the actual enhancement is 1.35. To apply these results to the gas switch, which has an enhancement of $\varepsilon_r = 2.4$, we will scale the applied voltage by the factor $2.4/1.35 = 1.8$.

Figure K-3 shows some of the paths that avalanching electrons will take if released from the cathode at various places. The electrons are released from the center of various elements that are on the cathode. The integers printed just above the abscissa are element IDs that are included to make referring to the paths more convenient. We set the pressure at 3.8 atmospheres (2888 Torr = 55.86 psi = 44 psig).

In the following table, the first column is the starting element ID, which can be cross-referenced to Figure K-3. Column 2 is the external field imposed on the gas-switch geometry. In order to maintain the proper field in the gap region, the voltage in the simulation is multiplied by the 1.8 factor discussed above. For example, if the gas switch is excited by a field of 70 kV/cm (column 2), the simulation would have a voltage difference of 1.8×70 volts between electrodes. The next two columns are the result of the integration using two different sources for the SF_6 α data. The data from Reference [K-2] is a best fit to data from several workers in the field. It is better documented and extends over a larger range than Reference [K-1]. The last column is the length of the path that the electron follows. In order to reach streamer threshold, αd must attain a value of approximately 18.

We see that even for the highest field tried (500 kV/cm), streamer threshold is never approached. For

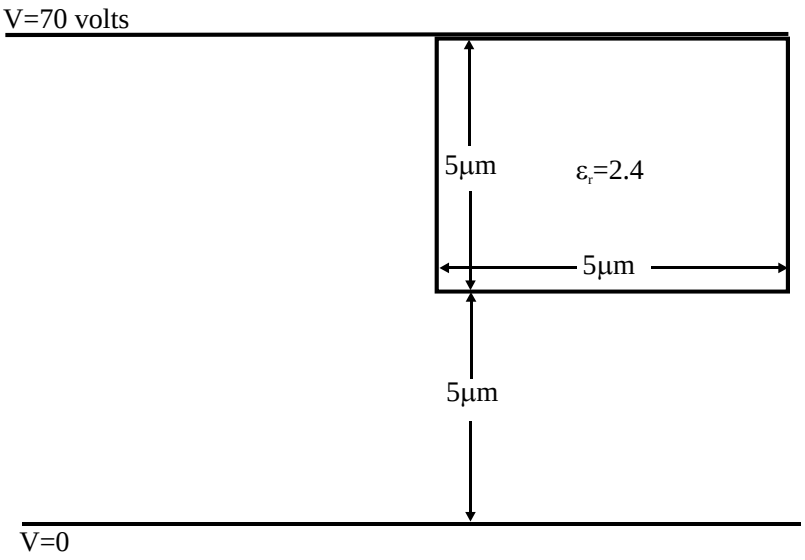

Figure K-2. Sharp dielectric edge.

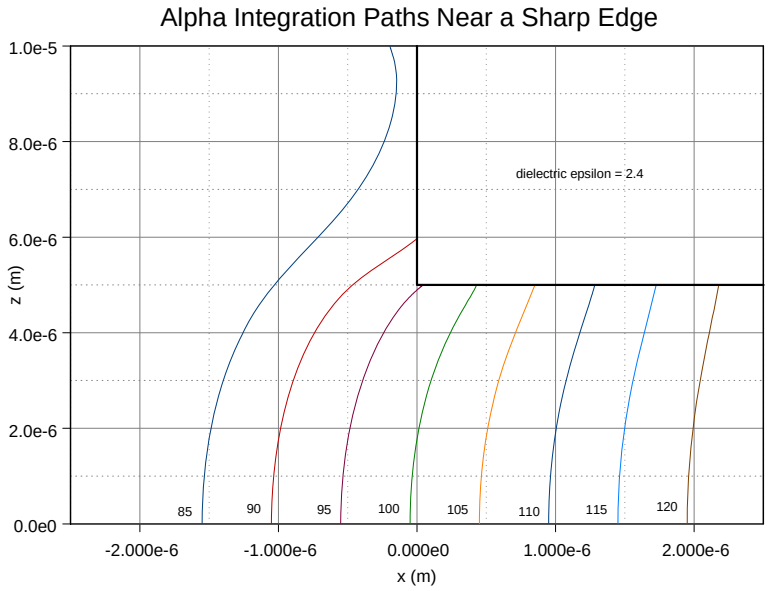

Figure K-3. Integration paths between cathode and sharp edge.

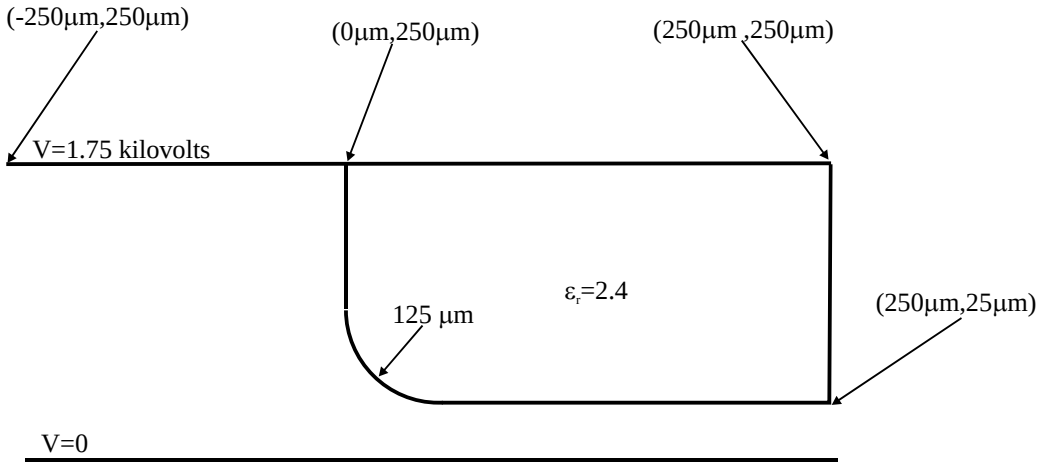

Figure K-4. Rounded edge.

the 70 kV/cm and 140 kV/cm fields, the values of αd are negative, implying that there is no net gain of electrons along this path. The path that approaches the edge (95) has a smaller value of αd than neighboring paths, which implies that the high field in the vicinity of the edge is too localized to overcome the net loss of electrons along the remainder of the path in the smaller field region. The avalanche shows more growth in the uniform field region between the dielectric and the cathode.

Element ID	Field (kV/cm)	αd [K-1]	αd [K-2]	Path (μm)
90	70	-3.37	-5.08	6.13
	140	-0.95	-1.46	
	280	+3.89	+3.33	
	500	+11.49	+9.60	
95	70	-2.61	-3.92	5.06
	140	-0.44	-0.80	
	280	+3.90	+3.37	
	500	+10.72	+8.85	
100	70	-2.54	-3.82	5.03
	140	-0.32	-0.68	
	280	+4.10	+3.54	
	500	+11.06	+9.10	
120	70	-2.42	-3.64	5.00
	140	-0.12	-0.47	
	280	+4.49	+3.88	
	500	+11.73	+9.58	

Rounded Edge

We next looked at a more realistic geometry where the edge has been rounded and the gap is five times as large (25 μm) as shown in Figure K-4. Here we must enhance the field by a factor of 1.13. Figure K-5 shows some of the integration paths.

The following table shows the same type of information as the previous table. A column has been

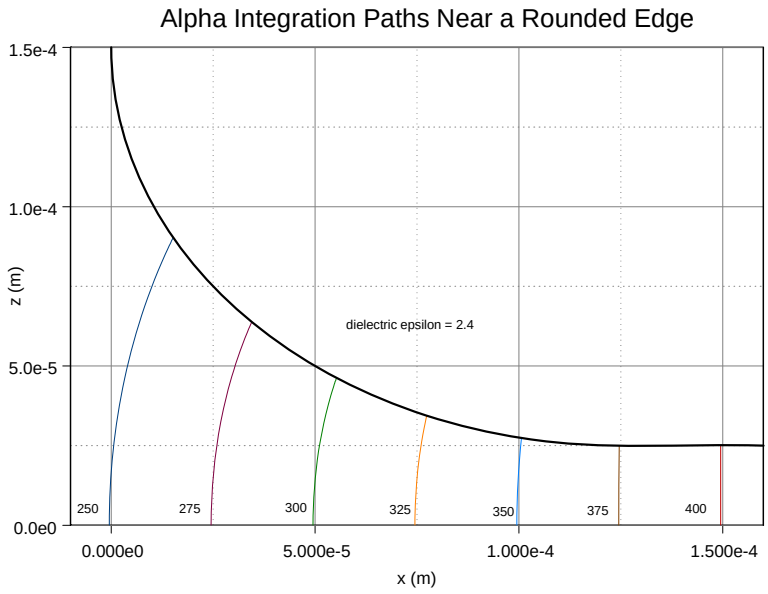

Figure K-5. Integration paths between cathode and rounded edge.

added entitled "Threshold," which documents the distance along the path at which the threshold value of $\alpha d = 18$ was exceeded based on the data from Reference [K-2]. Note that for this geometry, the lowest field that causes streamering is 264 kV/cm. At this field streamering occurs along the element 450 path in the uniform field region. At 280 kV/cm, the longer paths (element 300 and element 350 paths) are streamering as well.

Element ID	Field (kV/cm)	αd [K-1]	αd[K-2]	Path(μm)	Threshold (μm)
250	70	-62.0	-93.8	92.2	
	140	-36.9	-55.2		
	280	+13.2	+6.65		
300	70	-27.5	-41.5	46.8	
	140	-10.8	-15.7		
	280	+22.6	+19.3		43.9
350	70	-13.5	-20.4	27.4	
	140	-1.2	-3.1		
	280	+23.5	+20.3		24.7
450	70	-11.8	-17.8	25.0	
	140	-0.04	-1.8		
	280	+23.5	+20.3		22.3

Beveled Edge

We next looked at a realistic geometry where the edge has been beveled, as shown in Figure K-6. We must again enhance the field by a factor of 1.13. Figure K-7 shows some of the integration paths.

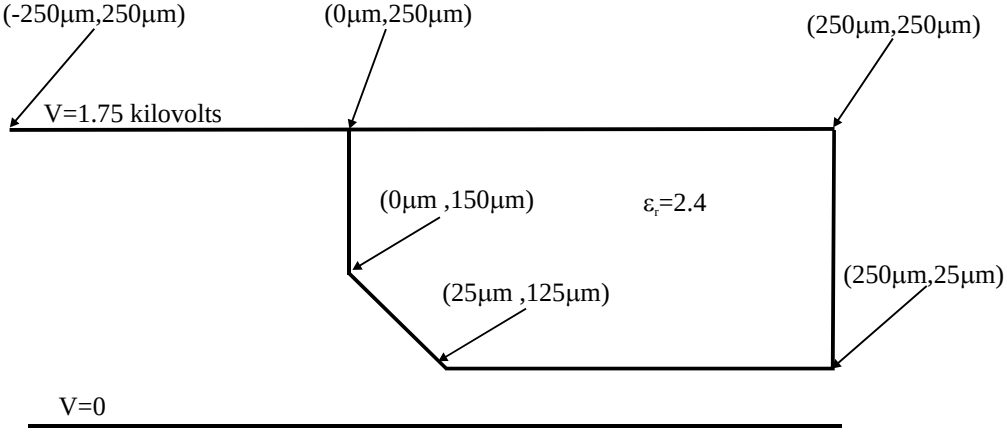

Figure K-6. Beveled edge.

The following table is for the beveled geometry. For this geometry, the lowest voltage that causes streamering is 261 kV/cm along the element 400 path (the uniform field region). The bevel causes the path length to grow more rapidly away from the uniform field region than the rounded geometry and so the paths that will streamer at 280 kV/cm are more confined to the vicinity of the uniform field region (element 350 and higher).

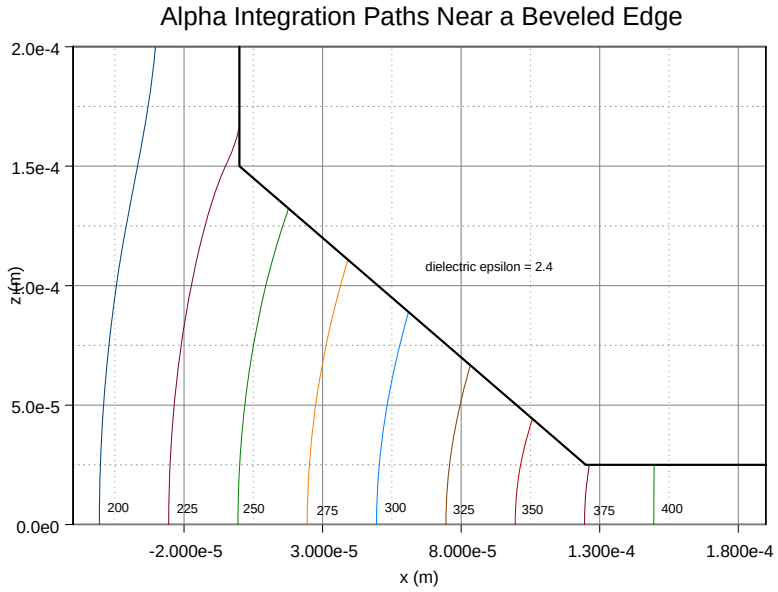

Figure K-7. Integration paths between cathode and beveled edge.

Element ID	Field (kV/cm)	αd[K-2]	Path(μm)	Threshold (μm)
250	70	-139.0	133.9	
	140	-85.6		
	280	+2.7		
300	70	-88.4	89.9	
	140	-47.7		
	280	+14.6		
350	70	-39.1	44.8	
	140	-13.8		
	280	+20.0		39.5
400	70	-17.5	25	
	140	-1.5		
	280	+20.8		22.3

Sharp Edge

Finally, we re-examine the sharp edge geometry with 25− μm gaps as shown in Figure K-8 to compare with the rounded and beveled edges. Again we must enhance the field by a factor of 1.13. Figure K-9 shows some of the integration paths.

The following table is for the sharp edge geometry. For this geometry, the lowest voltage that causes streamering is 276 kV/cm along the element 400 path, which is in the uniform field region.

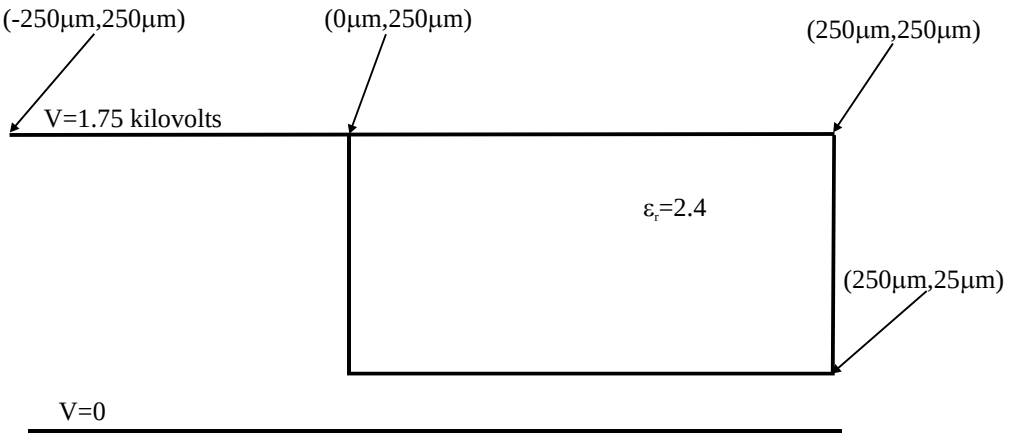

Figure K-8. Sharp dielectric edge.

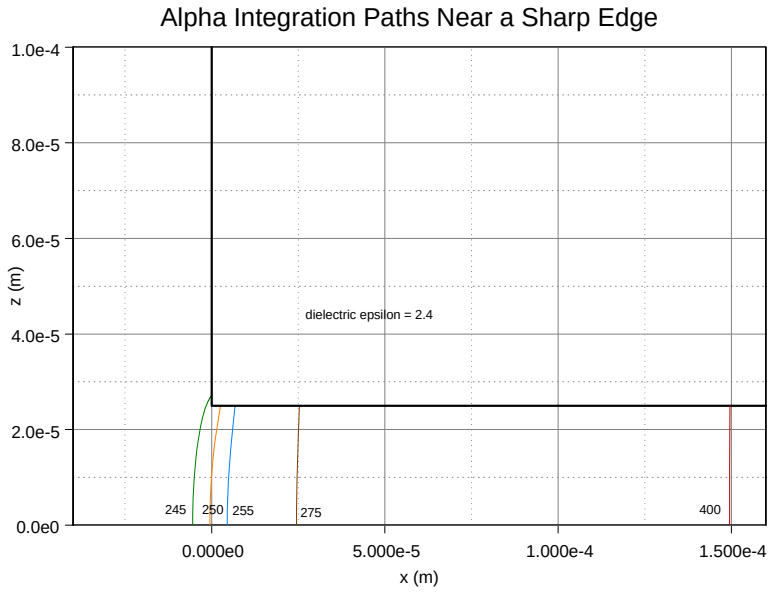

Figure K-9. Integration paths between cathode and sharp edge.

Element ID	Field (kV/cm)	αd[K-2]	Path(μm)
245	70	-25.8	28.2
	140	-11.1	
	280	+9.6	
250	70	-21.9	25.3
	140	-7.7	
	280	+11.5	
255	70	–21.3	25.1
	140	-6.6	
	280	+12.6	
275	70	-20.1	25.0
	140	-4.8	
	280	+15.1	
400	70	-18.5	25.0
	140	-2.8	
	280	+18.6	

Conclusions

In this section we examined how much the static field in the switch (70 kV/cm) needed to be enhanced by dynamic effects in order for an electron avalanche to progress to streamering. We looked at four geometries: a sharp dielectric edge with a 5-μm gap, a rounded dielectric edge with a 25-μm gap, a beveled edge with a 25-μm gap, and a sharp edge with a 25-μm gap. The 5 μm gap needed the field to be enhanced by a factor greater than 4, while the 25-μm gaps needed the field to be enhanced by a factor of around 3.8 (3.8 for round, 3.7 for beveled, and 3.9 for sharp). This implies that for the levels of field expected in the gas switch, only an enhancement due to dynamic effects of greater than 3.8 will cause streamering from the envelope-cathode triple points with 25-μm gaps.

References

[K-1]E. Kuffel, W. S. Zaengl, and J. Kuffel, *High Voltage Engineering Fundamentals*, Butterworth-Heinemann, Oxford, 2000, pp. 345-348.

[K-2]L. G. Christophorou and J. K. Olthoff, "Electron Interactions with SF_6", J. Phys. Chem. Ref. Data, v. 29, no. 3, 2000, pp. 267-330.

APPENDIX L. Electromagnetic Modeling of the Z_{20} Gas Switch

This activity developed a computational model of the gas switch based on a priori breakdown criteria that are applied to all gaps in the switch. The model enables an electromagnetic simulation of the hypothetical system performance, which can then be compared to experimental measurements (electrical by Corley and optical by Woodworth). Iteration of the a priori criteria to better match the measurements should provide boundaries on the physics models. The following summarizes the steps undertaken.

1. Convert TWOQUICK gas switch model to QUICKSILVER.
2. Adjust parameters to obtain cascade run time similar to the experiment range (avg = 37 ns; strong peak at 20 ns with many shots; and out to 70+ ns, with large spread).
3. $\sigma/\sigma_{max}=10^{-6}$ is the level at which cascade gap fields are observed computationally to become noticeably affected by conduction current. With the conductance-channel cross-sectional area (=1.9e-3 m^2) and σ_{max} (= 1.6e4 $[\Omega\text{-m}]^{-1}$), this 10^{-6} point corresponds to a gap conductance of 3.5e-3 Ω^{-1}.
4. Two components of the individual gap breakdown time (and therefore of full cascade time) are incorporated into the prescription for cascade-gap conductivity evolution to enable the study of the effect of each: *aft* (arc formation time) is the streamer production time, [in QUICKSILVER this is the time starting when E exceeds the set threshold (300 kV/cm) to when $\sigma/\sigma_{max} = 10^{-6}$] and *cgt* (conductivity growth time) [the time for the transition from 10^{6} to 10^{-4}]; essentially, the full breakdown time for a single gap is *aft* + *cgt*. (The time to 50% σ_{max} is then *aft* + 3.333 *cgt*.).
5. The following matrix of cases that produce cascade total times (ctt) of 14-28 ns, while distinguishing *aft* from *cgt*, were simulated. These choices of *aft* and *cgt* comprise two sets of 10^{-6} -times (*aft*): 10 ns and 15 ns. For each of these, we test three *cgt* values: 0.3, 3, and 6 ns for total cascade times (ctt) of 14 through 28 ns.

aft	cgt	ctt	aft	cgt	ctt
10	0.3	14	15	0.3	19
10	3	19	15	3	24
10	6	23	15	6	28

6. After the trigger gap closes, the resulting overvoltage wave first hits a group of the nearest n_{group} (~ 4) of cascade gaps and it slowly spreads out to eventually just barely overvolt (and that means threshold test is passed) out to the last cascade gap, at an average rate of an additional gap every 0.2 ns. The choice of *aft* and *cgt* leads to an expected total cascade time, ctt. In this geometry, overvoltage first hits cascade gaps 1 through n_{group} at 191 ns (2 ns after trigger-gap closure). The field threshold is subsequently reached for any gap n at $191+(n-n_{group})*0.2$, for n = 5 to 25. Adding *aft*+*cgt*

to the last cascade gap's (n = 25) time (relative to trigger breakdown) provides a good estimate [= 2+(n-n_{group})*0.2 + *aft*+*cgt*] of ctt. Remember the 10^{-6} and 10^{-4} σ/σ_{max} points that allow this prediction are actually telling us what conductance times are important for predicting cascade behavior. (See point #3.) Because of the sensitivity to the threshold, these results will change for threshold greater than the 300 kV/cm assumed, and this will be explored.

7. Arc formation time *aft* has negligible effect on the inside-gas-housing electric field during and after the cascade closure.
8. For either of the 2 *aft* values considered, increasing *cgt* lessens significantly the housing field (from 500 kV/cm for several ns down to below 300 kV/cm).
9. Once the total switch closure time ctt is correctly modeled in QUICKSILVER it is apparent that we could nevertheless be producing an inaccurate representation of the gas switch if our *aft* and *cgt* parameters are not individually correct even though their sum leads to the experimental ctt. More work is needed matching a single a priori parameter pair to optical measurements on several switches. Are there cases of long *aft* with shorter *cgt* when cascade-housing failure occurs?
10. Key new experimental physics necessary to exploit this finding will show what we can control (e.g., electrode shape, SF_6 pressure, etc.) that would change *cgt* and not just *aft*. If experimentally our ~30 ns ctt is due primarily to *aft* (e.g., *aft* = 29 ns), we will need to learn how to increase *cgt* for less housing field.
11. Annular channel radial width in the QUICKSILVER simulations is 4.06 mm (r_o = 7.698 cm, r_i = 7.291 cm). Experimental observations show the cross-sectional area should be four azimuthally spaced, 1-mm diameter channels. This is not feasible numerically as it would require a sub-cell-sized annular channel thickness. Equivalently, σ_{max} can be reduced by factor of 1/609. Eventually we might consider dynamic channel thickness during *cgt* phase from 0.1 to 1 mm.
12. Point 11 leads to our plan to generate the time dependence of σ/σ_{max} not by explicit time function with adjustable parameters (even though they were physically motivated choices), but by a higher-level physical model, perhaps Braginskii-based, that would self-adjust for experimental independent variables such as gas pressure and electric field, etc.

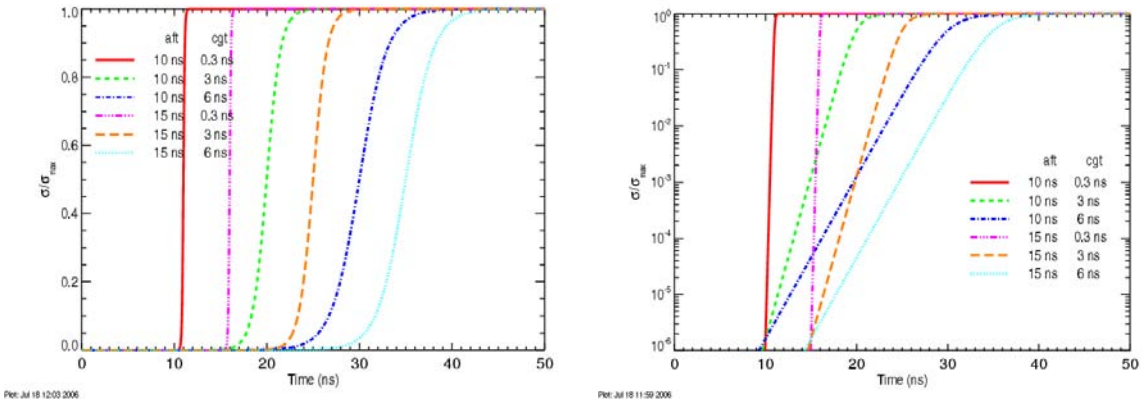

Figure L-1. Linear and log-scale plots of the σ/σ_{max} time dependence for the six combinations of aft and cgt.

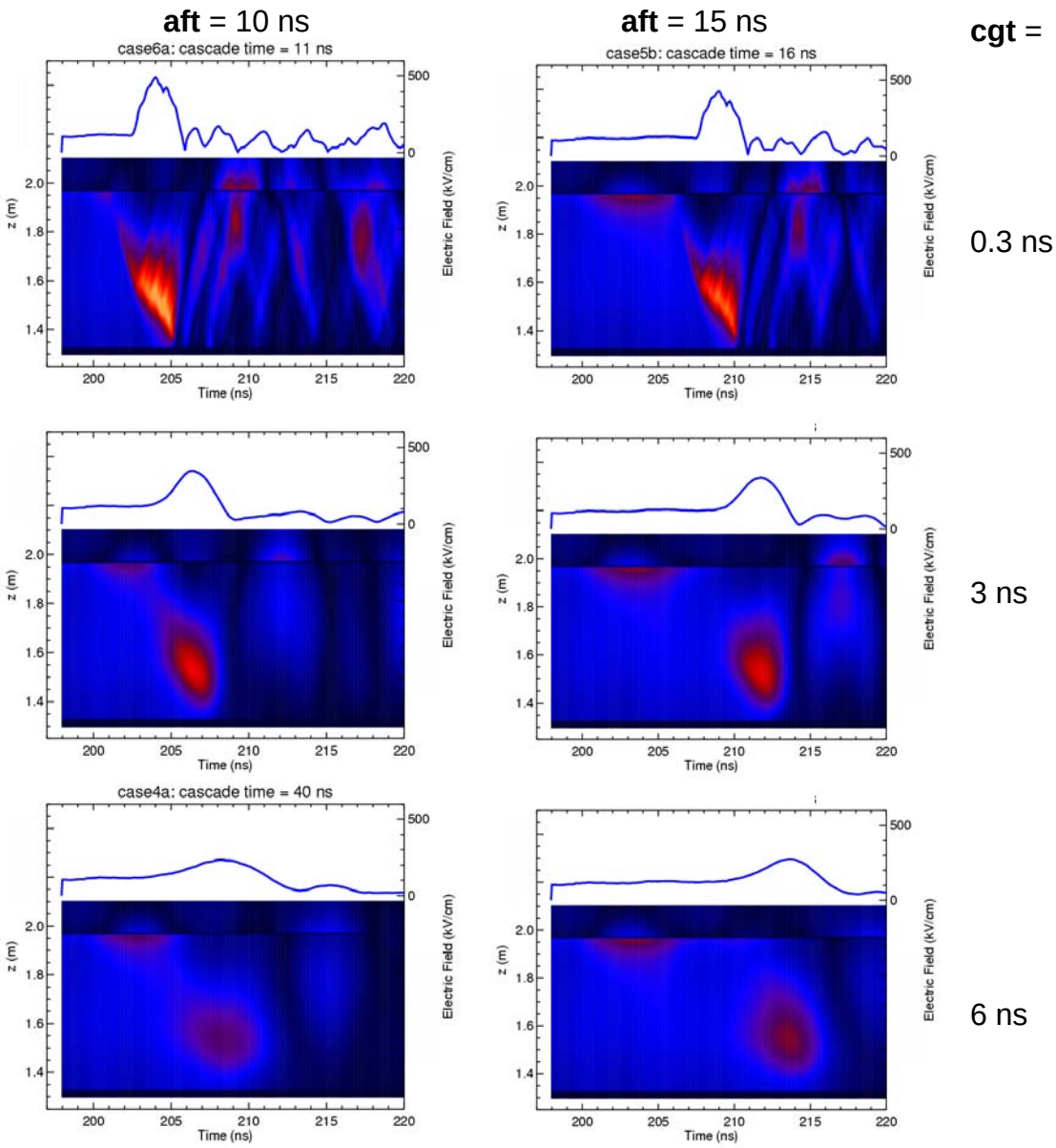

Figure L-2. Simulated streak images of the total electric field at the inside surface of the gas housing for the six cases of aft and cgt. Note that the second case, second row (aft = 15, cgt = 3), and the first case, third row (aft = 10, cgt = 6) both exhibit roughly the same total cascade times, yet also have different housing field strengths. Longer cgt, for the same cascade time, leads to less housing field.

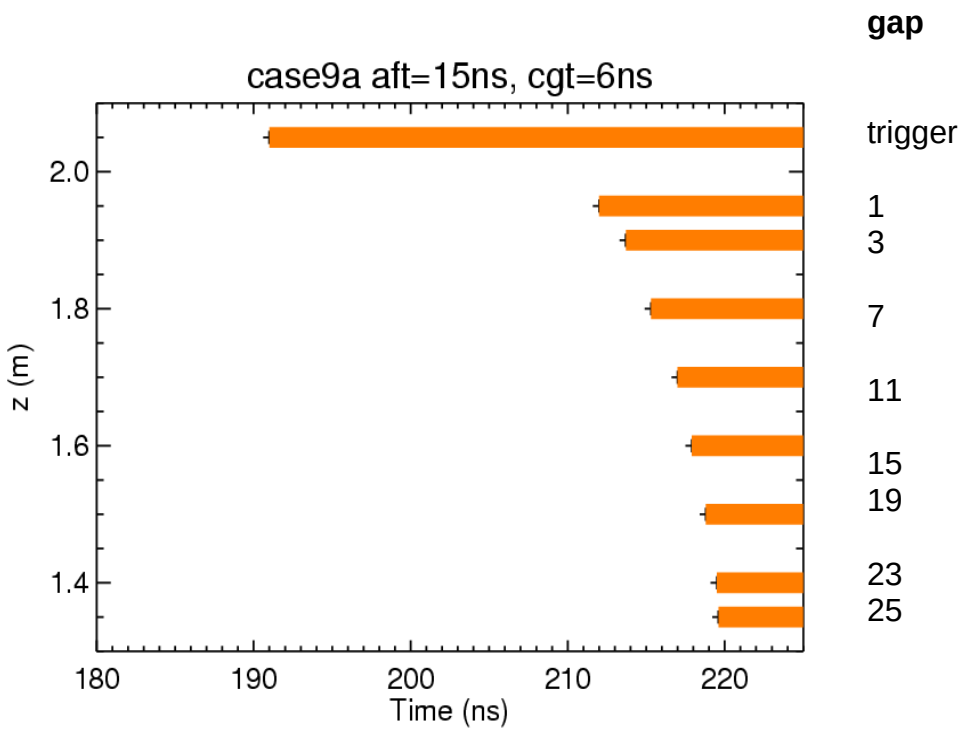

Figure L-3. A plot of typical cascade breakdown dynamics. Each bar corresponds to a particular gap. The time at the start of the bar is the time when the axial electric field exceeds the threshold (300 kV/cm) plus aft+cgt for the gap (i.e., the time when the axial field has first dropped to near zero). These times appear to match Joe Woodworth's light-output data (for a ctt = 30 ns case, Z_{20} Shot 1304) quite well. The trigger-to-cascade-gap#1 time is 17-20 ns (case 9a is 21 ns), and the ctt is 30 ns (28 ns for case 9a) gap/ns in this view increases away from the trigger. It is difficult to resolve the slightly positive rate increase unless cgt is significant.

APPENDIX M. Computational Modeling of High Pressure Gases in External Electric Fields

M.1 Introduction

This report summarizes progress in FY 2006 on computational modeling efforts directed towards fundamental processes associated with the breakdown of high-pressure gases. Voss Scientific personnel, in collaboration with Dr. L. Warne and Dr. R. Jorgenson at Sandia National Laboratories, have developed new computational models of gas breakdown for use in particle-in-cell (PIC) codes. These modeling efforts are key first steps in comprehensive and fundamental studies of the physics of high-pressure gas switches. The computational algorithms described in this report are of two types: a Monte Carlo type collision (MCC) model whereby PIC macro-particles undergo random elastic and inelastic interactions, and a semi-fluid scattering model.

In Section M.2, a description of a newly implemented attachment algorithm, important for electronegative gases such as SF_6, is given along with a detailed description of the modeling assumptions that are made to make this model computationally tractable. The details of the cross-section compilations for H_2 and SF_6 for use in the MCC algorithm are given in Section M.3. This section also includes the results of detailed swarm calculations using these cross sections and comparisons with experimental data. In Section M.4, the existing implicit collision model in the PIC code LSP is used to carry out two-dimensional 2D (r,z) streamer simulations. These simulations track the formation and evolution of a streamer from a small seed electron population in different applied electric fields. Swarm calculation results in H_2 are compared with experimental data in Section M.4.1. Several improvements were made to the algorithm as part of this study and overall the agreement with the MCC model is demonstrated. Conclusions are given in Section M.5. We note that streamer calculations using the MCC model are presently being carried out for both H_2 and SF_6. The results of these simulations will be given in a future report.

H.2 Attachment algorithm

We have previously developed an MCC model for LSP that has been used to simulate breakdown in weakly-ionized gases.[1,2] This model, including electron elastic, inelastic, and ionization processes with neutrals, was benchmarked for noble gases, such as He and Ar, in which no significant electron sink is present. For an electronegative gas such as SF_6, electron attachment processes play a key role in inhibiting breakdown at low field values. To allow for SF_6 modeling by LSP, we have developed an attachment algorithm that has been added to the MCC model previously developed for noble gases. The algorithm has also been implemented to work with the more approximate scattering model in LSP, but has not yet been tested.

Initially, a small code was written to do 0D-3V swarm simulations of electrons in a neutral SF_6 background and with a uniform electric field. In the initial MCC swarm code, ion products are not followed. However, in general it is necessary to track the ions to do self-consistent PIC simulations. The Monte-Carlo attachment algorithm has been ported into LSP with some notable simplifications:

1. LSP inputs only 1 attachment channel for each neutral species ($e + X \rightarrow X^-$). This simplifies the input, and keeps the number of ion species down. For example, for SF_6 the three significant attachment cross sections (for production of the negative ions SF_6^-, SF_5^-, and F^-) are summed to get a total attachment cross section, and all ion macro-particles are created as SF_6^-. Unless detailed ion dynamics become important this simplification should be adequate for a weakly ionized gas. The algorithm may be easily extended to a more general form allowing for multiple attachment processes if necessary.

2. The neutral temperature is not considered in the LSP-MCC implementation. This is fine if the electrons have velocities much larger than the neutrals. Since the neutrals are usually around room temperature ($v \sim 10^{-5}\ c$) and the electrons have energies of several eV ($v \sim 0.001$--$0.005c$) for large applied fields, this simplification is justified.

3. The attachment algorithm works with both the MCC model and the approximate scattering algorithm also implemented in LSP for inter-species collisions. The attachment algorithm has only been tested with the MCC model.

4. Recombination (a second-order effect in a weakly ionized gas) and electron detachment of negative ions (believed to occur on very long time scales) are not included at present.

We also note here that ion neutral collisions can also be modeled by the MCC model in LSP, but this has not yet been tested. Ion collisions are neglected in swarm calculations described below.

When running the MCC algorithm with attachment, two interaction input files are now necessary. The usual discrete events interaction file gives electron-neutral cross sections for elastic, ionization, and inelastic processes as a function of energy, as well as details on energy loss by the electron in an inelastic collision. Details on this file and its format can be found in Reference 1. The additional attachment interaction input file contains cross-section data as a function of energy for electron-neutral attachment processes that generate negative ions.

The full MCC model for electron-neutral collisions, including ionization and attachment channels, allows for accurate kinetic simulations of weakly ionized plasmas.[3] One major drawback to using the MCC model is the need to resolve to the electron-neutral collision frequency. The approximate scattering algorithm allows LSP to be run at time steps that exceed the collision frequency, although with a loss of detailed kinetic information regarding the electron distribution. This algorithm assumes like particles scatter off locally constructed drifting Maxwellian distributions. Collisions between dissimilar particles such as between electrons and neutrals are handled with a lumped frictional force and Ohmic heating term. By contrast, going to the MCC algorithm may require a prohibitively small (sub-picosecond) time step in large simulations. It is of great interest to assess the relative accuracy of the two scattering methods. One important goal is to find and validate an algorithm that may sacrifice some detailed kinetic information, but that provides approximately the right transport coefficients when with used a larger time step. Ultimately the use of the MCC model or an approximate alternate, of course, requires good cross-section data for gases of interest. Cross-section data for H_2 and SF_6 are considered in more detail in the following section.

M.3 Cross-Section Data for H_2 and SF_6

While some measured data is available for gases of interest, cross sections cannot be directly measured for all important processes. As an example, for SF_6, the excitation cross section is not well known, although the threshold is known to be around 10 eV.[4] But the transport properties, such as drift velocity, temperature, and effective ionization rates of electron swarms in a gas, can be readily measured. One common technique for determining a self-consistent set of cross sections for a gas is to numerically solve for the transport coefficients while iteratively adjusting the unknown cross sections (a lumped excitation cross section in the case of SF_6) until good agreement is found with measured data. This is not a trivial procedure as the cross sections are, in general, functions of electron energy. So both the functional shape and magnitude of the cross sections can be adjusted to match the transport coefficients over some range of applied electric field values. Typically, the numerical values of the transport coefficients are calculated by a Boltzmann code. For this work, the authors used the EEDF (an acronym for electron energy distribution function) code.[5] Like many similar codes described in the literature, EEDF solves iteratively for the steady-state electron energy distribution function *f(E)* where *E* is the electron energy. The transport coefficients are then calculated by appropriate integrals of the distribution function. Note that the electron number density can increase or decrease exponentially, but the shape of the distribution function and values of the transport coefficients are time-independent. The standard method of solution is to expand the distribution function in spherical harmonics and then to truncate the expansion to two terms: an isotropic leading term, and a small anisotropic correction term that is due to the applied field. Clearly this perturbative treatment is only valid when the electron drift velocity is small compared to the thermal velocity. But a more careful analysis[6] of the higher-order terms in the expansion shows that the two-term expansion is, in addition, only valid for electron energies for which the elastic cross section is much larger than the cross section for inelastic processes. If these conditions are not satisfied, higher-order terms in the expansion are required.[7] An alternate method is to directly simulate a swarm of particles using a PIC code. We used LSP to push electron macro-particles in a background neutral gas with a uniform applied electric field. The simulations were performed in a single cell. The particles were confined to the cell by suppressing the position push. Since the particles are not allowed to move spatially, spatial transport coefficients like the diffusion coefficient cannot be determined. Note also that only the applied electric field is present; the particle charges and currents were not allowed to feed back onto the fields. The electron neutral scattering was modeled by the MCC algorithm described in the previous section. The LSP-MCC swarm simulations must push electron macro-particles in the time-domain for a given set of initial conditions until steady-state conditions are achieved. As mentioned above, the MCC algorithm also requires a time step small enough to resolve the collision times of the scattering processes. For this reason the particle simulations are quite lengthy compared to the Boltzmann code. But the MCC algorithm does not make any assumptions *a priori* about the distribution function and should generate the correct kinetic behavior to all orders for an adequately small time step and large enough particle number. The results of the two methods should be the same as long as the two-term expansion is valid.

The transport coefficients that will be considered here are the electron drift velocity v_D, temperature T_e, and the ionization, attachment, and effective ionization rates. These rates are

denoted α, η, and $\bar{\alpha}$, respectively, and all are proportional to the neutral density n_n, which is taken to be constant for a weakly ionized gas. Integrating the Boltzmann equation over energy gives a rate equation for electron number density n_e

$$\frac{d}{dt} n_e = (\alpha - \eta) n_e = \bar{\alpha} n_e ,$$

which gives an exponential time dependence

$$n_e \propto e^{\bar{\alpha} t} .$$

The number of positive and negative ions n_{pi} and n_{ni} are then given by

$$\frac{d}{dt} n_{pi} = \alpha n_e ,$$
$$\frac{d}{dt} n_{ni} = \eta n_e .$$

An initial seed population of electrons will either increase or decrease exponentially depending on the sign of the difference of the ionization and attachment rates. All the transport coefficients v_D, T_e, α, η, and $\bar{\alpha}$ are functions of E/n_n where E is the local electric field strength (actually for small enough field values the transport coefficients are also functions of the neutral temperature, but this regime is not considered here). The data for E/n_n are generally given in units of Townsends, where 1 Td = 10^{-17} V-cm^2.

M.3.1 Cross Sections for H2

Since streamer calculations have been performed for H_2 using the approximate scattering model, it is of interest to develop interaction data for the MCC algorithm for the same gas. The two scattering algorithms can then be benchmarked. The EEDF code has a database of cross sections for most gases of interest including H_2. For most of the processes a reference is included for the cross-section data. However, many of these references cite preprints. The H_2 database contains an attachment cross section, but it is limited to a very narrow energy band and is about six orders of magnitude smaller than the elastic cross section in the same energy range. For this reason, absorption is neglected entirely for this gas. In addition to elastic and ionization cross sections, the database has several different excitation and vibrational cross sections included, both of which are treated as general inelastic collisions by the MCC algorithm in LSP. The electron loses the threshold energy for the process and is then scattered elastically. The algorithm does not track the excited or vibrational states of the neutrals. This omission is justified only for a weakly ionized plasma. Several of the excited states have threshold energies that are very similar. For simplicity some of these processes have been lumped together. Note that inelastic processes that have very different thresholds should not be summed. The MCC algorithm needs to differentiate between the processes to determine which threshold energy to subtract from the electron.

A rotational cross section is also given, but it has a very low threshold and acts effectively only as a small addition to the elastic cross section. For this reason this process is dropped. A measured cross-section for a dissociation process ($e + H_2 \rightarrow e + H + H$) is also included in EEDF.[8] From our calculations, it has been determined that inclusion of the dissociation process in the interaction tables gives avalanche rates that are significantly smaller than published experimental results. For this reason the dissociation process is dropped as well. It is possible that the remaining hydrogen cross sections have already been modified in EEDF in some ad hoc way to include the effect of the dissociation process. It has energy dependence similar to the excitation processes. If the excitation cross sections were to be elevated somewhat it could roughly compensate for the missing dissociation process. This reasoning is, of course, quite speculative. We have, in any case, chosen to take a pragmatic approach to the issue for the present, namely, cross sections that produce transport coefficients in agreement with experiment are retained.

Figure M-1 shows the cross-section data used in the LSP swarm simulations and EEDF runs. Figure M-1(a) compares the elastic cross section and the sum of all the inelastic processes (including ionization). Recall that the two-term expansion of the Boltzmann equation is valid when the elastic cross section is much larger than the inelastic. For H_2 this is seen to be the case for energies up to several tens of eV. Figure M-1(b) shows the total collision frequency as a function of energy

$$\frac{\nu_{Tot}(E)}{c} = n_n \sigma_{Tot} v = n_n \sigma_{Tot} \sqrt{\frac{2E}{m_e c^2}} ,$$

where σ_{Tot} is the sum of all cross sections. Since the total collision frequency needs to be resolved by the LSP-MCC algorithm, the plot shows that for electrons up to a few tens of eV the constraint on the time step is

$$c\Delta t << 10^{-2} \text{ cm} .$$

Figure M-2 shows the swarm results from an LSP simulation for H_2 at 100 Td. A time step ($c\Delta t$) of about 10^{-4} cm was used, and the simulation was started with 10,000 macro-electrons. Figure M-2(a) shows the electron temperature (in eV) as a function of time. The LSP simulation is run in the time domain with some initial electron distribution until a steady-state is reached (generally on the order of a few hundred collision times ν_{Tot}^{-1}). EEDF gives only steady-state temperature without any transient behavior. The EEDF result (3.23 eV) is shown as a vertical line in the figure. Figure M-2(b) shows the results for the drift velocity, and Figure M-2(c) shows the electron energy steady-state distribution function

$$g(E) = \sqrt{E}\, f(E) ,$$

with the normalization condition

$$\int_0^\infty g(E) dE = 1 .$$

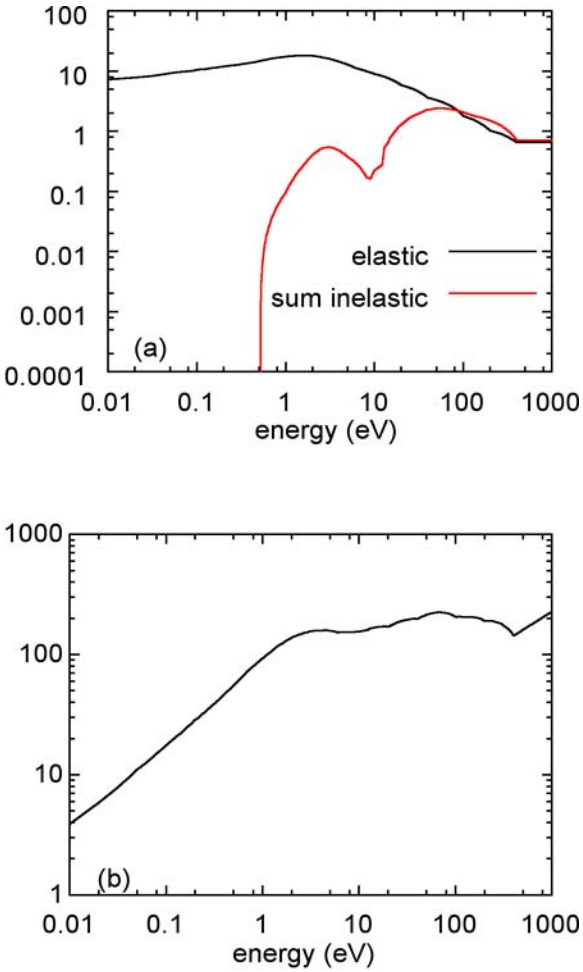

Figure M-1. Cross-section data for H_2 used in LSP and EEDF to calculate transport coefficients. (a) Elastic cross section compared to the cross section for the sum of all inelastic processes. The elastic cross section is much larger until around 100 eV. (b) Total collision frequency as a function of energy. The time step required to resolve the collision frequency will need to be significantly smaller than 10^{-2} cm.

For a Maxwellian electron distribution, $f(E) \propto \exp[-E/T_e]$. The LSP distribution is obtained statistically, that is, macro-electrons are binned in energy. The distribution function results show that there are essentially no electrons above about 20 eV. For this energy range the two-term Boltzmann expansion should be applicable (see Figure M-1(a)). Figure M-2(d) shows a plot of the log of the electron number density in the simulations. The steady-state slope gives an effective ionization rate of $\overline{\alpha} = 0.71\,\mathrm{ns}^{-1}$. Overall there is very good agreement between the LSP and EEDF results, although the electron temperature is a few percent higher for the LSP run.

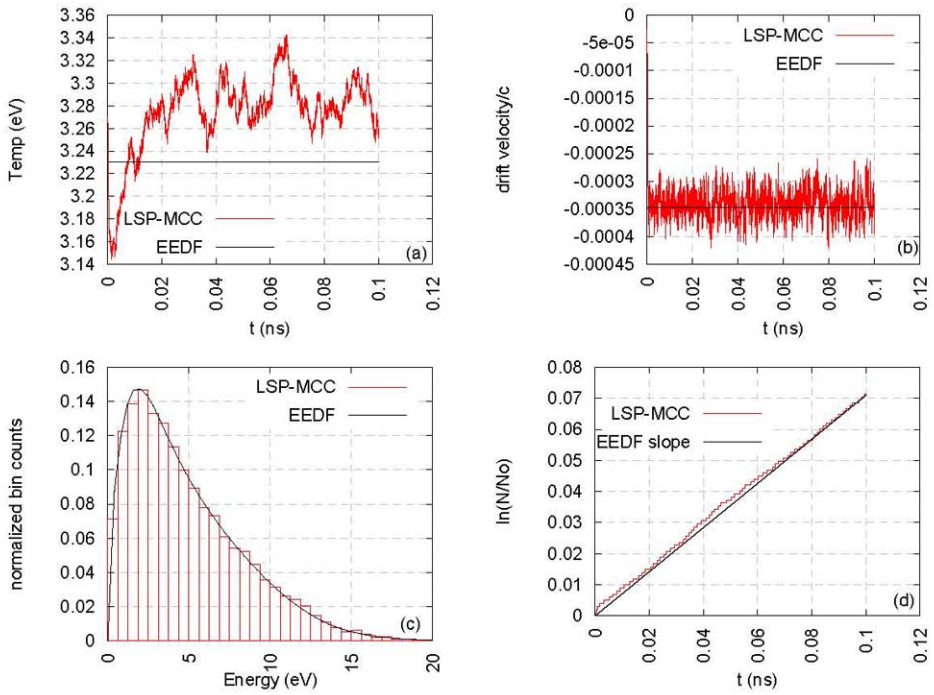

Figure M-2. Results from LSP and EEDF for H_2 at 100 Td. (a) Electron temperature in eV, (b) Drift velocity (normalized by c), (c) Electron energy distribution function, (d) Log of electron number density.

Figures M-3 and M-4 show comparisons of LSP and EEDF results for H_2 at STP in the range 10-160 Td with experimental data tabulated by Engelhardt and Phelps.[9] Figure M-3 shows the drift velocity (denoted "w" on the plot). The data in Engelhardt's paper[9] is for H_2 at 77K while the LSP and EEDF results are for STP; however, above 10 Td the transport coefficients do not depend on neutral temperature. Figure M-3 also shows the characteristic energy ε_K , a transport coefficient not directly calculated by LSP. Figure M-4 shows the LSP and EEDF results for ionization rate compared with the experimental data. Note that Engelhardt and Phelps plot normalized ionization rate "α_I / N" in units of cm^2. In this report we have defined ionization rate α in units of inverse time. This difference only results from slightly different definitions for the transport coefficient in question. To compare the LSP and EEDF directly with the data in Figure M-4, we have plotted $\alpha / v_D n_n$ in cm^2. Figure M-4 also shows experimental data for the excitation rate "α_e / N" which was not calculated for the LSP and EEDF results, as well as data for a D_2 gas. The experimental references can be found in the Engelhardt paper.[9] Although a limited amount of data was collected, both the LSP and EEDF results are seen to be in good agreement with experimental data in the parameter space that was considered for the cross sections discussed above.

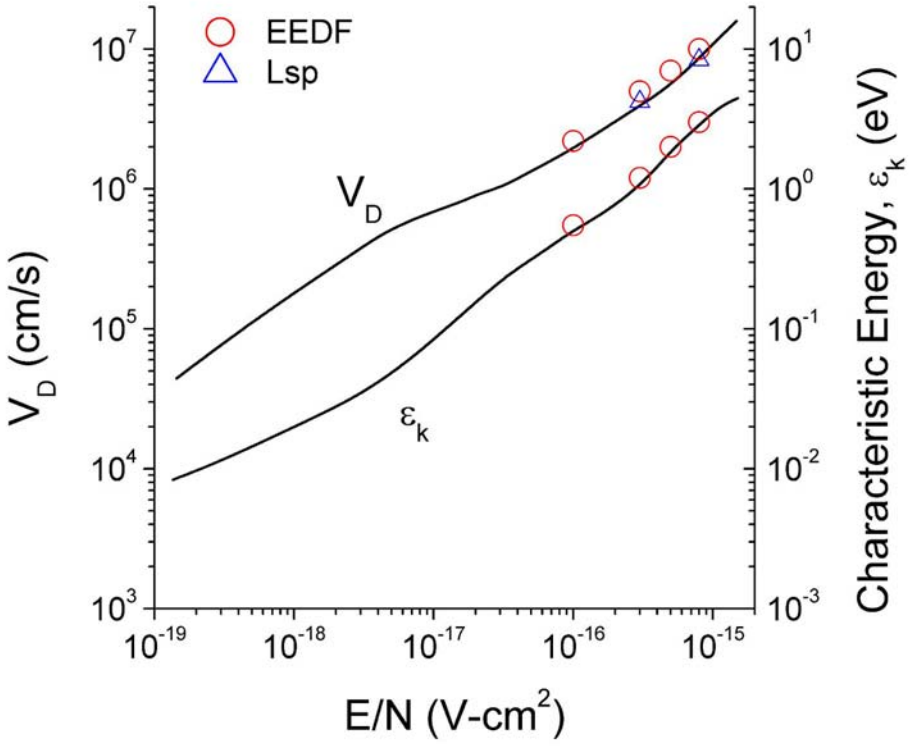

Figure M-3. Results for drift velocity and characteristic energy for H_2. Experimental data tabulated by Engelhardt and Phelps are compared to limited results from LSP and EEDF.

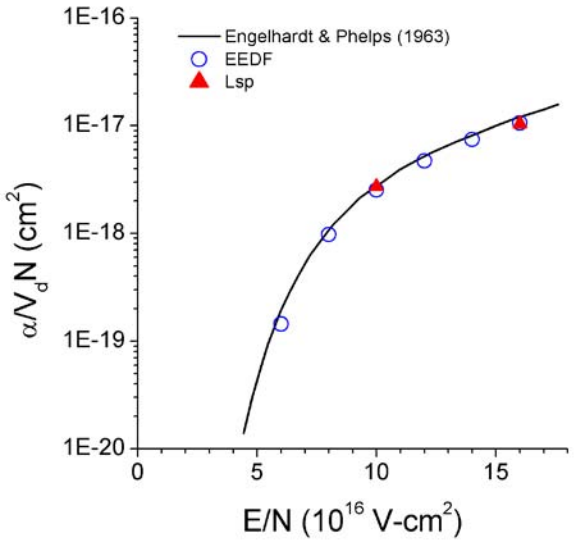

Figure M-4. Results for ionization rate for H_2. Experimental data tabulated by Engelhardt and Phelps are compared to limited results from LSP and EEDF. See the text for explanation of normalizations.

M.3.2 Cross Sections for SF_6

The important processes in SF_6 are listed along with a set of "self-consistent" cross sections in the paper by Kline.[4] These include an elastic and ionization cross section, a single excitation cross section, a vibrational cross section, and three attachment cross sections for making the negative ions SF_6^-, SF_5^-, and F^-. As explained by Kline, the excitation cross section is adjusted to obtain the proper breakdown threshold (value of E/n_n where $\bar{\alpha} = 0$) of 362 Td, and to obtain the proper slope of $\bar{\alpha}(E/n_n)$ near the breakdown threshold. The effective ionization rate is calculated by Kline by a Boltzmann code similar to EEDF that uses the two-term expansion. Running EEDF with the Kline cross sections gives results in good agreement with the Kline paper. (The cross sections in EEDF database differed somewhat from the Kline cross sections and gave a breakdown threshold that was substantially too large. For this reason the Kline cross sections were ported into EEDF.) Running LSP-MCC swarm simulations with the same set of cross sections led to significantly different results for the effective ionization rate. The breakdown threshold from the swarm simulation is found to be ~430 Td and the slope of $\bar{\alpha}$ is much lower around the threshold than the EEDF result. Figure M-5 shows the Kline cross sections for SF_6 as a function of electron energy. Again the elastic cross section is compared to the sum of all of the inelastic processes, including attachment. Attachment can, of course, be thought of as the ultimate inelastic collision, as the electron disappears entirely. For SF_6, the condition that the elastic cross section exceed the inelastic cross section is violated both at high energies ($E > 20$ eV), and at low energies where the attachment cross section dominates. This is in contrast to the case for H_2 (see Figure M-1) where the inelastic cross sections only exceed the elastic cross section when E > 100 eV.

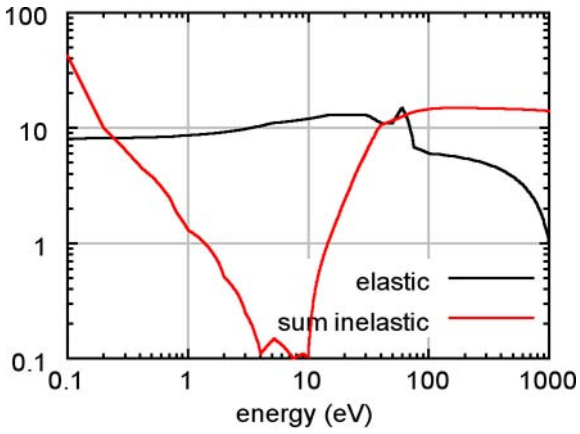

Figure M-5. Kline cross-section data for SF_6 used in LSP and EEDF to calculate transport coefficients. The elastic cross section is compared to the cross section for the sum of all other (inelastic) processes.

The cross sections used for He have been presented in another report,[1] but it is of interest here to discuss the results from LSP and EEDF for this gas. The MCC and Boltzmann code results are in good agreement for He until the electric field becomes high enough to generate a large drift velocity and/or to cause a significant number of electrons to have high enough energies for which the inelastic cross section exceeds the elastic cross section. In either case, the validity of the two term expansion in the Boltzmann method is in doubt. In He, the inelastic cross sections only exceed the elastic cross section at high energies (exceeding 20 eV). In SF_6 the situation is complicated by the presence of very large attachment cross sections at low energies as well. For both He and H_2 our comparisons between the methods always show good agreement when the conditions for the two-term expansion are satisfied, and break down only when they are violated. For this reason we suspect the discrepancies between the MCC swarm simulations and EEDF are due to the breakdown of the two-term expansion in the Boltzmann. It is, however, important to note that a publication by Itoh[10] reports that the two-term expansion is valid for SF_6 in the range from about 100 to 700 Td. Moreover, a companion paper by Satoh[11] also reports good agreement between Monte Carlo and Boltzmann results. These claims are still being investigated by the authors.

The paper by Itoh also reports a new set of SF_6 cross sections in which some modifications to the cross sections of Kline are introduced. The main differences are in the vibrational process, which is about a factor of 10 larger for Itoh than Kline, and in the excitation process. Itoh reports a maximum excitation cross section that is about a factor of three smaller than Kline's value. The elastic and attachment cross sections of Itoh and Kline are not identical but are very similar. Using Itoh's cross sections with LSP yielded a breakdown threshold that was too small (~250 Td), while the Kline cross sections gave too large a threshold.

As mentioned above, the discrepancies between LSP and the results of Itoh are still under investigation. However, a new set of self-consistent cross sections for SF_6 has been developed for use specifically with the LSP Monte Carlo scattering algorithm. The cross sections are those of Itoh with the modification that the magnitude (although not the threshold and functional dependence on energy) of the excitation cross section has been increased by a factor of about four from that reported in Itoh. With this modification, swarm simulations with the LSP-MCC algorithm showed fairly good agreement with experimental data of effective ionization and drift velocity as a function of E/n_n over the range from 100 to 700 Td. This can be seen in Figures M-6, M-7, and M-8 (all adapted from Kline). From Figure M-7 it is seen that these modified cross sections predict a breakdown threshold of close to 360 Td, in agreement with experiment, and give approximately the right slope for the effective ionization rate (labeled "λ_I / N" in the figure) near the threshold. Figure M-8 shows that the effective ionization rate agrees pretty well with experiments for values of E/n_n up to around 2000 Td, although LSP does predict a slightly higher rate at large values. Using the LSP output it is also possible to calculate the ionization and attachment rates, α and η, separately. Although the difference of the two, $\bar{\alpha}$, is in good agreement with experiment, α and η are both larger than the experimental results by a factor of about two, which could result in an elevated number of positive and negative ions in a full PIC simulation. Nonetheless, since the electron transport properties are captured fairly well by this set of cross sections, they will be used for SF_6 simulations until more study can be given to the SF_6 cross sections and the remaining discrepancies between LSP and literature cited above.

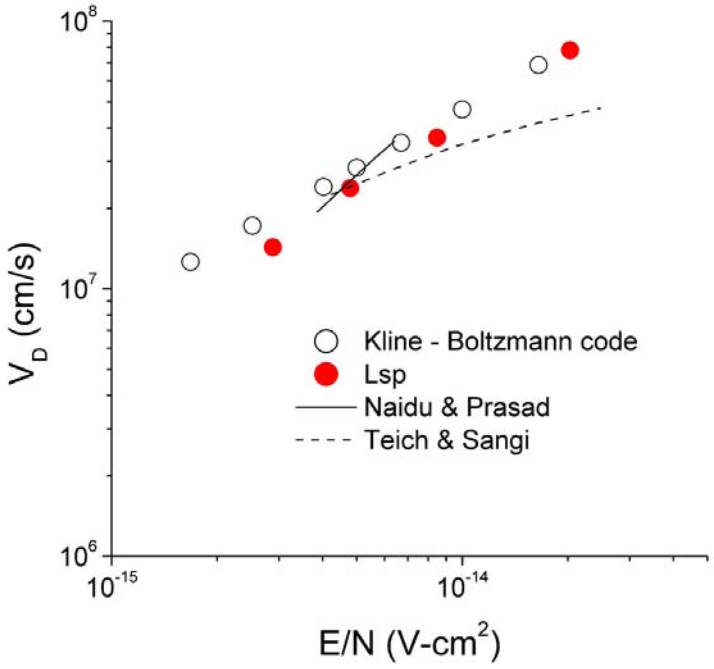

Figure M-6. Drift velocity for SF_6 as a function of E/n_n. Experimental data tabulated by Kline are shown in black, and LSP simulation results are shown as red circles.

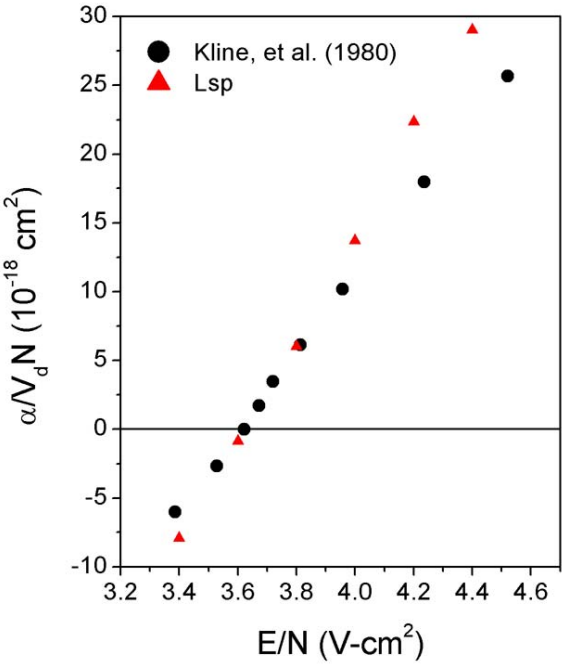

Figure M-7. Effective ionization rate near the breakdown threshold for SF_6 as a function of E/n_n. Experimental data tabulated by Kline are shown in black, and LSP simulation results are shown as red triangles.

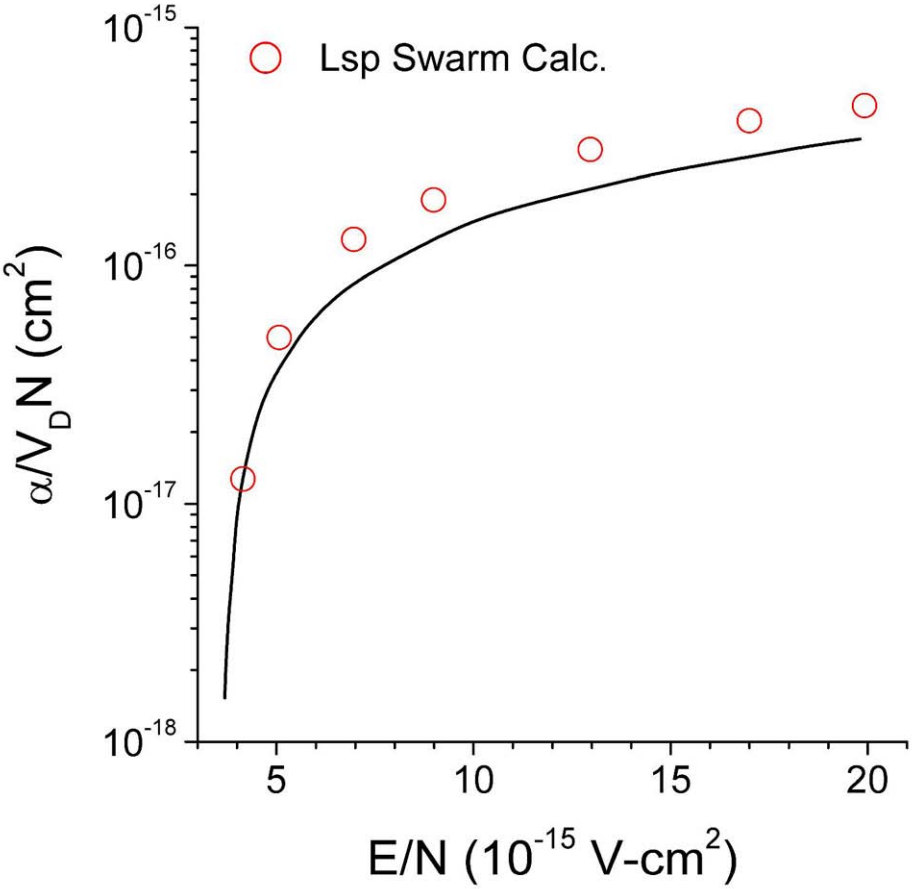

Figure M-8. Effective ionization rate above the breakdown threshold for SF_6 as a function of E/n_n. Experimental data tabulated by Kline are shown in black, and LSP simulation results are shown as red circles.

M.4 Comparison of LSP Swarm Calculation Results with Experimental Data

We first make use of the existing collision algorithms in LSP to study the behavior of an electron swarm in hydrogen gas with an applied electric field. The goal of these simulations was to ascertain the sensitivity of the electron distribution function to numerical properties such as time step and macro-particle number. In the simulations, a 3×10^8 cm^{-3} number density plasma "seed" was initialized and allowed to evolve in time under the influence of the applied electric field only. The electron swarm behavior in the gas is modeled in Monte Carlo fashion with ionization, energy loss, charge exchange, and scattering processes. Electron attachment had not been implemented in the code at the time of these simulation and thus was not included. We found that after some improvements the results in the one-dimensional (1D) simulations changed little with time step. These improvements involved the treatment of ionizing electrons and the Ohmic term in the scattering algorithm. The original LSP algorithm did not decrement the energy of the primary ionizing electron, which strongly influences the energy distribution. We modified this algorithm such that the primary and secondary electron each share half of the

available energy reduced by the ionization potential. In the old model, energetic electrons did not lose sufficient energy, which in turn overestimated the avalanche rate. Because the breakdown is driven by a plasma electron temperature of roughly ¼ the ionization potential or 3-4 eV, only electrons in the tail of the distribution actually ionize the gas. Thus, the number of electrons and energy associated with this correction is minimal. This problem is not an issue with the MCC model discussed in the previous section.

The second problem was noted in two-dimensional (2D) numerical tests discussed in the next section involving varying time steps with 18 kV/cm external field. We found that more avalanche ionization occurred for larger time step. The difference was traced to an inadequate Ohmic heating term in the collision algorithm. Near the edges of the streamer, insufficient statistics yielded non-physical drift velocities which then heated the local plasma electrons due to collisions. The model had assumed that the distributions of different plasma species were equilibrating (difference in their drift velocities decreasing in time), not actually in a steady state relative drift. The problem was effectively fixed by not permitting the drift velocity to fall below $v_{drift} = eE/m\nu_m$ where E is the ambient field and ν_m is the momentum transfer frequency. The new term for the change in temperature is now given by

$$\Delta T_{Ohmic} = \frac{2}{3}\max\left[v_{drift}{}^2 \exp(-0.5\nu_m \Delta t), \frac{E^2}{\nu_m{}^2} \right] \nu_m \Delta t,$$

where Δt is the time step. In the maximum function test above, the new drifting limit is on the right, the equilibration limit on the left. Subsequent tests give avalanche rates within 10% for a factor of 4 variations in time step.

M.4.1 Swarm Calculations

Using a fixed applied electric field, a uniform seed population of electrons is initialized in a 1D periodic region. As shown in Table M-1, the electron avalanche rate, temperature, drift velocity, and momentum transfer frequency are calculated for an atmosphere of hydrogen ($N = 2.6 \times 10^{19}$ cm^{-3} molecules). The avalanche rate α (in units of cm^{-1}) is normalized by $c/V_{drift}N$ where V_{drift} is the drift velocity and N is gas number density. The breakdown field strength is of the order 10 kV/cm with strong electron avalanche calculated at E=100 kV/cm. These results are in reasonable agreement with values from Dutton[12] shown (in red font) in Table M-1. Note that these tabulated values are consistent with the corresponding data values shown in Figures M-3 and M-4.[9]

Table M-1. Results of LSP swarm calculation in H_2 and experimental value from Dutton[12] (in red font) are shown. The field stress is given in units of E/p (kV/cm-atm) and E/N (V/cm^2).

E (kV/cm-atm) (V/cm^2)	Avalanche $\alpha c/V_{drift}N$ (cm^2)	T_e (eV)	V_{drift} (cm/s)	ν_m/c (cm^{-1})
5 1.9e-16	0 0	0.23 .4	2.35e6 2.5e6	125 133
10 3.8e-16	3.5e-19 3e-20	1.33 1.4	4.75e6 3.2e6	124 184
25 9.e-16	3e-18 2e-18	2.01 2.4	1.12e7 9e6	131 163
50 1.9e-15	3e-17 2.5e-17	2.74 3	2.41e7 2e7	122 147
100 3.8e-15	4.1e-17 5e-17	4.6 4.5	5.04e-4 5.e7	116 116

In the first simulations without the special treatment of ionization, the onset of avalanche occurs at lower *E*/*p* and was less abrupt. The electron temperature and drift velocities were not as sensitive.

M.4.2 Simulation of Streamer Propagation in Hydrogen

In this section, we use an implicit collisional electromagnetic-particle method[13] to study the 2D propagation of a streamer in an atmosphere of hydrogen. In 2D cylindrical (*r*,*z*) simulations, we can study the streamer evolution from wispy electron swarm to high density without the need to resolve the plasma electron oscillation frequency or the Debye length and maintain reasonable energy conservation. These constraints severely hamper the densities that can be simulated with explicit PIC algorithms. In these calculations, a coax feeds the voltage wave, giving electric fields of roughly 6-100 kV/cm across an 8-mm AK gap. A 3×10^8 cm^{-3} plasma was initialized 1 mm from the cathode on axis. We found that in all but the lowest field, a streamer propagated with increasing towards the anode. The streamer front velocities increased from 10 to 160 cm/μs. Typically, as shown in Figure M-9 for the 30 kV/cm field, a weak streamer initially formed a small distance from the seed. As the streamer drifted and the density increased, eventually the tail of the electrons became anchored in space by the increasing space charge. At this point the density of the plasma electrons and ions became comparable and the plasma begins to shield out the electric field. Shown in Figure M-10, the field is enhanced at the streamer edges to roughly twice the initial field. The electron temperature at the edges is roughly 4-eV, sufficient to enable a weak avalanche that sustains the streamer.

The sensitivity of the electron avalanche to time step is illustrated in Figure M-11. Here, the time step was varied from 0.67-2.67 ps with electron-neutral collision times $\tau_{en} \sim 0.28$ ps. Thus, the time step is actually as high as 10 τ_{en}. We see that except for early time initiation, the exponential growth of the electrons in the three simulations is quite close. This good agreement was not evident before the algorithm changes were made. As stated in the previous section, the difference was traced to an inadequate Ohmic heating term in the collision algorithm. Near the edges of the streamer, insufficient statistics yielded non-physical drift velocities which then heated the local plasma electrons due to collisions. The calculated avalanche rates are now within 10% for a factor of 4 variations in time step with steps as high as 10 collision times.

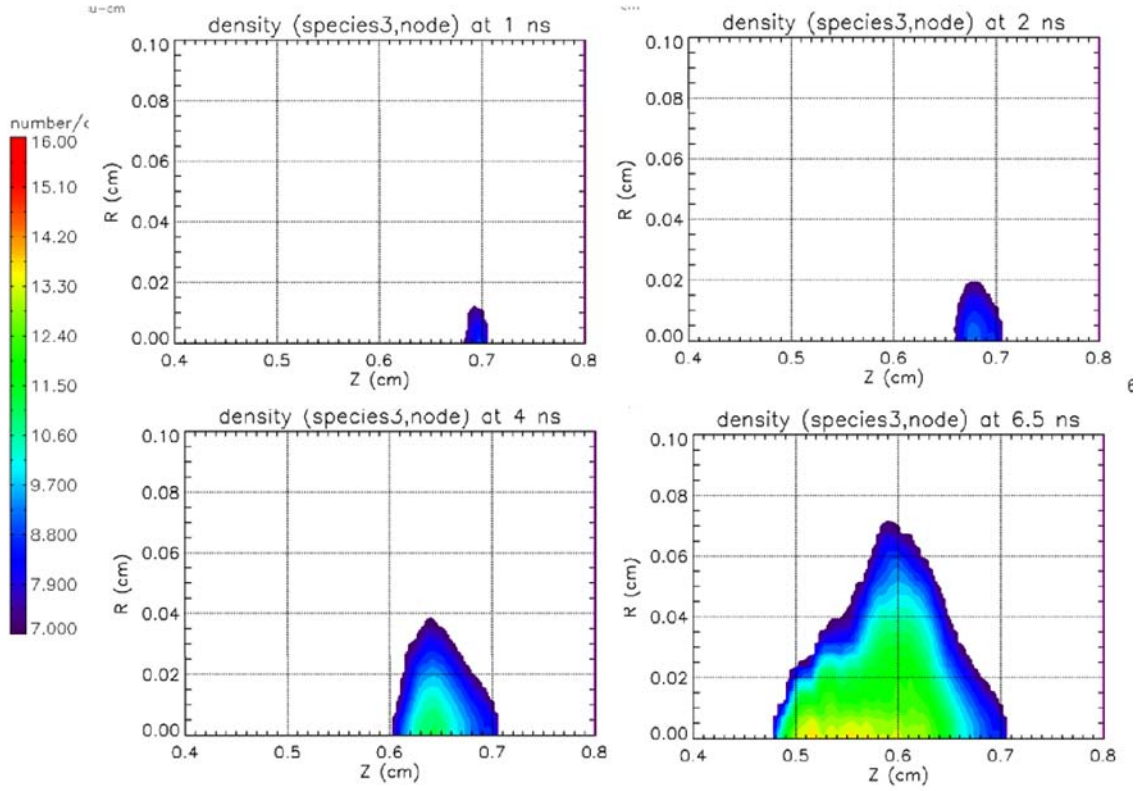

Figure M-9. The plasma ion density is plotted 1, 2, 4, and 6.5 ns into the 30 kV/cm-atm 2D LSP simulation. A small 3 x 10^8 cm^{-3} plasma seed is initialized at t = 0.

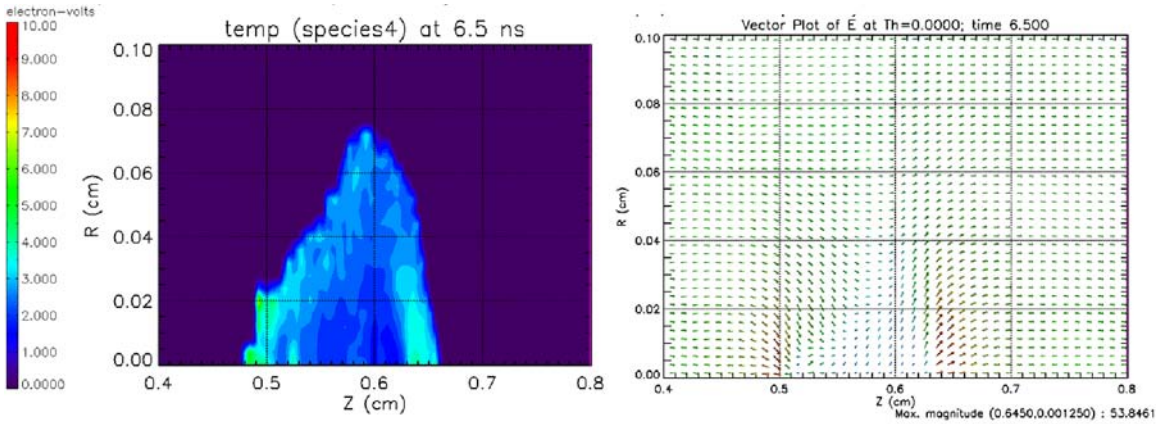

Figure M-10. For the 30 kV/cm-atm 2D simulation, the electron temperature (left) and electric field vectors (right) are plotted after 6.5 ns.

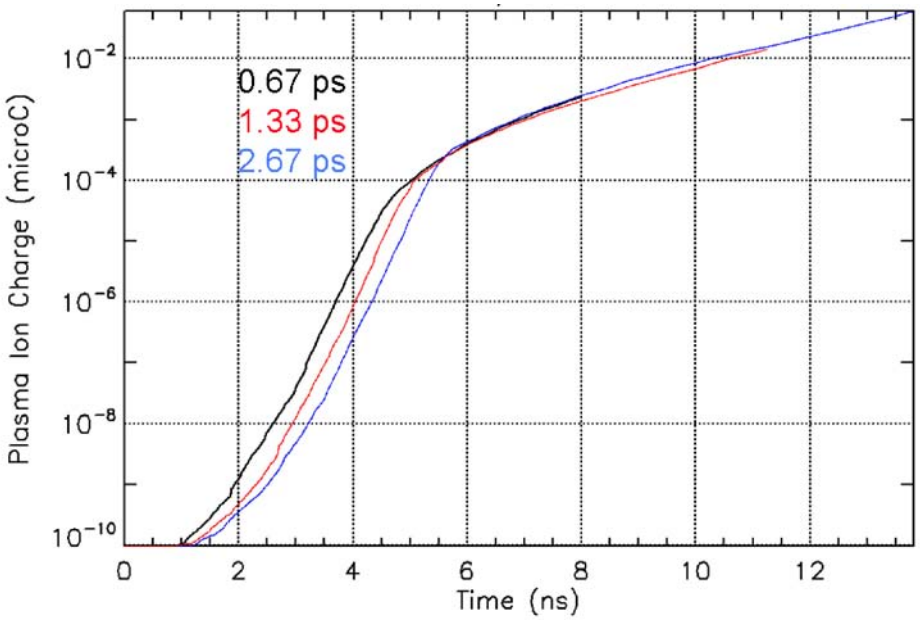

Figure M-11. The total ion charge in the 3 stream simulations with time steps of 0.67, 1.33, and 2.67 ps are shown versus time.

The 12 kV/cm electric field simulation exhibited a weak streamer that we were able to follow for the longest time (22.5 ns). Shown in Figure M-12, the streamer extends 4 mm with a radial extent of < 0.4 mm with peak density at 22.5 approaching 10^{12} cm^{-3}. The streamer front in this case moves at ~10 cm/μs. As the field increases, the front velocity does as well with a velocity of 160 cm/μs for E = 100 kV/cm.

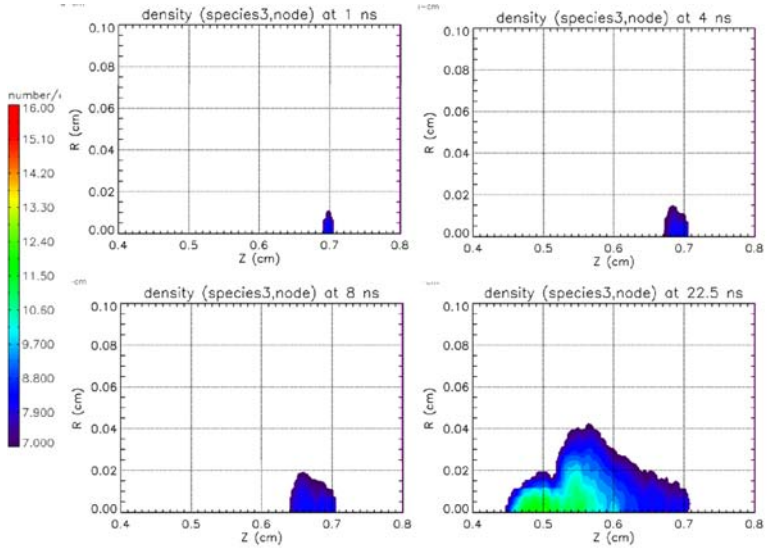

Figure M-12. The evolution of the plasma ion density is shown for the 12 kV/cm-atm 2-D simulation. The snapshots of the density are shown at 1, 4, 8, and 22.5 ns.

M.5 Conclusions

A MCC model has been implemented and tested in swarm calculations for H_2 and SF_6. The algorithm includes an attachment process that is important for electronegative gases such as SF_6.

A series of hydrogen breakdown simulations has been carried out with the LSP simulation code. Swarm simulations calculate electron avalanche rate, drift velocity, and electron temperatures in reasonable agreement with experiments. Sensitivity of the results to simulation time step was investigated. Results were shown to be insensitive to time step after handling of ionization and the Ohmic heating term were modified. Two-dimensional simulations of streamer propagation were carried out showing front velocities 3-5 times that of the 1D mean electron drift velocity. These results were consistent with a factor of 2-3 enhancement of the ambient electric field due to 2D geometry of the streamer. Electric fields are increasingly shorted within the streamer, and enhanced at edges as the streamer density increases. Electron temperatures are typically 4-5 eV at edge, sufficient for a weak avalanche in > 6 kV/cm fields. Future work will focus on advanced particle management algorithms to speed simulations that will allow for larger-scale switch simulations.

Streamer calculations are presently being carried out using the MCC model in 2D. Initial results show good agreement with the 2-D streamer simulations in H_2 that are reported in Section M.4.2. A complete report of the streamer calculations in both H_2 and SF_6 will be given when these simulations are complete.

M.6 References

1. C. Thoma, T.P. Hughes, N.L. Bruner, T.C. Genoni, D.R. Welch, and R.E. Clark, *Benchmarks for the Monte-Carlo Collision Model in LSP*, ATK-Mission Research Technical Report No. MRC-ABQ-R-2193, July 2005.

2. C. Thoma, T.P. Hughes, N.L. Bruner, T.C. Genoni, D.R. Welch, and R.E. Clark, Monte-Carlo vs. bulk conductivity modeling of RF breakdown in helium, *IEEE Trans. Plasma Sci.*, 34(3), 910, 2006.

3. It should be noted that some numerical concerns about the combination of MCC models and explicit PIC codes have been expressed in M.M. Turner, Kinetic properties of particle-in-cell simulations compromised by Monte Carlo collisions, *Phys. Plasmas*, 13, 033506, 2006.

4. See for example, L.E. Kline, D.K. Davies, C.L. Chen, and P.J. Chantry, Dielectric properties for SF_6 and SF_6 mixtures predicted from basic data, *J. Appl. Phys.*, 50, 6789, 1979.

5. A. Napartovich, *EEDF User's Guide*, unpublished.

6. See, for example, T. Holstein, Energy Distribution of Electrons in High Frequency Gas Discharges, *Phys. Rev.*, 70, 367, 1946.

7. L.C. Pitchford, S.V. O'Neil, and J.R. Rumble Jr., Extended Boltzmann analysis of electron swarm experiments, *Phys. Rev.*, A 23, 294, 1981.

8. S.J.B. Corrigan, Dissociation of Molecular Hydrogen by Electron Impact, *J. Chem. Phys.*, 43, 4381 (1965).

9. A.G. Engelhardt and A.V. Phelps Elastic and Inelastic Collision Cross Sections in Hydrogen and Deuterium from Transport Coefficients, *Phys. Rev.*, 131, 2115, 1963.

10. H. Itoh, Y. Miura, Y. Nakao, and H. Tagashira Electron Swarm Development in SF_6: Boltzmann Equation Analysis, *J. Phys. D: Appl. Phys.*, 21, 922, 1988.

11. K. Satoh, H. Itoh, Y. Nakao, and H. Tagashira Electron swarm development in SF_6: Monte Carlo simulation, *J. Phys. D: Appl. Phys.*, 21, 931, 1988.

12. J. Dutton, A Survey of Electron Swarm Data, *J. Phys. Chem. Ref. Data*, 4, 582, 1975.

13. D.R. Welch, D.V. Rose, M.E. Cuneo, R.B. Campbell, and T.A. Mehlhorn, Integrated Simulation of the Generation and Transport of Proton Beams from Laser-Target Interaction, *Phys. Plasmas*, 13, 063105, 2006.

APPENDIX N. Modeling Streamer Formation in SF_6 Using Electromagnetic Particle-in-Cell (PIC) and Swarm Models at High Pressures

High-pressure gas models for PIC typically solve the continuity (or rate) equations for gas ionization as auxiliary equations in terms of the continuous electron, n_e, negative ion, n_-, and positive ion n_+ concentrations

$$\frac{\partial n_e}{\partial t} = S - (\alpha - g)n_e - \beta n_+ n_e$$

$$\frac{\partial n_-}{\partial t} = \alpha n_e - \Gamma n_+ n_-$$

$$\frac{\partial n_+}{\partial t} = S + g n_e - \beta n_+ n_e - \Gamma n_+ n_-$$

where S is the source ionization rate, α is the electron attachment rate, g is the electron ionization (avalanche) rate, β is the electron-positive ion recombination rate, and Γ is the positive ion-negative ion recombination rate. Typically charge neutrality is assumed

$$n_+ = n_e + n_-$$

Discrete PIC seed electrons are used to trigger the ionization of the gas. A continuous slowing-down approximation (CSDA) is used to decelerate the PIC electrons in the background gas by using either a Bohr-Bethe-Block approximation or an electron loss function

$$L(T) = \frac{1}{N}\frac{dT}{dx}$$

where T is the energy and N is the concentration. The energy lost by the electrons is compared to the mean impact ionization energy for the gas to provide the source ionization rate, S. The electron and ion concentrations are then used to compute a conductivity from the electron, positive, and negative ion mobilities

$$\sigma = e(\mu_e n_e + \mu_+ n_+ + \mu_- n_-)$$

which couples the effects of the rate equations into the electromagnetic fields through Ampere's Law.

Attempting to use the above model to represent the formation of streamers propagates the steamer at the equilibrium velocity of the seed electrons. This equilibrium velocity is determined by balancing the rate of energy loss in the CSDA and rate of energy gain by the acceleration due to the constant electric field. In Figure N-1 this equilibrium energy is shown for a 9 MV/m electric field applied a across a 40-mm gap with SF_6 at 1 atm.

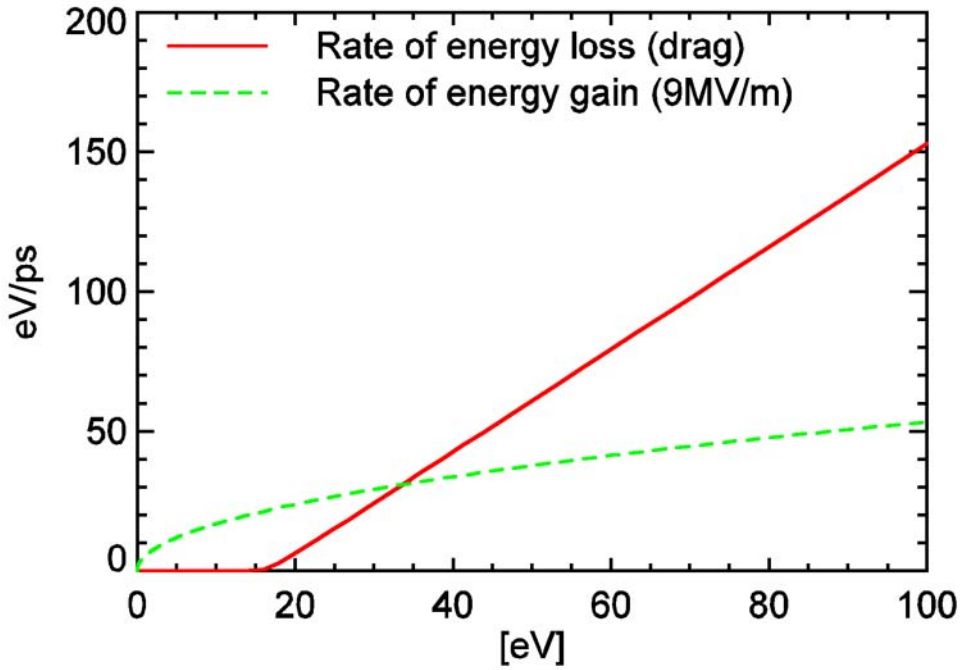

Figure N-1. Equilibrium energy.

The equilibrium energy of the electrons was observed to be 33 eV, which corresponds to a velocity of 0.011c. The propagation of the streamer head matched the equilibrium velocity rather than the drift velocity of 0.00063c observed for the continuity equation terms. Since the motions of the seed electrons were responsible for the propagation of the streamer, we concluded that an alternative scheme for seeding the streamer formation needed to be investigated to enable the use of the continuity equation model.

Upwind Donor Cell Technique

Previously, Morrow had success modeling streamer and streamer channels in SF_6 using a one-dimensional continuity equation approach.[1] Our approach is similar, but rather than including the drift terms in the continuity equations, it uses an upwind donor cell technique motivated by a physical interpretation of the phenomena. Concentrations are convected between neighboring cells using the appropriate drift velocities. The assumption of charge neutrality is dropped and the electron and ion concentrations are individually tracked.

One-Dimensional Case

To investigate the validity of our approach we prototyped a one-dimensional implementation of an upwind donor cell technique in IDL. We assume no magnetic fields and a conduction current given by

$$\vec{J} = \sigma\vec{E}$$

Ampere's Law gives an ordinary differential equation for the electric field, which is consistent with the continuity equation for the current

$$\frac{\partial \vec{E}}{\partial t} + \frac{\sigma}{\varepsilon}\vec{E} = 0$$

The electric field can then be expressed by solving the above equation using an integrating factor.

We have applied our prototype to the problem of Morrow[1] consisting of a 0.5-cm gap with an applied electric field of 9.2 MV/m with SF_6 at 1 atm. Using 181 cells across the gap and 400 seed electrons in the first cell, yields density of 1.84e15 m^{-3} for the assumed 100-μm-diameter channel. Shown in Figures N-2, N-3, and N-4 are the electron densities, negative ion densities, and the electric field magnitude in the gap at various times computed by our upwind donor cell technique. Observe that the streamer head is observed to move at a uniform velocity of 0.0013c.

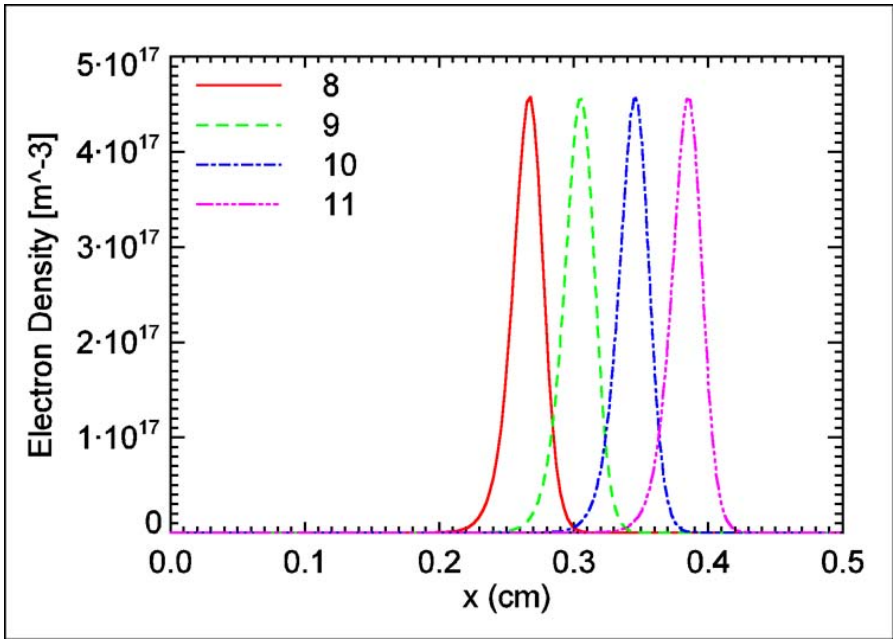

Figure N-2. Electron density vs position at various times [ns].

Note that the electric field shown in Figure N-4 is only reduced from the constant applied field. This result is consistent with our one-dimensional field solution. However, Davies[2] notes the importance of solving for the fields in three dimensions to allow for the finite radial extent of the charge distribution in the channel. Using the method of disks (or a thin-wire kernel approximation), an expression for the electric field which only depends on the electrode geometry is derived (Equation 4 in Reference 3). We have used this expression for the field to obtain results that more closely follow the results of Morrow.[1] However, some differences have been observed that are currently being investigated. Nonetheless, we feel that the one-dimensional case has validated our upwind donor cell technique and has served to emphasize the importance of modeling the three-dimensional nature of the field perturbations.

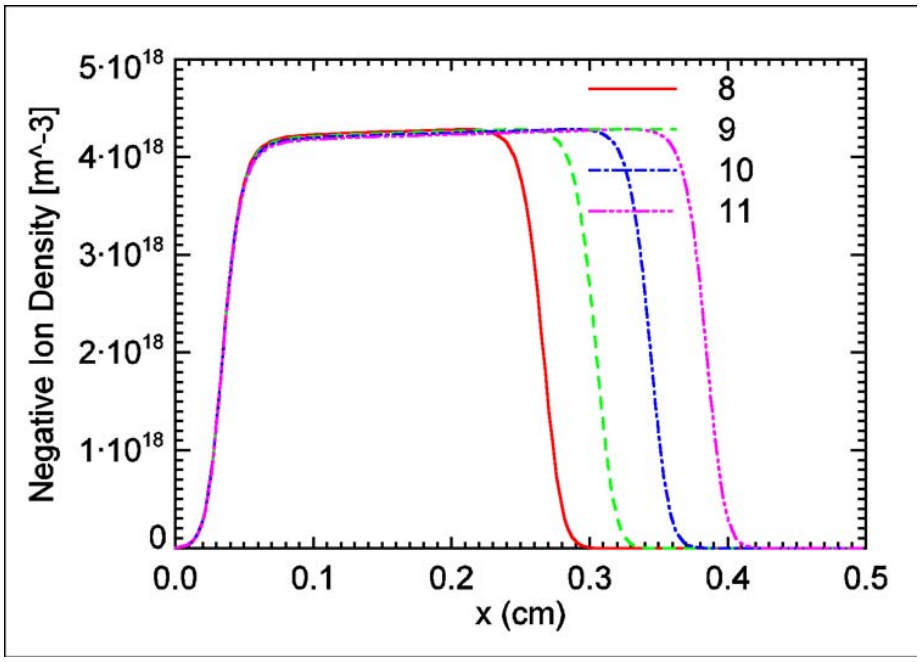

Figure N-3. Negative-ion density vs position at various times [ns].

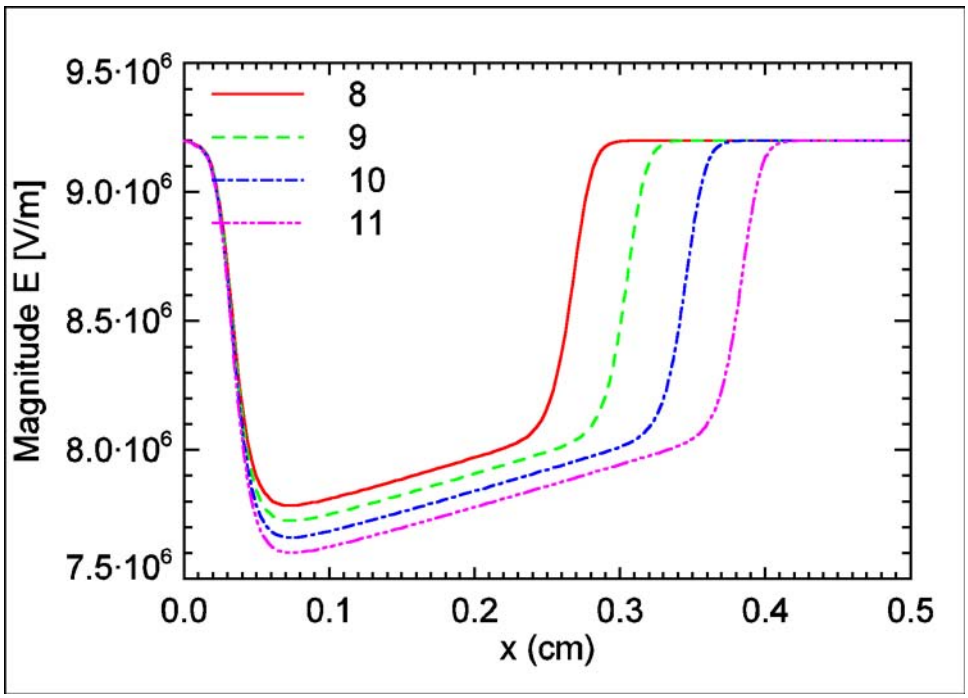

Figure N-4. Electric field magnitude vs position at various times [ns].

Three-Dimensional Case

We are currently in the process of testing an implementation of the upwind donor cell technique in the three-dimensional electromagnetic PIC code QUICKSILVER. QUICKSILVER has been modified to allow rate equation coefficient values for SF_6 to be loaded from a data file. Initial attempts at using PIC electrons to seed the streamer formation propagated the streamer at the equilibrium energy of the electrons, which is significantly larger than the drift velocities used for convecting the continuous concentrations. We are currently looking at seeding the streamer formation by setting the continuous rate equation concentration in a single cell.

Calculation of Rate Coefficients

The attachment, avalanche, and electron-ion recombination rate coefficients are computed using the NRL code MCSwarm.[4] MCSwam models electron transport in a gas with an applied electric field using the Monte Carlo method. MCSwarm creates an initial distribution of 20,000 particles in a 100-keV beam. A time accurate[5] null collision technique is applied to determine interactions. Interactions are simulated over an interval (<500 ns) until an equilibrium energy is reached. For SF_6, MCSwarm models nine reactions including four excited states, one ionization, and three attachment states. Currently electron-ion recombination rates are approximated from the average electron energy and the measured recombination rate as a function of energy specific to N_2 (Reference 6). In order to obtain good statistics, at periodic intervals the particle count is examined. Particles are randomly regrouped to a target count once a maximum threshold count is exceeded. Particles are cloned once the count drops below a minimum threshold, which is important when attachment dominates. Transport coefficients generated with MCSwarm compare favorably with two-term solutions to the Boltzmann equation and Febetron experiments.

Figure N-5 compares the mobility and Figure N-6 compares the effective ionization and attachment rates computed with MCSwarm to a variety of sources for SF_6.[7,8]

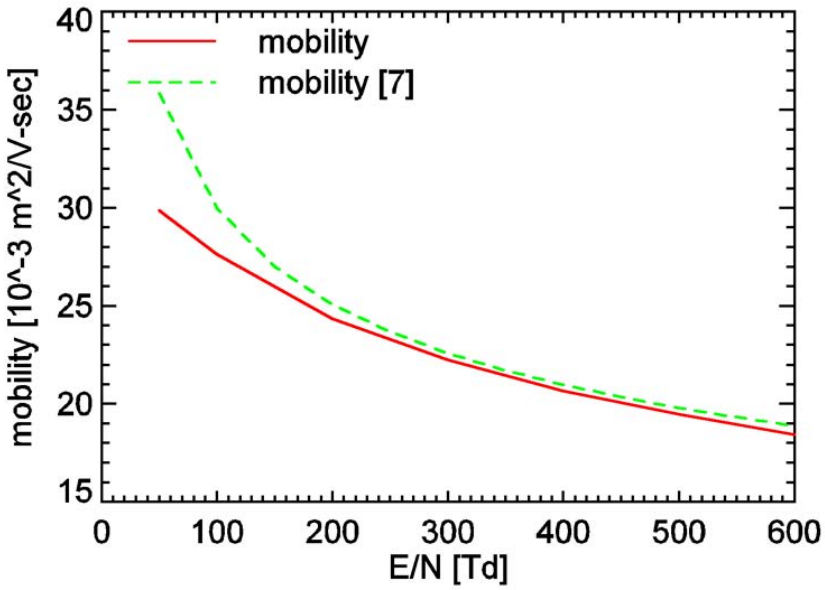

Figure N-5. Comparison of mobility for SF_6.

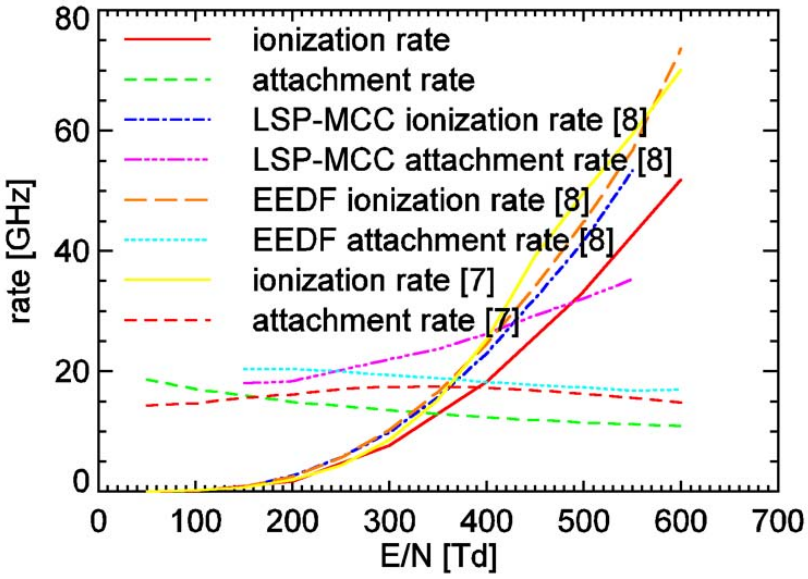

Figure N-6. Comparison of rate coefficients for SF_6.

References

1. R. Morrow, Properties of streamers and streamer channels in SF_6, *Phys. Rev. A*, vol. 35, #4, pp. 1778-1785, 1985.

2. A.J. Davies, C.S. Davies, and C.J. Evans, Computer Simulation of Rapidly Developing Gaseous Discharges, *Proc IEE,* Vol. 118, #6, pp. 816-823, 1971.

3. R. Morrow, Theory of Negative Corona in Oxygen, *Phys. Rev. A*, vol. 32, #3, pp. 1799-1809, 1985.

4. S. Swanekamp, P.F. Ottinger, S.D. Strasburg, J.W. Schumer, D.D. Hinshelwood, D. Mosher, B.V. Weber, M.L. Kiefer, D.B. Seidel, and T.D. Pointon, A Monte-Carlo Code for Computing Transport Coefficients in Weakly Ionized Gases, *33rd IEEE Conference on Plasma Sciences (ICOPS 2006),* Travis City, MI, June 2006.

5. V. Vahedi and M. Surendra, A Monte Carlo Collision Model for the Particle-in-Cell Method: Applications to Argon and Oxygen Discharges, *Comp. Phys. Comm.*, vol. 87, #2, pp. 179-198, 1995.

6. J.R. Peterson, *et al*. Dissociative Recombination and Excitation of N_2^+: Cross Sections and Product Branching Ratios, *J. Chem. Phys.*, vol. 108, #5, pp. 1978-1988, 1998.

7. R. Morrow, A Survey of the Electron and Ion Transport Properties of SF_6, *IEEE Trans. Plasma Sci.*, vol. PS-14, #3, pp. 234-239, 1986.

8. C. Thoma, D.V. Rose, and D.R. Welch, *Update on SF_6 kinetic modeling in LSP*, Voss Scientific, April 26, 2006.

APPENDIX O. Static Charge Measurements

Measurements of the switch were performed on the benchtop as well as in-situ to the pulser. A Prostat© PFM-711A electrostatic fieldmeter was used to perform the measurements. One of the in-situ measurements was performed immediately following installation of the switch and before any shots. Two other measurements were made following shots. Listed in the table is the maximum reading for each of the positions on the switch.

Switch measured external to pulser (benchtop).

Degrees	Pos 1	Pos 2	Pos 3	Spark Gap
0	850	2100	2100	nm
90	260	10	70	440
180	nm	nm	nm	nm
270	580	320	380	400

Switch measured in-situ to pulser (immediately following installation and before oil fill).

Degrees	Pos 1	Pos 2	Pos 3	Spark Gap
0	370	1300	900	260
90	90	200	200	200
180	nm	nm	nm	200
270	60	430	300	280

Switch measured in-situ to pulser (following shots and oil drain- max readings over multiple shots listed).

Degrees	Pos 1	Pos 2	Pos 3	Spark Gap
0	20	50	100	10
90	90	80	80	50
180	60	50	10	50
270	30	10	20	50

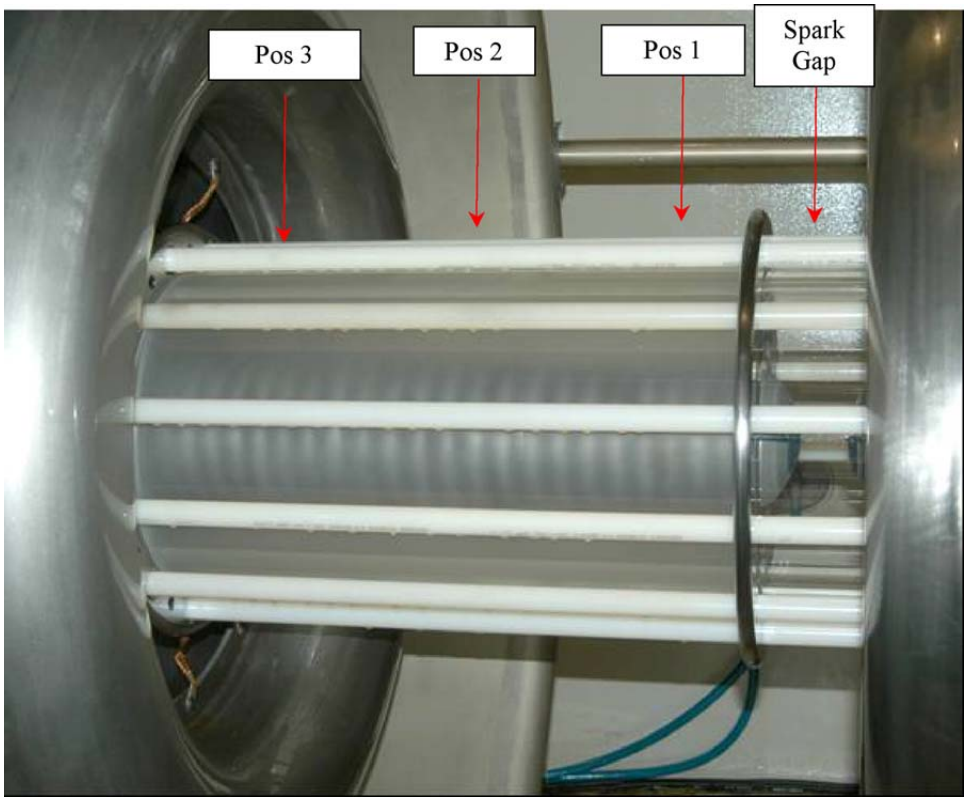

Figure O-1. Switch position orientation for measurements.

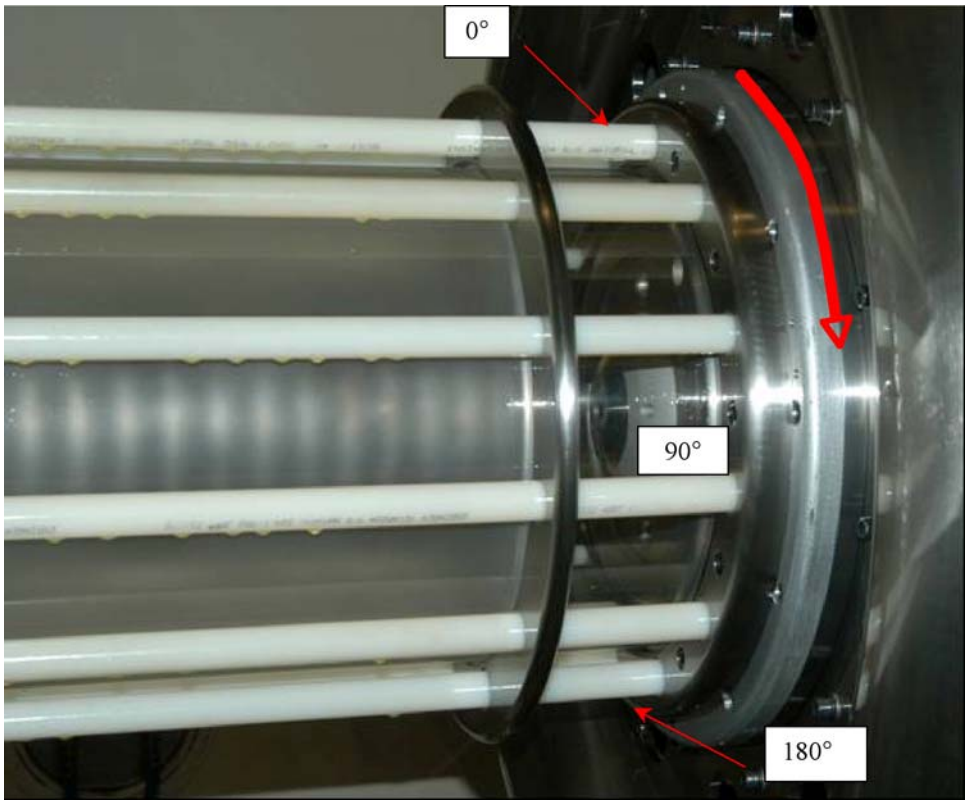

Figure O-2. Switch angle orientation for measurements.

Figure O-3. Electrostatic Fieldmeter PFM-711A Prostat.

APPENDIX P. Physics of Volumetric and Dielectric Surface Flashover in SF_6

High Voltage Technologies Group
Institute for Energy and Environment
Department of Electrical and Electronic Engineering
University of Strathclyde

Introduction

The laser triggered gas switch (LTGS) is used in Sandia National Laboratories' (SNL's) pulsed power Z_{20} machine. The switch consists of a laser triggered section and the cascade section with 20 toroidal symmetrical floating electrodes. A laser pulse results into a gas breakdown of the first triggered gap of the switch and the rest cascade inter-electrode gaps become stressed by high voltage. This in turn results into the cascade gaps breakdown and the closure of the entire switch. The work conducted at the University of Strathclyde has been concentrated on:

- study of a single cascade gap subjected to high voltage, and
- study of dielectric materials used to make a LTGS body.

The single cascade gap studies included the following tasks:

- Modeling of the electrical field distribution in the cascade gap with a special attention paid to triple points and sharp edges in the electrode/insulator system,
- Developing of a single gap test cell,
- Developing of a pulsed power supply and high-voltage (HV) diagnostics,
- Developing of the system for surface conductivity measurements,
- Study of mechanical damage of the LTGS body (section of acrylic dielectric) caused by HV spark channel.

During the course of the project a review of pulse breakdown data in SF_6, water, and insulating oil has been conducted. Specific attention has been paid to volt-time characteristics as they are of great importance for evaluation of the switch performance. This background information can be used in planning of the tests and analysis of the original breakdown experimental data obtained during the project.

Volt-Time Breakdown Information for SF_6, Oil and Water

Comparison of Breakdown Data in Water and SF_6

Figure P-1 shows breakdown field vs delay time to breakdown, for water with different conductivities and SF_6 at different pressures. The maximum breakdown field for water is about 1 MV/cm for pulses of 15- 20 ns, and it reduces to 0.2 MV/cm for much longer, 10 μs pulses. As it can be seen from this figure, the conductivity does not affect the breakdown strength of water for those short pulse durations in the interval 15-100 ns. The breakdown curves for SF_6 lie

lower that that for water (SF_6 has lower breakdown voltages). The breakdown voltage grows with increasing gas pressure. The highest gas breakdown voltages shown on this graph, for 6 bar SF_6, are close to the breakdown voltages for water.

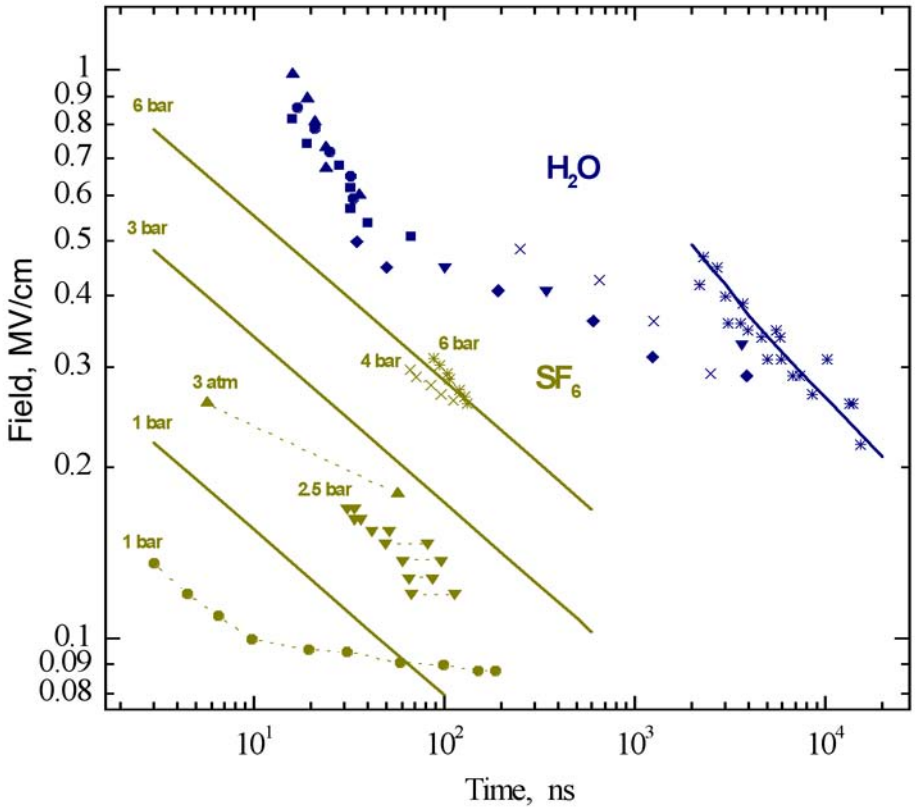

Figure P-1. Breakdown field as a function of breakdown delay time for water and SF_6.

Description of Breakdown Data for Water

Data from paper[1]:

Blue circles, distilled water (conductivity is not available)
Blue up triangles, NaCl water solution, 3.3 mS/m
Blue squares, NaCl water solution, 30 mS/m

Data description: The total breakdown time is considered as the combination of a statistical time lag and a formative time lag.

Experimental parameters: A water pulse forming line that was charged using a four-stage Marx bank was used to apply 100-ns, ≤80-kV positive pulses to the water. Voltage rise time was 3 ns. The electrodes had a Rogovskii profile with 20 mm in diameter. The gap spacing was 1.1 mm.

Data from paper[2]:

Blue down triangles, 500 μS/m
Blue diamonds, 33 μS/m

Data description: The breakdown time shown on the graph is the sum of a statistical time lag and a formation time lag.

Experimental parameters: Unnamed pulsed power supply provided pulses with an output voltage between 100 kV and 300 kV. The gap spacing was 5 mm, and the electrodes had a spherical shape with a 30 mm gap spacing. It was reported that streamers always started from the positive electrode and developed towards the negative electrode.

Data from paper[3]:

Blue crosses, 1 μS/m

Experimental parameters: A Marx generator had an output voltage of 0.5-1.7 MV and total capacitance of 6700 μF. The pulse's shape was described by $U=U_0(1\ cos(\omega t))$, and the HV pulses had negative polarity. The gap spacing was in the range between 10 mm and 60 mm, and the electrodes had a Rogovskii profile with a diameter of 100 mm.

Data from paper[4]:

Blue stars, 5.6 μS/m.

Experimental parameters: The voltage source was a 10-stage Marx generator capable of 500 kV maximum. The voltage rise time was approximately 4 μs. The polarity of pulses was positive. The electrode configuration was a hemisphere-plane geometry with the radius of the hemispherical electrode of 25.4 mm. The gap spacing was in the interval between 2.8 mm and 6.4 mm.

The blue line was fitted by: $E_{max}(t_{break}\text{-}0.53)^{1/3}=0.562$, [4]
where E_{max} is in MV/cm, t_{break} is in μs

Description of Breakdown Data for SF_6

Data from paper[5]:

Dark yellow down triangles, 2.5 bar.

Data description: Jitter and delay measurements for triggered breakdown at 2.5 bar.
Experimental parameters: not available

Data from paper[6]:

Dark yellow crosses, 4 bar; dark yellow stars, 6 bar.

Data description: Delay time to breakdown for self-breakdown.

Experimental parameters: A Blumlein cable generator capable of delivering rectangular pulses of 120 ns duration and with 20 ns rise time was employed. Plane-plane electrode configuration with 7 mm gap spacing was used. A hemispherical protrusion of known radius (1-2.5 mm) was introduced onto the stressed electrodes. The inter-electrode gap length (7 mm) was used for calculation of the electrical field values shown on the graph.

Data from paper[7]:

Dark yellow circles, 1 bar.

Data description: Formative time lag for negative polarity, 1 bar.

Experimental parameters: Cable generator capable of delivering rectangular pulses of 200 ns duration and with 1.5 ns rise time was employed. In order to eliminate the statistical time lag, primary electrons were generated by UV illumination. Electrodes of different radiuses with an 8-mm gap spacing were used. This value was used for calculations of the electric field shown on the graph.

Experiments by J. C. Martin (AWE), data from paper[8]:

Dark yellow up triangles, 3 bar.

Data description: not available.

Experimental parameters: not available.

J. C. Martin's formula (AWE), 1, 3, 6 bar[8]:

The dark yellow line was fitted using, $\rho\, t_{break} = 97800(E/\rho)^{-3.44}$

E_{max} is the average electric field in MV/cm, t_{break} is the breakdown delay in seconds, ρ is the gas density in g/cm^3.

Review of Volt-Time Characteristics for SF_6

The review of volt-time breakdown characteristics for SF_6 has been continued. V-t data for cylindrical electrodes are presented in Figures P-2 and P-3. These breakdown data were measured for coaxial electrode systems with 150/520 mm and 100/250 mm electrodes. Positive and negative pulses were applied to the central electrode. In one case, a dielectric spacer was placed between the coaxial electrodes. An average electric field strength shown on Figures P-2 and P-3 was calculated as applied voltage/inter-electrode distance.

Figure P-2 shows volt-time breakdown data for SF_6 at 3 bar in the 150/520 mm cylindrical coaxial electrode system with a conical dielectric spacer and without any spacer.[9] The conical spacer made of unnamed material was introduced between the central high-voltage electrode and the outer ground electrode. The graph shows that the pre-breakdown delay time is reduced by the spacer (orange squares), and there is no significant difference in the delay time for positive (solid orange squares) and negative (open orange squares) polarities in this case.

In the case of the electrode system without the dielectric spacer, the difference between positive (solid blue up triangles) and negative (open blue up triangles) polarities is more pronounced and

the pre-breakdown delay time is longer for negative pulses at the same level of the applied voltage.

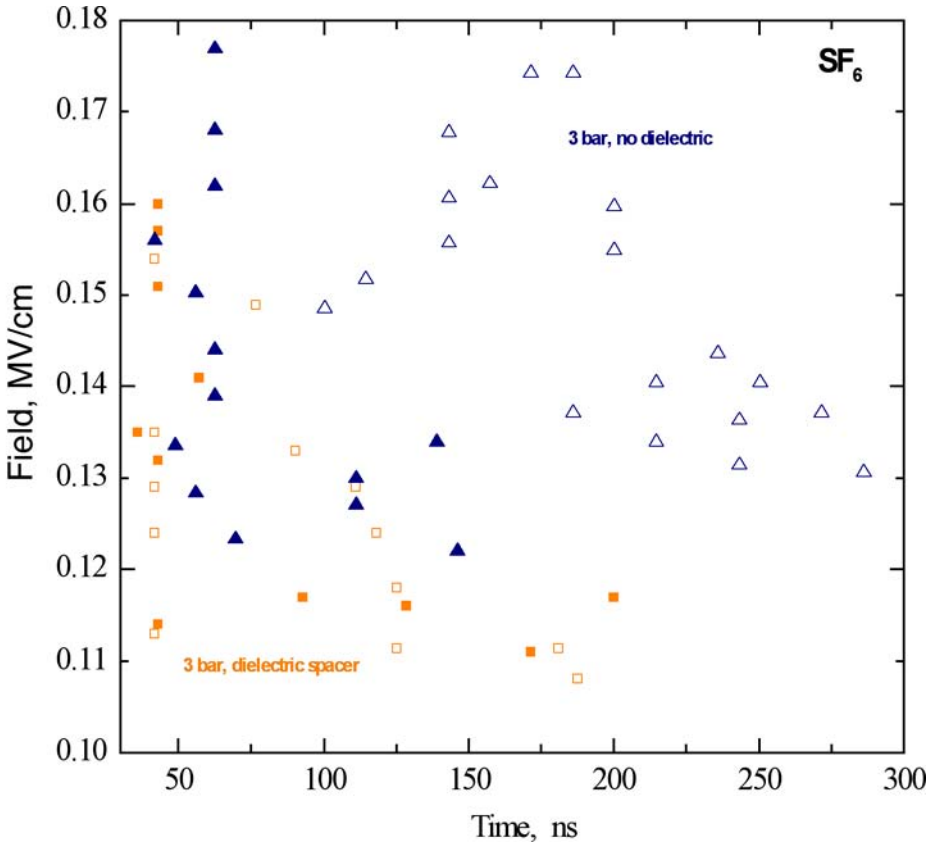

Figure P-2. Breakdown field as a function of breakdown delay time for SF_6.

Solid squares - spacer, positive polarity; open squares- spacer, negative polarity

Solid up triangles - no spacer, positive polarity; open up triangles- no spacer, negative polarity.

Figure P-3 shows volt-time breakdown data for SF_6 at 1.5 and 2.5 bar in the 100/250 mm cylindrical coaxial electrode system.[10] No dielectric spacer was introduced in this system. The data shows that SF_6 at higher pressure (2.5 bar) has a higher breakdown strength as compared with the SF_6 at 1.5 bar. It can be seen from the figure that the difference between positive and negative pulses is not very substantial, although pre-breakdown times shown on Figure P-3 are longer than pre-breakdown times on Figure P-2.

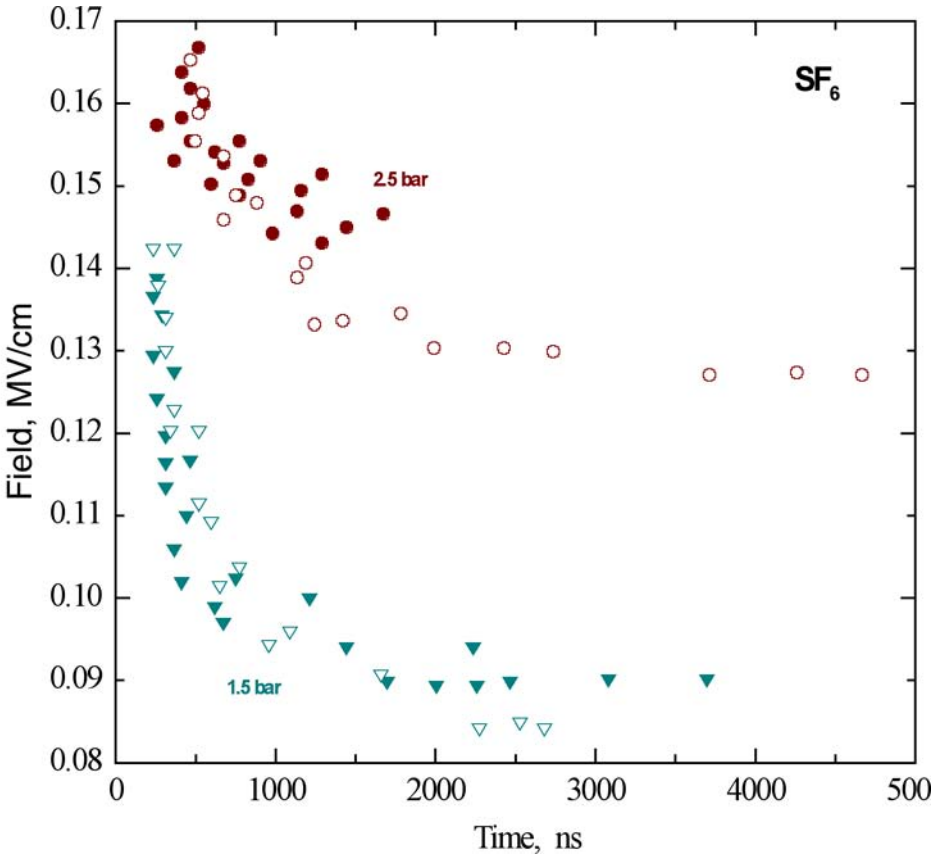

Figure P-3. Breakdown field as a function of breakdown delay time for SF_6.

Solid circles - 2.5 bar, positive polarity; open circles - 2.5 bar, negative polarity.

Solid down triangles - 1.5 bar, positive polarity; open down triangles - 1.5 bar, negative polarity.

It is difficult to make any firm conclusion from Figures P-2 and P-3 as no detailed description of experimental data such as statistical and formative time lags, parameters of HV pulses were available from References 9 and 10. This is probably because the data used were reproduced from other works. Analysis of V-t characteristics of SF_6 and mechanisms of breakdown will be continued.

Study of the Electric Field Distributions

"Electro" Models of the Cascade Section

The distribution of electrical field in the cascade multi-electrode LTGS switch and the single gap test chamber has been analyzed using "Electro" software. The model of the test chamber used in this analysis is shown in Figure P-4. The electrodes and the internal spacer have been developed from the drawings and specifications provided by SNL. They are identical to those employed in the large-scale cascade switch. The dielectric spacer material between electrodes is Lucite (shatter-resistant plastic with low dielectric permittivity of 2.4). Two versions of the test

chamber model have been developed. One version is the model with a solid spacer between electrodes (Figure P-4(a)) and second version is the model with two separate dielectric spacers separated by a gap (Figure P-4(b)).

In the model with the single solid spacer, the spacer has no holes to allow gas into the internal cavity. These holes with sharp edges could potentially generate high electrical fields. The second version models the presence of these holes by using a slot whose width is equal to the diameter of the holes drilled in the original spacer. This slot represents a limiting case, as there is no possibility to model real three-dimensional configurations using the "Electro" software.

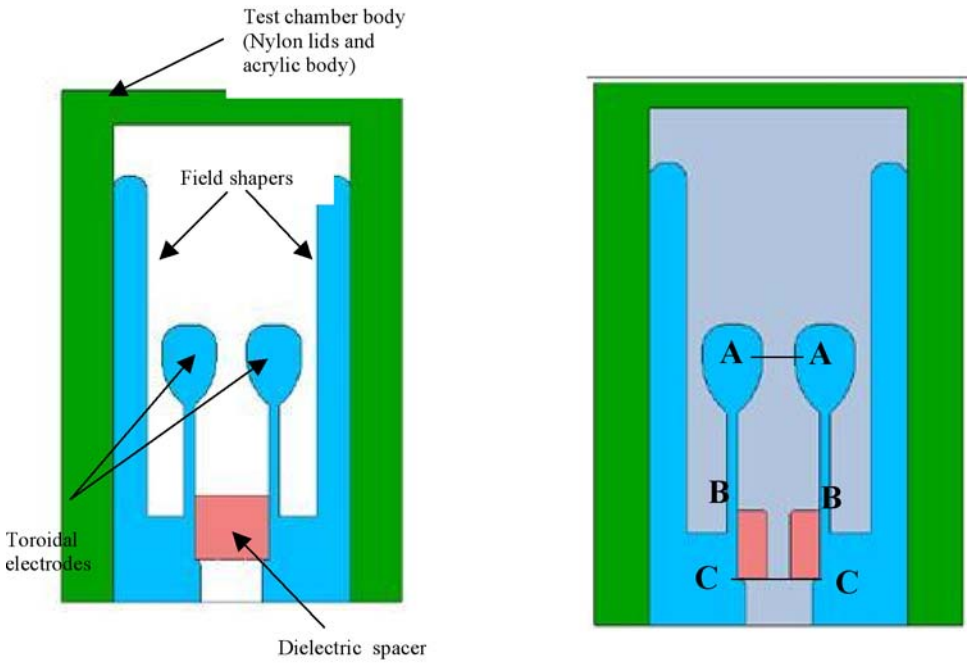

Figure P-4. Single gap test chamber design used in "Electro" calculations. (a) Solid dielectric spacer; (b) Dielectric spacer with a gap. A-A, B-B, C-C indicate lines across which electric field has been obtained.

The field distribution in the spark gaps between the floating toroidal electrodes of the cascade switch is shown in Figure P-5(a). This field distribution has been calculated for two closest points between electrodes in the multi-cascade switch. This is compared with the distribution in the proposed single gap test system shown in Figure P-5(b).

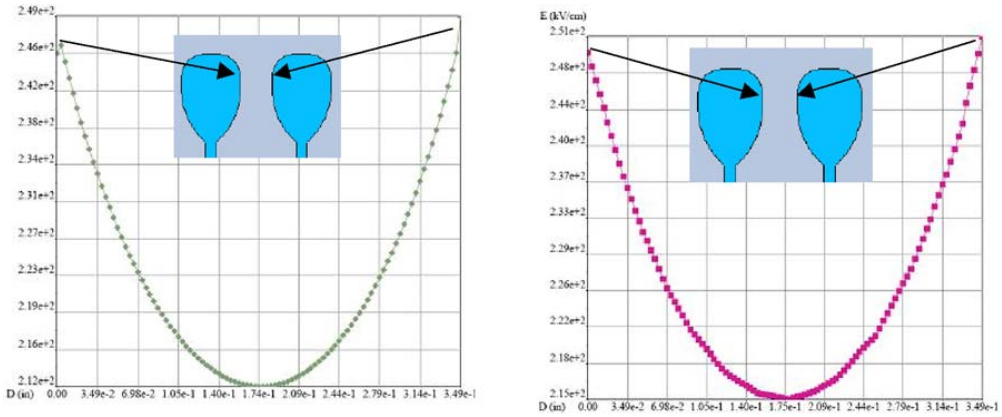

Figure P-5. Electric field distribution between two floating electrodes in the cascade switch (a), and in the single gap test chamber (line A-A, Figure P-4(b)).

Figure P-6 shows the field distribution along top surface of the solid dielectric spacer (Figure P-6(a)) and the combination of two spacers and the empty slot (Figure P-6(b)). As can be seen from Figure P-6(b) the magnitude of electric field at the edges of the spacers could reach values which are similar to the maximum electrical field in the gap between electrodes. The maximum field between electrodes is ~250 kV/cm (Figure P-5(a)), whereas the field peak at the top edge of the slot is ~193 kV/cm (Figure P-6(b)). Such high values of the electric field could potentially play a role in the initiation of breakdown. In the multi-cascade switch model supplied by SNL the central dielectric spacer has no boreholes to allow the gas into the cavity. In this case the field on the top surface of the dielectric spacer is much lower (~90 kV/cm, Figure P-6(a)) than the maximum field between electrodes.

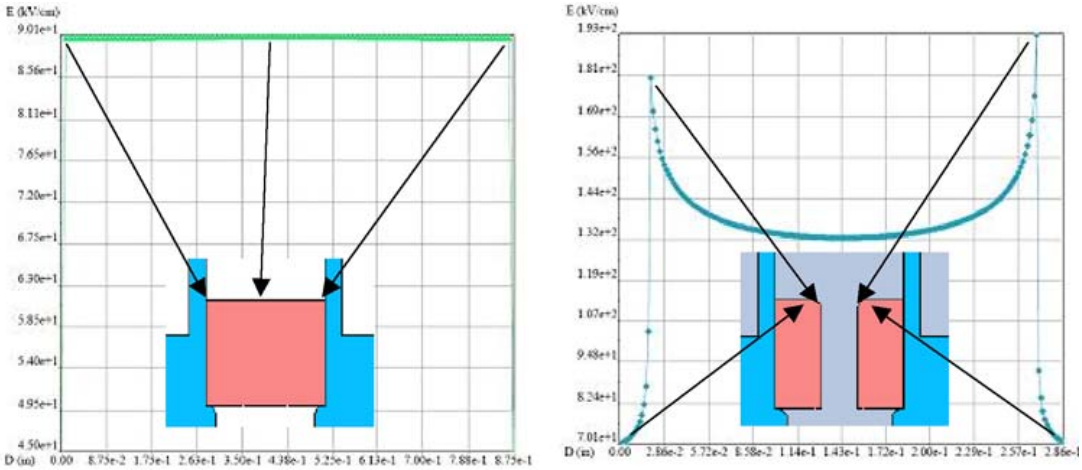

Figure P-6. Electric field along top surface of the dielectric spacer between electrodes.

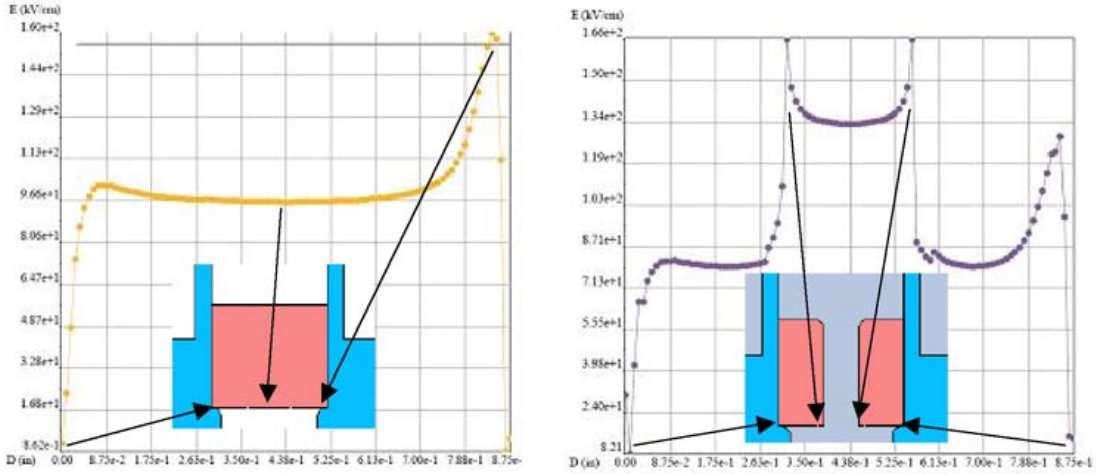

(a) (b)

Figure P-7. Electric field along bottom surface of the dielectric spacer between electrodes.

Figure P-7 shows the field distributions along the bottom surface of the dielectric spacer between electrodes. Again, as could be seen from Figure P-7(b) the sharp edges potentially could generate extremely high electrical fields. In the actual spacer with holes, the field values probably would be lower as compared with the fields calculated at the edge the slot because of screening processes. However, even in the case of solid bottom surface the field near the triple point on the high-potential electrode could be extremely high (~160 kV/cm), whereas the field near the ground electrode is low (Figure P-7(a)). Such effects have not been observed in the "Electro" model supplied by SNL, probably because of differences in the geometries of triple points.

Differences in Models of the Cascade Switch and the Single Gap Test Switch

In order to study the field distribution in the cascade switch and the single gap test switch designed at the University of Strathclyde, the model of the single gap switch has been developed in the "Electro" software and compared with the cascade "Electro" model provided by SNL. Figure P-8 shows sections of the "Electro" models of the cascade switch and the single gap test switch. These sections represent a triple point between an internal surface of the central dielectric spacer, an electrode support ledge and gas inside the dielectric spacer. In the SNL model the internal diameter of the dielectric spacer is 1.00 foot and the diameter of the central ledge which supports this spacer is 0.9543 foot. According to the drawings provided by SNL the diameter of the support ledge is 0.995±0.001 foot. This difference in the internal diameter of the spacer and the diameter of the support ledge is reflected in Figure P-8(a), where the gap between the internal edge of the spacer and the support ledge can be clearly seen. This gap, which is the vertical distance between first (red) point from the top and forth point (red), is 0.022845 foot. There is no such gap in the test chamber model, which has been designed as close to the SNL specifications as possible (Figure P-8(b)). y on Figure P-8(a) represents radial coordinate, the internal radius of the spacer is $y = 0.5$ foot, the radius of the ledge is $y = 0.477155$ foot in the case of the SNL model (Figure P-8(a)) and $y = 0.477155$ foot in the case of the single gap test chamber (Figure P-8(b)).

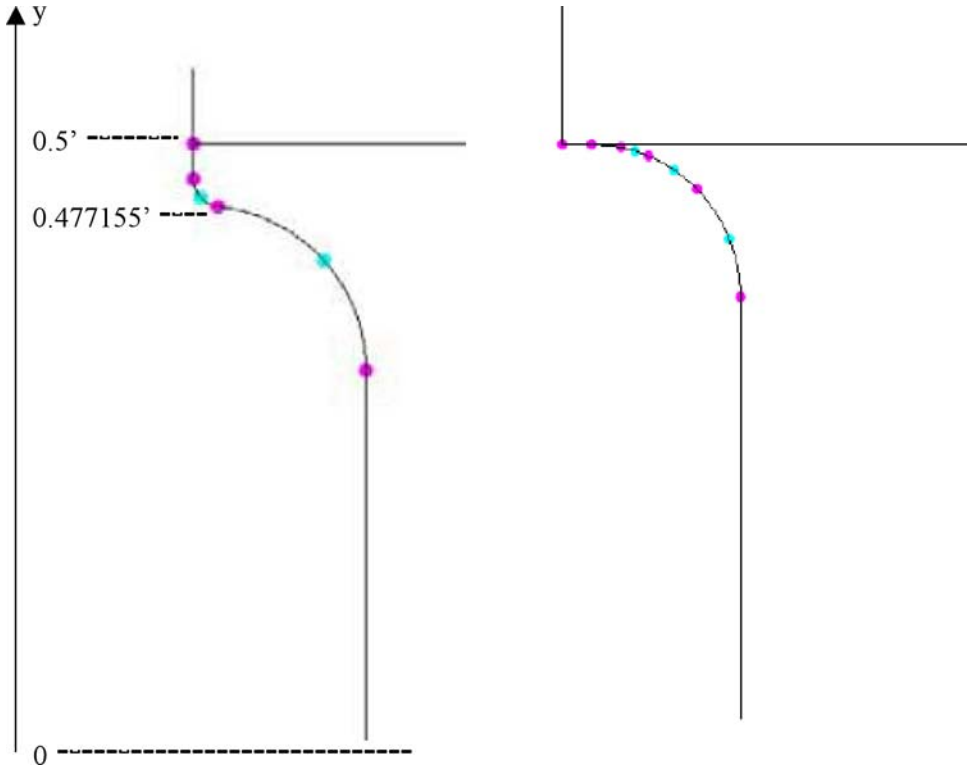

Figure P-8. Model of triple point in "Electro" software. (a) SNL "Electro" model, (b) single gap test switch model developed using SNL engineering drawings (numbers R79015 and R79017).

Calculations of the Electric Field in "Electro" Software Using the Single Gap Test Chamber Model

The analysis of the electric field distributions along the bottom surface of the dielectric spacer between electrodes (Figure P-7(a,b)) has been extended by looking at the field close to the surface. These calculations are shown in Figures P-9 and P-11.

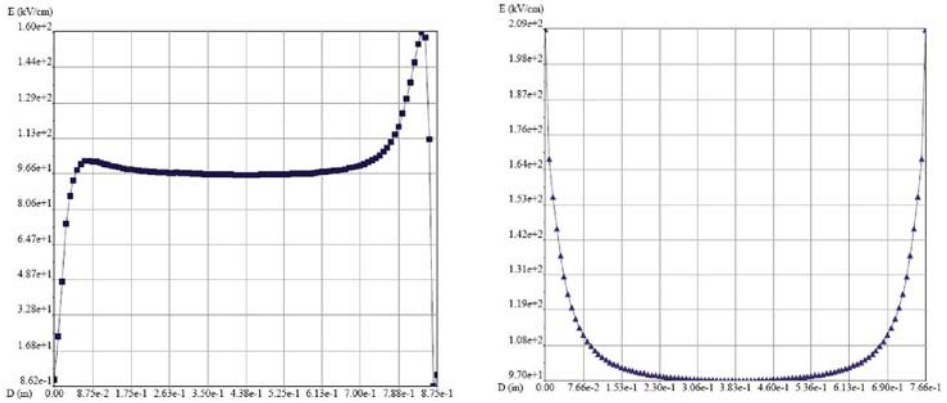

Figure P-9. Field distributions along the bottom line of the central dielectric spacer. (a) Field distribution along the bottom line of the spacer (y = 0.5 foot), (b) the field distribution 0.0176 foot away from the bottom of the spacer (y = 0.4824 foot).

Figure P-9 shows the electric field distributions at the bottom edge of the spacer in the approximation of the solid spacer without boreholes. The section of the "Electro" model for this case is shown in Figure P-10.

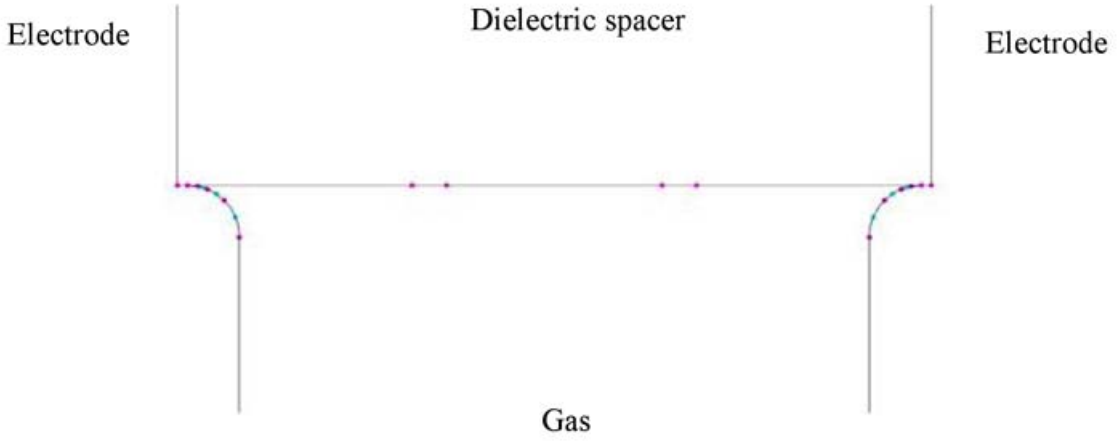

Figure P-10. Section of the single gap chamber model with the solid dielectric spacer between electrodes.

Figure P-11 shows the field distributions along the bottom line in the approximation of the combination of two dielectric spacers and the empty slot between them.

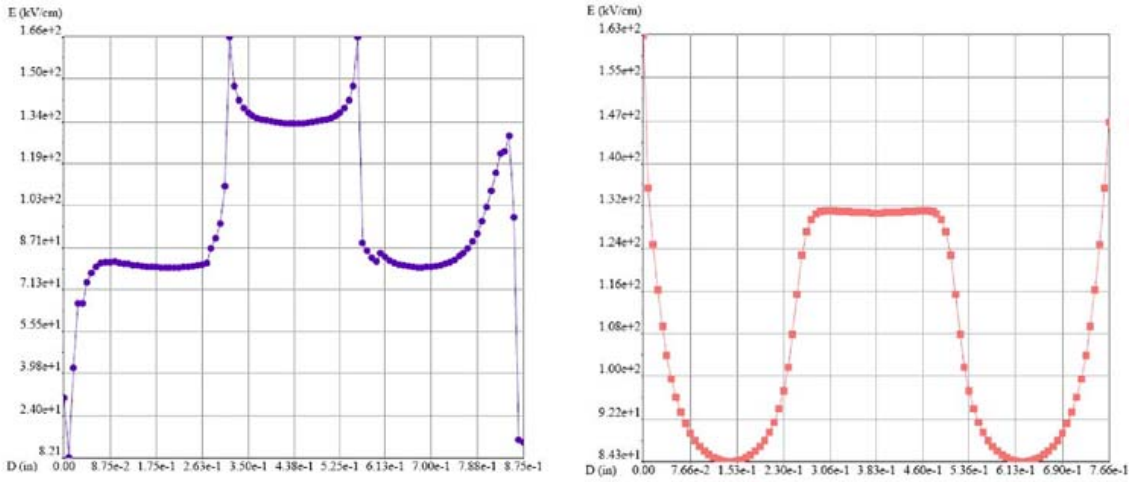

Figure P-11. Field distributions along the bottom of the combination of dielectric spacers and the empty slot. (a) Field distribution precisely along the bottom line of the spacers (y = 0.5 foot, (b) field distribution the 0.0176 foot away from the bottom of the spacers (y = 0.4824 foot).

The section of the "Electro" model for the combination of two dielectric spacers and the empty slot between them is shown in Figure P-12. This case represents an approximation of two boreholes in the central spacers shown in the SNL drawings. The slot width equals to the diameter of the boreholes (0.25 foot).

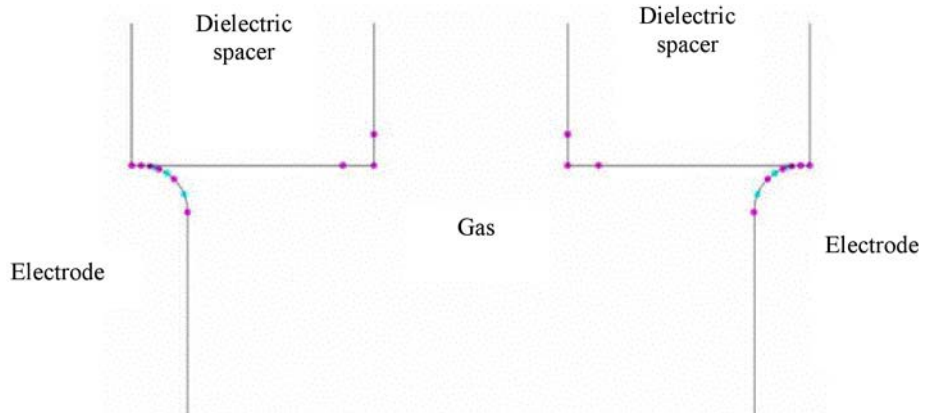

Figure P-12. Section of the single gap model with the two dielectric spacers and the empty slot between them.

Visual analysis of the field distributions presented in Figures P-9 and P-11 shows that the electric field is not symmetrical when calculated precisely along the bottom line of the dielectric spacer (cases (a)). The field distributions calculated away from the interface between the spacer and the gas show symmetrical spatial behavior. This could be potentially attributed to difficulties in numerical calculation of the electric field in the narrow regions of triple point junctions. The field distributions along the bottom line of the spacer were obtained in order to investigate the field effects of sharp dielectric edges (including hole edges). As could be seen from Figures P-9 and P-11 the sharp dielectric edges and triple points cause substantial enhancement and could make a contribution to the initiation of the spark discharge in the switch. Also, calculations given in Figure P-9(b) and P-11(b) show that the maximum field at triple points reduces with an introduction of a slot in the dielectric spacer. The maximum field at the triple point for the configuration shown in Figure P-9 is 209 kV/cm while the maximum field at the same triple point for the configuration with the slot (Figure P-10) is 163 kV/cm.

Development of the Marx Pulsed Power Supply

Development of the Marx Pulsed Power Supply

In order to study the pulse breakdown characteristics of the single gap switch mode a Marx pulse generator has been developed. This 10-stage generator has a total erected capacitance of 8 nF and is configured to deliver HV pulses with magnitudes up to 750 kV with a rise time of a few tens of ns. The generator is equipped with high-speed high-voltage diagnostics consisting of a resistive copper-sulfide voltage probe and a current shunt. These diagnostic devices are to be used for measurements of the voltage and current wave forms during switch breakdown. A photograph of the Marx generator is shown in Figure P-13.

Figure P-13. Picture of the 10-stage Marx generator.

Tuning Parameters of the Marx Generator

To satisfy the voltage rise and fall time conditions observed in SNL experiments, the Marx generator has been modified. Using an additional RC circuit the voltage rise time has been increased up to ~1 μs, which is close to the SNL experimental parameters.

Design of the Test Facility

The test chamber to study pulsed breakdown properties of SF_6 in a single gap, modeling part of the cascade switch, has been designed and developed. The set of 4.5 inches symmetrical toroidal electrodes and the dielectric spacer received from SNL has been used in the chamber. Figure P-14 shows the photograph of the electrodes and the spacer.

Figure P-14. Symmetrical toroidal electrodes received from SNL.

The single gap chamber also has a pair of flat disk field shapers that were manufactured in the departmental workshop. Figures P-15 and P-16 show engineering drawings of the field shapers and the top and bottom lids of the chamber. The acrylic body of the chamber uses a housing of the laser triggered gap provided by SNL.

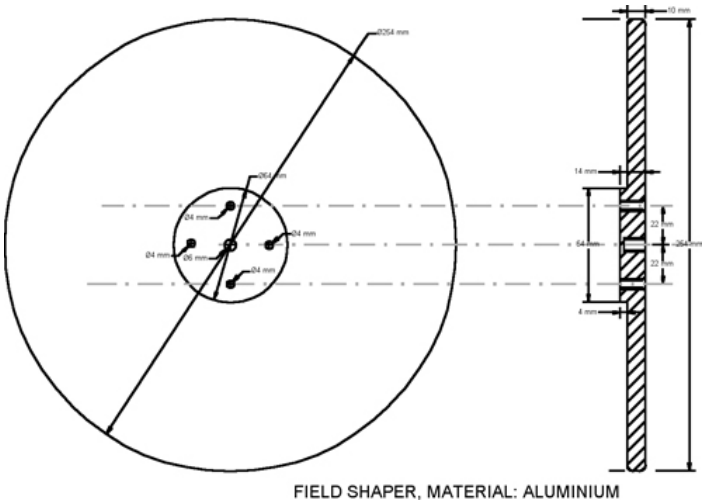

Figure P-15. Field shaper of the test chamber.

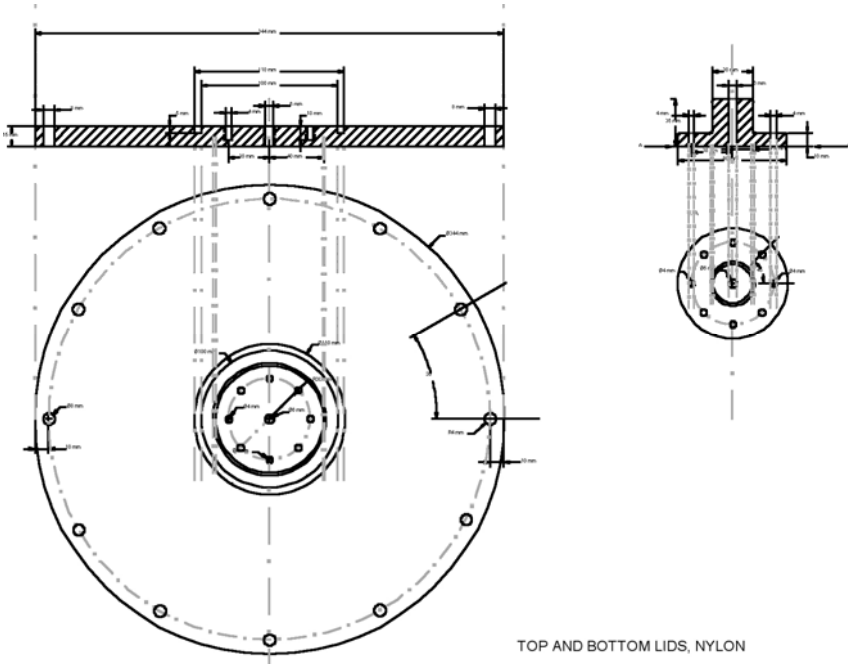

Figure P-16. Top and bottom lids of the test chamber.

Figures P-17 and P-18 show an external look of the assembled test cell and an internal view of the cell.

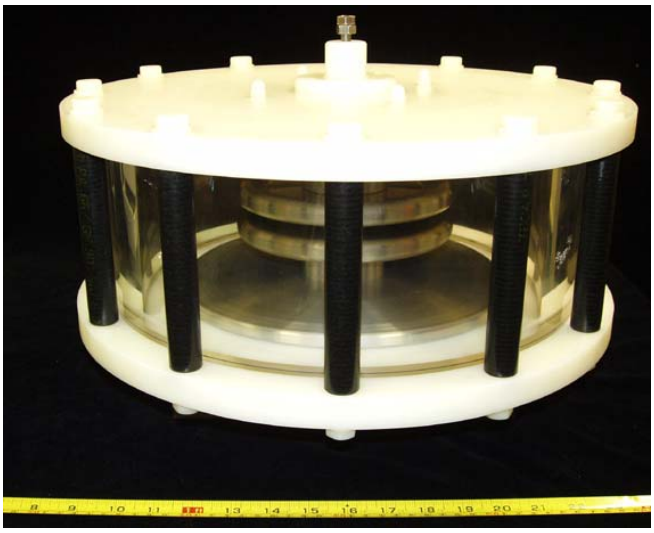

Figure P-17. The photograph of the test cell.

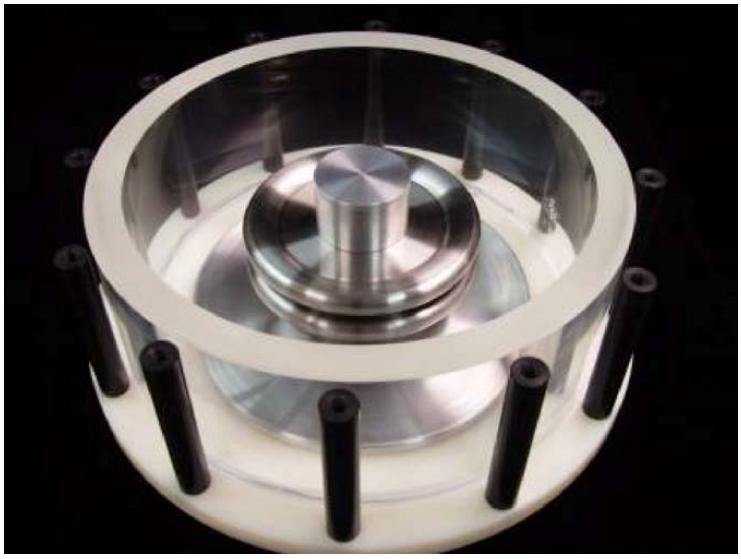

Figure P-18. Internal view of the test cell.

Cascade Switch Design Considerations

Initiation of the Discharge in the Cascade Section

The LTGS consists of two sections. Gas discharge in first section is initiated by a laser pulse; this causes the second cascade stage to become overvolted, which results in breakdown of the cascade gaps and switch closure. It was indicated by SNL[11] that overvolting is one of the main mechanisms of discharge initiation in the cascade section. The switch is designed so that the

nominal fields in the cascade gaps are 250 kV/cm. When the trigger section switches, the fields on the first few (2-3) cascade sections can go up by a factor of 2 from that nominal field level. Understanding the mechanisms by which discharges are initiated could lead to improvements in the LTGS design and operation.

It is clear that initiation of the discharge in the first stage of the switch occurs due to the dissipation of laser energy in the gas. In the case of the cascade section of the switch there are several possible initiation mechanisms for the discharge.

First, the discharge could be triggered in the gas by energetic electrons that could be produced due to the overvolting of the cascade sections, or by UV photons. These photons could be produced by the operation of the first section of switch or by local partial flashovers in the cascade section. Second, an electron avalanche could be triggered by field emission from the cascade electrodes.

Red arrows on Figure P-19 show potential sites for the emission of UV photons from the internal edges of the dielectric spacer. These photons could be generated by local discharges at the edge of the hole in the internal dielectric spacer. The electric field enhancement that would be responsible for this has been studied and discussed in previous sections titled "'Electro' Models of the Cascade Section" and "Calculations of the Electric Field in "'Electro' Software," where it was shown that the peak field peak at the inner edge of the hole in the dielectric could be as high as ~160 kV/cm. Such high values of the electric field could potentially lead to local breakdowns and play a noticeable role in initiation of the breakdown across the cascade gap at the points A and B through photoemission and photoionization.

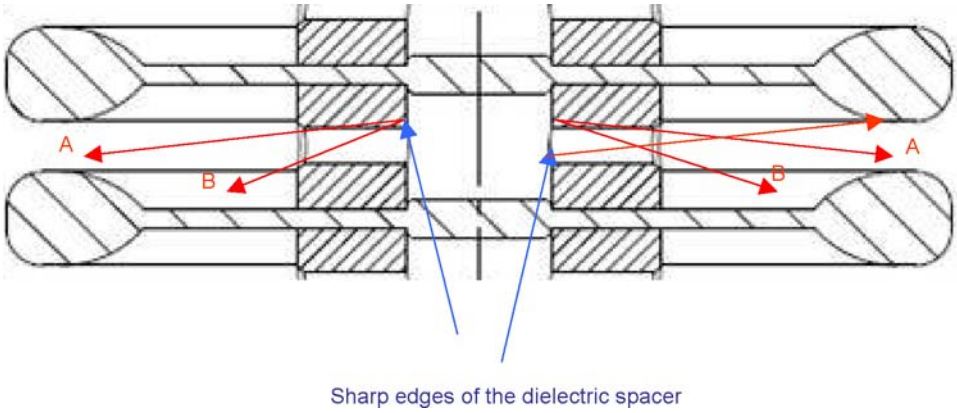

Figure P-19. Potential emission of photons from the edges of dielectric spacer into inter-electrode gap.

If the laser-triggered section is "line of sight" blind from the cascade gaps, then photoemission and photoionization from the laser section can be ruled out as the source for initiatory electron production in the cascade section. This therefore means that free electrons from background radiation, field emission from the cascade electrodes or photons from local flashovers are the only electron sources. The background ion-pair production rate (2-20 ion pairs per cc per sec)

coupled with the short window of opportunity make it unlikely that a free electron will be produced in the switch gas volume due to background radiation at a time immediately following closure of the laser gap. The problems of local discharges within the gap due to the spacer configuration can be addressed by modifying its design to reduce the local field enhancements. This would leave field emission as the only source of initiatory electron production. Even though the gap breakdown mechanism is described as overvolting, there must be a production mechanism for the initiatory electrons. Field emission occurs for electric fields above 100 kV/cm. If the field on the electrodes is similar to the gas field, which is retained to a level below 250 kV/cm, then field emission must be considered. The big question is "not if but when" does this start.

In addition, field emission may already have started before laser triggering occurs and the rapid acceleration of existing ionization processes is affected following the closure of the laser gap due to enhanced overvolting. Alternatively, the temporal statistics of field induced electron emission may be such that the cascade gaps are "silent" until laser gap closure, at which point the enhanced field causes spontaneous electron emission from the cascade electrodes (possibly from multiple sites causing multi-channeling) leading to breakdown. It would therefore be useful to consider how the field emission could be controlled to ensure better switch performance.

Control of Cascade Section Operation

Uni-Directional Electrodes

Concept of the Uni-Directional Electrodes

If the initiatory electron production does occur through field emission then there is no advantage in using symmetrical cascade electrodes. Non-symmetrical floating "toroidal" electrodes as shown in Figure P-20(b) will reduce the field enhancement at the negative electrodes and reduce field emission. This approach may allow the performance of the cascade section to be improved.

Non-symmetrical uni-directional electrodes will provide a field profile that influences electron production through field emission. It has been shown in paper[12] that the breakdown voltage for a system with a protrusion on a flat electrode surface behaves differently for negative and positive pulses. Figure P-21 shows the electrode configuration considered in this paper with a hemispherical protrusion on the top electrode.

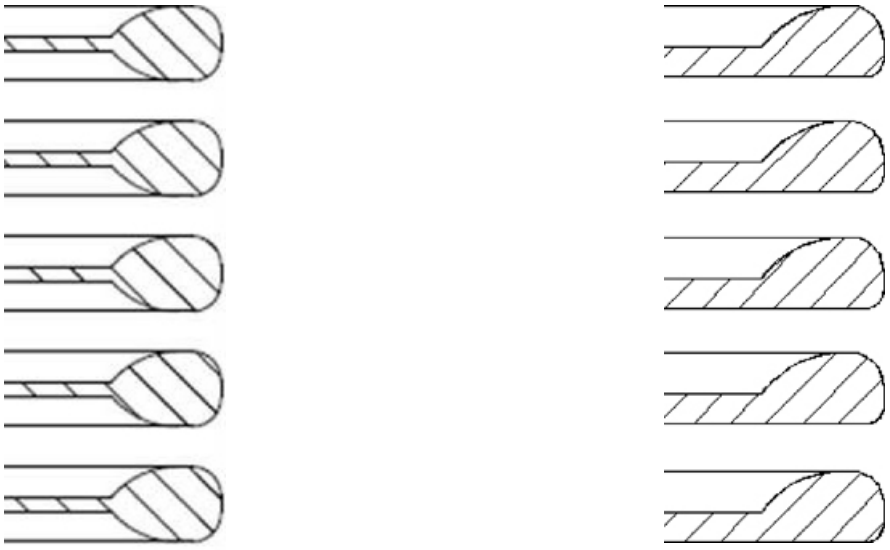

(a) (b)

Figure P-20. (a) Cross-section view of the Sandia symmetrical toroidal cascade electrodes; (b) conceptual design of the uni-directional cascade electrodes.

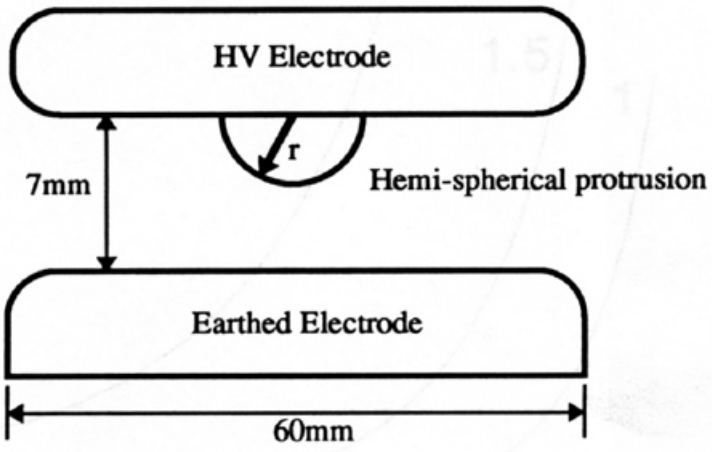

Figure P-21. Parallel plane electrode configuration with hemispherical protrusion.

The protrusion results in a local enhancement of the electric field, as shown in Figure P-22.

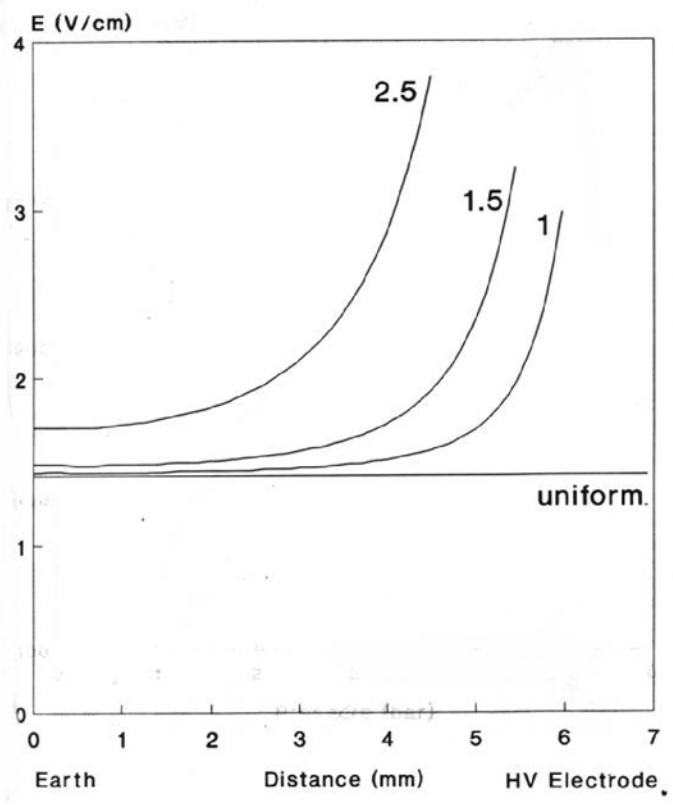

Figure P-22. Field distribution between electrodes. 1, 1.5, and 2.5 are radiuses of the protrusion in mm.

When positive pulses are applied to the gap, electron emission occurs from the flat electrode without a protrusion. The field near the flat electrode is not significantly affected by the presence of the protrusion on the opposite electrode, and therefore for positive pulses the breakdown voltage will be very similar to the breakdown field for a pair of flat electrodes and will not be significantly affected by the size of the protrusion (Figure P-23).

If negative pulses are applied the electron emission is affected by the local field near the protrusion, which is much higher than the average field between electrodes. This causes the breakdown voltage to be smaller than the voltage for flat electrodes without a protrusion (Figure P-24). This breakdown voltage also tends to reach a saturation value as the SF_6 gas pressure is increased.

Therefore there are advantages in designing an electrode system where the electrodes on the negative sides of the gap are flat, with protrusions on the electrodes on the positive side of the gap. This will allow the switch to be operated at higher pressures without the saturation effect on breakdown voltage observed in Figure P-24 occurring. This would make it possible to operate the cascade gaps at higher fields without breakdown before the operation of the laser triggered section.

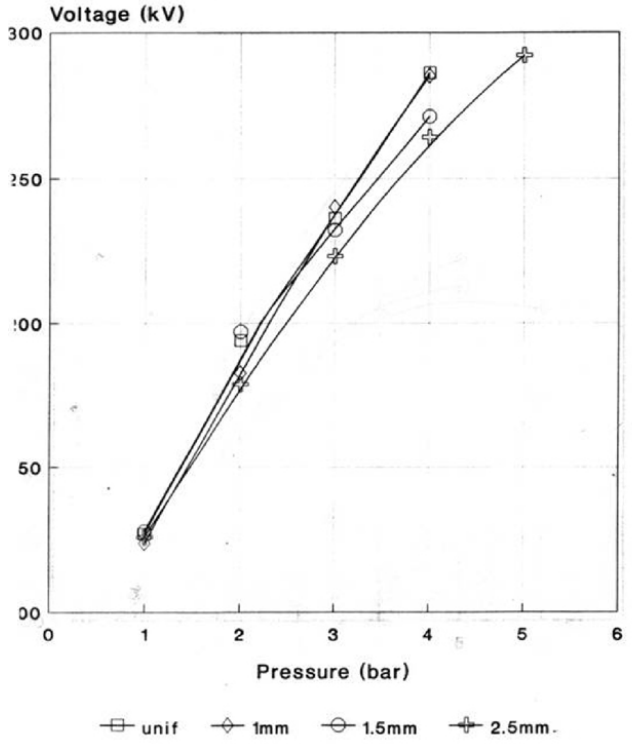

Figure P-23. Breakdown voltage in the electrode configuration with positive HV protrusion as function of SF_6 pressure.

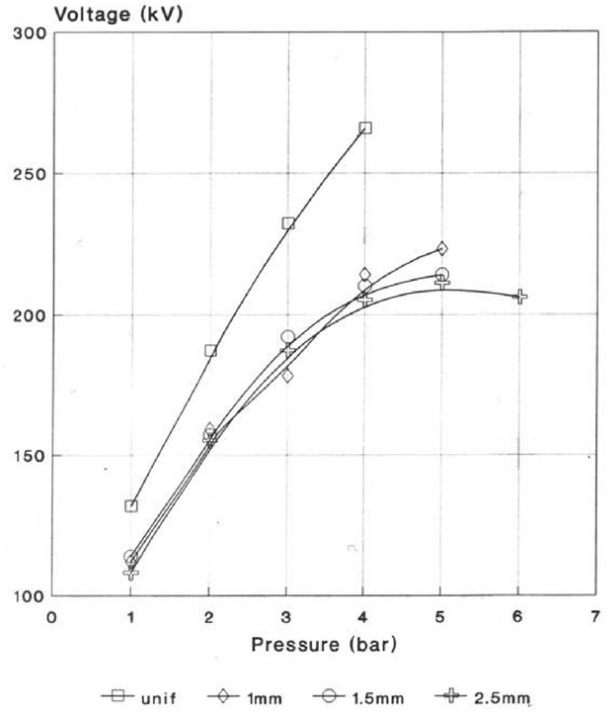

Figure P-24. Breakdown voltage in the electrode configuration with positive HV protrusion as function of SF_6 pressure.

Electrostatic Modelling of the Uni-Directional Electrodes

A model of the test chamber with non-symmetrical electrodes has been developed in "Electro" software. Electrical field distribution in this electrode geometry has been analyzed. It is planned to study different geometries of uni-directional electrode configurations. Figure P-25(a) shows non-symmetrical electrode design with electrodes of identical radius. Figure P-25(b) shows the field strength along the surface of the flat electrode. The electrical field in the vicinity of the top of the flat electrode is high, which is not desirable. In order to reduce the field in this region the radius of the left flat electrode could be made larger that the radius of the opposite toroidal electrode. The electric field in this design has been analyzed. Figure P-26(a) shows non-symmetrical electrode design with electrodes of different radiuses. Figure P-26(b) shows the field strength along the flat electrode. In this situation the field along the surface of the flat electrode does not change significantly and has its maximum near the apex of the toroidal electrode. This field distribution would be preferable in the cascade section electrode design.

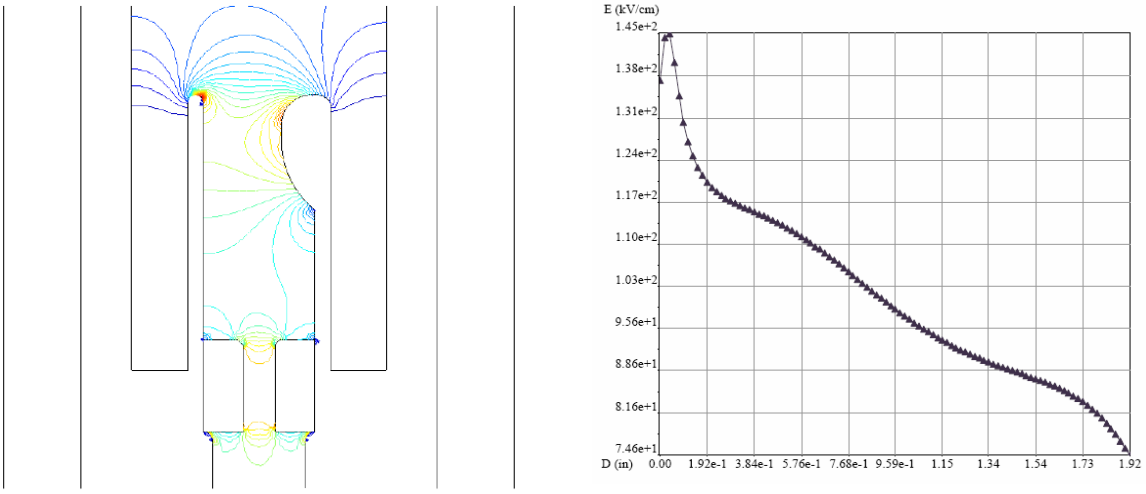

(a) (b)

Figure P-25. "Electro" model of uni-directional electrode configuration. Flat and toroidal electrodes have identical radiuses.

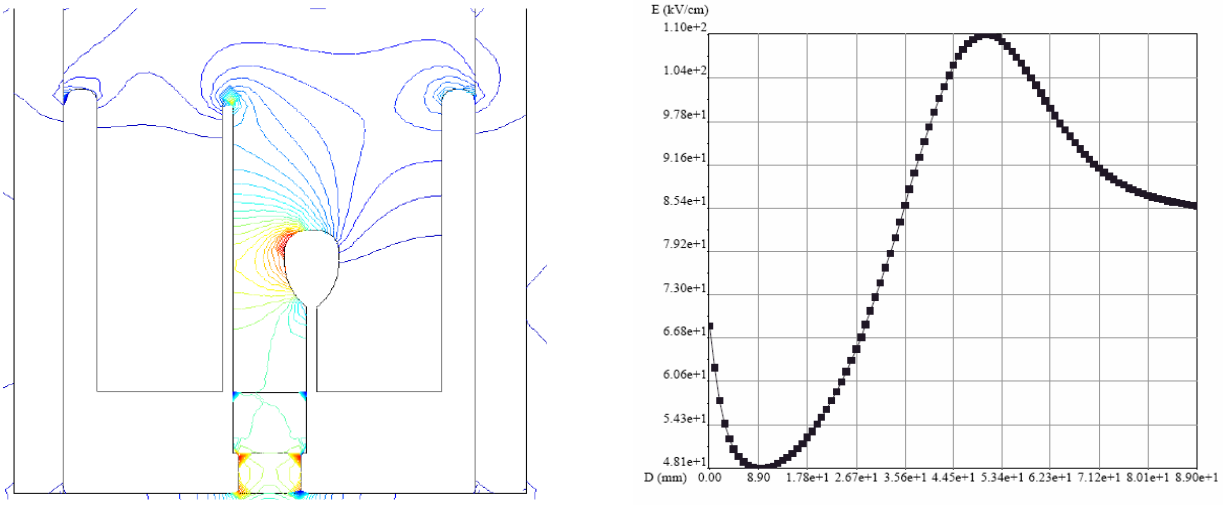

(a) (b)

Figure P-26. "Electro" model of uni-directional electrode configuration. Flat and toroidal electrodes have different radiuses.

In practical situations it is preferable to keep the radiuses of the cascade electrodes identical. Figure P-27 shows the proposed design of the cascade electrodes with identical radiuses but preferential field emission conditions from the right toroidal electrode. Figure P-27(b) shows the field strength along the flat electrode with a maximum field area located opposite to the toroidal prominence.

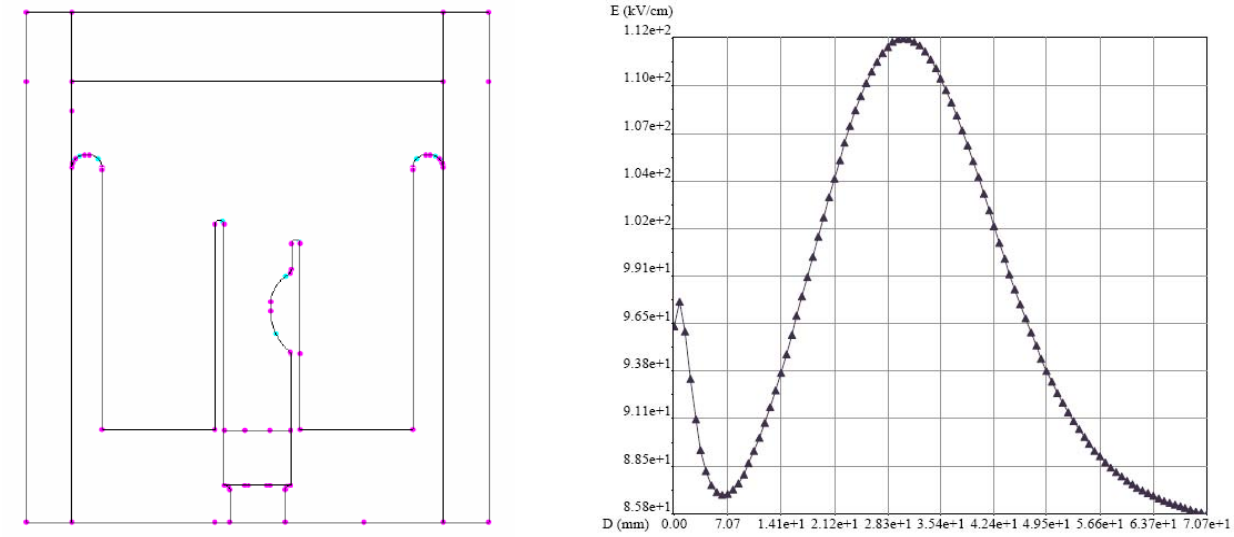

(a) (b)

Figure P-27. "Electro" model of uni-directional electrode configuration. Flat and toroidal electrode have identical radiuses but maximum field is achieved on the toroidal electrode.

Practical Design of the Toroidal Electrodes

Engineering drawing of the toroidal uni-polar electrode has been developed and discussed with the departmental workshop (Figure P-28). It is planned to start investigation of the uni-polar electrode configuration during the following phase of the project.

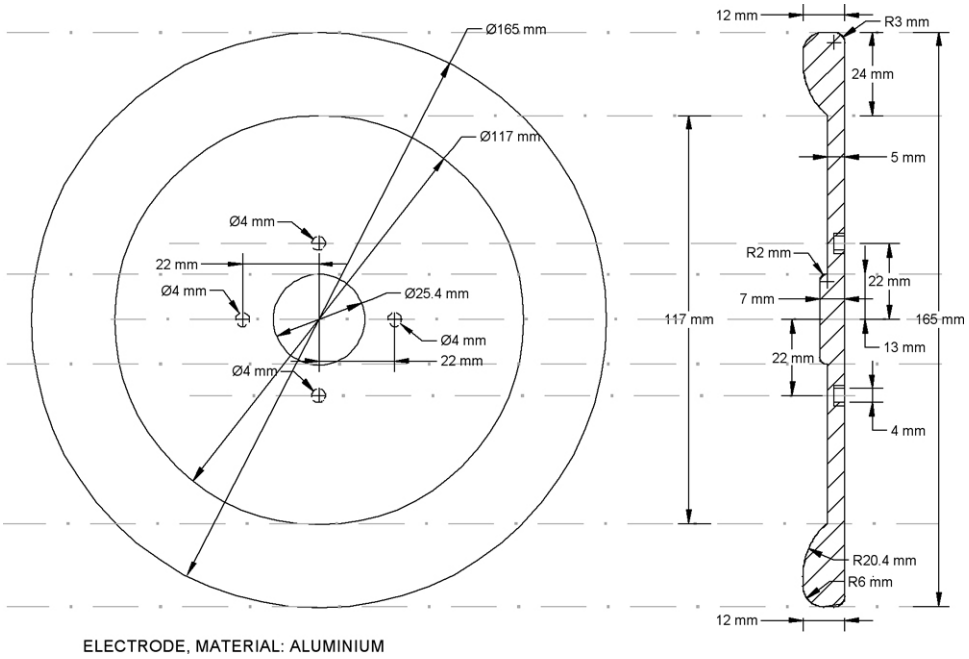

Figure P-28. Engineering drawing of the toroidal uni-polar electrode.

Capacitive Distribution of Voltage, Spacers with Different Permittivities, Different Gap Spacing

There would be advantages in ensuring that the voltage distribution across the cascade section was graded. This would help to ensure that the cascade broke down in a fixed rather than random sequence, which should allow more reliable and consistent switching behavior to be achieved. This grading could be implemented in various ways, which are discussed in this section. Capacitive distribution of the voltage amongst the gaps in the cascade section may be achieved by introduction of non-uniform grounding. This could provide sequential breakdown of the spark gaps, in a way similar to that introduced for Marx banks. The conceptual picture of the non-uniform grounding is shown in Figure P-29.

Introduction of dielectric spacer with different permittivities (Figure P-30) would also result in re-distribution of the electrical field and could help to control the breakdown sequence in the cascade section. Another approach to this problem would be different spacing of the inter-electrode gaps shown in Figure P-31.

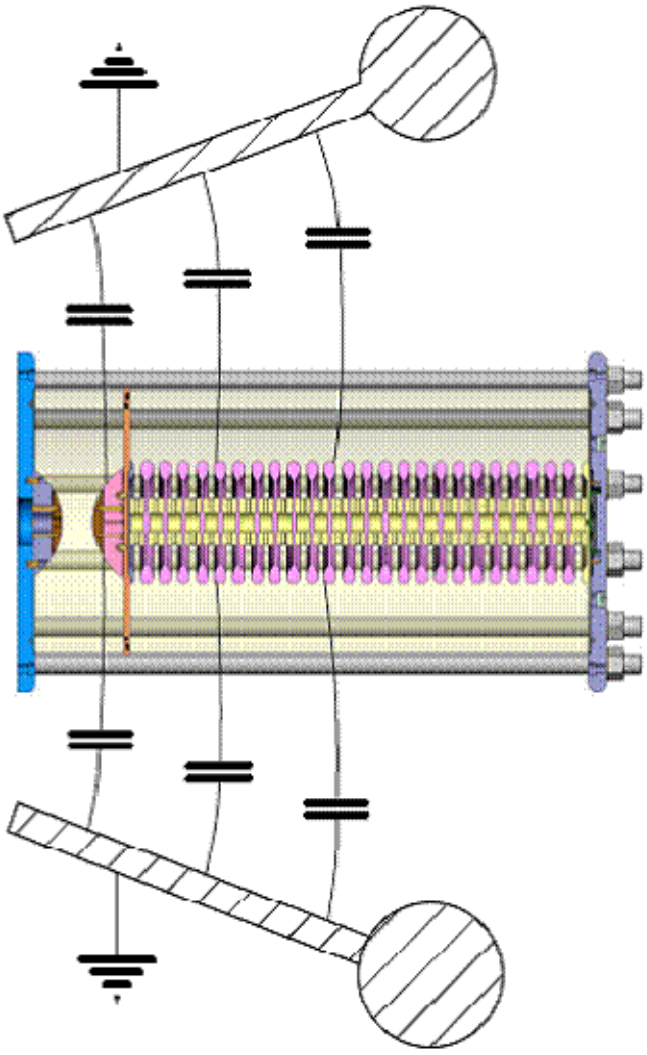

Figure P-29. Potential non-uniform grounding to provide sequential breakdown of the gaps in the cascade section.

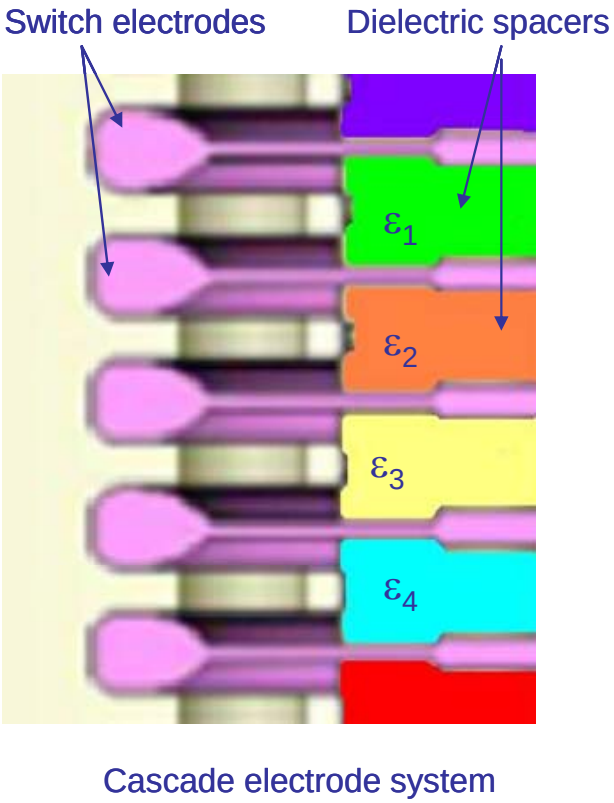

Figure P-30. Conceptual design of the cascade section with spacers of different permittivities.

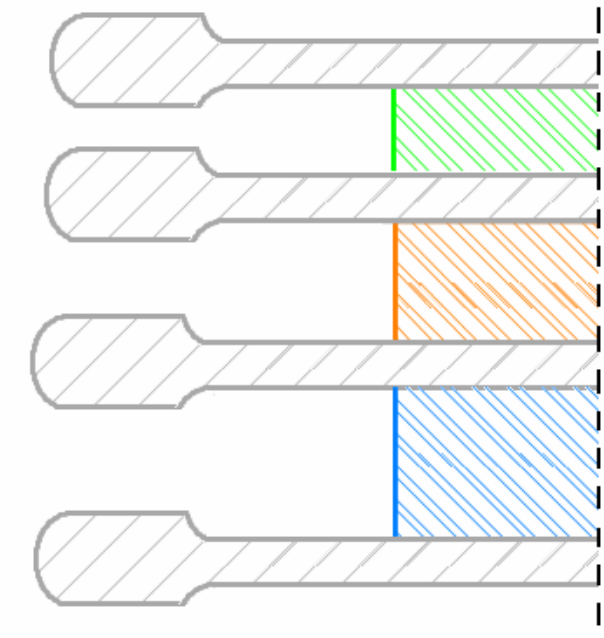

Figure P-31. Conceptual design of the cascade section with different gap spacing.

Other Possibilities: Leader Transition Effects, Gas Mixtures, Dielectric Coating

Better understanding of the leader-streamer transition in a non-uniform field could result in improvements in the design and operation of the cascade switch. It has been shown that for impulses with a rise time of ~1 μs the minimum impulse breakdown voltage is equal to the DC breakdown voltage at the minimum streamer-to-leader transition pressure and remains constant as pressure increases. In the range above the minimum streamer-to-leader transition pressure the DC breakdown voltage passes through a maximum.

The leader mechanism in SF_6 determines the breakdown characteristics in non-uniform gaps in SF_6 and the conditions necessary for the leader propagation are not fully understood yet. It has been suggested that a corona streamer discharge could turn into a stepping leader that propagates into the inter-electrode gap. At each step the leader precursor forms a short channel that propagates toward the cathode. The presence of ion near the tips of a streamer could be responsible for the formation and propagation of the leader, but the precise mechanism is not clear; it has been suggested that the presence of ions may permit the creation of a net charge at the corona streamer tip, which will result into development of electron avalanches. In Figure P-32 the streamer-to-leader transition pressures have been labeled for the SF_6 and two gas mixtures (A, B, C) and it indicates that this pressure increases as more air is added to the mixture.

This suggests that the use of gas mixtures could be another possibility of improving the cascade switch performance. As can be seen from Figure P-32, although adding 18% or 36% of air to SF_6 reduces the breakdown voltage at lower pressures, as the pressure is increased the breakdown voltage continues to rise smoothly rather than saturating or collapsing. This indicates that higher breakdown voltages can be achieved with a SF_6 mixture and it is possible to operate at higher pressures.

Figure P-33 shows that pure SF_6 (100%) at 2 bar has lower breakdown strength that the gas mixture that contains between ~50-75% of SF_6.

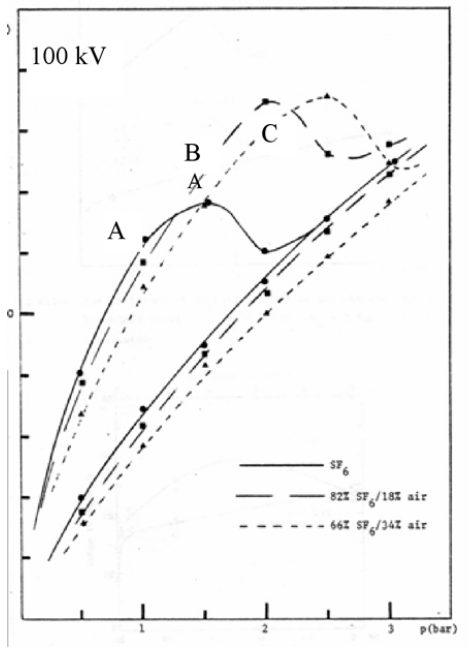

Figure P-32. Corona inception voltages (smooth lines) and DC breakdown voltages (curved lines) for SF_6 and SF_6/air mixtures.

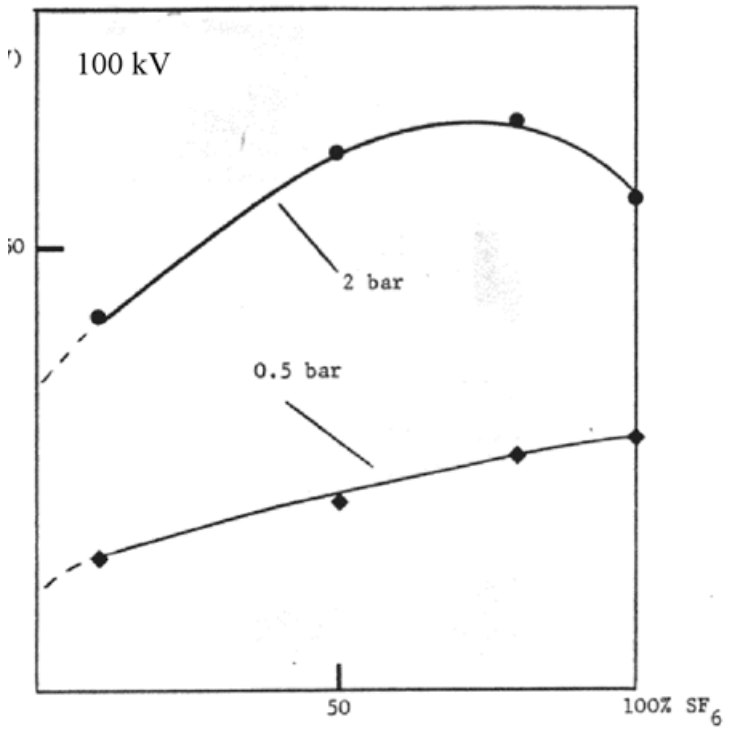

Figure P-33. Breakdown voltage as a function of SF_6 concentration for 0.5 and 2 bar pressures.

A possible approach to reduce the probability of misfires in the cascade section is to reduce field emission from undesirable locations. This could be achieved by coating regions of the cascade electrodes with a dielectric layer. This dielectric coating would minimize the electron emission from problematic places such as triple points and would reduce the open area of the electrodes. Therefore, the probability of the discharge initiation from the uncovered electrode areas will be increased, which would allow increased control of the cascade switch operation. The study of potential dielectric coatings for the electrodes is in progress.

Analysis of the Acrylic Switch Insulator Provided by SNL

Analysis of Shock Wave Action

Development of the Test Facility

The frame and an electrode system that allow point-point electrodes or thin conductive wire to be located on the dielectric surface have been manufactured (see Figure P-34). The frame has an electrode system that allows a thin conductive wire to be placed near the dielectric surface. This test system was used to generate 80-mm wire-guided discharges. In this arrangement the wire-guided discharge causes the development of a high-power ultrasound (HPU) pulse that impacts on the surface of the switch housing. This system allows the mechanical processes that will occur when the switch housing flashes over to be simulated at relatively low voltages and energies.

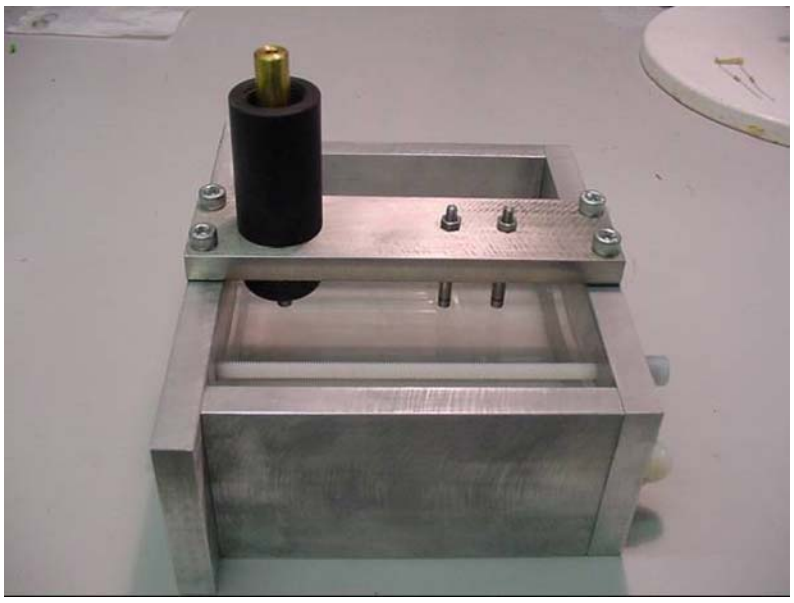

Figure P-34. Photograph of the test frame with a section of the dielectric material.

The complete HPU test facility includes the sample holder with the electrode system, the support frame and the rod to which the sample is attached, the cylindrical water tank, and the pulsed power supply. The photograph of the test rig is shown in Figure P-35. Using this system it is possible to produce wire-guided and free discharges with energies up to 1 kJ as a source of HPU.

Figure P-35. Water tank with metal support frame.

A section from the damaged insulation that was received from SNL has been cut into sections. Some of these sections have been used to study potential damage that shock pressure pulses could inflict on the dielectric body.

The section of the housing used in the HPU tests is shown in Figure P-36.

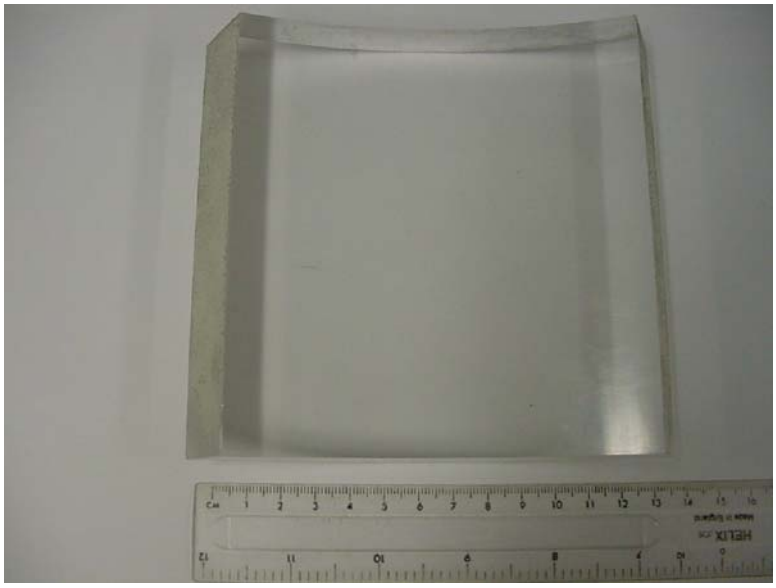

Figure P-36. Switch housing part before HPU tests.

Low-Energy HPU Tests

In first series of the tests the HPU pulses have been generated by relatively low energy wire-guided spark discharges near the surface of the acrylic insulator. The distance between the wire and the acrylic surface was a few millimetres. Other experimental parameters were as follows:

Charging voltage: 35 kV
Storage capacitance: 60 nF
Pulse energy: ~37 J
Wire length: 80 mm

In total 35 single shots were fired with an exploding wire between the electrodes. The picture of the housing section after HPU treatment is shown in Figure P-37.

Figure P-37. Switch housing part after HPU tests.

As can be seen from Figure P-37, the surface of the sample has not been damaged by the wire-guided spark discharges. Further tests with higher electrical energy are currently being undertaken.

High-Energy HPU Tests

In the second series of HPU tests higher pulse energies (up to 900 J) have been used. The section of the switch housing received from SNL has been used in the tests. The section of the housing before the high-energy HPU tests is shown in Figure P-38. The same sample holder as described previously has been used in the high-energy tests. As in the previous experiments a wire close to the surface of the polymer housing was used to guide the discharge.

Figure P-38. The section of acrylic dielectric before high-energy tests.

Other experimental parameters were as follows:

Charging voltage:	32 kV
Storage capacitance:	up to 1.68 μF
Pulse energy:	430-900 J
Wire length:	80 mm

The picture of the housing section after a 900 J pulse is shown in Figures P-39 though P-41. The housing part has been shattered.

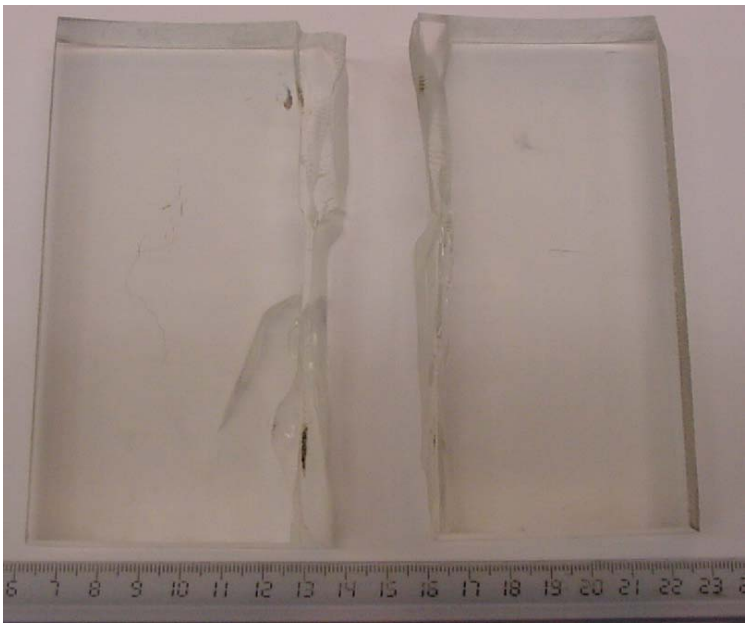

Figure P-39. Shattered acrylic insulator after a single 900-J pulse.

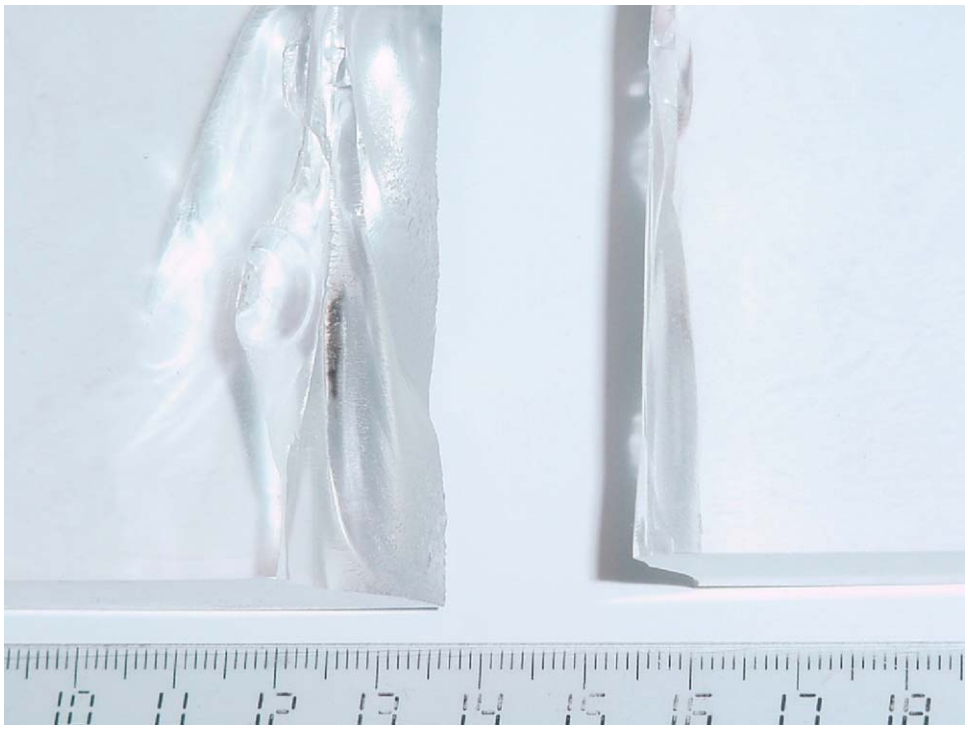

Figure P-40. Closeup view of destroyed section of the acrylic insulator (900 J).

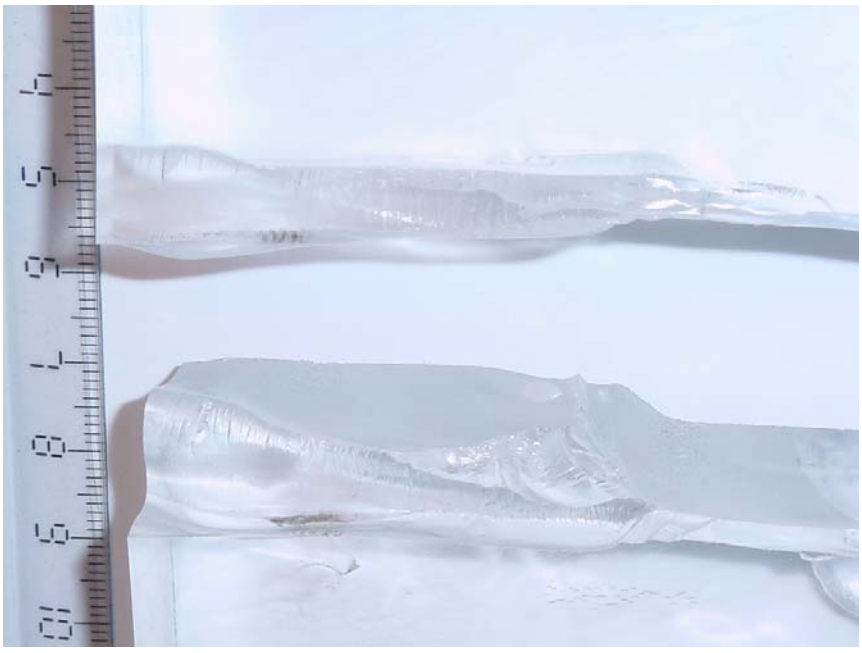

Figure P-41. Closeup view of destroyed section of the acrylic insulator (900 J).

Tests with lower energies (340-717 J) provided clear evidence of fracturing in the acrylic sample similar to that observed in the original SNL samples but at a much less extent (Figure P-42). Two symmetrical lines on the insulator surface indicate small fractures have been produced by the acoustic wave. Energies of 300-900 J are currently being investigated and multiple HPU pulses will be applied to the housing parts.

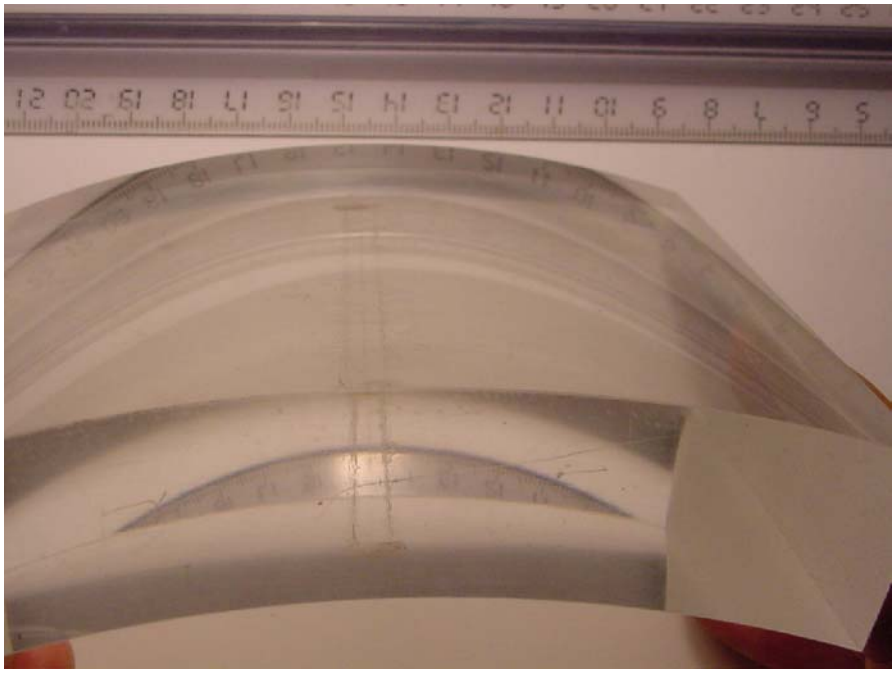

Figure P-42. Closeup view of damaged section of the acrylic insulator (573 J). Symmetrical fracturing (two parallel lines) of the insulator is visible in this picture.

Surface Conductivity Measurements on the Acrylic Switch Housing

The surface conductivity of the acrylic switch housing may have a significant impact on its flashover behavior. A experimental system to measure the surface conductivity of the housing of the laser triggered gap is currently being developed and tested. Once the design parameters and the performance of this equipment have been established they will be used to establish the effects the various processing and cleaning techniques used on the switch housing have on its surface conductivity.

For surface conductivity measurements to be meaningful it is necessary to design the measurement system so that the electric field applied to the sample is close to parallel to the surface of the sample and to design the measurement electrodes to ensure that the sensing electrode where the current flow is observed only detects the current that has passed along the surface of the sample and does not detect any current that has flowed through the bulk of the sample. In addition it is important that the field across the surface of the sample in the region where the measurements are to be taken is uniform and parallel to the surface. In the case of the Switch housing this is made more complicated due to its cylindrical geometry.

Basic Design of Sensing Electrodes

The first requirement can be met by designing the current sensing electrode so that it consists of a thin plate used to measure the current surrounded by a larger electrode that acts as a guard ring. This concept is shown in Figure P-43.

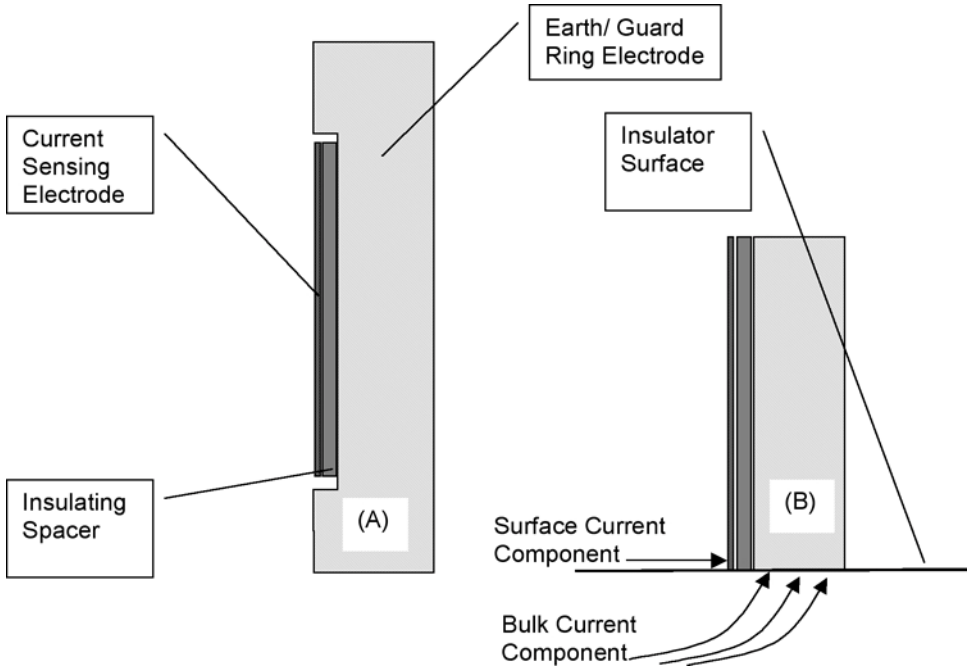

Figure P-43. Surface current sensing electrode. (A) View from above the electrode system. (B) Cross section showing current paths.

The thin current sensing electrode presents a very small cross-sectional area to the surface of the dielectric. This means that this electrode collects a very small proportion of the bulk current. The design of the earth/guard ring electrode ensures that the field in the region close to the sensing electrode will be close to uniform. The insulating layer prevents current flow between the guard and the sensing electrodes. In operation the potential of the sensing electrode will be controlled to ensure that it is at the same potential as the guard electrode.

Field Across Surface of the Housing

In the SNL switch housing, surface conductivity measurements are made more complex by the curvature of the surface and the thickness of the insulator housing. This complicates the design of the electrodes required to ensure that the electric field is parallel to the surface of the insulator. This has been addressed by using electrodes with surfaces normal to the insulator, and by having pairs of electrodes on the outer and inner surfaces of the sample.

A schematic of the side view of such an experimental system is shown in Figure P-44.

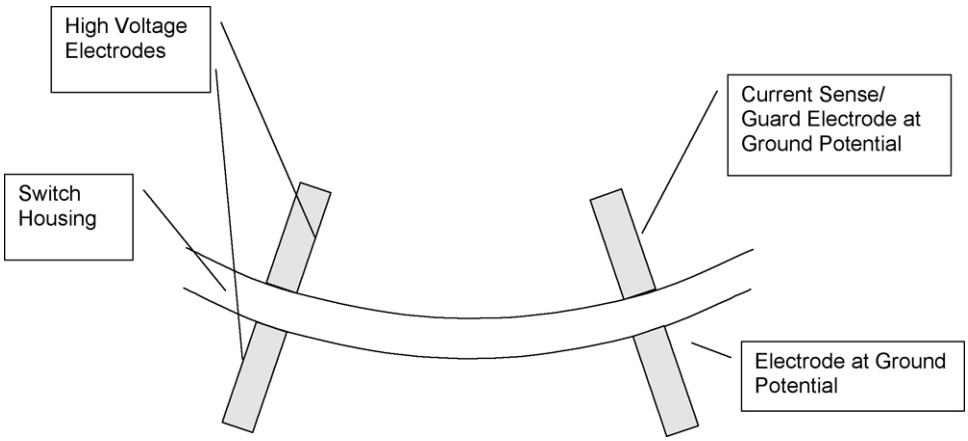

Figure P-44. Schematic of planned surface conductivity measurement system with pairs of electrodes.

To confirm that the proposed measurement system would perform correctly, field plots have been obtained for the electrode/insulator geometry using the Quick Field Finite element analysis package. Two pairs of radial electrodes (HV and grounded) have been located on both sides of the curved section of the dielectric, as shown in Figure P-35. The end surface of polymer has been set to the potential of the adjacent electrode. The equipotential between the electrodes are normal to the insulator surface with the field lines inside the dielectric following the curvature of the acrylic switch housing section. This means that a normal component of the electric field across the air/dielectric interface will be minimal and that the current flowing along the surface will follow the tangential field component.

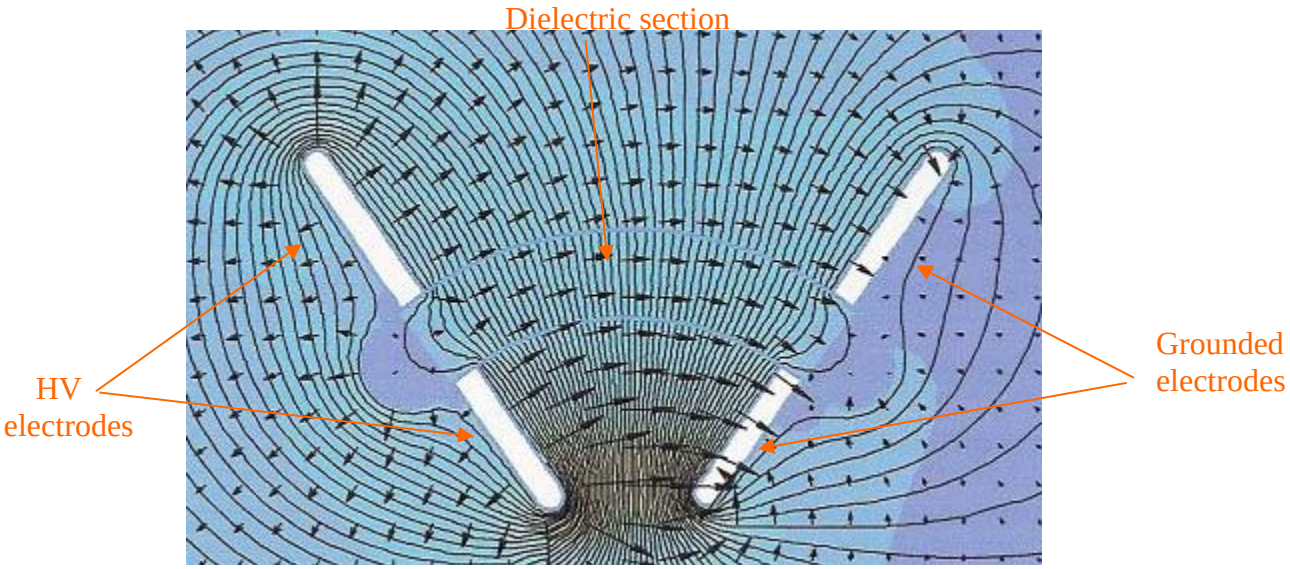

Figure P-45. Field distribution in the section of the acrylic insulator. Rectangular electrode shape. Polymer section is inverted compared to schematic in Figure P-44.

For an electrode system such as has been modeled in Figure P-45 to work effectively the surface of the electrodes must make a good contact with the insulator surface. As the switch housing has a curved surface, this may present fabrication problems. An alternative approach is to design electrodes, each of which has two sharp straight edges that will make contact with the surface of the switch housing. Field plots for such a design are shown in Figures P-46 and P-47.

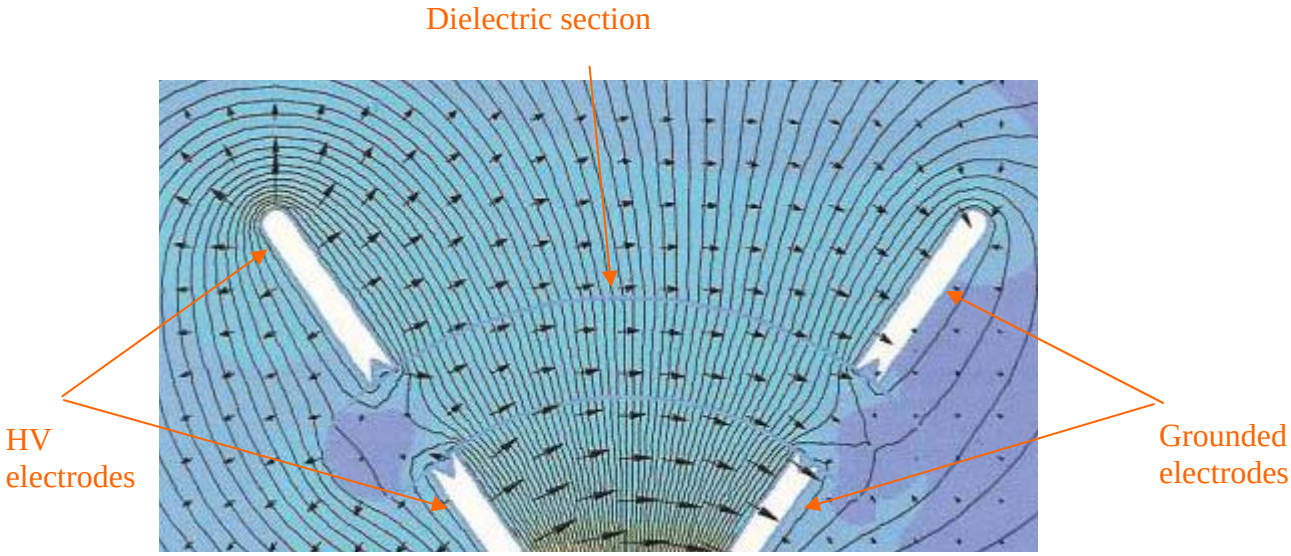

Figure P-46. Field distribution in the section of the acrylic insulator. Sharp edge electrodes. Polymer section is inverted compared to schematic in Figure P-44.

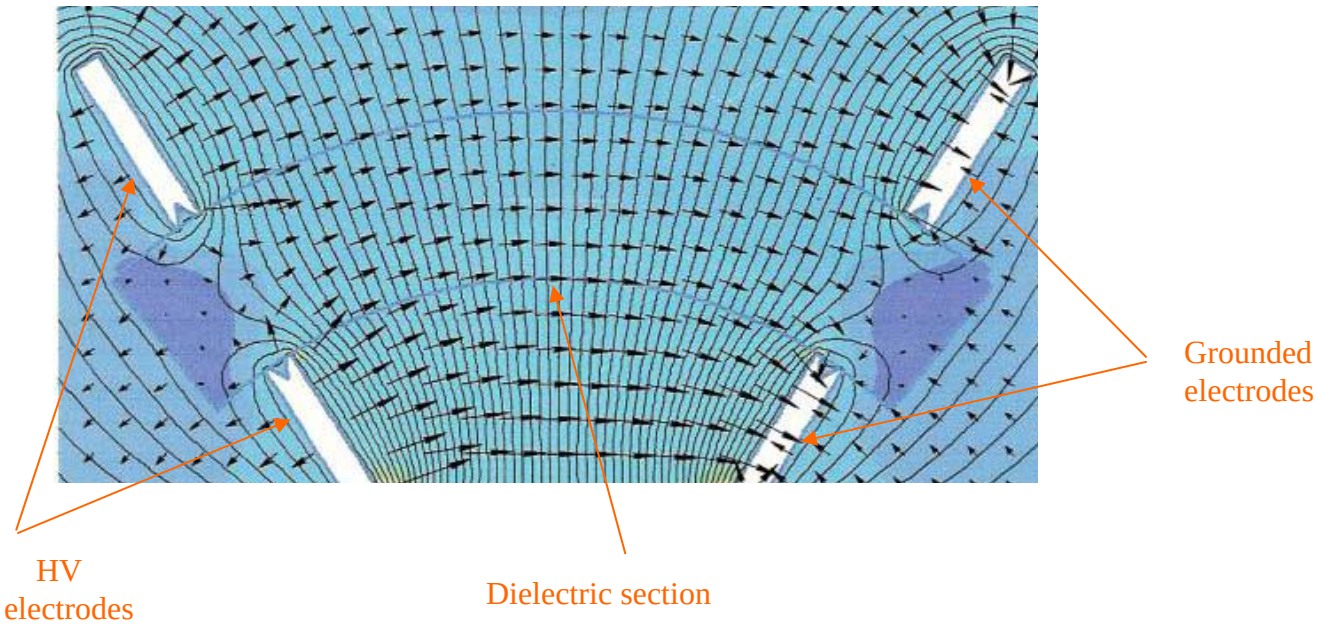

Figure P-47. Field distribution in the section of the acrylic insulator. Sharp edge electrodes. Polymer section is inverted compared to schematic in Figure P-44.

It can be seen that this approach also results in a reasonable field distribution across the surface of the curved dielectric spacer; however, there is an indication of some field distortion in the region close to the electrodes. There is also concern of the possibility the sharp edges might damage the samples or introduce mechanical stresses into the polymer when they are clamped onto the surface.

Fabrication of Surface Conductivity Test Rig

From the field plots reported in the previous section it has been decided to fabricate a measurement system based on a design using electrodes machined to match the curved surfaces of the switch housing. To simplify the design only the inner surfaces of the electrodes will be normal to the housing. Figures P-48 and P-49 show the electrode designs for contact with the outer and inner surfaces of the switch housing.

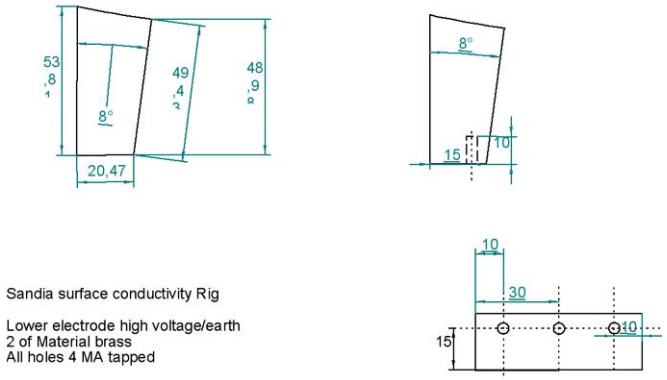

Figure P-48. Design of electrode to contact outer surface of switch housing for surface conductivity measurements.

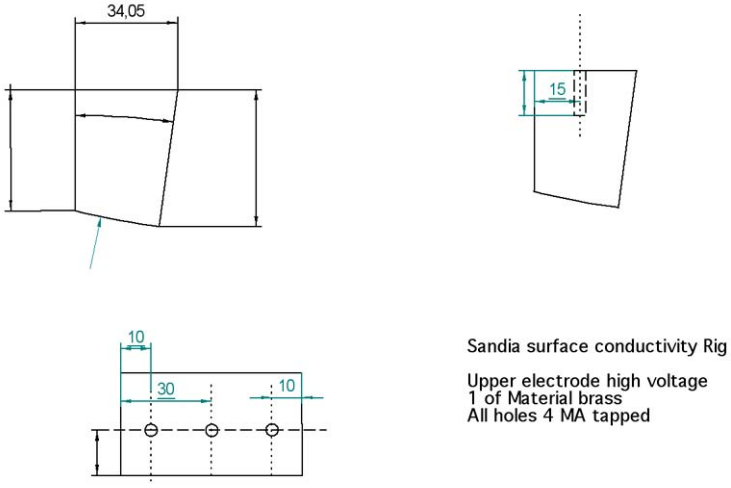

Figure P-49. Design of electrodes for contact with inner surface of switch housing for surface conductivity measurements.

The components to fabricate the measurement system are currently been manufactured in the HVT workshop facilities.

Conclusions and Future Work

In 2005-2006 the main aims of the Strathclyde University project team were

- Review improvements in the design of the Rimfire switch,
- Review SF_6, water, and oil volt-time breakdown characteristics,
- Design and develop a single gap test bed facility,
- Analyze field distribution in the cascade section of the laser triggered switch and the single gap test bed, and
- Analyze and test SNL insulation materials.

During this period the single test cell has been designed and developed and the study of the breakdown characteristics of SF_6-filled cell has been started. The customized pulsed power supply provides flexibility in pulse parameters, which is needed for breakdown properties investigation.

Electrostatic analysis of the cascade toroidal electrodes and the spacer between them allowed the problematic places to be identified and potential improvements in the cascade design have been proposed and discussed based on this analysis. One of the potential improvements could be introduction of additional gaps in the dielectric spacer (puck), as these gaps could potentially reduce the field values at triple points.

Conceptual design of uni-directional cascade electrodes has been proposed and several uni-directional configurations have been analyzed from the electrostatic point of view.

Action of HPU pulses on the acrylic dielectric has been studied. It has been shown that high-energy HPU pulses (900 J discharge energy) could cause complete disintegration of the acrylic housing. Lower energy pulses (300-700 J) caused local damage on the dielectric surface but did not result in the dielectric breakage.

Electrostatic analysis of the electrode system for surface conductivity measurements has been performed and the electrode system has been designed.

Future work will be concentrated on switching performance characterization and assessment and will include the following tasks:

- Identification of areas of the switch where there would be a benefit in reducing the electric field (areas of excessive aging), and regions where switch failure occurs.

- Identification of areas of the switch where there could be a benefit in increasing the electric field such as those regions that control the operation and sequence of the cascade section of switch or minimizing lateral discharges to the switch housing.

- Investigation of existing data for switch characterization.
- Delay times, dV/dt, jitter, V-t characteristic, V-p.
- Influence of operating voltage and switching waveforms.
- Correlation to failures/problems with switches.
- Statistical analysis/data-mining.
- Electrodes, their design and gas handling.
- Development of potential condition monitoring strategies.
- Development of switch designs and switching features for consideration.

The study on dielectric properties of the materials used in the switch design will be continued. This work will include surface conductivity measurements, investigation of mechanical degradation through surface damage, charge injection, electrical tree growth, mechanical stress etc.

It is planned to study charge injection into the material bulk. This is an electric field related phenomenon, which is likely to occur at the junction between metal electrodes. It is intended to determine whether significant charge injection can occur into the insulation at conductor interfaces when subjected to LTGS switching conditions.

References

1. H.M. Jones and E.E. Kunhardt, The influence of pressure and conductivity on the pulsed breakdown in water, *IEEE Trans. Dielectr. and Electr. Insul*., v. 1, n. 6, 1994, pp. 1016-1024.

2. A.P. Alkhimov, V.V. Vorob'ev, V.F. Klimkin, A.G. Ponomaranko, and R.I. Soloukhin, The development of electrical discharge in water, *Sov. Phys. - Doklady*, v. 15, n. 10, 1971, pp. 959-961.

3. V.D. Tarasov, V.A Balakin, and O.P. Pecherskii, Electrical breakdown in water by 0.5 1.7 MV pulses 0.5-5 μs long, *.Sov. Phys. – Tech. Phys*, v. 8, 1972, pp. 1379-1380.

4. D.B. Fenneman and R.J. Gripshover, Electrical breakdown in water in the microsecond regime, *2nd International Pulsed Power Conference*, Lubbock, TX, 1979, p. 122.

5. S.J. MacGregor, O. Farish, and I.D. Chalmers, The switching properties of SF_6 gas mixtures, *IEEE 7th Int. Pulsed Power Conf.*, Monterey, CA, 1989, pp. 510-513.

6. F. Tuema, Methods of improving the pulse repetition frequency of high pressure gas switches, PhD thesis, University of Strathclyde, 1996.

7. M. Giesselmann, I. Kusuma, W. Pfeiffer, and J. Wolf, Breakdown development of pulsed N_2 and SF_6 gaps, *5th IEEE Int. Pulsed Power Conf.*, Arlington, pp. 84-87, 1985.

8. T.H. Martin, An empirical formula for gas switch breakdown delay, *7th IEEE Int. Pulsed Power Conf.*, Monterey, CA, pp. 73-79, 1989.

9. A.H. Cookson, Review of high voltage gas breakdown and flashover of insulators in compressed sulfur hexafluoride, *Proc. Of the 3rd Int. Conf. on Properties and Applications of Dielectric Materials*, Tokyo, Japan, July 8-12, pp. 369-376, 1991.

10. J. Ozawa, Voltage-time characteristics of impulse breakdown in SF_6 gas, *Proc. of 5th Int. Symposium on Gaseous Dielectrics*, Knoxville, TN, USA, pp. 438-444, 1987.

11. J. Lehr, Sandia National Laboratories, Private communication, 2006.

12. S.J. MacGregor, S. Turnbull, F. Tuema, and O. Farish, Enhanced spark gap switch recovery using nonlinear V/p curves, *IEEE Trans. Plasma Sci.*, v. 23, no. 4, pp. 260-266, 1995.

APPENDIX Q. Physics of Dielectric Surface Flashover at Atmospheric Conditions

Center for Pulsed Power and Power Electronics
Texas Tech University

Introduction

With the new requirements in switching voltage, the present Z switch design is deemed inadequate due to switch failure occurring after only a few shots. The primary failure mode is surface flashover in the high-pressure gas (SF_6 > 40 psig) on the inside of the PMMA envelope. This surface flashover occurs initially during the regular cascade switching process without affecting the switch's electrical performance. However, the switch will prefire in the successive shot. The damage to the envelope has to be repaired before normal switch operation can resume. The following presents experimental results of pulsed surface flashover across different dielectric materials in SF_6 primarily at atmospheric pressure as well as flashover and volume breakdown in SF_6 at pressures from 10 Torr to 40 psig. Besides fast voltage and current monitoring of the breakdown event, an increased emphasis was put on imaging the event as well as gathering optical emission spectra (~200 nm to 700 nm) from it. The role of ultraviolet (UV) emission due to a volume SF_6 arc as a potential flashover holdoff reducing cause is discussed. As much as possible, the small-scale experiments were designed to reproduce at least partly the conditions as they are found in the large 5 MV Z switch.

Experimental Setup

The gas pressure in the Z rimfire switch is typically 40 psig. It was decided at the beginning of the project that an immediately available flashover chamber operating exclusively at atmospheric pressure was initially to be used to gather some baseline flashover data. Parallel to this effort, a new 40 psig chamber was designed and constructed. This chamber can handle pressures starting from a few Torr absolute to 40 psig. Both chambers are excited with an eight-stage Marx generator with up to 45 kV charging voltage per stage.

Atmospheric Flashover Chamber

The dielectric testing setup was an adaptation from a previous project in which extensive field simulations and impedance matching between the transmission line and electrode feed-throughs was done to ensure minimal signal distortion and system robustness. The design utilizes a coaxial geometry of 52 Ω impedance (see Figure Q-1). The dielectric testing chamber was created from half-inch-thick polycarbonate to allow for easy optical access. Dashed lines in Figure Q-1 represent a removable outer conductor which contains a small hole for imaging of the gap. Two ports, located at the base of the chamber, allow for a continuous flow of SF_6 or any other desired gas. The chamber is kept at a slight overpressure to prevent outside contamination. A photograph of the setup can be seen in Figure Q-2.

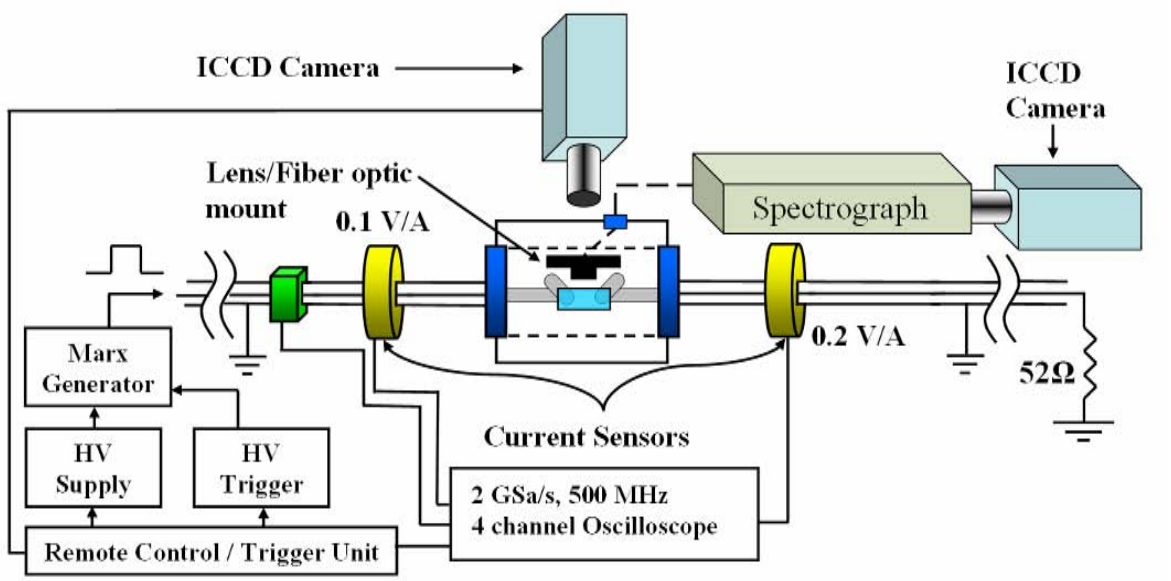

Figure Q-1. Experimental setup for surface flashover. The dashed lines within the dielectric flashover chamber represent a removable section of the outer conductor. Gas lines have been omitted for clarity.

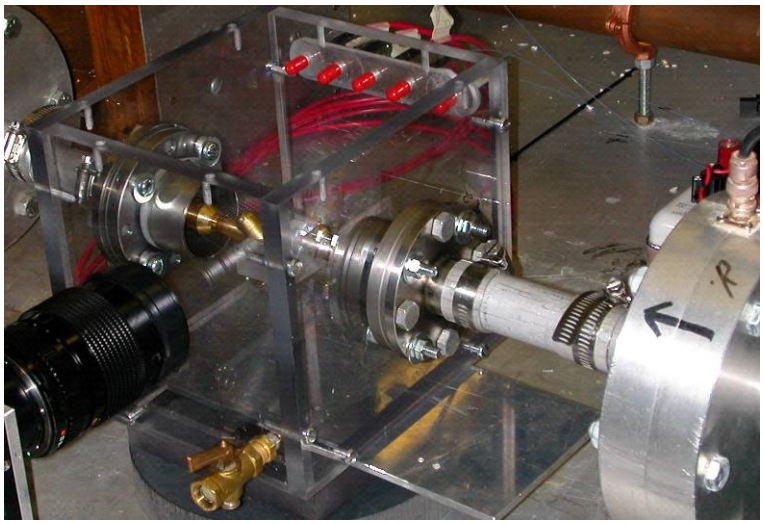

Figure Q-2. Image of atmospheric chamber including imaging and current measurement diagnostics.

Transient excitation is achieved via an eight-stage 360 kV maximum pulse Marx generator. The Marx generator is remotely charged with a high-voltage (HV) DC power supply capable of generating up to 125 kV at a maximum of 2 mA. A TTL trigger unit is utilized to trigger a 40 kV high-voltage pulser, which in turn triggers the Marx generator. When triggered, the voltage pulse from the Marx generator travels down a 1 m transmission line, through a 52 Ω water resistor (cupric sulfate), and then to the electrodes in the flashover chamber. The Marx

output voltage was typically set to 90 kV, which corresponds to a coulomb transfer of 60 μC for the atmospheric surface flashover testing with this chamber.

High-Pressure Breakdown Chamber

In order to accurately simulate the conditions within the Z_{20} gas switch a test chamber has been devised that can support pressures from 10 torr absolute to 40 psig. In order to achieve this pressure range the chamber is constructed of stainless steel. The chamber contains a variety of access ports to allow for the various diagnostics as well as pump-down and fill-line access. The high-voltage connection to the chamber inside is made by a custom fabricated feedthrough using an RG-220 cable fed through a compression port. The cable acts as a holder for one of the electrodes, while a sliding assembly attached to the chamber holds the ground electrode. This assembly enables changing samples as well as adjusting of the gap spacing. An overview of the chamber can be seen in Figure Q-3 and the entire setup is shown in Figure Q-4.

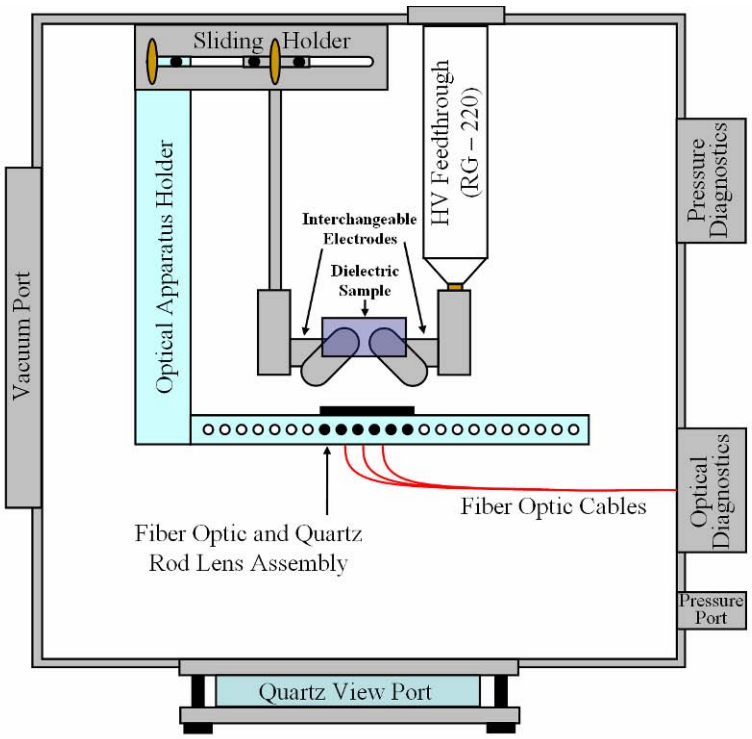

Figure Q-3. Overview of the high-pressure chamber (10 inches x 10 inches x 10 inches). Additional electrodes and flashover surfaces are omitted for clarity, but can be seen in Figure Q-5.

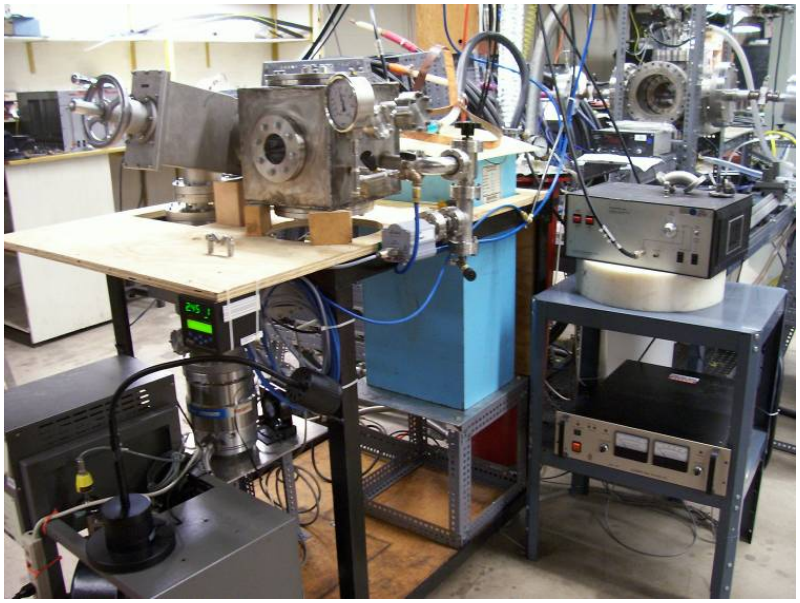

Figure Q-4. Photograph of entire setup including Marx generator, HV power supply, and pulser, and all associated peripheral equipment.

The Marx output voltage for the experiments with this high-pressure chamber was typically set to 320 kV, which corresponds to a coulomb transfer of 216 μC. In addition to the primary spark gap, the chamber also contains provisions for two additional surface flashover gaps. These surfaces are located directly above and below the primary gap, as seen in Figure Q-5. The purpose of these gaps is to study the effects of a primary arc, e.g., the UV radiation generated by it or accumulation of volume arc products, on the adjacent dielectric surfaces. A voltage stress can be applied to each surface by way of spring-mounted electrodes driven independently of the primary excitation.

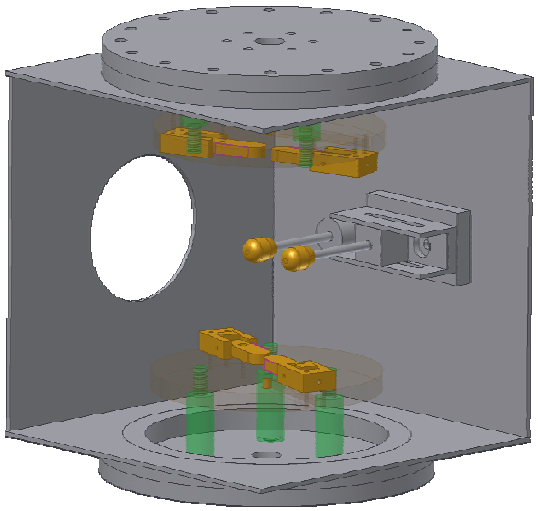

Figure Q-5. Three-dimensional view of high-pressure chamber, showing the relative position of the secondary flashover apparatus in relation to the primary spark gap. Shown with volume breakdown electrodes designed to match the edge radii of the backbone disks in the Z_{20} switch.

Diagnostics

Voltage and Current Measurements

Measurement of the dielectric flashover requires instrumentation with high temporal resolution. For this reason, capacitive voltage dividers with a sensitivity of 3.7 mV/kV and a rise time better than 1 ns were incorporated on to the 52 Ω transmission line in both setups. Traveling wave current sensors are utilized for the current measurements and have a sensitivity of 0.1 V/A with a ~1 ns rise time. All signals were then recorded using a 500 MHz bandwidth, 2 GSa/s, Agilent Infinium oscilloscope.

Imaging

Imaging of the flashover event is achieved using either a digital SLR camera with open shutter exposure, or an Andor Technology Intensified CCD DH-734 camera with nanosecond temporal resolution. The SLR is primarily used with the high-pressure setup due to the intense EMI generated by the discharge that could damage the ICCD. In both cases the camera is fitted with a zoom lens and is positioned directly outside the flashover chamber. In the atmospheric chamber the camera is focused on the dielectric gap through a small hole in the detachable outer conductor. Optical gate times of 3 to 300 ns were utilized for the flashover experiments. In the high-pressure chamber the camera can either be focused on the gap through the quartz view port or through the HV feedthrough hole in the upper flange on the chamber. The second method is utilized to allow for both imaging of the gap and collection of optical emission spectra concurrently.

Optical Emission Spectroscopy

In order to help determine some of the processes contributing to the flashover, a spectrograph is utilized to analyze the emissions from the discharge. The spectrograph is an Oriel MS 257 ¼ meter imaging spectrograph. It is equipped with a 4 grating turret and automatic grating switching. The MS 257 is a multi-track or imaging spectrograph. While normal spectrographs are designed for spectral (horizontal) resolution at the expense of vertical resolution, the MS 257 has toroidal mirrors designed to allow multiple vertical points, or fiber optic inputs, to be diffracted at one time. This feature is used to collect spectra from multiple points along the discharge path. A specially designed apparatus, shown in Figure Q-6, uses cylindrical quartz lenses to focus optical light emission from three rectangular areas between the electrodes into three fiber optic cables leading back to the spectrograph. In this way spatially resolved emission can be collected. The spectrum is recorded with an additional Andor ICCD camera.

Of specific interest is the UV range, since photoemission of electrons from the dielectric surface is unlikely at the longer wavelengths in the VIS. A literature survey yielded light absorption cross sections for SF_6 (see Figure Q-7). For comparison, the cross section for O_2 is also shown. Molecular nitrogen exhibits only notable absorption in the UV/VUV range for wavelengths shorter than ~ 120 nm and is therefore not shown.

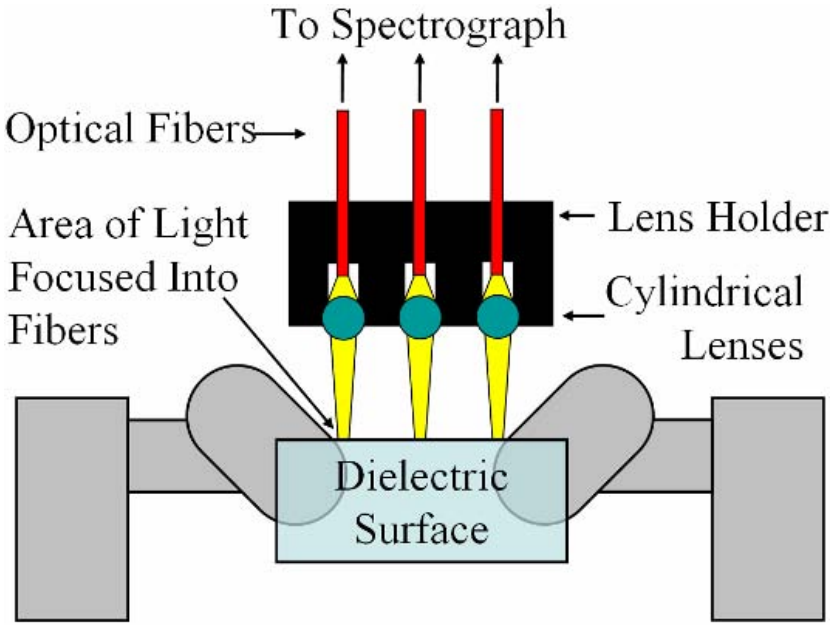

Figure Q-6. Cross section of the optical emission collection apparatus.

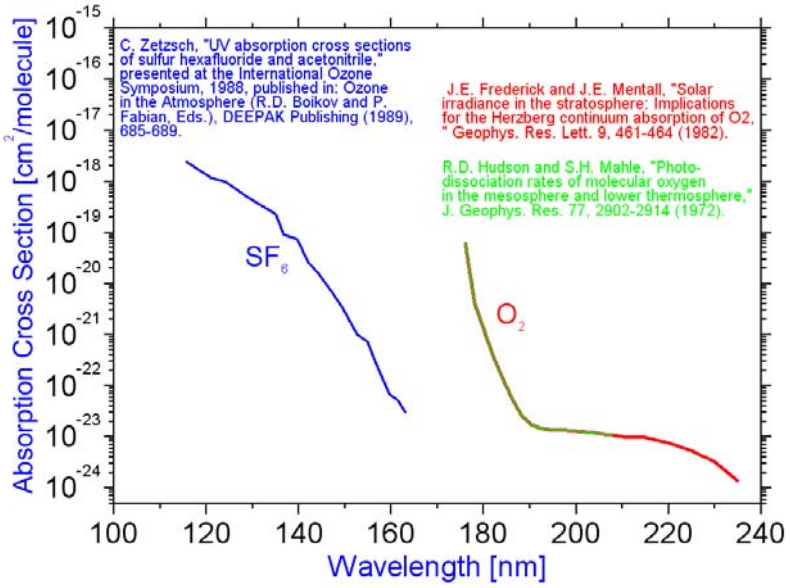

Figure Q-7. Absorption cross sections for molecular oxygen and sulfur hexafluoride.

For a given distance, the expected light transmission can be calculated from the cross section by

$$T = I / I_0 \cdot \exp(-\sigma n d) \qquad \text{(Q-1)}$$

with the transmission T, intensity of the incident/transmitted light I_0 or I, respectively, absorption cross section σ [cm^2], n molecule density (2.5×10^{19} cm^{-3} for STP), and d distance [cm]. The resulting transmission for the switch conditions, d = 2.75 inches, n corresponding to 40 psig of gas, reveals that light above 160 nm is easily transmitted in an SF_6 atmosphere, while this limit is roughly 180 nm for molecular oxygen (see Figure Q-8).

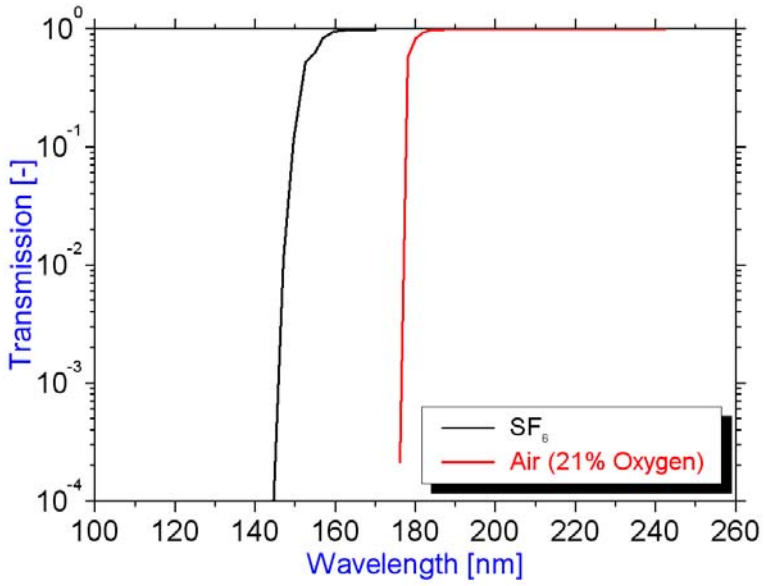

Figure Q-8. Light transmission for molecular oxygen and SF_6 through 2.75 inches of gas at a pressure of 40 psig.

Previous studies at TTU revealed that the surface flashover path can be affected by external UV illumination if the wavelength range is extending down to ~ 320 nm as a minimum (no noticeable impact for light in wavelength range > 400 nm).[1] While these tests were done in a nitrogen environment at atmospheric pressure across a polycarbonate surface (Lexan), it still indicates that wavelengths higher than the 165 nm, i.e., the limit of the data in Figure Q-8, will likely be of importance.

In order to verify that UV is easily transmitted in high-pressure SF_6, a broadband UV source was utilized to measure the spectral transmission through 5 inches of SF_6 and N_2 (see Figure Q-9). Overall, the SF_6 and the N_2 reference curve match well, clearly indicating very little, if any, absorption for SF_6 in the range from 250 to 800 nm for the conditions found in the Rimfire

[1] K. P. Morales, J. T. Krile, A. A. Neuber, and H. G. Krompholz, Pulsed Dielectric Surface Flashover in Atmospheric Conditions, to be published in the *IEEE Transactions on Dielectrics and Electrical Insulation*, 2006.

switch. It should be noted that the signal below ~ 250 nm becomes very noisy, which is due to the decreasing light output of the broadband source at shorter wavelength and the also smaller spectral response of the utilized spectroscopy system at shorter wavelength. Since there is presently no known absorption resonance of SF_6 between 165 nm and 250 nm, it should be assumed that virtually all light between 165 and 800 nm is transmitted easily through 2.75 inches of SF_6 at 40 psig.

While the above clearly shows that UV/VUV light can easily propagate in the conditions found in the Rimfire switch, experimental optical emission spectra of SF_6 discharges need to confirm that light in the relevant wavelength range ($\lambda < 320$ nm) is actually generated during switching.

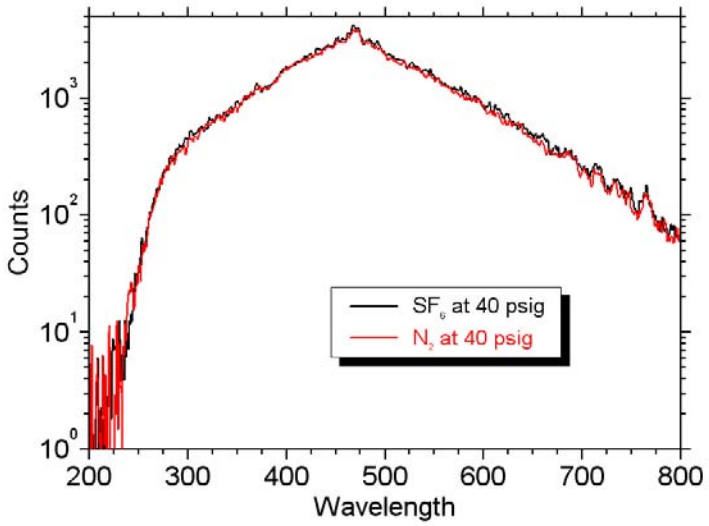

Figure Q-9. Measured spectral response of the TTU spectroscopy system to a broadband Xe high-pressure lamp for transmission through 5 inches of SF_6 or N_2, respectively.

When interpreting measured spectra, the spectral sensitivity of the spectroscopic system needs to be taken into account. The spectral sensitivity of the system is primarily determined by the spectrograph grating, the fiberoptics (UV grade fused silica fiber), and the camera's photocathode quantum efficiency. What is desired is an inverse apparatus function that can be multiplied by the collected data to yield the actual spectra. This function is determined using two calibration sources with known outputs. The first source is a deuterium lamp (a #63162 bulb from Newport) and the second is a xenon lamp (a #6254 bulb from Oriel). Both sources have a relatively well-defined output in specific wavelength ranges and the combined response was used to calculate the apparatus function. Any raw data recorded by the ICCD is typically in counts, while the scaled data, which accounts for the losses in the collection system, is labeled as relative intensity in arbitrary units. All data shown in this report was corrected using this calculated calibration curves, shown in Figure Q-10.

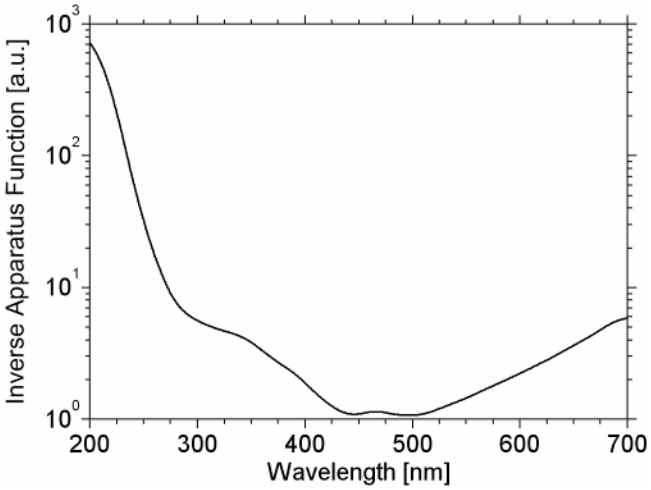

Figure Q-10. Scaling curve for all collected spectra, accounting for internal loss in the collection apparatus.

Electrode Properties

Two distinct sets of electrodes were used, one for surface flashover and one for volume breakdown. The dielectric flashover experiments were conducted with angled electrode geometry, as shown in Figure Q-11. The electrodes used in the atmospheric chamber are machined from brass and are mounted at a 180-degree angle from each other and are embedded approximately 0.54 inch into the dielectric material. Electrodes with identical dimension made of stainless steel were used in the high-pressure chamber. This was done primarily to match the material, 410 stainless steel (ASTM A240), used in the actual switch in the Z_{20}. A set of brass, angled electrodes is also available for testing in the high-pressure chamber if desired. A second set of stainless steel electrodes, designed to mimic the individual "vertebrae" in the Rimfire switch, was used for volume breakdown and is shown in Figure Q-12.

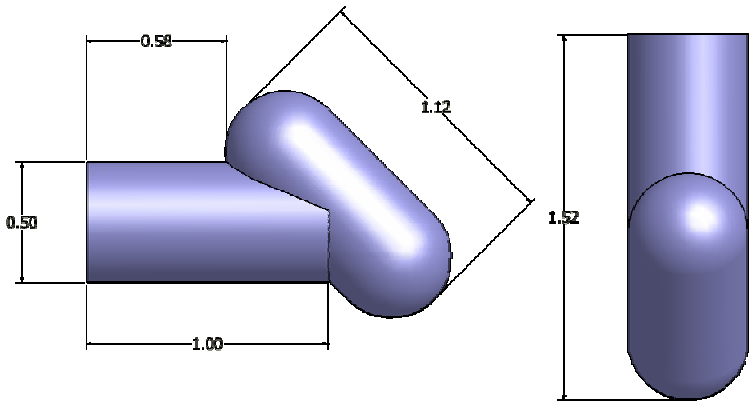

Figure Q-11. Drawing of angled electrodes used for surface flashover experiments.

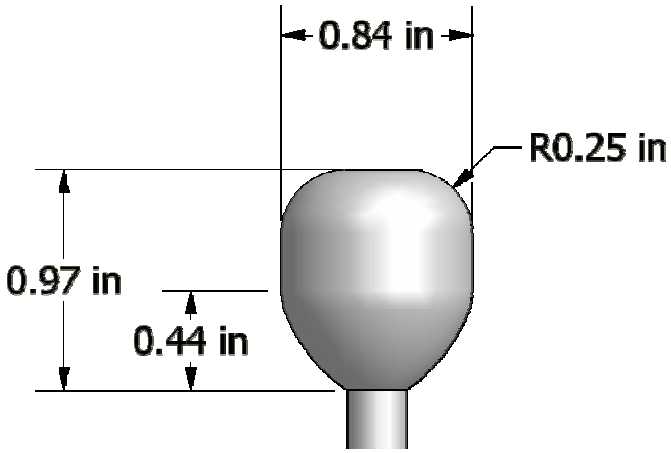

Figure Q-12. Electrodes used for volume breakdown in the high-pressure chamber. The electrodes are designed to mimic outside edge of the "vertebrae" in the Z_{20} Rimfire switch.

Dielectric Sample Geometry

Extensive field simulations were done on multiple electrode designs using Ansoft's Maxwell three-dimensional (3D) simulation program. The angled electrode design produced strong electric field components normal to the dielectric surface, and as such was utilized in the experiments. An example of the magnitude of the electric field between the electrodes with the application of 72 kV can be seen in Figure Q-13. During the experiments a variety of dielectric materials, listed in Table Q-1, were tested.

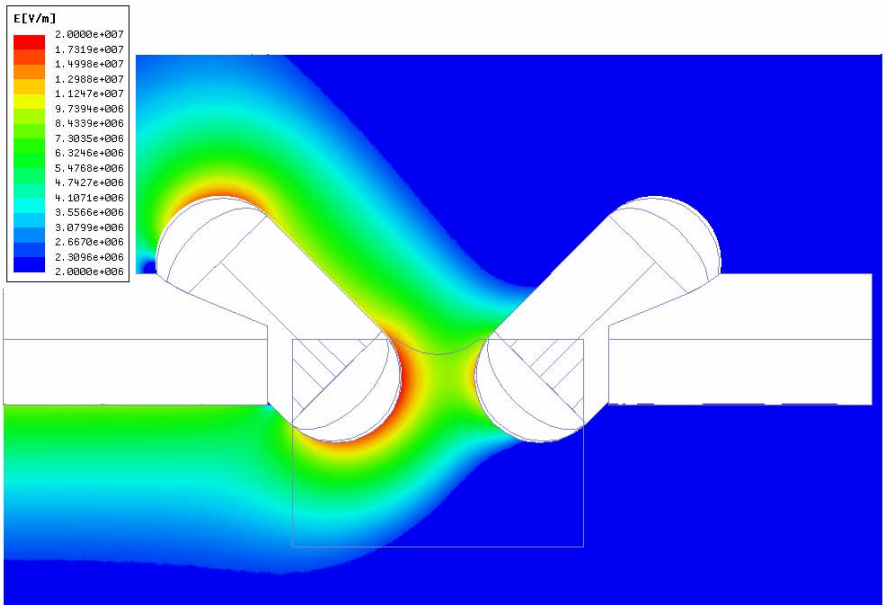

Figure Q-13. Maxwell 3D simulation of electric field magnitude for the angled electrode geometry in a cut plane normal to the dielectric surface.

Table Q-1. List of dielectric materials used during testing.

Optical Grade Lexan	Rexolite
Virgin Teflon	Epox 826
High Density Polyethylene (HDP)	826/D-400/KF-865 80 °C 3 days
Plexiglas	

For each of the materials, three different surface geometries were tested. However, the dimensions of the dielectric samples remained the same, and can be viewed in Figure Q-14. The surface geometries were defined as follows: a smooth surface is a dielectric sample whose surface is one that was not altered or machined except for the electrode slots; a rough surface is a dielectric sample whose surface was sanded with fine-grit sandpaper to create micro protrusions on the surface (in the explanation of the results, the sandpaper grit and number of passes will be associated with the sample); and a grooved surface is a dielectric sample having a groove machined along the surface of the sample. For the path of the groove along the surface, refer to Figure Q-14. Although considerable effort went into creating uniformity in each sample and surface type, the machining of the groove depth varied slightly. This variation, although slight, showed an effect on the behavior of the flashover event, which will be discussed later.

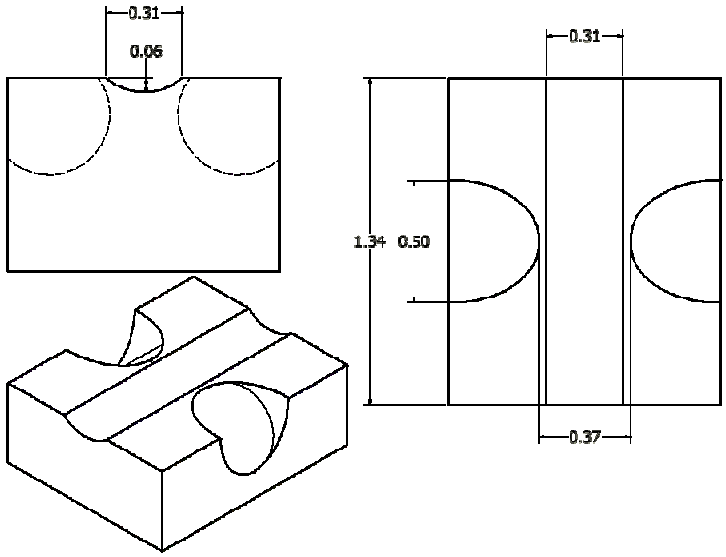

Figure Q-14. Dielectric sample geometry and dimensions used for testing.

Procedure

Uniformity of testing procedures and the machining of dielectric samples was crucial to the accuracy of the recorded data. After machining, each sample was cleaned with cyclohexane and then inserted between the angled electrodes in the flashover chamber. Once inserted, the ICCD camera was then focused on the surface path between the electrodes. In the atmospheric chamber, the flow valves for the gas of choice are adjusted until the gas flow in the chamber is observed. The chamber is purged for about 2 minutes before testing to minimize pre-existing

contaminants. The gas is then set to a slight overpressure and allowed to flow at a constant rate throughout the experiment to prevent further contamination. In the second setup, the chamber is pumped down to 10s of torr before being backfilled with SF_6 until the desired pressure is achieved.

SF_6 Surface Flashover Material Studies

Reference Waveforms

For each flashover event, the camera gate (when applicable), current, and voltage waveforms were acquired and recorded. A representative set of surface flashover oscilloscope waveforms is depicted in Figure Q-15. The typical flashover voltage waveform is characterized by a sharp rise in voltage as the voltage pulse is applied to the gap, followed by a distinct drop in voltage as flashover occurs. The collapse of the voltage due to flashover is then accompanied by the simultaneous rise in current. It should be noted that the Marx generator used was set to output a negative voltage pulse. The time interval between negative voltage rise and current rise will be referred to as breakdown delay time in the following.

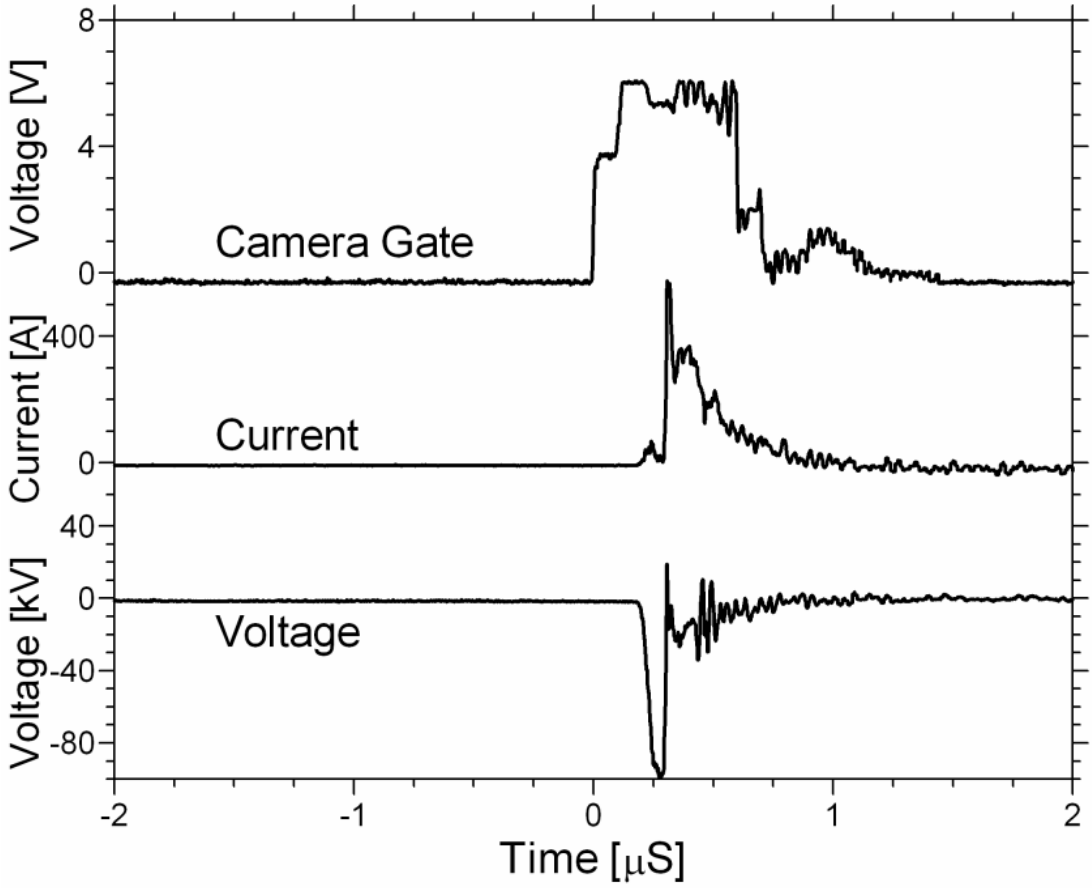

Figure Q-15. Representative waveforms for camera gate, current, and voltage signals for flashover in SF_6 at 1 atmosphere absolute pressure.

Material Flashover Analysis

As stated previously, the flashover analysis process consisted of many steps. One of the first steps that allowed us to obtain information on the flashover behavior was the data recorded from the ICCD camera. The images taken during the flashover event were angled on the surface of the dielectric such that the path of the event could be seen. This proved important in the investigation of whether the flashover event followed the electric field lines or the surface of the dielectric. The results of the liftoff occurrences for each dielectric material are listed in the following section. Below, images of Teflon are shown because of its high percentage of liftoff occurrences (see Figures Q-16 through Q-18). An interesting observation was that although it can be seen that Teflon flashover did follow the surface for some instances and distances, the flashover did not leave visible tracking on the surface. Even under scanning electron microscopy (SEM) imaging, surface distortions or abnormalities could not be detected. The same was observed for the one sample of Plexiglas used in testing. Further investigation into Plexiglas is required.

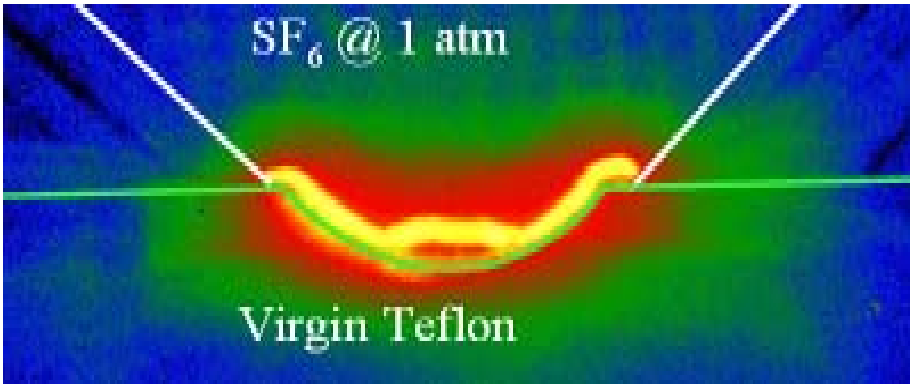

Figure Q-16. Grooved virgin Teflon sample at 1 atm of SF_6. Gap = 10.53 mm, T_{delay} = 92 ns, V_{pulse} = ~91 kV.

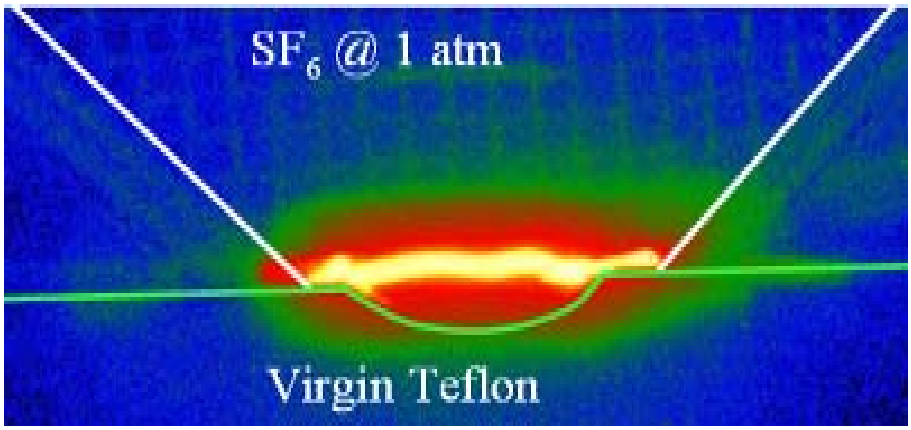

Figure Q-17. Grooved virgin Teflon sample at 1 atm of SF_6. Gap = 9.48 mm, T_{delay} = 307.3 ns, V_{pulse} = ~90 kV.

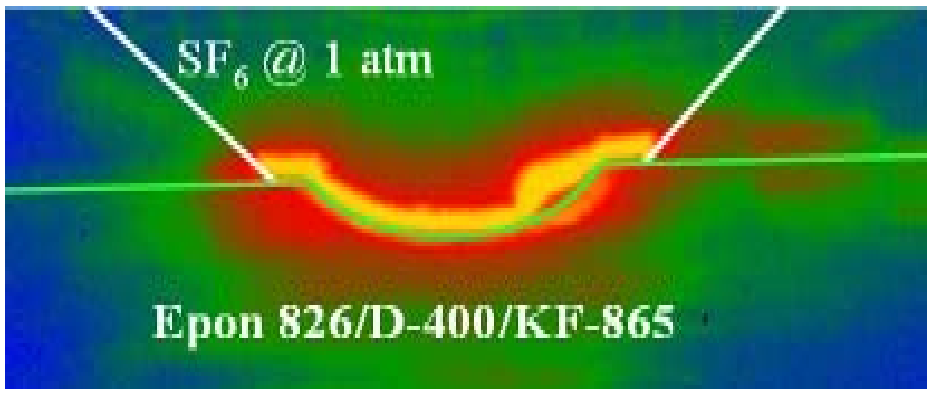

Figure Q-18. Grooved Epon 826/D-400/KF-865 sample at 1 atm of SF_6. Gap = 10.8 mm, T_{delay} = 50 ns, V_{pulse} = ~69 kV.

Material Comparisons

For the comparison of the materials, two methods were chosen. The first was to compare the materials percentage of liftoff for total samples of that material. That is to say, out of all the flashover events recorded for the specific material, how many lifted off the surface. It should be noted that in relation to the other materials, only one sample of Rexolite, HDP (High Density Polyethylene), and Plexiglas was tested.

Table Q-2. Dielectric material comparisons of liftoff during flashover event. Each of the dielectric samples was flashed typically 10 times.

Material	Liftoff Percen-tage	Number of Samples	Permittivity	Comments
Teflon	50%	12	2-2.1	Partial liftoff (Grooved samples)
Lexan	0%	11	3	
HDP	0%	1	2.26@ 1Mhz	
Rexolite	0%	1	2.53 through 500 Ghz	
Plexiglas	50%	1	2.2-3.4	Very partial liftoff (Grooved sample)
Epon 826/T-403	13%	4	~5	Partial liftoff (Grooved samples)
826/D400/KF-865	18 %	3	~5	Partial liftoff (Grooved samples)

Teflon with the highest number and most distinct liftoffs is known to have a comparably small photoemission coefficient compared to most dielectrics. As the arc itself emits UV radiation (see the section titled "SF_6 Volume Breakdown"), the observed behavior would underline the importance of photoemitted electrons from the surface for the flashover dynamics.

While the observation of liftoff or no liftoff is relevant to understanding the flashover dynamics, including erosion effects, the study of time delay for breakdown is most revealing for the pulsed voltage holdoff capabilities of different materials; see as an example Teflon in Figure Q-19.

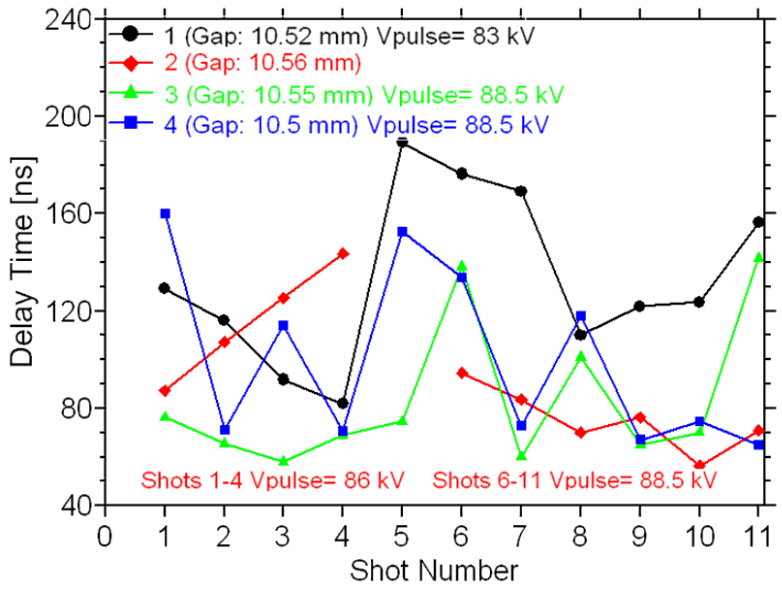

Figure Q-19. Surface flashover delay times across Teflon for four samples.

Since resources were limited, some of the materials had but one sample tested. As such, a direct comparison of the time delays is not straightforward and has to be approached with caution. Nevertheless, the average delay times of the tested materials are depicted in Figure Q-20 sorted by applied field strength. Note that in the ideal case the field strength of all tested samples would be identical. However, due to gap adjustments necessary to fall within the initial breakdown chamber voltage limits, the field strength varies between samples. Nevertheless, Figure Q-20 can be interpreted such that if a material exhibits a longer breakdown delay time at a larger applied field than another material, its holdoff strength can be considered superior.

Despite the limited number of tested samples, Figure Q-20 indicates that Teflon has a longer breakdown delay time even at a higher applied field when compared to the epoxies and the HDP. Teflon also seems to be superior to Rexolite and most likely Lexan. It should be noted that between samples of a specific material, with several samples tested, the average breakdown voltage varied approximately 1-2 kV. The one sample of Plexiglas (material taken directly from the Z switch envelope) exhibited the best performance at 1 atmosphere of SF_6 without any external source of UV illumination. Note that the volume arcs between the backbone electrodes can be considered producing external UV radiation (see the section titled "SF_6 Volume Breakdown"), that impacts the inside surface of the Plexiglas switch envelope.

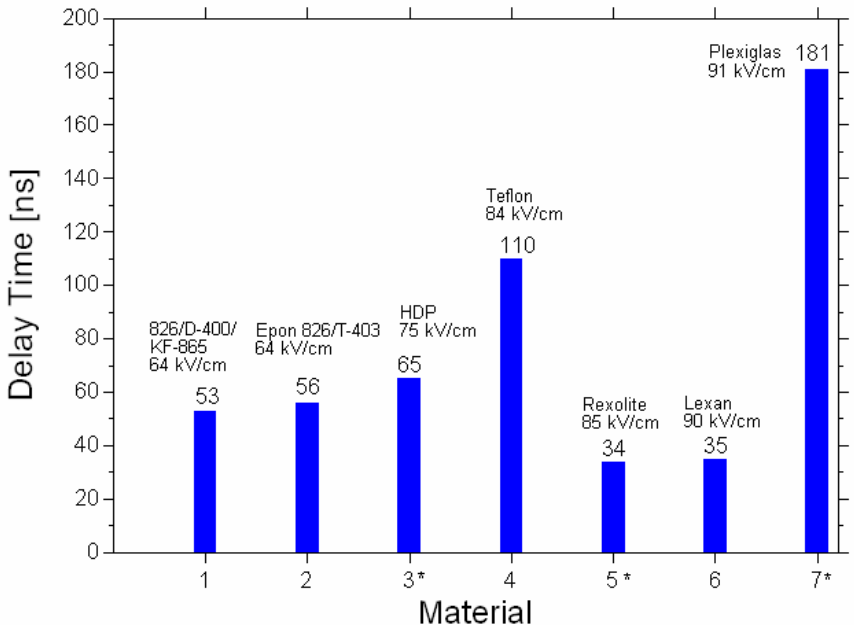

Figure Q-20. Dielectric material comparison of average time delays. Samples arranged by field strength (asterisk indicates one sample only tested).

Post-Flashover Analysis

In order to better understand the effects of flashover on the dielectric material, several dielectric samples underwent a postmortem imaging analysis, which took place at the Texas Tech University Imaging Center. First each dielectric was imaged and photographed using a stereoscopic microscope. This process enables verifying if visible damage could be seen on the surface of the material. The second step was to utilize a scanning electron microscope to view the surface of the material and compare the images to the stereoscope. This proved useful when damage could not be seen or was vague under a stereoscope. The third step was to use X-ray spectroscopy to identify elements on the surface of the dielectric. This has the potential to give some insight into interactions between the arc, gas, and the dielectric.

Optical Microscope Images

The microscope images allowed for a better perception of visible surface damage (see, for instance, Figure Q-22).

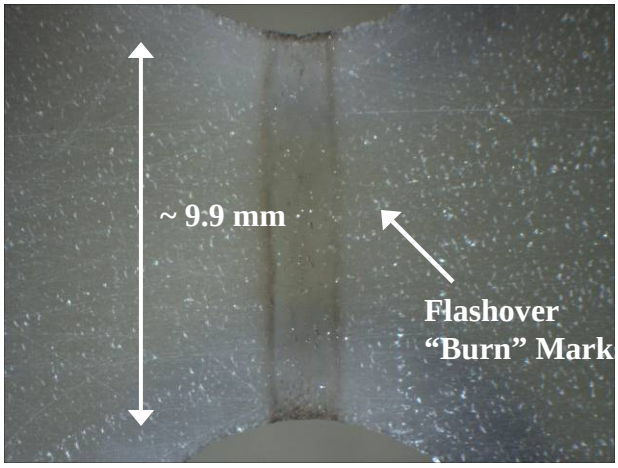

Figure Q-21. Smooth surface dielectric sample 826/D400/KF-865 cured at 80 °C for three days after 38 discharges (1 atm SF_6, 30 µC).

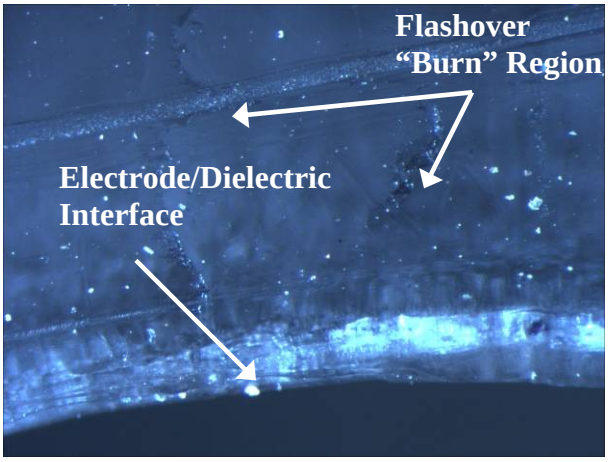

Figure Q-22. Smooth optical grade Lexan after 10 discharges (1 atm SF_6, 30 µC).

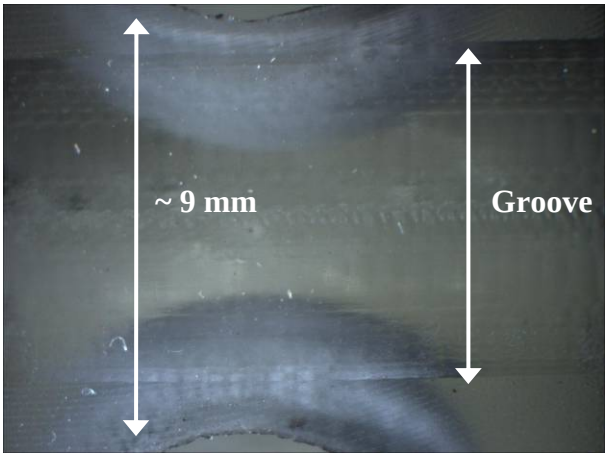

Figure Q-23. Grooved Plexiglas after 10 discharges (1 atm SF_6, 30 µC). No damage visible other than groove machining.

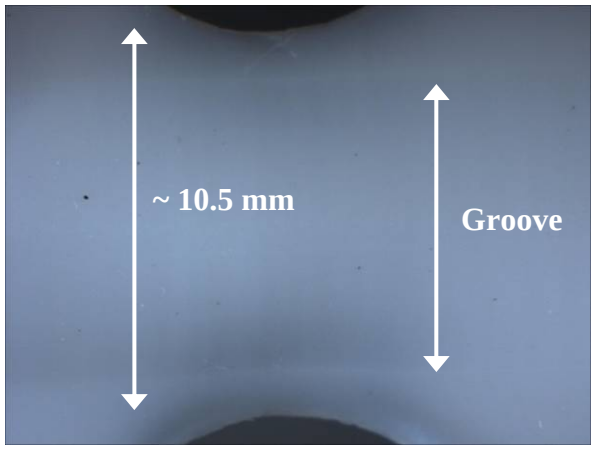

Figure Q-24. Grooved Teflon after 10 discharges (1 atm SF_6, 30 μC). No damage visible other than groove machining.

SEM and X-Ray Spectroscopy Analysis of Dielectric

The scanning electron microscope was utilized to obtain a closer view of the damage caused by the flashover. Although SEM can be used for obtaining topography, morphology, composition, and crystallographic information, the main utilization was on topography and composition. Through topography, images of the surface damage were obtained and compared to those of light microscopes. The following images were taken with a Hitachi S-4300SE/N scanning electron microscope.

It should be noted that the employed SEM imaging does not show what is on the surface, but rather what lies just below the surface. As such, surface damage should not be seen, but in Figure Q-25 it is apparent that damage has occurred. Typically when an area becomes charged, that is, when the SEM negatively charges an area, the image becomes brighter, but in Figure Q-25 the flashover path boundaries are black, which means that the region is not expelling electrons. Speculation could be made that a positive charge is being left behind after surface flashover, or that there is a difference in the material. Further investigation is required on the subject.

Figure Q-27 is that of a dielectric material after flashover in the second chamber. The material is optical grade Lexan, and was flashed 40 times. Flashover occurred five times at each of the following pressures: 10 Torr, 20 Torr, 50 Torr, 100 Torr, 250 Torr, 680 Torr, 20 psig, and 40 psig. It should be noted that in comparison to the Lexan discharged in the first chamber, this sample exhibited some cracking, which is only visible in the flashover region. Also, since changes in the structure of the material will show up in the SEM images as well, it could be speculated that the internal cracking and discoloration of the material is due to a change in the composition of the material.

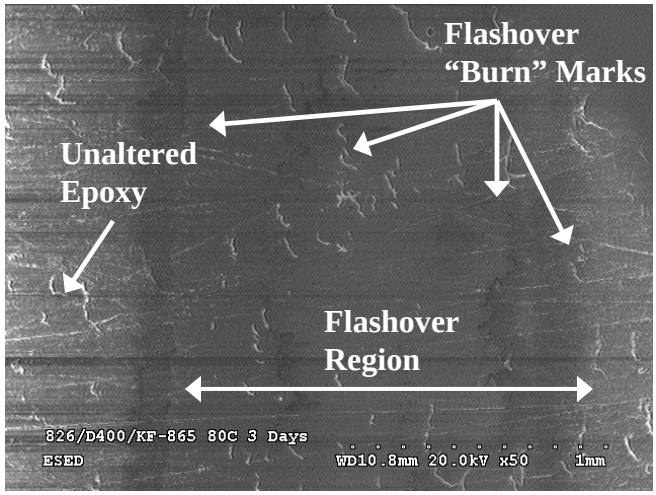

Figure Q-25. SEM image of smooth surface dielectric sample 826/D400/KF-865 cured at 80 °C for three days after 38 discharges (1 atm SF_6, 30 µC). Distinct difference between flashover region unaltered Epoxy surface.

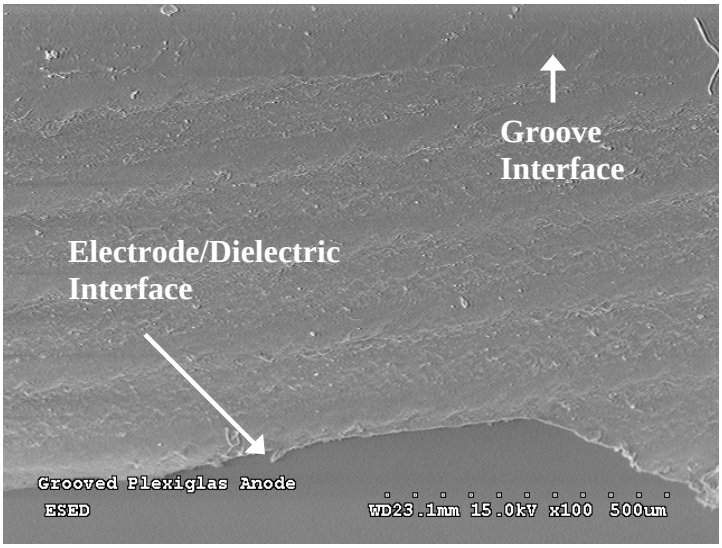

Figure Q-26. SEM image of grooved Plexiglas after 10 discharges (1 atm SF_6, 30 µC). No damage visible other than groove machining.

After obtaining images from the scanning electron microscope, X-ray spectroscopy analysis was then performed on the sample surfaces. Typically, the difficulty of the analysis spawns mainly from finding a suitable representative location or object to perform the analysis. Yet after obtaining SEM images, a random pattern of white flakes could be seen on the surfaces. An example of this can be seen in Figure Q-27. After performing the X-ray spectroscopy on some random white flakes, it was found that the flakes where comprised of sulfur. These arc by-products were found for all dielectric materials[2] tested, although in some of the materials such as Figure Q-28, sulfur spheres were identified rather than flakes.

[2] Virgin Teflon material proved inconclusive due to the inability to locate a suitable location or object to perform the X-ray fluoroscopy.

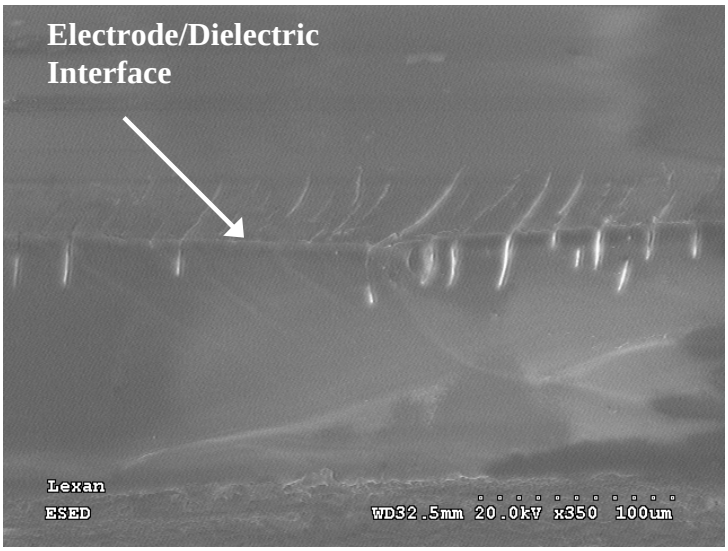

Figure Q-27. SEM image of smooth-surfaced optical grade Lexan. Discharges occurred 40 times at eight various pressures (varied pressure SF_6, 108 µC). Cracks in image are located at the electrode/dielectric interface.

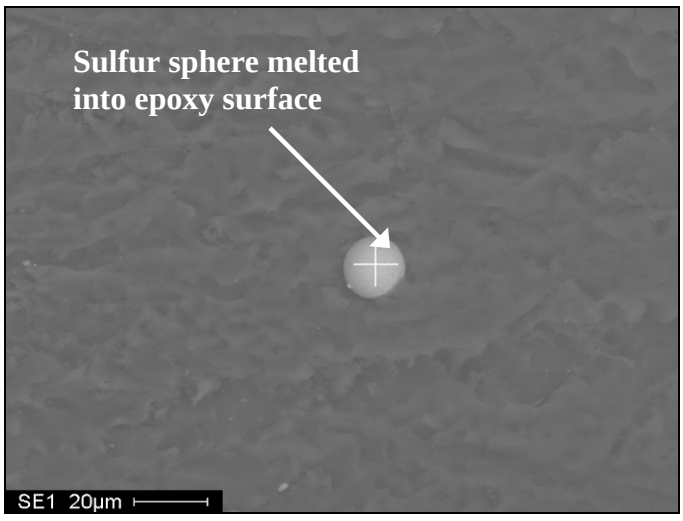

Figure Q-28. SEM image from dielectric material 826/D400/KF-865 used for X-ray spectroscopy analysis (1 atm SF_6, 30 µC).

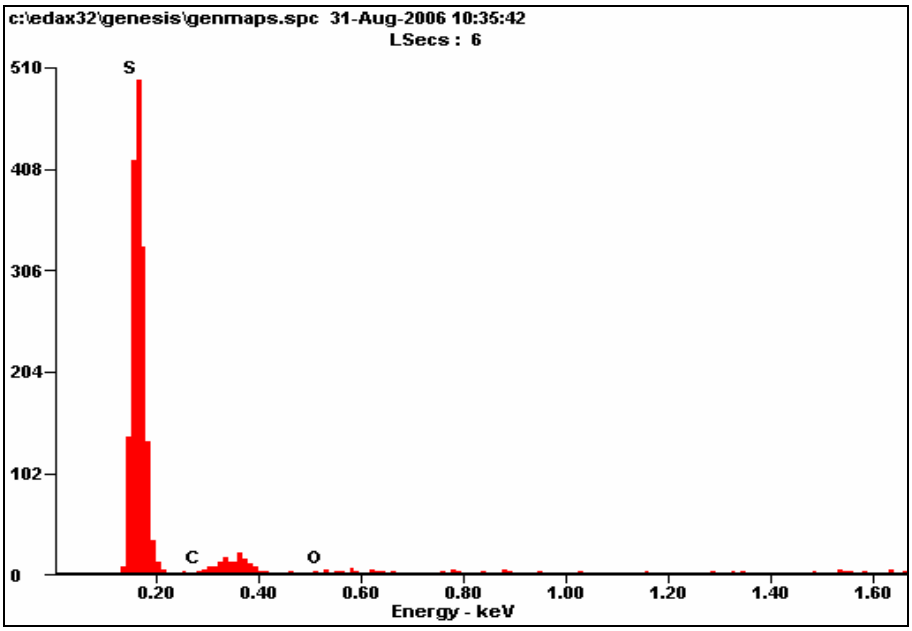

Figure Q-29. X-ray spectroscopy results for crosshair location in Figure Q-28. X-ray spectroscopy indicates sulfur deposit.

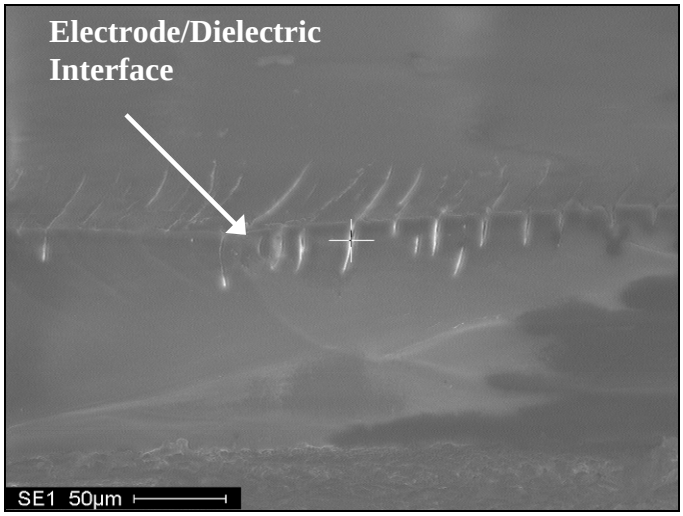

Figure Q-30. Lexan image used for X-ray spectroscopy (varied pressure SF_6, 108 µC). Crosshair denotes point at which elemental composition was performed.

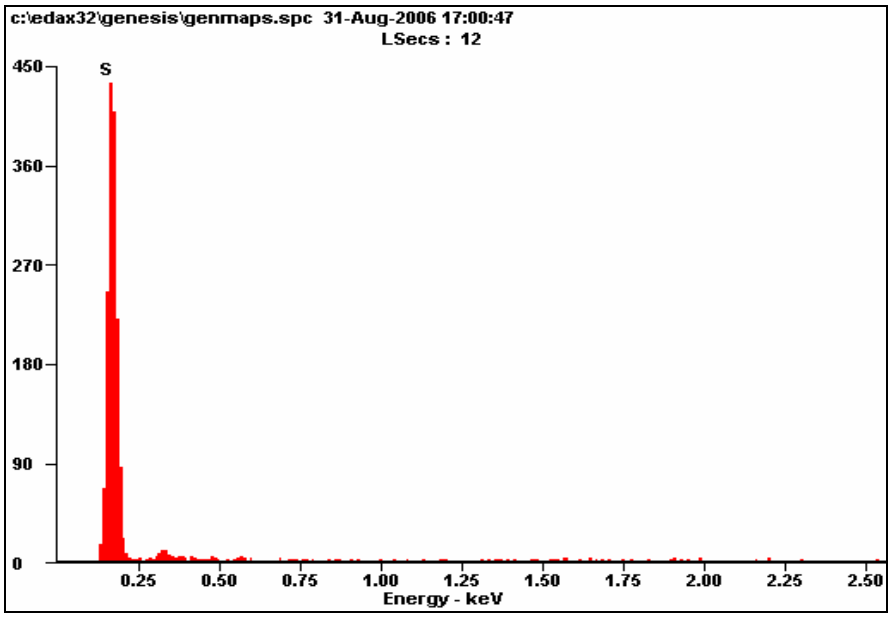

Figure Q-31. X-ray spectroscopy results for crosshair location in Figure Q-30. X-ray spectroscopy indicates sulfur deposit.

SF_6 Surface Flashover, 10 torr to 40 psig

Representative Waveforms

Representative current and voltage waveform for SF_6 breakdowns are depicted in Figure Q-32. The breakdown will occur on the rising edge of the voltage pulse for the lowest pressures. The droop of the voltage signal before breakdown is a result of the capacitive voltage divider and is not real. The peak voltage is maintained until breakdown.

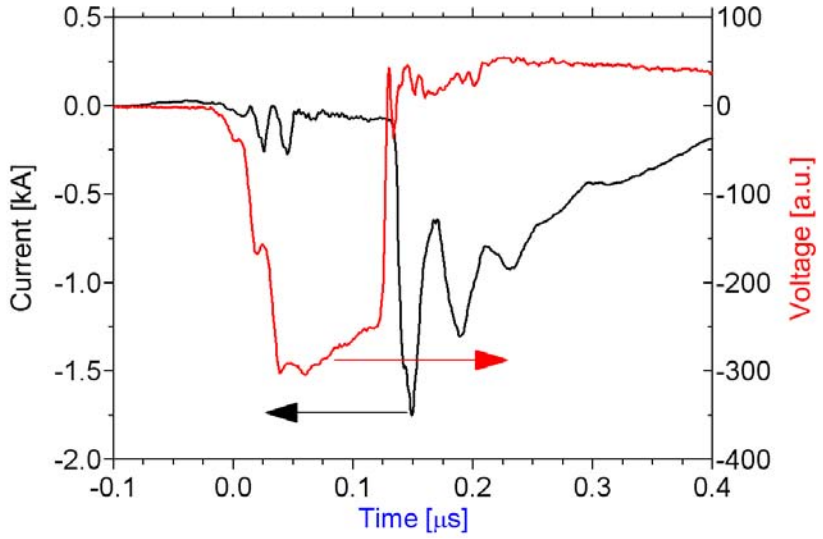

Figure Q-32. Current and voltage waveform of SF_6 breakdown. Peak voltage is about 320 kV. The voltage signal is not corrected for the voltage sensor droop.

Representative Images

While collecting spectra the gap is simultaneously imaged. These images are time-integrated over the entire discharge. During testing the shutter is held open and the aperture is set to the minimum. Flashovers at lower pressures yield dimmer and more diffuse arc channel, which forms near the surface as in Figure Q-33. As the pressure is increased the discharge becomes more intense and begins to move away from the surface, as shown in Figures Q-34 and Q-35.

Figure Q-33. Time-integrated image of surface flashover of a polycarbonate surface in SF_6 at 10 torr. Charged electrode is on the left.

Figure Q-34. Time-integrated image of surface flashover of a Lexan surface in SF_6 at 500 torr.

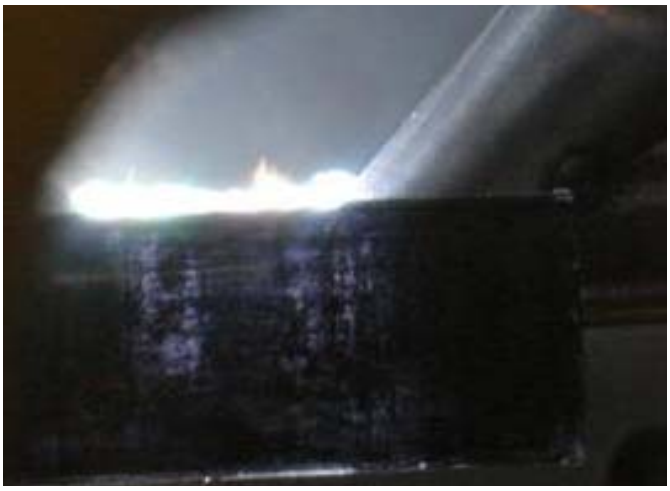

Figure Q-35. Time-integrated image of surface flashover of a polycarbonate surface in SF_6 at 40 pisg. Camera shifted position, resulting in the limited visibility of the changing electrode.

Optical Emission Spectra, Surface Flashover

Using the optical emission collection apparatus described earlier, spectra are collected from three points along the arc channel (see Figure Q-6). The first lens collects optical emissions from just in front of the excitation electrode, the second observes the middle of the gap, and the third observes just in front of the grounded electrode. Figure Q-36 shows several of the peaks that have been identified so far, including sulfur, fluorine, hydrogen, and carbon. The carbon and hydrogen is of particular significance because it indicates the discharge is removing material from the surface and exciting it.

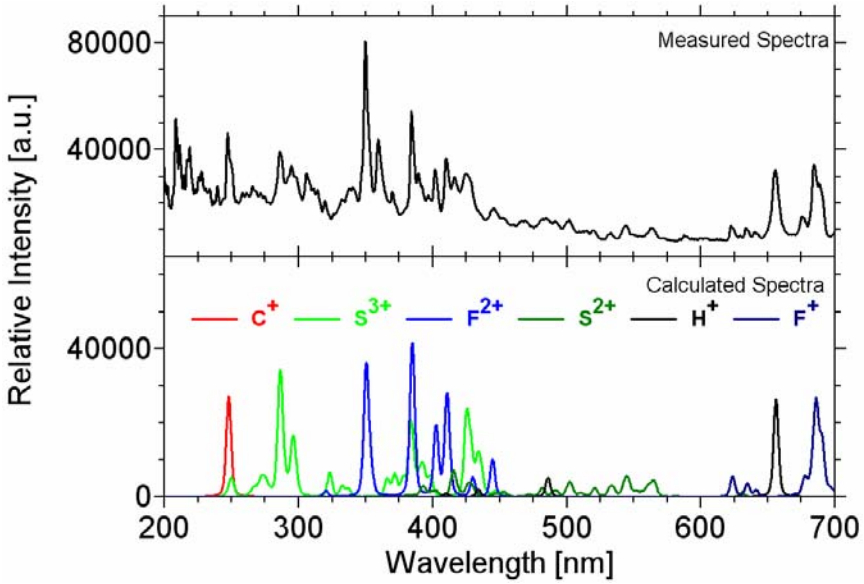

Figure Q-36. Spectra peak identification using calculated atomic spectra. Measured spectra collected in SF_6 environment, across a polycarbonate sample, at 50 torr. The calculated spectra is given for an temperature of 30,000 K.

In order to isolate any peaks that have not yet been identified, and to illustrate the underlying broadband spectra, the identified peaks are added together and subtracted from the original signal. The convolution profiles used in the calculation of the atomic spectra are adjusted to match those of the actual setup. Figure Q-37 shows the result of this subtraction. It can be seen that most of the peaks in the 450 nm to 700 nm range have been identified and removed, leaving an approximation of the broadband spectra, which is most likely due to contributions from excited SF_6 molecules and recombination. At the lower wavelengths it becomes clear that additional peaks exist, and their identification is currently under way.

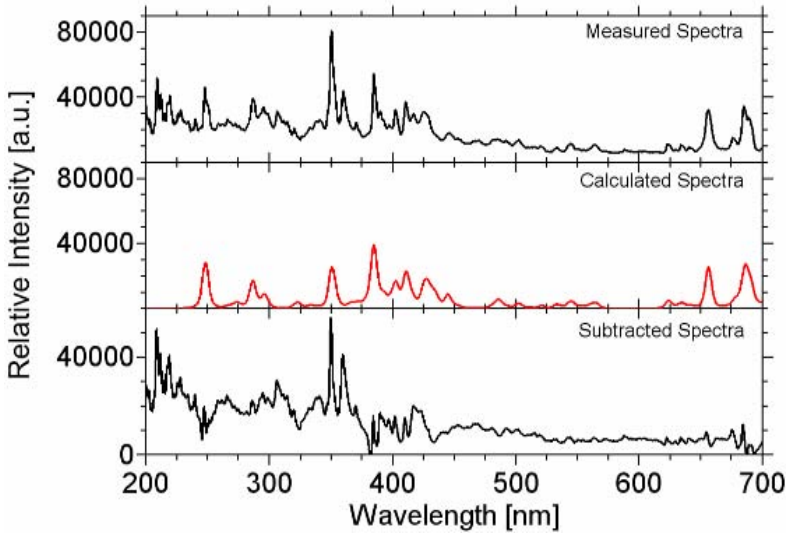

Figure Q-37. Calculation of remaining spectra after identified atomic spectra lines are removed. Measured spectra collected in SF_6 environment, across a polycarbonate sample, at 50 torr. The calculated spectra is given for an temperature of 30,000 K.

Spectra are collected from three points along the discharge path, as in Figure Q38, and in general the spectra are very consistent over the length of the gap. One notable difference is the increased UV content just in front of the charging electrode. Typically, metal lines would be present in the regions near the electrodes; however, in this case the Marx generator is unable to provide sufficient current to erode the stainless steel electrodes. This is further supported by the lack of significant damage to the electrodes after repeated firing. A series of shots were performed while varying the pressure of SF_6 in the chamber. Figures Q-39 through Q-41 show the results of the 10 torr to 40 psig series of tests. Due to the consistency of the spectra along the discharge path, only the center of the gap is shown. All presented spectral data has been scaled by the correction factor to account for internal losses in the collection system discussed previously. In addition to the distinct peaks, there is a broadband contribution to the spectra as well. This broad signature becomes more and more pronounced at higher pressures, where the discharge is more intense and as a minimum pressure broadened. At higher pressures the carbon line is dominant, which could be due to a more constricted arc channel, or the increased gas/ion temperature of the discharge. The more intense discharge is able to effectively remove the carbon from the surface and excite it.

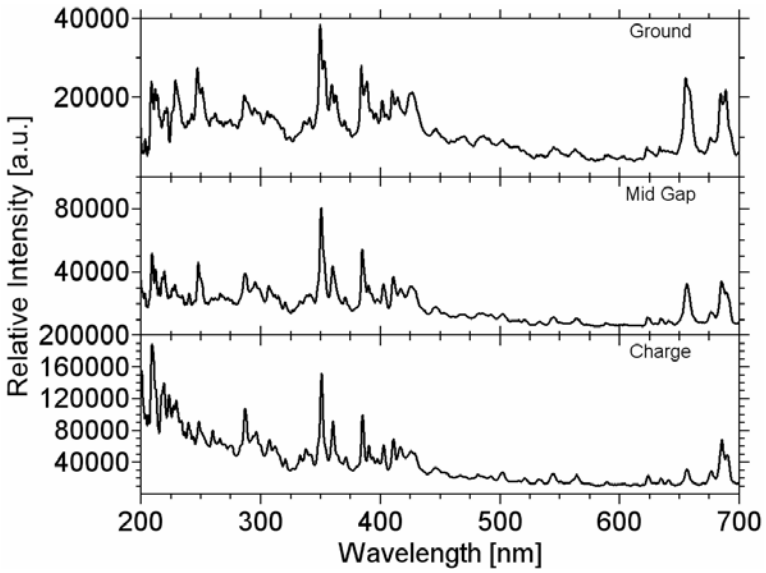

Figure Q-38. Spectra collected from a surface flashover of a polycarbonate surface in an SF_6 environment at 50 torr. Spectra is collected from three points along the discharge path, as denoted.

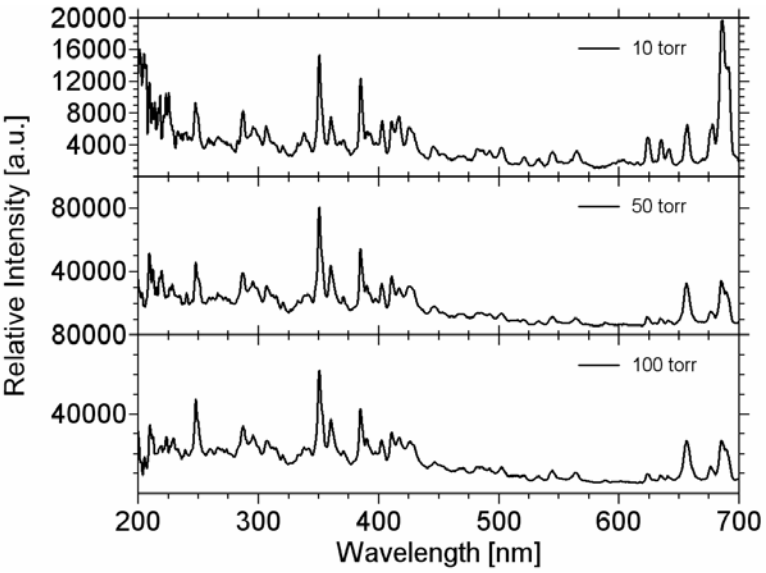

Figure Q-39. Spectra collected from a surface flashover of a polycarbonate surface in an SF_6 environment at various pressures. Spectra is collected from middle of the gap at each noted pressure.

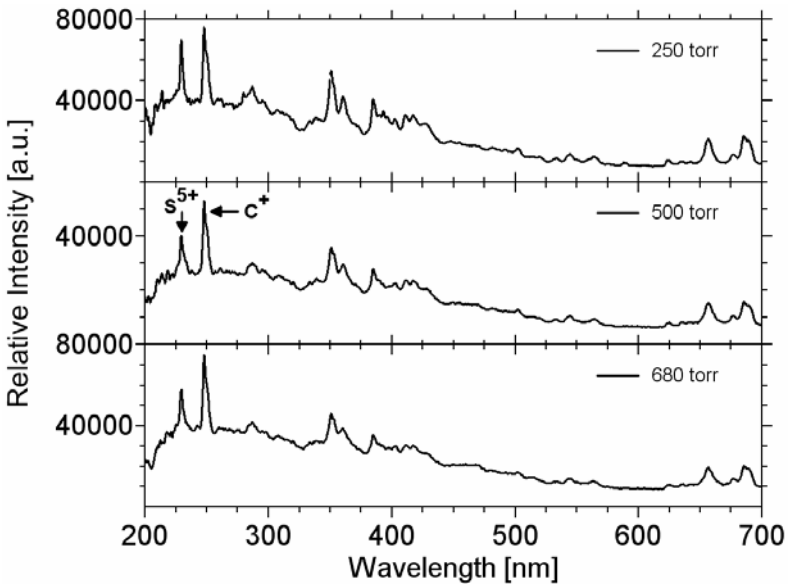

Figure Q-40. Spectra collected from a surface flashover of a polycarbonate surface in an SF_6 environment at various pressures. Spectra is collected from middle of the gap at each noted pressure.

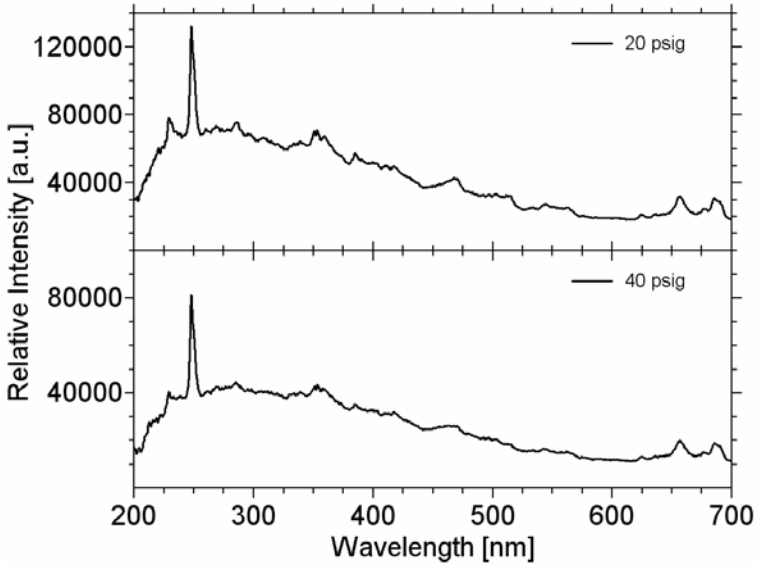

Figure Q-41. Spectra collected from a surface flashover of a polycarbonate surface in an SF_6 environment at various pressures. Spectra is collected from middle of the gap at each noted pressure.

SF_6 Volume Breakdown, 10 torr to 40 psig

Representative Images

Breakdown events occurring without a dielectric surface are also investigated at a range of pressures. For volume breakdown the stainless steel electrodes with similar geometries to those in the Z_{20} switch are utilized with a 3/8-inch gap. As before, the gap is imaged while the spectra are collected. These images are time-integrated over the entire discharge. During testing the shutter is held open and the aperture is set to the minimum. Flashovers at lower pressures yield dimmer and more diffuse arc channel, with multichannel arcs, as in Figure Q-42, occurring roughly a fifth of the time. As the pressure is increased the discharge becomes more intense and lacks obvious multichannel formation, as seen in Figures Q-42 through Q-44. It is possible that multichannel arcs form at higher pressure, greater than 680 torr; however, in future experiments the optical emission must be attenuated in order to detect these events.

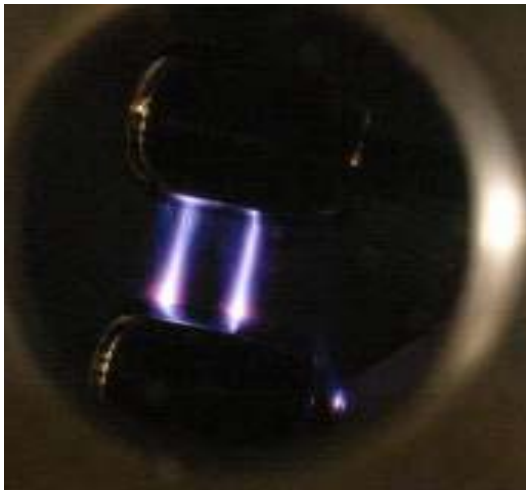

Figure Q-42. Time-integrated image of volume breakdown between two stainless steel electrodes in SF_6 at 10 torr. Charged electrode is on the bottom.

Figure Q-43. Same as Figure Q-42 at 500 torr.

Figure Q-44. Same as Figure Q-42 at 40 psig.

Optical Emission Spectra, Volume Breakdown

In this case the three fibers were all focused between the electrodes, and the spectra collected at different points along the discharge path are almost identical. Given the similarities, only the middle fiber will be shown at each pressure. Spectra line identification, as shown in Figure Q-45, indicates three important differences in optical emissions of surface flashover across polycarbonate and that of volume breakdown. The first is the lack of carbon and hydrogen lines, which tends to support the initial conclusion that they were the result of damage to the surface. The second is the absence of some of the sulfur and fluorine lines, which were initially assumed to be a result of the disassociation of the SF_6 gas in the environment. Their absence in volume breakdown could indicate that they were a result of damage to the polycarbonate surface, which contains both elements. Finally, there is the presence of nitrogen line, which is likely due to small leak in the system at the time, allowing small amounts of air into the chamber. It should be noted that previous research under controlled mixing conditions has revealed that small amounts of nitrogen (few percent) in SF_6 already show up prominently in the emission spectrum of a spark. Looking at the intensity of the lines with respect to background pressure in Figures Q-46 through Q-48 reveals that the N_2 lines fade as the pressure increases, disappearing altogether at 500 torr. Obviously, a small leak has lesser consequences at the higher pressures.

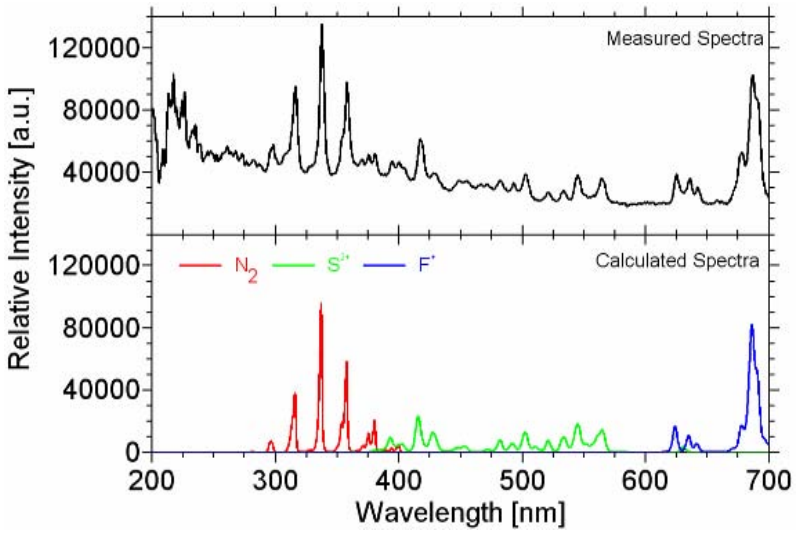

Figure Q-45. Spectra peak identification using calculated atomic and diatomic spectra. Measured spectra collected in SF_6 environment at 100 torr.

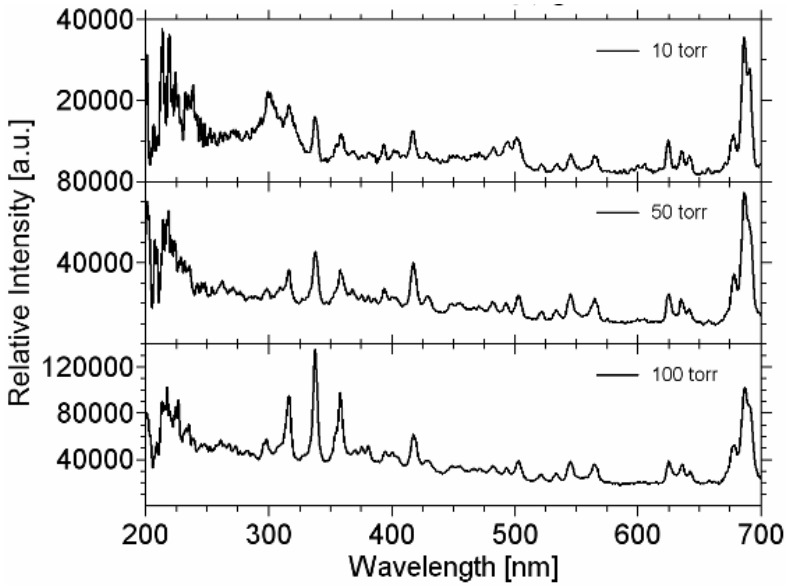

Figure Q-46. Spectra collected from a volume discharge in SF_6 at various pressures. The 100 torr spectrum exhibits more N_2 contamination.

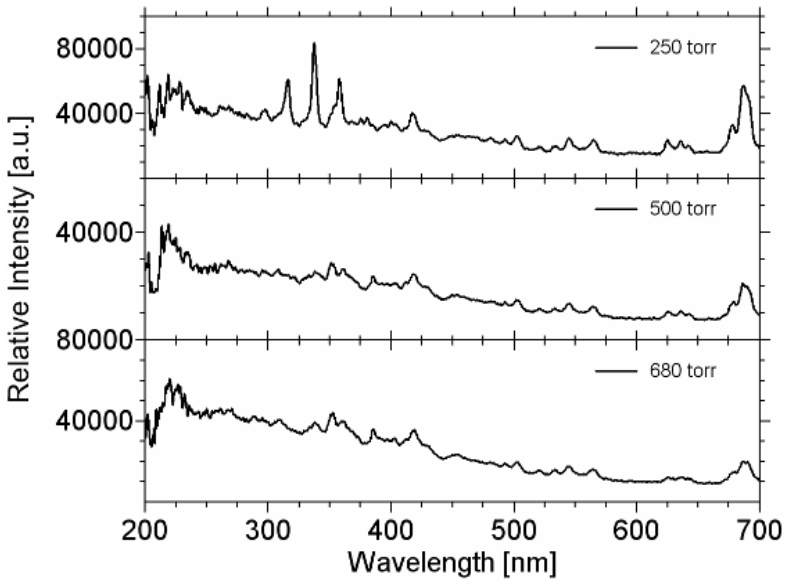

Figure Q-47. Spectra collected from a volume discharge in SF_6 at various pressures.

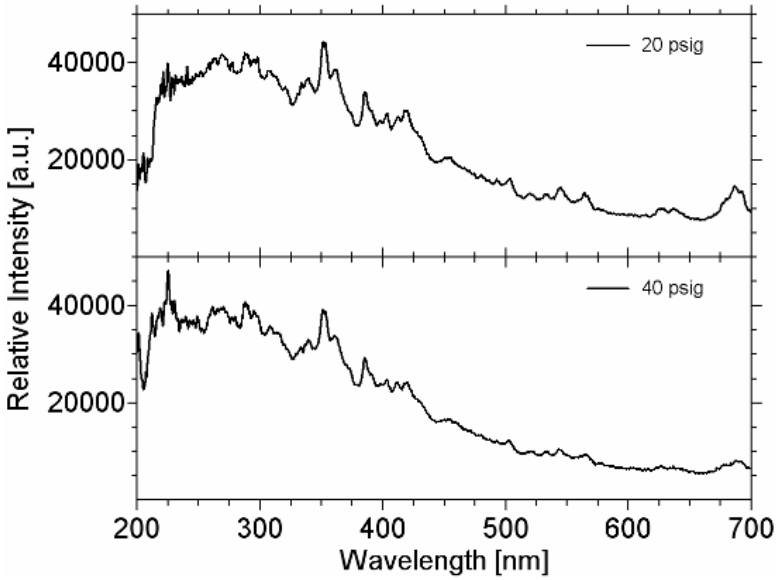

Figure Q-48. Spectra collected from a volume discharge in SF_6 at various pressures.

Conclusions

Photoemission of electrons by UV photons impacting the envelope is one of the suspected reasons that can initiate the unwanted tracking along the inside envelope surface in the ZR switch. We have quantitatively shown that a significant amount of UV light is produced by both a volume arc and surface flashover in high-pressure SF_6. As a matter of fact, the more intense light output is in the wavelength regime below 320 nm; a regime that has been identified in previous research as having a distinct effect on the arc path of flashover in atmospheric nitrogen. The majority of species contributing to the observed optical emission spectra between 200 and 700 nm has been identified. While it was possible to estimate the volume arc's electronic temperature (~35,000 K) for the lower pressures (50 torr), the spectra at 40 psig are problematic due to their more broadband features that mask distinct atomic or molecular lines. The differences between volume and surface flashover become apparent in Figure Q-49.

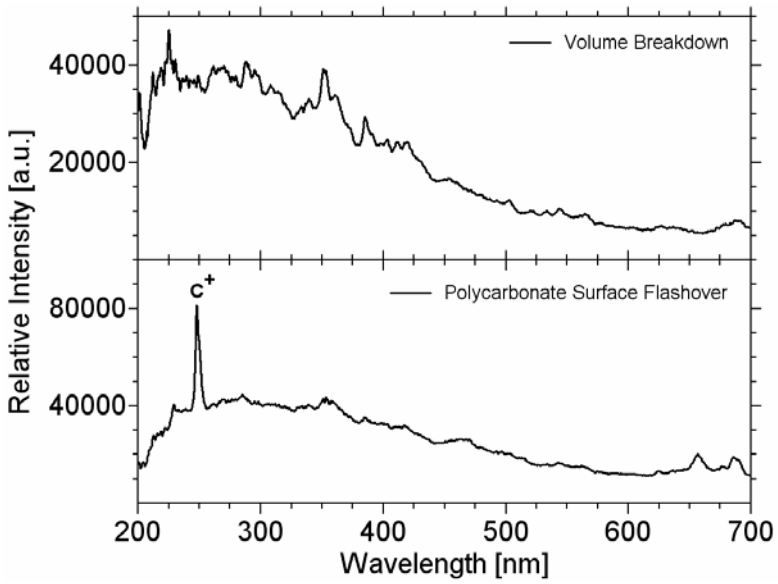

Figure Q-49. Volume breakdown (top) and surface flashover (bottom) at 40 psig SF_6.

Most prominently, the peak at 250 nm in the surface flashover spectrum is due to singly ionized carbon produced by erosion followed by electron impact ionization and excitation of dielectric material (all tested materials were hydrocarbon-based). The absence of metal lines in any of the observed spectra is a result of the rather low coulomb transfer and low current amplitude (~ 2 kA) in the test setup. It should be assumed that the spectral shape will change with the current amplitude increased into the 100 kA regime in future research. Overall, our results support the hypothesis of UV radiation contributing to the initiation of switch failure.

The breakdown delay time of several dielectric materials was recorded and compared for several dielectric materials with the initial setup limited to 1 atmosphere of SF_6. Most of the materials (Lexan, Teflon, HDP, Rexolite, Plexiglass) have dielectric constants between ~ 2 to 3, while the Epoxy-based materials fall out of this range with a permittivity of ~ 5. Of all tested materials,

Teflon and Plexiglass performed the best, i.e., they exhibited the longest flashover delay time at a given pulsed voltage amplitude. One should note, however, that thus far only one Plexiglass sample was tested. Clear differences in erosion became apparent. For instance, Epoxy and Rexolite exhibited very distinct surface damage. Teflon on the other hand exhibited the least surface damage, and postmortem surface analysis (40 psig flashover) did not reveal any sulfur deposits. With the recent completion of the high-pressure SF_6 breakdown chamber, it will now be possible to test the diverse materials more rigorously with improved statistics.

Postmortem analysis of surface flashover samples revealed sulfur deposits on the dielectric surface, essentially a layer of sulfur with some sulfur drops. Depending on the material, the deposits were more or less distinct; virtually no sulfur was found on Teflon. The occurrence of sulfur on the dielectric surface is consistent with the more prevalent appearance of sulfur ionic lines in the flashover spectrum (SII and SIII) as compared to the volume breakdown spectra (SII only).

Future Plans

Besides continuation of the spectral analysis, testing of different dielectric materials, and postmortem surface analysis, the biggest step will be increasing the arc current amplitude from a few kA to 100 kA. While the 40 psig breakdown chamber will be used as is, the external excitation circuit will have to be designed and built. One possible solution is depicted in Figure Q-50, utilizing the already used Marx generator to break down the volume gap, while the magnetic switch is used to push current through the gap after the gap has broken down.

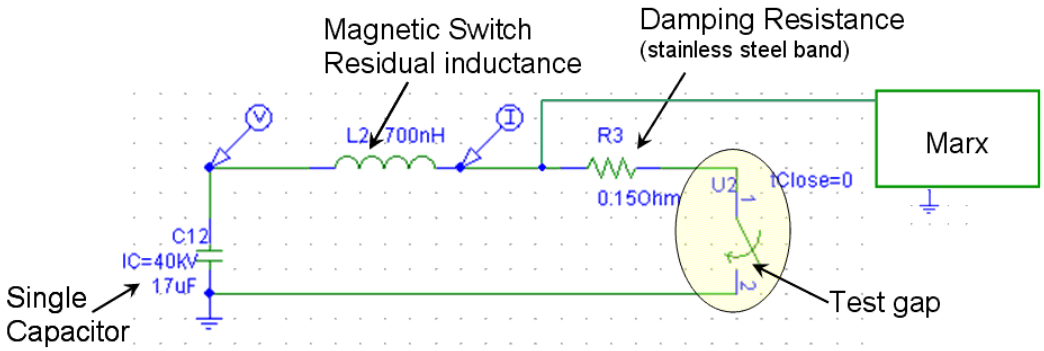

Figure Q-50. Planned high-current arc setup for 40 psig SF_6.

The expected current amplitude is compared to the Z switch current as modeled with Sandia National Laboratories' Screamer code (see Figure Q-51).

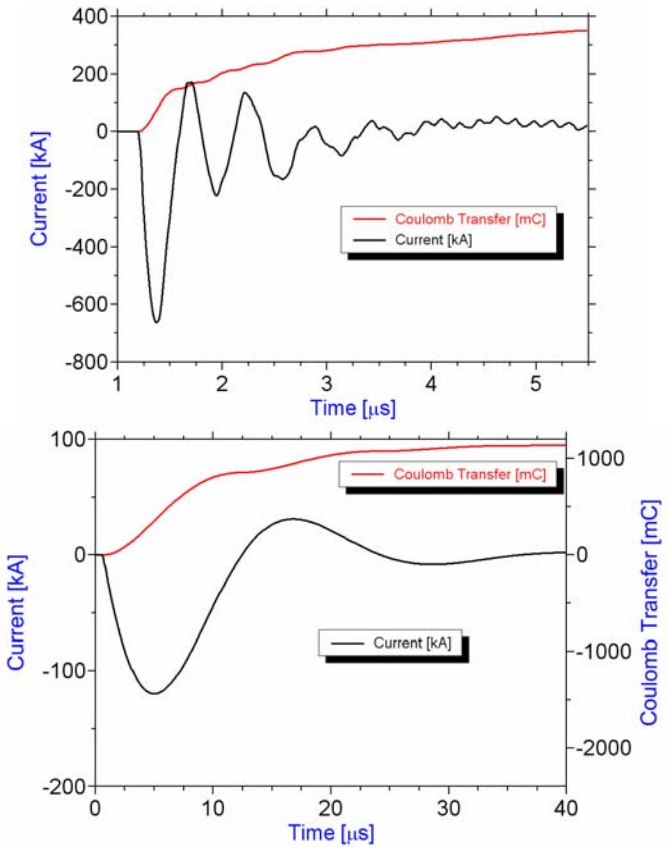

Figure Q-51. (a) Z switch current (Screamer): Current divided into multiple arcs. (b) Planned simulation setup: Single arc

Note the 600 kA current amplitude in the Z switch is divided into several arcs so that the ~ 100 kA current of the test setup becomes comparable to a single arc in the switch. The expected coulomb transfer is roughly three times higher in the planned test setup, thus providing sufficient electrode erosion and generation of arc by-products. As outlined in the section titled "SF_6 Surface Flashover Material Studies," two secondary flashover gaps, simulating the ZR switch envelope, are incorporated into the flashover chamber. It is planned to investigate the response of these secondary gaps to the high-current volume arc. Possible results are decreased flashover holdoff voltage dynamically due to UV illumination from the volume arc or statically due to surface contamination of arc by-products. Note that the distance between volume arc and secondary flashover gaps is identical to the distance between backbone electrodes to envelope in the ZR switch.

APPENDIX Q1. SF_6 Optical Emission Spectroscopy (OES)

Not much quantitative spectroscopic data is available for sparks or arcs in SF_6 at conditions relevant to the present research. As a rare example, Figure Q.1-1 depicts a spectrum taken from a corona discharge in SF_6 at close to atmospheric pressure.

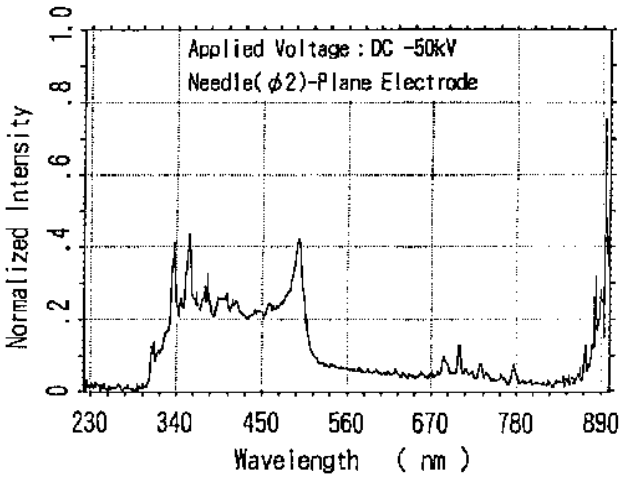

Figure Q.1-1. Emission spectrum of a corona discharge in 0.12 MPa SF_6.[3]

Note that the lines around 340 nm have been identified as emission from molecular nitrogen. Contamination of SF_6 with N_2 is a common problem in spectra found in the literature as 1% or less N_2 will easily show up in an SF_6 discharge. The cross section for electron impact excitation and coefficients for spontaneous emission must be strongly in favor of N_2 vs. SF_6, not at least due to the more narrowband nature of the N_2 emission.

A similar spectrum was measured with the present apparatus in pulsed mode with a current amplitude of a few kA (~ 100 ns pulse), however at a much lower pressure of 10 Torr (see Figure Q.1-2). The step at in the spectrum at ~ 500 nm is a dominant feature in both spectra (Figures Q.1-1 and Q.1-2).

[3] K. Fujii, M. Yamada, A. Tanaka, and K. Kurosawa, Emission Spectrum of Partial Discharge Light in SF_6 Gas, *Record of the 1992 IEEE International Symposium on Electrical Insulation*, Baltimore, MD, USA, June 7-10, 1992.

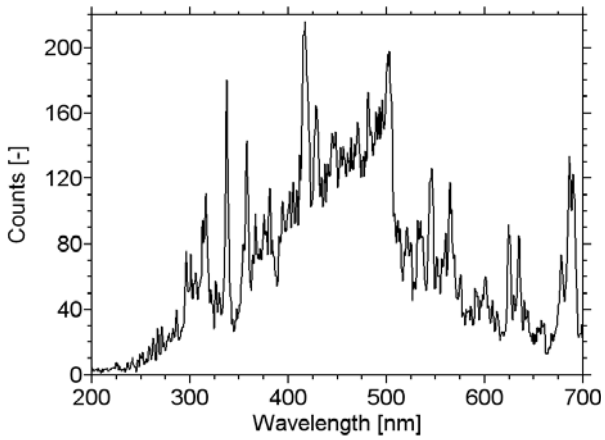

Figure Q.1-2. Volume arc in 10 torr SF_6 and < 0.5 torr N_2.

When interpreting such spectra, the spectral sensitivity of the spectroscopic system needs to be taken into account. In this particular case, the sensitivity is primarily determined by the spectrograph grating, the fiberoptics (UV grade fused silica fiber), and the camera's photocathode quantum efficiency. Two lamps with known spectral output (Xenon high pressure and deuterium lamp) were utilized to generate the inverse apparatus function of the entire system (Figure Q.1-3). Any measured spectrum needs to be corrected with (multiplied by) the inverse apparatus function to yield the true emitted spectrum as it would be measured with a spectroscopic system having an ideal flat response. Note that the short wavelength range below 250 nm is significantly attenuated by the spectroscopic system.

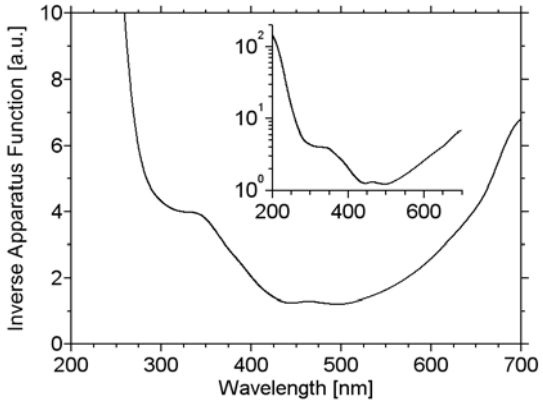

Figure Q.1-3. Apparatus function of OES system.

The corrected spectrum may look quite different from the raw spectrum (see Figures Q.1-2 and Q.1-3). It should be noted that the apparatus function is quite typical for a grating spectrograph with some photocathode-based sensor. Hence, since neither the spectrum in Figure Q.1-2 or Figure Q.1-3 is corrected, the similarity is more than a coincidence. For further spectral analysis, e.g., calculation of intensity and comparison with calculated spectra, the corrected spectrum, i.e., Figure Q.1-4, should be used.

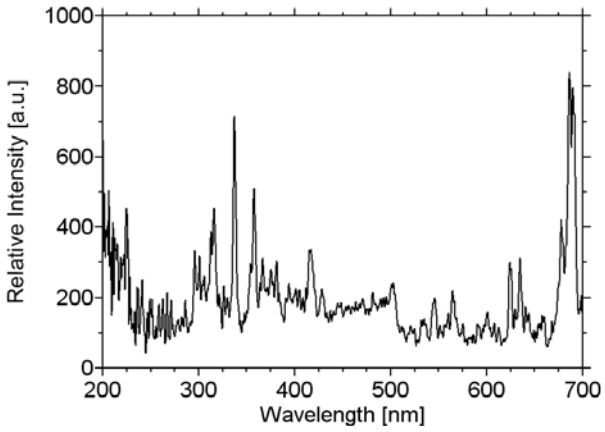

Figure Q.1-4. Corrected spectrum from Figure Q.1-2. The increase in UV intensity below 250 nm is most likely not real and due to the relatively small signal-to-noise ratio of this lower-pressure spectrum (spectral correction amplifies this noise).

APPENDIX R. Experiments at the University of Missouri

Department of Electrical and Computer Engineering
University of Missouri – Columbia

Introduction

High-pressure, SF_6-filled gas switch design requires a balance between reliable triggering, voltage hold-off, current handling, and flashover of dielectric housing materials. At high voltages, dielectric flashover can become a more stringent design consideration, as housing size and cost increases, while the potential for flashover also increases. As a consequence, a study of flashover in several atmospheres of SF_6 and at 1 to 1.5 MV has been undertaken.

Insulator flashover is a very broad and important problem, which has received a great deal of attention for many decades. One well-known discussion of flashover in vacuum occurs in J.C. Martin's review of pulsed power.[1] Flashover in SF_6 has also been extensively studied, as SF_6 insulation of switch gear and other devices in the electric power industry are common.[2,3] However, flashover in certain conditions, such as high pressure, has been largely overlooked due to focus on flashover in other areas. As a result, flashover at high pressure is not fully understood.

To examine dielectric flashover in high voltage, laser triggered and self-break switches, a test-switch has been developed at the University of Missouri Terawatt Test Stand (MUTTS). The experiments conducted at MU focus on the importance of parameters like triple point field enhancement, time at high voltage, or t-effective (teff) and ultraviolet (UV) effects on the insulator.

Experimental Setup

The MUTTS Marx bank is composed of 32 100-kV, 0.7-μF capacitors that are switched with 16 Physics International T508 spark gaps. The Marx bank negatively charges a 7-nF water intermediate store capacitor (I-store). The test switch connects the intermediate store into a resistive load of 2.5 ohms. An impedance mismatch between the Marx bank and intermediate store causes a voltage ring-up at the switch to approximately 1.4 times the Marx bank voltage.[5]

For all switch and insulator tests, voltage was measured with a resistive divider on the switch cathode field shaping conductor. Current through the load was measured with four current viewing resistors near ground that summed to give the total current. The Marx bank voltage and current were also monitored. A photodiode and fiber optic were used to measure light coming from the trigger gap for timing considerations. Open shutter pictures were also taken of the trigger gap as the switch fired.

To enable optical diagnosis of the spark gap switch experiments, fused silica fiber optics have been embedded in a test switch insulator. These optical fibers will be used to measure the time-resolved UV flux on the insulator surface and also to collect spectrally resolved measurements of the optical emission from the switch arc.

For the time-resolved UV flux measurements, silica fibers with a 0.22 numerical aperture and a 200 μm diameter are being used to interrogate the switch. The fiber optic pass band ranges from 100 to 1200 nm. Each fiber collects and transmits light to a SiC photodiode sensitive from 210 to 380 nm. The induced photocurrent is amplified and measured on an oscilloscope. The time-resolved measurement is currently being installed in the MUTTS switch and has not yet been used to collect meaningful data.

The switch arc light emission is collected with a 400-μm-diameter fiber with a 200 to 800 nm pass band for spectroscopy. Time-gated emission spectra are collected with an Acton SpectraPro-300i spectrograph coupled with a Princeton Instruments intensified CCD camera. The spectrograph has a focal length of 300 mm with an aperture ratio f/4 and is sensitive over the 200 to 1000 nm range.

Results obtained on MUTTS are useful for comparison to other ongoing spark gap switch tests at Sandia National Laboratories (SNL) and other universities. The Switch Test Bed (STB) facility at SNL is a higher voltage and current switch test facility compared to MUTTS. The differences between the two labs allow for more testing to be completed while including a wider range of independent variables. MUTTS is designed for quick experimental turnaround and allows the Rimfire switch or subsections of the Rimfire switch to be operated for a large number of shots at a voltage level of 1 to 1.5 MV, while STB usually operates near 3.5 MV. MUTTS has an intermediate store charge time of about 550 ns compared to 800 ns for STB. However, both machines have similar rates of charge. The peak current level of MUTTS is around 150 kA into a 2.5 ohm load, while STB generally operates with a peak current of 250 kA. The very reliable voltage output of MUTTS makes it a good facility for testing effects of high voltage across single gap switches. The lower voltage of the MUTTS facility, compared to STB, enables the incorporation of many diagnostics on or near the test switch.

On the MUTTS facility, a 4 MV Rimfire LTGS has been modified to test only the trigger gap section of the original switch. The cascade section of the switch has been electrically shorted for the purpose of only testing the trigger gap. Most of the cascade electrodes have been removed so that the cascade section fits in a single switch envelope insulator. The trigger gap electrodes are made of stainless steel and have copper-tungsten inserts near the center of the hemispheres, where the arc usually forms. The endplates of the switch are made of aluminum. The trigger section insulator envelope is PMMA acrylic that was machined by SNL to a length of 12.57 cm. The insulator inner diameter is 25.4 cm with a thickness of 1.9 cm. Any additional modifications to the insulator envelopes have been machined by the University of Missouri.

Figure R-1 shows the test switch. The trigger gap has two hemispherical electrodes and is above the shorted Rimfire section. The switch has four field shaping rings surrounding it. The two larger rings are made of aluminum and have a cross-sectional diameter of 3.91 cm. The two smaller field shapers are made of copper and have a cross-sectional diameter of 2.54 cm. The length of the trigger gap is 4.59 cm and the length of the switch from outside of the endplates is 30.77 cm.

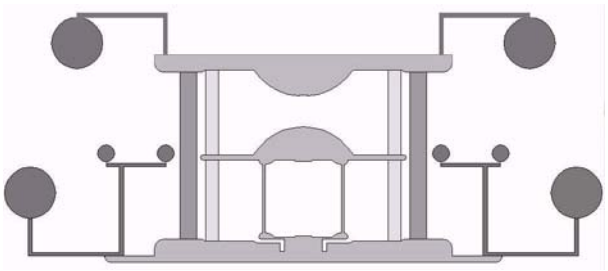

Figure R-1. MUTTS trigger gap switch with electric field shaping conductors.

For comparison purposes, the electric field near the insulator of the MUTTS switch was matched closely with the field of a Z_{20} switch trigger gap. The copper and aluminum rings were added to the switch geometry to shape the electric field across trigger envelope. Electrostatic fields near the MUTTS switch have been simulated with Ansoft Maxwell 2D. Figure R-2 shows the electric field along the insulator of the MUTTS switch with 938 kV across the trigger gap and the electric field of a Z_{20} trigger gap. The electric field on the insulator varies less than 4% between the two switches.

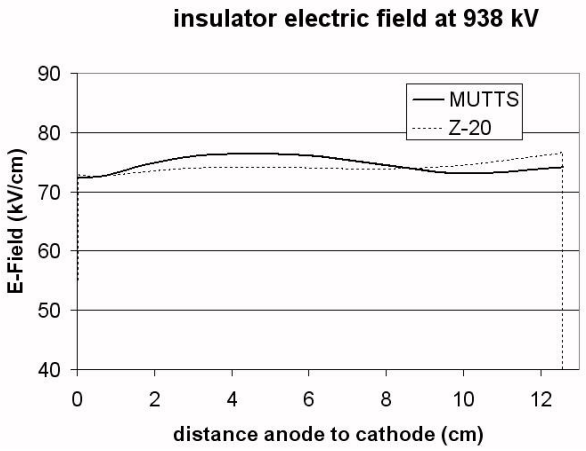

Figure R-2. Magnitude of total electric field for MUTTS and Z_{20} along the trigger gap of the switch insulator with 938 kV applied. The electric fields are basically the same, varying less than 4% between the two insulators.

The switch was configured to operate in both self-break and laser-triggered mode. The grounded anode end of the switch has a 1.27 cm hole to allow a focused laser into the trigger gap. The majority of data gathered for the initial part of this experiment was obtained by operating the switch in self-break mode. The switch trigger laser is a New Wave Research, frequency quadrupled Nd-YAG at 266 nm.

Each switch in the flashover study was cleaned according a standard cleaning procedure before testing. The metal components of the switch were cleaned with a diluted ethanol solution and then wiped with hexanes and a lint-free cloth. The acrylic components of the switch were wiped

with Simple Green when heavily coated with oil and then wiped with hexanes and a lint-free cloth before being installed. The nylon rods holding the endplates of the switch were tightened to 61 N-m unless otherwise stated. The switch was then pressure tested up to 5.1 atm.

Experiment

Self-Break Curve

Testing began by creating a self-break curve of the MUTTS switch under a pressure range of 1.34 to 5.42 atm. The self-break voltage was 600 kV for a 1.34 atm and reached 1.6 MV at 5.42 atm. Flashover did not occur during the self-break shots. Figure R-3 shows the self-break curve generated for the MUTTS trigger gap switch. Figure R-4 shows the spread of the breakdown voltage for each pressure.

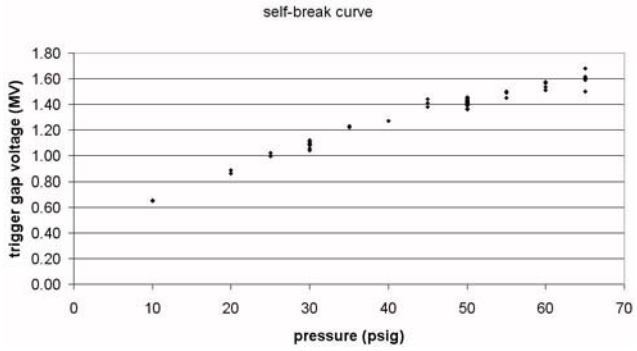

Figure R-3. Self-break curve of MUTTS trigger gap switch.

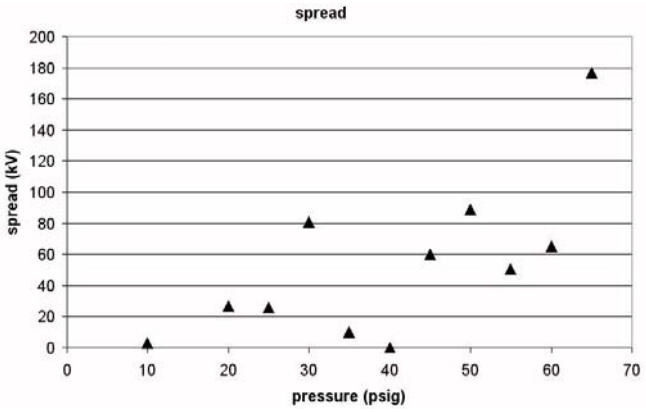

Figure R-4. Breakdown voltage range at each switch pressure.

A typical self-break curve shot at 4.40 atm had a Marx risetime of 400 ns with an insulator stress effective time (teff) time of 190 ns. Teff time was defined as the time the insulator was stressed at or above 63 percent of the breakdown voltage.[1] The mean breakdown voltage at 4.40 atm was 1.4 MV with an average maximum current of 100 kA flowing through the load. The 1.4 MV on the switch resulted in a peak electric field of 114 kV/cm along the inside surface of the insulator and an average electric field of 111 kV/cm.

Asymmetric Torque

The effect of cantilevering shift on the insulator due to the mounting of the switch was tested initially. In order to mimic a cantilevered shift on the insulator with a vertically mounted switch, an asymmetric torque was put on the nylon rods holding the switch together. Figure R-5 shows the torque that was applied to the nylon rods holding the endplates together. This created a measurable difference in the endplate-to-endplate dimension of the switch. Measured at the outer edge of the endplate diameter, length of the switch from endplate to endplate became 25.17 cm on the 0 N-m side and 24.85 cm on the 81 N-m side. The length near the 41 N-m nylon rod was 25.02 cm.

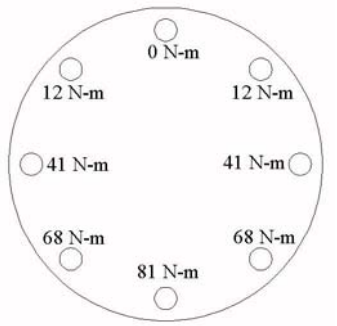

Figure R-5. Torque applied to nylon rods through switch endplate.

The switch was tested over a range of 4.40 to 5.08 atm without flashover. Twenty-six shots were taken on the asymmetrically torqued switch. The average breakdown voltage at 4.40 atm was 1.33 MV with an average teff of 180 ns. Figure R-6 shows the voltage of a typical asymmetrically torqued shot.

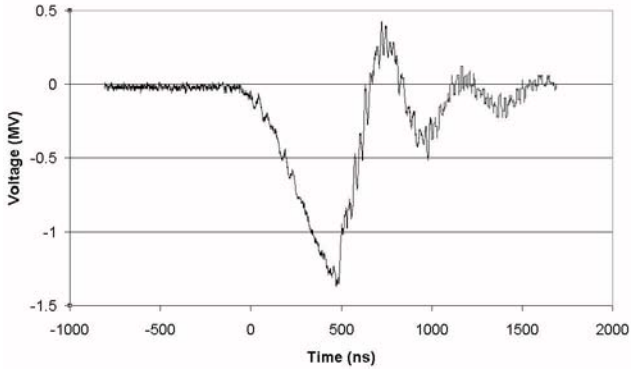

Figure R-6. Switch voltage for a 4.40 atm shot on an asymmetrically torqued switch.

Grooved Insulator

The possibility of flashover caused by small gaps between endplate and insulator was also tested. Field enhancement caused by these gaps is considered to be a possible cause of insulator flashover. Gaps were machined into the insulator in two separate tests. The first insulator tested included a 1.6 mm by 1.6 mm square gap machined into the cathode side of the insulator for 1/8th of the circumference of the envelope.

The switch was tested from 4.40 to 5.08 atm over 17 shots and did not result in flashover along the insulator. The mean breakdown voltage at 4.40 atm was 1.31 MV. This resulted in a peak electric field of 121 kV/cm near the insulator groove. Figure R-7 shows the electric field along the inside surface of the insulator from anode to cathode. Plots of both a 938 kV and 1.31 MV trigger gap voltage are shown.

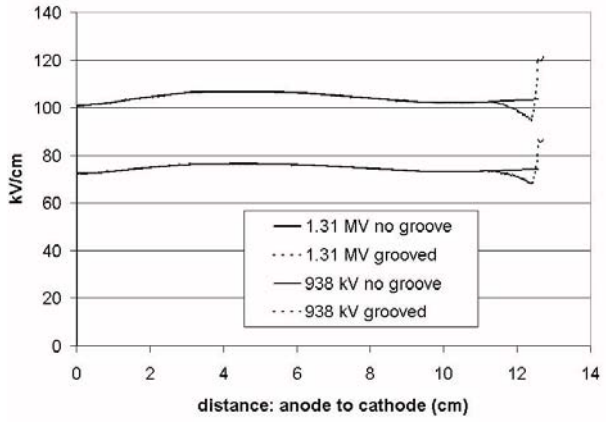

Figure R-7. Electric field along the insulator inside surface from anode to cathode. The grooved surface causes a significant increase in field magnitude near the cathode triple point.

Another tested insulator had a series of gaps increasing in depth around the circumference of the switch. The gap was machined 1.6 mm into the radius of the insulator and increased from zero to 3.6 mm away from the cathode in eight steps of 0.5 mm. This test showed the effect of both very small and very large gaps near the insulator-cathode junction. Figure R-8 is a drawing of a section of the multi-grooved insulator. The section shown is of the largest and smallest grooves separated by a section with no groove.

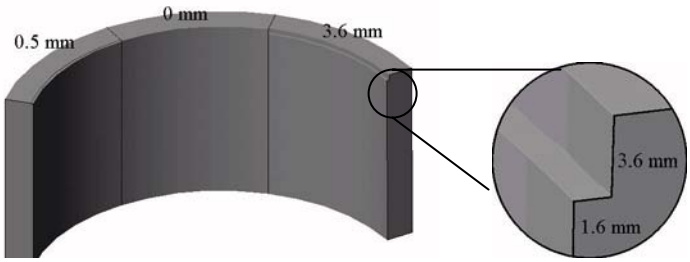

Figure R-8. Section of multi-grooved insulator.

During testing on the multi-grooved insulator, the pressure of the switch was increased from 4.40 to 5.08 atm. For 4.40 atm the mean breakdown voltage was 1.3 MV. The multi-grooved insulator did not result in flashover. A multi-grooved insulator near the anode was also tested and no flashover was observed.

Field simulations showed that the maximum electric field due to enhancement by machined grooves was found for the 3.6 mm and 1.5 mm insulator. The field strength on these insulators reached 134 kV/cm near the cathode. The 0.5 mm insulator also showed a significant field enhancement directly at the triple point. The field at the triple point of the 0.5 mm groove reached 130 kV/cm. On the 1 mm insulator, a minimum field enhancement was seen. Simulations with groove size smaller than 0.5 mm showed that the electric field enhancement in the cathode region decreased. Figure R-9 shows the electric field near the grooved region for insulators with zero, 0.5, 1, and 1.5 mm grooves.

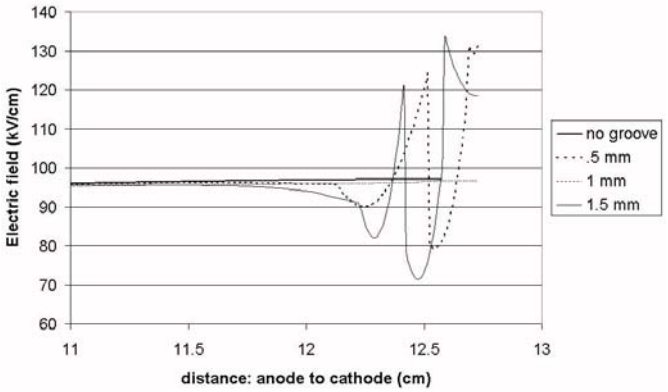

Figure R-9. Electric field near cathode region for zero, 0.5, 1, and 1.5 mm grooves. A minimum field enhancement results from a 1 mm groove.

Removed Trigger Hemispheres

In an effort to force the insulator to flash, the trigger hemispheres were removed from the endplate and trigger plate of the switch in order to increase the trigger gap to insulator length ratio. The bronze laser tube was left in place extending 2.54 cm from the anode into the trigger gap. The electric field profile along the insulator surface remained relatively flat. The first shot with this configuration caused an arc to jump from the bronze tube to the cathode plate. A second, less intense arc formed near the insulator, flashing the insulator for the first time. This occurred with a peak voltage of 1 MV. The switch was immediately removed after one shot for inspection. Figures R-10 and R-11 are pictures of the trigger gap during breakdown. Figure R-10 shows the switch during operation without the trigger hemispheres with the more intense arc and the less intense flashover. Figure R-11 shows the switch under normal operating conditions. The trigger hemisphere electrodes were replaced in the switch after this test.

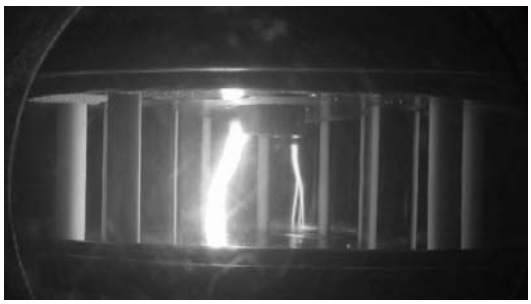

Figure R-10. Shot 212 with trigger hemispheres removed. The flashover event is less intense than the arc near the switch center.

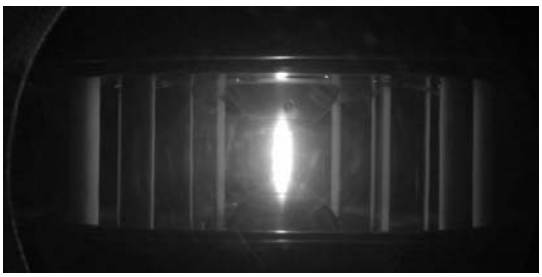

Figure R-11. A typical shot.

Increased Teff

In order to change the teff on the insulator, an inductance was added between the Marx bank and the I-store. The dV/dt on the switch was decreased from 2920 kV/microsecond to 2710 kV/microsecond. Thirty-five shots were taken with a decreased rate of voltage rise and shots with similar rise times were compared. Figure R-12 shows two shots with similar rise times and a different dV/dt.

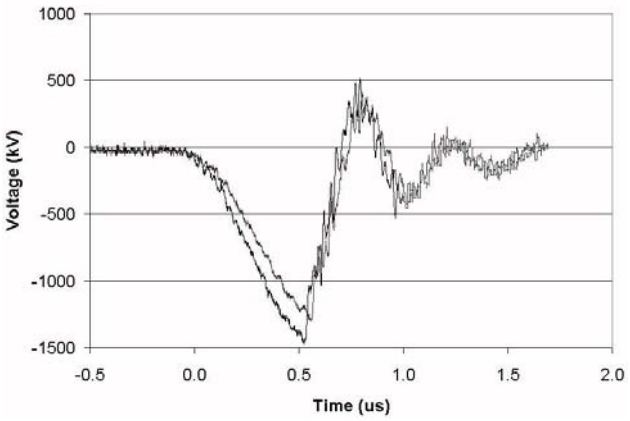

Figure R-12. Switch voltages before and after changing teff.

The increased charge time induced a lower breakdown voltage in the switch at the same pressure. The mean breakdown voltage for the teff shots at 4.40 atm fell to 1.26 MV. Increasing teff did not result in insulator flashover. Figure R-13 shows the effect of a decreased dV/dt on switch breakdown voltage at 4.40 atm. The multi-grooved insulator was shot an additional 20 times with the inductance added to decrease di/dt; no flashover was observed.

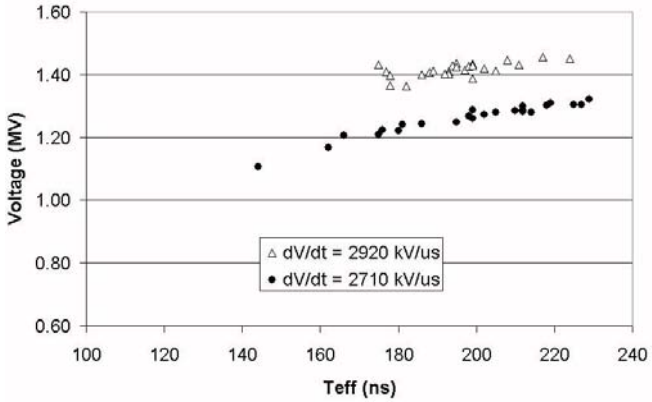

Figure R-13. Decreased dV/dt effect on breakdown voltage at 4.40 atm.

Isolated Trigger Hemispheres

In an attempt to increase the UV levels near the insulator triple point, in order to induce flashover, the cathode trigger hemisphere was separated from trigger plate with several layers of Kapton tape. The separation resulted in an arc forming between the hemisphere and trigger plate. This created a UV source shining more directly on the triple point, as shown in Figure R-14. Twelve shots were taken with the cathode hemisphere isolated and no flashover was observed. After this final test to try to induce flashover by reasonable switch modification, the experiment focus shifted to examining conditions created by the arc in the switch.

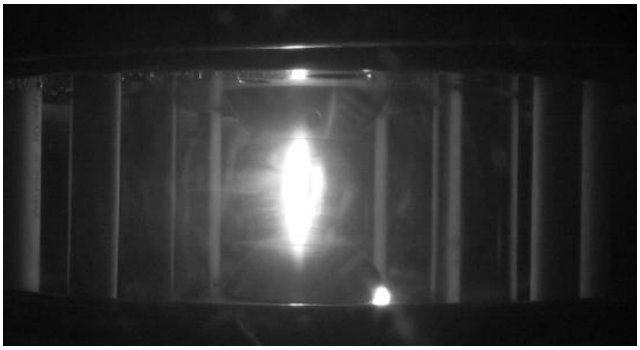

Figure R-14. With the trigger plate hemisphere slightly removed from the cathode, a spark forms between the hemisphere and cathode, shining directly on the triple point.

Transmissivity of PMMA

The percentage of UV light transmitted, reflected, and absorbed were measured for samples prepared with various cleaning procedures on a UV-visible spectrophotometer. Nine samples of PMMA were tested. These samples were split into three sets of three. The first set was wiped clean with a lint-free cloth. The second set was cleaned with hexane using a lint-free cloth. The third set was cleaned with Windex using a lint-free cloth.

Three sets of data were taken per set of samples. A spectrum ranging from 190 to 1000 nm was taken on the first sample set (three pieces) with all three cleaning procedures. The last two sample sets (six pieces) were scanned at very low speed from 370 to 410 nm to focus on the transmissivity cutoff. Percent transmitted (%T), percent reflected (%R), and absorption were all measured.

PMMA exhibits a distinct cutoff region between 380 nm and 400 nm. Over this range the %T and %R of light drop nearly 80% while absorption increases dramatically. The PMMA cleaned with hexane exhibits slightly lower %T nearing cutoff. Figure R-15 shows the transmissivity near cutoff.

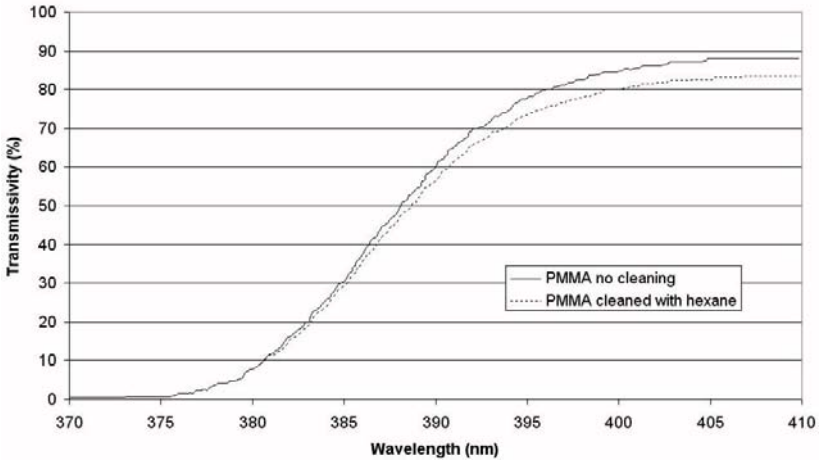

Figure R-15. Percent transmitted vs. wavelength through the sample of PMMA.

No sizable difference between %T, %R, and absorption was found for the three cleaning procedures, although hexane appears to absorb slightly more near the cutoff region.

Fiber Optic Probe

Fiber optics were embedded into a PMMA insulator to collect light from the arc at various points on the insulator. Six holes were drilled through the insulator with bore slightly larger than the fiber optic diameter. Five holes were spaced equally along the length of the insulator, with the top fiber 0.64 cm from the anode and the bottom fiber 0.64 cm from the cathode. The vertical distance between these fibers was 2.8 cm. The fibers holes were drilled 22.5 degrees apart moving along the insulator circumference, spanning 90 degrees total of the switch circumference. The fibers were set with epoxy, penetrating the insulator inner surface by 0.5 mm. These five fibers will collect UV light incident on the insulator surface for time-resolved measurements of the relative UV flux on the insulator. Figure R-16 shows the placement of the fibers on the switch insulator.

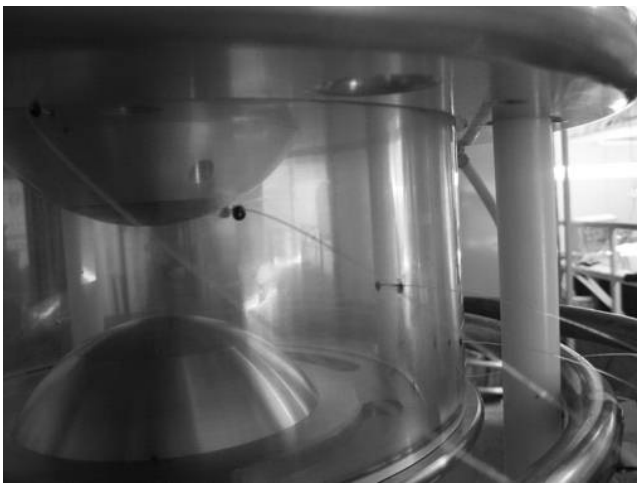

Figure R-16. Fiber optic cables placed into the switch insulator.

A sixth fiber penetrates the switch, looking at the center of the switch arc. This fiber collects light for optical emission spectroscopy. Several initial spectra have been collected at various wavelength resolutions. Figure R-17 is a composite spectrum spanning the UV to near infrared, taken with a 1200 groove/mm grating blazed at 300 nm. Component spectra were collected over several self-break switch shots, with similar electrical parameters, ICCD timing, and gate width. Each component spectrum covered about 30 nm of the spectrum. Timing of the camera gate relative to the switch voltage is shown in Figure R-18. No relative spectral corrections have been applied to this data, so the inference of relative intensity in any spectral range is difficult or impossible at this stage. However, it is clear that ample continuum radiation is produced in the UV portion of the spectrum. The absence of individual spectral lines is also notable. Spectroscopy experiments are ongoing, and calibrated spectral irradiance lamps have been acquired to enable calibration of relative intensity across the spectrum.

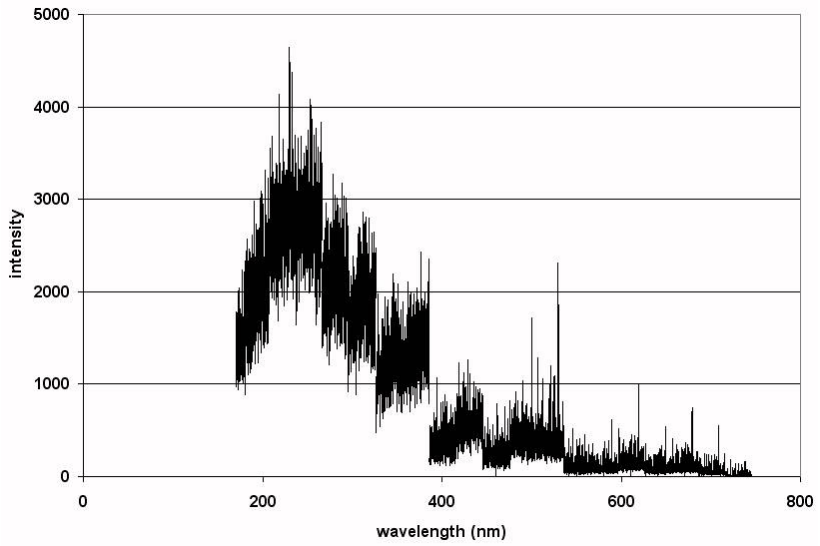

Figure R-17. Composite spectrum of the switch arc emission.

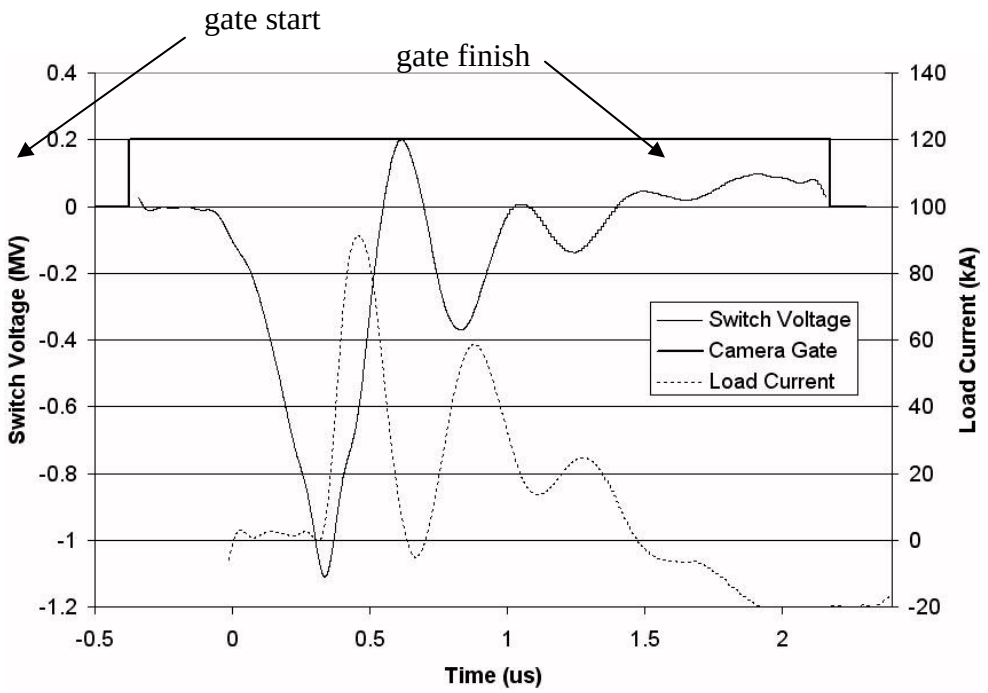

Figure R-18. Camera gate timing shown with voltage and current of the switch.

During shots taken for spectroscopic measurements, the switch was pressurized at 3.0 atm. The average breakdown voltage for these shots was 1.1 MV. This resulted in an average peak current of 91 kA through the load.

Conclusions

Over 350 shots have now been taken on the trigger gap switch and flashover has occurred on the trigger gap insulator only once, when the switch hemispheres were removed. The tests that were performed on the trigger gap switch have not pointed to an exact cause for flashover of the trigger envelope. One of the more interesting observations of this study was that significant triple point field enhancement did not lead to any flashover events in this configuration. A cantilever effect due to a horizontal switch mount was also not shown to lead to flashover.

The null flashover results in these experiments do not point to a specific cause or problem area for dielectric flashover in high-voltage switches. They do, however, span a significant range of experimental design space, pointing out regions of operation where flashover is less likely to occur. The experiments also provide some perspective on the relative importance of parameters like triple point field enhancement and teff. We believe that these experiments will provide some guidance in designing future experiments that directly test the causes and mitigating factors of switch flashover.

The new diagnostics discussed in this report are intended to quantify the arc optical and UV emissions from the Rimfire trigger section switch. These diagnostics are being optimized on MUTTS and will provide a unique tool and test facility. Both time-resolved and spectrally resolved analyses will be possible on the switch in the near future. Insulator surface charge may also be an important factor in causing flashover. New measurement techniques may provide insight on the levels of charge on the insulator surface while the switch is operating.

References

1. J.C. Martin, *JC Martin on Pulsed Power,* Vol. 3 of the Advances in Pulses Power Technology Series, Plenum, New York, 1991.

2. T. Yamagiwa, Particle Initiated Breakdown Characteristics on a Ribbed Surface for SF_6 Gas Insulated Switchgear, *IEEE Transactions on Power Delivery*, Vol. 3, No. 3, July 1988.

3. J.D. Morgan and M. Abdellah, Impulse Breakdown of Covered Cylinders in SF_6 and SF_6 Gas Mixtures, *IEEE Transactions on Electrical Insulation*, Vol. 23, No. 3, June 1988.

4. J.S. Rajan, Investigation on Correlation Between Surface Flashover and Surface Roughness of Insulating Spacers, *IEEE Conference on Electrical Insulation and Dielectric Phenomena*, Vol. 2, pp. 472-5, 1998.

5. K.R. LeChien, J.M. Gahl, M.A. Kemp, R.D. Curry, J.M. Elizondo, and K.W. Struve, Development of a terawatt test stand at the University of Missouri for fast, multichannel switching analysis, *14th IEEE International Pulsed Power Conference*, Vol. 2, pp. 1051-3, 2003.

6. E.M. Veldhuizen, Streamer Branching in a Short Gap: The Influence of the Power Supply, *IEEE Transactions on Plasma Science*, Vol. 30, No. 1, 2002.

7. M. Arrayas, Spontaneous Branching of Anode-Directed Streamers between Planar Electrodes, *Phys. Rev. Lett*., 88, 2002.

8. Sandia National Laboratories, personal communication, unpublished data.

9. M.A. Noras, Charge Detection Methods for Dielectrics, *Trek Appl. Notes*, No. 3005.

DISTRIBUTION

1 Chris Deeney
Director, Office of Defense Science
NA-11, Forrestal Building
U.S. Department of Energy
1000 Independence Ave. SW
Washington, DC 20585

1 Ralph Schneider
Office of Defense Science
NA-11, Forrestal Building
U.S. Department of Energy
1000 Independence Ave. SW
Washington, DC 20585

4 Professor Scott Kovaleski
Electrical and Computer Engineering
University of Missouri-Columbia
349 Engineering Building West
Columbia, MO 65211

4 Scott J. MacGregor
University of Strathclyde
Institute for Energy and Environment
Department of Electronic and Electrical Engineering
204 George Street
Royal College Building
Glasgow, Scotland G1 1XW
UNITED KINGDOM

4 Professor Andreas Neuber
Center for Pulsed Power & Power Electronics
Department of Electrical & Computer Engineering
Texas Tech University
Box 43102
Lubbock, TX 79409-3102

2 MS 9018 Central Technical Files, 8944

1 MS 0104 Thomas Bickel, 1200
1 MS 0511 Carol Adkins, 1210
1 MS 0511 Wendy Cieslak, 1010
1 MS 0511 John Maenchen, 1212
1 MS 0513 Rick Stulen, 1000
6 MS 1152 Jane Lehr, 1654

1	MS 1152	Larry Warne, 1652
1	MS 1152	Roy Jorgenson, 1652
1	MS 1178	Doug Bloomquist, 1630
1	MS 1178	Ed Weinbrecht, 1635
1	MS 1178	Woody Weed, 1635
1	MS 1178	Finis Long, 1637
1	MS 1178	Randy McKee, 1639
1	MS 1178	Pete Wakeland, 1639
1	MS 1181	Larry Schneider, 1650
1	MS 1181	Tom Mehlhorn, 1640
1	MS 1190	Keith Matzen, 1600
1	MS 1191	John Porter, 1670
2	MS 1193	John Corley, 1671
1	MS 1193	David L. Johnson, 1645
1	MS 1193	Keith LeChien, 1671
3	MS 1193	David Rose, 1645
1	MS 1193	Ken Prestwich, 1645
1	MS 1193	Joe Woodworth, 1671
1	MS 1194	Dave Bliss, 1671
1	MS 1194	Mark Savage, 1671
1	MS 1194	Ken Struve, 1671
2	MS 0899	Technical Library, 4536